INNOVATIVE IMAGING TECHNIQUES IN PRECLINICAL MODELS OF NEURODEGENERATIVE DISEASES

EDITED BY: Rodolfo Gabriel Gatto and Yu-Chien Wu
PUBLISHED IN: Frontiers in Neuroscience

frontiers Research Topics

ISSN 1664-8714
ISBN 978-2-88974-316-2
DOI 10.3389/978-2-88974-316-2

About Frontiers

Frontiers is more than just an open-access publisher of scholarly articles: it is a pioneering approach to the world of academia, radically improving the way scholarly research is managed. The grand vision of Frontiers is a world where all people have an equal opportunity to seek, share and generate knowledge. Frontiers provides immediate and permanent online open access to all its publications, but this alone is not enough to realize our grand goals.

Frontiers Journal Series

The Frontiers Journal Series is a multi-tier and interdisciplinary set of open-access, online journals, promising a paradigm shift from the current review, selection and dissemination processes in academic publishing. All Frontiers journals are driven by researchers for researchers; therefore, they constitute a service to the scholarly community. At the same time, the Frontiers Journal Series operates on a revolutionary invention, the tiered publishing system, initially addressing specific communities of scholars, and gradually climbing up to broader public understanding, thus serving the interests of the lay society, too.

Dedication to Quality

Each Frontiers article is a landmark of the highest quality, thanks to genuinely collaborative interactions between authors and review editors, who include some of the world's best academicians. Research must be certified by peers before entering a stream of knowledge that may eventually reach the public - and shape society; therefore, Frontiers only applies the most rigorous and unbiased reviews.
Frontiers revolutionizes research publishing by freely delivering the most outstanding research, evaluated with no bias from both the academic and social point of view.
By applying the most advanced information technologies, Frontiers is catapulting scholarly publishing into a new generation.

What are Frontiers Research Topics?

Frontiers Research Topics are very popular trademarks of the Frontiers Journals Series: they are collections of at least ten articles, all centered on a particular subject. With their unique mix of varied contributions from Original Research to Review Articles, Frontiers Research Topics unify the most influential researchers, the latest key findings and historical advances in a hot research area! Find out more on how to host your own Frontiers Research Topic or contribute to one as an author by contacting the Frontiers Editorial Office: frontiersin.org/about/contact

INNOVATIVE IMAGING TECHNIQUES IN PRECLINICAL MODELS OF NEURODEGENERATIVE DISEASES

Topic Editors:
Rodolfo Gabriel Gatto, Mayo Clinic, United States
Yu-Chien Wu, Indiana University Bloomington, United States

Citation: Gatto, R. G., Wu, Y.-C., eds. (2022). Innovative Imaging Techniques in Preclinical Models of Neurodegenerative Diseases. Lausanne: Frontiers Media SA. doi: 10.3389/978-2-88974-316-2

Table of Contents

frontiers in Neuroscience

EDITORIAL
published: 23 December 2021
doi: 10.3389/fnins.2021.801037

Editorial: Innovative Imaging Techniques in Preclinical Models of Neurodegenerative Diseases

Rodolfo G. Gatto[1]* *and Yu-Chien Wu*[2]

[1] *Department of Bioengineering, University of Illinois at Chicago, Chicago, IL, United States,* [2] *Department of Radiology and Imaging Sciences, Indiana University School of Medicine, Indianapolis, IN, United States*

Keywords: neuroimaging technologies, neurodegenerative diseases, preclinical animal models, neuroscience methods, axonal connectivity

Editorial on the Research Topic

Innovative Imaging Techniques in Preclinical Models of Neurodegenerative Diseases

Edited by:
Zhengwang Wu,
University of North Carolina at Chapel Hill, United States

Reviewed by:
Andrii Domanskyi,
Orion Corporation, Finland

****Correspondence:***
Rodolfo G. Gatto
rodogatto@gmail.com;
rgatto@uic.edu
orcid.org/0000-0003-2170-6662

Specialty section:
This article was submitted to Brain Imaging Methods, a section of the journal Frontiers in Neuroscience

Received: *24 October 2021*
Accepted: *22 November 2021*
Published: *23 December 2021*

Citation:
Gatto RG and Wu Y-C (2021) Editorial: Innovative Imaging Techniques in Preclinical Models of Neurodegenerative Diseases. Front. Neurosci. 15:801037. doi: 10.3389/fnins.2021.801037

Neurodegenerative disorders have been forecast as the next global pandemic. Besides the growing understanding of the basic molecular mechanisms associated to neurodegenerative diseases (NDDs), the current number of disease-modifying treatments remains quite limited. Considering the high social impact among such diseases, technical resources have been focused on the investigation of early biomarkers aiming to maximize the treatment exposures and improve the patient's prognosis.

Improvements in imaging systems and more precise genetic manipulations in biological models are possible new routes toward quantifying diseases progression or developing disease-modifying therapy. In invertebrate models, such as the fruit fly, the compound eye is a premier experimental system for modeling human neurodegenerative diseases. The disruption of the retinal geometry has been historically assessed using time-consuming and poorly reliable techniques such as histology manual counting. Recent semiautomated quantification approaches rely either on manual region-of-interest delimitation or automated methods to estimate the extent of degeneration. The work from Diez-Hermano et al. presents a fully automated classification pipeline of bright-field images, based on orientated gradient descriptors and machine learning (ML) techniques. As an example, the author's initial region-of-interest (ROI) extraction was performed applying image classification algorithms by different ML approaches on independent datasets (Diez-Hermano et al.). Therefore, the authors proved ML as a useful tool to combine imaging techniques in the early detection of AD and screen for mild cognitive impairment (MCI). On the other side, the work of Pan et al. used convolutional neural network (CNN) taking advantage to its excellent efficiency in automated feature learning from a variety of multilayer perceptrons. As such, ensemble learning (EL) has shown robustness as a learning-system performance via multi-model integration. Therefore, combining CNN and EL on a set of MRI images, the authors were able to identify subjects with MCI or AD (Pan et al.).

Understanding non-human microstructural brain alterations in the course of neurodegenerative diseases (NDDs) has substantially improved by incorporating non-invasive imaging techniques such as MRI. The development of diffusion-weighted sequences and techniques, such as diffusion tensor imaging (DTI) is currently integrated into MRI medical systems. DTI-based studies also allow the application of a variety of animal models for the study of NDDs (Müller et al.). Further, microscopic tissue examination can also be achieved by DTI at high fields ultra-high fields (Gatto et al., 2018). In a rodent (rat) model of Duchenne muscular dystrophy (DMD), investigators used DTI and high-resolution Localized MR spectroscopy (MRS) to study the brain and temporalis muscle structure *in-vivo*. Imaging findings of this study indicated a disturbed motor and sensory signaling, resulting in dysfunctional neurotransmission, as well unstable osmoregulation in this genetically modified preclinical brain tissue (Xu et al.). On the other hand, DTI and 18F-Fludeoxyglucose (FDG) PET were also used to evaluate the effects on morphology and glucose utilization levels during pulsed Focused Ultrasound (pFUS) and microbubbles (MB) sessions in the rat cortex and hippocampus, which can be used as the benchmarks for the future study of NDDs (Tu et al.). In the line of more complex diffusion model, Diffusion Basis Spectrum Imaging (DBSI) was applied to assess axonal loss after transient dexamethasone treatment in optic neuritis (ON) of mice models experimental autoimmune encephalomyelitis (EAE) related to multiple sclerosis (MS). More important, their finding supported the potential use of DBSI as an *in vivo* imaging outcome measure to assess NDDs related pathologies (Lin et al.). Further on, DTI has been also a valuable tool to study the link between tauopathies (AD) and traumatic brain injury (TBI) n P301L mutant-tau-transgenic-pR5-mice. In combination with immunohistochemistry techniques, the results showed that different parameters from the DTI signal were associated with the co-occurrence of tau-phosphorylation and glial activity following TBI (Soni et al.). Recently, X-ray phase-contrast tomography (XPCT), has contributed to the additional description of high-resolution 3D imaging features in AD and MS animal models' vascular tissues (Palermo et al.).

A more comprehensive approach has been the combination of biological models and multi-modal imaging modalities in the investigation of neurological diseases. Multimodal techniques, including magnetization transfer (MT), DTI, and relaxation along a fictitious field (RAFF) in the rotating frame of rank 4 (RAFF4), were used to detect the changes in the myelin content and microstructure (myelin sheets modifications by gliosis) during the remyelination phase by lysophosphatidylcholine (LPC) induced demyelination in the corpus callosum of rats (Holikova et al.). Moreover, multiparametric approaches have been used to assess different aspects of demyelinating (MS) disease in clinical settings (Mustafi et al., 2019).

Preclinical animal models are a fundamental link between the discovery of basic molecular mechanisms from single-cell organisms and full-scale clinical trials. From the acceleration of pharmacological outcomes to the evaluation of feasibility in revolutionary gene therapies, animal models have been making it possible to improve clinical image acquisition procedures and the setup of more comprehensive neuromonitoring protocols. As an example, Parkinson's Disease (PD), a major neurodegenerative disease, is characterized by massive degeneration of dopaminergic neurons in the substantia nigra pars compacta, alpha-synuclein-containing Lewy bodies, and neuroinflammation. In these cases, magnetic resonance (MR) imaging plays a crucial role in the diagnosis and monitoring of disease progression and treatment. A variety of MR methods are available to characterize neurodegeneration and other disease features such as iron accumulation and metabolic changes in PD animal models (Petiet). Neuroimaging changes were also been characterized in a PD patient with excessive daytime sleepiness (PD-EDS), revealing regional hypertrophy of the striatum in the cohort, concluding that this early bioimaging marker would provide valuable information when investigating PD-EDS (Gong et al.).

In this Research Topic, we found that the contribution of new computational approaches, combined imaging techniques, and animal models keeps expanding the neuroscience field and the discovery of new imaging biomarkers of NDDs. Therefore, we provide the reader with a wide-ranging overview of current innovative imaging techniques that are sensitive to novel biological paradigms and animal models to aid translational research in the diagnosis and monitoring of patient populations suffering from these devastating illnesses. Ultimately, this article collection demonstrates the expanding integration of artificial and biological models to improve translational and therapeutical approaches among these exciting and significant fields.

AUTHOR CONTRIBUTIONS

Both authors listed have made a substantial, direct, and intellectual contribution to the work and approved it for publication.

REFERENCES

Gatto, R. G., Amin, M. Y., Deyoung, D., Hey, M., Mareci, T. H., and Magin, R. L. (2018). Ultra-high field diffusion mri reveals early axonal pathology in spinal cord of als mice. *Transl. Neurodegener.* 7:20. doi: 10.1186/s40035-018-0122-z

Mustafi, S. M., Harezlak, J., Kodiweera, C., Randolph, J. S., Ford, J. C., Wishart, H. A., and Wu, Y. (2019). Detecting white matter alterations in multiple sclerosis using advanced diffusion magnetic resonance imaging. *Neural Regen. Res.* 14, 114–123. Available online at: https://www.nrronline.org/article.asp?issn=1673-5374;year=2019;volume=14;issue=1;spage=114;epage=123;aulast=Mustafi

Conflict of Interest: The authors declare that this article collection was conducted in the absence of any commercial or financial relationships that could be interpreted as a potential conflict of interest.

frontiers in Neuroscience

ORIGINAL RESEARCH
published: 09 January 2020
doi: 10.3389/fnins.2019.01353

Striatum Shape Hypertrophy in Early Stage Parkinson's Disease With Excessive Daytime Sleepiness

*Liang Gong[1], Huaisu Li[1], Dan Yang[1], Yinwei Peng[1], Duan Liu[1], Ming Zhong[1], Bei Zhang[1], Ronghua Xu[1] and Jian Kang[2]**

[1] *Department of Neurology, Chengdu Second People's Hospital, Chengdu, China,* [2] *Hospital of Chengdu University of Traditional Chinese Medicine, Chengdu, China*

Introduction: Excessive daytime sleepiness (EDS) is one of the common and burdensome non-motor symptoms of Parkinson's disease (PD). However, the underlying neuropathology mechanism in PD patients with EDS (PD-EDS) remains unclear. The present study aims to delineate potential locations of structural alteration of subcortical regions in early stage and drug-naïve PD-EDS.

Methods: The study had 252 patients with PD and 92 matched healthy controls (HC). EDS was estimated with the Epworth Sleepiness Scale, with a cutoff of 10. Ultimately, 59 patients were considered as PD-EDS. The remaining 193 were PD patients without EDS (PD-nEDS). FMRIB's Integrated Registration and Segmentation Tool (FIRST) was employed to assess the volumetric and surface alterations of subcortical nuclei in PD and PD-EDS.

Results: Volumetric analyses found no difference in the subcortical nucleus volume between PD and HC, or PD-EDS and PD-nEDS groups. The shape analyses revealed the local atrophic changes in bilateral caudate and right putamen in patients with PD. In addition, the hypertrophic changes were located in the right putamen and left pallidum in PD-EDS than in PD-nEDS.

Conclusion: Our findings revealed the regional hypertrophy of the striatum in PD-EDS. Our results indicate that local hypertrophic striatum would be a valuable early biomarker for detecting the alteration in PD-EDS. The shape analysis contributes valuable information when investigating PD-EDS.

Keywords: Parkinson's disease, excessive daytime sleepiness, striatum, shape analysis, structure

Edited by:
Rodolfo Gabriel Gatto,
University of Illinois at Chicago,
United States

Reviewed by:
Sandeep Kumar Barodia,
The University of Alabama
at Birmingham, United States
Patrice Péran,
Institut National de la Santé et de la
Recherche Médicale (INSERM),
France

****Correspondence:***
Jian Kang
0181@cdutcm.edu.cn

Specialty section:
This article was submitted to
Neurodegeneration,
a section of the journal
Frontiers in Neuroscience

Received: *08 September 2019*
Accepted: *02 December 2019*
Published: *09 January 2020*

Citation:
Gong L, Li H, Yang D, Peng Y,
Liu D, Zhong M, Zhang B, Xu R and
Kang J (2020) Striatum Shape
Hypertrophy in Early Stage
Parkinson's Disease With Excessive
Daytime Sleepiness.
Front. Neurosci. 13:1353.
doi: 10.3389/fnins.2019.01353

INTRODUCTION

Parkinson's disease (PD) is the second most common neurodegenerative disorder associated with both motor and numerous non-motor symptoms (De Lau and Breteler, 2006). Excessive daytime sleepiness (EDS), a non-motor feature, is described as inappropriate and undesirable sleepiness during waking hours, affecting 16–50% of patients with PD (Knie et al., 2011). As EDS has a significant negative impact on the quality of life and driving safety (Meindorfner et al., 2005;

Chahine et al., 2017), it is quite essential to fully understand the neurobiological mechanism underlying this symptom.

Although studies have shown associations with EDS symptoms in PD including non-tremor dominant phenotype, autonomic dysfunction, depression, anxiety, and disorders of rapid eye movement sleep behavior (Simuni et al., 2015; Amara et al., 2017; Wen et al., 2017), the neural mechanism of EDS in PD remains poorly understood. The lack of correlation between EDS and disease severity of PD [Hoehn & Yahr stage (H&Y)] has led to the notion that the EDS might be associated with PD-specific pathology (Yousaf et al., 2018b). However, *in vivo* neuroimaging quantification has been used to detect early pathophysiological changes in PD with EDS (PD-EDS), potentially serving as a biomarker for disease progression and treatment monitoring (Chondrogiorgi et al., 2016; Wen et al., 2017; Ashraf-Ganjouei et al., 2019). Molecular imaging studies using positron emission tomography (PET) and single-photon emission computed tomography (SPECT) implicate EDS with dopaminergic dysfunction in subcortical regions (Happe et al., 2007; Pagano et al., 2016). However, molecular imaging is expensive and radioactive, so it would not be a conventional and regular scan. T1-weighted magnetic resonance imaging (MRI) is one of the most widely used sequences in neuroimaging studies; it can be acquired in all scanners and is commonly used in conventional clinical MRI protocols. Presently, three studies have used the whole-brain gray matter analysis and revealed widespread volume reductions in the frontal, occipital, temporal, and limbic lobes in PD patients with EDS (PD-EDS) (Gama et al., 2010; Kato et al., 2012; Chondrogiorgi et al., 2016). However, for the subcortical nucleus, these studies have contradictory findings, reporting both increased and decreased gray matter volumes (GMs) in the hippocampus and parahippocampus in patients with PD-EDS. One reason for inconsistent findings might be the small sample size and antiparkinsonian medication in previous studies. Another important factor might be attributed to the limitation of the voxel-based morphometry (VBM) analysis, which is based on a standard template. A previous volumetric analysis of PD pathology also showed conflicting results on subcortical structures (Uitti et al., 2005; Gama et al., 2010; Péran et al., 2010).

Several surface-based subcortical region shape analyses of PD patients have revealed local atrophy in the subcortical nucleus, including the caudate nucleus and the putamen, and a correlation between cognitive function and atrophy of the caudate nucleus and the putamen (Apostolova et al., 2010; Sterling et al., 2013; Menke et al., 2014; Nemmi et al., 2015). Recently, Nemmi et al. (2015) showed that the shape analysis was the most sensitive method for observing atrophy-related differences between PD patients and control subjects. They also found that the information from the shape analysis was able to discriminate PD patients from healthy control subject best when compared with the standard volumetric and gray matter density analysis (Nemmi et al., 2015). Thus, we hypothesize that the shape analysis could be a useful tool to detect localized subcortical nuclei alterations in PD-EDS.

To test our hypothesis, we used a fully automated segmentation method (FIRST, Oxford Centre, FMRIB) and the replicable vertex-based shape analysis in our study. We compared the subcortical nuclei shape difference between early stage and drug-naïve PD patients and matched healthy controls (HC). The PD patients group was further divided into PD-EDS and PD without EDS subgroups (PD-nEDS) according to the Epworth Sleepiness Scale (ESS; with a cutoff of 10), and the shape difference between these two PD groups was conducted in each subcortical nucleus, separately. We also performed a traditional volumetric-based analysis between groups.

MATERIALS AND METHODS

Participants

All participants were enrolled in PPMI (Parkinson's Progression Markers Initiative), an observational, international, multicenter investigation of clinical, biological, and neuroimaging markers of PD progression, where all patients with PD were newly diagnosed and untreated at baseline (Marek et al., 2011). Study aims, methodology, and details of study assessments are available on the PPMI website[1]. The inclusion and exclusion criteria were described previously in detail (Wen et al., 2016; Chahine et al., 2019). Institutional review boards approved the study at PPMI sites, and written informed consent was obtained.

As of August 4, 2019, the participants in the PPMI database include 454 patients and 215 matched HC. Only participants with T1 structural MRI data and an ESS assessment were included in the present study; 350 participants were selected for MRI processing, and six were excluded based on image-processing quality control (poor segmentation). The final sample included 252 patients with PD and 92 HC subjects.

Assessments and Subgroup of Parkinson's Disease

The ESS was used for EDS evaluation; this scale has high test–retest correlation and high internal consistency (Johns, 1991). ESS is recommended for assessing and measuring the severity of EDS in PD by the Movement Disorders Society Sleep Scale Task Force (Högl et al., 2010). According to the ESS cutoff score recommend, patients with PD were categorized as having EDS (PD-EDS group) if ESS was equal or above 10 and not having EDS (PD-nEDS group) if ESS score was lower than 10 (Arnulf et al., 2002; Matsui et al., 2006; Högl et al., 2010; Amara et al., 2017). As indicated by the ESS cutoff score, 192 PD patients were subdivided to PD-EDS group, and 53 PD patients were subdivided to PD-nEDS group. The Movement Disorders Society Unified Parkinson's Disease Rating Scale score (UPDRS) part III was used to measure motor function (Goetz et al., 2008), and the Montreal Cognitive Assessment (MoCA) was used to test global cognitive function (Nasreddine et al., 2005). The 15-item Geriatric Depression Scale (GDS) to test mood symptoms (Weintraub et al., 2006) and the Rapid Eye Movement Sleep Behavior Disorder Screening Questionnaire (RBDSQ) was selected as a measure of rapid eye movement sleep behavior disorder (RBD) (Stiasny–Kolster et al., 2007).

---

[1] http://www.ppmi-info.org/study-design

MRI Acquisition

The MRI acquisition procedures were displayed in detail at http://www.ppmi-info.org/wp-content/uploads/2017/06/PPMI-MRI-Operations-Manual-V7.pdf. In brief, a three-dimensional (3D), T1-weighted sequence (e.g., MPRAGE or SPGR) is required. The field of view (FOV) must include the vertex, cerebellum, and pons. The T1-weighted image must be acquired as a 3D sequence and have a slice thickness of 1.5 mm or less with no interslice gap. The PPMI core optimized the acquisition sequence across sites to minimize bias in data between sites and maximize comparability of data in the study. Typical MRI parameters were as follows: repetition time 5–11 ms; echo time 2–6 ms; thickness 1.2 mm; gap 0 mm; voxel size 1 × 1 × 1.2 mm; matrix 256 × 256 × 170–200.

Image Preprocessing

MRI data analyses were performed using the tools from FSL (version 5.0.9[2]; FMRIB Software Library, Oxford University, Oxford, United Kingdom) (Jenkinson et al., 2012).

First, the SIENAX[3] was used to estimate the total intracranial volume (eTIV), white matter volume (WM), and GM for all the subjects. All reported brain volumes were normalized to a "normalized" skull size (Smith et al., 2002).

Second, the subcortical structures were segmented using the FMRIB's Integrated Registration and Segmentation Tool (FIRST[4], part of FSL, version 5.0.9) (Patenaude et al., 2011). FIRST is an automated tool to segment the subcortical nuclei and has been used to study several neuropsychiatric disorders (van den Bogaard et al., 2011; Seifert et al., 2015).

Third, after the automated segmentation (fun_first_all), the quality of segmentation for each subject was checked manually (first_roi_slicesdir). The outcome file of FIRST was then used for the volume and vertex analysis. For the standard volumetric analysis, the raw volume subcortical structure was normalized for the inter-individual variability of brain size (raw volume/eTIV).

Statistical Analysis

A two-sample *t*-test was conducted to compare various demographic data between the two groups, whereas the chi-squared test was used to compare sex and H&Y stage. An analysis of covariance (ANCOVA) was used to estimate the group differences in the whole brain volume (eTIV) and normalized subcortical structure volume, with age, sex, and eTIV (not in the eTIV comparison) as covariates (SPSS 20, Inc., Chicago, IL, United States). Pearson correlation was employed to examine the relationship between ESS, MoCA, GDS, and EBDSQ scores in the PD group. Statistical significance was set at p-values < 0.05, after correction for multiple comparisons using the false discovery rate (FDR).

Surface-Based Shape Analysis

The new version of vertex-wise analysis was employed to investigate localized shape differences in the subcortical nucleus between HC and PD, as well as the group differences between PD-EDS and PD-nEDS, separately. The shape analyses were all adjusted for age, sex, and eTIV (first_utils and randomize, FSL 5.0.9). This approach calculates the group differences on a per-vertex basis. The threshold-free cluster enhancement (TFCE), a new method for finding significant "clusters" in the statistic image without having to define clusters in a binary way, was used for multiple comparison correction (Smith and Nichols, 2009). As the traditional surface-based vertex analysis comprises the vectors in each significant vertex, we used it to display the direction of group differences.

RESULTS

Demographic and Behavioral Features

Detailed subject characteristics and clinical parameters for each group are summarized in **Table 1**. There are no significant differences in age, sex, education, ESS score, GDS score, or eTIV between PD and HC groups. The EBDSQ score was higher and MoCA score was lower in the PD group than in the HC group. Similarly, except the difference in ESS, there are no intergroup differences in age, sex, education, disease duration, age of onset, H&Y stage, UPDRS-III, MoCA, GDS, EBDSQ score, or eTIV between PD-nEDS and the PD-EDS groups.

The correlation analyses revealed that the EDS scores were significant and positively correlated with EBDSQ scores ($r = 0.223$, $p = 0.004$) and GDS scores ($r = 0.126$, $p = 0.046$) in the PD group. However, the relationship between EDS and GDS was not significant after FDR correction. The EDS scores did not correlate significantly with cognitive function (MoCA) and motor symptom (UPRDS-III) in the PD group. In addition, the EDS score in patients with H&Y stage 2 was significantly higher than that in H&Y stage 1 (7.43 vs. 6.47, $p = 0.03$).

Subcortical Nuclei Global Normalized Volume Comparison

There was no significant difference in any of the subcortical nucleus volumes between PD and HC and between PD-EDS and PD-nEDS groups in the global normalized volume of each nucleus after FDR correlation (**Table 2**).

Shape Comparisons of Parkinson's Disease and Control Subcortical Structures

As shown in **Figure 1**, the new vertex analysis revealed that the body and right tail caudate, the left head caudate, and the right ventrolateral putamen showed significant group differences in the PD group than in the HC group (TFCE corrected). The traditional surface-based vertex analysis showed an inward displacement in these significantly different regions of the bilateral caudate and right putamen (**Figure 2**), whereas the findings of shape analysis indicated a localized caudate and putamen volume atrophy in the PD group than in the HC group. No significant areas of hypertrophy were observed. No significant

---

[2] https://fsl.fmrib.ox.ac.uk/fsl

[3] https://fsl.fmrib.ox.ac.uk/fsl/fslwiki/SIENA

[4] https://fsl.fmrib.ox.ac.uk/fsl/fslwiki/FIRST

TABLE 1 | Demographic and clinical characteristics of all participants.

Subject groups	HC	PD	PD-EDS	PD-nEDS	*p*-value (HC vs. PD)	*p*-value (PD-EDS vs. PD-nEDS
N	**92**	**252**	**59**	**193**		
Age (years)	59.81 ± 10.44	61.34 ± 9.51	62.23 ± 8.91	60.54 ± 10.05	0.203	0.361
Gender (female/male)	30/62	96/156	25/34	70/123	0.210†	0.445†
Education (years)	15.78 ± 2.88	15.31 ± 3.14	15.83 ± 3.10	16.01 ± 3.00	0.216	0.763
Disease duration (months)	–	6.80 ± 7.44	7.19 ± 7.29	6.61 ± 7.44	–	0.682
Onset (years)		59.27 ± 10.07	60.52 ± 8.83	58.26 ± 10.76	–	0.249
H&Y (1/2)		118/134	23/36	95/98	–	0.285†
UPDRS-III	0.54 ± 1.22	19.60 ± 9.17	21.34 ± 10.67	18.62 ± 8.40	<0.001	0.129
MoCA	28.30 ± 1.30	27.14 ± 2.42	27.06 ± 2.81	27.48 ± 2.20	<0.001	0.376
ESS	6.71 ± 3.67	6.99 ± 3.57	12.08 ± 2.18	5.44 ± 2.21	0.510	<0.001
GDS	5.25 ± 1.55	5.32 ± 1.43	5.35 ± 2.01	5.35 ± 1.43	0.673	0.993
EBDSQ	3.77 ± 2.28	5.55 ± 2.77	5.67 ± 3.09	5.08 ± 2.86	<0.001	0.178
eTIV	1, 525.98 ± 593.29	1, 534.63 ± 564.14	1, 383.31 ± 497.73	1, 518.73 ± 534.80	0.900	0.178

All values are presented as means and standard deviation (SD). †*p-value was calculated using chi-squared test. HC, healthy control; PD, Parkinson's disease; EDS, excessive daytime sleepiness; PD-EDS, PD patients with EDS; PD-nEDS, PD patients without EDS; H&Y, Hoehn–Yahr stage; UPDRS-III, Unified Parkinson's Disease Rating Scale part III; MoCA, Montreal Cognitive Assessment; ESS, Epworth Sleepiness Scale; GDS, Geriatric Depression Scale; EBDSQ, rapid eye movement episode sleep behavior disorder (RBD) screening questionnaire; eTIV, estimated total intracranial volume.*

TABLE 2 | Mean normalized volume of subcortical structure among groups.

Subcortical region	HC (*n* = 92)	PD (*n* = 252)	*t*-value	*p*-value	PD-EDS (*n* = 59)	PD-nEDS (*n* = 193)	*t*-value	*p*-value
Left accumbens	0.38 ± 0.15	0.36 ± 0.17	0.86	0.39	0.35 ± 0.14	0.38 ± 0.14	−1.10	0.27
Left amygdala	1.10 ± 0.39	1.09 ± 0.40	0.11	0.91	1.07 ± 0.33	1.20 ± 0.39	−1.86	0.07
Left caudate	2.48 ± 0.85	2.51 ± 0.88	−0.28	0.78	2.46 ± 0.78	2.68 ± 0.76	−1.46	0.15
Left hippocampus	2.80 ± 1.01	2.83 ± 1.00	−0.30	0.76	2.80 ± 0.86	3.10 ± 0.97	−1.75	0.08
Left pallidum	1.33 ± 0.47	1.38 ± 0.48	−0.79	0.43	1.33 ± 0.42	1.45 ± 0.42	−1.56	0.12
Left putamen	3.54 ± 1.22	3.61 ± 1.27	−0.45	0.65	3.57 ± 1.11	3.78 ± 1.09	−1.03	0.31
Left thalamus	5.96 ± 2.06	6.03 ± 2.04	−0.26	0.79	6.00 ± 1.78	6.41 ± 1.79	−1.18	0.24
Right accumbens	0.30 ± 0.12	0.30 ± 0.14	0.26	0.80	0.30 ± 0.13	0.30 ± 0.11	−0.02	0.99
Right amygdala	1.11 ± 0.41	1.16 ± 0.42	−0.98	0.33	1.13 ± 0.33	1.25 ± 0.36	−1.93	0.06
Right caudate	2.54 ± 0.89	2.60 ± 0.89	−0.52	0.60	2.54 ± 0.76	2.81 ± 0.81	−1.85	0.07
Right hippocampus	2.89 ± 1.04	2.89 ± 1.03	−0.01	0.99	2.87 ± 0.92	3.05 ± 0.87	−1.01	0.32
Right pallidum	1.36 ± 0.48	1.39 ± 0.48	−0.43	0.67	1.37 ± 0.43	1.45 ± 0.41	−1.08	0.28
Right putamen	3.59 ± 1.25	3.66 ± 1.29	−0.41	0.68	3.61 ± 1.11	3.85 ± 1.09	−1.12	0.27
Right thalamus	5.83 ± 1.99	5.92 ± 2.00	−0.34	0.73	5.93 ± 1.77	6.25 ± 1.74	−0.93	0.35

The values represent the mean and standard deviation of the ratio between structures' volume and eTIV. eTIV, estimated total intracranial volume.

group differences were found in the shape analysis of the other subcortical nuclei.

Shape Comparisons of Parkinson's Disease With Excessive Daytime Sleepiness and Parkinson's Disease Without Excessive Daytime Sleepiness Subcortical Structures

The shape analyses also revealed significant group differences in the left dorsolateral pallidum and the right dorsal putamen between the PD-EDS and PD-nEDS groups (**Figure 3**). The traditional surface-based vertex analysis showed an outward displacement in these significantly different regions of pallidum and putamen (**Figure 4**); thus, the shape analysis results indicate a localized pallidum and putamen volume hypertrophy in PD-EDS than in PD patients without EDS (PD-nEDS). No significant group differences were found in the shape analysis of the other subcortical nuclei.

DISCUSSION

The current study employed surface-based shape analysis to investigate the spatial distribution change of subcortical nuclei in drug-naïve early stage patients with PD and PD-EDS. This study has two main findings: First, we verified that the atrophy of striatum volume is not global but regional in the patients with PD. Specifically, the regional atrophy in PD was located in the right tail caudate nuclei, left head caudate nuclei, and right ventrolateral putamen. Second, the PD-EDS showed regional

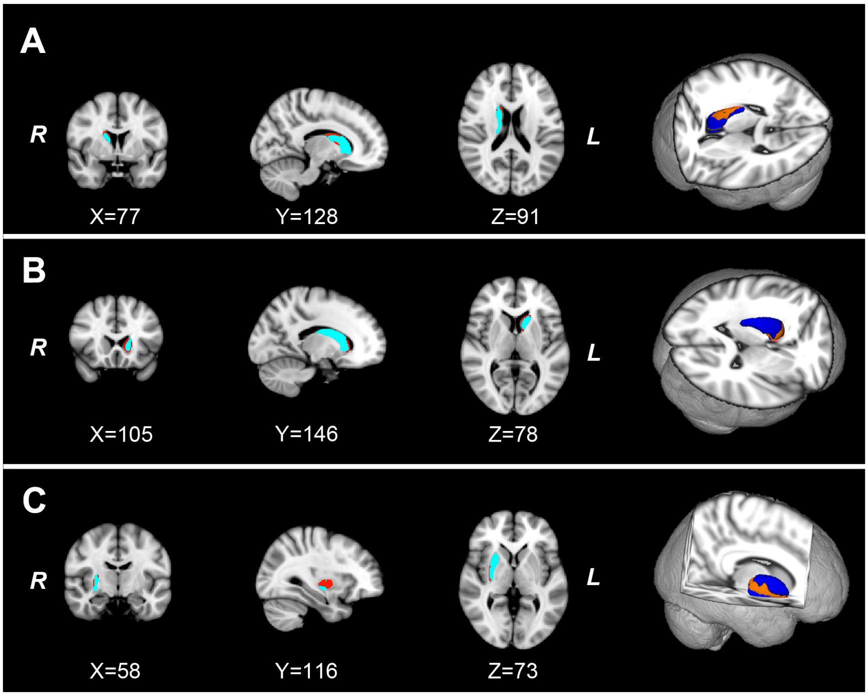

FIGURE 1 | The localized shape differences between HC and PD groups using vertex-wise surface analyses of each subcortical nucleus. The regions in orange indicate the different regions of the characteristic subcortical nuclei between PD and HC groups. **(A)** Group differences of the right caudate are located in the body and tail subdivisions. **(B)** Group differences of the left caudate are located in the head subdivision. **(C)** The group differences of the right putamen are located in the ventrolateral subdivision of putamen. HC, healthy control; PD, Parkinson's disease.

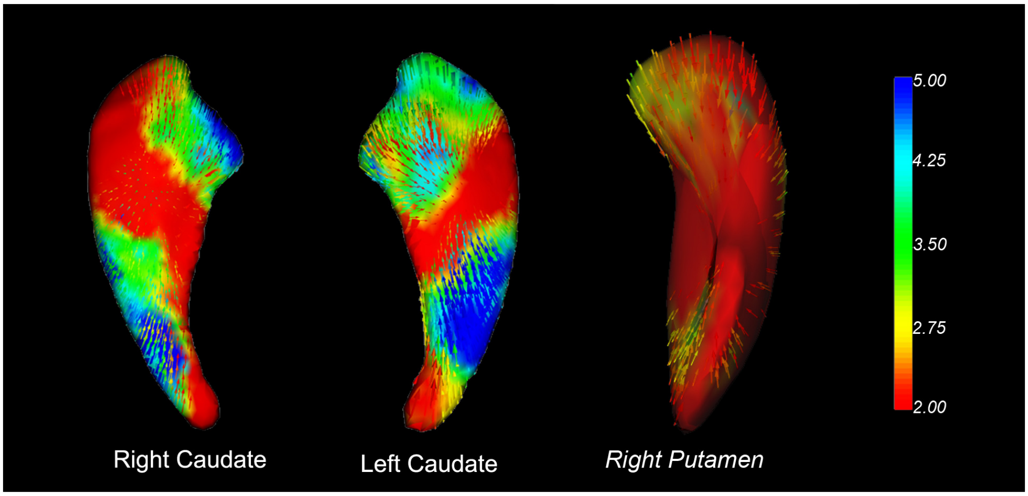

FIGURE 2 | Vector graphs of the bilateral caudate and right putamen according to the traditional surface-based vertex analysis displayed by 3D mesh. The color bar indicates the statistical values; an increase from red to blue indicates a lower to higher statistical significance. The small arrows shown on the surface indicate the direction of change. The inward arrows indicate the direction of difference, suggesting that these subcortical nuclei are smaller/thinner here than in the healthy control groups.

hypertrophic volume alteration in the striatum when compared with PD-nEDS. The hypertrophied striatum was located in the left dorsolateral pallidum and right dorsal putamen. To our knowledge, this is the first study demonstrating PD-EDS-related shape differences in the striatum. Our findings indicate that the region-specific striatum shape alteration would be the early biomarker in PD-EDS.

The results of the present study are consistent with previous reports of striatal shape atrophy in patients with PD and indicate that striatal shape alteration between PD and control subjects

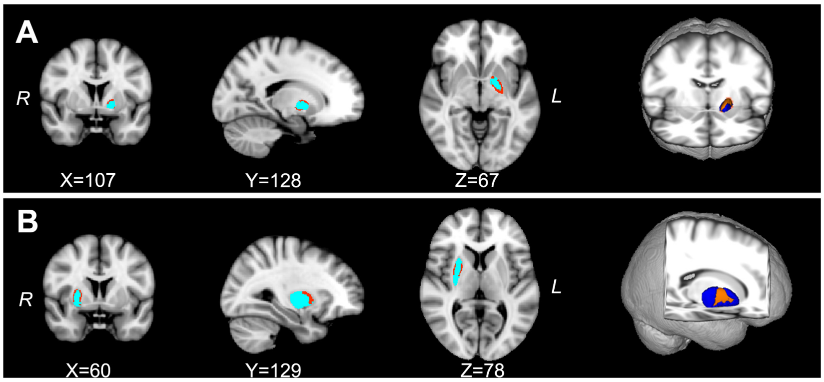

FIGURE 3 | The localized shape differences between PD-EDS and PD-nEDS subgroups using vertex-wise surface analyses of each subcortical region. The regions in orange indicate the different regions of the special subcortical nuclei between PD-EDS and PD-nEDS groups. **(A)** The group differences of the left pallidum are located in the left dorsolateral subdivision of pallidum; **(B)** the group differences of the right putamen are located in the middle subdivision of putamen. PD-EDS, Parkinson's disease with excessive daytime sleepless; PD-nEDS, Parkinson's disease without excessive daytime sleepless.

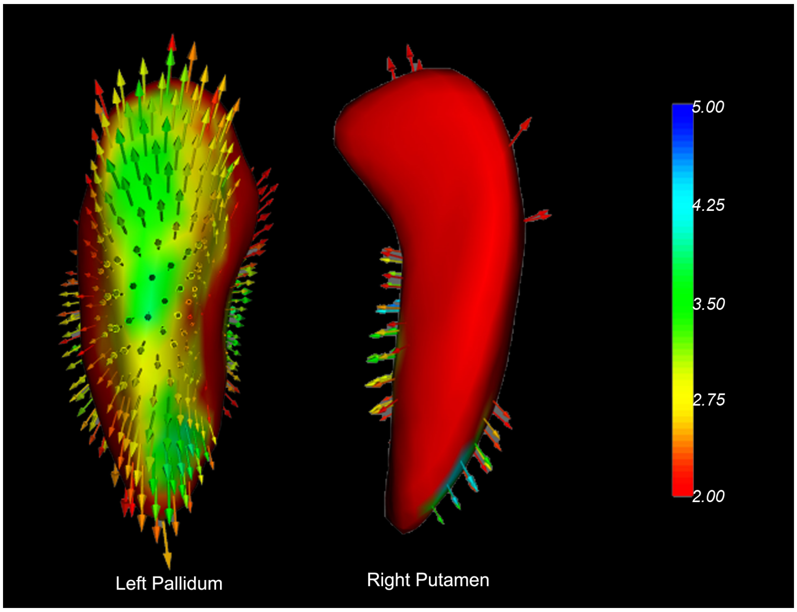

FIGURE 4 | Vector graphs of the bilateral caudate and right putamen according to the traditional surface-based vertex analysis displayed by 3D mesh. The color bar indicates the statistical values; an increase from red to blue indicates a lower to higher statistical significance. The small arrows shown on the surface indicate the direction of change. The inward arrows indicate the direction of difference is such that these subcortical nuclei are smaller/thinner here than in the healthy control groups.

are most robust in the caudate nuclei and putamen (Apostolova et al., 2010; Sterling et al., 2013; Nemmi et al., 2015). Previous studies used manual, semi-automated, and machine learning approaches for subcortical structure region segmentation and shape analysis (Apostolova et al., 2010; Pitcher et al., 2012; Sterling et al., 2013). Apostolova et al. (2010) reported that PD with dementia showed atrophy in the left medial and lateral and right medial of the caudate. Sterling et al. (2013) found that the most significant atrophic putamen in PD was localized in the caudal and ventrolateral areas, and the most atrophic caudate was located at the rostral caudate head. They also reported the association between cognition performance and the altered region of putamen (Sterling et al., 2013). The local putamen atrophy would attribute to the reduced dopaminergic activity and striatal dopamine depletion spine loss in the putamen in early disease stages of PD (Geng et al., 2006; Burguière et al., 2013; Sterling et al., 2013). In addition, the atrophied caudate nuclei were located in the right tail and left head region. The results indicate a hemispheric difference in PD patients, supporting the notion of an endogenous, inter-hemispheric dopamine imbalance in the mesostriatal dopaminergic system (Molochnikov and Cohen, 2014).

The existing neuroimaging studies on the EDS symptom in PD patients have found EDS-related alteration at brain structural, functional, and metabolic levels (for review, see Yousaf et al., 2018b). PD-EDS showed dopamine transporter (DAT) uptake reduction in the caudate, which correlated with clinical EDS symptom (Yousaf et al., 2018a). Happe et al. (2007) reported that the DAT binding in the striatum and putamen inversely correlates with EDS score in early PD. To our knowledge, no neuroimaging study focused on the structural shape alteration of the striatum in PD-EDS. In our study, the hypertrophic alteration in the left dorsolateral pallidum and right dorsal putamen was found in PD-EDS than in PD without EDS. The results are consistent with previous structural studies on sleep disorders. Hypertrophic cortical and subcortical alterations have been reported in other sleep disorders, such as obstructive sleep apnea and primary insomnia (Rosenzweig et al., 2013; Baril et al., 2017; Yu et al., 2018). The hypertrophic structural change of the striatum in the sleep disorders implied the intricate endogenous repair systems in the brain, and the preconditioning and enhanced neurogenesis mechanism might be included (Lledo et al., 2006; Dirnagl et al., 2009). EDS also impacts the striatum in the early stage of PD. Our study supports the notion that EDS might be a preclinical marker of PD (Arnulf et al., 2002), and the EDS symptom in the drug-naïve and early stage PD might be attributed to the compensatory mechanism of the striatum. Further studies with longitudinal designs are warranted to clarify whether the compensation will reverse to maladaptation during the disease progression.

It is interesting to note that the normalized global volume of the subcortical nuclei did not show a significant difference for any of the structures between the PD and HC, PD-EDS, and PD-nEDS groups. These findings are consistent with previous observations on patients with PD where volume did not show any difference between the PD and HC groups, but the shape analysis was able to detect the significant difference (McKeown et al., 2008; Apostolova et al., 2010; Nemmi et al., 2015; Tanner et al., 2017). Several studies have found decreased subcortical nuclei volumes in the putamen, thalamus, and hippocampus in the PD group than in the HC group; the PD patients recruited in these studies were in the late stage of the of disease, were at mild stage, have dementia, and undergoing dopaminergic treatment (Halliday, 2009; Pitcher et al., 2012; Nemmi et al., 2015; Tanner et al., 2017). These findings all suggested that the surface-based shape analysis would be more sensitive to detect the early change of subcortical structures in patients with PD and in PD-EDS.

There are several limitations to our study. First, there are no objective measures of EDS in the present study, and the subjective assessment may result in underestimation of this symptom (Kaynak et al., 2005). Second, structural association of the striatum with EDS in PD patients could not be explained as a causal relationship, and further longitudinal studies would be necessary to confirm the hypertrophic shape change as dynamic components of the progression in PD-EDS. Third, the PD patients were all in the early stage, and the severity of EDS in our group is moderate (below 16). We proposed that the hypertrophic alteration in striatum might be a compensatory mechanism in the mild severity of EDS in PD patients. Further studies should enroll severe EDS patients to verify our speculation. Lastly, all patients in our study were drug naïve; however, another cause of EDS is drug therapy, including dopamine agonists and levodopa (Knie et al., 2011). How the striatum structural alteration in PD with the EDS occurred after treatment with dopaminergic agents should be investigated in future studies.

CONCLUSION

In summary, the present study verified the localized atrophic striatum in patients with PD. In addition, we found the regional putamen and pallidum hypertrophy in PD-EDS. Our results indicate that compensatory mechanisms might be involved in the early stage of PD-EDS, and the shape alteration of stratum would be a useful biomarker for early detection in the PD-EDS.

DATA AVAILABILITY STATEMENT

Publicly available datasets were analyzed in this study. This data can be found here: www.ppmi-info.org/data.

AUTHOR CONTRIBUTIONS

LG and JK designed the study. LG, HL, DY, and JK analyzed and drafted the manuscript. YP, MZ, DL, BZ, and RX made substantial contribution to the data interpretation, critically revised, and drafted the manuscript. All the authors read and approved the final version of the manuscript.

FUNDING

This work was partially supported by the Chengdu Medical Research Project (2015076 and 2019115) and Sichuan Medical Research Project (16PJ032).

ACKNOWLEDGMENTS

Data used in the preparation of this article were obtained from the Parkinson's Progression Markers Initiative (PPMI) database (www.ppmi-info.org/data). For up-to-date information on the study, visit www.ppmi-info.org. PPMI – a public–private partnership – is funded by The Michael J. Fox Foundation for Parkinson's Research and funding partners, including AbbVie, Avid, Biogen, BioLegend, Bristol-Myers Squibb, GE Healthcare, GeneTech, GSK, Lilly, Lundbeck, Merck, Meso Scale Discovery, Pfizer, Piramal, Roche, Sanofi Genzyme, Servier, Takeda, Teva, UCB, and Golub Capital.

REFERENCES

Amara, A. W., Chahine, L. M., Caspell-Garcia, C., Long, J. D., Coffey, C., Högl, B., et al. (2017). Longitudinal assessment of excessive daytime sleepiness in early Parkinson's disease. *J. Neurol. Neurosurg. Psychiatry* 88, 653–662. doi: 10.1136/jnnp-2016-315023

Apostolova, L. G., Beyer, M., Green, A. E., Hwang, K. S., Morra, J. H., Chou, Y. Y., et al. (2010). Hippocampal, caudate, and ventricular changes in Parkinson's disease with and without dementia. *Mov. Disord.* 25, 687–695. doi: 10.1002/mds.22799

Arnulf, I., Konofal, E., Merino–Andreu, M., Houeto, J., Mesnage, V., Welter, M., et al. (2002). Parkinson's disease and sleepiness: an integral part of PD. *Neurology* 58, 1019–1024. doi: 10.1212/wnl.58.7.1019

Ashraf-Ganjouei, A., Kheiri, G., Masoudi, M., Mohajer, B., Mojtahed Zadeh, M., Saberi, P., et al. (2019). White matter tract alterations in drug-naïve Parkinson's disease patients with excessive daytime sleepiness. *Front. Neurol.* 10:378. doi: 10.3389/fneur.2019.00378

Baril, A.-A., Gagnon, K., Brayet, P., Montplaisir, J., De Beaumont, L., Carrier, J., et al. (2017). Gray matter hypertrophy and thickening with obstructive sleep apnea in middle-aged and older adults. *Am. J. Respir. Crit. Care Med.* 195, 1509–1518. doi: 10.1164/rccm.201606-1271OC

Burguière, A., De Bundel, D., Valjent, E., Roger, J., Smolders, I., Fagni, L., et al. (2013). Combination of group I mGlu receptors antagonist with dopaminergic agonists strengthens the synaptic transmission at corticostriatal synapses in culture. *Neuropharmacology* 66, 151–157. doi: 10.1016/j.neuropharm.2012.03.017

Chahine, L., Dos Santos, C., Fullard, M., Scordia, C., Weintraub, D., Erus, G., et al. (2019). Modifiable vascular risk factors, white matter disease and cognition in early Parkinson's disease. *Eur. J. Neurol.* 26:246-e18. doi: 10.1111/ene.13797

Chahine, L. M., Amara, A. W., and Videnovic, A. (2017). A systematic review of the literature on disorders of sleep and wakefulness in Parkinson's disease from 2005 to 2015. *Sleep Med. Rev.* 35, 33–50. doi: 10.1016/j.smrv.2016.08.001

Chondrogiorgi, M., Tzarouchi, L. C., Zikou, A. K., Astrakas, L. G., Kosta, P., Argyropoulou, M. I., et al. (2016). Multimodal imaging evaluation of excessive daytime sleepiness in Parkinson's disease. *Int. J. Neurosci.* 126, 422–428. doi: 10.3109/00207454.2015.1023437

De Lau, L. M., and Breteler, M. M. (2006). Epidemiology of Parkinson's disease. *Lancet Neurol.* 5, 525–535.

Dirnagl, U., Becker, K., and Meisel, A. (2009). Preconditioning and tolerance against cerebral ischaemia: from experimental strategies to clinical use. *Lancet Neurol.* 8, 398–412. doi: 10.1016/S1474-4422(09)70054-7

Gama, R. L., Távora, D. G., Bomfim, R. C., Silva, C. E., De Bruin, V. M., and De Bruin, P. F. (2010). Sleep disturbances and brain MRI morphometry in Parkinson's disease, multiple system atrophy and progressive supranuclear palsy - a comparative study. *Parkinson. Relat. Disord.* 16, 275–279. doi: 10.1016/j.parkreldis.2010.01.002

Geng, D. Y., Li, Y. X., and Zee, C. S. (2006). Magnetic resonance imaging-based volumetric analysis of basal ganglia nuclei and substantia nigra in patients with Parkinson's disease. *Neurosurgery* 58, 256–262; discussion 256–262.

Goetz, C. G., Tilley, B. C., Shaftman, S. R., Stebbins, G. T., Fahn, S., Martinez-Martin, P., et al. (2008). Movement disorder society-sponsored revision of the Unified Parkinson's Disease Rating Scale (MDS-UPDRS): scale presentation and clinimetric testing results. *Mov. Disord.* 23, 2129–2170. doi: 10.1002/mds.22340

Halliday, G. M. (2009). Thalamic changes in Parkinson's disease. *Parkinson. Relat. Disord.* 15(Suppl. 3), S152–S155. doi: 10.1016/S1353-8020(09)70804-1

Happe, S., Baier, P. C., Helmschmied, K., Meller, J., Tatsch, K., and Paulus, W. (2007). Association of daytime sleepiness with nigrostriatal dopaminergic degeneration in early Parkinson's disease. *J. Neurol.* 254, 1037–1043. doi: 10.1007/s00415-006-0483-6

Högl, B., Arnulf, I., Comella, C., Ferreira, J., Iranzo, A., Tilley, B., et al. (2010). Scales to assess sleep impairment in Parkinson's disease: critique and recommendations. *Mov. Disord.* 25, 2704–2716. doi: 10.1002/mds.23190

Jenkinson, M., Beckmann, C. F., Behrens, T. E., Woolrich, M. W., and Smith, S. M. (2012). FSL. *Neuroimage* 62, 782–790. doi: 10.1016/j.neuroimage.2011.09.015

Johns, M. W. (1991). A new method for measuring daytime sleepiness: the Epworth sleepiness scale. *Sleep* 14, 540–545.

Kato, S., Watanabe, H., Senda, J., Hirayama, M., Ito, M., Atsuta, N., et al. (2012). Widespread cortical and subcortical brain atrophy in Parkinson's disease with excessive daytime sleepiness. *J. Neurol.* 259, 318–326. doi: 10.1007/s00415-011-6187-6

Kaynak, D., Kiziltan, G., Kaynak, H., Benbir, G., and Uysal, O. (2005). Sleep and sleepiness in patients with Parkinson's disease before and after dopaminergic treatment. *Eur. J. Neurol.* 12, 199–207. doi: 10.1111/j.1468-1331.2004.00971.x

Knie, B., Mitra, M. T., Logishetty, K., and Chaudhuri, K. R. (2011). Excessive daytime sleepiness in patients with Parkinson's disease. *CNS Drugs* 25, 203–212.

Lledo, P. M., Alonso, M., and Grubb, M. S. (2006). Adult neurogenesis and functional plasticity in neuronal circuits. *Nat. Rev. Neurosci.* 7, 179–193. doi: 10.1038/nrn1867

Marek, K., Jennings, D., Lasch, S., Siderowf, A., Tanner, C., Simuni, T., et al. (2011). The parkinson progression marker initiative (PPMI). *Prog. Neurobiol.* 95, 629–635.

Matsui, H., Nishinaka, K., Oda, M., Hara, N., Komatsu, K., Kubori, T., et al. (2006). Excessive daytime sleepiness in Parkinson disease: a SPECT study. *Sleep* 29, 917–920. doi: 10.1093/sleep/29.7.917

McKeown, M. J., Uthama, A., Abugharbieh, R., Palmer, S., Lewis, M., and Huang, X. (2008). Shape (but not volume) changes in the thalami in Parkinson disease. *BMC Neurol.* 8:8. doi: 10.1186/1471-2377-8-8

Meindorfner, C., Körner, Y., Möller, J. C., Stiasny–Kolster, K., Oertel, W. H., and Krüger, H. P. (2005). Driving in Parkinson's disease: mobility, accidents, and sudden onset of sleep at the wheel. *Mov. Disord.* 20, 832–842. doi: 10.1002/mds.20412

Menke, R. A., Szewczyk–Krolikowski, K., Jbabdi, S., Jenkinson, M., Talbot, K., Mackay, C. E., et al. (2014). Comprehensive morphometry of subcortical grey matter structures in early-stage Parkinson's disease. *Hum. Brain Mapp.* 35, 1681–1690. doi: 10.1002/hbm.22282

Molochnikov, I., and Cohen, D. (2014). Hemispheric differences in the mesostriatal dopaminergic system. *Front. Syst. Neurosci.* 8:110. doi: 10.3389/fnsys.2014.00110

Nasreddine, Z. S., Phillips, N. A., Bédirian, V., Charbonneau, S., Whitehead, V., Collin, I., et al. (2005). The Montreal cognitive assessment, MoCA: a brief screening tool for mild cognitive impairment. *J. Am. Geriatr. Soc.* 53, 695–699. doi: 10.1111/j.1532-5415.2005.53221.x

Nemmi, F., Sabatini, U., Rascol, O., and Péran, P. (2015). Parkinson's disease and local atrophy in subcortical nuclei: insight from shape analysis. *Neurobiol. Aging* 36, 424–433. doi: 10.1016/j.neurobiolaging.2014.07.010

Pagano, G., Molloy, S., Bain, P. G., Rabiner, E. A., Chaudhuri, K. R., Brooks, D. J., et al. (2016). Sleep problems and hypothalamic dopamine D3 receptor availability in Parkinson disease. *Neurology* 87, 2451–2456. doi: 10.1212/wnl.0000000000003396

Patenaude, B., Smith, S. M., Kennedy, D. N., and Jenkinson, M. (2011). A Bayesian model of shape and appearance for subcortical brain segmentation. *Neuroimage* 56, 907–922. doi: 10.1016/j.neuroimage.2011.02.046

Péran, P., Cherubini, A., Assogna, F., Piras, F., Quattrocchi, C., Peppe, A., et al. (2010). Magnetic resonance imaging markers of Parkinson's disease nigrostriatal signature. *Brain* 133, 3423–3433. doi: 10.1093/brain/awq212

Pitcher, T. L., Melzer, T. R., Macaskill, M. R., Graham, C. F., Livingston, L., Keenan, R. J., et al. (2012). Reduced striatal volumes in Parkinson's disease: a magnetic resonance imaging study. *Transl. Neurodegen.* 1:17.

Rosenzweig, I., Kempton, M. J., Crum, W. R., Glasser, M., Milosevic, M., Beniczky, S., et al. (2013). Hippocampal hypertrophy and sleep apnea: a role for the ischemic preconditioning? *PLoS One* 8:e83173. doi: 10.1371/journal.pone.0083173

Seifert, C. L., Magon, S., Sprenger, T., Lang, U. E., Huber, C. G., Denier, N., et al. (2015). Reduced volume of the nucleus accumbens in heroin addiction. *Eur. Arch. Psychiatry Clin. Neurosci.* 265, 637–645. doi: 10.1007/s00406-014-0564-y

Simuni, T., Caspell-Garcia, C., Coffey, C., Chahine, L. M., Lasch, S., Oertel, W. H., et al. (2015). Correlates of excessive daytime sleepiness in de novo Parkinson's disease: a case control study. *Mov. Disord.* 30, 1371–1381. doi: 10.1002/mds.26248

Smith, S. M., and Nichols, T. E. (2009). Threshold-free cluster enhancement: addressing problems of smoothing, threshold dependence and localisation in cluster inference. *Neuroimage* 44, 83–98. doi: 10.1016/j.neuroimage.2008.03.061

Smith, S. M., Zhang, Y., Jenkinson, M., Chen, J., Matthews, P., Federico, A., et al. (2002). Accurate, robust, and automated longitudinal and cross-sectional brain change analysis. *Neuroimage* 17, 479–489. doi: 10.1006/nimg.2002.1040

Sterling, N. W., Du, G., Lewis, M. M., Dimaio, C., Kong, L., Eslinger, P. J., et al. (2013). Striatal shape in Parkinson's disease. *Neurobiol. Aging* 34, 2510–2516. doi: 10.1016/j.neurobiolaging.2013.05.017

Stiasny–Kolster, K., Mayer, G., Schäfer, S., Möller, J. C., Heinzel–Gutenbrunner, M., and Oertel, W. H. (2007). The REM sleep behavior disorder screening questionnaire—a new diagnostic instrument. *Mov. Disord.* 22, 2386–2393. doi: 10.1002/mds.21740

Tanner, J. J., Mcfarland, N. R., and Price, C. C. (2017). Striatal and hippocampal atrophy in idiopathic Parkinson's disease patients without dementia: a morphometric analysis. *Front. Neurol.* 8:139. doi: 10.3389/fneur.2017.00139

Uitti, R. J., Baba, Y., Whaley, N., Wszolek, Z. K., and Putzke, J. (2005). Parkinson disease: handedness predicts asymmetry. *Neurology* 64, 1925–1930. doi: 10.1212/01.wnl.0000163993.82388.c8

van den Bogaard, S. J., Dumas, E. M., Ferrarini, L., Milles, J., Van Buchem, M. A., Van Der Grond, J., et al. (2011). Shape analysis of subcortical nuclei in Huntington's disease, global versus local atrophy–results from the TRACK-HD study. *J. Neurol. Sci.* 307, 60–68. doi: 10.1016/j.jns.2011.05.015

Weintraub, D., Oehlberg, K. A., Katz, I. R., and Stern, M. B. (2006). Test characteristics of the 15-item geriatric depression scale and Hamilton depression rating scale in Parkinson disease. *Am. J. Geriatr. Psychiatry* 14, 169–175. doi: 10.1097/01.jgp.0000192488.66049.4b

Wen, M. C., Chan, L., Tan, L., and Tan, E. (2017). Mood and neural correlates of excessive daytime sleepiness in Parkinson's disease. *Acta Neurol. Scand.* 136, 84–96. doi: 10.1111/ane.12704

Wen, M. C., Ng, S. Y., Heng, H. S., Chao, Y. X., Chan, L. L., Tan, E. K., et al. (2016). Neural substrates of excessive daytime sleepiness in early drug naïve Parkinson's disease: a resting state functional MRI study. *Parkinson. Relat. Disord.* 24, 63–68. doi: 10.1016/j.parkreldis.2016.01.012

Yousaf, T., Pagano, G., Niccolini, F., and Politis, M. (2018a). Excessive daytime sleepiness may be associated with caudate denervation in Parkinson disease. *J. Neurol. Sci.* 387, 220–227. doi: 10.1016/j.jns.2018.02.032

Yousaf, T., Pagano, G., Wilson, H., and Politis, M. (2018b). Neuroimaging of sleep disturbances in movement disorders. *Front. Neurol.* 9:767. doi: 10.3389/fneur.2018.00767

Yu, S., Feng, F., Zhang, Q., Shen, Z., Wang, Z., Hu, Y., et al. (2018). Gray matter hypertrophy in primary insomnia: a surface-based morphometric study. *Brain Imaging Behav*. doi: 10.1007/s11682-018-9992-z [Epub ahead of print].

Conflict of Interest: The authors declare that the research was conducted in the absence of any commercial or financial relationships that could be construed as a potential conflict of interest.

frontiers
in Neuroscience

ORIGINAL RESEARCH
published: 13 May 2020
doi: 10.3389/fnins.2020.00259

Early Detection of Alzheimer's Disease Using Magnetic Resonance Imaging: A Novel Approach Combining Convolutional Neural Networks and Ensemble Learning

Dan Pan[1], *An Zeng*[1,2]*, *Longfei Jia*[1], *Yin Huang*[1], *Tory Frizzell*[3] *and Xiaowei Song*[3] *for the Alzheimer's Disease Neuroimaging Initiative (ADNI)*[†]

[1] School of Computers, Guangdong University of Technology, Guangzhou, China, [2] Guangdong Key Laboratory of Big Data Analysis and Processing, Guangzhou, China, [3] SFU ImageTech Lab, Surrey Memorial Hospital, Fraser Health, Surrey, BC, Canada

Edited by:
Yu-Chien Wu,
Indiana University Bloomington,
United States

Reviewed by:
Giuseppe Jurman,
Fondazione Bruno Kessler, Italy
Han Zhang,
University of North Carolina at
Chapel Hill, United States

Correspondence:
An Zeng
zengan@gdut.edu.cn

[†] Alzheimer's Disease Neuroimaging Initiative – Data used in preparation of this article were obtained from the Alzheimer's Disease Neuroimaging Initiative (ADNI) database (adni.loni.usc.edu). As such, the investigators within the ADNI contributed to the design and implementation of ADNI and/or provided data but did not participate in analysis or writing of this report. A complete listing of ADNI investigators can be found at: http://adni.loni.usc.edu/wp-content/uploads/how_to_apply/ADNI_Acknowledgement_List.pdf

Specialty section:
This article was submitted to
Brain Imaging Methods,
a section of the journal
Frontiers in Neuroscience

Received: *27 September 2019*
Accepted: *09 March 2020*
Published: *13 May 2020*

Citation:
Pan D, Zeng A, Jia L, Huang Y, Frizzell T and Song X (2020) Early Detection of Alzheimer's Disease Using Magnetic Resonance Imaging: A Novel Approach Combining Convolutional Neural Networks and Ensemble Learning. Front. Neurosci. 14:259. doi: 10.3389/fnins.2020.00259

Early detection is critical for effective management of Alzheimer's disease (AD) and screening for mild cognitive impairment (MCI) is common practice. Among several deep-learning techniques that have been applied to assessing structural brain changes on magnetic resonance imaging (MRI), convolutional neural network (CNN) has gained popularity due to its superb efficiency in automated feature learning with the use of a variety of multilayer perceptrons. Meanwhile, ensemble learning (EL) has shown to be beneficial in the robustness of learning-system performance via integrating multiple models. Here, we proposed a classifier ensemble developed by combining CNN and EL, i.e., the CNN-EL approach, to identify subjects with MCI or AD using MRI: i.e., classification between (1) AD and healthy cognition (HC), (2) MCIc (MCI patients who will convert to AD) and HC, and (3) MCIc and MCInc (MCI patients who will not convert to AD). For each binary classification task, a large number of CNN models were trained applying a set of sagittal, coronal, or transverse MRI slices; these CNN models were then integrated into a single ensemble. Performance of the ensemble was evaluated using stratified fivefold cross-validation method for 10 times. The number of the intersection points determined by the most discriminable slices separating two classes in a binary classification task among the sagittal, coronal, and transverse slice sets, transformed into the standard Montreal Neurological Institute (MNI) space, acted as an indicator to assess the ability of a brain region in which the points were located to classify AD. Thus, the brain regions with most intersection points were considered as those mostly contributing to the early diagnosis of AD. The result revealed an accuracy rate of 0.84 ± 0.05, 0.79 ± 0.04, and 0.62 ± 0.06, respectively, for classifying AD vs. HC, MCIc vs. HC, and MCIc vs. MCInc, comparable to previous reports and a 3D deep learning approach (3D-SENet) based on a more state-of-the-art and popular Squeeze-and-Excitation Networks model using channel attention mechanism. Notably, the intersection points accurately located the medial temporal lobe and several other structures of the limbic system, i.e., brain regions known to be struck early in AD. More interestingly, the classifiers disclosed multiple patterned MRI changes in the brain in AD and MCIc, involving these key regions. These results suggest that as a data-driven method, the combined CNN and EL approach can locate the most discriminable brain regions indicated by the trained ensemble model while the generalization ability of the ensemble model was maximized to successfully capture AD-related brain variations early in the disease process; it can also provide new insights into understanding the complex heterogeneity of whole-brain MRI changes in AD. Further research is needed to examine the clinical implication of the finding, capability of the advocated CNN-EL approach to help understand and evaluate an individual subject's disease status, symptom burden and progress, and the generalizability of the advocated CNN-EL approach to locate the most discriminable brain regions in the detection of other brain disorders such as schizophrenia, autism, and severe depression, in a data-driven way.

Keywords: Alzheimer's disease, mild cognitive impairment, convolutional neural networks, ensemble learning, magnetic resonance imaging, MRI biomarkers, MCI-to-AD conversion, Alzheimer's Disease Neuroimaging Initiative

INTRODUCTION

Alzheimer's disease (AD) is a chronic, progressive, and irreversible neurodegenerative disease clinically manifested by amnesia, cognitive dysfunction, and gradual loss of multiple other brain functions and daily living independency (Ulep et al., 2018). The number of patients with AD worldwide is expected to increase from the current 47 million to 152 million by 2050, causing serious economic, medical, and societal consequences (Christina, 2018). The pathogenesis of AD remains not fully elucidated and no available therapy can cure AD or completely stop disease progression. Amnestic mild cognitive impairment (MCI) is a transitional stage between cognitively normal aging and AD, and patients with MCI are more likely to develop AD than age-matched healthy cognition (HC) (Liu et al., 2014). Early detection of AD by screening MCI is crucial both for effective management and care strategies and for developing new drugs and measures to prevent further deterioration of the disease.

Brain magnetic resonance imaging (MRI) has enabled non-invasive *in vivo* investigations of AD-related changes in the brain. A large number of promising machine learning applications have used MRI for AD prediction (Mateos-Pérez et al., 2018), which include random forests (RF) (Tripoliti et al., 2011), support vector machine (SVM) (Leemput et al., 2002), and boosting algorithms (Hinrichs et al., 2009). Even so, existing machine learning approaches typically involve manual selection of pre-defined brain regions of interest (ROIs) based on known MRI features of AD. Given the limited understanding of definitive MRI biomarkers for AD, it is likely that pre-selected ROIs cannot include all the information potentially useful to uncover the complexity of AD. Manual selection can also be prone to subjective errors and be time-consuming and labor-intensive (Li et al., 2018).

Deep learning represents a more advanced approach; methods such as stacked auto-encoder (SAE) (Vincent et al., 2010), deep belief networks (DBNs) (Hinton, 2009), and convolutional neural networks (CNNs) (LeCun, 2015) can automatically build a more abstract high-level representation of the learning system by integrating low-level features embedded in the data (Sun et al., 2012). The CNN model has been widely used for classification (Krizhevsky et al., 2012), segmentation (Long et al., 2015), and object detection (Girshick et al., 2014), due to several advantages: CNNs can directly accept images data as input, utilize spatial information embedded in adjacent pixels, and effectively reduce the number of model parameters by using local receptive fields, weights sharing, and subsampling. When a CNN model is trained with MRI slices, image features can be automatically retrieved, eliminating the need of manual selection of features for the learning process (Lin et al., 2018). Meanwhile, ensemble learning (EL) has shown beneficial in the performance and robustness via integrating multiple learning systems (Opitz and Maclin, 1999), which has also been applied to MRI (Ortiz et al., 2016).

So far, some researchers have combined deep learning and EL on MRI data for AD. A method for AD and early AD diagnosis by fusing functional and structural imaging data based on the use of the Deep Learning paradigm, and more specifically, deep belief networks (DBN) has been advocated (Ortiz et al., 2016). Gray matter (GM) images from each brain area have been split into 3D patches according to the regions defined by the Automated Anatomical Labeling (AAL) atlas, and these patches were used to train a set of DBNs. The DBNs were then ensembled where the final prediction was determined by a voting scheme. Two deep learning based structures and four different voting schemes were implemented and compared, giving as a result a potent classification architecture where discriminative features were computed in an unsupervised fashion (Ortiz et al., 2016). Islam and Zhang (2018) proposed an ensemble of three deep CNNs with slightly different configurations for Alzheimer's disease diagnosis using brain MRI data analysis. In addition, sparse regression models were combined with deep neural networks for AD diagnosis (Suk et al., 2017). Here, sparse regression models with different regularization control values outputted their own prediction values. To obtain the final prediction values, CNNs discovered the optimal weights to ensemble multiple sparse regression models in a hierarchical and non-linear way (Suk et al., 2017). In 2019, 20 white matter and GM slices with significant brain structures from MR images were selected to train an ensemble of ConvNet networks (Ji et al., 2019). In Li et al. (2018), a whole MR brain image was partitioned into different local regions and a number of 3D patches were extracted from each region. Subsequently, the authors grouped the patches from each region into different clusters with the K-Means clustering method. Next, a DenseNet was constructed to learn the patch features for each cluster and the features acquired from the discriminative clusters of each region were ensembled for classification. At the end, the authors combined the classification results from different local regions to improve final image classification.

In the present study, we proposed a novel CNN–EL approach based on an established eight-layer CNN network structure (Wang et al., 2018), to automatically retrieve features from brain MRI data that can be used to differentiate subjects with clinical diagnosed AD and MCI from HC, and those with MCIc and MCInc. We are also interested in identifying patterns of MRI brain changes that characterize AD and MCIc. To achieve the study objectives, we first derived a CNN model using each set of the sagittal, coronal, or transverse MRI slices; then, we developed a classifier ensemble based on three-axis slices using EL. A number of sophisticated techniques were employed in our approach, which included six ways of data augmentation (DA) to facilitate an equal and relatively large number of instances of each class in the training dataset, top-performance enforcing to achieve a high classification accuracy and robustness of the model training, and parallel processing to improve the time efficiency of the system function.

In the CNN-EL, a data-driven, homogeneous ensemble learning approach was employed. A base classifier based on 2D CNN model was trained using each set of the sagittal, coronal, or transverse MRI slices; that is, a trained base classifier corresponds to a slice dataset, which is composed of slices in a specific position in brain from the subjects in the training dataset. The preparations of training datasets didn't depend on prior experience or domain knowledge. In order to reduce the loss of information as much as possible during the process of slicing the 3D volume into 2D slices, we have utilized as many and meaningful 2D-sagittal, -coronal, or -transverse slices from all over the brain as we can at the same time to train the base classifiers. Among them, the trained base classifiers with the best generalization performance on the validation datasets were selected and combined to generate a refined final classifier ensemble based on three-axis slices. In this data-driven way, the slices corresponding to the selected trained base classifiers were considered as those with the strongest capabilities to classify AD. The number of the intersection points determined by the most discriminable slices separating two classes in a binary classification task among the sagittal, coronal, and transverse slice-sets, transformed into the standard Montreal Neurological Institute (MNI) space, acted as an indicator to assess the ability of a brain region in which the points were located to classify AD. Thus, we located the most discriminable brain regions indicated by the trained CNN-EL model while its generalization abilities were maximized and superior to those of the compared methods. That is, we can understand the predictions made by the trained CNN-EL model to some extent. However, the compared methods, i.e., PCA + SVM (Christian et al., 2015) and a 3D deep learning approach (3D-SENet) based on a more state-of-the-art and popular Squeeze-and-Excitation Networks model using channel attention mechanism, which was derived from the paper (Hu et al., 2018), were unable to do the same thing as the above-mentioned and failed to provide meaningful explanations for predictions since the models achieved with those compared methods were still like a "black-box". To our knowledge, this is the first attempt to do the above way with both CNN and EL, and at the same time, the promising experimental results have been achieved.

In detail, the CNN-EL was different from the above-mentioned methods which combined the deep learning with the ensemble learning to analyze MRI data for detecting AD in the base classifiers (Ortiz et al., 2016; Suk et al., 2017; Islam and Zhang, 2018; Li et al., 2018), the ensemble methods (Ortiz et al., 2016; Suk et al., 2017; Islam and Zhang, 2018), the model interpretability (Ortiz et al., 2016; Suk et al., 2017; Islam and Zhang, 2018), or the preparation of training datasets (Ortiz et al., 2016; Li et al., 2018; Ji et al., 2019).

Furthermore, in the paper (Wen et al., 2019), the authors firstly systematically and critically reviewed the state-of-the-art on classification of Alzheimer's disease based on convolutional neural networks and T1-weighted MRI. Next, they proposed an open-source framework for reproducible evaluation of classification approaches. In this study, the fivefold cross validation procedure was strictly followed and repeated ten times for each binary experiment, i.e., AD vs. HC, MCIc vs. HC, and MCIc vs. MCInc. The potential data leakage among binary classification tasks was avoided and therefore the experimental results were unbiased and reproducible.

MATERIALS AND METHODS

Participants and Datasets

Data used in the study were obtained from the Alzheimer's Disease Neuroimaging Initiative (ADNI) database.[1] The ADNI was launched in 2003 as a public–private partnership, led by Principal Investigator, Michael W. Weiner, MD. The primary goal of ADNI has been to test whether serial MRI, positron emission tomography (PET), other biological markers, and clinical and neuropsychological assessment can be combined to measure the progression of MCI and early AD.

To facilitate comparison of our results with those reported previously, we used the same MRI dataset from the ADNI database as utilized by Christian et al. (2015) in building the eight-layer CNN networks (Wang et al., 2018) to train the base classifiers, as well as to test the performance of the final classifier ensemble based on three-axis slices (n = 509 subjects:

---

[1] adni.loni.usc.edu

TABLE 1 | Characteristics of participants in **(A)** the training and testing dataset (upper panel) and **(B)** the validation dataset (lower panel).

Variable	AD	MCIc	MCInc	HC
(A)				
N	137	76	134	162
Gender (male:female)	67:70	43:33	84:50	86:76
Age (year; mean, std)	76.0,7.3	74.8, 7.3	74.5, 7.2	76.3, 5.4
Weight (kg; mean, std)	70.9, 14.0	72.7, 14.3	76.2, 12.9	73.8, 13.6
MMSE (mean, std)	23.2, 2.0	26.47, 1.84	27.19, 1.71	29.18, 0.96
CDR (mean, std)	0.75, 0.25	0.50, 0.00	0.50, 0.00	0.00, 0.00
GDS (mean, std)	1.59, 1.32	1.38, 1.14	1.52, 1.37	0.80, 1.08
(B)				
N	100	39	39	100
Gender (male:female)	60:40	23:16	29:10	45:55
Age (years; mean, std)	74.24, 7.82	74.15, 7.10	76.02, 7.00	73.36, 5.70
Weight (kg; mean, std)	76.04, 15.83	73.59, 14.14	78.35, 12.99	76.16, 15.66
MMSE (mean, std)	23.84, 2.08	27.05, 1.59	27.56, 1.83	28.92, 1.25
CDR (mean, std)	0.82, 0.24	0.50, 0.00	0.50, 0.00	0.00, 0.00
GDS (mean, std)	1.81, 1.56	1.92, 1.35	1.79, 1.45	0.83, 1.34

AD, Alzheimer's disease patients; MCIc, mild cognitive impairment patients who will convert to AD; MCInc, mild cognitive impairment patients who will not convert to AD; HC, healthy controls; MMSE, Mini Mental State Examination; CDR, Clinical Dementia Rating; GDS, Global Deterioration Scale.

$AD = 137$, 18 months MCIc = 76 and MCInc = 134, and $HC = 162$; **Table 1A**). We enrolled 162 cognitively normal elderly controls (HC), 137 patients with diagnosis of AD, 76 patients with diagnosis of MCI who converted to AD within 18 months (MCIc), and 134 patients with diagnosis of MCI who did not convert to AD within 18 months (MCInc). MCI patients who had been followed less than 18 months were not considered (Christian et al., 2015). A total of 509 subjects from 41 different radiology centers were considered. Inclusion criteria for HC were as follows: Mini Mental State Examination (MMSE) scores between 24 and 30; Clinical Dementia Rating (CDR) (Morris, 1993) of zero; and absence of depression, MCI, and dementia. Inclusion criteria for MCI were as follows: MMSE scores between 24 and 30; CDR of 0.5; objective memory loss, measured by education adjusted scores on Wechsler Memory Scale Logical Memory II (Wechsler, 1987); absence of significant levels of impairment in other cognitive domains; and absence of dementia. Inclusion criteria for AD were as follows: MMSE scores between 20 and 26; CDR of 0.5 or 1.0; and NINCDS/ADRDA criteria for probable AD (McKhann et al., 1984; Dubois et al., 2007).

To facilitate the development of the EL process, an additional validation dataset of 278 subjects ($AD = 100$, 36 months MCIc = 39 and MCInc = 39, and $HC = 100$; **Table 1B**) was also retrieved from the ADNI database and used to identify the base classifiers showing the best generalization performance. The validation data of 278 subjects had no overlapping with the aforementioned data of 509 subjects, i.e., the validation data were used for neither training the base classifiers nor testing the acquired final classifier ensemble based on three-axis slices (**Table 1B**). Here, among 164 patients with diagnosis of pMCI (progressive MCI) used by Moradi et al. (2015), i.e., if diagnosis was MCI at baseline but conversion to AD was reported after baseline within 1, 2, or 3 years, and without reversion to MCI or HC at any available follow-up (0–96 months), 39 patients who were not in the 509 subjects were selected as MCIc subjects in the validation dataset. Meanwhile, among 100 patients with diagnosis of sMCI (stable MCI) used by Moradi et al. (2015), i.e., if diagnosis was MCI at all available time points (0–96 months) but at least for 36 months, 39 patients who were not in the aforementioned 509 subjects were chosen as MCInc subjects in the validation dataset. In order to keep the validation dataset relatively balanced, we enrolled 100 cognitively normal elderly controls (HC) and 100 patients with diagnosis of AD who were not in the aforementioned 509 subjects as well.

MRI Preprocessing

Upon downloading, the T1-weighted MRI data in.nii format were processed using the CAT12 toolkit[2] with default value setting. The preprocessing pipeline included skull extraction, registration to the MNI space, and image smoothing, so that after processing, all the images had a dimension of $121 \times 145 \times 121$ ($X \times Y \times Z$) with a spatial resolution of $1.5 \times 1.5 \times 1.5\ \text{mm}^3$ per voxel. Voxel-based MRI signal intensity normalization was then performed for each image; i.e., the value of each voxel was normalized as the original value divided by the original maximal value of the image, yielding a value between 0 and 1. The complete preprocessing pipeline is summarized in **Figure 1**.

To facilitate the CNN training, verification, and testing, a 3D image set of each subject was re-sliced into three 2D image sets, each of the sagittal, coronal, or transverse orientation (with X, Y, and Z axes perpendicular to the sagittal, coronal, and transverse planes, respectively). A preprocessed 3D MRI image (of $121 \times 145 \times 121$) was thus re-sliced into 121 sagittal, 145 coronal, and 121 transverse slices; the values on the X, Y, and Z axis were $\{-90, -88, -87, \ldots 90\}$, $\{-126, -125, -123, \ldots 90\}$, and $\{-72, -71, -69, \ldots 108\}$, respectively. For example, $X(i)$, $i \in \{-90, -88, -87, \ldots 90\}$ is the sagittal slice through the point $[i, 0, 0]$. Here, the numbers within the brackets were the MNI coordinates. To reduce the number of base classifiers without compromising the effectiveness of the classification, every other slice was used (given the relatively small difference between two adjacent slices) and slices near either end of an axis were discarded (given the relatively less amount of information useful for classification), which lay outside the blue rectangle shown in **Figure 2**. The CNN model training, testing, and verification involved use of only 40 sagittal slices $\{X(-61), X(-58), X(56)\}$, 50 coronal slices $\{Y(-91), Y(-88), Y(56)\}$, and 33 transverse

---

[2] http://dbm.neuro.uni-jena.de/cat/

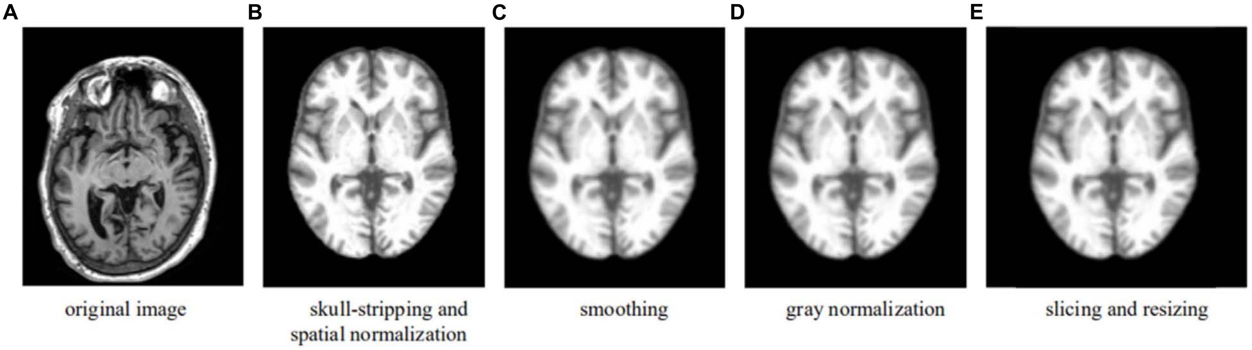

FIGURE 1 | Preprocessing pipeline—an example showing the formation of a transverse slice used in the learning. **(A)** Original image. **(B)** Skull-stripping and spatial normalization. **(C)** Smoothing. **(D)** Gray normalization. **(E)** Slicing and resizing.

slices $\{Z(-28), Z(-25), Z(68)\}$, i.e., in total, 123 slices of a subject's 3D brain image.

Given the dimension of the 3D MRI (121 × 145 × 121), the sizes of the sagittal, coronal, and transverse slices obtained through re-slicing were 145 × 121, 121 × 121, and 121 × 145, respectively. Each of the 2D slices was reformatted to 145 × 145 using edge padding and zero filling, so that the 2D slice is squared, while the center and the spatial resolution of the resized image remained unchanged.

Convolutional Neural Network

As an automated image recognition method, the CNN has attracted widespread research attention with tremendous success in recent years. Hubel and Wiesel first described receptive fields, binocular interactions, and the functional architecture of cat primary visual cortex about 55 years ago (Hubel and Wiesel, 1962, 1965). Kunihiko Fukushima proposed a neural network model nicknamed "Neocognitron" (Fukushima, 1980) that is structurally similar to the hierarchy model of the visual nervous system proposed by Hubel and Wiesel. This unique network structure can effectively reduce the complexity of feedback neural networks, which characterizes the CNN model. With the CNN, each input image is passed through a series of convolution layers: filtering layers (kernels), pooling layers, and fully connected layers (FCs). A softmax function is then applied to classify an image with probabilistic values between 0 and 1, making the CNN suitable for learning representations of image features (Schmidhuber, 2015).

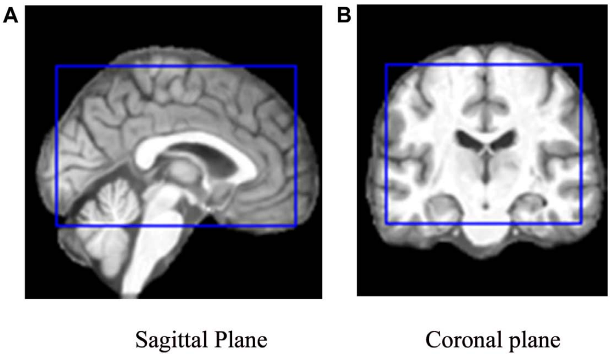

FIGURE 2 | The cropping range (inside the blue rectangle) of the slices used to train the model on **(A)** a sagittal plane and **(B)** a coronal plane, respectively. **(A)** Sagittal Plane. **(B)** Coronal plane.

A convolution layer in the CNN model is typically composed of two segments: feature extraction and feature mapping (Krizhevsky et al., 2012). In the feature-extraction segment, each neuron is connected to the local receptive field of the upper layer to extract local features. Once the local feature is extracted, its spatial relationship with other features is also determined. In the feature-mapping segment, convolution is performed on the input data using a learnable filter or kernel to produce a feature map. Feature mapping computes the outputs of neurons connected to receptive fields in the input, with each neuron computing a dot product between its weight (i.e., filter) and a local receptive field (equivalent to filter size) to which it is connected (the input volume). Multiple feature maps can be calculated with a set of learnable filters. In this way, the number of parameters to be tuned in the CNN is effectively reduced. A convolutional layer is followed by a pooling layer, e.g., max-pooling layer (Weng et al., 1992), which performs a down-sampling operation along the spatial dimensions (e.g., X, Y for a transverse slice). This unique dual-feature extraction method can effectively reduce the feature resolution (Krizhevsky et al., 2012). The basic structures of the convolutional layer and the pooling layer of the CNN model are shown in **Figure 3**.

In this study, the CNN was utilized mainly to recognize 2D images with displacement, scaling, and other non-deformed distortions. Data were reconstructed, so that an image was inputted into the CNN model as a vector for easy feature extraction and classification. The effectiveness of the CNN was improved as the pooling layer learned the features from training data without manual extraction. Applying the learnable kernels and convolution operation, the CNN was trained in parallel, while the local weight-sharing effectively reduced its complexity.

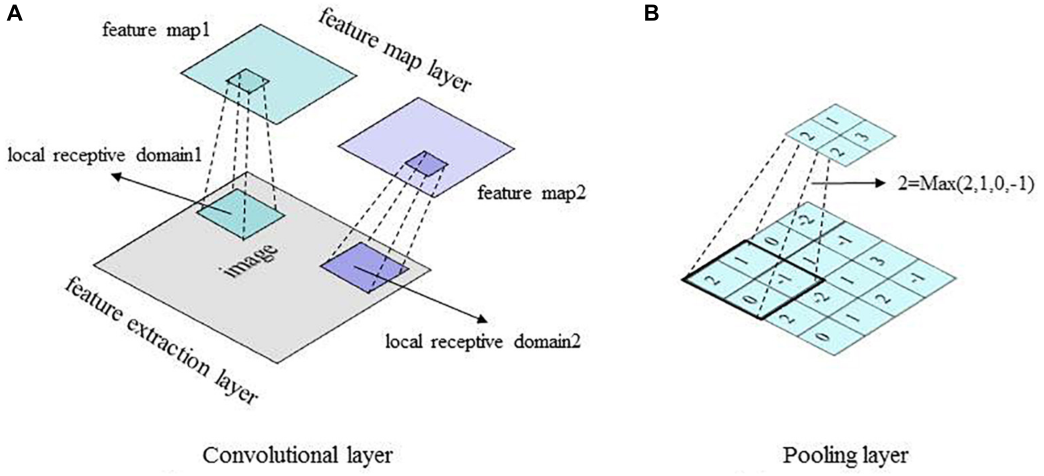

FIGURE 3 | Basic structures of the CNN convolutional layer and pooling layer. **(A)** Convolutional layer. **(B)** Pooling layer.

Ensemble Learning

EL algorithms including Bagging (Breiman, 1996), Boosting (Freund and Schapire, 1997), and Random Forest (Breiman, 2001) have been typically used to construct a set of base classifiers in solving a given problem. Using a training dataset, EL discriminates features to produce a weighted vote for classes, which is then applied in classifying more cases in new datasets. Based on the methods with which a base learner is generated, each of the EL algorithms can be divided into two general approaches: the heterogeneous approach, which applies different learning algorithms in the same training data, and the homogeneous approach, which applies the same learning algorithm in different training data (Zhang and Zhang, 2011). Both approaches have been shown to significantly improve the generalizability and robustness of a learning system.

In the present study, the homogeneous EL approach was adopted from the stratified Bagging method. The same CNN algorithm was employed to train different base classifiers using different 2D MRI slices. The outputs from the multiple trained base classifiers with the best generalization performance on the validation dataset were then combined to generate a refined final classifier ensemble based on three-axis slices that was used to predict classification results for new cases, i.e., 3D MRI data.

Classification Experiment

A total of 787 subjects' 3D MR images from the ADNI database were partitioned into three datasets: training and testing datasets to build the base classifiers and examine the performance of the final classifier ensemble based on three-axis slices (n = 509; **Table 1A**) and a verification dataset to evaluate and select the best base classifiers (n = 278; **Table 1B**). For training and testing, a stratified fivefold cross-validation method was employed, such that each binary classification task (e.g., MCIc vs. MCInc) was conducted five times. No images in the training/testing datasets were used to select the best base classifiers, and thus potential data leakage among binary classification tasks was avoided.

In each binary classification task, a total of 123 2D sagittal, coronal, and transverse slices extracted from each 3D MRI were employed to generate 123 trained base classifiers. Using classification of AD (n = 137) vs. HC (n = 162) as an example, 299 labeled 3D MRI (**Table 1A**), were partitioned into 80% training and 20% testing cases with stratified random sampling. The 299 2D slices of $X(i)$ [or $Y(j)$, or $Z(k)$] were compiled as a 2D dataset, where $i \in \{-61, -58, \ldots 56\}$, $j \in \{-91, -88, \ldots 56\}$, and $k \in \{-28, -25, \ldots 68\}$; 239 (or 80%) of stratified randomly selected cases were employed to train the $X(i)$ [or $Y(j)$, or $Z(k)$] base classifier, while the remaining slices of 60 (or 20%) cases were used to test the trained classifier ensemble based on three-axis slices. In this way, all 123 trained base classifiers to classify AD vs.HC were acquired.

Then, the 123 labeled 2D MR images from each of AD (n = 100) and HC (n = 100) cases were altogether used as the validation dataset (**Table 1B**): they were employed to select the five base classifiers (i.e., in total 15) with the best generalization performance, as determined by classification accuracy, among the sagittal, coronal, and transverse slice-based base classifiers, respectively. The number of five was determined by the experiments. Finally, after building three classifier ensembles based on single-axis slices (i.e., sagittal, coronal, and transverse), a classifier ensemble based on three-axis slices, which was composed of all the three classifier ensembles based on single-axis slices, was finally built using these 15 base classifiers, following a simple majority voting scheme (Arora et al., 2012). The 2D slices that were extracted from the 3D MR images of the remaining 60 (or 20%) cases in the training and testing dataset and were corresponding to the 15 base classifiers were used to test the performance of the built classifier ensemble based on three-axis slices.

TABLE 2 | Numbers of augmented images in the MCIc and MCInc datasets.

Augmentation methods	MCIc	MCInc	Total
Original slices	76	134	210
Rotation	1368	1340	2708
Translation	1368	1340	2708
Gamma correction	1368	1340	2708
Random noise	1368	1340	2708
Scaling	1368	1340	2708
Random affine transformation	1368	1340	2708
Total number of images in the augmented dataset	8284	8174	16,458

Data Augmentation

To overcome the possible over-fitting problem in training robust CNN models and to incorporate possible image discrepancy, augmented images were generated from the original slices by six operations: rotation, translation, gamma correction, random noise addition, scaling, and random affine transformation. The augmented data were added to the original training dataset to allow a sufficiently large sample size (**Table 2**). Data augmentation was also used to mitigate the originally imbalanced dataset (e.g., there were more subjects with MCInc than those with MCIc), for which the preset number of augmented slices to be generated varied from class to class. For example, to classify MCIc vs. MCInc, there were 76 MCIc and 134 MCInc cases. Using six data augmentation operations, 10 new slices were generated from an MCInc case and 18 from an MCIc case with each operation. In this way, slice ratios of MCInc:MCIc became ∼1:1 after data augmentation from the original ∼1.8:1.

RESULTS

Base Classifiers

To address the objective of the study, i.e., binary classification of AD or MCIc vs. HC, and MCIc vs. MCInc, three corresponding classifier ensembles based on the three slice orientation groups (sagittal, coronal, and transverse), i.e., classifier ensembles based on three-axis slices, were trained. The overall architecture of the proposed classifier ensemble based on three-axis slices is shown in **Figure 4** and the flow chart of the experiment is shown in **Figure 5**.

Each base classifier consisted of six convolution layers (conv) and two fully connected layers (FCs). The last FC layer had only two nodes, and the softmax function was used to implement the binary classification. The network architecture and corresponding hyper-parameters are shown in **Figure 6** and **Table 3**, respectively. Each base classifier was trained for 30 epochs, as 30 epochs proved sufficient for a base classifier to converge. That is, after 30 epochs, a trained base classifier could achieve 100% classification accuracy on the original slices (rather than the augmented slices) in the training dataset. Activation functions in all convolutional layers were of the leaky rectifier linear activation (LReLU) type (Shan et al., 2016), while the Adam optimization algorithm (Kingma and Ba, 2014) was used

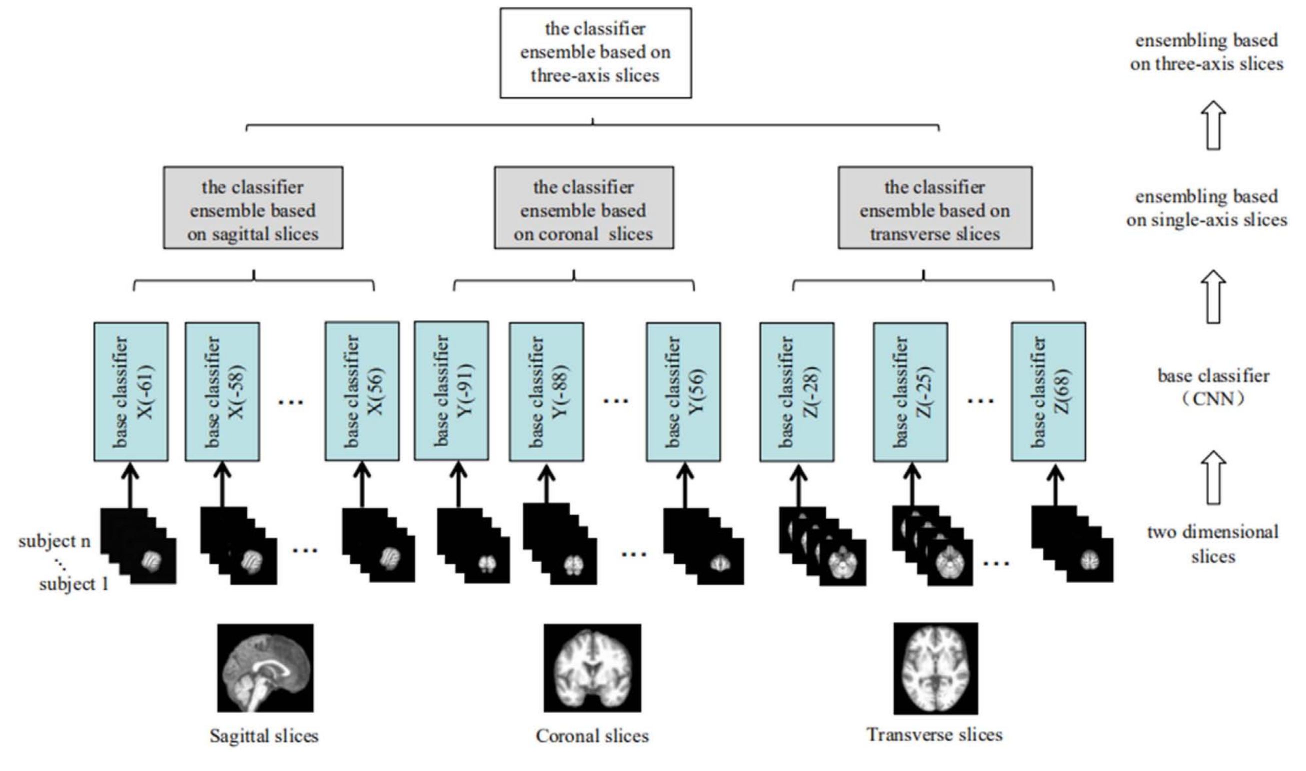

FIGURE 4 | The architecture of the classifier ensemble based on the three sets of 2D slices (from left to right: sagittal, coronal, and transverse).

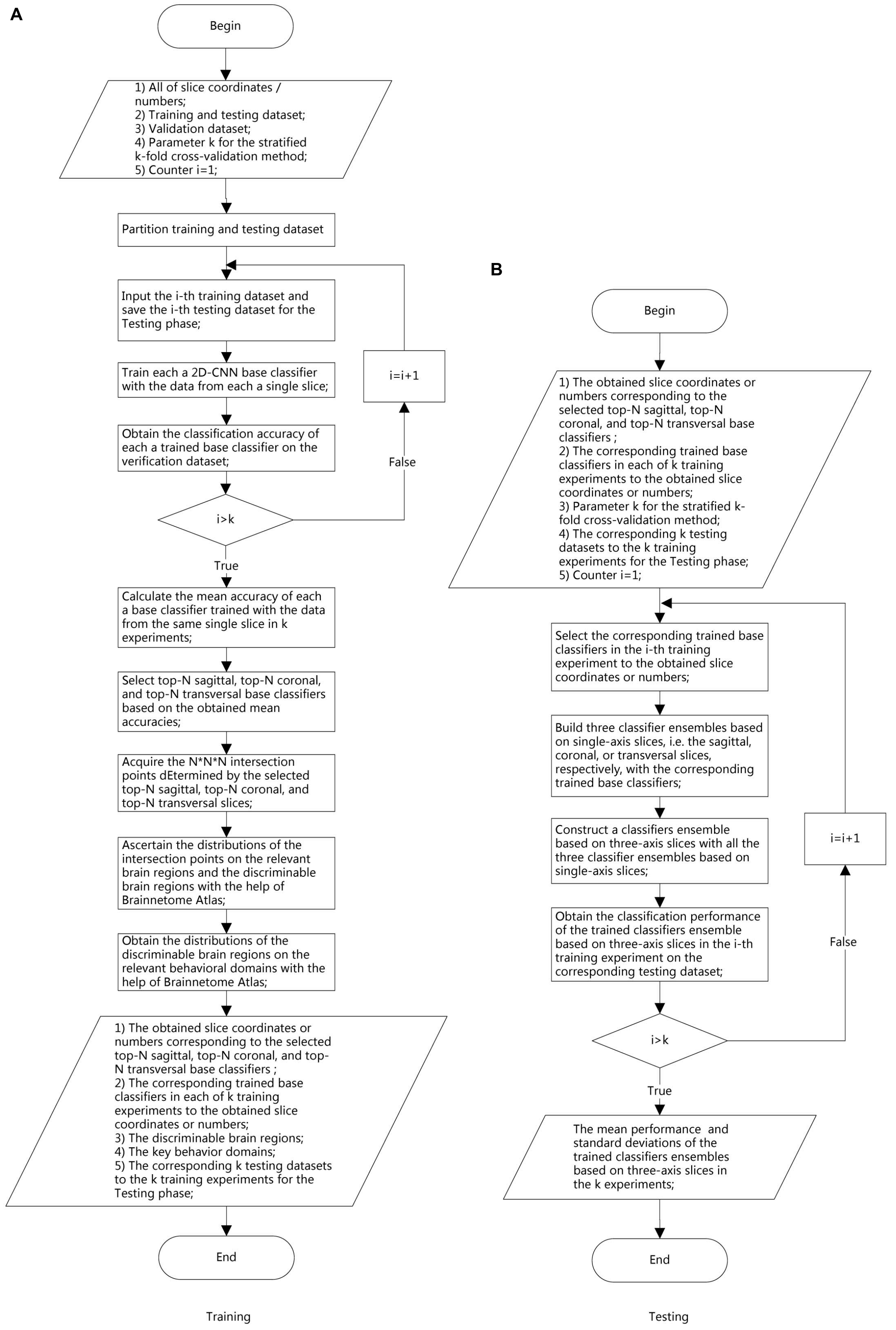

FIGURE 5 | Experimental flow chart. **(A)** Training phase. **(B)** Testing phase.

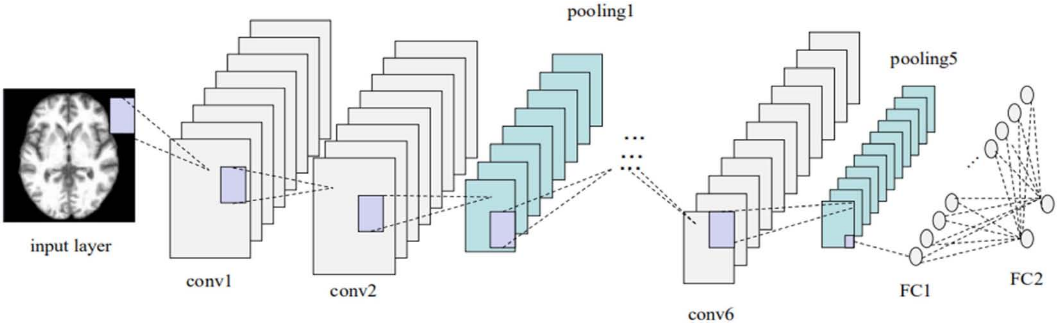

FIGURE 6 | Base-classifier architecture used in the CNN-EL approach proposed here.

to update network weights. The learning rate and the batch size were set to 0.0001 and 200, respectively.

Ensemble Learning

The proposed model employed a two-stage EL scheme. Phase 1 involved building three classifier ensembles based on single-axis slices (i.e., sagittal, coronal, and transverse) and Phase 2 involved constructing a classifier ensemble based on three-axis slices, which was composed of all the three classifier ensembles based on single-axis slices acquired in Phase 1. In total, 40 sagittal, 50 coronal, and 33 transverse base classifiers were acquired. Then, the five base classifiers with the best generalization performance for each slice orientation were selected using the verification dataset, yielding three classifier ensembles based on single-axis slices, each with the 5 best base classifiers. The output of a classifier ensemble based on single-axis slices was generated by combining the outputs of the five best base classifiers. Finally, a simple majority voting scheme was used to combine the predictions of these three classifier ensemble based on single-axis slices to yield the output of the classifier ensemble based on three-axis slices. Experimental results demonstrated that this EL method greatly improved the generalizability and robustness of early stage AD detection.

TABLE 3 | Detailed hyper-parameters of base classifiers of the CNN-EL approach advocated here.

Layer #	Layer name	Kernel size	Strides	Input channels	Output channels
1	conv1	3*3	3	1	32
2	conv2	3*3	3	32	64
	pooling1	3*3	1	N/A	N/A
3	conv3	3*3	3	64	128
	pooling2	3*3	1	N/A	N/A
4	conv4	1*1	1	128	256
	pooling3	3*3	1	N/A	N/A
5	conv5	1*1	1	256	512
	pooling4	3*3	1	N/A	N/A
6	conv6	1*1	1	512	1024
	pooling5	3*3	3	N/A	N/A
7	FC1	N/A	N/A	4096	100
8	FC2	N/A	N/A	100	2

Classification Performance

Using the stratified fivefold cross-validation procedure and repeating it 10 times, the average classification accuracies were 84% for AD vs. HC, 79% for MCIc vs. HC, and 62% for MCIc vs. MCInc. The average classification accuracies for AD vs. HC and MCIc vs. HC were statistically significantly higher than those achieved using principal component analysis (PCA) plus the SVM method described in a previous study (Christian et al., 2015), while the average classification accuracy for MCIc vs. MCInc was not statistically significantly lower (Christian et al., 2015). As for the reason why the classification accuracy for MCIc vs. MCInc task was relatively low, we suppose the performance of the proposed CNN-EL method, as a deep learning approach, which usually demands more training data, was a little bit more negatively affected by the insufficient training samples in the MCIc vs. MCInc classification task. Plus, one additional possible reason might be the cutoff threshold of follow-up duration to define MCIc and MCInc, and the cohorts of MCIc and MCInc subjects might be highly heterogeneous regardless of the threshold used (Li et al., 2019).

More importantly, the standard deviations of the classification accuracies were only 0.05 for AD vs. HC, 0.04 for MCIc vs. HC, and 0.06 for MCIc vs. MCInc, all of which were about one-third of those reported previously (Christian et al., 2015).

In this study, all of the experiments were run on one node in a GPU cluster with five nodes, each of which had two NVIDIA Tesla P100-PCIe-16GB 250W cards. For a 1 × 5-fold cross-validation process, the computing time of the CNN-EL proposed here in AD vs. HC, MCIc vs. HC, and MCIc vs. MCInc task was about 21, 19, and 15 h, respectively.

At the same time, the proposed approach here was compared with the 3D-SENet. As the central building block of CNNs, the convolution operator could enable networks to acquire informative features by fusing both spatial and channel-wise information within local receptive fields at each layer. To achieve better generalization performance, the SENet automatically learned the weight of each feature channel to enhance the useful features and suppress the useless features for the task to be tackled, by introducing "Squeeze-and-Excitation" block as a self-attention function on channels (Hu et al., 2018). Here, the architecture of the compared 3D-SENet model and corresponding detailed hyper-parameters are shown in **Figure 7**

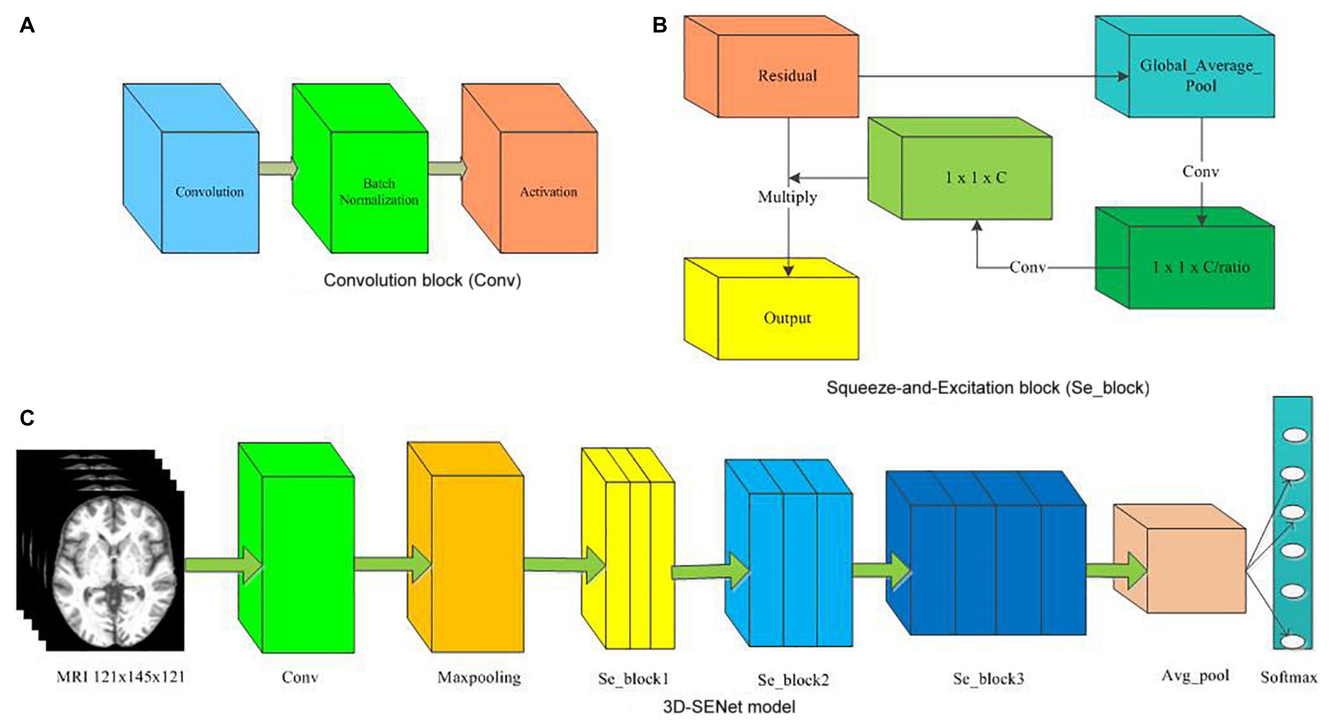

FIGURE 7 | The architecture of the 3D-SENet model. **(A)** Convolution block (Conv), **(B)** Squeeze-and-Excitation block (Se_block), **(C)** 3D-SENet model.

TABLE 4 | Detailed hyper-parameters of 3D-SENet model.

Layer name	Sub-layer name	Kernel size	Strides	Filters	Output size
MRI_images	N/A	N/A	N/A	N/A	121 × 145 × 121
Conv	N/A	3 × 3 × 3	1	64	121 × 145 × 121
Maxpooling	N/A	3 × 3 × 3	2	N/A	60 × 72 × 60
Se_block1	Block1	3 × 3 × 3	2	256	30 × 36 × 30
Se_block1	Block2	3 × 3 × 3	1	256	30 × 36 × 30
Se_block1	Block3	3 × 3 × 3	1	256	30 × 36 × 30
Se_block2	Block1	3 × 3 × 3	2	512	15 × 18 × 15
Se_block2	Block2	3 × 3 × 3	1	512	15 × 18 × 15
Se_block2	Block3	3 × 3 × 3	1	512	15 × 18 × 15
Se_block3	Block1	3 × 3 × 3	2	1024	8 × 9 × 8
Se_block3	Block2	3 × 3 × 3	1	1024	8 × 9 × 8
Se_block3	Block3	3 × 3 × 3	1	1024	8 × 9 × 8
Se_block3	Block4	3 × 3 × 3	1	1024	8 × 9 × 8
Avg_pool	N/A	8 × 9 × 8	1	1024	1 × 1 × 1024
Softmax	N/A	N/A	N/A	N/A	2

and **Table 4**, respectively. With 10 × 5-fold cross-validation processes, the accuracy rates of 0.80 ± 0.05, 0.75 ± 0.07, and 0.57 ± 0.11 were obtained, respectively, for classifying AD vs. HC, MCIc vs. HC, and MCIc vs. MCInc. For a 1 × 5-fold cross-validation process, the computing time of the 3D-SENet in AD vs. HC, MCIc vs. HC, and MCIc vs. MCInc task was about 11.5, 10.9, and 10.6 h, respectively.

In order to evaluate the classification performance more comprehensively, the Area Under the Curve (AUC) and Matthews Correlation Coefficient (MCC) (Matthews, 1975) have been used as the performance metrics in this study as well. To verify whether or not our performance is different from those of two methods, i.e., Christian et al. (2015) and the 3D-SENet model, we have further run six hypothesis tests (*p*-value approach) for three binary experiments, i.e., AD vs. HC, MCIc vs. HC, and MCIc vs. MCInc. After the homogeneity of variance test was performed, the Student's *t*-test with the Cox-Cochran correction for unequal variances was applied if

TABLE 5 | Comparison of experimental results with PCA + SVM (Christian et al., 2015) and 3D-SENet.

Experiment model	AD vs. HC			MCIc vs. HC			MCIc vs. MCInc		
	ACC	**AUC**	**MCC**	**ACC**	**AUC**	**MCC**	**ACC**	**AUC**	**MCC**
PCA + SVM	0.76 ± 0.11	–	–	0.72 ± 0.12	–	–	0.66 ± 0.16	–	–
3D-SENet	0.80 ± 0.05	0.88 ± 0.04	0.62 ± 0.09	0.75 ± 0.07	0.79 ± 0.07	0.42 ± 0.16	0.57 ± 0.11	0.57 ± 0.08	0.11 ± 0.15
CNN + EL proposed here	0.84 ± 0.05	0.92 ± 0.03	0.68 ± 0.10	0.79 ± 0.04	0.83 ± 0.06	0.49 ± 0.12	0.62 ± 0.06	0.59 ± 0.07	0.10 ± 0.15

the homogeneity of variance test failed. Experimental results and corresponding statistical performance comparisons with p-values are summarized in **Tables 5**, **6**, respectively. For all three binary classification tasks, the average classification accuracies of the CNN-EL were statistically significantly higher than those achieved using the 3D-SENet, while the standard deviations of the CNN-EL were lower than or equal to those of the 3D-SENet.

It can be seen that the proposed early detection model for Alzheimer's disease based on CNN and EL was more accurate and robust than the PCA plus SVM method (Christian et al., 2015) and the 3D-SENet model.

Discriminable Brain Regions

In the first phase of EL, the validation set was employed to examine each base classifier and subsequently to acquire three classifier ensembles based on each of the three single-axis slice datasets, each comprising of the best five sagittal, coronal, and transverse base classifiers in generalization capabilities. As a base classifier corresponds to a slice dataset, all 15 best base classifiers correspond to 15 slices in the X–Y–Z coordinate system, which can define $5 \times 5 \times 5$ points in the X–Y–Z coordinate system. As an example, the sagittal, coronal, and transverse slice numbers corresponding to the 15 best base classifiers for the first time to run the stratified fivefold cross-validation procedure are shown in **Table 7**.

Take the AD vs. HC classification task for the first time to run the stratified fivefold cross-validation procedure as an example. One hundred twenty-five points in the X–Y–Z coordinate system were determined by the top 5 sagittal, coronal, and transverse slices, respectively, e.g., (22, −5, −23), (20, −17, −25)… (28, −7, −11). These 125 points were mapped onto various brain regions using the Brainnetome Atlas (Fan et al., 2016), which can facilitate investigation of structure-function relationships and comparative neuroanatomical studies. The Brainnetome Atlas currently contains 246 regions of the bilateral hemispheres. Moreover, the atlas connectivity-based parcellation-yielded regions are functionally defined according to behavioral domain and paradigm class meta-data labels of the BrainMap database[3] using forward and reverse inferences. The brain regions corresponding to the 125 points in the standard MNI space were located with the help of the Brainnetome Atlas. In this way, the brain regions with particularly significant contributions to the classification were identified according to the number of intersection points located in those regions. Here, the number of the intersection points determined by the most discriminable slices separating two classes in a binary classification task among the sagittal, coronal, and transverse slice sets, transformed into the standard MNI space, acted as an indicator to assess the contributions of a brain region in which the points were located to classifying AD. Given that the brain regions in a discriminable slice contribute to the classification

TABLE 6 | Statistical comparisons with p-values about accuracy mean of the three methods for **(A)** AD vs. HC task (upper panel), **(B)** MCIc vs. HC task (middle panel), and **(C)** MCIc vs. MCInc task (lower panel).

Model	PCA + SVM	3D-SENet	CNN + EL proposed here
(A)			
PCA + SVM	N/A	$p > 0.05$	$p < 0.05$
3D-SENet	$p > 0.05$	N/A	$p < 0.05$
CNN + EL proposed here	$p < 0.05$	$p < 0.05$	N/A
(B)			
PCA + SVM	N/A	$p > 0.05$	$p < 0.05$
3D-SENet	$p > 0.05$	N/A	$p < 0.05$
CNN + EL proposed here	$p < 0.05$	$p < 0.05$	N/A
(C)			
PCA + SVM	N/A	$p < 0.05$	$p > 0.05$
3D-SENet	$p < 0.05$	N/A	$p < 0.05$
CNN + EL proposed here	$p > 0.05$	$p < 0.05$	N/A

TABLE 7 | Sagittal, coronal, and transverse slice numbers corresponding to the 15 best base classifiers for the first time to run the stratified fivefold cross-validation procedure.

Experiment	Rank	Sagittal slice #	Coronal slice #	Transverse slice #
AD vs. HC	1	22	−5	−23
	2	20	−17	−25
	3	16	−13	−19
	4	−20	−23	−17
	5	28	−7	−11
MCIc vs. HC	1	16	−13	−17
	2	20	−7	−25
	3	14	−11	−7
	4	26	−31	−23
	5	−20	−5	−29
MCIc vs. MCInc	1	−46	−13	−23
	2	−16	7	−19
	3	−44	−1	55
	4	−56	−79	−25
	5	−50	−35	−29

---

[3] http://www.brainmap.org/taxonomy

of AD, we cannot deny the fact that a brain region at which an intersection point formed by three discriminable sagittal, coronal, and transverse slices is located contributes most to the classification of AD among all the brain regions that existed in the sagittal, coronal or transverse discriminable slice since the brain region exists in the three slices at the same time.

In this way, for all the 10 × 5-fold cross-validation processes, the number of all the intersection points located in the same brain region is summed to measure the ability of the brain region to classify AD. The brain regions identified with the most intersection points might be the most discriminable for a binary classification task. Thus, the details of the identified brain regions with the classification capacity are shown in **Figure 8** and **Tables 8a–c**. It is notable that the sum of the last column (i.e., the number of points located in a brain region) in each of the three tables was less than 1250 since some intersection points were located in the unlabeled brain regions. In **Figure 8**, values on the vertical and the horizontal axes represent the brain region labels and the number of intersection points located in each brain region, respectively. The prefix capital letters R and L of a brain region label (e.g., R.rHipp) refer to the right and left cerebral hemispheres, respectively.

From the above figures and tables, the most discriminable brain regions in the AD vs. HC classification task were the rostral hippocampus (Greene et al., 2012), medial amygdala (Nelson et al., 2018), globus pallidus (Baloyannis, 2006), lateral amygdala (Kile et al., 2009), area 28/34 (EC, entorhinal cortex), and caudal area 35/36, i.e., parahippocampal gyrus (van Hoesen et al., 2000), while those in the MCIc vs. HC classification task were rostral hippocampus (Ighodaro et al., 2015), medial

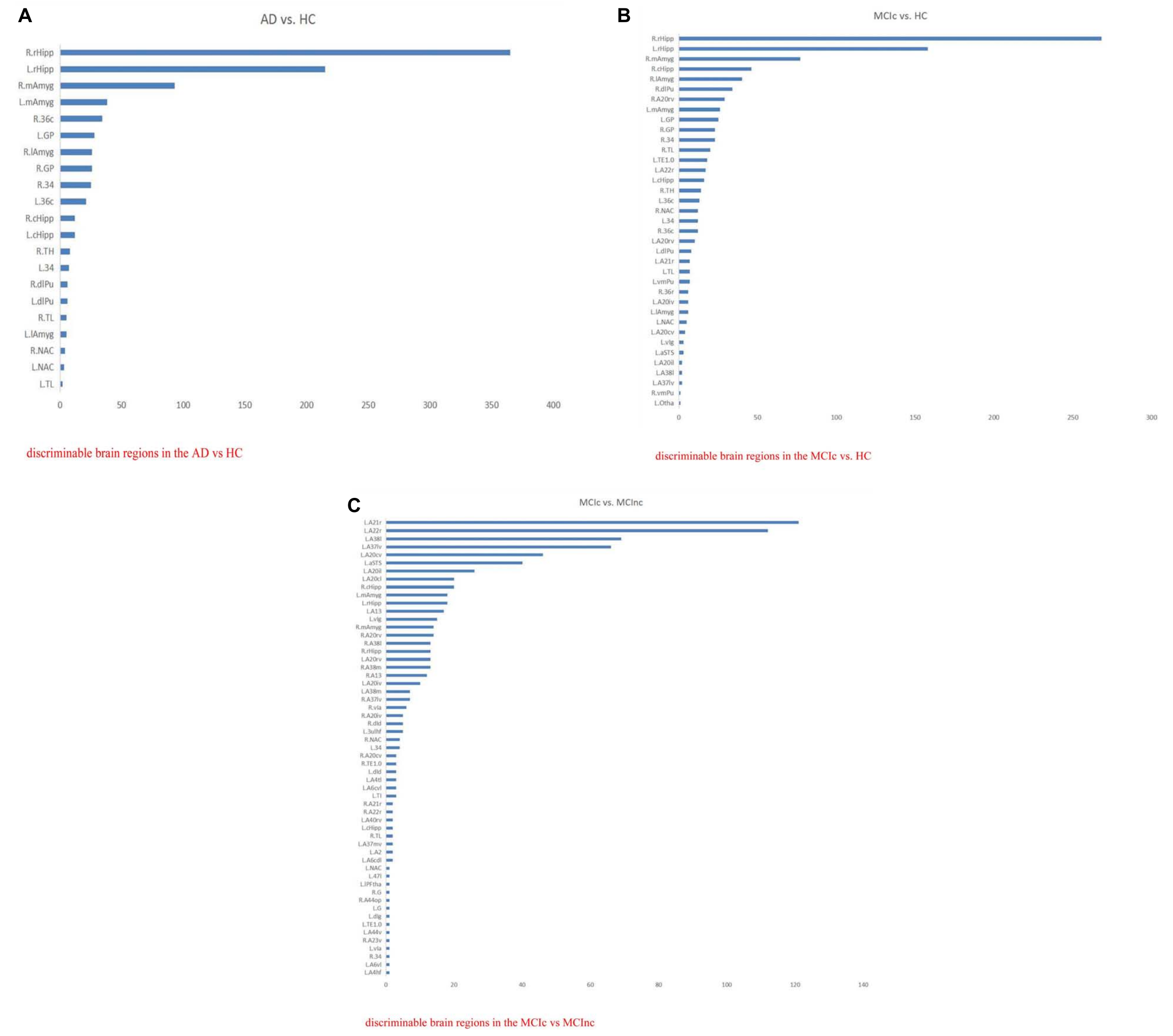

FIGURE 8 | The list of brain regions with the classification capacity in each classification task. **(A)** Discriminable brain regions in the AD vs. HC. **(B)** Discriminable brain regions in the MCIc vs. HC. **(C)** Discriminable brain regions in the MCIc vs. MCInc.

TABLE 8a | Details of the discriminable brain regions in the AD vs. HC task.

Label of a brain region	Name of a brain region	# of points located in a brain region
R.rHipp	Rostral hippocampus	365
L.rHipp	Rostral hippocampus	215
R.mAmyg	Medial amygdala	93
L.mAmyg	Medial amygdala	38
R.36c	Caudal area 35/36	34
L.GP	Globus pallidus	28
R.GP	Globus pallidus	26
R.lAmyg	Lateral amygdala	26
R.34	Area 28/34 (EC, entorhinal cortex)	25
L.36c	Caudal area 35/36	21
L.cHipp	Caudal hippocampus	12
R.cHipp	Caudal hippocampus	12
R.TH	Area TH (medial PPHC)	8
L.34	Area 28/34 (EC, entorhinal cortex)	7
L.dlPu	Dorsolateral putamen	6
R.dlPu	Dorsolateral putamen	6
L.lAmyg	Lateral amygdala	5
R.TL	Area TL (lateral PPHC, posterior parahippocampal gyrus)	5
R.NAC	Nucleus accumbens	4
L.NAC	Nucleus accumbens	3
L.TL	Area TL (lateral PPHC, posterior parahippocampal gyrus)	2

TABLE 8b | Details of the discriminable brain regions in the MCIc vs. HC task.

Label of a brain region	Name of a brain region	# of points located in a brain region
R.rHipp	Rostral hippocampus	268
L.rHipp	Rostral hippocampus	158
R.mAmyg	Medial amygdala	77
R.cHipp	Caudal hippocampus	46
R.lAmyg	Lateral amygdala	40
R.dlPu	Dorsolateral putamen	34
R.A20rv	Rostroventral area 20	29
L.mAmyg	Medial amygdala	26
L.GP	Globus pallidus	25
R.34	Area 28/34 (EC, entorhinal cortex)	23
R.GP	Globus pallidus	23
R.TL	Area TL (lateral PPHC, posterior parahippocampal gyrus)	20
L.TE1.0	TE1.0 and TE1.2	18
L.A22r	Rostral area 22	17
L.cHipp	Caudal hippocampus	16
R.TH	Area TH (medial PPHC)	14
L.36c	Caudal area 35/36	13
R.36c	Caudal area 35/36	12
L.34	Area 28/34 (EC, entorhinal cortex)	12
R.NAC	Nucleus accumbens	12
L.A20rv	Rostroventral area 20	10
L.dlPu	Dorsolateral putamen	8
L.vmPu	Ventromedial putamen	7
L.TL	Area TL (lateral PPHC, posterior parahippocampal gyrus)	7
L.A21r	Rostral area 21	7
L.lAmyg	Lateral amygdala	6
L.A20iv	Intermediate ventral area 20	6
R.36r	Rostral area 35/36	6
L.NAC	Nucleus accumbens	5
L.A20cv	Caudoventral of area 20	4
L.aSTS	Anterior superior temporal sulcus	3
L.vIg	Ventral dysgranular and granular insula	3
L.A37lv	Lateroventral area 37	2
L.A38l	Lateral area 38	2
L.A20il	Intermediate lateral area 20	2
L.Otha	Occipital thalamus	1
R.vmPu	Ventromedial putamen	1

amygdala (Cavedo et al., 2014), caudal hippocampus (Chen et al., 2015), lateral amygdala (Kile et al., 2009), dorsolateral putamen (Reeves et al., 2010), rostroventral area 20, i.e., Fusiform gyrus (Bokde et al., 2006), globus pallidus (Hernández et al., 2020), area 28/34 (EC, entorhinal cortex) (Du et al., 2001; Burggren et al., 2011; Tward et al., 2017), and area TL (lateral PPHC, posterior parahippocampal gyrus) (Devanand et al., 2007). Finally, the most discriminable brain regions in the MCIc vs. MCInc classification task were rostral area 21 and anterior superior temporal sulcus, i.e., middle temporal gyrus (Karas et al., 2008); rostral area 22 and lateral area 38, i.e., superior temporal gyrus (Karas et al., 2008); lateroventral area 37, i.e., fusiform gyrus (Guillozet et al., 2003); and caudoventral of area 20 and intermediate lateral area 20 and caudolateral of area 20, i.e., inferior temporal gyrus (Scheff et al., 2011) and caudal hippocampus (Thomann et al., 2012). The top 10 most discriminable brain regions are mapped onto brain images in **Figure 9**.

In the paper (Yang et al., 2019), the results showed that the patients with aMCI (elderly patients with amnestic MCI) merely had slight atrophy in the inferior parietal lobe of the left hemisphere but a significant difference was NOT found in comparison with the NC (normal controls). The results are consistent with the highly lateralized MCIc vs. MCInc-related features acquired in this study, to some degree. Plus, the most discriminable brain regions identified in the MCIc vs. MCInc classification task in our study were in agreement with the conclusion of the paper (Yang et al., 2019) that the atrophy of cortical thickness and surface area in aMCI began in the temporal lobe but the range of atrophy gradually expanded with the progression of disease, to a great extent. Furthermore, in the paper (Karas et al., 2008), the obtained results were that MCI converters (patients with MCI who will progress to AD) had more left lateral temporal lobe atrophy (superior and middle temporal gyrus) and left parietal atrophy (angular gyrus and inferior parietal lobule) than MCI non-converters, i.e., stable patients with MCI, and the drawn conclusion was that by studying two MCI converter vs. non-converter populations, atrophy beyond the medial temporal lobe was found to be characteristic of converters and atrophy

TABLE 8c | Discriminable brain regions in the MCIc vs. MCInc classification task.

Label of a brain region	Name of a brain region	# of points located in a brain region
L.A21r	Rostral area 21	121
L.A22r	Rostral area 22	112
L.A38l	Lateral area 38	69
L.A37lv	Lateroventral area 37	66
L.A20cv	Caudoventral of area 20	46
L.aSTS	Anterior superior temporal sulcus	40
L.A20il	Intermediate lateral area 20	26
R.cHipp	Caudal hippocampus	20
L.A20cl	Caudolateral of area 20	20
L.rHipp	Rostral hippocampus	18
L.mAmyg	Medial amygdala	18
L.A13	Area 13	17
L.vIg	Ventral dysgranular and granular insula	15
R.A20rv	Rostroventral area 20	14
R.mAmyg	Medial amygdala	14
R.A38m	Medial area 38	13
L.A20rv	Rostroventral area 20	13
R.rHipp	Rostral hippocampus	13
R.A38l	Lateral area 38	13
R.A13	Area 13	12
L.A20iv	Intermediate ventral area 20	10
R.A37lv	Lateroventral area 37	7
L.A38m	Medial area 38	7
R.vIa	Ventral agranular insula	6
L.3ulhf	Area 1/2/3 (upper limb, head and face region)	5
R.dId	Dorsal dysgranular insula	5
R.A20iv	Intermediate ventral area 20	5
L.34	Area 28/34 (EC, entorhinal cortex)	4
R.NAC	Nucleus accumbens	4
L.TI	Area TI (temporal agranular insular cortex)	3
L.A6cvl	Caudal ventrolateral area 6	3
L.A4tl	Area 4 (tongue and larynx region)	3
L.dId	Dorsal dysgranular insula	3
R.TE1.0	TE1.0 and TE1.2	3
R.A20cv	Caudoventral of area 20	3
L.A6cdl	Caudal dorsolateral area 6	2
L.A2	Area 1/2/3 (tongue and larynx region)	2
L.A37mv	Medioventral area 37	2
R.TL	Area TL (lateral PPHC, posterior parahippocampal gyrus)	2
L.cHipp	Caudal hippocampus	2
L.A40rv	Rostroventral area 40 (pfop)	2
R.A22r	Rostral area 22	2
R.A21r	Rostral area 21	2
L.A4hf	Area 4 (head and face region)	1
L.A6vl	Ventrolateral area 6	1
R.34	Area 28/34 (EC, entorhinal cortex)	1
L.vIa	Ventral agranular insula	1
R.A23v	Ventral area 23	1
L.A44v	Ventral area 44	1
L.TE1.0	TE1.0 and TE1.2	1
L.dIg	Dorsal granular insula	1
L.G	Hypergranular insula	1
R.A44op	Opercular area 44	1
R.G	Hypergranular insula	1
L.lPFtha	Lateral pre-frontal thalamus	1
L.47l	Lateral area 12/47	1
L.NAC	Nucleus accumbens	1

of structures such as the left parietal cortex and left lateral temporal lobe might independently predict conversion. The results and conclusion were consistent with most of our results to some extent.

After location mapping, the corresponding behavioral domains to every identified brain region were obtained from

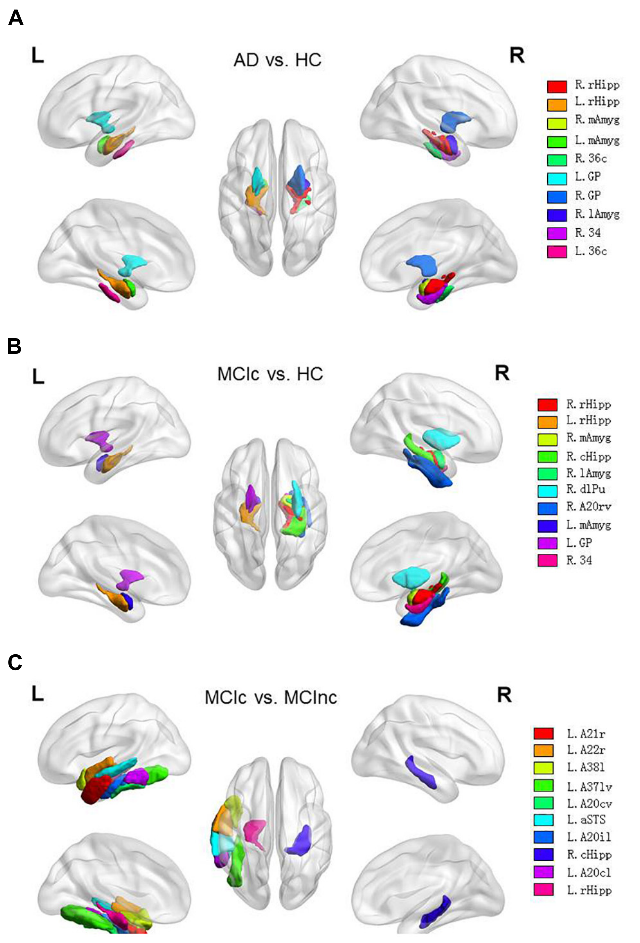

FIGURE 9 | Top 10 most discriminable brain regions in each binary classification task: **(A)** AD vs. HC; **(B)** MCIc vs. HC; **(C)** MCIc vs. MCInc.

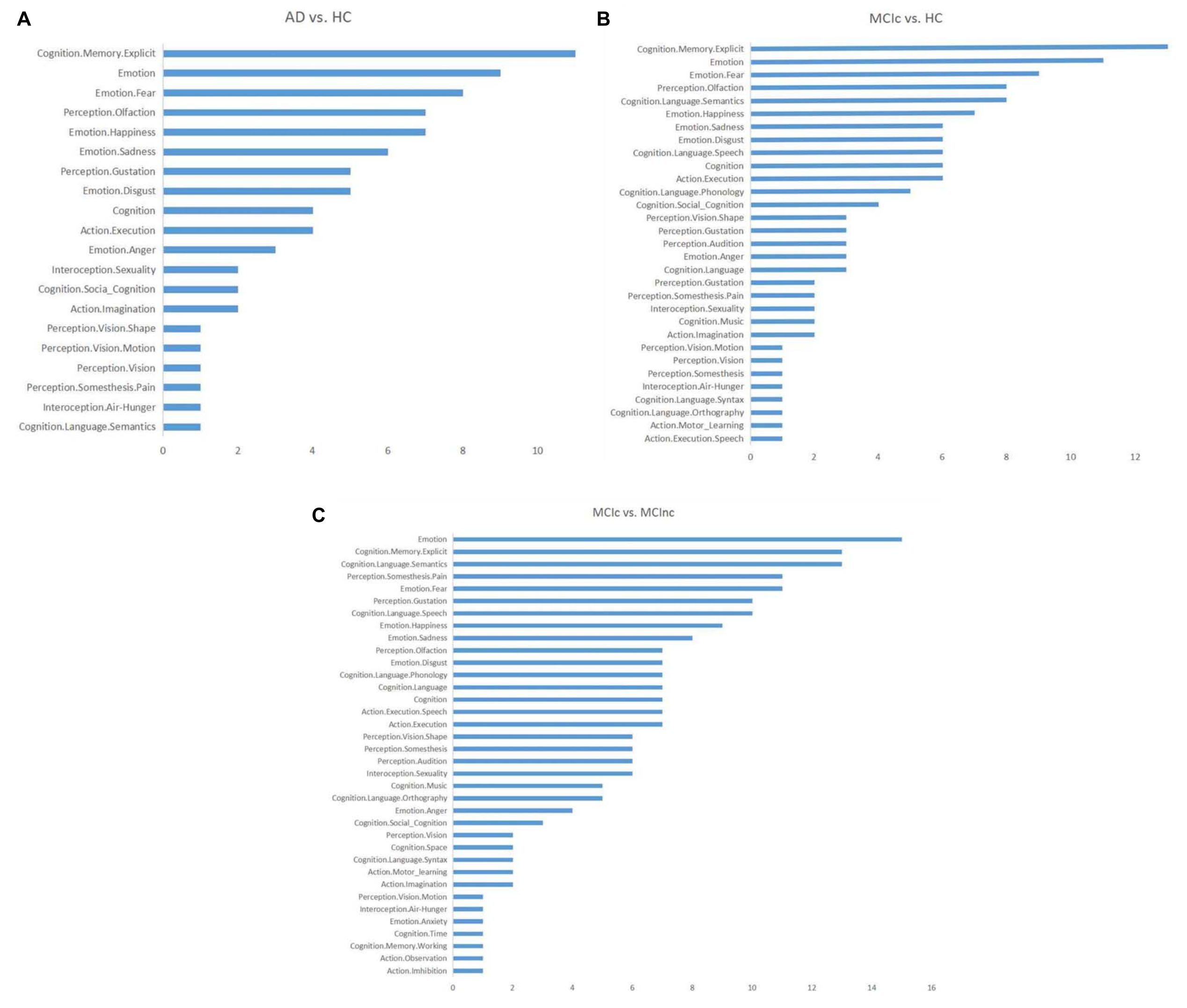

FIGURE 10 | Distributions of the identified brain regions on the relevant behavioral domains in each binary classification task: **(A)** AD vs. HC; **(B)** MCIc vs. HC; **(C)** MCIc vs. MCInc.

the Brainnetome Atlas official website,[4] and the functions of these identified brain regions were analyzed. Then, the number of identified brain regions corresponding to each AD-related behavioral domain was calculated for each task (**Figure 10**) to reveal the distribution of structures showing the largest differences between classes and thus most informative for classification (e.g., emotion-related structures for AD vs. HC). In the figure, the vertical and horizontal axes show the relevant behavioral domains and the number of identified brain regions associated with these relevant behavioral domains, respectively.

From **Figure 10**, it can be seen that the functions related to these identified brain regions with the discriminability were mainly involved with the behavioral domains of emotion, memory, language, perception, internal feelings, and activity. The most common symptoms of AD, especially in the early stage, include memory loss that disrupts daily life, challenges in planning or problem solving, difficulty completing familiar tasks at home, at work, or at leisure, confusion with time or place, trouble understanding visual images and spatial relationships, new problems with words in speaking or writing, misplacing things and losing the ability to retrace steps, decreased or poor judgment, and changes in mood and personality (Mantzavinos and Alexiou, 2017). Thus, the behavioral domains relevant to the identified brain regions were generally consistent with the common symptoms of AD.

DISCUSSION

In this study, we developed a novel deep learning approach that combined CNN and EL and applied it to the most commonly acquired anatomical MRI of the brain, i.e., T1WI. We aimed to

---

[4] www.Brainnetome.org

achieve two objectives: i.e., classification of AD or MCIc vs. HC, and MCIc vs. MCInc and identification of the complex change patterns associated with AD.

In comparison with a previous PCA plus SVM method (Christian et al., 2015), the current method does not require manual selection of ROIs, but automatically extracts the discriminable features from the MR images using a CNN-based adaptive representation learning method in a data-driven way. The proposed method employs a two-stage EL scheme to improve generalization and robustness. The model achieved average classification accuracies (± standard deviation) of 0.84 ± 0.05 for AD vs. HC, 0.79 ± 0.04 for MCIc vs. HC, and 0.62 ± 0.06 for MCIc vs. MCInc. Compared to the PCA plus SVM method, the proposed method showed statistically substantially improved accuracy and robustness for distinguishing among the AD, MCIc, and HC groups, while model accuracy was NOT statistically lower than that achieved by the PCA plus SVM method for distinguishing MCIc from MCInc. At the same time, compared to the 3D-SENet model, the CNN-EL method achieved statistically higher accuracy and robustness for all the three binary classification tasks.

For a 1 × 5-fold cross-validation processes, we also identified the 15 slices and resultant 125 (i.e., 5 × 5 × 5) intersection points in the standard MNI space based on the five best base classifiers trained respectively with sagittal, coronal, or transverse slice data. These points were then mapped onto the Brainnetome Atlas to identify the corresponding brain regions with the discriminability in the three binary classification tasks. For all the 10 × 5-fold cross-validation processes, the number of all the intersection points located in the same brain region was summed to evaluate the capability of the brain region to help diagnose AD. The identified brain regions included hippocampus, amygdala, and temporal lobe, which are known to be affected by AD and involved in neurological processes impaired in AD (Schroeter et al., 2009). Also, we acquired the corresponding behavioral domains based on all identified brain regions, which were generally consistent with the common symptoms of AD.

In two-dimensional convolutional neural network (2D-CNN)-based models for early detection of AD, only sagittal, coronal, or transverse slices of 3D MR images are usually used as the training dataset. A specific slice, such as a transverse slice through the hippocampus, was often selected based on experience or prior domain knowledge (Wang et al., 2018). Using only the data from a single 2D slice of a 3D MR image removes potentially valuable information. In comparison, the novel CNN-EL approach that we proposed here has the following significant features:

(1) Six data augmentation (DA) methods are used to deal with the imbalanced data problem by disproportionately increasing the number of image slices in classes with fewer samples. As a result, each class can have approximately an equal increased number of training instances in the augmented dataset.
(2) The proposed ensemble model combines features identified from the sagittal, coronal, and transverse slices of a 3D MRI dataset together, to improve classification accuracy and model adaptability. Each of the base 2D CNN classifier was trained with the data from a single slice orientation. Then, the top "N" trained base classifiers were selected according to the generalization performance on the verification dataset to build the final ensemble. In this way, the method effectively improved classification accuracy and robustness. The slices used as training data to construct base classifiers were not necessarily specified based on prior domain knowledge; rather, each available and valid slice (sagittal, coronal, or transverse) in the dataset was used to train the corresponding base classifier.
(3) Compared to the length of time spent on building a model with data from only a single slice orientation, it may take more time to build the proposed model since many more base classifiers need to be trained. To effectively solve this problem, the parallel processing method was adopted to train the base classifiers used to build the ensemble model. This greatly improved the training efficiency and made the proposed model scalable.
(4) According to the classification performances of all trained base classifiers on the verification dataset, the three sets of top "N" base classifiers trained using data from sagittal, coronal, and transverse slices, respectively, were determined. Since a base classifier was trained with the data from only a specific slice orientation, the most important sagittal, coronal, or transverse slice for a binary classification task (e.g., AD vs. HC) could be located according to the three sets of top "N" base classifiers in a data-driven way. Furthermore, the brain regions corresponding to the intersection points determined by the top "N" sagittal, coronal, and transverse slices could be located with the help of the Brainnetome Atlas. The brain regions identified with the most intersection points might be the most discriminable for a binary classification task, given that the number of the intersection points could be an indicator to measure the ability of a brain region in which the points were located to classify AD.
(5) The performance of the proposed classifier ensemble was compared to that of other machine learning models using the same dataset. The experimental results showed that the proposed model achieved better classification accuracy and robustness.

The relatively low classification accuracy for MCIc vs. MCInc warrants further investigation and the classification performance needs to be improved with the optimization methods and/or other deep learning models to identify the brain regions with stronger discriminability.

For an individual subject to be diagnosed, the votes of base classifiers in the trained classifier ensemble based on the three-axis slices and the number of resulting intersection points located in each brain region might be employed to disclose the extent to which AD impaired each brain region and each behavioral domain, which could help understand and evaluate the subject's disease status, symptom burden and, more importantly, progress. Plus, with the advancements of brain atlases and advanced ultra-high-field scanners, chances are that the positions and the number of the intersection points determined by the proposed CNN-EL methods might provide more details on and insights into the progress of AD pathology.

Furthermore, the advocated method may be useful for identifying additional candidate neuroimaging biomarkers for AD as well as for other brain diseases such as Parkinson's disease, autism, schizophrenia and severe depression, especially for identifying candidate neuroimaging biomarkers for other little-known brain disorders, in a data-driven way.

The above-mentioned discussions, the clinical implication of the finding applying other samples, and the generalizability of the advocated CNN-EL approach need to be examined in the future research.

DATA AVAILABILITY STATEMENT

The datasets analyzed for this study can be found in the Alzheimer's Disease Neuroimaging Initiative (ADNI) database (adni.loni.usc.edu).

AUTHOR CONTRIBUTIONS

DP and AZ designed and coordinated the study. LJ, DP, YH, and AZ carried out experiment and data process. XS reviewed the study design and data processing, and edited results interpretation and presentation. All authors drafted and revised the manuscript, and approved the final version of the submitted manuscript.

ACKNOWLEDGMENTS

We thank the reviewers for their constructive comments on this article. This study was supported by NSF of China (Grant Nos. 61976058 and 61772143), Science and Technology Planning Project of Guangdong (Grant No. 2019A050510041), R&D projects in key areas of Guangdong (Grant No. 2019B010109001), and Science and Technology Planning Project of Guangzhou (Grant Nos. 202002020090 and 201804010278). Additional funding for neurological research was from Surrey Hospital & Outpatient Centre Foundation (FHG2017-001). Data collection and sharing for this project were funded by the Alzheimer's Disease Neuroimaging Initiative (ADNI) (National Institutes of Health Grant U01 AG024904) and DOD ADNI (Department of Defense Award No. W81XWH-12-2-0012). ADNI was funded by the National Institute on Aging, the National Institute of Biomedical Imaging and Bioengineering, and through generous contributions from the following: AbbVie, Alzheimer's Association; Alzheimer's Drug Discovery Foundation; Araclon Biotech; BioClinica, Inc.; Biogen; Bristol-Myers Squibb Company; CereSpir, Inc.; Cogstate; Eisai Inc.; Elan Pharmaceuticals, Inc.; Eli Lilly and Company; EuroImmun; F. Hoffmann-La Roche Ltd and its affiliated company Genentech, Inc.; Fujirebio; GE Healthcare; IXICO Ltd.; Janssen Alzheimer Immunotherapy Research & Development, LLC.; Johnson & Johnson Pharmaceutical Research & Development LLC.; Lumosity; Lundbeck; Merck & Co., Inc.; Meso Scale Diagnostics, LLC.; NeuroRx Research; Neurotrack Technologies; Novartis Pharmaceuticals Corporation; Pfizer Inc.; Piramal Imaging; Servier; Takeda Pharmaceutical Company; and Transition Therapeutics. The Canadian Institutes of Health Research was providing funds to support ADNI clinical sites in Canada. Private sector contributions are facilitated by the Foundation for the National Institutes of Health (www.fnih.org). The grantee organization is the Northern California Institute for Research and Education, and the study is coordinated by the Alzheimer's Therapeutic Research Institute at the University of Southern California. ADNI data are disseminated by the Laboratory for Neuro Imaging at the University of Southern California. Additional funding support for the manuscript preparation was from the Surrey Hospital & Outpatient Centre Foundation of Fraser Health, Canada.

REFERENCES

Arora, S., Hazan, E., and Kale, S. (2012). The multiplicative weights update method: a meta-algorithm and applications. *Theory Comput.* 8, 121–164.

Baloyannis, S. J. (2006). Mitochondrial alterations in Alzheimer's disease. *J. Alzheimer's Dis.* 9, 119–126.

Bokde, A. L. W., Lopez-Bayo, P., Meindl, T., Pechler, S., Born, C., Faltraco, F., et al. (2006). Functional connectivity of the fusiform gyrus during a face-matching task in subjects with mild cognitive impairment. *Brain* 129, 1113–1124. doi: 10.1093/brain/awl051

Breiman, L. (1996). Bagging predictors. *Mach. Learn.* 24, 123–140. doi: 10.1007/bf00058655

Breiman, L. (2001). Random forest. *Mach. Learn.* 45, 5–32. doi: 10.1023/A:1010933404324

Burggren, A. C., Renner, B., Jones, M., Donix, M., Suthana, N. A., Martin-Harris, L., et al. (2011). Thickness in entorhinal and subicular cortex predicts episodic memory decline in mild cognitive impairment. *Int. J. Alzheimer's Dis.* 2011:9.

Cavedo, E., Pievani, M., Boccardi, M., Galluzzi, S., Bocchetta, M., Bonetti, M., et al. (2014). Medial temporal atrophy in early and late-onset Alzheimer's disease. *Neurobiol. Aging* 35, 2004–2012. doi: 10.1016/j.neurobiolaging.2014.03.009

Chen, J., Zhang, Z., and Li, S. (2015). Can multi-modal neuroimaging evidence from hippocampus provide biomarkers for the progression of amnestic mild cognitive impairment? *Neurosci. Bull.* 31, 128–140. doi: 10.1007/s12264-014-1490-8

Christian, S., Antonio, C., Petronilla, B., Gilardi, M. C., Aldo, Q., and Isabella, C. (2015). Magnetic resonance imaging biomarkers for the early diagnosis of Alzheimer's disease: a machine learning approach. *Front. Neurosci.* 9:307. doi: 10.3389/fnins.2015.00307

Christina, P. (2018). *World Alzheimer Report 2018 – The State of the Art of Dementia Research: New Frontiers*. London: Alzheimer's Disease International.

Devanand, D. P., Pradhaban, G., Liu, X., Khandji, A., De Santi, S., Segal, S., et al. (2007). Hippocampal and entorhinal atrophy in mild cognitive impairment: prediction of Alzheimer disease. *Neurology* 68, 828–836. doi: 10.1212/01.wnl.0000256697.20968.d7

Du, A. T., Schuff, N., Amend, D., Laakso, M. P., Hsu, Y. Y., Jagust, W. J., et al. (2001). Magnetic resonance imaging of the entorhinal cortex and hippocampus in mild cognitive impairment and Alzheimer's disease. *J. Neurol. Neurosurg. Psychiatry* 71, 441–447. doi: 10.1136/jnnp.71.4.441

Dubois, B., Feldman, H. H., Jacova, C., DeKosky, S. T., Barberger-Gateau, P., Cummings, J., et al. (2007). Research criteria for the diagnosis of Alzheimer's disease: revising the NINCDS–ADRDA criteria. *Lancet Neurol.* 6, 734–746. doi: 10.1016/S1474-4422(07)70178-3

Fan, L., Hai, L., Zhuo, J., Yu, Z., Wang, J., Chen, L., et al. (2016). The human brainnetome atlas: a new brain atlas based on connectional architecture. *Cereb. Cortex* 26, 3508–3526. doi: 10.1093/cercor/bhw157

Freund, Y., and Schapire, R. E. (1997). A decision-theoretic generalization of on-line learning and an application to boosting. *J. Comput. Syst. Sci.* 55, 119–139. doi: 10.1006/jcss.1997.1504

Fukushima, K. (1980). Neocognitron: a self-organizing neural network model for a mechanism of pattern recognition unaffected by shift in position. *Biol. Cybernet.* 36, 193–202. doi: 10.1007/bf00344251

Girshick, R. B., Donahue, J., Darrell, T., and Malik, J. M. (2014). "Rich feature hierarchies for accurate object detection and semantic segmentation," in *Proceedings of the IEEE Conference on Computer Vision and Pattern Recognition* (San Juan: IEEE).

Greene, S. J., Killiany, R. J., Alzheimer's Disease, and Neuroimaging Initiative. (2012). Hippocampal subregions are differentially affected in the progression to Alzheimer's disease. *Anatom. Rec.* 295, 132–140. doi: 10.1002/ar.21493

Guillozet, A. L., Weintraub, S., Mash, D. C., and Mesulam, M. M. (2003). Neurofibrillary tangles, amyloid, and memory in aging and mild cognitive impairment. *Arch. Neurol.* 60, 729–736.

Hernández, M. C. V., Clark, R., Wang, S. H., Guazzo, F., Calia, C., Pattan, V., et al. (2020). The striatum, the hippocampus, and short-term memory binding: volumetric analysis of the subcortical grey matter's role in mild cognitive impairment. *NeuroImage Clin.* 25:102158. doi: 10.1016/j.nicl.2019.102158

Hinrichs, C., Singh, V., Mukherjee, L., Xu, G., Chung, M. K., and Johnson, S. C. (2009). Spatially augmented LPboosting for AD classification with evaluations on the ADNI dataset. *Neuroimage* 48, 138–149. doi: 10.1016/j.neuroimage.2009.05.056

Hinton, G. E. (2009). Deep belief networks. *Scholarpedia* 4:5947. doi: 10.4249/scholarpedia.5947

Hu, J., Shen, L., and Sun, G. (2018). "Squeeze-and-excitation networks," in *Proceedings of the IEEE conference on Computer Vision and Pattern Recognition* (New York, NY: IEEE), 7132–7141.

Hubel, D. H., and Wiesel, T. N. (1962). Receptive fields, binocular interaction and functional architecture in the cat's visual cortex. *J. Physiol.* 160, 106–154. doi: 10.1113/jphysiol.1962.sp006837

Hubel, D. H., and Wiesel, T. N. (1965). Receptive fields and functional architecture in two nonstriate visual areas (18 and 19) of the cat. *J. Neurophysiol.* 28, 229–289. doi: 10.1152/jn.1965.28.2.229

Ighodaro, E. T., Jicha, G. A., Schmitt, F. A., Neltner, J. H., Abner, E. L., Kryscio, R. J., et al. (2015). Hippocampal sclerosis of aging can be segmental: two cases and review of the literature. *J. Neuropathol. Exp. Neurol.* 74, 642–652. doi: 10.1097/nen.0000000000000204

Islam, J., and Zhang, Y. (2018). Brain MRI analysis for Alzheimer's disease diagnosis using an ensemble system of deep convolutional neural networks. *Brain Inform.* 5:2.

Ji, H., Liu, Z., Yan, W. Q., and Klette, R. (2019). "Early diagnosis of alzheimer's disease using deep learning," in *Proceedings of the 2nd International Conference on Control and Computer Vision* (New York, NY: Association for Computing Machinery), 87–91.

Karas, G., Sluimer, J., Goekoop, R., Van Der Flier, W., Rombouts, S. A. R. B., Vrenken, H., et al. (2008). Amnestic mild cognitive impairment: structural MR imaging findings predictive of conversion to Alzheimer disease. *Am. J. Neuroradiol.* 29, 944–949. doi: 10.3174/ajnr.a0949

Kile, S. J., Ellis, W. G., Olichney, J. M., Farias, S., and DeCarli, C. (2009). Alzheimer abnormalities of the amygdala with Klüver-Bucy syndrome symptoms: an amygdaloid variant of Alzheimer disease. *Arch. Neurol.* 66, 125–129.

Kingma, D., and Ba, J. (2014). Adam: a method for stochastic optimization. *Comput. Sci.*

Krizhevsky, A., Sutskever, I., and Hinton, G. E. (2012). "ImageNet classification with deep convolutional neural networks," in *Proceedings of the International Conference on Neural Information Processing Systems* (Cambridge, MA: MIT Press), 1097–1105.

LeCun, Y. (2015). *LeNet, Convolutional Neural Networks.* Available online at: http: //yann. lecun. com/exdb/lenet.

Leemput, K., Van Maes, F., Vandermeulen, D., and Suetens, P. (2002). Automated model-based tissue classification of MR images of the brain. *IEEE Trans. Med. Imaging* 18, 897–908. doi: 10.1109/42.811270

Li, F., Liu, M., and Alzheimer's Disease and Neuroimaging Initiative. (2018). Alzheimer's disease diagnosis based on multiple cluster dense convolutional networks. *Computer. Med. Imag. Graph.* 70, 101–110. doi: 10.1016/j.compmedimag.2018.09.009

Li, H., Habes, M., Wolk, D. A., Fan, Y., Alzheimer's Disease, and Neuroimaging Initiative. (2019). A deep learning model for early prediction of Alzheimer's disease dementia based on hippocampal magnetic resonance imaging data. *Alzheimer's & Dementia* 15, 1059–1070. doi: 10.1016/j.jalz.2019.02.007

Lin, W., Tong, T., Gao, Q., Guo, D., Du, X., Yang, Y., et al. (2018). Convolutional neural networks-Based MRI image analysis for the Alzheimer's disease prediction from mild cognitive impairment. *Front. Neurosci.* 12:777. doi: 10.3389/fnins.2018.00777

Liu, S., Liu, S., Cai, W., Pujol, S., Kikinis, R., and Feng, D. (2014). "Early diagnosis of Alzheimer's disease with deep learning," in *Proceedings of the IEEE International Symposium on Biomedical Imaging* (New York, NY: IEEE).

Long, J., Shelhamer, E., and Darrell, T. (2015). "Fully convolutional networks for semantic segmentation," in *Proceedings of the IEEE Conference on Computer Vision and Pattern Recognition* (Boston, MA: IEEE).

Mantzavinos, V., and Alexiou, A. (2017). Biomarkers for Alzheimer's disease diagnosis. *Curr. Alzheimer Res.* 14:1149. doi: 10.2174/156720501466617020312 5942

Mateos-Pérez, J. M., Dadar, M., Lacalle-Aurioles, M., Iturria-Medina, Y., Zeighami, Y., and Evans, A. C. (2018). Structural neuroimaging as clinical predictor: a review of machine learning applications. *NeuroImage Clin.* 20, 506–522. doi: 10.1016/j.nicl.2018.08.019

Matthews, B. W. (1975). Comparison of the predicted and observed secondary structure of T4 phage lysozyme. *Biochim. Biophys. Acta (BBA)-Protein Struct.* 405, 442–451. doi: 10.1016/0005-2795(75)90109-9

McKhann, G., Drachman, D., Folstein, M., Katzman, R., Price, D., and Stadlan, E. M. (1984). Clinical diagnosis of Alzheimer's disease report of the NINCDS-ADRDA Work Group* under the auspices of department of health and human services task force on Alzheimer's disease. *Neurology* 34, 939–939. doi: 10.1212/wnl.34.7.939

Moradi, E., Pepe, A., Gaser, C., Huttunen, H., Tohka, J., Alzheimer's Disease, et al. (2015). Machine learning framework for early MRI-based Alzheimer's conversion prediction in MCI subjects. *Neuroimage* 104, 398–412. doi: 10.1016/j.neuroimage.2014.10.002

Morris, J. C. (1993). The Clinical Dementia Rating (CDR): current version and scoring rules. *Neurology* 43, 2412–2414. doi: 10.1212/WNL.43.11.2412-a

Nelson, P. T., Abner, E. L., Patel, E., Anderson, S., Wilcock, D. M., Kryscio, R. J., et al. (2018). The amygdala as a locus of pathologic misfolding in neurodegenerative diseases. *J. Neuropathol. Exp. Neurol.* 77, 2–20.

Opitz, D., and Maclin, R. (1999). Popular ensemble methods: an empirical study. *J. Artif. Intell. Res.* 11, 169–198. doi: 10.1613/jair.614

Ortiz, A., Munilla, J., Gorriz, J. M., and Ramirez, J. (2016). Ensembles of deep learning architectures for the early diagnosis of the Alzheimer's disease. *Int. J. Neural Syst.* 26:1650025. doi: 10.1142/s0129065716500258

Reeves, S., Mehta, M., Howard, R., Grasby, P., and Brown, R. (2010). The dopaminergic basis of cognitive and motor performance in Alzheimer's disease. *Neurobiol. Dis.* 37, 477–482. doi: 10.1016/j.nbd.2009.11.005

Scheff, S. W., Price, D. A., Schmitt, F. A., Scheff, M. A., and Mufson, E. J. (2011). Synaptic loss in the inferior temporal gyrus in mild cognitive impairment and Alzheimer's disease. *J. Alzheimer's Dis.* 24, 547–557. doi: 10.3233/jad-2011-101782

Schmidhuber, J. (2015). Deep learning in neural networks: an overview. *Neural Netw.* 61, 85–117. doi: 10.1016/j.neunet.2014.09.003

Schroeter, M. L., Stein, T., Maslowski, N., and Neumann, J. (2009). Neural correlates of Alzheimer's disease and mild cognitive impairment: a systematic and quantitative meta-analysis involving 1351 patients. *Neuroimage* 47, 1196–1206. doi: 10.1016/j.neuroimage.2009.05.037

Shan, S. L., Khalil-Hani, M., and Bakhteri, R. (2016). Bounded activation functions for enhanced training stability of deep neural networks on visual pattern recognition problems. *Neurocomputing* 216, 718–734. doi: 10.1016/j.neucom.2016.08.037

Suk, H. I., Lee, S. W., Shen, D., and Alzheimer's Disease Neuroimaging Initiative (2017). Deep ensemble learning of sparse regression models for brain disease diagnosis. *Med. Image Anal.* 37, 101–113. doi: 10.1016/j.media.2017.01.008

Sun, Z., Xue, L., Xu, Y., and Wang, Z. (2012). Overview of deep learning. *J. Comput. Res. Dev.* 29, 2806–2810. doi: 10.3969/j.issn.1001-3695.2012.08.002

Thomann, A. P., Seidl, U., Brinkmann, J., Hirjak, D., Traeger, T., Christian Wolf, R., et al. (2012). Hippocampal morphology and autobiographic memory in mild cognitive impairment and Alzheimer's disease. *Curr. Alzheimer Res.* 9, 507–515. doi: 10.2174/156720512800492558

Tripoliti, E. E., Fotiadis, D. I., and Argyropoulou, M. (2011). A supervised method to assist the diagnosis and monitor progression of Alzheimer's disease using data from an fMRI experiment. *Artif. Intell. Med.* 53, 35–45. doi: 10.1016/j.artmed.2011.05.005

Tward, D. J., Sicat, C. S., Brown, T., Bakker, A., Gallagher, M., Albert, M., et al. (2017). Entorhinal and transentorhinal atrophy in mild cognitive impairment using longitudinal diffeomorphometry. *Alzheimer's & Dementia: Diagn. Assess. Dis. Monitor.* 9, 41–50. doi: 10.1016/j.dadm.2017.07.005

Ulep, M. G., Saraon, S. K., and McLea, S. (2018). Alzheimer disease. *J. Nurse Practit.* 14, 129–135.

van Hoesen, G. W., Augustinack, J. C., Dierking, J., Redman, S. J., and Thangavel, R. (2000). The parahippocampal gyrus in Alzheimer's disease: clinical and preclinical neuroanatomical correlates. *Ann. N. Y. Acad. Sci.* 911, 254–274. doi: 10.1111/j.1749-6632.2000.tb06731.x

Vincent, P., Larochelle, H., Lajoie, I., Bengio, Y., and Manzagol, P. A. (2010). Stacked denoising autoencoders: learning useful representations in a deep network with a local denoising criterion. *J. Mach. Learn. Res.* 11, 3371–3408. doi: 10.1016/j.mec hatronics.2010.09.004

Wang, S. H., Phillips, P., Sui, Y., Liu, B., Yang, M., and Cheng, H. (2018). Classification of Alzheimer's disease based on eight-layer convolutional neural network with leaky rectified linear unit and max pooling. *J. Med. Syst.* 42, 85. doi: 10.1007/s10916-018-0932-7

Wechsler, D. (1987). *Manual: Wechsler Memory Scale-Revised*. San Antonio, TX: Psychological Corporation.

Wen, J., Thibeau-Sutre, E., Samper-Gonzalez, J., Routier, A., Bottani, S., Durrleman, S., et al. (2019). Convolutional neural networks for classification of alzheimer's disease: overview and reproducible evaluation. *arXiv preprint arXiv* [Preprint].

Weng, J., Ahuja, N., and Huang, T. S. (1992). "Cresceptron: a self-organizing neural network which grows adaptively," in *Proceedings Int'l Joint Conference on Neural Networks*, Vol. 1, Baltimore, MD, 576–581. doi: 10.1109/IJCNN.1992.287150

Yang, H., Xu, H., Li, Q., Jin, Y., Jiang, W., Wang, J., et al. (2019). Study of brain morphology change in Alzheimer's disease and amnestic mild cognitive impairment compared with normal controls. *Gen. Psychiatry* 32:e100005. doi: 10.1136/gpsych-2018-100005

Zhang, C. H., and Zhang, J. (2011). A survey of selective ensemble learning algorithm. *Chin. J. Comput.* 34, 1399–1410. doi: 10.3724/sp.j.1016.2011.01399

Conflict of Interest: The authors declare that the research was conducted in the absence of any commercial or financial relationships that could be construed as a potential conflict of interest.

frontiers
in Neuroscience

METHODS
published: 04 June 2020
doi: 10.3389/fnins.2020.00516

Machine Learning Representation of Loss of Eye Regularity in a *Drosophila* Neurodegenerative Model

Sergio Diez-Hermano[1,2]*, *Maria D. Ganfornina*[1], *Esteban Vegas-Lozano*[3]† and *Diego Sanchez*[1]†

[1] Instituto de Biologia y Genetica Molecular-Departamento de Bioquimica y Biologia Molecular y Fisiologia, Universidad de Valladolid-CSIC, Valladolid, Spain, [2] Departamento de Biodiversidad, Ecologia y Evolucion, Unidad de Biomatematicas, Universidad Complutense, Madrid, Spain, [3] Departamento de Genetica, Microbiologia y Estadistica, Universidad de Barcelona, Barcelona, Spain

Edited by:
Rodolfo Gabriel Gatto,
University of Illinois at Chicago,
United States

Reviewed by:
Santhosh Girirajan,
Pennsylvania State University (PSU),
United States
Praveen Agarwal,
Anand International College
of Engineering, India
Angelique Christine Paulk,
Massachusetts General Hospital,
Harvard Medical School,
United States

***Correspondence:**
Sergio Diez-Hermano
serbiodh@gmail.com

†These authors have contributed equally to this work and share senior authorship

Specialty section:
This article was submitted to
Brain Imaging Methods,
a section of the journal
Frontiers in Neuroscience

Received: 21 February 2020
Accepted: 27 April 2020
Published: 04 June 2020

Citation:
Diez-Hermano S, Ganfornina MD, Vegas-Lozano E and Sanchez D (2020) Machine Learning Representation of Loss of Eye Regularity in a Drosophila Neurodegenerative Model. Front. Neurosci. 14:516. doi: 10.3389/fnins.2020.00516

The fruit fly compound eye is a premier experimental system for modeling human neurodegenerative diseases. The disruption of the retinal geometry has been historically assessed using time-consuming and poorly reliable techniques such as histology or pseudopupil manual counting. Recent semiautomated quantification approaches rely either on manual region-of-interest delimitation or engineered features to estimate the extent of degeneration. This work presents a fully automated classification pipeline of bright-field images based on orientated gradient descriptors and machine learning techniques. An initial region-of-interest extraction is performed, applying morphological kernels and Euclidean distance-to-centroid thresholding. Image classification algorithms are trained on these regions (support vector machine, decision trees, random forest, and convolutional neural network), and their performance is evaluated on independent, unseen datasets. The combinations of oriented gradient + gaussian kernel Support Vector Machine [0.97 accuracy and 0.98 area under the curve (AUC)] and fine-tuned pre-trained convolutional neural network (0.98 accuracy and 0.99 AUC) yielded the best results overall. The proposed method provides a robust quantification framework that can be generalized to address the loss of regularity in biological patterns similar to the *Drosophila* eye surface and speeds up the processing of large sample batches.

Keywords: ***Drosophila melanogaster***, **neurodegeneration, rough eye phenotype, spinocerebellar ataxia, machine learning, classification, deep learning**

INTRODUCTION

Drosophila melanogaster stands out as one of the key animal models in today's modern genetic studies, with an estimated 75% of human disease genes having orthologs in flies (Reiter et al., 2001). Its growth as a powerful experimental model of choice has been supported by the wide array of genetic and molecular biology tools designed with the fruit fly in mind (Johnston, 2002), easing

---

Abbreviations: AdaBoost, adaptative boosting; AUC, area under the ROC curve; BN, batch normalization; CNN, convolutional neural network; DT, decision tree; gmr, glass multimer reporter; HOG, histogram of oriented gradients; IREG, regularity index; MLP, multilayer perceptron; NN, neural network; PolyQ, polyglutaminated; RBF, radial basis function; RGB, red, green, blue (colorspace); RF, random forest; ROC, receiver operating characteristic; ROI, region of interest; SCA, spinocerebellar ataxia; SEM, scanning electron micrograph; SGD, stochastic gradient descent; SVM, support vector machine; UAS, upstream activating sequence; WT, wild type.

the creation of genetic deletions, insertions, knock-downs, and transgenic lines. Fly biologists have greatly contributed to our knowledge of mammalian biology, making *Drosophila* the historical premier research system in the fields of epigenetics, cancer molecular networks, neurobiology, and immunology (Wangler et al., 2015). The relative simplicity of *Drosophila* genetics (four pairs of homologous chromosomes, in contrast to 23 in humans) and organization (i.e., $\sim 2 \times 10^5$ neurons in opposition to roughly 10^{11} neurons in humans) makes the fruit fly an especially well-suited model for the analysis of subsets of phenotypes associated with complex disorders.

Specifically, the retinal system in *Drosophila* has been widely used as an experimental setting for high-throughput genetic screening and for testing molecular interactions (Thomas and Wassarman, 1999). Eye development is a milestone in the *Drosophila* life cycle, with a massive two-thirds of the essential genes in the fly genome required at some point during the process (Thaker and Kankel, 1992; Treisman, 2013). Therefore, it constitutes an excellent playground to study the genetics underlying general biological phenomena, from the basic cellular and molecular functions to the pathogenic mechanisms involved in multifactorial human diseases, such as diabetes or neurodegeneration (Garcia-Lopez et al., 2011; Lenz et al., 2013; He et al., 2014).

The fruit fly compound eye is a biological system structured as a stereotypic array of 800 simple units, called ommatidia, which display a highly regular hexagonal pattern (**Figure 1**). This strict organization precisely allows to evaluate the impact of altered gene expression and mutated proteins on the external eye morphology and to detect subtle alterations on the ommatidia geometry due to cell degeneration. One special type of cellular deterioration largely studied using *Drosophila* retina encompasses polyglutamine-based neurodegenerative diseases, namely, Huntington's and spinocerebellar ataxias (SCA) (Ambegaokar et al., 2010).

The overexpression of polyQ-expanded proteins *via* the UAS/Gal4 system in the fly retina results in a depigmented, rough eye phenotype caused by the loss of interommatidial bristles (see the wild-type pattern in the inset of **Figure 1B**), ommatidial fusion, and necrotic tissue (**Figure 2**). The vast majority of studies assessing the rough eye morphology rely on qualitative examination (i.e., visual inspection) of its external appearance to manually rank and categorize mutations based on their severity (Roederer et al., 2005; Bilen and Bonini, 2007; Cukier et al., 2008). Even though evident degenerated phenotypes are easily recognizable, weak modifiers or subtle alterations may go undetected for the naked eye. Quantitative approaches addressing this issue involve histological preparations from which to evaluate the retinal thickness and the regularity of the hexagonal array or scoring scales for the presence of expected features in the retinal surface (Jonshon and Cagan, 2009; Jenny, 2011; Caudron et al., 2013; Mishra and Knust, 2013; Song et al., 2013). Recently, there have been efforts to fully computerize the analysis of *Drosophila*'s rough eye phenotype in bright-field and scanning electron micrograph (SEM) images in the form of ImageJ plugins, called FLEYE and Flynotiper (Diez-Hermano et al., 2015; Iyer et al., 2016). Whereas both methods propose automatized workflows, the former prompts the user to manually delimit the region of interest (ROI) to extract the hand-crafted features from it, which serve as input to a statistical model and finally output a regularity index (IREG) to the user. The second method relies upon a single engineered feature and lacks statistical background to support it.

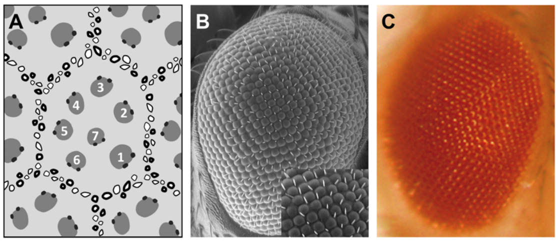

FIGURE 1 | *Drosophila* compound eye structure. Different eye imaging techniques demonstrating the hexagonal packing of the ommatidia and the trapezoidal arrangement of the photoreceptors. **(A)** Schematic representation of a tangential section through the eye. Numbers depict photoreceptors. **(B)** Scanning electron micrograph (SEM). Higher magnification view in inset. **(C)** Bright field microscope picture.

Hence, there is a need to tackle a fully automatized, statistically multivariate assessment of *Drosophila* eye's quantification, given its utmost relevance as a simple, yet comprehensive, model for testing general biology hypotheses and human neurological diseases. Particularly, machine learning algorithms have proven to be incredibly efficient image classifiers during the past decade (Bishop, 2006), rapidly permeating in the fields of cell biology and biomedical image-based screening (Sommer and Gerlich, 2013; Chessel, 2017; Tyagi, 2019). Machine learning methods greatly ease the analysis of complex multi-dimensional data by learning processing rules from examples that can be later on generalized to classify new, unseen data (**Figure 3A**).

The machine learning techniques typically applied to image classification includes support vector machines (SVM) (Ben-Hur et al., 2008; Chauhan et al., 2019), decision trees (DT) (Orrite et al., 2009), random forests (RF) (Schroff et al., 2008), and neural networks (NNs) (Giacinto and Roli, 2001). Alongside processing power and graphic card-dedicated coding, deep learning methods have exponentially grown in importance during the last few years (LeCun et al., 2015; Po-Hsien et al., 2015). The conventional machine learning algorithms aforementioned require data processing and feature enrichment prior to the training phase as they are not suited to work with raw input. In contrast, the deep learning procedures are general-purpose learners in the sense that they can be fed with raw data, automatically suppress irrelevant information, and select discriminant characteristics, composing simple layers of non-linear transformations into a higher, more abstract level of representation (**Figure 3B**). The convolutional neural networks (CNNs) are a well-known architecture for deep learning and have been continuously outperforming the previous machine learning techniques, especially in computer vision and audio recognition (Po-Hsien et al., 2015). With the increasing availability of large biological datasets, its popularity in bioinformatics and bioimaging has quickly escalated, and

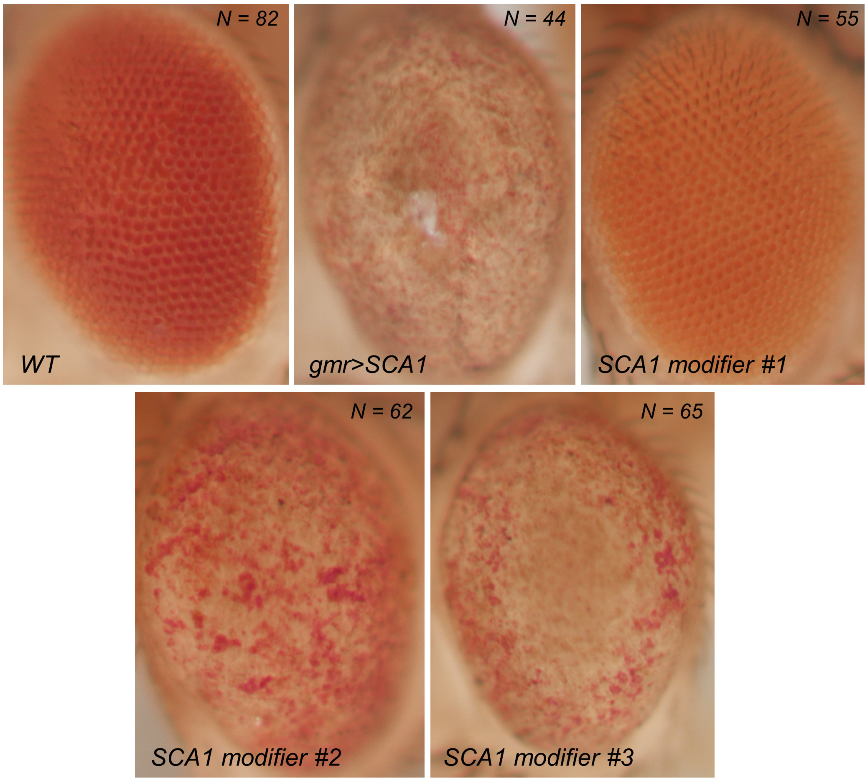

FIGURE 2 | Bright field photographs of rough eye phenotype surfaces. SCA1 gene modifiers can be tested on the fly eye using the UAS/Gal4 system. Complete loss of surface regularity and depigmentation can be appreciated between the WT and SCA1 phenotypes. SCA1 modifiers show intermediate levels of degeneration.

currently CNNs are addressing problems hardly resolvable by former top-notch analysis techniques (Angermueller et al., 2016; Chen et al., 2016; Kraus et al., 2016; Spanhol et al., 2016; Yang et al., 2016; Anwar et al., 2018; Badar et al., 2020). The striking advantage of these networks is that a feature's hand-crafting and engineering are completely avoided as they implement functions insensitive to perturbations, thanks to the multilayer mapping representation of discriminant details.

The novelty of the present work consists in applying and comparing the different image classification strategies mentioned so far in an extensively used biological model, *D. melanogaster*, which has been scarcely addressed before and is in dire need of a state-of-the-art quantification framework.

MATERIALS AND METHODS

Fly Lines and Maintenance

All stocks and crosses were grown in a temperature-controlled incubator at 25°C, 60% relative humidity, and under a 12-h light–dark cycle. They were fed on conventional medium containing wet yeast 84 g/L, NaCl 3.3 g/L, agar 10 g/L, wheat flour 42 g/L, apple juice 167 ml/L, and propionic acid 5 ml/L. To drive transgene expression to the eye photoreceptor, we used the line gmr:GAL4. Rough eye phenotype was triggered using the UAS:hATXN182Q transgene (Fernandez-Funez et al., 2000) that models human type 1 spinocerebellar ataxia (SCA1), and different UAS:modifier-gene constructs were used to test the system capability to recognize intermediate phenotypes.

Sample Size

A total of 308 image files were saved using NIS-Elements software in TIFF format. The number of pictures by category is as follows: 82 wild type (WT), 44 gmr > SCA1, 55 modifier #1, 62 modifier #2, and 65 modifier #3.

External Eye Surface Digital Imaging

Digital pictures (2,880 × 2,048 pixels) of the surface of fly eyes were taken with a Nikon DS-Fi3 digital camera and viewed with a Nikon SMZ1000 stereomicroscope equipped with a Plan Apo× 1 WD70 objective. The flies were anesthetized with CO_2 and their bodies were immobilized on dual adhesive tape, with their heads oriented to have an eye parallel to the microscope objective. The fly eyes were illuminated with a homogeneous fiber optic light passing through a translucid cylinder so that the light rays were dispersed and did not directly reach the eyes. The images taken with this method show a better representation of the surface retinal texture in contrast to the pictures where light fell upon the eye and the lens' reflection was captured by the camera, forming bright-spotted grids. The additional settings include an 8× optical zoom in the stereomicroscope.

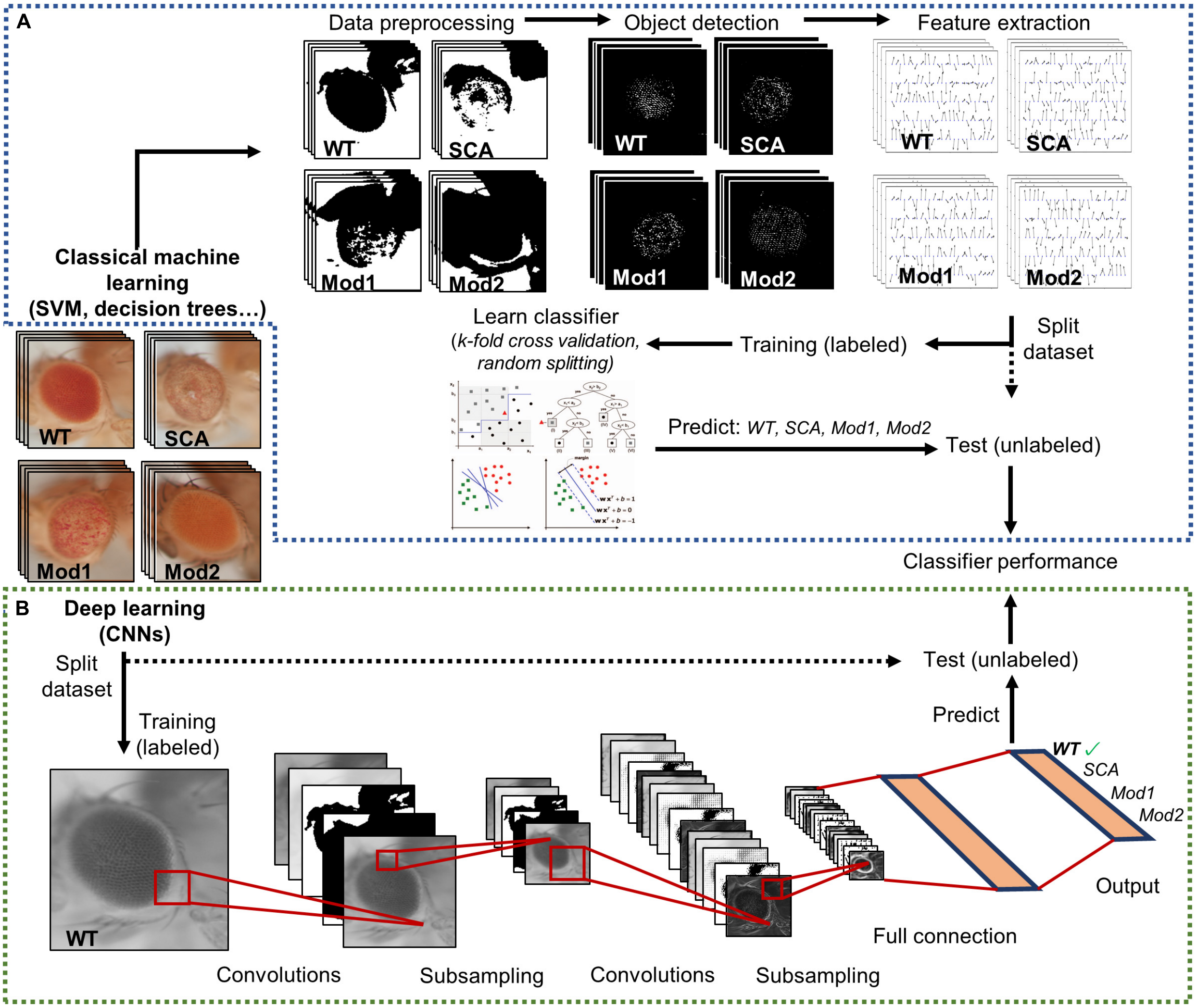

FIGURE 3 | Supervised image classification pipelines. Both workflows start with a dataset labeled with predefined classes. A final performance assessment is also mandatory to test whether the classifier is able to generalize to independent datasets. **(A)** Conventional machine learning methods heavily depend on raw data preprocessing. Splitting into training and test sets occurs only after relevant features have been extracted from the curated data. **(B)** Deep learning techniques receive raw pixel intensities directly as input, so the pipeline begins by splitting the datasets. A simple CNN architecture is depicted as an example. Relevant feature representation occurs in the inner layers of the network, after subsequent convolution and pooling steps. Adapted from Tarca et al. (2007) and Sommer and Gerlich (2013).

ROI Selection Algorithm

All image analyses were performed using R programming language (R Core Team, 2018). The eye images in red/green/blue (RGB) color space were first resized to one-fourth of their original resolution to help fit the image data to the memory capacity of the computer system used. White TopHat morphological transformation with a disc kernel of size 9 was applied using the package EBImage (Pau et al., 2010). The transformed images are converted to grayscale and thresholded to keep only pixels with intensity >0.99 quantile. The overall centroid of the remaining pixels is estimated using the Weiszfeld L1-median (Vardi and Cun-Hui, 2000). For each pixel, the Euclidean distance to the centroid is calculated, and those with distances >0.8 quantile are discarded. A 0.90 confidence level ellipse is estimated on the final selected pixels, and its area is superimposed to the original resized picture to extract the final ROI.

HOG Descriptor and Machine Learning Classifiers

Firstly, RGB ROIs were converted to grayscale while maintaining the original luminance intensities. The histogram of gradient (HOG) features was extracted using the OpenImageR package (Mouselimis, 2017). A 5 × 5 cell descriptor with five orientations covering a gradient range of 0–180° was estimated per cell in the gradient, resulting in a final 125-dimensional vector for each ROI.

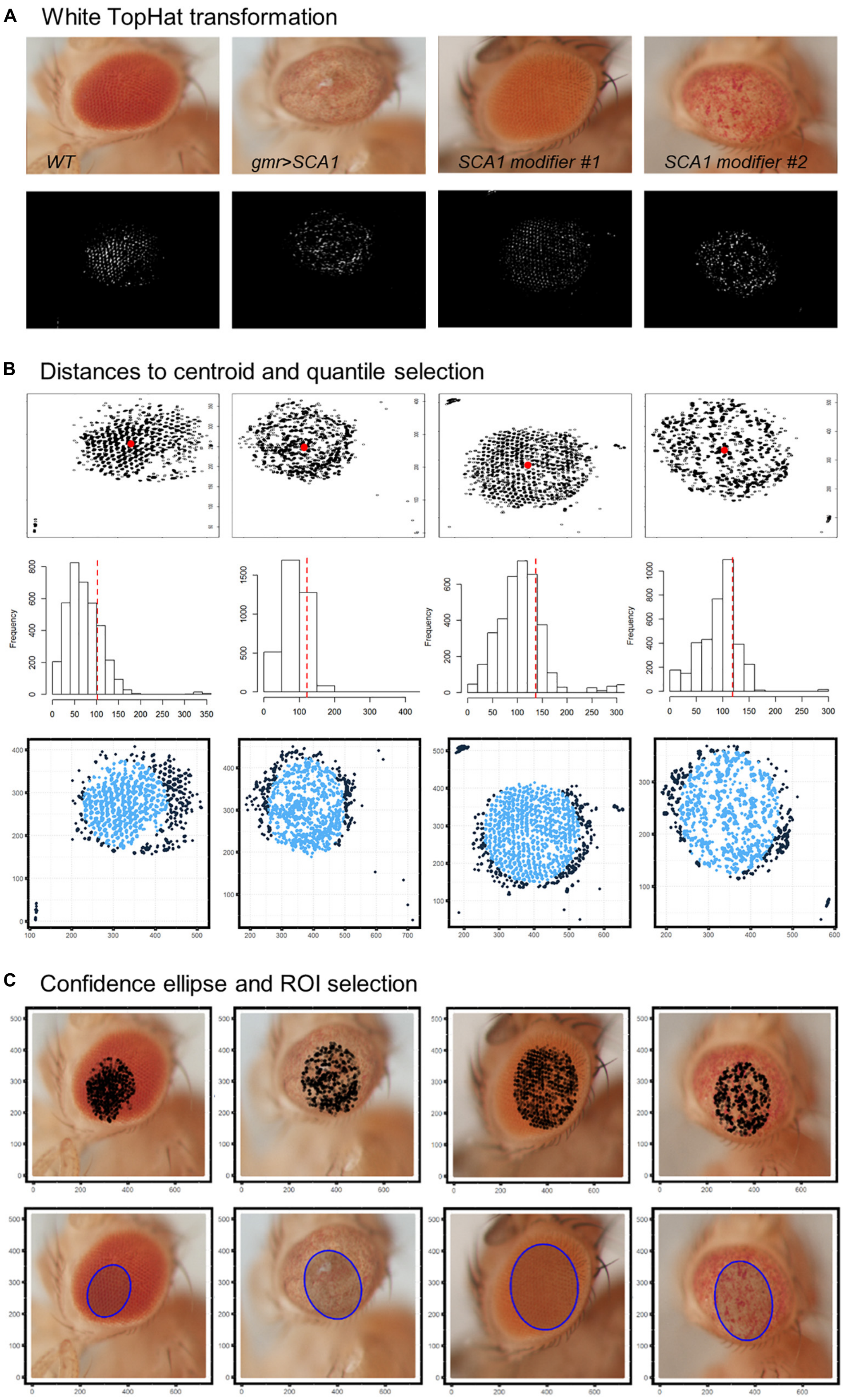

FIGURE 4 | *Drosophila* eye ROI detection strategy. Representative examples of healthy and degenerated eyes are shown. **(A)** Morphological transformation and intensity thresholding extract pixels mostly contained within the eye. **(B)** Euclidean distance to the centroid (red dot) and frequency histogram for quantile selection. Dark blue points are discarded as potential pixel outliers outside the eye limit. **(C)** Selected pixels are superposed to the original image and those within the area of a 0.90 confidence ellipse are extracted as the final ROI (blue shaded ellipse).

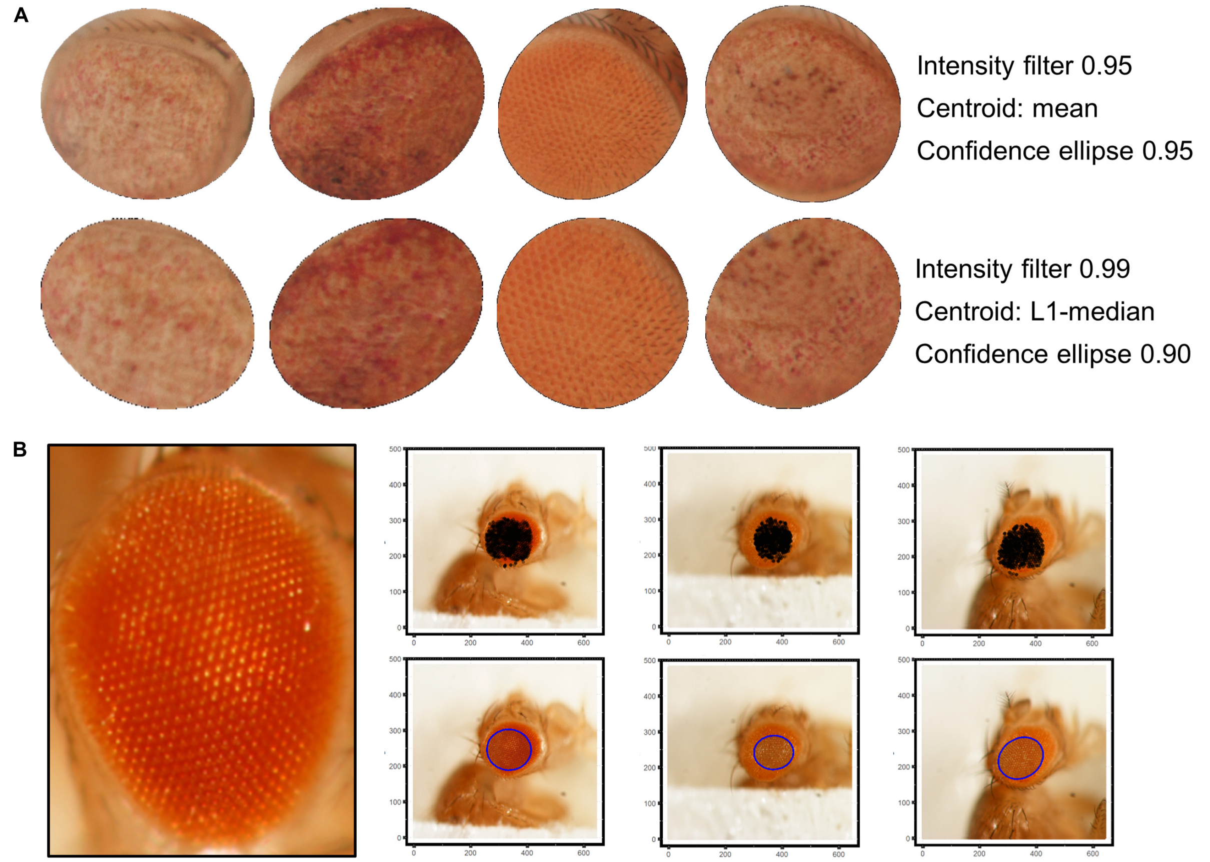

FIGURE 5 | ROI selection optimization and extensibility. **(A)** L1-median centroid alongside stricter thresholds improve the eye area detection. **(B)** Bright-spotted fly eye images can also be successfully segmented using this method.

TABLE 1 | Machine learning classifier confusion matrix.

	Reference																			
Predicted	**WT**				**gmr > SCA**				**SCA modifier #1**				**SCA modifier #2**				**SCA modifier #3**			
WT	20	16	20	20	0	2	2	2	1	4	3	1	0	0	0	1	0	4	3	1
gmr > SCA	0	2	0	0	11	7	7	8	0	2	0	0	0	1	1	0	0	2	3	0
SCA modifier #1	0	0	0	0	0	0	2	0	12	7	10	11	0	0	0	0	0	0	0	0
SCA modifier #2	0	1	0	0	0	0	0	0	0	0	0	1	14	12	11	12	0	3	0	0
SCA modifier #3	0	1	0	0	0	2	0	1	0	0	0	0	1	2	3	2	16	7	10	15

Colors scheme: SVM, DT, Boost DT, RF.

The SVM, DT, and RF algorithms were trained on the extracted HOG features. The dataset was split into training and test sets with a 75/25 ratio using stratified random sampling to ensure class representation. The modeling strategy for all classifiers included cross-validation to assess generalization, grid search for parameter selection and performance evaluation on test set *via* confusion matrix, global accuracy, Kappa statistic, and multiclass pairwise area under the curve (AUC) (Ferri et al., 2003). We tested a radial basis function (RBF) kernel SVM, DT, adaptative boosting DT, and 1,000-trees RF using the R packages *kernlab*, *C50*, and *caret* (Karatzoglou et al., 2004; Kuhn et al., 2015).

Deep Learning Classifiers

The extracted ROIs were resized to a 224 × 224 × 3 RGB array and stored in vectorized form, resulting in a final data frame of 308 × 150,528 dimensions. The dataset was split into training and test sets with a 75/25 ratio using stratified random sampling to ensure class representation. We further confirmed that the training and test partitions were representative of the sample variability *via* a loss plot (**Supplementary Figure S1**). Two CNNs were trained on this data:

(i) A simple CNN trained from scratch, with hyperbolic tangent as activation function, two convolutional layers,

TABLE 2 | Machine learning performance evaluation metrics on test data.

	Classifier			
Metric	**SVM RBF**	**DT**	**AdaBoost DT**	**1000 RF**
Accuracy	0.973 (0.907–0.997)	0.653 (0.535–0.760)	0.773 (0.662–0.862)	0.880 (0.784–0.944)
Kappa	0.966	0.560	0.711	0.847
Multiclass AUC	0.978	0.665	0.763	0.906

True positives are shaded in gray.

two pooling layers, two fully connected layers (200 and five nodes), 30 epochs, and a typical softmax output. Each convolutional layer uses a 5 × 5 kernel and 20 or 50 filters, respectively. The pooling layers apply a classical "max pooling" approach. All the parameters in kernels, bias terms, and weight vectors are automatically learned by back-propagation with a learning rate equal to 0.05 and a stochastic gradient descent (SGD) optimizer to ensure that the magnitude of the updates stayed small (Bottou, 2010).

(ii) A fine-tuned CNN using an ImageNet pretrained model with a batch-normalization network structure (Deng et al., 2009; Ioffe and Szegedy, 2015), 30 epochs, a very slow learning rate (0.05), and a SGD optimizer. The final fully connected (five nodes) and softmax output layers are tuned to fit the new fly eye ROIs.

For the CNN training, the R package *MXNet* compiled for the central processing unit (CPU) was used (Tianqi et al., 2015). Performance was assessed in terms of confusion matrix and global accuracy using the *caret* package (Kuhn, 2008).

RESULTS

Automatized Detection of *Drosophila* Eye ROIs From Bright-Field Images

The first step in the quantification workflow is the extraction of pixels corresponding to the fly eye from the rest of the image. One concern is that the eye is not flat but convex in morphology, so under white light only the central surface is at the camera focus. To address this issue, white TopHat morphological transformations were performed, defined as the difference between the input image and its opening by a structuring kernel. The opening operation involves erosion followed by a dilation of the image, retrieving the objects of the input image that are simultaneously smaller than the structuring element and brighter than their neighbors.

Best results were obtained using a 9 × 9 disc-shaped kernel followed by a thresholding of pixels with intensities over the 0.99 percentile (**Figure 4A**). Afterward, the centroid of the selected pixels was calculated as the L1-median, which is a more robust estimator of the central coordinates than the arithmetic mean. Points with Euclidean distance to the centroid greater than 0.8 percentile are more likely to lie outside the eye area and were discarded (**Figure 4B**). A 0.90 confidence ellipse calculated on the selected pixels conforms the area of the final ROI, which was superimposed and cropped from the original eye image (**Figure 4C**). As can be appreciated in the example images, the method is invariant to the location of the eye within the image. Various combinations of the thresholds and the centroid estimator were tested (**Figure 5A**). The proposed segmentation method also works well on bright-field images where light falls directly onto the ommatidium and the eye is seen as a region enriched in reflection spots (**Figure 5B**). The full array of the final ROIs is represented in **Supplementary Figure S2**.

We also addressed whether there was any anatomical preference in the ROI extraction that could be biasing the classification procedure. To this extent, heatmaps overlaying all the elliptic ROIs were generated genotype-wise (**Supplementary Figure S3**). There were a few instances in which the selected ROI included areas outside the eye. This happened more easily in the modifier genotypes and can be seen in the figure as shades that lay outside the eye border. Overall, the ROI extraction seems to be robust against the different ommatidial distribution and eye shapes.

HOG Feature Extraction

Region of interests cannot be directly input to classical machine learning techniques, so the information contained in their pixels must be extracted beforehand. This is done by estimating a HOG, which can be interpreted as a feature descriptor of a picture that outputs summarized information about predominant shapes and structures. The HOG technique starts by dividing the picture into cells and identifying whether a given cell is an edge or not. HOG provides the edge direction as well, which is done by extracting the gradient and orientation (magnitude and direction) of the edges across neighbor cells. These cells comprise the local regions of related pixels, from which the HOG generates a histogram using the gradients and the orientations of the pixel values, hence the name "histogram of oriented gradients."

Prior to the HOG extraction, the ROIs were transformed to grayscale, preserving the luminance of the original RGB image. Then, a 125-dimensional feature vector is extracted for each ROI, representing the frequency of a certain gradient within the image (**Supplementary Figure S4**). The matrix formed by the 125-D vectors of all ROIs conforms to the input for the machine learning classifiers.

Note that HOG is only used to feed the classical machine learning algorithms (SVM, DT, and RF), not the deep learning CNN, which directly uses the pixels' values as input. This is due to the internal structure of the CNN, the inner layers of which serve as border and edge detectors themselves. This is a reason that led us to believe that pigmentation was not affecting the classification procedure, given that all the methods we used relied on structure detectors rather than color differences.

Comparison of Machine Learning Classifiers

Support vector machine with RBF kernel, DT, AdaBoost DT, and 1,000-trees RF algorithms were tested on the extracted HOG features. The sample consisted in 308 fly eye images distributed in five different phenotype classes with varying

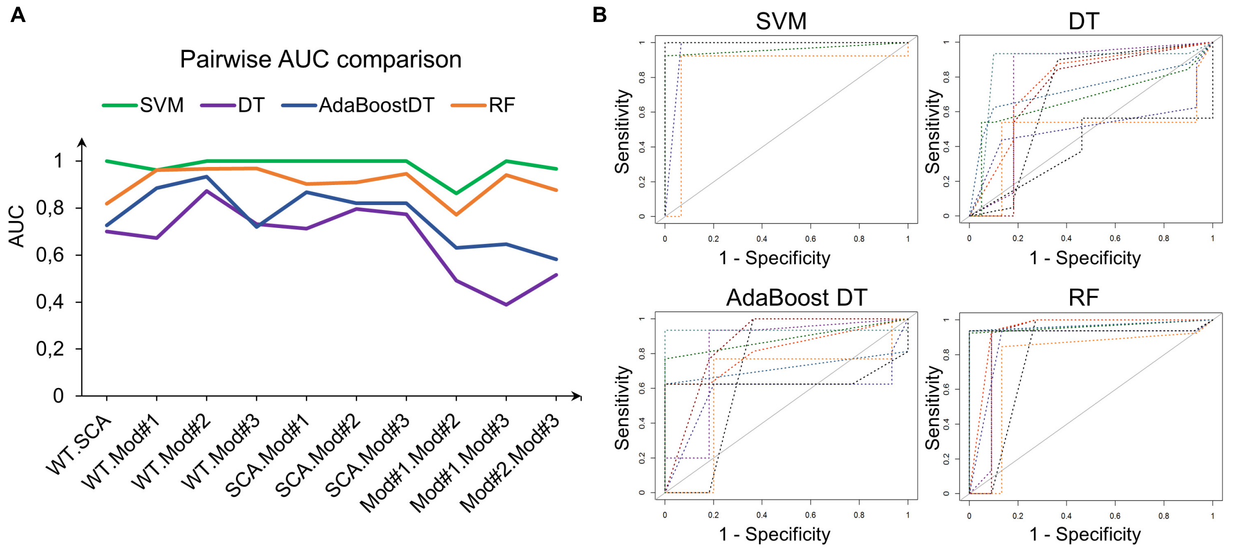

FIGURE 6 | Class pairwise AUC and ROC. **(A)** SVM with RBF kernel outperforms the other classifiers in all comparisons. **(B)** ROC plots corresponding to the AUCs in **(A)**.

degrees of retinal surface degeneration. The data were split using stratified random sampling in 75% training and 25% test set. The optimal parameters for each classifier were found using 10-fold cross-validation on the training set. **Table 1** shows the confusion matrix, and **Table 2** represents the global accuracy, Kappa statistic, and multiclass AUC, defined as the average AUC of class pairwise comparisons (**Figure 6A**), which was calculated on the test data. The pairwise receiver operating characteristic (ROC) plots are represented in **Figure 6B**.

In general, the four classifiers performed fairly well on unseen data. Both DT algorithms fell on the low spectrum either in accuracy and AUC (<0.80), whereas RF achieved a remarkable AUC of 0.90. Overall, SVM accomplished the best results among all the error metrics evaluated, with a global accuracy of 0.97 (0.90–0.99), Kappa of 0.96, and a multiclass AUC of roughly 0.98. The parameters that yield these results were a Gaussian kernel, a cost penalty = 1, and sigma = 0.005. The WT eyes were the most correctly classified phenotype by the four methods.

From the SVM estimated class probabilities, it is possible to derive a IREG that ranges from 0 (total degeneration) to 1 (healthy eye) (Diez-Hermano et al., 2015). It is based on the knowledge of the degeneration intensity of the phenotypes involved in the model: WT < modifier #1 < modifier #2 < modifier #3 < SCA1, from absence to full presence of rough eye phenotype. IREG is then calculated as:

$$\text{IREG} = \frac{\begin{array}{c}4 \cdot P\left(\text{eye} = \text{WT}\right) + 3 \cdot P\left(\text{eye} = \text{Mod\#1}\right)\\ +2 \cdot P\left(\text{eye} = \text{Mod\#2}\right) + P(\text{eye} = \text{Mod\#3})\end{array}}{4}$$

when estimated on the test data, the IREG distribution fits to the expected values and properly reflects the intrinsic variability of the fly model and the rough eye phenotype (**Figure 7**).

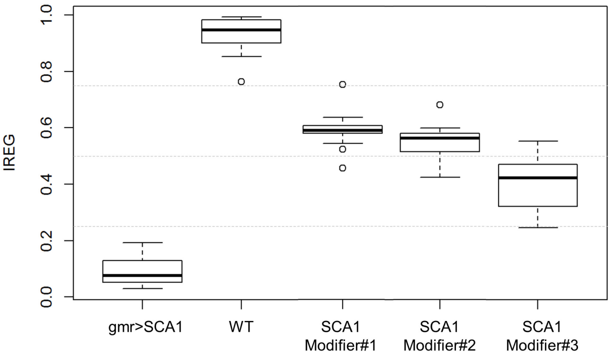

FIGURE 7 | IREG boxplots. WT and SCA1 eyes show opposing IREG values and no distribution overlap. SCA modifiers show intermediate rough eye phenotypes and slight distribution overlapping, but the median and central boxes differentiate them. Gray dotted lines mark 0.25, 0.5 and 0.75 IREG values. Sample sizes are as follows: 82 WT, 44 gmr > SCA1, 55 modifier #1, 62 modifier #2, and 65 modifier #3.

Deep Learning Classifiers

In contrast with the previous machine learning classifiers that needed a transformation of the cropped images into an enriched feature space (HOG), deep learning algorithms directly use the ROI pixel intensity arrays as input. The features are automatically learned during the learning process, from gross edge and contour detection to discrimination of fine details the deeper the layer in the network.

Two different strategies were followed to train the deep networks: learning a *de novo* model and transfer learning. The latter approach takes advantage of CNNs pre-trained on very large samples, which is especially well suited for classifying new small datasets as the majority of patterns and motifs commonly

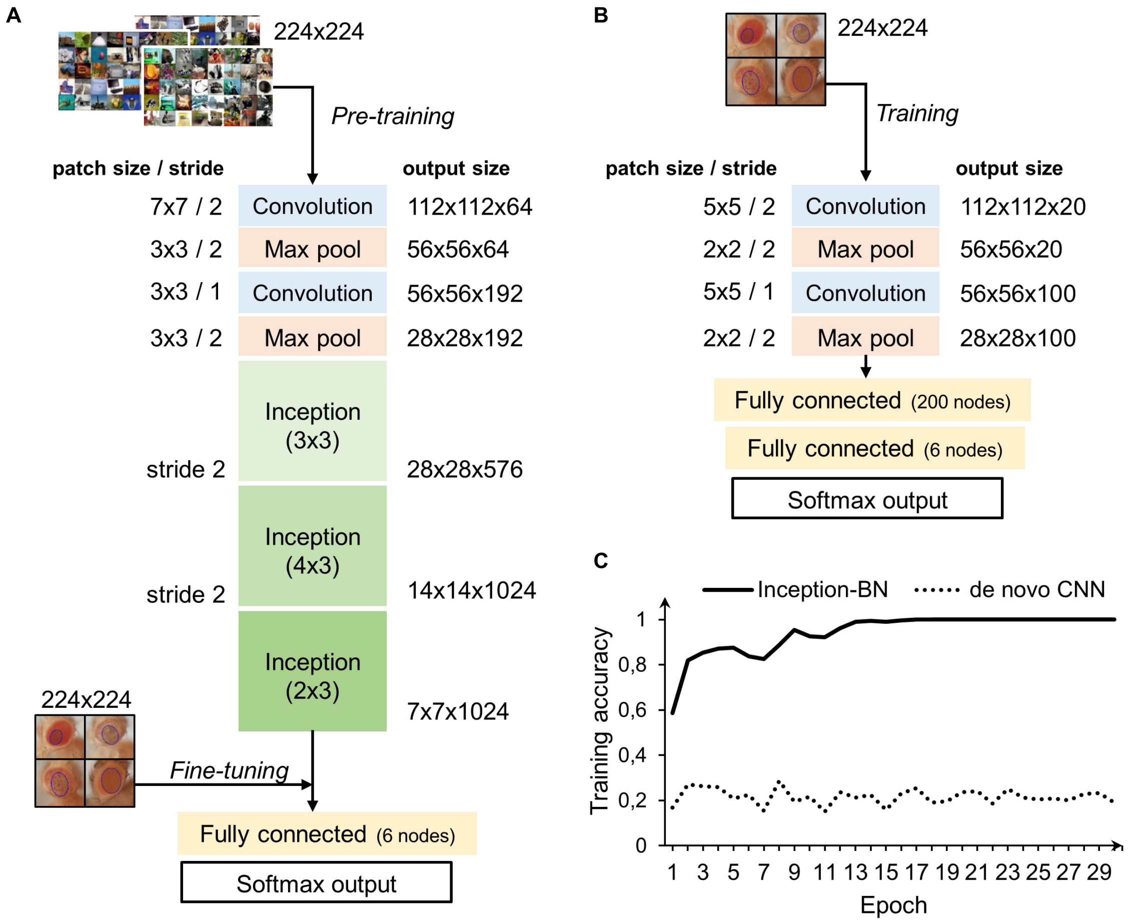

FIGURE 8 | CNN architectures and learning curve. **(A)** Inception-BN is a 15-layered CNN pre-trained on thousands of natural images. A six-nodes fully connected layer and softmax output are trained with new fly eye images on top of the Inception blocks. **(B)** *De novo* CNN with five layers and a six-nodes fully connected and softmax output. **(C)** Training accuracy in the pre-trained model starts pretty high and quickly rises in the first few epochs. In contrast, *de novo* model accuracy remains low and fluctuates around the initial value with no apparent signs of improvement.

TABLE 3 | Convolutional neural networks classifier confusion matrix.

	Reference									
Predicted	**WT**		**gmr > SCA**		**SCA modifier #1**		**SCA modifier #2**		**SCA modifier #3**	
WT	20	20	0	11	0	13	0	15	0	16
gmr > SCA	0	0	11	0	0	0	0	0	0	0
SCA modifier #1	0	0	0	0	13	0	0	0	0	0
SCA modifier #2	0	0	0	0	0	0	14	0	0	0
SCA modifier #3	0	0	0	0	0	0	1	0	16	0

Color scheme: Inception-BN de novo CNN.

found in the images are already known to the model internal representation. Thus, it is only necessary to fine-tune the final layers to learn the particularities of the new images, which is many times faster than training a CNN from scratch and does not require thousands of labeled examples. The architectures of both *de novo* and pre-trained CNN are depicted in **Figures 8A,B**. The pre-trained model chosen uses the inception structure, characterized by including mini-batch normalization (BN) for each training epoch, which allows for high learning rates and acts as regularizer. In comparison, the *de novo* CNN is much shallower due to computational constraints.

Accuracy during the training phase is usually a reliable indicator of a CNN capability to learn the discriminative features with the available sample size (**Figure 8C**). The curve of the *de novo* CNN is a clear sign that either the network is not deep enough or the training sample is too small for the complexity

TABLE 4 | Convolutional neural networks performance evaluation metrics on test data.

	Classifier	
Metric	**Inception-BN**	***De novo* CNN**
Accuracy	0.986	0.146
Multiclass AUC	0.997	0.5

True positives are shaded in gray.

of the classification task at hand. One major concern with the pre-trained inception-BN was the possibility that the network was memorizing the training set, given the few epochs it needed to achieve perfect training accuracy. A performance assessment in an independent test set of unseen images gave impressive accuracy and AUC values close to 1 (**Tables 3**, **4**), refuting the possibility of overfitting. The CNN trained from scratch predicted every eye to be WT, indicative of the weak classifying rule learned in training.

Transfer learning CNN was also the only model capable of properly quantifying the pictures taken under drastically different illumination techniques, relative to the sample that it was trained on (dispersed indirect light). The genetic background also differed from the training sample and corresponds to tau-related neurodegeneration, the accumulation of which contributes to the pathology of Alzheimer disease (Lasagna-Reeves et al., 2016; Rousseaux et al., 2016; Galasso et al., 2017). **Supplementary Figure S5** shows how IREG estimations coming from CNN were more representative of the surface regularity than IREG coming from the SVM, which was the top-performance machine learning technique. In fact, the SVM predicted all eyes to have essentially the same IREG value. Additionally, retraining all models with our original sample of bright-spotted eyes (**Supplementary Figure S2B**) resulted in transfer learning CNN being the only model that could successfully generalize to a set of new eyes (**Supplementary Table S1**).

Given its classification accuracy and versatility, transfer learning with the pre-trained inception-BN model is arguably the top performer classifier among all the methods tested in this work.

DISCUSSION

The present work provides a novel and fully automated method to quantitatively assess the degeneration intensity of the fruit flies' compound eye using reliable and robust state-of-the-art machine learning techniques. This new method consists in the acquisition of bright-field images from the external retinal surface, the automatic extraction of a ROI enriched in information of the eye morphology, and a classification algorithm built around a pre-trained deep learning algorithm, fine-tuned to the particularities of the eye degeneration's images. Additionally, a model based on the combination of HOG features extraction and Gaussian kernel SVM offered performance on par with the CNN and, in fact, required much less training time.

In contrast with previous quantification approaches (Caudron et al., 2013; Diez-Hermano et al., 2015; Iyer et al., 2016), this method does not rely on patterns that are created by light reflecting in the eye lenses, so it can be applied to extract ROIs from a variety of illumination conditions. While performing the experiment to validate the method, we have estimated the total time that it takes for a researcher to analyze an experimental group of 50 flies: 1.5 h from anesthetizing the flies until the final IREG plot was statistically assessed. It is noteworthy that the most part of that estimation was devoted to capturing the images, which is a mandatory step, whether the flies are to be manually or automatically classified later on. The proposed pipeline can process a 2,880 × 2,048-resolution image in less than 10 s and batches of 50 images in approximately 90 s, depending on the hardware that it runs on.

One of the major goals of this work was to analyze the potentiality of deep learning techniques to extract feature maps directly from the raw pixel array, which could be used as input to other conventional machine learning algorithms (i.e., SVM). Due to computational constraints, it was not possible to tune up the graphics processing unit-compiled versions of the software utilized, and the prohibitive CPU computational time and memory usage in its absence made the evaluation of the former objective not feasible. HOG was chosen as an alternative descriptor, given its successful application in object detection (Dalal and Triggs, 2005; Orrite et al., 2009; Li et al., 2012), and ended up resulting in a surprisingly powerful classifier in combination with conventional SVM. Nonetheless, the pre-trained CNN will still be preferable for pictures taken under illumination conditions different from the ones the models were trained on as it has been shown to have greater discriminative power.

A drawback of CNNs is the staggering amount of labeled training examples that they need to learn adequate internal representations of image patterns and motifs. Although the sample size in *Drosophila* experiments ranks among the largest of any animal model in genetics, it is still a titanic effort to go beyond 1,000 images in a typical fruit fly assay. This limitation affected the performance of the *de novo* CNN, which led to the alternative strategy of transfer learning. Using inception-BN, a CNN pre-trained on millions of natural images (Ioffe and Szegedy, 2015), proved to be a well-thought solution that definitely opens up the field of deep learning to small-scale biology setups.

Future lines of work include developing the fly eye detection algorithm further to make it extensible to other image capturing techniques (i.e., SEM). A more immediate priority is the creation of a user-friendly Shiny application (Winston et al., 2017) that will allow the researcher to tweak the ROI selection parameters to fit the peculiarities of its own dataset prior to the degeneration quantification. Depending on the particular hardware settings, the app may also offer the user the possibility to train its own SVM or deep learning model.

The aim of this work is to provide a workflow that results in a quantitative assessment of the degree of eye degeneration of hundreds of flies in a quick and unbiased manner. This makes our method particularly suitable for discriminating potential genetic rescues or aberrations. We believe that our algorithm could be easily implemented in fully robotized environments as the final quantification step. The highlighted strengths of the proposed framework will enhance the sensitivity of high-throughput genetic screens based on rough eye phenotypes and demonstrate that fly eye imaging is a top-notch technique for the quantitative modeling of human diseases.

DATA AVAILABILITY STATEMENT

The datasets generated and analyzed for this study, alongside the R scripts, can be found in the FigShare repository at https://tinyurl.com/un8tacu.

AUTHOR CONTRIBUTIONS

SD-H performed the experiments, took the fly eye pictures, analyzed the data, and wrote the manuscript. MG and DS designed the genetic background of the flies, took the fly eye pictures, and helped with the manuscript writing. EV-L analyzed the data and helped with the manuscript writing.

FUNDING

This work was supported by grants to MG and DS [Ministerio de Ciencia e Innovación (MICINN), grants BFU2011-23978 and BFU2015-68149-R co-financed by the European Regional Development Fund].

ACKNOWLEDGMENTS

The authors thank Candido P. Segurado, for his contribution to the fly lines maintenance and the eye pictures collection, and Dr. Ismael Al-Ramahi and Dr. Maria de Haro, for loaning a set of pictures comprising different illumination conditions and genetic backgrounds, which were used for validation purposes. The authors also note that this work includes content that first appeared in the master's thesis of Diez-Hermano (2017).

SUPPLEMENTARY MATERIAL

The Supplementary Material for this article can be found online at: https://www.frontiersin.org/articles/10.3389/fnins.2020.00516/full#supplementary-material

REFERENCES

Ambegaokar, S. S., Roy, B., and Jackson, G. R. (2010). Neurodegenerative models in Drosophila: polyglutamine disorders, Parkinson disease, and amyotrophic lateral sclerosis. *Neurobiol. Dis.* 40:1. doi: 10.1016/j.nbd.2010.05.026

Angermueller, C., Parnamaa, T., Parts, L., and Stegle, O. (2016). Deep learning for computational biology. *Mol. Syst. Biol.* 12:7. doi: 10.15252/msb.20156651

Anwar, S. M., Majid, M., and Qayyum, A. (2018). Medical image analysis using convolutional neural networks: a review. *J. Med. Syst.* 42:226. doi: 10.1007/s10916-018-1088-1

Badar, M., Haris, M., and Fatima, A. (2020). Application of deep learning for retinal image analysis: a review. *Comput. Sci. Rev.* 35:100203. doi: 10.1016/j.cosrev.2019.100203

Ben-Hur, A., Ong, C. S., Sonnenburg, S., Schölkopf, B., and Rätsch, G. (2008). Support vector machines and kernels for computational biology. *PLoS Comput. Biol.* 4:173. doi: 10.1371/journal.pcbi.1000173

Bilen, J., and Bonini, N. M. (2007). Genome-wide screen for modifiers of ataxin-3 neurodegeneration in Drosophila. *PLoS Genet.* 3:30177. doi: 10.1371/journal.pgen.0030177

Bishop, C. M. (2006). *Pattern Recognition And Machine Learning*. Berlin: Springer.

Bottou, L. (2010). "Large-scale machine learning with stochastic gradient descent," in *Proceedings of the COMPSTAT'2010*, eds Y. Lechevallier, and G. Saporta, (Cham: Physica-Verlag HD).

Caudron, Q., Lyn-Adams, C., Aston, J. A. D., Frenguelli, B. G., and Moffat, K. G. (2013). Quantitative assessment of ommatidial distortion in Drosophila melanogaster: a tool to investigate genetic interactions. *J. Neurogenet.* 24:87.

Chauhan, V. K., Dahiya, K., and Sharma, A. (2019). Problem formulations and solvers in linear SVM: a review. *Artif. Intell. Rev.* 52, 803–855. doi: 10.1007/s10462-018-9614-6

Chen, C. L., Mahjoubfar, A., Tai, L. C., Blaby, I. K., Huang, A., Niazi, K. R., et al. (2016). Deep learning in label-free cell classification. *Sci. Rep.* 6:21471. doi: 10.1038/srep21471

Chessel, A. (2017). An Overview of data science uses in bioimage informatics. *Methods* 115, 110–118. doi: 10.1016/j.ymeth.2016.12.014

Cukier, H. N., Perez, A. M., Collins, A. L., Zhou, Z., Zoghbi, H. Y., and Botas, J. (2008). Genetic modifiers of MeCP2 function in Drosophila. *PLoS Genet.* 4:179. doi: 10.1371/journal.pgen.1000179

Dalal, N., and Triggs, B. (2005). "Histograms of oriented gradients for human detection," in *Proceedings of the 2005 IEEE Computer Society Conference on Computer Vision and Pattern Recognition (CVPR'05)*, San Diego, CA.

Deng, J., Dong, W., Socher, R., Li, L. J., Li, K., and Fei-Fei, L. (2009). "Imagenet: A large-scale hierarchical image database," in *Proceedings of the 2009 IEEE Conference on Computer Vision and Pattern Recognition*, Miami, FL.

Diez-Hermano, S. (2017). *Machine Learning Regularity Representation From Biological Patterns: A Case Study In A Drosophila Neurodegenerative Model*. Master thesis, Open University of Catalonia (UOC), Spain.

Diez-Hermano, S., Valero, J., Rueda, C., Ganfornina, M. D., and Sanchez, D. (2015). An automated image analysis method to measure regularity in biological patterns: a case study in a Drosophila neurodegenerative model. *Mol. Neurodegener.* 10:9. doi: 10.1186/s13024-015-0005-z

Fernandez-Funez, P., Nino-Rosales, M. L., de Gouyon, B., She, W. C., Luchak, J. M., Martinez, K., et al. (2000). Identification of genes that modify ataxin-1-induced neurodegeneration. *Nature* 408:6808. doi: 10.1038/35040584

Ferri, C., Hernandez-Orallo, J., and Salido, M. A. (2003). "Volume under the ROC surface for multi-class problems. exact computation and evaluation of approximations," in *Proceedings of the 14th European Conference on Machine Learning*, València.

Galasso, A., Cameron, C. S., Frenguelli, B. G., and Moffat, K. G. (2017). An AMPK-dependent regulatory pathway in tau-mediated toxicity. *Biol. Open* 6:10. doi: 10.1242/bio.022863

Garcia-Lopez, A., Llamusi, B., Orzaez, M., Perez-Paya, E., and Artero, R. D. (2011). In vivo discovery of a peptide that prevents CUG-RNA hairpin formation and reverses RNA toxicity in myotonic dystrophy models. *Proc. Natl. Acad. Sci. U.S.A.* 108:29. doi: 10.1073/pnas.1018213108

Giacinto, G., and Roli, F. (2001). Design of effective neural network ensembles for image classification purposes. *Image Vis. Comp.* 19:9. doi: 10.1016/S0262-8856(01)00045-2

He, B. Z., Ludwig, M. Z., Dickerson, D. A., Barse, L., Arun, B., and Vilhjalmsson, B. J. (2014). Effect of genetic variation in a Drosophila model of diabetes-associated misfolded human proinsulin. *Genetics* 196:2. doi: 10.1534/genetics.113.157800

Ioffe, S., and Szegedy, C. (2015). Batch normalization: Accelerating deep network training by reducing internal covariate shift. *arXiv* [Preprint], Available online at: https://arxiv.org/abs/1502.03167 (accessed May 15, 2017).

Iyer, J., Wang, Q., Le, T., Pizzo, L., Grönke, S., and Ambegaokar, S. (2016). Quantitative assessment of eye phenotypes for functional genetic studies using Drosophila melanogaster. *G3* 3:5. doi: 10.1534/g3.116.027060/-/DC1

Jenny, A. (2011). Preparation of adult Drosophila eyes for thin sectioning and microscopic analysis. *J. Vis. Exp.* 54:2959. doi: 10.3791/2959

Johnston, D. (2002). The art and design of genetic screens: Drosophila melanogaster. *Nat. Rev. Genet.* 3, 176–188.

Jonshon, R. I., and Cagan, R. L. (2009). A Quantitative method to analyze Drosophila pupal eye patterning. *PLoS One* 4: e7008. doi: 10.1371/journal.pone.0007008.g001

Karatzoglou, A., Smola, A., Hornik, K., and Zeileis, A. (2004). kernlab - An S4 Package for kernel methods in R. *J. Stat. Soft.* 11:9. doi: 10.18637/jss.v011.i09

Kraus, O. Z., Ba, J. L., and Frey, B. J. (2016). Classifying and segmenting microscopy images with deep multiple instance learning. *Bioinformatics* 32:12. doi: 10.1093/bioinformatics/btw252

Kuhn, M. (2008). Building predictive models in R using the caret package. *J. Stat. Soft.* 28:5. doi: 10.18637/jss.v028.i05

Kuhn, M., Weston, S., Coulter, N., and Culp, M. (2015). *C50: C5.0 Decision Trees and Rule-Based Models R Package Version 0.1.0-24*. Available online at: https://CRAN.R-project.org/package=C50 (accessed February 10, 2017).

Lasagna-Reeves, C. A., de Haro, M., Hao, S., Park, J., Rousseaux, M. W., and Al-Ramahi, I. (2016). Reduction of Nuak1 decreases tau and reverses phenotypes in a tauopathy mouse model. *Neuron* 92:2. doi: 10.1016/j.neuron.2016.09.022

LeCun, Y., Bengio, Y., and Hinton, G. (2015). Deep learning. *Nature* 521:7553. doi: 10.1038/nature14539

Lenz, S., Karsten, P., Schulz, J. B., and Voigt, A. (2013). Drosophila as a screening tool to study human neurodegenerative diseases. *J. Neurochem.* 127:4. doi: 10.1111/jnc.12446

Li, S., Xiabi, L., Ling, M., Chunwu, Z., Xinming, Z., and Yanfeng, Z. (2012). "Using HOG-LBP features and MMP learning to recognize imaging signs of lung lesions," in *Proceedings of the 2012 25th IEEE International Symposium on Computer-Based Medical Systems (CBMS)*, Rome.

Mishra, M., and Knust, E. (2013). Analysis of the Drosophila compound eye with light and electron microscopy. *Meth. Mol. Biol.* 935, 161–182. doi: 10.1007/978-1-62703-080-9_11

Mouselimis, L. (2017). *OpenImageR: An Image Processing Toolkit. R Package Version 1.0.5*.

Orrite, C., Gañán, A., and Rogez, G. (2009). "HOG based decision tree for facial expression classification," in *Pattern Recognition and Image Analysis, 5524 (Lecture Notes in Computer Science)*, eds H. Araujo, A. Mendonça, A. Pinho, and M. Torres, (Berlin: Springer), 176–183.

Pau, G., Fuchs, F., Sklyar, O., Boutros, M., and Huber, W. (2010). EBImage - an R package for image processing with applications to cellular phenotypes. *Bioinformatics* 26:7. doi: 10.1093/bioinformatics/btq046

Po-Hsien, L., Shun-Feng, S., Ming-Chang, C., and Chih-Ching, H. (2015). "Deep Learning and its application to general image classification," in *Proceedings of the 2015 International Conference on Informative and Cybernetics for Computational Social Systems (ICCSS)*, Chengdu. doi: 10.1186/s12859-017-1954-8

R Core Team, (2018). *R: A Language And Environment For Statistical Computing*. Vienna: R Foundation for Satistical Computing.

Reiter, L. T., Potocki, L., Chien, S., Gribskov, M., and Bier, E. (2001). A systematic analysis of human disease-associated gene sequences in Drosophila melanogaster. *Genome Res.* 11, 1114–1125. doi: 10.1101/gr.169101

Roederer, K., Cozy, L., Anderson, J., and Kumar, J. P. (2005). Novel dominant-negative mutation within the six domain of the conserved eye specification gene sine oculis inhibits eye development in Drosophila. *Dev. Dyn.* 232:3. doi: 10.1002/dvdy.20316

Rousseaux, M. W., de Haro, M., Lasagna-Reeves, C. A., De Maio, A., Park, J., and Vilanova-Velez, L. (2016). TRIM28 regulates the nuclear accumulation and toxicity of both alpha-synuclein and tau. *eLife* 5:19809. doi: 10.7554/eLife.19809

Schroff, F., Criminisi, A., and Zisserman, A. (2008). "Object class segmentation using random forests," in *Proceedings of the British Machine Vision Conference 2008*, Leeds.

Sommer, C., and Gerlich, D. W. (2013). Machine learning in cell biology - teaching computers to recognize phenotypes. *J. Cell Sci.* 126:24. doi: 10.1242/jcs.123604

Song, W., Smith, M. R., Syed, A., Lukacsovich, T., Barbaro, B. A., and Purcell, J. (2013). Morphometric analysis of Huntington's disease neurodegeneration in Drosophila. *Meth. Mol. Biol.* 1017, 14–57. doi: 10.1007/978-1-62703-438-8_3

Spanhol, F. A., Oliveira, L. S., Petitjean, C., and Heutte, L. (2016). "Breast cancer histopathological image classification using convolutional neural networks," in *Proceedings of the 2016 International Joint Conference on Neural Networks (IJCNN)*, Vancouver, BC.

Tarca, A., Carey, V. J., Chen, X. W., Romero, R., and Draghici, S. (2007). Machine learning and its applications to biology. *PLoS Comput. Biol.* 3:e116. doi: 10.1371/journal.pcbi.0030116

Thaker, H. M., and Kankel, D. R. (1992). Mosaic analysis gives an estimate of the extent of genomic involvement in the development of the visual system in Drosophila melanogaster. *Genetics* 131, 883–894.

Thomas, B. J., and Wassarman, D. A. (1999). A fly's eye view of biology. *Trends. Genet.* 15, 184–190.

Tianqi, C., Qiang, K., and Tong, H. (2015). *Mxnet: MXNet. R Package Version 0.9.4*. Available online at: https://github.com/dmlc/mxnet/tree/master/R-package (accessed March 3, 2017).

Treisman, J. E. (2013). Retinal differentiation in Drosophila. *Interdiscip. Rev. Dev. Biol.* 2:4. doi: 10.1002/wdev.100

Tyagi, V. (2019). A review on image classification techniques to classify neurological disorders of brain MRI. *IEEE ICICT* 1, 1–4. doi: 10.1109/ICICT46931.2019.8977658

Vardi, Y., and Cun-Hui, Z. (2000). The multivariate L1-median and associated data depth. *PNAS* 97, 1423–1426. doi: 10.1073/pnas.97.4.1423

Wangler, M. F., Yamamoto, S., and Bellen, H. J. (2015). Fruit flies in biomedical research. *Genetics* 199:3. doi: 10.1534/genetics.114.171785

Winston, C., Joe, C., Allaire, J. J., Yihui, X., and McPherson, J. (2017). *Shiny: Web Application Framework for R. R Package Version 1.1.0*. Available online at: https://CRAN.R-project.org/package=shiny (accessed May 25, 2017).

Yang, X., Yeo, S. Y., Hong, J. M., Wong, S. T., Tang, W. T., and Wu, Z. Z. (2016). A deep learning approach for tumor tissue image classification. *IASTED Biomed. Eng.* 832. doi: 10.2316/p.2016.832-025

Conflict of Interest: The authors declare that the research was conducted in the absence of any commercial or financial relationships that could be construed as a potential conflict of interest.

BRIEF RESEARCH REPORT
published: 14 July 2020
doi: 10.3389/fnins.2020.00739

Abnormalities in Brain and Muscle Microstructure and Neurochemistry of the DMD Rat Measured by *in vivo* Diffusion Tensor Imaging and High Resolution Localized ^{1}H MRS

Su Xu[1,2], Shiyu Tang[1,2], Xin Li[1], Shama R. Iyer[3] and Richard M. Lovering[3]*

[1] Department of Diagnostic Radiology and Nuclear Medicine, University of Maryland School of Medicine, Baltimore, MD, United States, [2] Center for Advanced Imaging Research, University of Maryland School of Medicine, Baltimore, MD, United States, [3] Department of Orthopaedics, University of Maryland School of Medicine, Baltimore, MD, United States

Edited by:
Rodolfo Gabriel Gatto,
University of Illinois at Chicago,
United States

Reviewed by:
Paola Porcari,
Memorial Sloan Kettering Cancer
Center, United States
Sean Forbes,
University of Florida, United States

***Correspondence:**
Richard M. Lovering
rlovering@som.umaryland.edu

Specialty section:
This article was submitted to
Neurodegeneration,
a section of the journal
Frontiers in Neuroscience

Received: 18 March 2020
Accepted: 22 June 2020
Published: 14 July 2020

Citation:
Xu S, Tang S, Li X, Iyer SR and
Lovering RM (2020) Abnormalities
in Brain and Muscle Microstructure
and Neurochemistry of the DMD Rat
Measured by in vivo Diffusion Tensor
Imaging and High Resolution
Localized ^{1}H MRS.
Front. Neurosci. 14:739.
doi: 10.3389/fnins.2020.00739

Duchenne muscular dystrophy (DMD) is an X-linked disorder caused by the lack of dystrophin with progressive degeneration of skeletal muscles. Most studies regarding DMD understandably focus on muscle, but dystrophin is also expressed in the central nervous system, potentially resulting in cognitive and behavioral changes. Animal models are being used for developing more comprehensive neuromonitoring protocols and clinical image acquisition procedures. The recently developed DMD rat is an animal model that parallels the progressive muscle wasting seen in DMD. Here, we studied the brain and temporalis muscle structure and neurochemistry of wild type (WT) and dystrophic (DMD) rats using magnetic resonance imaging and spectroscopy. Both structural and neurochemistry alterations were observed in the DMD rat brain and the temporalis muscle. There was a decrease in absolute brain volume ($WT = 1579$ mm^3; $DMD = 1501$ mm^3; $p = 0.039$, Cohen's $d = 1.867$), but not normalized ($WT = 4.27$; $DMD = 4.02$; $p = 0.306$) brain volume. Diffusion tensor imaging (DTI) revealed structural alterations in the DMD temporalis muscle, with increased mean diffusivity (MD), axial diffusivity (AD), and radial diffusivity (RD). In the DMD rat thalamus, DTI revealed an increase in fractional anisotropy (FA) and a decrease in RD. Smaller normalized brain volume correlated to severity of muscle dystrophy ($r = -0.975$). Neurochemical changes in the DMD rat brain included increased GABA and NAA in the prefrontal cortex, and GABA in the hippocampus. Such findings could indicate disturbed motor and sensory signaling, resulting in a dysfunctional GABAergic neurotransmission, and an unstable osmoregulation in the dystrophin-null brain.

Keywords: duchenne muscular dystrophy, rat model, neuroimaging, magnetic resonance imaging, ^{1}H magnetic resonance spectroscopy, diffusion tensor imaging

INTRODUCTION

Duchenne muscular dystrophy (DMD) is an X-linked muscle disorder that presents clinically with significant and progressive muscle wasting and loss of muscular function (Brooke et al., 1989; McDonald et al., 1995; Lovering et al., 2005), due to the absence of the protein, dystrophin. Dystrophin is a large sarcolemma-associated protein expressed in striated muscle

(Tinsley et al., 1994; Blake et al., 1996). Our understanding about the function of dystrophin has been derived from studies of dystrophin-deficient animals, with the most common model being the *mdx* mouse.

Dystrophin is also expressed in the central nervous system (CNS), but there is a dearth of knowledge regarding its role in the brain. Cognitive impairment, including mental retardation (Cotton et al., 2005) can occur in DMD patients (Duchenne, 1861; Anderson et al., 2002; Nardes et al., 2012). This can include diminished memory function, especially short term memory (Hinton et al., 2007; Wingeier et al., 2011), as well as language impairments, long-term memory problems, and limited executive functions (Cotton et al., 2001, 2005; Wicksell et al., 2004; Marini et al., 2007). Both CT and *in vivo* ^{1}H MRS studies indicate a slow, progressive cerebral degeneration in DMD patients (Yoshioka et al., 1980; Uchino et al., 1994; Rae et al., 1998; Chen et al., 1999), with findings of cortical atrophy and ventricular dilation in older patients, and patients with large amounts of physical disability (Yoshioka et al., 1980).

In muscle, dystrophin protects the sarcolemma against mechanical stress (Koenig et al., 1988) and contributes to force and signal transduction (Ervasti and Campbell, 1993; Petrof et al., 1993; Lovering and De Deyne, 2004). Dystrophin also regulates intracellular calcium and the cascade of calcium-related events (Lansman and Franco, 1991; Lovering et al., 2009), the aggregation of neurotransmitter receptors (Kong and Anderson, 1999; Pratt et al., 2013), and reactive oxygen species (Whitehead et al., 2006; Khairallah et al., 2012). In the brain, various dystrophin isoforms are distributed unequally, but dystrophin is expressed in the post-synaptic neurons of the cortex, hippocampus, and cerebellum, which are regions integral to cognition (Cyrulnik and Hinton, 2008). Thus, cognitive impairment in DMD patients could be due to its absence. However, the specific function of dystrophin in brain is not fully understood. In muscle, dystrophin has functional and structural roles. Identifying how dystrophin's absence affects the brain would be helpful in monitoring disease progression or effectiveness of therapies that are being developed for DMD.

The most commonly studied animal model of DMD is the *mdx* mouse, which similar to patients with DMD, lacks dystrophin (Sicinski et al., 1989). However, even though *mdx* mice have muscle pathology, the phenotype is much less severe than patients with DMD. Thus, the utility of the *mdx* mouse as a model for DMD is questionable (Allamand and Campbell, 2000). Novel rat models of DMD have become available (Larcher et al., 2014; Nakamura et al., 2014), but have still not been fully characterized. The rat model appears to better mimic DMD than the *mdx* mouse, with progressive muscle fibrosis, fatty infiltration, muscle weakness, decreased activity, and altered diastolic function (Larcher et al., 2014; Nakamura et al., 2014). A recent report showed that the DMD rat shows significant changes in neuromotor behavior (Caudal et al., 2020). The DMD rat more closely parallels the phenotype of DMD than *mdx* mice in terms of histology and life span, but there are no imaging studies of the rat DMD brain. In this brief research report, we used *in vivo* magnetic resonance imaging (MRI), diffusion tensor imaging (DTI) and high resolution localized ^{1}H magnetic resonance spectroscopy (^{1}H MRS) to investigate alterations in brain structure and neurochemicals in the DMD rat brain and adjacent temporalis muscle. The use of these *in-vivo* neuroimaging technologies will be helpful in clarifying the function of dystrophin in the brain. Furthermore, the development of these neuroimaging techniques is important as non-invasive tools for diagnosis, monitoring disease progression, planning rehabilitation, and determining the effectiveness of therapeutic interventions.

METHODS

Animals

DMD rats were generated using a CRISPR-based approach targeting exon 22 to exon 26 of dystrophin (gRNA pairs GTCTAA TAGTAGGTGATAAGAGG and CAGCTCTTGTACCCGATTG CTGG), resulting in a ~1080 bp mutant dystrophin mRNA that is undetectable. Two-month old dystrophic (DMD, $N = 4$, 356 ± 26 g) and age-matched littermate wild type (WT, $N = 4$, 384 ± 29 g) male rats were used. Body weight was not significantly different between DMD and WT rats. All experimental procedures were approved by the University of Maryland School of Medicine Institutional Animal Care and Use Committee.

MRI Protocol

The MRI/MRS experiments were performed on a Bruker BioSpec 70/30USR Avance III 7T scanner. A Bruker four-element ^{1}H surface coil array was used as the receiver and a Bruker 72 mm linear-volume coil as the transmitter. Each rat was anesthetized in an animal chamber using a gas mixture of O_2 (1 L/min) and isoflurane (3%) then later maintained at 1–2% isoflurane during scanning. An MR compatible small-animal monitoring system was used to monitor the animal respiration rate and body temperature. The animal body temperature was maintained at 35–37°C using warm water circulation.

T_2-weighted anatomic head (including brain and the surrounding muscle tissues) images were obtained using a 2D rapid acquisition with relaxation enhancement (RARE) sequence in the axial plane [repetition time (TR)/echo time (TE) = 4600/30 ms, RARE factor = 4, field of view (FOV) = 32 × 32 mm^2, slice thickness = 1 mm, image matrix = 320 × 320, in-plane resolution = 100 × 100 μm^2, number of averages (NA) = 2, number of slices = 16]. Brain volume analysis was performed in MIPAV (Medical Image Processing, Analysis, and Visualization[1]). Skull-stripping was performed manually on images. The total brain volume was calculated by adding the slice-by-slice volume from 13 slices that were consistently acquired across animals as shown in **Figure 1A**.

In vivo DTI images on rat heads were acquired with a gradient echo-planar imaging (EPI) sequence (TR/TE = 2,500/18.82 ms, diffusion directions = 30, NA = 1, image matrix = 92 × 92, in-plane resolution = 348 × 348 μm^2, the FOV was the same as T_2-weighted images). Two *b*-values (1,000 and 2,000 s/mm^2)

---

[1] https://mipav.cit.nih.gov/

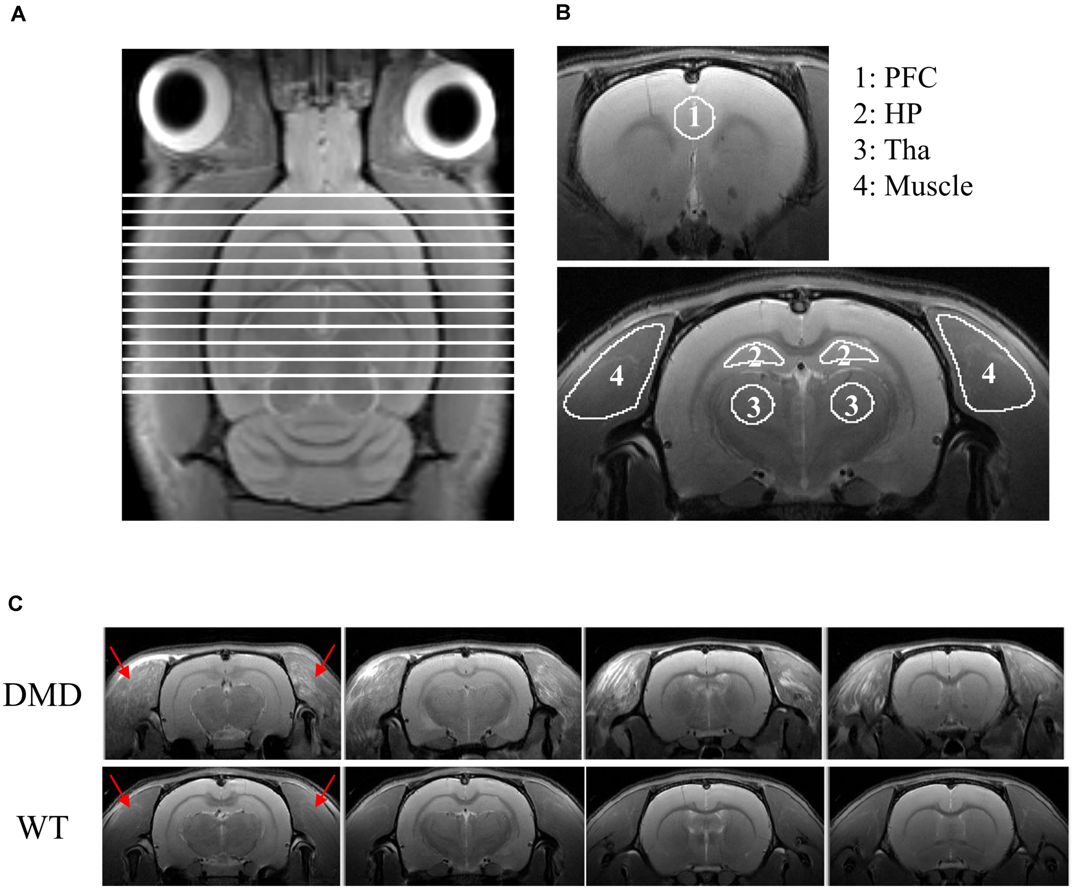

FIGURE 1 | (A) T_2-weighted image of a rat brain showing all slices included for the calculation of brain volume. **(B)** Regions of interest (ROIs) used for DTI data analysis. ROIs were drawn in the prefrontal cortex (PFC; ROI 1), hippocampus (HP; ROI 2), thalamus (Tha, ROI 3) and temporalis muscle (ROI 4). **(C)** RARE T_2-weighted MRI axial view of the muscle surrounding the cranium (temporalis muscle, red arrows) of the head of each wild-type (WT) and dystrophic (DMD) rat. In the WT rats, the temporalis muscles were homogeneously dark with no focal hyperintense regions, whereas in the DMD rats, the temporalis muscles were heterogeneous, with multiple, unevenly distributed focal hyperintensities. There were no apparent anatomic differences between WT and DMD brains. RARE: rapid acquisition with relaxation enhancement sequence.

were acquired for each direction. Five additional images at $b = 0$ s/mm^2 were also acquired. Typically for routine brain evaluations, the b-values (a measure of the sensitivity to diffusion) in DTI experiments are at 1,000 s/mm^2 (Xu et al., 2011; Zhuo et al., 2012). The $b = 2000$ s/mm^2 was added in the current study to test whether better characterized gray matter microstructure would yield differences in brain maturation (Cheung et al., 2009; Zhuo et al., 2012). However, no significant differences were found in the current age group of DMD and WT rats. The acquisition of multiple images acquired at $b = 0$ s/mm^2 was utilized to obtain a strong signal to noise ratio for non-diffusion weighted map to improve the estimation of diffusion parameters (Jones et al., 1999).

Custom-made diffusion kurtosis software (Xu et al., 2013) was used to generate the maps of mean diffusivity (MD), axial diffusivity (AD), radial diffusivity (RD), and fractional anisotropy (FA). MD measures the average water diffusion within the head. AD measures the water diffusion along the neuronal axons. RD measures the water diffusion perpendicular to the axons. FA measures the degree of diffusion anisotropy of the head. The regions of interest (ROIs), including prefrontal cortex, hippocampus, thalamus, and the temporalis muscle were manually defined on the FA images while using the T_2-weighted image for anatomic reference in FSLeyes[2] (**Figure 1B**). Values of MD, AD, RD, and FA were extracted, respectively, from each generated map using the manually defined ROIs. The details of this procedure have been published previously (Zhuo et al., 2012).

A ^{1}H short-TE Point-RESolved Spectroscopy (PRESS) pulse sequence (Xu et al., 2013) (TR/TE = 2,500/10 ms, NA = 360) was used for MRS data acquisition with the voxel centered on the prefrontal cortex (PFC, 3 mm × 3 mm × 3 mm) and hippocampus (HP, 8 mm × 2 mm × 2 mm), respectively. The unsuppressed water signal from each of the prescribed voxels was obtained to serve as a reference for determining the specific metabolite concentrations. Quantification of the MRS was based

---

[2] https://git.fmrib.ox.ac.uk/fsl/fsleyes/fsleyes

on frequency domain analysis using a "Linear Combination of Model spectra" (LCModel) (Provencher, 1993). Absolute concentrations were estimated with the LCModel automatic procedure (version 6.3-0G).

Statistics

All *in vivo* MRI and MRS measurements between DMD and WT rats were compared using *t*-tests with an alpha level set at $p < 0.05$. Cohen's d was used to measure effect size. Correlations between normalized brain volume, MRS measurements, and DTI parameters of MD, AD, RD, and FA were calculated using Pearson's correlation coefficient.

RESULTS

DMD rats clearly had muscle lesions (**Figure 1C**), which showed a similar pattern to what we have reported in *mdx* mice (Xu et al., 2015). The MRI of WT temporalis muscles were homogeneous, but these muscles of DMD rats showed signal heterogeneity, with numerous focal hyperintensities clearly present. There were no apparent anatomical differences in T_2-weighted images of the brains between the WT and DMD rats (**Figure 1C**). A significant reduction of whole brain volume was detected in DMD rats compared to WT rats ($p = 0.039$, Cohen's $d = 1.867$) (**Figure 2A**), however, this difference was not significant when the brain volume was normalized to body weight ($p = 0.306$) (**Figure 2B**).

All of the diffusivities were significantly increased in the temporalis muscles of the DMD rats compared to WT rats (MD: $p = 0.024$, Cohen's $d = 2.255$; AD: $p = 0.024$, Cohen's $d = 2.234$; RD: $p = 0.034$, Cohen's $d = 1.199$) (**Figure 3A**). FA significantly increased ($p = 0.028$, Cohen's $d = 2.041$) while RD significantly decreased ($p = 0.014$, Cohen's $d = 2.5$) in the thalamus of DMD rats compared to WT rats (**Figure 3B**), which could signify either increased myelination, or decreased fiber diameters. A correlation analysis was performed between the normalized brain volume and the MD, AD, and RD value of temporalis muscles in WT and DMD rats using Pearson's correlation analysis. Significant negative correlation was detected in DMD rats between normalized brain volume and muscle MD ($r = -0.974$, $p = 0.026$), and normalized brain volume and muscle RD ($r = -0.975$, $p = 0.025$), respectively (**Figure 3C**). No significant correlations were observed in WT rats. This finding suggests that the level of brain atrophy is associated with the severity of dystrophic muscle in DMD rats. No significant difference between WT and DMD rats was detected in any of the diffusion measures in prefrontal cortex and hippocampus (data not shown).

Representative high resolution localized *in vivo* MRS spectra from the PFC and HP of a DMD rat are shown in **Figure 4A**. Several neurochemicals were detected, such as total creatine (tCr, creatine + phosphocreatine), γ-aminobutyric acid (GABA), glucose (Glc), glutamate (Glu), glutamine (Gln), glutathione (GSH), *myo*-inositol (Ins), *N*-acetyl-aspartate (NAA), *N*-acetylaspartateglutamate (NAAG), taurine (Tau), Choline (Cho), and macro molecules (MM). Compared to WT mice, DMD rats demonstrated significant elevations in GABA ($p = 0.045$) and NAA ($p = 0.044$) in the PFC, as well as a marginal elevation in GABA ($p = 0.062$) in the HP (**Figures 4A,B**). No significant differences were seen in other neurochemicals from these regions. The relationship between MRS and DTI results was also performed, but no significant correlation was found (data not shown).

DISCUSSION

This brief study demonstrated that multi-modal MR neuroimaging modalities can identify changes in the structure (MRI/DTI) and neurobiochemistry (MRS) of muscle and brain in young DMD rats. DMD rats had smaller brain volumes and body weights, although there was no significant difference in normalized brain volume. Interestingly, a recent study looking at aged *mdx* mice showed a progressive, age-dependent decline

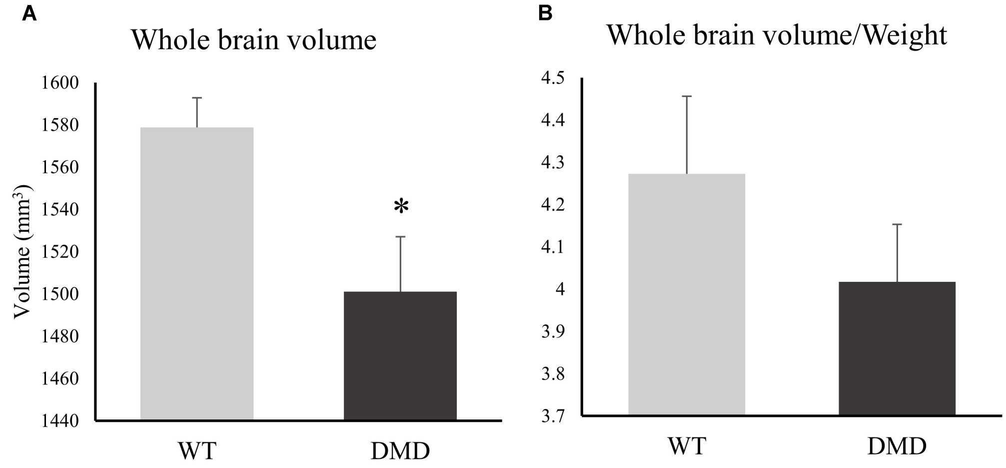

FIGURE 2 | (A) Bar graph showing differences between the whole brain volume of dystrophic (DMD) and wild-type (WT) rats. **(B)** Bar graph showing differences between the normalized brain volume of DMD and WT animals. *significantly different from the corresponding values in WT rats (un-paired *t*-test, $p < 0.05$).

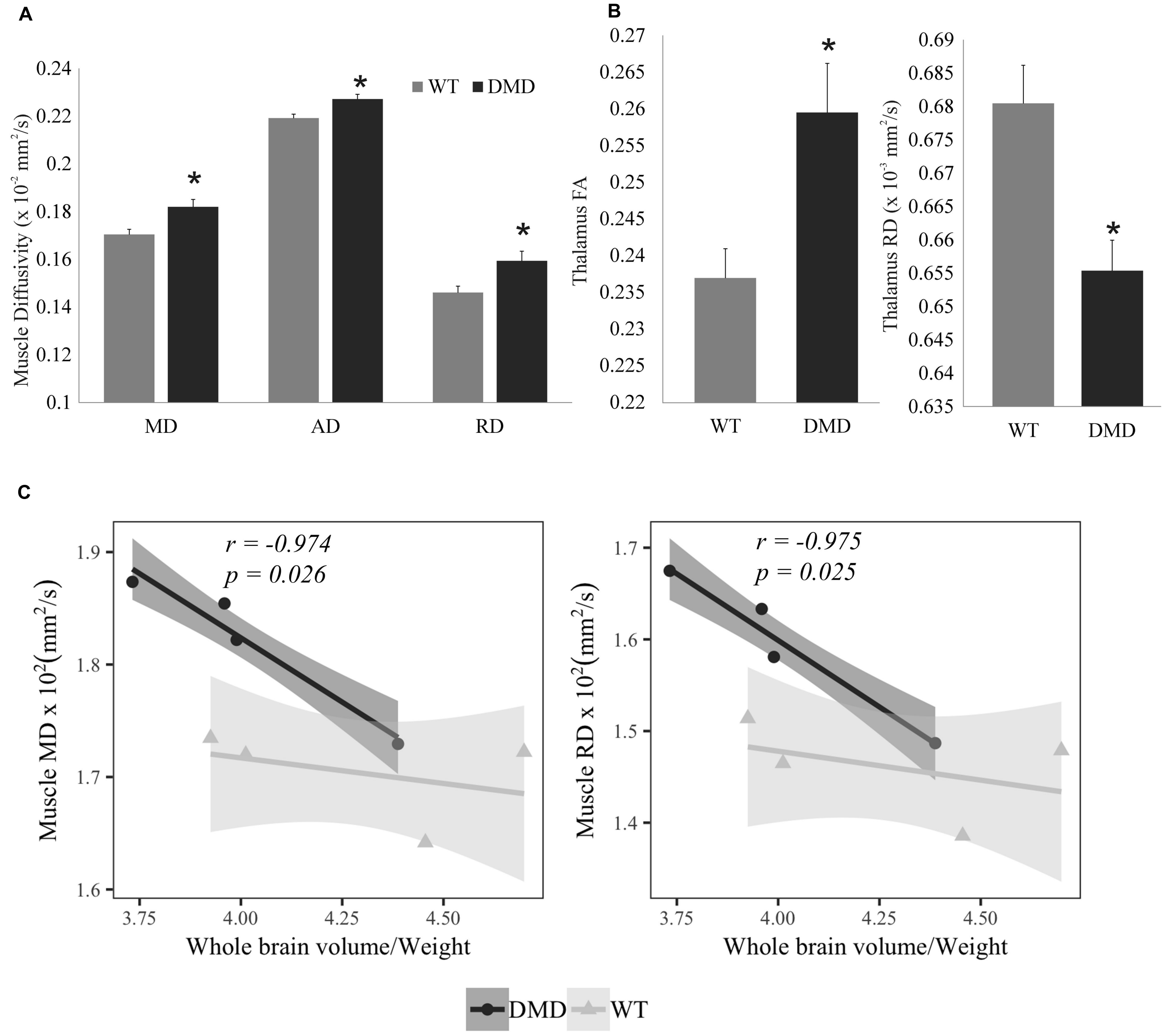

FIGURE 3 | (A) Bar graph showing the increased values in muscle mean diffusivity (MD), axial diffusivity (AD), and radial diffusivity (RD) in dystrophic (DMD) rats compared to wild-type (WT) rats. **(B)** Bar graph showing that fractional anisotropy (FA) was significantly increased, while RD was reduced in the thalamus of DMD rats compared to WT rats. **(C)** Correlation plots between normalized whole brain volume and both muscle MD (left) and muscle RD (right) in DMD and WT rats. *Significantly different from the corresponding value in WT rats (un-paired *t*-test, $p < 0.05$).

in cognitive function (Bagdatlioglu et al., 2020). The authors suggested that the absence of dystrophin causes a late onset neurodegeneration that is not readily detected in the *mdx* mice because most testing has been performed in relatively young animals before the onset of this degeneration. Such a finding is consistent with MRI findings in older DMD patients, showing reduced total brain volume compared to healthy controls (although such findings are difficult to separate from effects of steroid therapy) (Doorenweerd et al., 2014). Although we did not assess aged rats, the slight reduction in total brain volume in the DMD rat might reflect a phenotype that, compared to *mdx* mice, more closely resembles DMD.

Mastication is impaired in DMD patients, for example patients have a decrease in normal bite force. Thus, it's plausible that the reduced body weights of the DMD rats compared to controls could be due to reduced food consumption secondary to the muscle pathology in the temporalis muscles (Bagdatlioglu et al., 2020), although this was not assessed.

MD, AD, and RD were significantly increased in the temporalis muscles of the DMD rats compared to WT rats, MD and RD values had significant negative correlations to normalized brain volume in DMD rats, but not in WT rats. This finding suggests that the level of brain atrophy is associated with the severity of muscular dystrophy in DMD rats. The

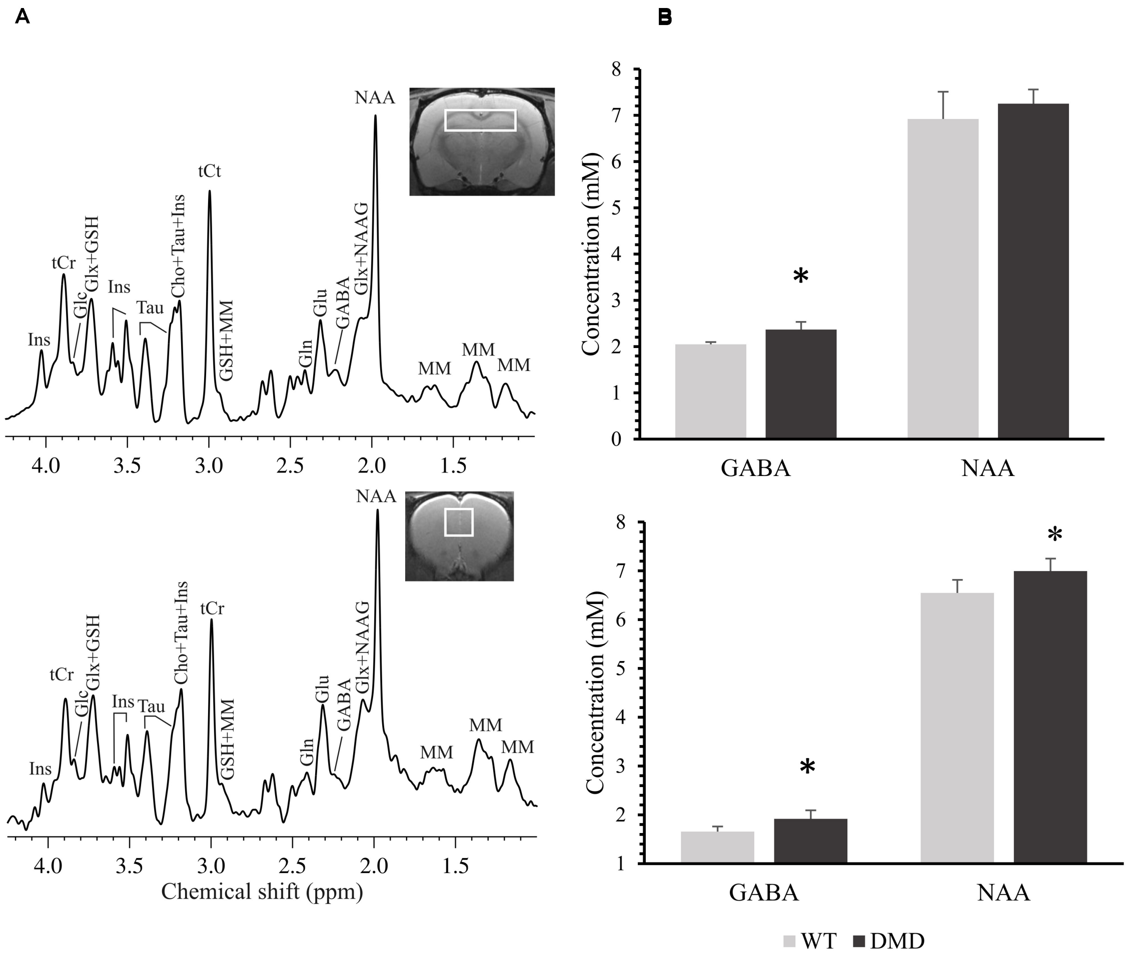

FIGURE 4 | (A) Representative *in vivo* ^{1}H MR spectra acquired from the prefrontal cortex (PFC, bottom) and the hippocampus (HP, top) of a dystrophic (DMD) rat brain. Main metabolites shown in the spectra are: γ-aminobutyric acid (GABA), glutamine (Gln), glutamate (Glu), glucose (Glc), glutathione (GSH), *myo*-inositol (Ins), *N*-acetylaspartate (NAA), *N*-acetylaspartateglutamate (NAAG), taurine (Tau), total creatine (tCr; phosphocreatine + creatine), choline (Cho), glutamate/glutamine complex (Glx), and macro molecules (MM). **(B)** Comparison of the neurochemical concentrations (mM) between wild-type (WT) and DMD rats in PFC (bottom) and HP (top). Data are expressed as mean ± standard error. *Significantly different from the corresponding value in WT rats (un-paired *t*-test, $p < 0.05$).

structural alterations seen in DMD rats included increased FA and decreased RD in thalamus, a structure that has extensive nerve connections to the cerebral cortex and the midbrain. The primary function of the thalamus is to relay motor and sensory signals to and from the cerebral cortex. Thus, the microstructural alteration in the thalamus may reflect the movement disorder caused by the muscular dystrophy.

The changes in concentrations of neurochemicals in the DMD rat brains were in the HP and PFC regions, where dystrophin is normally present (Caudal et al., 2020). Elevations in GABA (in PFC and HP) and NAA (in PFC) were observed in DMD rats. A disruption in the amount or relative proportions of these neurochemicals likely has consequences on dystrophin's functions, such as GABAergic neurotransmission and osmoregulation in the brain.

The elevations in GABA in the both PFC and HP in the DMD rat brains may indicate a dysfunction of GABAergic neurotransmission. It is known that full-length dystrophin co-localizes with $GABA_A$ receptors in the mouse cerebellum, cerebral cortex and hippocampus (Knuesel et al., 1999). Dystrophin likely contributes to neurotransmitter receptor aggregation, potentially due to the reduction of $GABA_A$ resulting in the elevation of GABA in the brain (Knuesel et al., 1999; Kueh et al., 2011).

NAA is a known osmolyte, providing ∼7% of neuronal osmolarity (Baslow, 2000). Missing cerebral dystrophin may lead to modification of the microenvironment of the neurons and thus may result in a perturbed osmoregulation. The NAA elevation may work as a beneficial compensatory mechanism in the brain.

The subcellular distribution of dystrophin neurons is restricted and varies within the brain, including in the rat (Caudal et al., 2020). If dystrophin can play different roles in different areas of the brain, this could explain why our findings are restricted to some, and not all, brain regions. Interestingly, our findings were restricted to brain regions known to be related to cognitive function. Since distribution of dystrophin is limited in the brain, this could explain why only mild cognitive dysfunction is seen in patients with DMD. Here, we report changes in DTI parameters and GABA and NAA in several brain areas. Such findings indicate small brain volume that correlated to severity of muscle dystrophy, disturbed motor and sensory signal sending, dysfunction of GABAergic neurotransmission, and perturbed osmoregulation in the DMD rat brain. The prefrontal cortex and hippocampus are two regions that show the absence of dystrophin and feasibility of MRS. Therefore, we put these two regions in the localized MRS protocol. Now that we know from the DTI results that the microstructure of the thalamus can be affected by DMD, we will add the thalamus as a target region in our future study for MRS.

Our results in this study on DMD rat brain reflect similar findings found in both the *mdx* mouse model and patients with DMD. Behavioral studies indicate learning impairments in *mdx* mice (Muntoni et al., 1991; Vaillend et al., 1995; Perronnet et al., 2012). A handful of studies that have explored *in vivo* ^{1}H MRS indicate low ratios of Cr/Cho and NAA/Cho in *mdx* brains compared to wild type controls (Tracey et al., 1996). Using MRI and MRS, we previously reported structural and biochemical changes in brains of 7-month old *mdx* mice (Xu et al., 2015). Our results showed enlarged lateral ventricles in *mdx* brains when compared to WT. Other structural alterations were observed by *ex vivo* DTI. In the prefrontal cortex, elevations in diffusivities were detected in the prefrontal cortex and a reduction of FA was measured in the hippocampus. Biochemical changes included elevations in phospfholine and glutathione, and a reduction in GABA in the hippocampus of the *mdx* mice. In addition, we found an elevation in taurine in the prefrontal cortex. Such findings indicate a regional structural change, altered cellular antioxidant defenses, modified GABAergic neurotransmission, and disrupted osmoregulation in the brain lacking dystrophin. Significant increases in ratios of choline-containing compounds to *N*-acetylaspartate (Cho/NAA) and Cho/Cr have been detected in the cerebellum of DMD boys compared to age-matched controls (Rae et al., 1998). A progressive nature was further reflected by a larger effect in 12 year old patients with DMD than in 8 year old patients with DMD. Conversely, another study showed a significant decrease in absolute Cho levels in both the cerebellum and the temporo-parietal cortex of the DMD patients (Kreis et al., 2011).

The impact of dystrophin's absence on behavior has also recently been studied in the DMD rat, showing clear alterations in overall neuromotor function (Caudal et al., 2020). The current study sheds further light on dystrophin's role in the brain. Replacing dystrophin in the brain would be the most logical solution to resolving cognitive issues, but such a therapy is not imminent, despite ongoing efforts (Goyenvalle et al., 2015). The non-invasive imaging methods employed here could be effective in monitoring the efficiency of the potential therapeutic agents, including the brain if such treatments are developed.

In summary, we studied the structure (brain and muscle) and neuro biochemistry of healthy and dystrophic rats with MRI/MRS and found in dystrophic rats: smaller brain volume that correlated to severity of muscular dystrophy, alterations in diffusion of the muscle and thalamus, and several biochemical alterations in prefrontal cortex and hippocampus.

DATA AVAILABILITY STATEMENT

All datasets generated for this study are included in the article.

ETHICS STATEMENT

The animal study was reviewed and approved by the University of Maryland School of Medicine Institutional Animal Care and Use Committee.

AUTHOR CONTRIBUTIONS

SX and RL contributed to the conception and design. XL and ST contributed to the acquisition and analysis of data. SX, ST, SI, and RL contributed to the interpretation of the results. All authors contributed to the manuscript writing.

FUNDING

This work was supported by grants to RL (R56AR073193) from the NIAMS, National Institutes of Health (NIH) and from UMB Institute for Clinical and Translational Research (ICTR), and to SI from the Muscular Dystrophy Association (MDA 577897) and (K01 AR074048), NIAMS/NIH.

ACKNOWLEDGMENTS

We thank the Myologica LLC. for graciously providing the WT and DMD rats. We also thank the University of Maryland School of Medicine Center for Innovative Biomedical Resources, Translational Research in Imaging @ Maryland (CTRIM) for providing the imaging services.

REFERENCES

Allamand, V., and Campbell, K. P. (2000). Animal models for muscular dystrophy: valuable tools for the development of therapies. *Hum. Mol. Genet.* 9, 2459–2467. doi: 10.1093/hmg/9.16.2459

Anderson, S. I., Head, C., Rae, S., and Morley, J. W. (2002). Brain function in Duchenne muscular dystrophy. *Brain* 125, 4–13. doi: 10.1093/brain/awf012

Bagdatlioglu, P., Porcari, E., Greally, A. M., Blamire, N., and Straub, V. (2020). Cognitive impairment appears progressive in the mdx mouse. *Neuromuscul Disord.* 30, 368–388. doi: 10.1016/j.nmd.2020.02.018

Baslow, M. H. (2000). Functions of N-acetyl-L-aspartate and N-acetyl-L-aspartylglutamate in the vertebrate brain: role in glial cell-specific signaling. *J. Neurochem.* 75, 453–459. doi: 10.1046/j.1471-4159.2000.0750453.x

Blake, J. M., Tinsley, J., and Davies, K. (1996). Utrophin: a structural and functional comparison to dystrophin 1. *Brain Pathol.* 6, 37–47. doi: 10.1111/j.1750-3639.1996.tb00781.x

Brooke, G. M., Fenichel, R. C., Griggs, J. R., Mendell, R., Moxley, J., Florence, W. M., et al. (1989). Duchenne muscular dystrophy: patterns of clinical progression and effects of supportive therapy. *Neurology* 39, 475–481.

Caudal, V., Francois, A., Lafoux, M., Ledevin, I., Anegon, C., Le Guiner, T., et al. (2020). Characterization of brain dystrophins absence and impact in dystrophin-deficient Dmdmdx rat model. *PLoS One* 15:e0230083. doi: 10.1371/journal.pone.0230083

Chen, Y., Takeshima, Y., Ishikawa, Y., Ishikawa, R., Minami, P., and Matsuo, M. (1999). A novel deletion of the dystrophin S-promoter region cosegregating with mental retardation. *Neurology* 52, 638–640.

Cheung, E. S., Hui, K. C., Chan, J. A., Helpern, L., and Wu, E. (2009). Does diffusion kurtosis imaging lead to better neural tissue characterization? A rodent brain maturation study. *Neuroimage* 45, 386–392. doi: 10.1016/j.neuroimage.2008.12.018

Cotton, N. J., Voudouris, N., and Greenwood, K. (2001). Intelligence and Duchenne muscular dystrophy: full-scale, verbal, and performance intelligence quotients. *Dev. Med. Child Neurol.* 43, 497–501. doi: 10.1111/j.1469-8749.2001.tb00750.x

Cotton, N. J., Voudouris, S., and Greenwood, K. (2005). Association between intellectual functioning and age in children and young adults with Duchenne muscular dystrophy: further results from a meta-analysis. *Dev. Med. Child Neurol.* 47, 257–265. doi: 10.1017/s0012162205000496

Cyrulnik, S. E., and Hinton, V. J. (2008). Duchenne muscular dystrophy: a cerebellar disorder? *Neurosci. Biobehav. Rev.* 32, 486–496. doi: 10.1016/j.neubiorev.2007.09.001

Doorenweerd, C. S., Straathof, E. M., Dumas, P., Spitali, I. B., Ginjaar, B. H., Wokke, D. G., et al. (2014). Reduced cerebral gray matter and altered white matter in boys with Duchenne muscular dystrophy. *Ann. Neurol.* 76, 403–411. doi: 10.1002/ana.24222

Duchenne, G. (1861). *De I'electrisation Localisee Et Son Application a La Pathologie Et a Al Therapeutique*, 2nd Edn. Paris: Bailliere et Fils, 354–356.

Ervasti, J., and Campbell, K. P. (1993). Dystrophin and the membrane skeleton. *Curr. Opin. Cell Biol.* 5, 82–87. doi: 10.1016/s0955-0674(05)80012-2

Goyenvalle, G., Griffith, A., Babbs, A. S., El, K., Ezzat, A., Avril, B., et al. (2015). Functional correction in mouse models of muscular dystrophy using exon-skipping tricyclo-DNA oligomers. *Nat. Med.* 21, 270–275. doi: 10.1038/nm.3765

Hinton, R. J., Fee, E. M., Goldstein, M., and De Vivo, D. (2007). Verbal and memory skills in males with Duchenne muscular dystrophy. *Dev. Med. Child Neurol.* 49, 123–128. doi: 10.1111/j.1469-8749.2007.00123.x

Jones, M. A., Horsfield, B., and Simmons, A. (1999). Optimal strategies for measuring diffusion in anisotropic systems by magnetic resonance imaging. *Magn. Reson. Med.* 42, 515–525. doi: 10.1002/(sici)1522-2594(199909)42:3<515::aid-mrm14>3.0.co;2-q

Khairallah, G., Shi, F., Sbrana, B. L., Prosser, C., Borroto, M. J., Mazaitis, E. P., et al. (2012). Microtubules underlie dysfunction in duchenne muscular dystrophy 2. *Sci. Signal.* 5:ra56. doi: 10.1126/scisignal.2002829

Knuesel, M., Mastrocola, R. A., Zuellig, B., Bornhauser, M. C., Schaub, M., and Fritschy, J. M. (1999). Short communication: altered synaptic clustering of GABAA receptors in mice lacking dystrophin (mdx mice). *Eur. J. Neurosci.* 11, 4457–4462. doi: 10.1046/j.1460-9568.1999.00887.x

Koenig, A. P., Monaco, M., and Kunkel, L. (1988). The complete sequence of dystrophin predicts a rod-shaped cytoskeletal protein. *Cell* 53, 219–228. doi: 10.1016/0092-8674(88)90383-2

Kong, J., and Anderson, J. E. (1999). Dystrophin is required for organizing large acetylcholine receptor aggregates 1. *Brain Res.* 839, 298–304. doi: 10.1016/s0006-8993(99)01737-0

Kreis, K., Wingeier, P., Vermathen, E., Giger, F., Joncourt, K., Zwygart, F., et al. (2011). Kaufmann, C. Boesch, and M. Steinlin, Brain metabolite composition in relation to cognitive function and dystrophin mutations in boys with Duchenne muscular dystrophy. *NMR Biomed.* 24, 253–262. doi: 10.1002/nbm.1582

Kueh, J., Dempster, S. I., Head, S., and Morley, J. W. (2011). Reduced postsynaptic GABAA receptor number and enhanced gaboxadol induced change in holding currents in Purkinje cells of the dystrophin-deficient mdx mouse. *Neurobiol. Dis.* 43, 558–564. doi: 10.1016/j.nbd.2011.05.002

Lansman, J. B., and Franco, A. (1991). What does dystrophin do in normal muscle? *J. Muscle Res. Cell Motil.* 12, 409–411. doi: 10.1007/bf01738325

Larcher, A., Lafoux, L., Tesson, S., Remy, V., Thepenier, V., Francois, C., et al. (2014). Characterization of dystrophin deficient rats: a new model for Duchenne muscular dystrophy. *PLoS One* 9:e110371. doi: 10.1371/journal.pone.0110371

Lovering, L., Michaelson, R., and Ward, C. W. (2009). Malformed mdx myofibers have normal cytoskeletal architecture yet altered EC coupling and stress-induced Ca2+ signaling. *Am. J. Physiol. Cell Physiol.* 297, C571–C580.

Lovering, N. C., Porter, R., and Bloch, R. J. (2005). The muscular dystrophies: from genes to therapies. *Phys. Ther.* 85, 1372–1388. doi: 10.1093/ptj/85.12.1372

Lovering, R., and De Deyne, P. (2004). Contractile function, sarcolemma integrity, and the loss of dystrophin after skeletal muscle eccentric contraction-induced injury. *Am. J. Physiol. Cell Physiol.* 286, C230–C238.

Marini, M. L., Lorusso, M. G., D'Angelo, F., Civati, A. C., Turconi, F., and Fabbro, N. (2007). Evaluation of narrative abilities in patients suffering from Duchenne Muscular Dystrophy. *Brain Lang.* 102, 1–12. doi: 10.1016/j.bandl.2007.02.003

McDonald, R. T., Abresch, G. T., Carter, W. M., Fowler, E. R., Johnson, D. D., and Kilmer, R. (1995). Profiles of neuromuscular diseases. Duchenne muscular dystrophy. *Am. J. Phys. Med. Rehabil.* 74, S70–S92.

Muntoni, A., Mateddu, T., and Serra, G. (1991). Passive avoidance behaviour deficit in the mdx mouse. *Neuromuscul. Disord.* 1, 121–123. doi: 10.1016/0960-8966(91)90059-2

Nakamura, W., Fujii, M., Tsuboi, J., Tanihata, N., Teramoto, S., Takeuchi, K., et al. (2014). Generation of muscular dystrophy model rats with a CRISPR/Cas system. *Sci. Rep.* 4:5635.

Nardes, A. P., Araujo, F., and Ribeiro, M. G. (2012). Mental retardation in Duchenne muscular dystrophy. *J. Pediatr.* 88, 6–16.

Perronnet, C., Chagneau, B. P., Le, N., Samson-Desvignes, D., Mornet, S., Laroche, S., et al. (2012). Upregulation of brain utrophin does not rescue behavioral alterations in dystrophin-deficient mice. *Hum. Mol. Genet.* 21, 2263–2276. doi: 10.1093/hmg/dds047

Petrof, J. B., Shrager, H. H., Stedman, A. M., Kelly, A., and Sweeney, H. (1993). Dystrophin protects the sarcolemma from stresses developed during muscle contraction. *Proc. Natl. Acad. Sci. U.S.A.* 90, 3710–3714. doi: 10.1073/pnas.90.8.3710

Pratt, S. B., Shah, C. W., Ward, M. P., Inacio, J. P., Stains, R., and Lovering, M. (2013). Effects of in vivo injury on the neuromuscular junction in healthy and dystrophic muscles 1. *J. Physiol.* 591, 559–570. doi: 10.1113/jphysiol.2012.241679

Provencher, S. W. (1993). Estimation of metabolite concentrations from localized in vivo proton NMR spectra. *Magn. Reson. Med.* 30, 672–679. doi: 10.1002/mrm.1910300604

Rae, R. B., Scott, C. H., Thompson, R. M., Dixon, I., Dumughn, G. J., Kemp, A., et al. (1998). Brain biochemistry in Duchenne muscular dystrophy: a 1H magnetic resonance and neuropsychological study. *J. Neurol. Sci.* 160, 148–157. doi: 10.1016/s0022-510x(98)00190-7

Sicinski, Y., Geng, A. S., Ryder-Cook, E. A., Barnard, M. G., Darlison, M., and Barnard, P. (1989). The molecular basis of muscular dystrophy in the mdx mouse: a point mutation. *Science* 244, 1578–1580. doi: 10.1126/science.2662404

Tinsley, D. J., Blake, R. A., Zuellig, R., and Davies, K. (1994). Increasing complexity of the dystrophin-associated protein complex 1. *Proc. Natl. Acad. Sci. U.S.A.* 91, 8307–8313. doi: 10.1073/pnas.91.18.8307

Tracey, J. F., Dunn, H. G., Parkes, R., and Radda, G. (1996). An in vivo and in vitro H-magnetic resonance spectroscopy study of mdx mouse brain: abnormal development or neural necrosis? *J. Neurol. Sci.* 141, 13–18. doi: 10.1016/0022-510x(96)00135-9

Uchino, K., Yoshioka, T., Miike, M., Tokunaga, E., Uyama, H., Teramoto, H., et al. (1994). Naoe, and M. Ando, Dystrophin and dystrophin-related protein in the brains of normal and mdx mice. *Muscle Nerve* 17, 533–538. doi: 10.1002/mus.880170511

Vaillend, A., Rendon, R., Misslin, C., and Ungerer, A. (1995). Influence of dystrophin-gene mutation on mdx mouse behavior. I. Retention deficits at long delays in spontaneous alternation and bar-pressing tasks. *Behav. Genet.* 25, 569–579. doi: 10.1007/bf02327580

Whitehead, E. W., Yeung, R., and Allen, D. G. (2006). Muscle damage in mdx (dystrophic) mice: role of calcium and reactive oxygen species. *Clin. Exp. Pharmacol. Physiol.* 33, 657–662. doi: 10.1111/j.1440-1681.2006.04394.x

Wicksell, M., Kihlgren, L., Melin, R., and Eeg-Olofsson, O. (2004). Specific cognitive deficits are common in children with Duchenne muscular dystrophy. *Dev. Med. Child Neurol.* 46, 154–159. doi: 10.1111/j.1469-8749.2004.tb00466.x

Wingeier, E., Giger, S., Strozzi, R., Kreis, F., Joncourt, B., Conrad, S., et al. (2011). Neuropsychological impairments and the impact of dystrophin mutations on general cognitive functioning of patients with Duchenne muscular dystrophy. *J. Clin. Neurosci.* 18, 90–95. doi: 10.1016/j.jocn.2010.07.118

Xu, D., Shi, S. J., Pratt, W., Zhu, A., Marshall, A., and Lovering, R. (2015). Abnormalities in brain structure and biochemistry associated with mdx mice measured by in vivo MRI and high resolution localized (1)H MRS. *Neuromuscul. Disord.* 25, 764–772. doi: 10.1016/j.nmd.2015.07.003

Xu, J., Zhuo, J., Racz, D., Shi, S., Roys, G., Fiskum, P., et al. (2011). Early microstructural and metabolic changes following controlled cortical impact injury in rat: a magnetic resonance imaging and spectroscopy study. *J. Neurotrauma* 28, 2091–2102. doi: 10.1089/neu.2010.1739

Xu, Y., Ji, X., Chen, Y., Yang, R. P., Gullapalli, R., and Masri, R. (2013). In vivo high-resolution localized (1) H MR spectroscopy in the awake rat brain at 7 T. *Magn. Reson. Med.* 69, 937–943. doi: 10.1002/mrm.24321

Yoshioka, T., Okuno, Y., Honda, R., and Nakano, Y. (1980). Central nervous system involvement in progressive muscular dystrophy. *Arch. Dis. Child* 55, 589–594. doi: 10.1136/adc.55.8.589

Zhuo, S., Xu, J. L., Proctor, R. J., Mullins, J. Z., Simon, G., Fiskum, L., et al. (2012). Diffusion kurtosis as an in vivo imaging marker for reactive astrogliosis in traumatic brain injury. *Neuroimage* 59, 467–477. doi: 10.1016/j.neuroimage.2011.07.050

Conflict of Interest: The authors declare that the research was conducted in the absence of any commercial or financial relationships that could be construed as a potential conflict of interest.

frontiers
in Neuroscience

ORIGINAL RESEARCH
published: 25 August 2020
doi: 10.3389/fnins.2020.00908

Diffusion Tensor Imaging and Chemical Exchange Saturation Transfer MRI Evaluation on the Long-Term Effects of Pulsed Focused Ultrasound and Microbubbles Blood Brain Barrier Opening in the Rat

Tsang-Wei Tu[1,2,3]*, Zsofia I. Kovacs[2,4], Maggie Sundby[2], Jaclyn A. Witko[2,3], Georgios Z. Papadakis[5], William C. Reid[5], Dima A. Hammoud[5] and Joseph A. Frank[2,6]

[1] Molecular Imaging Laboratory, Department of Radiology, Howard University College of Medicine, Washington, DC, United States, [2] Frank Laboratory, Radiology and Imaging Sciences, Clinical Center, National Institutes of Health (NIH), Bethesda, MD, United States, [3] Center for Neuroscience and Regenerative Medicine, Henry Jackson Foundation, Bethesda, MD, United States, [4] Institute for Biomedical Engineering, Swiss Federal Institute of Technology, Zurich, Switzerland, [5] Center for Infectious Disease Imaging, Clinical Center, National Institutes of Health (NIH), Bethesda, MD, United States, [6] National Institute of Biomedical Imaging and Bioengineering, National Institutes of Health (NIH), Bethesda, MD, United States

OPEN ACCESS

Edited by:
Yu-Chien Wu,
Indiana University Bloomington,
United States

Reviewed by:
Iris Yuwen Zhou,
Massachusetts General Hospital
and Harvard Medical School,
United States
Zhongliang Zu,
Vanderbilt University, United States
Michael C. Veronesi,
Indiana University, United States

***Correspondence:**
Tsang-Wei Tu
tut@howard.edu

Specialty section:
This article was submitted to
Brain Imaging Methods,
a section of the journal
Frontiers in Neuroscience

Received: *30 May 2020*
Accepted: *05 August 2020*
Published: *25 August 2020*

Citation:
Tu T-W, Kovacs ZI, Sundby M,
Witko JA, Papadakis GZ, Reid WC,
Hammoud DA and Frank JA (2020)
Diffusion Tensor Imaging
and Chemical Exchange Saturation
Transfer MRI Evaluation on
the Long-Term Effects of Pulsed
Focused Ultrasound
and Microbubbles Blood Brain Barrier
Opening in the Rat.
Front. Neurosci. 14:908.
doi: 10.3389/fnins.2020.00908

Blood-brain barrier opening (BBBO) with pulsed Focused Ultrasound (pFUS) and microbubbles (MB) has received increasing interest as a method for neurotherapeutics of the central nervous system. In general, conventional MRI [i.e., T2w, T2*w, gadolinium (Gd) enhanced T1w] is used to monitor the effects of pFUS+MB on BBBO and/or assess whether sonication results in parenchymal damage. This study employed multimodal MRI techniques and ^{18}F-Fludeoxyglucose (FDG) PET to evaluate the effects of single and multiple weekly pFUS+MB sessions on morphology and glucose utilization levels in the rat cortex and hippocampus. pFUS was performed with 0.548 MHz transducer with a slow infusion over 1 min of Optison$^{\mathrm{TM}}$ (5–8 $\times$ 10^7 MB) in nine focal points in cortex and four in hippocampus. During pFUS+MB treatment, Gd-T1w was performed at 3 T to confirm BBBO, along with subsequent T2w, T2*w, DTI and glucose CEST (glucoCEST)-weighted imaging by high field 9.4 T and compared with FDG-PET and immunohistochemistry. Animals receiving a single pFUS+MB exhibited minimal hypointense voxels on T2*w. Brains receiving multiple pFUS+MB treatments demonstrated persistent T2w and T2* abnormalities associated with changes in DTI and glucoCEST when compared to contralateral parenchyma. Decreased glucoCEST contrast was substantiated by FDG-PET in cortex following multiple sonications. Immunohistochemistry showed significantly dilated vessels and decreased neuronal glucose transporter (GLUT3) expression in sonicated cortex and hippocampus without changes in neuronal counts. These results suggest the importance to standardize MRI protocols in concert with advanced imaging techniques when evaluating long term effects of pFUS+MB BBBO in clinical trials for neurological diseases.

Keywords: pFUS microbubble, blood brain barrier, T2* abnormality, DTI, CEST, FDG-PET

INTRODUCTION

MRI guided (MRIg) pulsed Focused Ultrasound (pFUS) is a non-invasive technique being advocated for the blood brain barrier opening (BBBO) to facilitate the delivery of neurotherapeutics (i.e., drugs, genes, biologics) in the treatment of primary and metastatic central nervous system (CNS) tumors (Park et al., 2012, 2020) or neurodegenerative diseases, such as amyotrophic lateral sclerosis (Abrahao et al., 2019) and Alzheimer's disease (Baseri et al., 2012; Kovacs et al., 2014; Lipsman et al., 2018). pFUS coupled with an infusion of ultrasound contrast agent microbubbles (MB) causes BBBO primarily by mechanical effects from acoustic cavitation forces on the endothelium that alters the integrity of tight junction proteins (TJP) and changes calcium fluxes within vasculature (Sheikov et al., 2004, 2008; Deng, 2010; Burgess and Hynynen, 2014; Gorick et al., 2020). MRIg pFUS+MB targeting delivery of neurotherapeutics in CNS diseases has been performed in preclinical experimental studies (Jones et al., 2018) and ongoing clinical trials (NCT03608553, NCT03739905, NCT04118764, NCT03551249, NCT03616860, NCT03714243)[1]. Aside from the positive results, the pFUS+MB BBBO has also been reported to induce a sterile inflammatory response (SIR) in the targeted parenchyma (Banks, 2016; Kovacs et al., 2017b, 2018b; McMahon and Hynynen, 2017; McMahon et al., 2017, 2020). The magnitude of the expression of cytokines, chemokines and trophic factors (CCTF) and cell adhesion molecules (CAM) may be related to the sonication parameters used along with MB dosing (Silburt et al., 2017; Kovacs et al., 2018a). The long-term effects of the induced SIR in pFUS+MB BBBO requires further investigation.

MRI is a sensitive and commonly used technique to assess changes in the brain following pFUS+MB. Gadolinium-based contrast agents (GBCA)-T1-weighted (w) MRI are used to document BBBO following sonication, confirmed by extravasation of dyes or plasma proteins into the parenchyma on histology (Yang et al., 2009; Chai et al., 2018; Stavarache et al., 2018; Morse et al., 2019). The level of contrast enhancement in GBCA-T1w MRI may be related to the magnitude of sonication parameters and the amount of CCTF expression (Nance et al., 2014; Mooney et al., 2016; Olumolade et al., 2016; Kovacs et al., 2017b; McMahon et al., 2017). T2w (Alkins et al., 2013; Aryal et al., 2015; Meng et al., 2017) and T2*w (Hynynen et al., 2001) images have also been used to examine the structural damage and microhemorrhages following pFUS induced BBBO (Gan et al., 2012; McDannold et al., 2012; Kovacs et al., 2014; Downs et al., 2015b; Alecou et al., 2017; Horodyckid et al., 2017). In addition, immunohistochemistry (IHC) techniques have also been used to document changes in cellular activation following sonication and BBBO (Hynynen et al., 2001; Aryal et al., 2015). However, investigations using advanced high-resolution imaging techniques that can assess changes in tissue morphology and glucose utilization, such as diffusion tensor imaging (DTI) (Basser and Pierpaoli, 1996) and chemical exchange saturation transfer (CEST) (Ward et al., 2000). MRI have received little attention despite their potential for assessing treatment effects following single or multiple sonication sessions.

The purpose of this study was to evaluate the long-term effects of single and multiple pFUS+MB BBBO in the rat cortex and hippocampus by high-resolution advanced MRI techniques and correlate radiological findings to pathology. MRI was performed at 9.4 T at 1 day, 2 and 6 weeks post 1×, 2×, and 6× pFUS+MB using T2w, T2*w, DTI and CEST imaging. The imaging results were compared to 2-[^{18}F] Fluoro-deoxyglucose (FDG) positron emission tomography (PET) performed after the sixth sonication and IHC results for glucose transporters and neuronal density. The results underscore the value of incorporating advanced MRI imaging techniques in assessing metabolic and morphological changes in the brain following sonication.

MATERIALS AND METHODS

Animal Care

For all the animal experiments, barrier-raised and specific pathogen-free 6–8-week-old female Sprague-Dawley rats were used (Charles River Laboratory, Wilmington, MA). Rats were housed individually in a temperature- and light-controlled room on a 12-h light–dark cycle and were fed commercial rodent chow (2018 Teklad Global 18% Protein Rodent Diet; Harlan Laboratories Inc., Indianapolis, IN) and tap water *ad libitum*. This study was approved by our Institutional Animal Care and Use Committee and all experiments were complied with the National Research Council's Guide for the Care and Use of Laboratory Animals (2011).

Experiment Design

Figure 1 is a diagram outlining the timing of the imaging experiments performed. Rats had *in vivo* MRI using a Bruker 9.4T scanner (Bruker Corp., Billerica, MA) and a radiofrequency quadrature coil (Doty Scientific, Inc., Columbia, SC). Before starting pFUS+MB treatments, anatomical T2w imaging was used to screen for baseline brain abnormalities, including spontaneous ventriculomegaly previously found in the Wistar rats (Tu et al., 2014), which served as exclusion criteria. The imaging parameters included: rapid acquisition with refocused echoes (RARE) sequence, repetition time/echo time (TR/TE) 3000/11 ms, RARE factor 8, in-plane resolution 100 × 100 μm^2, slice thickness 500 μm, slice number 30. Throughout the MRI scans, a circulating water warming pad was placed under the animals to ensure a constant 37°C body temperature while anesthesia was ensured by isoflurane (1–1.5%) in 100% O_2 via nosecone. A steady respiratory rate was monitored using a pressure sensor (SA Instruments Inc., Stony Brook, NY) and maintained at 40–50 breaths-per-minute by controlling the level of isoflurane/oxygen mixture. 21 rats were first scanned to screen for baseline abnormalities, 14 rats were determined to be normal, and 10 of these rats received further complete imaging examinations to serve as the baseline controls due to the limitation on the imaging resources. These 14 rats were randomly divided into two groups receiving either one (Group 1, *n* = 7) or 6 weekly (Group 2, *n* = 7) pFUS+MB treatments (**Figure 1**).

---

[1] clinicaltrials.gov

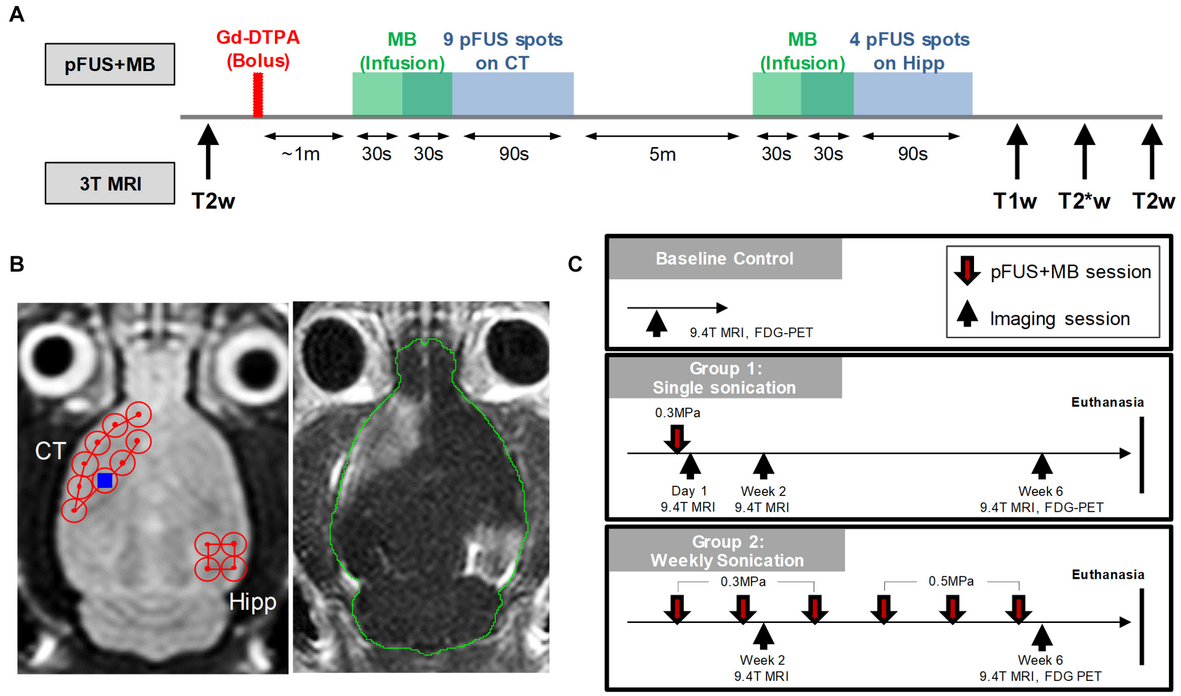

FIGURE 1 | Experimental design. **(A)** Workflow of the MRI-guided pFUS+MB treatments on 3 T MRI system. **(B)** Axial T2w images (left) were acquired for sonication planning of the treatment: nine 2 mm-diameter non-overlapping focal points were placed on the left cortex covering the area anterior to the lateral ventricle and four focal points were placed on the right hippocampus. After bolus Gd-DTPA injection, microbubbles were slowly infused via tail and followed by sonication starting 30 s after microbubble infusion. The total sonication time is 120 s for each treatment. Gd-T1w images (right) shows the opening of blood-brain barrier after pFUS+MB treatment. **(C)** Longitudinal imaging experiment timeline. Baseline T2w MRI were first obtained on 9.4 T MRI to rule out brain abnormalities prior to sonication. The other imaging protocols included T2*w, DTI, CEST and ^{18}F-FDG-PET. Animals were then euthanized in week 7 and brains were harvested for histological examination.

After receiving one pFUS+MB exposures, Group 1 rats had 9.4 T MRI performed on week 2 (1X-W6) and week 6 (1X-W6) post-sonication and were euthanized at week 7. Group 2 rats received 6 weekly pFUS+MB treatments and had MRI at week 2 (2X-W2) and week 6 (6X-W6) post-sonication, and were euthanized at week 7 (**Figure 1C**). ^{18}F-FDG-PET scans were performed on week 6 on a randomly selected subsets of control (*n* = 4), Group 1 (*n* = 6) and Group 2 (*n* = 4) rats. The imaging results presented in the current study were complementary to the data reported in Kovacs et al. (2018b).

MRI-Guided Pulsed Focused Ultrasound and Microbubbles

MRI-guided pFUS+MB treatments were performed using a preclinical pFUS instrument equipped with a surface coil (RK-100, FUS Instruments, Toronto, ON) on a Philips Achieva 3 T MRI system (Philips Healthcare, Andover, MA). The workflow of the pFUS+MB treatments is illustrated in **Figure 1A**. pFUS targeting coordinates for sonication were obtained from axial T2w images by turbo spin echo (TSE) with TR/TE 2000/70 ms, echo train length 12, in-plane resolution 273 × 273 μm^2, slice thickness 1.5 mm, average 4. Prior to pFUS sonication, rats were first infused intravenously (IV) with 100 μL Magnevist gadopentetate dimeglumine (Gd, Bayer Healthcare Pharmaceuticals, Inc., Whippany, NJ) via tail vein catheter for Gd-T1w MRI examination of BBBO. Thirty seconds before initiating sonication, an intravenous infusion (1.66 μL/s) of Optison^{TM} (GE Healthcare, Little Chalfont, Buckinghamshire, United Kingdom) was started that continued to 100 μL (i.e., 30 s) during sonication to targeted regions in the left cortex and the right hippocampus with non-overlapping 2-mm diameter focal spots as previously described (**Figure 1B**; Kovacs et al., 2017b, 2018a,b). Infusion of MB was separated by at least 5 min between sonications in the same rat. The initial dose (Day 0) of Optison^{TM} was ∼460 μL/kg and was fixed at 100 μL (5–8 × 10^7 MB) for all sonications independent of animal weight that was sufficient to cause BBBO (Kovacs et al., 2017b; Kovacs et al., 2018a). Immediately post-pFUS+MB, axial T1w images were obtained by spin echo (SE, TR/TE 215/10 ms, in-plane resolution 137 × 137 μm^2, slice thickness 1.5 mm, average 4). Pulsed FUS was performed with the following parameters: 0.3–0.5 MPa peak negative pressure (PNP) measured in water that was applied in 10 ms burst length and <1% duty cycle with a pulse repetition frequency (PRF) of ∼0.5–0.6 Hz (i.e., 120 s/9 focal points in the left frontal cortex anterior to the lateral ventricle including the striatum, 120 s/4 target points in the right hippocampus (**Figure 1B**), using a single-element spherical FUS transducer (center frequency: 548 kHz focal number: 0.8 active diameter: 7.5 cm; FUS Instruments, Toronto, Canada). For Group 2 rats the PNP was increased to 0.5 MPa from the 4th sonication due to the changes in skull thickness and weight gain causing an effective decrease in MB/kg concentration in the animals. The pFUS PNP of 0.3–0.5 MPa were chosen while the animals were on 100% O_2 that would result in detectible contrast enhancement on Gd-T1w images (McDannold et al., 2017; Kovacs et al., 2018b).

In vivo 9.4 T MRI for pFUS+MB Treatment Effects

High-resolution 9.4 T MRI scans were obtained in the rat brain for the longitudinal examinations after pFUS+MB exposures as outlined in **Figure 1C**. The 9.4 T MRI scans were performed within 3 days after sonication using the following imaging protocols: T2w images by RARE (TR/TE 3000/11.6 ms; RARE factor 8; in-plane resolution 200 × 200 μm^2; slice thickness 500 μm; average 3); three dimensional T2*w images by multiple gradient echo (MGE; TR/TE 50/3 ms; ΔTE 3 ms; number of echoes 10; flip angle 30°; resolution 200 μm^3 isotropic; average 2). The T2*w images were generated by combining the 10 MGE data with an effective TE 22.7 ms to enhance the presence of T2* abnormality. Quantitative T2* maps were obtained by fitting the signal intensity (S_i) of each voxel from MGE dataset to a mono-exponential decay as a function of TE:

$$S_i = S_0 \exp(-TE_i/T2^*) \quad (1)$$

Three dimensional DTI was acquired using spin echo (SE) echo-planar imaging (EPI; TR/TE 550/49 ms; EPI segment 6; Δ 15 ms; δ 5 ms; b-value 800 s/mm^2; 15 diffusion encoding directions with 2 B_0 images; average 1). The DTI imaging volume and voxel size were identical to the T2*w imaging. Diffusion-weighted images were corrected for B_0 susceptibility induced EPI distortion, eddy current distortions, and motion distortion with b-matrix reorientation using Tortoise v2.5 (NIH, Bethesda, MD). After correction, the diffusion tensor was calculated to derived DTI parameters, fractional anisotropy (FA), mean diffusivity (MD), axial diffusivity (AD), and radial diffusivity (RD) to evaluate the microstructural changes following pFUS+MB opening of the BBB. CEST MRI data were acquired by single slice RARE with (S_{MT}) and without (S_0) magnetization transfer (MT) pulses (TR/TE 3091.7/10.4 ms; RARE factor 8; in-plane resolution 200 × 200 μm^2; slice thickness 0.8 mm; MT pulse 1.5 μT, 1 s). The MT offset frequencies (Δω) were set from −1.6 to +1.6 kHz with 100 Hz stepping. Z-spectral interpolation and WAter Saturation Shift Referencing (WASSR) techniques were applied to correct the shifted water resonance frequency by B_0 inhomogeneity (TR/TE 1500/10.4 ms; RARE factor 8; MT pulse 0.3 μT, 250 ms; Δω −0.4 to +0.4 kHz with 60 Hz stepping). Magnetization transfer ratio asymmetry (MTR_{asym}) was calculated by $[S_{MT}(-\Delta\omega) - S_{MT}(\Delta\omega)]/S_0$. The CEST-weighted images were generated by integrating the area under the curves of MTR_{asym} for the proton signal of glucose metabolites (glucoCEST) exchanging at the center of 1.2 ppm (±0.5 ppm) in arbitrary unit (Van Zijl et al., 2007; Chan et al., 2012; Tu et al., 2018). One Group 2 animal had severe motion artifacts in the week 6 MRI scans. This dataset was excluded in the rest of analysis.

In vivo ^{18}F-FDG-PET

^{18}F-FDG-PET imaging was performed at week 6 for each group to evaluate the changes of glucose uptake and metabolism following pFUS+MB treatment using a small animal Inveon PET/CT scanner (Siemens Medical Solutions, Malvern, PA) with transaxial field of view (FOV) of 10 cm, axial FOV of 12.7 cm and full width at half maximum (FWHM) spatial resolution at center FOV of 1.4 mm. Rats were first anesthetized with 2–2.5% isoflurane-oxygen mixture and ^{18}F-FDG (dose based on the body weight of each animal; avg. dose = 0.951 mCi) was then injected as a bolus through the tail vein followed by a quick saline flush (300 μL). After the injection, the animals were allowed to recover at room temperature. Thirty minutes after radiotracer injection, the animals were anesthetized again and secured to an imaging bed, placing the head symmetrically in the center FOV. The animals' respiratory rate was carefully monitored to avoid any intra-subject variability of the anesthesia level (target respiratory frequency range = 40–60 breaths/min). The body temperature was maintained by a heating pad. Following a 30 min uptake period, PET emission scans were acquired in list mode following which emission sinograms were corrected for scatter, ^{18}F-decay, random and dead time. The resulting histograms were then reconstructed applying Fourier rebinning and ordered subject expectation maximization algorithm (4 OSEM iterations, 18 MAP iterations, matrix: 128 × 128, target resolution: 0.8 mm). Once scan was completed, the animals were allowed to recover from anesthesia under a heat lamp. The PET data were co-registered to a previously acquired T2w anatomical MR template and the standardized uptake values (SUVs) were processed using PMOD 3.7 (PMOD technologies, Zurich, Switzerland).

For all the MRI and PET data quantification, the regions of interest (ROIs) encompassing the ipsilateral treated and contralateral untreated regions were drawn for cortex and hippocampus by two experienced technologists (**Supplementary Figure S1**). ROIs for DTI and T2* maps also included external capsule (EC) to assess white matter integrity after pFUS+MB. Except for the aforementioned software, the imaging data were processed by in-house Matlab (Mathworks, Inc., Natick, MA) scripts.

Immunohistochemistry Analysis

Three animals in each group were randomly selected at week 7 after last scan for trans-cardiac perfusion with 4% PFA in PBS. The brains were extracted and sectioned at 10 μm for histological examination for neurons and glucose transporters per published protocol (Yu et al., 1995; Kovacs et al., 2018b). The following primary antibodies were used: glucose transporter 1 (GLUT1) (Invitrogen MA5-11315, Waltham, MA) at 1/200; glucose transporter 3 (GLUT3) (Abcam ab41525, Cambridge, United Kingdom) at 1/1500; hexaribonucleotide binding protein-3 (NeuN) (Cat. mab377, Millipore) at 1/1000. Secondary antibodies were used at 1/200 as follows: NeuN: goat anti-mouse F(ab') IgG- H&L Dylight 594 (Cat. ab96881, Abcam, Cambridge, United Kingdom); GLUT1: goat anti-mouse F(ab') IgG2a Dylight 594 (SAB4600328, Sigma Aldrich, St. Louis, MO); GLUT3: goat anti-rabbit F(ab') IgG- H&L Dylight 594 (Cat. ab102293, Abcam, Cambridge, United Kingdom). The IHC data were quantified from the corresponding locations matching to the ROIs for MRI data quantification to cover each pFUS treated and contralateral regions. In each IHC images, the positive fluorescent staining was quantified from three FOVs in 20X and averaged to represent the area percentage of the staining.

Statistical Analysis

Statistical analysis was performed using Prism v8.1.2 (GraphPad Software, Inc., La Jolla, CA). The experiment was powered around the MRI variables, including T2*, DTI, and CEST parameters. A sample size of $n = 6$ –10/group was determined necessary to detect differences in these key variables at an α level of $p < 0.05$ and 80% power. The quantification data of the T2* and DTI parameters passed the Shapiro–Wilk test for normality and were compared between the unsonicated animals of the baseline control, animals sonicated once and imaged at week 6 (1X-W6), and animals sonicated six times and imaged at week 6 (6X-W6) using paired *t*-test in significant level predetermined at $p < 0.05$. For glucoCEST and FDG-PET, the contrast ratios between the ipsilateral treated and contralateral untreated brain regions were calculated and reported for the cortex and hippocampus. Because of the non-normality of measured variables distribution, the nonparametric Kruskal–Wallis test followed by Dunn's *post-hoc* multiple comparisons test ($p < 0.05$) was used to compare the glucoCEST and FDG-PET contrast ratios among groups. The comparison included unsonicated animals of the baseline control, animals sonicated once and imaged at week 6 (1X-W6), and animals sonicated six times and imaged at week 6 (6X-W6). A separate longitudinal analysis was performed for Group 1 rats between glucoCEST ratios at 2 weeks (1X-W2) and at 6 weeks (1X-W6), and for Group 2 rats at week 2 (2X-W6) and at week 6 (6X-W6) scans. The IHC data passed normality test and compared using paired *t*-test between the ipsilateral treated and contralateral untreated regions. All data are reported as mean ± SD.

RESULTS

T2w, T2*w, and DTI

pFUS+MB exposure to the cortex and hippocampus resulted in significant contrast enhancement in Gd-T1w images indicative of BBBO (**Figure 1B**). In Group 1 rats, MRI demonstrated no qualitative differences between ipsilateral treated brain and contralateral parenchyma on T2w, T2*w, and DTI images 1-day post-pFUS+MB (**Figure 2**). MRI scans performed at week 2 and week 6 post-sonication revealed scattered hypointense voxels on T2*w images in the targeted cortex and hippocampus in five of seven rats (**Figures 2B,D,E**). DTI showed hyperintense voxels in the FA maps of the treated hippocampus (**Figure 2E**). In Group 2 rats that received 6 weekly pFUS+MB, there were clear differences after the second sonication on T2 and T2*w images with hypointense voxels in the targeted cortex and hippocampus (**Figure 3**). The hyperintense voxels appeared more clearly in the FA maps of the treated cortex and hippocampus that were consistent with areas of abnormalities on T2*w images (**Figures 3C–E**). Compared to the contralateral regions, quantitative analysis demonstrated significantly decreased T2*

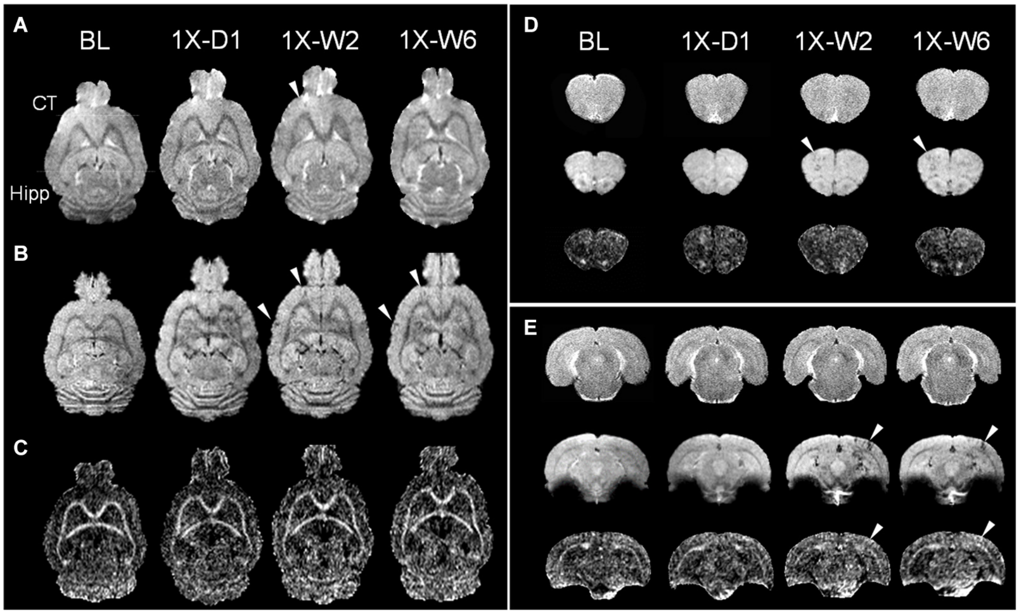

FIGURE 2 | Longitudinal MRI of the brain in a single pFUS+MB treatment group (1X) acquired in baseline (BL), day 1 (D1), week 2 (W2), and week 6 (W6) by **(A)** T2w, **(B)** T2*w, and **(C)** fractional anisotropy (FA) of 9.4 T MRI. The T2*w images in week 2 and 6 display apparent T2* abnormalities (arrowheads) in **(B,D)** the left cortex and **(E)** right hippocampus, where DTI shows increased FA correspondingly. No abnormal voxel is found in the FA images in (C) and (D). The horizontal lines in **(A)** denote the coronal section in **(D,E)**. **(D,E)** Images from upper to lower are T2w, T2*w, FA. CT, cortex; Hipp, hippocampus.

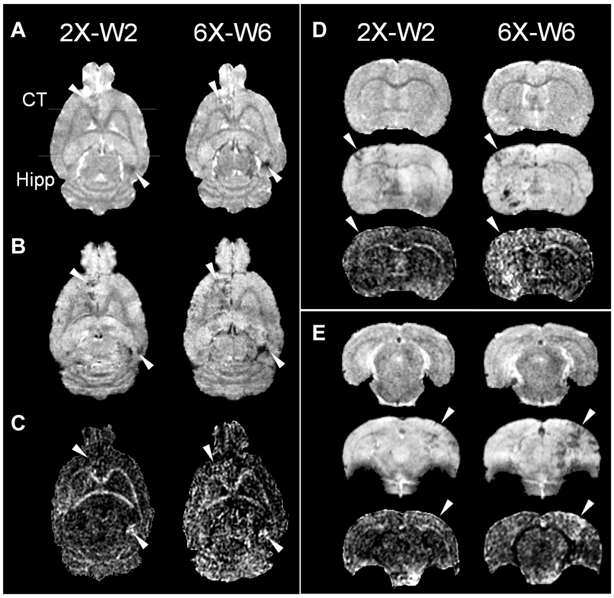

FIGURE 3 | Longitudinal MRI of the brain in the weekly pFUS+MB treatment group (2X or 6X) imaged in week 2 (W2) and week 6 (W6) by 9.4 T **(A)** T2w, **(B)** T2*w, and **(C)** fractional anisotropy (FA). The T2w and T2*w images demonstrate clear treatment effects after multiple pFUS+MB treatments, where DTI clearly shows increased FA. The arrowheads indicate the locations that show abnormalities after treatments. The horizontal lines in (A) denote the coronal section in **(D,E)**. **(D,E)** Images from upper to lower are T2w, T2*w, FA. CT, cortex; Hipp, hippocampus.

values in the cortex of the Group 2 rats (−23.71 ± 10.67%, $t_{(5)}$ = 5.818, $p < 0.01$), and in the hippocampus in both Group 1 [−29.8 ± 9.1%, $t_{(6)}$ = 8.226, $p < 0.001$] and Group 2 [−32.98 ± 14.06%, $t_{(5)}$ = 6.780, $p < 0.01$] rats at week 6 (**Figures 4A,F**). In Group 1 rats, a significant increase in RD was observed in the treated EC [+15.89 ± 13.08%, $t_{(6)}$ = 3.582, $p < 0.05$] (**Figure 4D**). All the rest of the DTI metrics were not different between the treated and untreated hemisphere at week 6 after one sonication. In Group 2 rats, compared to the contralateral untreated regions, FA increased significantly in the treated cortex [+11.67 ± 9.2%, $t_{(5)}$ = 3.220, $p < 0.05$] and hippocampus [+25.69 ± 13.61%, $t_{(5)}$ = 5.852, $p < 0.01$], while RD decreased in the cortex [−9.16 ± 6.41%, $t_{(5)}$ = 4.151, $p < 0.01$] and hippocampus [−18.07 ± 13.25%, $t_{(5)}$ = 3.436, $p < 0.05$] at week 6, along with significantly decreased FA [−10.55 ± 3.15%, $t_{(5)}$ = 7.719, $p < 0.001$], increased RD [+19.68 ± 14.69%, $t_{(5)}$ = 3.658, $p < 0.05$], and decreased AD [−7.96 ± 5.12%, $t_{(5)}$ = 3.680, $p < 0.05$] in the EC (**Figures 4G–J**). The T2* and DTI results are also listed in the **Supplementary Table S1**.

GlucoCEST Weighted Imaging

No obvious difference was seen in the glucoCEST-weighted images between the treated and untreated cortex and hippocampus in Group 1 rats at either 2 or 6 week time points following a single pFUS+MB treatment (**Figure 5**). There was significant difference in the glucoCEST contrast ratios between the treated and untreated cortex of the baseline control rats, rats sonicated once and imaged in week 6, and rats sonicated six times and imaged in week 6 [$H_{(3)}$ = 6.360, $p < 0.05$] (**Figure 8A**). The *post-hoc* tests showed the differences were between the animals of unsonicated baseline (0.998 ± 0.169) and the animals sonicated six times and imaged in week 6 (0.793 ± 0.126, $p < 0.05$). No significant difference was noted in the hippocampus. Longitudinally, in the Group 2 animals that had weekly sonication, there was a decrease trend in the contrast ratios in the cortex and hippocampus between week 2 and week 6 (**Supplementary Figure S2**). These changes were not significant in either of the location. **Figures 6**, **7** shows the group averaged Z-spectra and MTR_{asym} of the treated and untreated cortex and hippocampus.

FDG-PET

FDG-PET studies were performed in the baseline control rats, Group 1 and Group 2 rats at week 6. There was a significant difference in the cortex among the three groups [$H_{(3)}$ = 8.095, $p < 0.01$] (**Figures 5**, **8**). The *post-hoc* tests showed significant decreases in the ratios between the unsonicated rats (1.00 ± 0.02) and Group 2 rats (0.94 ± 0.04, $p < 0.01$), and between Groups 1 (0.99 ± 0.02) and Group 2 rats (0.94 ± 0.04, $p < 0.01$) (**Figure 8B**). No significant difference was seen in the hippocampus among the three groups (**Figure 8D**). The quantifications of glucoCEST and FDG-PET results are also listed in the **Supplementary Table S2**.

Histology

Histological evaluations were performed on the tissues harvested in week 7 after a single or six weekly pFUS+MB exposures (**Figure 9**). Group 1 rats demonstrated no difference in GLUT1 or GLUT3 expression on the immunofluorescent staining in either sonicated region. In Group 2 rats, increased GLUT1 was detected on the endothelium of the dilated vessels in the treated hippocampus [$t_{(2)}$ = 4.483, $p < 0.05$]. Compared to a homogenous expression in the contralateral parenchyma, the GLUT1 expression was demonstrated as a scattered depleted pattern on the microvasculature in the sonicated sites. Neuronal GLUT3 expression was significantly decreased in the sonicated cortex [$t_{(2)}$ = 4.726, $p < 0.05$] and hippocampus [$t_{(2)}$ = 5.334, $p < 0.05$] as compared to the contralateral regions. No significant change was observed in the NeuN staining for neurons.

DISCUSSION

The major focus of this study was to use advanced MRI techniques and FDG-PET to evaluate the rat brain following single or 6 weekly pFUS+MB induced BBBO sessions over time. The majority of rats in Groups 1 and 2 had clear evidence of morphological changes on high-resolution T2*w and T2w along with changes in FA on DTI images on MRI at 9.4 Tesla. In the animals receiving multiple weekly pFUS+MB, there was a decrease in the image contrast on the glucoCEST-weighted imaging and FDG-PET in the cortex when compared to unsonicated animals or the Group 1 rats sonicated once in week 6.

Various pFUS+MB protocols have been used in both experimental and clinical studies that result in BBBO, facilitating

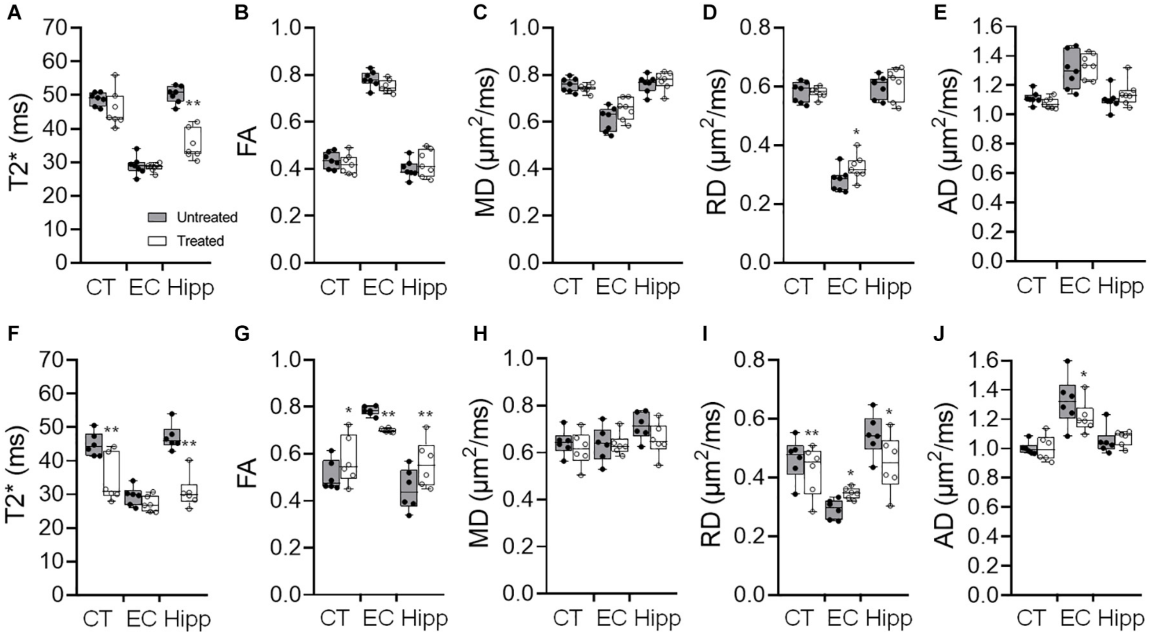

FIGURE 4 | (A–E) Quantification of the 9.4 T imaging data acquired in week 6 brains of Group 1 rats with a single pFUS+MB sonication (1X-W6), and (F-J) Group 2 with six weekly sonications (6X-W6) of T2* **(A,F)**, fractional anisotropy (FA) **(B,G)**, mean diffusivity (MD) **(C,H)** and radial diffusivity (RD) **(D,I)** and axial diffusivity (AD) **(E,J)**. Comparing to the brains with one sonication, changes in the DTI parameters are more significant between the ipsilateral treated and contralateral untreated regions of the cortex (CT), external capsule (EC) and hippocampus (Hipp) after 6 weekly pFUS+MB treatments. *$p < 0.05$, **$p < 0.01$ vs. contralateral untreated region, paired *t*-test (Group 1, $n = 7$; Group 2, $n = 6$).

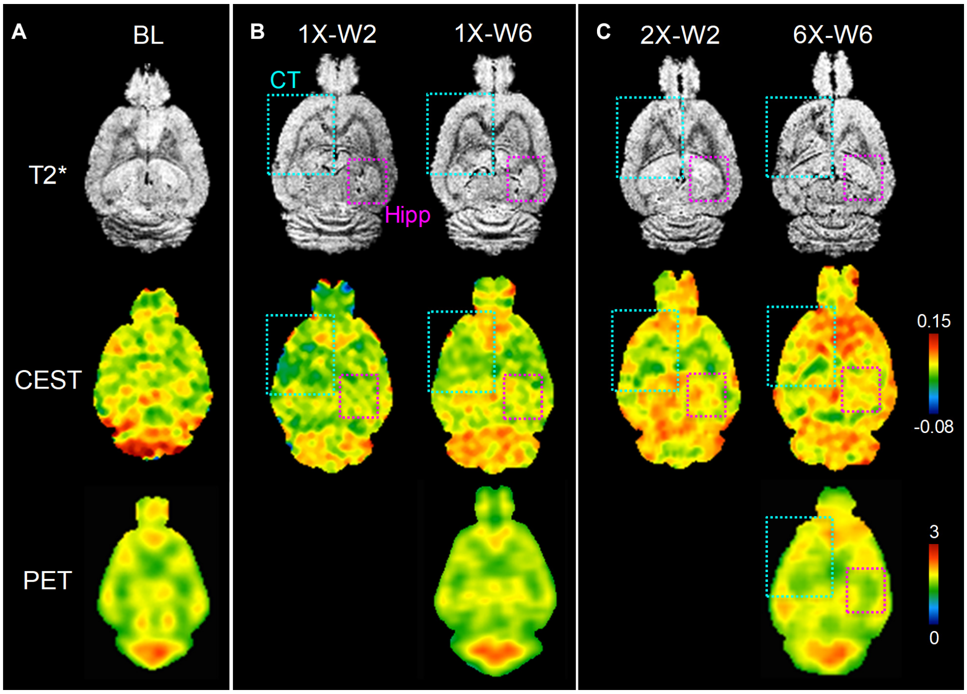

FIGURE 5 | *In vivo* MRI and FDG-PET images of rat brains of **(A)** baseline (BL), **(B)** one sonication (1X), **(C)** multiple weekly pFUS+MB treatments (2X, 6X) and images at week 2 (W2) and week 6 (W6). T2*w images clearly show the sonication sites in the left cortex and striatum (cyan square), and in the right hippocampus (purple square), where the glucoCEST-weighted images and FDG-PET images show changes correspondingly.

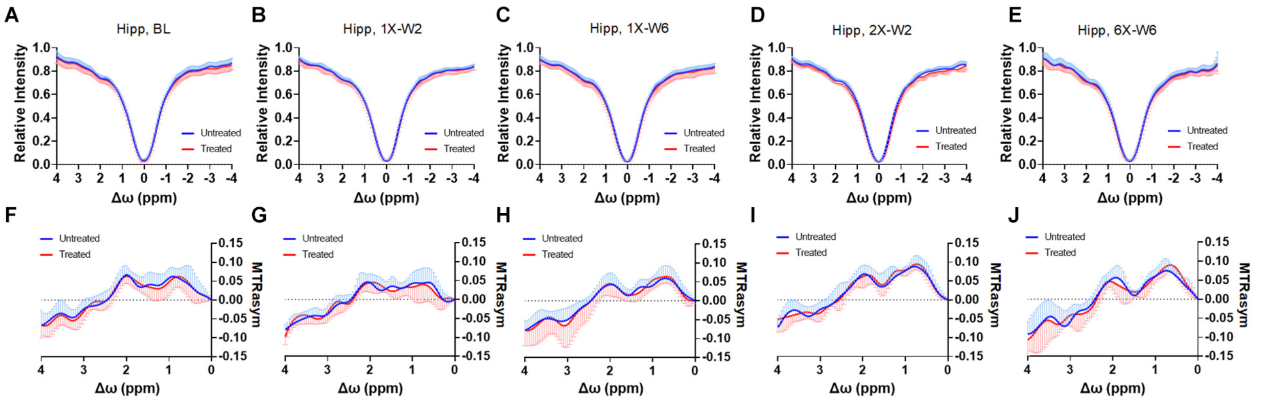

FIGURE 6 | (A–E) The CEST Z-spectra and **(F–J)** MTR$_{asym}$ of the treated and untreated hippocampus from baseline (**A,F**, *n* = 10), 1X-W2 (**B,G**, *n* = 7), 1X-W6 (**C,H**, *n* = 7), 2X-W2 (**D,I**, *n* = 7), 6X-W6 (**E,J**, *n* = 6) rats. Data are presented as mean ± SD.

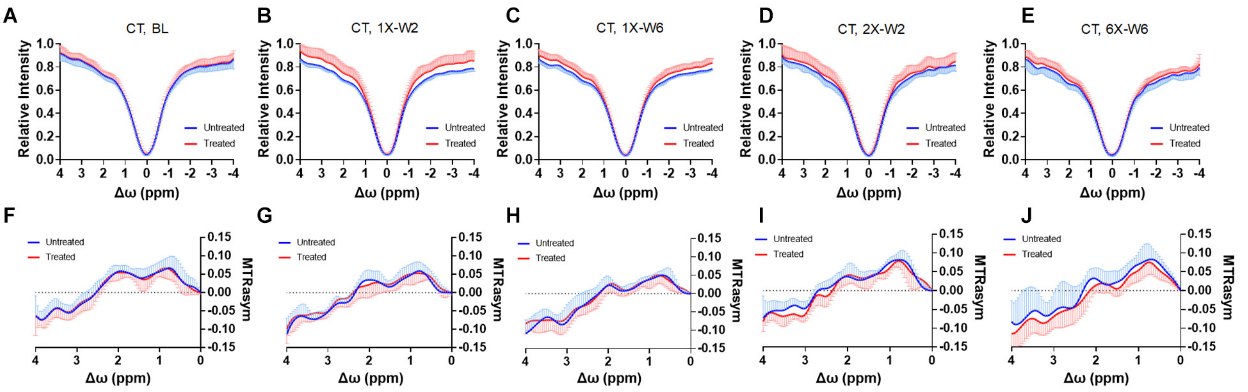

FIGURE 7 | (A–E) The CEST Z-spectra and **(F–J)** MTR$_{asym}$ of the treated and untreated cortex from baseline (A, F, *n* = 10), 1X-W2 (B, G, *n* = 7), 1X-W6 (C, H, *n* = 7), 2X-W2 (D, I, *n* = 7), 6X-W6 (E, J, *n* = 6) rats. Data are presented as mean ± SD.

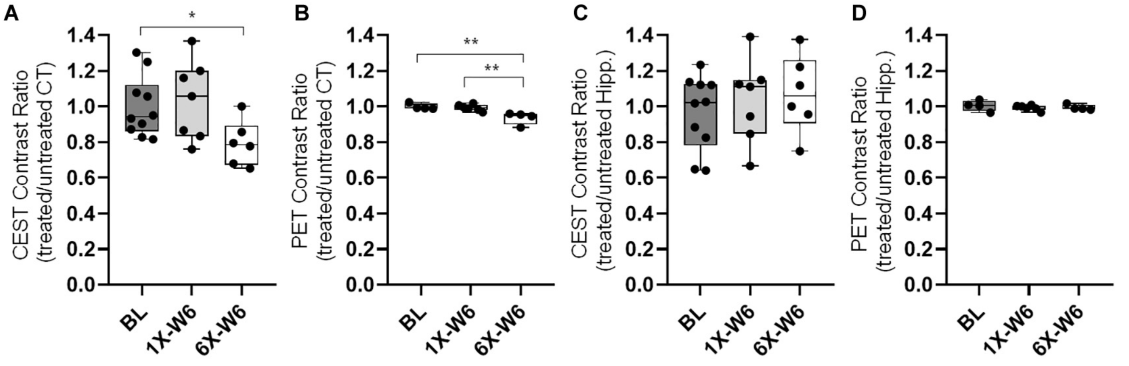

FIGURE 8 | (A) The quantification of glucoCEST shows significantly decreased contrast ratios (treated/untreated) in the cortex of the Group 2 rats compared to that of the baseline (BL) control rats. **(B)** The FDG-PET quantification shows significantly decreased SUV ratios (treated/untreated) in the cortex of the Group 2 rats sonicated six times (6X-W6) compared to control animals and Group 1 rats sonicated once (1X-W6). No significant difference is seen in the hippocampus in the **(C)** glucoCEST and (d) FDG-PET data. $^*p < 0.05$, $^{**}p < 0.01$ vs. BL, Kruskal–Wallis one-way ANOVA, Dunn's test (Group 1, *n* = 7; Group 2, *n* = 6).

the delivery of neurotherapeutics to targeted regions in the brain and potentially enhancing neurological outcomes (Kroll and Neuwelt, 1998; Hynynen et al., 2001; McDannold et al., 2008, 2017; Neuwelt et al., 2008; Gabathuler, 2010; Burgess et al., 2014; Chai et al., 2014; Horodyckid et al., 2017; Kovacs et al., 2017b, 2018a; McMahon et al., 2017; Wu et al., 2017). The interaction

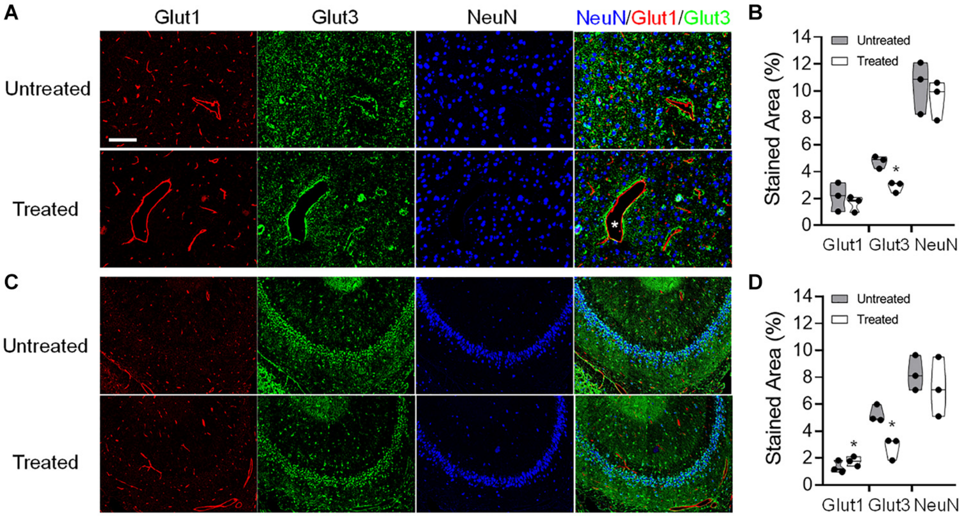

FIGURE 9 | Representative immunohistochemistry (IHC) staining of the endothelial glucose transporter 1 (GLUT1), neuronal glucose transporter 3 (GLUT3), and neuronal nuclei (NeuN) of a Group 2 rat brain that was obtained at week 7 after six pFUS+MB treatments. Dilated vessels were found in the treated hemisphere (asterisk). The IHC images were acquired and quantified from the **(A,B)** cortex and **(C,D)** hippocampus. $^{*}p < 0.05$, $^{**}p < 0.01$ vs. contralateral untreated region, paired *t*-test ($n = 3$/stain/group).

of the pFUS with the MB confined to the vascular space leads to stable cavitation and transient BBBO via stretching of endothelial cells coupled with the induced expression of proinflammatory molecular proteins from the neurovascular unit and alterations in TJP expression (Sheikov et al., 2008; Aryal et al., 2015; Downs et al., 2015b; Kovacs et al., 2017b; McMahon and Hynynen, 2017; McMahon et al., 2017). The evaluation of the sonicated brain by MRI has usually been limited to GdT1w, T2w, T2*w or susceptibility-weighted imaging along with quantitative metrics determining gadolinium leakage (Aryal et al., 2015; Downs et al., 2015b; Wu et al., 2017) and has rarely shown damage (Kovacs et al., 2018b). Conventional imaging techniques used following pFUS+MB BBBO are usually performed with relatively large voxels (>250 μm in-plane resolution and slices 0.8–1.5 mm) that are then correlated to pathological changes in the parenchyma (Treat et al., 2007, 2012; Chai et al., 2014; McDannold et al., 2016; Aryal et al., 2017; McMahon et al., 2017; O'Reilly et al., 2017; Kovacs et al., 2018b). In most of these imaging studies, pathological changes in the sonicated parenchyma could be missed especially when MRI is acquired at 3 T in small animal models (Treat et al., 2007; Marquet et al., 2011).

In the current study, MRI scans at 9.4 T were performed with in plane resolution of 200 × 200 μm^2 and 500 μm thickness for T2w images and T2*w and DTI images were performed at 200 μm thickness, thereby limiting partial volume effects and increasing the conspicuity of changes in signal intensity in the sonicated cortex and hippocampus compared to contralateral brain. T2w and T2*w images acquired 1-day post-pFUS+MB did not reveal any abnormalities, however after two weeks, 71.4% of the rats had hypointense voxels in T2*w images of the targeted cortex or hippocampus. It has recently been shown that 4 days following pFUS+MB in the rat, T2* hypo-intensities were detected suggesting vascular compromise in area of sonication (McMahon et al., 2017). Further investigation into the changes in vascular integrity would contribute to the evolution of pathological changes over time following pFUS+MB BBBO. Multiple weekly pFUS in the rat performed at higher PNP with Definity at 10 μL/kg diluted 10× demonstrated evidence of hypointense voxels on T2w image at 3 T associated with microhemorrhages (Kobus et al., 2016). In comparison, repeated pFUS+MB BBBO in non-human primates over 20 months did not show evidence of long term damage or hypointense voxels on SWI studies at 3 T (Downs et al., 2015b). It has recently been reported that T2w and T2*w pathological changes were conspicuous at 3 T following 2 weekly pFUS+MB and there was a quantitative increase in numbers of voxels with lower T2* values following six sonications (Kovacs et al., 2018b). The current study demonstrated similar pathological changes observed at 9.4 T on T2w and T2*w imaging following 2 and 6 weekly sonication to induce BBBO. The T2* pathology presumably due to microhemorrhages would evolve over time and either be metabolized by microglia and disappear or result in hemosiderin deposition in the brain and remain as an abnormality on T2* w images. The microhemorrhage changes in the rat brain following pFUS would be tracked on MRI similar to what is observed with ischemic disease, stroke or chronic traumatic encephalopathy in the rat.

There have been no reports to date in the rat employing DTI and CEST MRI to evaluate morphological and metabolic changes in targeted area in the brain. pFUS+MB induced changes on the FA maps of the targeted brain at 2 or 6 weeks compared to the contralateral brain. In comparison to the Group 1 rats, Group 2 rats exhibited decreased FA and AD in the sonicated external capsule that may reflect white matter damage, inflammation, neurite beading and disrupted glial cells (Budde and Frank, 2010; Tu et al., 2016). The increased FA in the sonicated cortex and hippocampus would suggest tissue damage in association with astrogliosis in the Group 2 rats (Budde et al., 2011). The decreases in RD in Group 2 rat cortex and hippocampus would be indicative of tissue swelling and/or increased cellularity, i.e., mononuclear cell infiltration and inflammation, in the sonicated regions, while the increased RD in the external capsule may be related to increased permeability or demyelination (Tu et al., 2014, 2016). For the 6 weekly pFUS+MB treated animals, there was greater significant T2* shortening in the cortex and hippocampus that could also contribute to the differences in the DTI metrics caused by local inhomogeneity, such as micro-hemorrhage and iron metabolites resulting in hyperintense regions on the FA maps compared to contralateral side. Further investigations are needed to determine the DTI metric changes immediately after sonication and how these changes relate to axonal integrity in the external capsule or neuronal damage within the parenchyma.

There have been few studies investigating glucose uptake or metabolism in normal brains by FDG-PET following BBBO by US combined with MB infusion (Yang et al., 2014; Horodyckid et al., 2017). Using a planar ultrasound transducer implanted in non-human primate skull with infusion of MB (SonoVue^{TM}; Bracco, Milan, Italy) every 2 weeks, the authors reported BBBO but no evidence of change in glucose metabolism by FDG-PET (Horodyckid et al., 2017). In comparison ^{18}F-FDG-PET performed immediately and 24 h after pFUS+MB showed decreased glucose uptake in the rat brain by inhibiting GLUT1 expression within the 24 h period of BBBO as documented by Evans blue extravasation into the parenchyma (Yang et al., 2014). The effect of pFUS+MB on glucose uptake was found to be transient and reversible after one sonication session. In the current study ^{18}F-FDG-PET detected decreased FDG uptake and metabolism in rats receiving 6 weekly pFUS+MB treatments in the cortex but not at the level of the hippocampus. Changes in FDG uptake were not apparent in the treated brain 6 weeks after a single sonication. We also demonstrated that the glucoCEST-weighted images provided sufficient contrast reflective of decreased glucose levels in corresponding areas of decreased FDG uptake in Group 2 rats (**Figures 5**, **8**). CEST-MRI has a voxel size 80–100 times smaller than PET scans by monitoring ^{1}H - water ^{1}H exchange on MRI without using radioisotope (Guivel-Scharen et al., 1998; Ward et al., 2000). The chemical exchange results in the transfer of magnetization from the small exchangeable proton pool (e.g., micromolar to millimolar range) to a much larger water proton pool (∼110 M) until a steady state is reached. The sensitivity of glucoCEST is higher than direct observation of the glucose through ^{1}H-NMR because the proton signal is amplified via many exchange events during the extended saturation period of magnetization transfer pulses (Van Zijl and Yadav, 2011).

In vivo glucoCEST-weighted imaging has been shown to detect delayed hypo-metabolism in a rat brain following traumatic brain injury (Tu et al., 2018). The imaging contrast in glucoCEST-weighted imaging may be related to the steady-state glucose level in the brain parenchyma which has been previously validated by 2DG autoradiography. CEST data acquisition using low saturation power (1.5 μT) and short saturation duration (1 s) minimizes extensive direct saturation effect to enhance the sensitivity for detecting glucose in the rat brain. Although the endogenous glucoCEST contrast may also be affected by other hydroxyl metabolites such as myo-Inositol, deriving the glucoCEST-weighted contrast by integrating the MTR_{asym} areas specifically on the glucose chemical shifts at 1.2 ppm provides the sensitivity and specificity to detect changes of glucose level in the sonicated parenchyma (**Figure 5**; Chan et al., 2012; Tu et al., 2018). In this study, the IHC analysis suggests that the changes of the cerebral glucose level could be related to decreased neuronal transporter GLUT3, and the re-distributed vascular glucose transporter GLUT1 after multiple pFUS+MB BBBO sessions. While no significant loss of neuronal cells was seen in the NeuN staining, the decreased GLUT3 expression may be associated with the prolonged inflammatory responses, neurogenesis and neurodegenerative processes induced by repeated BBBO in the treated parenchyma (Kovacs et al., 2018b). A clear pattern of altered endothelial GLUT1 expression on the dilated vessels or on the contracted vessels may also decrease the glucose level in the sonicated brain (**Figure 9**). Further investigations are needed to evaluate the longer-term effects of pFUS+MB on endothelial GLUT1 and neuronal GLUT3 expression and whether the changes would return to control levels.

The recent progress in the pFUS+MB BBB research has advanced this novel technology to an encouraging direction for clinical application for drug delivery in the CNS diseases (NCT03321487, NCT02986932, NCT03608553, NCT03616860, NCT03739905, NCT03714243) (see text footnote 1). This contemporary technology continues to require optimization of the FUS parameters with the use of advanced passive cavitation detection feedback approaches to limit non-linear stable or inertial cavitation that could result in parenchymal damage or excessive neuroinflammation (Jones et al., 2018). The translational work would be to see if it will be possible to apply DTI and CEST, or a comparison to FDG-PET, for the pFUS+MB treatment in brain tumors or Alzheimer's disease, and whether at higher resolution scans can detect subtle differences in glucose concentration which may reflect micrometastasis in the case of metastatic disease to the brain or glioblastoma multiforme spreading outside Gd enhanced area on FLAIR or T2w images. For Alzheimer's disease, these imaging methods could be correlated to areas of hypoperfusion.

The current study employed a pFUS+MB protocol with nine 2-mm diameter focal spots in the left frontal cortex and four in the right hippocampus to provide an example of almost complete coverage in the hemisphere to induce BBBO and deliver neurotherapeutics or stimulate an immune response in the diseased brain (Kovacs et al., 2017b, 2018b). The experimental results may not be related directly to other pFUS+MB experiments to cause BBBO performed with different FUS parameters, targeting approaches or MB type, dose and infusion rates in relationship to initiating sonication (Kovacs et al., 2018a). Another limitation of this study is the lack of longer-term follow-up in animals that received 6 weekly sonications. It will be important to apply advanced imaging techniques to monitor changes in the brain following multiple sonication treatments to determine both morphological and metabolic responses in relationship to pathology and functional outcomes (Downs et al., 2015a; Kobus et al., 2016; Horodyckid et al., 2017; Kovacs et al., 2017a; O'Reilly et al., 2017; Silburt et al., 2017). Our findings suggest that the structural damage in the T2* and DTI may be more permanent, and the CEST and PET observation of the altered glucose levels may be transient and reversible in the longer term. On the detection of glucose utilization, the FDG-PET was more sensitive to detect the treatment effect with fewer data variations and higher significance. The glucoCEST data varied due to the less abundant endogenous glucose signals and the susceptibility to the imaging artifacts, including motion and field inhomogeneity. Since glucose signal at 1.2 ppm is close to the water signal, large saturation pulses may diminish the glucose signals due to the direct saturation effect. In order to observe the glucose signal, our previous study uses relatively small saturation intensity (1.5 μT and 1 s) for acquiring glucoCEST data on the 9.4 T for the rat brain (Tu et al., 2018). Further study is required to investigate the CEST imaging parameters for optimizing endogenous glucoCEST. Furthermore, the glucoCEST weighted image was generated by integrating the MTR_{asym} centered in 1.2 ppm, ranging from 0.7 to 1.7 ppm. The MTR_{asym} at this range may contain interferences from other metabolite signals, including creatine centering in 1.95 ppm, myo-inositol in 0.6 ppm, and the upfield Nuclear Overhauser Enhancement (NOE). More sophisticated CEST contrast analysis, such as multi-pool Lorentzian fitting of the global Z-spectra (Desmond et al., 2014; Zhou et al., 2017), may enhance the specificity of glucose detection following pFUS+MB BBBO in the brain. GlucoCEST imaged with exogenous glucose injection should improve the sensitivity to detect the subtle treatment effect of the pFUS+MB. However, the exogenous glucoCEST may be predominantly affected by the increased vessel permeability and glucose agent leakage from the pFUS+MB induced BBBO, which may not be related to the static glucose levels in the treated brain. The feasibility of applying exogenous glucoCEST in the case of pFUS+MB BBBO would require further investigations.

CONCLUSION

This study describes the monitoring of the long-term effect using conventional and advanced imaging techniques such as DTI and CEST imaging following a single or multiple weekly pFUS+MB BBBO. The findings suggest the importance of using these imaging methods for monitoring the late effects in the brain tissue and be used for further investigations to evaluate the changes in the brain following low pressure pFUS+MB treatment.

DATA AVAILABILITY STATEMENT

All datasets generated for this study are included in the article/**Supplementary Material**.

ETHICS STATEMENT

The animal study was reviewed and approved by the National Institutes of Health.

AUTHOR CONTRIBUTIONS

JF, T-WT, and ZK: conceptualization. T-WT, ZK, MS, JW, GP, WR, DH, and JF: methodology. T-WT, ZK, MS, JW, and GP: formal analysis. DH and JF: resources. T-WT and JF: writing – original draft. T-WT, ZK, DH, and JF: writing – review and editing. T-WT, ZK, and MS: visualization. DH and JF: supervision. T-WT, DH, and JF: funding acquisition. All authors had full access to all the data in the study and take responsibility for the integrity of the data and the accuracy of the data analysis.

FUNDING

This work was supported by funding from the Department of Defense through the Center for Neuroscience and Regenerative Medicine (Henry M. Jackson Foundation Award #300604-8.01-60855 and #305500-8.01-60855), the Intramural Research Programs of the Clinical Center and of the National Institute of Biomedical Imaging and Bioengineering at the National Institutes of Health, and from the Center for Infectious Disease Imaging in the Clinical Center. T-WT was supported by extramural National Institutes of Health funding of NCATS 5UL1TR001409, NICHD 1U54HD090257, and NIMHD 2U54MD007597.

SUPPLEMENTARY MATERIAL

The Supplementary Material for this article can be found online at: https://www.frontiersin.org/articles/10.3389/fnins.2020.00908/full#supplementary-material

REFERENCES

Abrahao, A., Meng, Y., Llinas, M., Huang, Y., Hamani, C., Mainprize, T., et al. (2019). First-in-human trial of blood-brain barrier opening in amyotrophic lateral sclerosis using MR-guided focused ultrasound. *Nat. Commun.* 10:4373.

Alecou, T., Giannakou, M., and Damianou, C. (2017). Amyloid beta plaque reduction with antibodies crossing the blood-brain barrier, which was opened in 3 sessions of focused ultrasound in a rabbit model. *J. Ultrasound Med.* 36, 2257–2270. doi: 10.1002/jum.14256

Alkins, R. D., Brodersen, P. M., Sodhi, R. N., and Hynynen, K. (2013). Enhancing drug delivery for boron neutron capture therapy of brain tumors with focused ultrasound. *Neuro. Oncol.* 15, 1225–1235. doi: 10.1093/neuonc/not052

Aryal, M., Fischer, K., Gentile, C., Gitto, S., Zhang, Y. Z., and Mcdannold, N. (2017). Effects on P-glycoprotein expression after blood-brain barrier disruption using focused ultrasound and microbubbles. *PLoS One* 12:e0166061. doi: 10.1371/journal.pone.0166061

Aryal, M., Vykhodtseva, N., Zhang, Y. Z., and Mcdannold, N. (2015). Multiple sessions of liposomal doxorubicin delivery via focused ultrasound mediated blood-brain barrier disruption: a safety study. *J. Control Release* 204, 60–69. doi: 10.1016/j.jconrel.2015.02.033

Banks, W. A. (2016). From blood-brain barrier to blood-brain interface: new opportunities for CNS drug delivery. *Nat. Rev. Drug Discov.* 15, 275–292. doi: 10.1038/nrd.2015.21

Baseri, B., Choi, J. J., Deffieux, T., Samiotaki, G., Tung, Y. S., Olumolade, O., et al. (2012). Activation of signaling pathways following localized delivery of systemically administered neurotrophic factors across the blood-brain barrier using focused ultrasound and microbubbles. *Phys. Med. Biol.* 57, N65–N81.

Basser, P. J., and Pierpaoli, C. (1996). Microstructural and physiological features of tissues elucidated by quantitative-diffusion-tensor MRI. *J. Magn Reson B* 111, 209–219. doi: 10.1006/jmrb.1996.0086

Budde, M. D., and Frank, J. A. (2010). Neurite beading is sufficient to decrease the apparent diffusion coefficient after ischemic stroke. *Proc. Natl. Acad. Sci. U.S.A.* 107, 14472–14477. doi: 10.1073/pnas.1004841107

Budde, M. D., Janes, L., Gold, E., Turtzo, L. C., and Frank, J. A. (2011). The contribution of gliosis to diffusion tensor anisotropy and tractography following traumatic brain injury: validation in the rat using Fourier analysis of stained tissue sections. *Brain* 134, 2248–2260. doi: 10.1093/brain/awr161

Burgess, A., Dubey, S., Yeung, S., Hough, O., Eterman, N., Aubert, I., et al. (2014). Alzheimer disease in a mouse model: MR imaging-guided focused ultrasound targeted to the hippocampus opens the blood-brain barrier and improves pathologic abnormalities and behavior. *Radiology* 273, 736–745. doi: 10.1148/radiol.14140245

Burgess, A., and Hynynen, K. (2014). Drug delivery across the blood-brain barrier using focused ultrasound. *Expert Opin. Drug Deliv.* 11, 711–721. doi: 10.1517/17425247.2014.897693

Chai, W. Y., Chu, P. C., Tsai, C. H., Lin, C. Y., Yang, H. W., Lai, H. Y., et al. (2018). Image-Guided focused-ultrasound CNS molecular delivery: an implementation via dynamic contrast-enhanced magnetic-resonance imaging. *Sci. Rep.* 8:4151.

Chai, W. Y., Chu, P. C., Tsai, M. Y., Lin, Y. C., Wang, J. J., Wei, K. C., et al. (2014). Magnetic-resonance imaging for kinetic analysis of permeability changes during focused ultrasound-induced blood-brain barrier opening and brain drug delivery. *J. Control Release* 192, 1–9. doi: 10.1016/j.jconrel.2014.06.023

Chan, K. W., Mcmahon, M. T., Kato, Y., Liu, G., Bulte, J. W., Bhujwalla, Z. M., et al. (2012). Natural D-glucose as a biodegradable MRI contrast agent for detecting cancer. *Magn Reson Med.* 68, 1764–1773. doi: 10.1002/mrm.24520

Deng, C. X. (2010). Targeted drug delivery across the blood-brain barrier using ultrasound technique. *Ther. Deliv.* 1, 819–848. doi: 10.4155/tde.10.66

Desmond, K. L., Moosvi, F., and Stanisz, G. J. (2014). Mapping of amide, amine, and aliphatic peaks in the CEST spectra of murine xenografts at 7 T. *Magn Reson Med.* 71, 1841–1853. doi: 10.1002/mrm.24822

Downs, M. E., Buch, A., Karakatsani, M. E., Konofagou, E. E., and Ferrera, V. P. (2015a). Blood-brain barrier opening in behaving non-human primates via focused ultrasound with systemically administered microbubbles. *Sci. Rep.* 5:15076.

Downs, M. E., Buch, A., Sierra, C., Karakatsani, M. E., Teichert, T., Chen, S., et al. (2015b). Long-term safety of repeated blood-brain barrier opening via focused ultrasound with microbubbles in non-human primates performing a cognitive task. *PLoS One* 10:e0125911. doi: 10.1371/journal.pone.0125911

Gabathuler, R. (2010). Approaches to transport therapeutic drugs across the blood-brain barrier to treat brain diseases. *Neurobiol. Dis.* 37, 48–57. doi: 10.1016/j.nbd.2009.07.028

Gan, H. K., Burgess, A. W., Clayton, A. H., and Scott, A. M. (2012). Targeting of a conformationally exposed, tumor-specific epitope of EGFR as a strategy for cancer therapy. *Cancer Res.* 72, 2924–2930. doi: 10.1158/0008-5472.can-11-3898

Gorick, C. M., Mathew, A. S., Garrison, W. J., Thim, E. A., Fisher, D. G., Copeland, C. A., et al. (2020). Sonoselective transfection of cerebral vasculature without blood-brain barrier disruption. *Proc. Natl. Acad. Sci. U.S.A.* 117, 5644–5654. doi: 10.1073/pnas.1914595117

Guivel-Scharen, V., Sinnwell, T., Wolff, S. D., and Balaban, R. S. (1998). Detection of proton chemical exchange between metabolites and water in biological tissues. *J. Magn. Reson* 133, 36–45. doi: 10.1006/jmre.1998.1440

Horodyckid, C., Canney, M., Vignot, A., Boisgard, R., Drier, A., Huberfeld, G., et al. (2017). Safe long-term repeated disruption of the blood-brain barrier using an implantable ultrasound device: a multiparametric study in a primate model. *J. Neurosurg.* 126, 1351–1361. doi: 10.3171/2016.3.jns151635

Hynynen, K., Mcdannold, N., Vykhodtseva, N., and Jolesz, F. A. (2001). Noninvasive MR imaging-guided focal opening of the blood-brain barrier in rabbits. *Radiology* 220, 640–646. doi: 10.1148/radiol.2202001804

Jones, R. M., Deng, L., Leung, K., Mcmahon, D., O'reilly, M. A., and Hynynen, K. (2018). Three-dimensional transcranial microbubble imaging for guiding volumetric ultrasound-mediated blood-brain barrier opening. *Theranostics* 8, 2909–2926. doi: 10.7150/thno.24911

Kobus, T., Vykhodtseva, N., Pilatou, M., Zhang, Y., and Mcdannold, N. (2016). Safety validation of repeated blood-brain barrier disruption using focused ultrasound. *Ultrasound Med. Biol.* 42, 481–492. doi: 10.1016/j.ultrasmedbio.2015.10.009

Kovacs, Z., Werner, B., Rassi, A., Sass, J. O., Martin-Fiori, E., and Bernasconi, M. (2014). Prolonged survival upon ultrasound-enhanced doxorubicin delivery in two syngenic glioblastoma mouse models. *J. Control Release* 187, 74–82. doi: 10.1016/j.jconrel.2014.05.033

Kovacs, Z. I., Burks, S. R., and Frank, J. A. (2017a). Reply to Silburt et al.: concerning sterile inflammation following focused ultrasound and microbubbles in the brain. *Proc. Natl. Acad. Sci. U.S.A.* 114, E6737–E6738.

Kovacs, Z. I., Burks, S. R., and Frank, J. A. (2018a). Focused ultrasound with microbubbles induces sterile inflammatory response proportional to the blood brain barrier opening: attention to experimental conditions. *Theranostics* 8, 2245–2248. doi: 10.7150/thno.24181

Kovacs, Z. I., Kim, S., Jikaria, N., Qureshi, F., Milo, B., Lewis, B. K., et al. (2017b). Disrupting the blood-brain barrier by focused ultrasound induces sterile inflammation. *Proc. Natl. Acad. Sci. U.S.A.* 114, E75–E84.

Kovacs, Z. I., Tu, T. W., Sundby, M., Qureshi, F., Lewis, B. K., Jikaria, N., et al. (2018b). MRI and histological evaluation of pulsed focused ultrasound and microbubbles treatment effects in the brain. *Theranostics* 8, 4837–4855. doi: 10.7150/thno.24512

Kroll, R. A., and Neuwelt, E. A. (1998). Outwitting the blood-brain barrier for therapeutic purposes: osmotic opening and other means. *Neurosurgery* 42, 1083–1099. doi: 10.1097/00006123-199805000-00082

Lipsman, N., Meng, Y., Bethune, A. J., Huang, Y., Lam, B., Masellis, M., et al. (2018). Blood-brain barrier opening in Alzheimer's disease using MR-guided focused ultrasound. *Nat. Commun.* 9:2336.

Marquet, F., Tung, Y. S., Teichert, T., Ferrera, V. P., and Konofagou, E. E. (2011). Noninvasive, transient and selective blood-brain barrier opening in non-human primates in vivo. *PLoS One* 6:e22598. doi: 10.1371/journal.pone.0022598

McDannold, N., Arvanitis, C. D., Vykhodtseva, N., and Livingstone, M. S. (2012). Temporary disruption of the blood-brain barrier by use of ultrasound and microbubbles: safety and efficacy evaluation in rhesus macaques. *Cancer Res.* 72, 3652–3663. doi: 10.1158/0008-5472.can-12-0128

McDannold, N., Vykhodtseva, N., and Hynynen, K. (2008). Effects of acoustic parameters and ultrasound contrast agent dose on focused-ultrasound induced blood-brain barrier disruption. *Ultrasound Med. Biol.* 34, 930–937. doi: 10.1016/j.ultrasmedbio.2007.11.009

McDannold, N., Zhang, Y., and Vykhodtseva, N. (2016). Nonthermal ablation in the rat brain using focused ultrasound and an ultrasound contrast agent: long-term effects. *J. Neurosurg.* 125, 1539–1548. doi: 10.3171/2015.10.jns151525

McDannold, N., Zhang, Y., and Vykhodtseva, N. (2017). The effects of oxygen on ultrasound-induced blood-brain barrier disruption in mice. *Ultrasound Med. Biol.* 43, 469–475. doi: 10.1016/j.ultrasmedbio.2016.09.019

McMahon, D., Bendayan, R., and Hynynen, K. (2017). Acute effects of focused ultrasound-induced increases in blood-brain barrier permeability on rat microvascular transcriptome. *Sci. Rep.* 7:45657.

McMahon, D., and Hynynen, K. (2017). Acute Inflammatory response following increased blood-brain barrier permeability induced by focused ultrasound is dependent on microbubble dose. *Theranostics* 7, 3989–4000. doi: 10.7150/thno.21630

McMahon, D., Oakden, W., and Hynynen, K. (2020). Investigating the effects of dexamethasone on blood-brain barrier permeability and inflammatory response following focused ultrasound and microbubble exposure. *Theranostics* 10, 1604–1618. doi: 10.7150/thno.40908

Meng, Y., Volpini, M., Black, S., Lozano, A. M., Hynynen, K., and Lipsman, N. (2017). Focused ultrasound as a novel strategy for Alzheimer disease therapeutics. *Ann. Neurol.* 81, 611–617. doi: 10.1002/ana.24933

Mooney, S. J., Shah, K., Yeung, S., Burgess, A., Aubert, I., and Hynynen, K. (2016). Focused ultrasound-induced neurogenesis requires an increase in blood-brain barrier permeability. *PLoS One* 11:e0159892. doi: 10.1371/journal.pone.0159892

Morse, S. V., Pouliopoulos, A. N., Chan, T. G., Copping, M. J., Lin, J., Long, N. J., et al. (2019). rapid short-pulse ultrasound delivers drugs uniformly across the murine blood-brain barrier with negligible disruption. *Radiology* 291, 459–466. doi: 10.1148/radiol.2019181625

Nance, E., Timbie, K., Miller, G. W., Song, J., Louttit, C., Klibanov, A. L., et al. (2014). Non-invasive delivery of stealth, brain-penetrating nanoparticles across the blood-brain barrier using MRI-guided focused ultrasound. *J. Control Release* 189, 123–132. doi: 10.1016/j.jconrel.2014.06.031

Neuwelt, E., Abbott, N. J., Abrey, L., Banks, W. A., Blakley, B., Davis, T., et al. (2008). Strategies to advance translational research into brain barriers. *Lancet Neurol.* 7, 84–96. doi: 10.1016/s1474-4422(07)70326-5

O'Reilly, M. A., Jones, R. M., Barrett, E., Schwab, A., Head, E., and Hynynen, K. (2017). Investigation of the safety of focused ultrasound-induced blood-brain barrier opening in a natural canine model of aging. *Theranostics* 7, 3573–3584. doi: 10.7150/thno.20621

Olumolade, O. O., Wang, S., Samiotaki, G., and Konofagou, E. E. (2016). Longitudinal motor and behavioral assessment of blood-brain barrier opening with transcranial focused ultrasound. *Ultrasound Med. Biol.* 42, 2270–2282. doi: 10.1016/j.ultrasmedbio.2016.05.004

Park, E. J., Zhang, Y. Z., Vykhodtseva, N., and Mcdannold, N. (2012). Ultrasound-mediated blood-brain/blood-tumor barrier disruption improves outcomes with trastuzumab in a breast cancer brain metastasis model. *J. Control Release* 163, 277–284. doi: 10.1016/j.jconrel.2012.09.007

Park, S. H., Kim, M. J., Jung, H. H., Chang, W. S., Choi, H. S., Rachmilevitch, I., et al. (2020). Safety and feasibility of multiple blood-brain barrier disruptions for the treatment of glioblastoma in patients undergoing standard adjuvant chemotherapy. *J. Neurosurg.* Online ahead of print.

Sheikov, N., Mcdannold, N., Sharma, S., and Hynynen, K. (2008). Effect of focused ultrasound applied with an ultrasound contrast agent on the tight junctional integrity of the brain microvascular endothelium. *Ultrasound Med. Biol.* 34, 1093–1104. doi: 10.1016/j.ultrasmedbio.2007.12.015

Sheikov, N., Mcdannold, N., Vykhodtseva, N., Jolesz, F., and Hynynen, K. (2004). Cellular mechanisms of the blood-brain barrier opening induced by ultrasound in presence of microbubbles. *Ultrasound Med. Biol.* 30, 979–989. doi: 10.1016/j.ultrasmedbio.2004.04.010

Silburt, J., Lipsman, N., and Aubert, I. (2017). Disrupting the blood-brain barrier with focused ultrasound: perspectives on inflammation and regeneration. *Proc. Natl. Acad. Sci. U.S.A.* 114, E6735–E6736

Stavarache, M. A., Petersen, N., Jurgens, E. M., Milstein, E. R., Rosenfeld, Z. B., Ballon, D. J., et al. (2018). Safe and stable noninvasive focal gene delivery to the mammalian brain following focused ultrasound. *J. Neurosurg.* 130, 989–998. doi: 10.3171/2017.8.jns17790

Treat, L. H., Mcdannold, N., Vykhodtseva, N., Zhang, Y., Tam, K., and Hynynen, K. (2007). Targeted delivery of doxorubicin to the rat brain at therapeutic levels using MRI-guided focused ultrasound. *Int. J. Cancer* 121, 901–907. doi: 10.1002/ijc.22732

Treat, L. H., Mcdannold, N., Zhang, Y., Vykhodtseva, N., and Hynynen, K. (2012). Improved anti-tumor effect of liposomal doxorubicin after targeted blood-brain barrier disruption by MRI-guided focused ultrasound in rat glioma. *Ultrasound Med. Biol.* 38, 1716–1725. doi: 10.1016/j.ultrasmedbio.2012.04.015

Tu, T. W., Ibrahim, W. G., Jikaria, N., Munasinghe, J. P., Witko, J. A., Hammoud, D. A., et al. (2018). On the detection of cerebral metabolic depression in experimental traumatic brain injury using Chemical Exchange Saturation Transfer (CEST)-weighted MRI. *Sci. Rep.* 8:669.

Tu, T. W., Turtzo, L. C., Williams, R. A., Lescher, J. D., Dean, D. D., and Frank, J. A. (2014). Imaging of spontaneous ventriculomegaly and vascular malformations in Wistar rats: implications for preclinical research. *J. Neuropathol. Exp. Neurol.* 73, 1152–1165. doi: 10.1097/nen.0000000000000140

Tu, T. W., Williams, R. A., Lescher, J. D., Jikaria, N., Turtzo, L. C., and Frank, J. A. (2016). Radiological-pathological correlation of diffusion tensor and magnetization transfer imaging in a closed head traumatic brain injury model. *Ann. Neurol.* 79, 907–920. doi: 10.1002/ana.24641

Van Zijl, P. C., Jones, C. K., Ren, J., Malloy, C. R., and Sherry, A. D. (2007). MRI detection of glycogen in vivo by using chemical exchange saturation transfer imaging (glycoCEST). *Proc. Natl. Acad. Sci. U.S.A.* 104, 4359–4364. doi: 10.1073/pnas.0700281104

Van Zijl, P. C., and Yadav, N. N. (2011). Chemical exchange saturation transfer (CEST): what is in a name and what isn't? *Magn. Reson. Med.* 65, 927–948. doi: 10.1002/mrm.22761

Ward, K. M., Aletras, A. H., and Balaban, R. S. (2000). A new class of contrast agents for MRI based on proton chemical exchange dependent saturation transfer (CEST). *J. Magn. Reson* 143, 79–87. doi: 10.1006/jmre.1999.1956

Wu, S. K., Chu, P. C., Chai, W. Y., Kang, S. T., Tsai, C. H., Fan, C. H., et al. (2017). Characterization of Different microbubbles in assisting focused ultrasound-induced blood-brain barrier opening. *Sci. Rep.* 7:46689.

Yang, F. Y., Chang, W. Y., Chen, J. C., Lee, L. C., and Hung, Y. S. (2014). Quantitative assessment of cerebral glucose metabolic rates after blood-brain barrier disruption induced by focused ultrasound using FDG-MicroPET. *Neuroimage* 90, 93–98. doi: 10.1016/j.neuroimage.2013.12.033

Yang, F. Y., Liu, S. H., Ho, F. M., and Chang, C. H. (2009). Effect of ultrasound contrast agent dose on the duration of focused-ultrasound-induced blood-brain barrier disruption. *J. Acoust. Soc. Am.* 126, 3344–3349. doi: 10.1121/1.3242376

Yu, S., Tooyama, I., Ding, W. G., Kitasato, H., and Kimura, H. (1995). Immunohistochemical localization of glucose transporters (GLUT1 and GLUT3) in the rat hypothalamus. *Obes. Res.* 3(Suppl. 5), 753S–776S.

Zhou, I. Y., Wang, E., Cheung, J. S., Zhang, X., Fulci, G., and Sun, P. Z. (2017). Quantitative chemical exchange saturation transfer (CEST) MRI of glioma using image downsampling expedited adaptive least-squares (IDEAL) fitting. *Sci. Rep.* 7:84.

Conflict of Interest: The authors declare that the research was conducted in the absence of any commercial or financial relationships that could be construed as a potential conflict of interest.

frontiers
in Neuroscience

SYSTEMATIC REVIEW
published: 31 August 2020
doi: 10.3389/fnins.2020.00734

Diffusion Tensor Imaging-Based Studies at the Group-Level Applied to Animal Models of Neurodegenerative Diseases

Hans-Peter Müller[1]*, **Francesco Roselli**[1,2], **Volker Rasche**[3] **and Jan Kassubek**[1]

[1] Department of Neurology, University of Ulm, Ulm, Germany, [2] German Center for Neurodegenerative Diseases (DZNE), Ulm, Germany, [3] Core Facility Small Animal MRI, University of Ulm, Ulm, Germany

OPEN ACCESS

Edited by:
Yu-Chien Wu,
Indiana University Bloomington,
United States

Reviewed by:
Matthew D. Budde,
Medical College of Wisconsin,
United States
Matthew ManHin Cheung,
CUHK Medical Centre, Hong Kong
Nian Wang,
Duke University, United States

***Correspondence:**
Hans-Peter Müller
hans-peter.mueller@uni-ulm.de

Specialty section:
This article was submitted to
Brain Imaging Methods,
a section of the journal
Frontiers in Neuroscience

Received: 17 April 2020
Accepted: 22 June 2020
Published: 31 August 2020

Citation:
Müller H-P, Roselli F, Rasche V and Kassubek J (2020) Diffusion Tensor Imaging-Based Studies at the Group-Level Applied to Animal Models of Neurodegenerative Diseases. Front. Neurosci. 14:734.
doi: 10.3389/fnins.2020.00734

The understanding of human and non-human microstructural brain alterations in the course of neurodegenerative diseases has substantially improved by the non-invasive magnetic resonance imaging (MRI) technique of diffusion tensor imaging (DTI). Animal models (including disease or knockout models) allow for a variety of experimental manipulations, which are not applicable to humans. Thus, the DTI approach provides a promising tool for cross-species cross-sectional and longitudinal investigations of the neurobiological targets and mechanisms of neurodegeneration. This overview with a systematic review focuses on the principles of DTI analysis as used in studies at the group level in living preclinical models of neurodegeneration. The translational aspect from *in-vivo* animal models toward (clinical) applications in humans is covered as well as the DTI-based research of the non-human brains' microstructure, the methodological aspects in data processing and analysis, and data interpretation at different abstraction levels. The aim of integrating DTI in multiparametric or multimodal imaging protocols will allow the interrogation of DTI data in terms of directional flow of information and may identify the microstructural underpinnings of neurodegeneration-related patterns.

Keywords: DTI, magnetic resonance imaging, translational, *in vivo* animal model, neurodegeneration, group studies

INTRODUCTION

In this systematic review, principles of diffusion tensor imaging (DTI) analysis at the group level with the special focus on applications to animal models of neurodegeneration are summarized. Methodological aspects are addressed covering experimental design and DTI data acquisition as well as data analysis at the group level. The emphasis will be on the concept of translational imaging from *in-vivo* animal models of neurodegeneration to (clinical) applications in humans that may sometime form the basics for novel therapeutic approaches. The continuous and compulsive research is addressed in studying the patterns underlying cellular and molecular relations in living animals since there are at present no sufficient *in-vitro* or *in-silico* models that can serve as alternatives to the use of *in-vivo* animal models (Bennett and Ringach, 2016). Thus, insights into the spectrum of DTI-based neuroimaging data analysis is provided and interpretations at different abstraction levels in that context are summarized.

Neuroimaging of Neurodegenerative Diseases in Humans and Preclinical Models

Structural and microstructural neuroimaging findings especially by magnetic resonance imaging (MRI) have improved the longstanding notions regarding the pathophysiology of neurodegenerative diseases (Frisoni et al., 2010; Chiò et al., 2014; Politis, 2014; Blamire, 2018). The cellular mechanisms underlying the stereotypical progression of pathology in specific neurodegenerative diseases are not completely understood; however, there is increasing indication that misfolded protein aggregates can spread by a self-perpetuating neuron-to-neuron transmission (Braak et al., 2013; Jucker and Walker, 2013, 2018; Goveas et al., 2015). Neuroimaging techniques can identify specific lesion patterns and explain how these disorders spread across brain networks (Agosta et al., 2015). However, most neuroimaging studies have drawbacks, such as limited sample sizes in orphan diseases or insufficient clinical characterization of patients, absence of adequate controls, and scarcity of longitudinal assessments.

This review concentrates on DTI, as a subtechnique of diffusion-weighted imaging, in the application to animal models of neurodegenerative diseases. A special focus are animal models of dementia like Alzheimer's disease (AD), motor neuron disorders such as amyotrophic lateral sclerosis (ALS), and Parkinson's disease (PD), although the neuropathological disease-spreading concept in humans in predefined patterns related to the forming of pathogenic assemblies of disease-specific proteins ("prion-like paradigm") could not be demonstrated in an animal model yet.

Animal models of adult-onset neurodegenerative diseases have helped to understand the molecular pathogenesis of these diseases. Despite all limitations, the understanding of these disorders and the improvement of mechanistically designed therapeutics can still profit from these animal models and from the generation of animal models that more exactly recapitulate human disease (Dawson et al., 2018). However, the characterization of any new model is crucial and remains a bottleneck; efforts have to be performed to comprehensively catalog the phenotypes associated with each model, including studies such as *in-vivo* imaging (Dawson et al., 2018).

DTI Mapping of White Matter

White matter tracts of the central nervous system consist mainly of densely packed axons and various types of neuroglia. The axonal membrane and myelin layers are the predominant biological features that restrict the water diffusion perpendicular to the fiber orientation. This, leads to an anisotropic water diffusion in brain white matter. Additionally, myelin sheaths around the axons contribute to the anisotropy of diffusion for intra- as well as for extracellular water (Mori and van Zijl, 2002; Garin-Muga and Borro, 2014).

The quantitative description of this anisotropy is measured by DTI, imaging the local microstructural characteristics of water diffusion. The signal intensity in each recording voxel is attenuated depending on the amplitude and the direction of the diffusion-encoding gradients as well as on the local microstructure in which the water molecules diffuse (Basser et al., 1994). In the presence of anisotropy in white matter, diffusion properties can be described in first approximation by a tensor (Mattiello et al., 1994). The anisotropy of the diffusion processes is related to the presence and orientation of fiber tracts in white matter and is therefore influenced by its micro- and macrostructural features. On a macroscopic scale, the intra-voxel coherence in the orientation of all white matter tracts in an imaging voxel influences its degree of anisotropy, whereas the microstructural features, mainly the intraaxonal organization besides the density of fiber and cell packing, degree of myelination, and individual fiber diameter, influence diffusion anisotropy (Pierpaoli and Basser, 1996; Duan et al., 2015).

In DTI recordings of the human brain, the voxel dimensions are in the order of millimeters. Thus, a voxel always contains the averaged information of diffusion covering a high number of axons as well as the surrounding water molecules. In spite of this multidirectional environment, DTI recordings are sensitive to the orientation of the largest principal axis, which aligns to the predominant axonal direction, that is, the axonal contribution dominates the recorded signal (Mori and van Zijl, 2002; Brandstack et al., 2016).

DTI techniques provide basically several types of information about the property of water diffusion: first, the orientation-independent extent of diffusion anisotropy (Pierpaoli and Basser, 1996) and second, the predominant direction of water diffusion in image voxels, that is, the diffusion orientation (Pajevic and Pierpaoli, 1999; Marrale et al., 2016). The diffusion tensor model allows for the calculation of multiple parameters; out of these, the fractional anisotropy (FA) is the most commonly used parameter to measure directional dependence of water diffusion that way parameterizing the shape of the tensor and providing a normalized value to the degree of anisotropy (Sampaio-Baptista and Johansen-Berg, 2017).

DTI in the Animal Brain—Translational Imaging

DTI has become an important tool to study the anatomy of animal brains *in vivo*, for example, the mouse brain (Aggarwal et al., 2010; Harsan et al., 2010; Nouls et al., 2018), the rat brain (Gyengesi et al., 2014; Figini et al., 2015), the canine brain (Wu et al., 2011), or the primate brain (Feng et al., 2017; Risser et al., 2019). The non-invasive nature of MRI/DTI enables longitudinal studies of transgenic disease models (Haber et al., 2017; Petrella et al., 2018). Ultra-high fields at 11.7 T (Müller et al., 2012a) or 16.4 T (Brennan et al., 2013) and dedicated resonators [cryogenic cooled resonator (CCR)] allow the recording of high-resolution DTI datasets with in-plane resolutions down to $100 \times 100\,\mu$m for mouse models (or small rodents) with an axial slice thickness down to 200 μm (Müller et al., 2012a), while the development of fast DTI protocols has led to reduced acquisition times until about 30 min, enabling the logistics for the monitoring of larger cohorts (Müller et al., 2013).

In DTI, the diffusion in each voxel is assumed to be represented by a single tensor. In human brain imaging, where

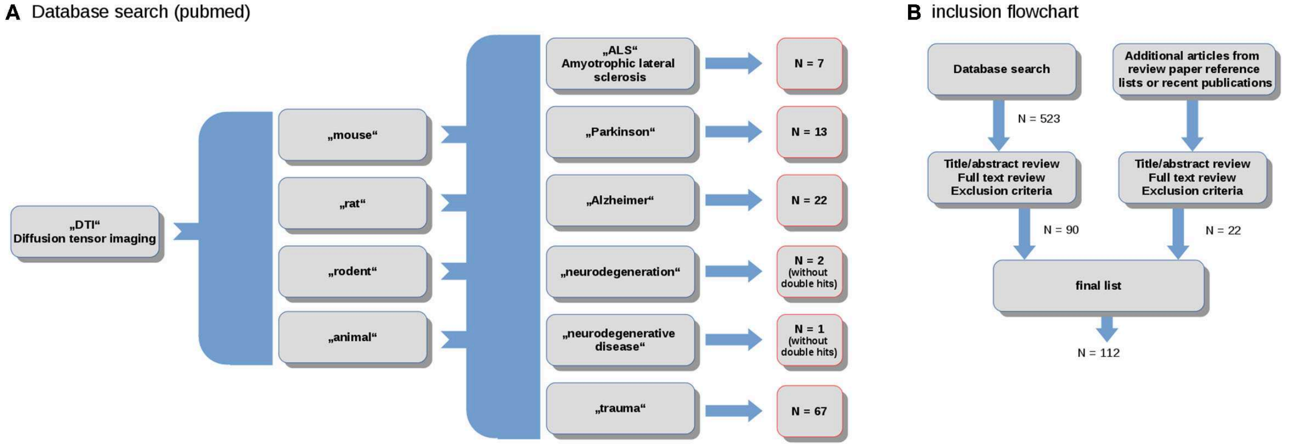

FIGURE 1 | (A) Selection diagram depicting the number of studies included for the spectrum of studied neurodegenerative diseases; and **(B)** PRISMA flowchart.

typical voxel sizes can be easily as high as $2 \times 2 \times 2$ mm^3, this assumption fails in regions where multiple fiber bundles of various spatial orientations may be packed together in a single voxel ("crossing fibers"). In the same line, DTI does not account for multiple tissue types within a voxel, and a number of different white matter microstructural features (including the cellular membranes of glial cells and the axon diameter and density) contribute to the obtained DTI indices (Sampaio-Baptista et al., 2019). The ratio of the microstructural feature size to voxel size is improved in small animal imaging where voxel sizes for mice and small rodents, typically in the order of $100 \times 100 \times 200$ µm^3 *in vivo* and even much higher spatial resolution up to isotropic some 10 µm *ex vivo*, are much closer to the fiber bundle diameters (Aggarwal et al., 2010; Kumar et al., 2014).

METHODS

Search Strategy and Study Selection

The literature review and study inclusion process were conducted in accordance with the PRISMA guidelines (Panic et al., 2013). In a systematic search conducted in April 2020, data were collected from the online library PubMed (https://www.ncbi.nlm.nih.gov/pubmed/). The search keywords were the combination of the terms ("DTI") and ("mouse," "rat," "rodent," "animal") and ("ALS," "Parkinson," "Alzheimer," "neurodegeneration," "neurodegenerative disease," "trauma"). In total, this search yielded more than 500 results. These studies were probed for original research and English language in peer-reviewed journals. Studies with models that do not refer to neurodegenerative diseases were excluded. The references were studied for further candidates. In total, 114 studies were included in the systematic review (**Figure 1**).

DTI Data Acquisition: Scanners and Coils

The major challenges in *in-vivo* DTI is the long acquisition time required to acquire the multi-directional diffusion data with sufficient signal-to-noise ratio (SNR) at the required spatial resolution. While scanning time for *ex-vivo* studies is in principle without direct limitation, *in-vivo* experiments require careful consideration of animal welfare. Since animals are usually anesthetized, longer scan times than in human application are possible, and adult animals can in principle be scanned for several hours, yielding high spatial resolution and sufficient SNR for subsequent DTI analysis with species-optimized MR scanning protocols and even systems (Oguz et al., 2012; Rumple et al., 2013; Zhang et al., 2013). Prolonged scan times might rise concerns regarding motion artifacts (Oguz et al., 2014; Zhang X. et al., 2016) despite the use of dedicated holders additionally to the general anesthesia (Herrmann et al., 2012; Müller et al., 2013; Zhang et al., 2015); however, drift or misalignment can readily be corrected during post-processing. Further, reduction of scan times is of general interest to enable large cohort studies.

Where non-human primate and rat studies have even been performed on clinical systems (Mayer et al., 2007; Zhang et al., 2013; Zhang R. Z. et al., 2016), recent advances in high-field MR imaging offer improved SNR and resolution. Especially for rodent imaging, typically specialized coils and high-field scanners (up to 17.6 T) are applied. DTI studies of the rodent brain have been reported using dedicated small animal systems from 4.7 T up to 17.6 T (Nair et al., 2005; Duong, 2010; Harsan et al., 2010; Lodygensky et al., 2010; Gatto et al., 2018a). For further improvement of SNR, the use of dedicated application-specific receive coils ranging from simple single-loop surface coils to complex phase array and micro-imaging coils (Zhao et al., 2008) has been introduced. In the field of rodent imaging, most promising are CCRs, which have demonstrated significant increase of the effective SNR (Ratering et al., 2008) at 9.4 T and are supposed to provide an SNR gain of at least a factor of 2 at 11.7 T systems (**Figure 2**). In mice, the use of CCR at 11.7 T has enabled the reduction of the DTI acquisition times to ∼30 min, which is considered feasible for cohort studies (Müller et al., 2012a).

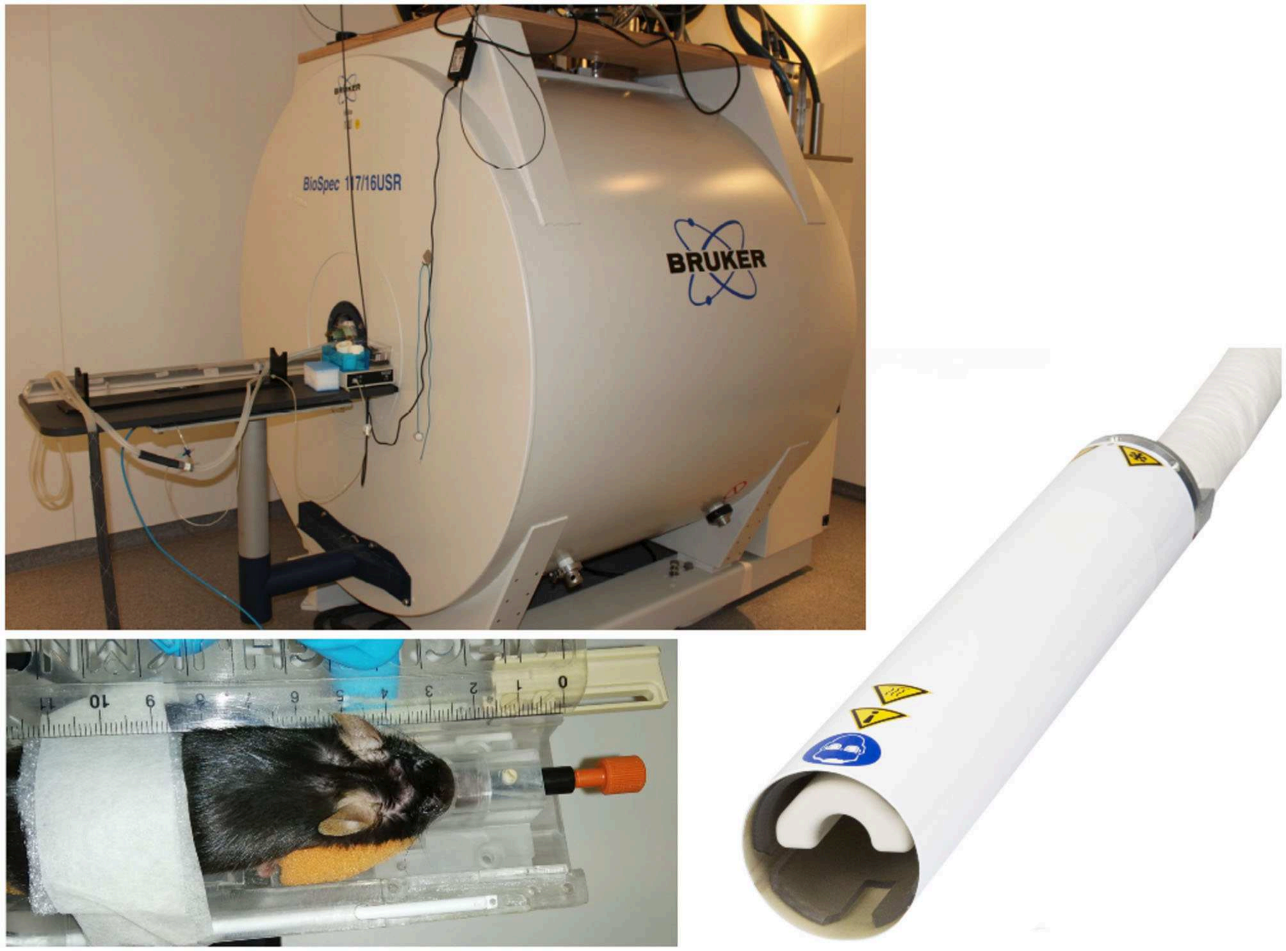

FIGURE 2 | Typical equipment for scanning of mouse cohorts. 11.7 T tomograph (Biospec 117/16, Bruker, Ettlingen, Germany), two-element transmit/receive ^{1}H mouse cryogenic surface coil (Cryo-Probe, Bruker BioSpin); the animals are placed in a stereotaxic head support (Bruker Biospin, Ettlingen, Germany) to immobilize the head. Data acquisition is performed under isoflurane anesthesia.

DTI Data Acquisition: Pulse Sequences

DTI relies on fast diffusion encoding imaging sequences. Although advanced acquisition techniques including spiral (Frank et al., 2010) and gradient and spin echo GRASE (Aggarwal et al., 2010) imaging techniques have been introduced to *in-vivo* DTI, independent of the field strength and animal model, most reported studies still rely on conventional single-shot or segmented echo planar imaging. Ideally, isotropic 3D imaging techniques are used to provide high-fidelity DTI data. However, with acquisition times in the several hour range (Cai et al., 2011; Wu et al., 2013), application to cohort studies is limited and conventional 2D multi-slice techniques are still broadly used. As the current standard for murine cohort studies (and other rodents), multi-slice echo planar imaging acquisitions with echo times between 50 and 100 ms and repetition times between 6,000 and 15,000 ms are frequently used. Spatial in-plane resolution and slice thickness is adapted to the size of the animal model with in-plane spatial resolution ranging from $100 \times 100\ \mu\text{m}^2$ (mice) to $650 \times 650\ \mu\text{m}^2$ (chimpanzee). For volume of interest coverage, typically 50–100 axial slices with 200 μm (mice) to 1,000 μm (chimpanzee) slice thickness are acquired. To ensure sufficient diffusion tensor fidelity, diffusion weighted (typically $b = 1{,}000$ s/mm²) images are acquired with 30 and more different encoding (gradient) directions plus one to five unweighted ($b = 0$ s/mm²) images. There is no general rule for the optimum sampling scheme in DTI; the performance of sampling schemes that use low numbers of sampling orientations and less efficient schemes with larger numbers of sampling orientations and the scenarios in which each type of scheme should be used (Jones, 2004) are still under discussion. Scanning times for sufficient spatial resolution, SNR, and DTI quality have been reported in the hour range. Even though still limited by SNR constraints, parallel imaging and compressed sensing techniques (Shi et al., 2015) have been introduced to further reduce scan times and high spatial resolution DTI in mice was shown to be feasible within 30-min scan times (Müller et al., 2012a), thus enabling application to large cohort studies.

Atlases

Animal MRI/DTI analysis requires atlases in analogy to the standardized coordinate frames for humans such as the Montreal Neurological Institute atlas (Brett et al., 2002). High-resolution images are used for the identification of rodent brain regions by human experts to delineate regions of interest (ROI) or tracts of interest (TOI). Prominently used atlases are summarized in the following (Oguz et al., 2012).

Mouse atlases:

- Waxholm atlas (Jiang and Johnson, 2009) includes four adult male C57 mice and includes T1, T2, T2*, and DTI images at high resolution.
- Developmental Mouse Atlas (Zhang et al., 2003; Aggarwal et al., 2009; Chuang et al., 2011) is a series of atlases of developing mouse embryos, including FA, T2w, and tensor maps collected from mouse fetuses at embryonic days.
- The mouse brain in stereotaxic coordinates (Paxinos and Franklin, 2007) providing both accurate stereotaxic coordinates for laboratory use, and detailed delineations and indexing of structures for reference.
- The online Allen Reference Brain Atlas (available at https://mouse.brain-map.org/static/atlas) including sagittal and coronal implementation of the Allen Mouse Common Coordinate Framework.

Rat atlases:

- A DTI-based atlas of the rat brain (Rumple et al., 2013)
- The rat brain in stereotaxic coordinates (Paxinos and Watson, 2013), providing both accurate stereotaxic coordinates for laboratory use, detailed delineations, and indexing of structures for reference.

Primate atlases:

- A digital 3D atlas of the marmoset brain based on multi-modal MRI (Liu C. et al., 2018).
- The marmoset brain in stereotaxic coordinates (Palazzi and Bordier, 2008).

Data Processing

For DTI analysis many automated and manual tools are available. With respect to the large amount of data that are recorded during a DTI experiment, only tools should be considered that are necessary to address the endpoints of the specific study, that way maintaining statistical power and reducing analysis time. Regardless of the tools selected, there are typically a number of steps necessary to acquire data from DTI images (Oguz et al., 2012).

In analogy to human DTI analysis, some preprocessing steps are necessary on DTI data (Liu et al., 2010). These include eddy current corrections, rigid registration of individual diffusion weighted images to the baseline image to minimize motion effects, correction of intensity inhomogeneities, quality control, and elimination of possible corrupted gradient directions (Müller et al., 2012a; Oguz et al., 2012) as well as the stereotaxic normalization to a brain atlas coordinate frame (cf. 2.3).

As an example for the data analysis cascade, data processing is described as performed with the *Tensor Imaging and Fiber Tracking* software package, which has been successfully applied both to human DTI group studies in neurodegenerative diseases (Kassubek and Müller, 2016) and to data of preclinical models of neurodegeneration (Müller et al., 2012a). Thus, with a rescaling, the same software analysis cascade can be applied to analysis of human and murine DTI data, that way consolidating the translational aspect both "from man to preclinical model" and vice versa "from preclinical model to man" (**Figure 3**). For animal as well as for human DTI studies, a slice thickness to in-plane resolution ratio between 1.0 and 1.5 is considered to be a good choice. For animal studies, the recorded brain grid could be adjusted to be in the same order as in human DTI studies, since the transformation to an iso-grid of 50 μm for mice (and corresponding values for other animals) corresponds to an iso-grid of 1 mm in human studies. After transformation of the recorded data into an iso-grid by nearest neighbor interpolation, spatial normalization to a stereotaxic standard space is performed using study-specific b0- and FA-templates (Müller et al., 2012a). Optimum normalization is obtained by an iterative process using scanner- and sequence specific b0- and FA-templates according to landmarks of a stereotaxic animal atlas (see section DTI Data Acquisition: Pulse Sequences).

DTI metrics maps (FA, axial diffusivity—AxD, radial diffusivity—RD, mean diffusivity—MD) are calculated from these stereotaxically normalized data sets and are in a following step smoothed with a Gaussian filter with a size of about two to three times the recording voxel size, that way providing a good balance between sensitivity and specificity. The axonal damage and myelin degradation is mirrored by DTI metrics; differences at the group level to assess microstructural alterations by statistical analysis of DTI metrics can be performed by various approaches (Müller and Kassubek, 2018): (1) unbiased voxelwise comparison by whole brain-based spatial statistics (WBSS) (Müller et al., 2012b) or tractwise comparison by tract-based spatial statistics (TBSS) (Smith et al., 2006) or (2) hypothesis-guided tract-based quantification by analyzing DTI metrics in tract systems by TOI-based tractwise FA statistics (TFAS) (Müller et al., 2007) (**Figure 4**).

Whole-Brain-Based Spatial Statistics

Unbiased voxelwise comparison of cohort brains can be performed for cross-sectional comparisons of mutant animals vs. *wt* animals at baseline or at follow-up, using WBSS (Müller et al., 2012a). Statistical comparisons of DTI metrics maps for mutant vs. *wt* are performed voxelwise by means of statistical testing [a good choice is an FA threshold of 0.2 (Kunimatsu et al., 2004) to concentrate the analysis on white matter], followed by correction for multiple comparisons (e.g., with the false-discovery-rate algorithm at $p < 0.05$ Genovese et al., 2002) and further reduction of the alpha error by a spatial correction algorithms in the size range of the smoothing kernel, leading to a minimum size of alteration clusters.

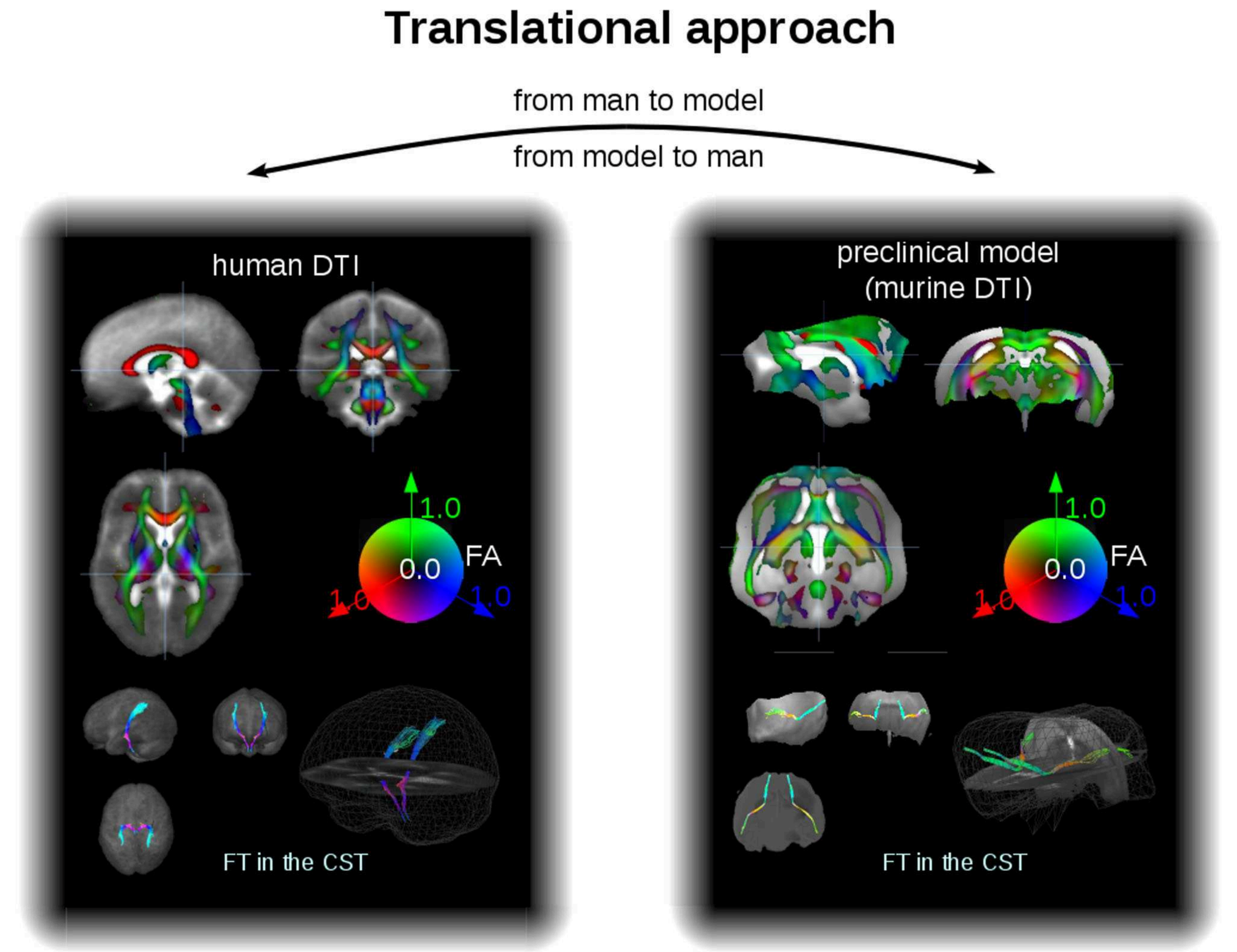

FIGURE 3 | Translational approach. In a different scale, DTI data of man and mice can be analyzed within the same software environment, that is, with the same analysis cascade. Examples for FA maps in coronar, sagittal, and axial orientation (upper panel) and projectional views of FT examples (lower panel) for human (left) and murine (right) group averaged data sets. The cerebellum of the mouse brains has been masked out. CST, corticospinal tracts.

Voxelwise comparison (e.g., by WBSS) of longitudinal DTI map differences could be performed by calculating voxelwise differences between DM maps of baseline and follow-up scans for mutant animals and *wt* animals; differences have then to be linearly normalized to an identical time-interval prior to statistical comparison. In analogy to cross-sectional WBSS, statistical comparisons of longitudinal DTI map differences are performed voxelwise by means of statistical testing, and results have to be corrected for multiple comparisons and also by clustering.

Whole-Brain Connectivity Analysis

A connectome refers to a comprehensive description of neuronal connections, for example, the wiring diagram of the entire brain. Given the enormous range of connectivity in the mammalian brain, such descriptions on a macro- or mesoscale range (Oh et al., 2014) can be inferred from imaging white matter fiber tracts through DTI in the living brain (Nouls et al., 2018). DTI-based connectomics have already been applied to mouse models of genetic risk factors for late onset AD for identifying vulnerable brain networks (Badea et al., 2019). Whole mouse brain structural connectomics (Shibata et al., 2015; Allan Johnson et al., 2019) have already been verified by neuron tracing data (Chen et al., 2015; Sinke et al., 2018; Wang et al., 2018).

Region-of-Interest Analyses

A hypothesis-guided approach is performed when using ROIs that are placed in defined anatomical regions and comparing the average DTI metrics values, that is, rotational invariant parameters of the diffusion tensor, within the respective ROI for the cohorts (e.g., Harsan et al., 2010; Müller et al., 2019) for quantitative comparisons of in-between ROIs or to show differences between various white matter regions. ROI analysis could be extensively performed by placing an arbitrary

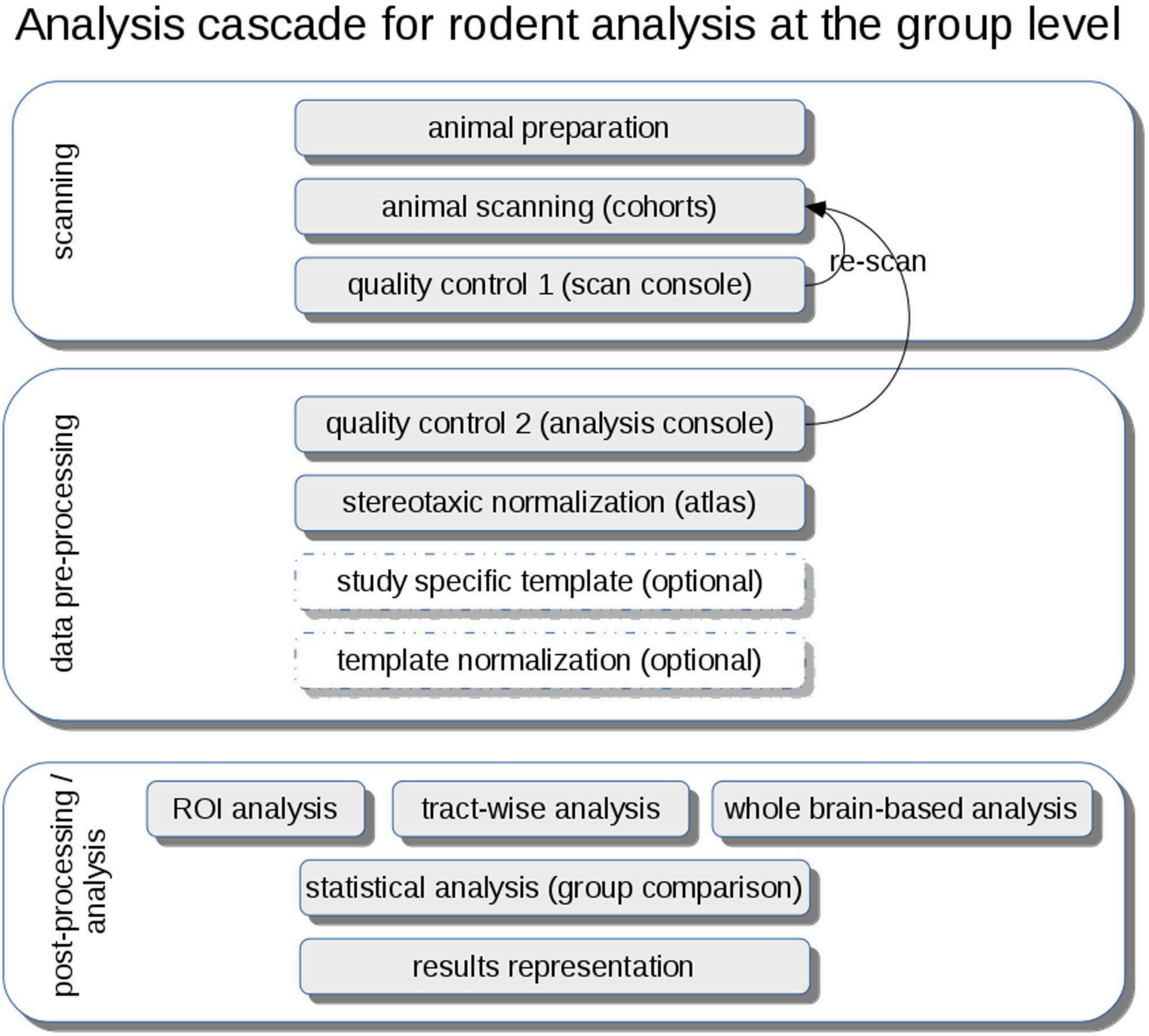

FIGURE 4 | Analysis cascade for rodent analysis at the group level. After animal preparation and scanning, quality control could be performed first at the scan console and second during the pre-processing at the analysis console with the option of re-scanning of low-quality data sets. A stereotaxic normalization to atlas coordinates can be refined by the creation of study-specific templates and a subsequent template normalization. Analysis at the group level can be performed by hypothesis-guided ROI analysis or tractwise analysis or by unbiased whole brain-based analysis, each followed by a statistical analysis extracting and representing significant results using a pre-defined significance level.

number of ROIs (e.g., Irie et al., 2018) with variable extension. The advantage of ROI analysis is that (in case of accurate anatomical placement) it can also be performed without any prior stereotaxical normalization; in this case, manual ROI identification can be supported by confocal microscopic image (Irie et al., 2018).

Tract-Based Analysis

In order to identify fiber structures in an atlas-based coordinate frame, different technical approaches can be applied. One technique is TBSS (Smith et al., 2006), a fully automated method to perform whole-brain tract DTI analyses by calculating a skeleton of fibers by projection onto an alignment-invariant tract representation. TBSS has been shown to be applicable not only to human DTI studies, but also to different animal models (Sierra et al., 2011). An additional more tract specific technique is the TOI-based approach for which an averaged data set is created from all contributing data sets after normalization to a common coordinate frame preserving all tensor-related information (Alexander et al., 2001; Field et al., 2005). Then, fiber tracking (FT) techniques could be applied, e.g., deterministic streamline tracking in order to obtain defined tract structures. These tract structures are used in order to obtain a quantitative access to the tractography results (TFAS—Müller et al., 2007) by comparing the average DTI metrics values within the respective TOI for the cohorts. This TOI analysis approach can be used for a hypothesis-guided analysis of FT bundles.

Advantages and Drawbacks of the Different Analysis Techniques

Unbiased comparison of cohort brains can be performed by WBSS or connectome/whole brain connectivity analysis either cross-sectionally or longitudinally. The drawback of these approaches is that they are less specific, and one has to deal with statistical correction algorithms, such as corrections for multiple comparisons and spatial cluster corrections. WBSS requires no fiber tracking algorithms, thus is not depending on all the accuracy challenges, which FT/connectome analysis has to deal with.

Hypothesis-guided techniques, that is, ROI analysis or tract-based analysis, have the advantage to specifically focus on certain brain regions also at the individual level with or without any prior stereotaxical normalization. However, the comparison of the results to reference regions is mandatory to obtain an impression about the validity of the results.

In general, FT-based techniques have the advantage to analyze also long-range structural connections, whereas ROI techniques are restricted to certain brain areas. However, as FT techniques are much more sophisticated and probably contain a higher sensitivity to widespread brain alterations, the possibility of misinterpretation and unspecific erroneous results is increased.

APPLICATIONS TO MODELS OF NEURODEGENERATIVE DISEASES

Methodological DTI Studies in Cohorts of Preclinical Models in General

DTI in mouse cohorts has successfully been applied to image microstructure organization with a resolution down to 50 μm (Aggarwal et al., 2010; Guilfoyle et al., 2011). The analyses have been performed by ROI analysis or fiber tracking techniques (Harsan et al., 2010; Müller et al., 2012a). As one example, the translational role of DTI in developmental pathologies has been extensively described (Oguz et al., 2012). Special focus has been put on the identification of rodent olfactory bulb structures with micro-DTI (Zhao et al., 2008) or DTI tractography analysis of infralimbic and prelimbic connectivity using high-throughput MRI (Gutman et al., 2012). In the following chapters, a summary for AD, PD, and ALS is provided; single studies are concerned with, for example, a risk-related biomarker in animal model of glaucoma (Hayashi et al., 2013) or neurodegeneration in Niemann-Pick type C mice (Totenhagen et al., 2012). A comprehensive review of DTI in preclinical studies of Huntington's disease has recently been published by Gatto and Weissmann (2019) so that Huntington's disease was not included in our review.

Cohort DTI Studies in Animal Models of Amyotrophic Lateral Sclerosis (ALS)

Cohort DTI studies have been performed for the SOD1 mouse model of ALS for the spinal cord (Kim et al., 2011; Underwood et al., 2011; Marcuzzo et al., 2017), detecting longitudinal white matter degeneration alongside histology and electron microscopy. DTI of ALS brains of SOD1-mice at 9.4 T and 16.7 T, respectively, have shown a presymptomatic decrease in axonal organization by FA and neurite content by Intracellular Volume Fraction across the spinal cord, corpus callosum, hippocampus, and cortex; the combination of DTI, neurite orientation dispersion, and density imaging (NODDI), and diffusion kurtosis imaging (DKI) (Marrale et al., 2016) models have proved to provide an assessment of the early microstructural changes in the ALS brain (Gatto et al., 2018b,c, 2019). Longitudinal DTI in the *TDP-43*^{G298S} ALS mouse model at the cohort level revealed cortical and callosal microstructure alterations (Müller et al., 2019); in this study, longitudinal DTI scans at 11.7 T of baseline and follow-up scans with an interval of several months were investigated by voxelwise comparison as well as by tractwise analysis, while histological investigations complemented the *in-vivo* results.

Cohort DTI Studies in Animal Models of Alzheimer's Disease (AD)

Seminal work on the application of DTI to AD mouse models has been obtained for the first time more than 15 years ago (Sun et al., 2005; Shepherd et al., 2006), with the identification of age-dependent white matter disturbances in mice overexpressing beta-amyloid precursor protein (APP) under control of the platelet-derived growth factor promoter (PDAPP mice) (Song et al., 2004). This work was followed up by a detailed cohort study of APPsw transgenic mouse (Tg2576), which revealed abnormal DTI metrics related to axonal damage (both in gray and white matter) in mice of 12 months of age (or older) and abnormal DTI metrics related to myelin damage at 16 and 18 months of age (Song et al., 2005). However, these findings were not confirmed in *ex-vivo* DTI measurements, which revealed no loss in white matter integrity (Harms et al., 2006), raising questions about the source of the signal actually lost upon formalin fixation. More recently, DTI abnormalities have been confirmed in multiple white matter tracts as well as in the hippocampus in different mouse models for AD (Kerbler et al., 2013; Snow et al., 2017) and imaged *in vivo* at different field strengths, for example, 7 T (Whittaker et al., 2018) or 11.7 T (Zerbi et al., 2013). Further investigation of the APP model has confirmed abnormalities in DTI metrics both in gray and in white matter (Bitner et al., 2012; Qin et al., 2013; Shu et al., 2013; Shen et al., 2018; Liu L. et al., 2020). Gray and white matter degeneration was detected by DTI in an unbiased approach in cohort studies of APP transgenic mice (Müller et al., 2013) and 3×Tg-AD model mice (Manno et al., 2019) or after Aβ injections (Sun et al., 2014; Nishioka et al., 2019). *Ex-vivo* DTI was used to identify vulnerable brain networks in mouse models for late onset AD (Hara et al., 2017; Badea et al., 2019).

Histological confirmation demonstrated that such abnormalities corresponded to cortical and hippocampal neuronal loss, dendritic dystrophy and plaque accumulation, perivascular space dilation, and myelin damage (Qin et al., 2013). However, study of the triple-transgenic AD mouse model carrying mutations in APP, PS1, and the P301L mutation in Tau genes could not detect abnormalities in DTI metrics (imaged at 7T) despite histological detection of plaques and tangles-like lesions (Kastyak-Ibrahim et al., 2013). More recently, DTI imaging has been used to study murine models of tauopathies, namely the rTg4510 carrying the Tau(P301L) transgene; FA was found to be significantly decreased in the corpus callosum of these mice when imaged at 8.5 months of age at 9.4 T (Wells et al., 2015). In this model, DTI was sensitive enough to detect changes, histologically confirmed, in several areas of corpus callosum as early as 2.5 months after birth (Sahara et al., 2014). In a similar model, DTI proved sensitive enough to detect the regeneration of myelin when the expression of mutant Tau was suppressed (Holmes et al., 2016).

Taken together, the majority of the DTI studies in AD murine models or rat models (Anckaerts et al., 2019) appear to detect abnormalities in FA and other metrics in white matter and, less consistently, in gray matter. Thus, DTI imaging appears to be a possible non-invasive approach to assess cortical and white matter integrity in AD mouse models.

Cohort DTI Studies in Animal Models of Parkinson's Disease (PD)

Animal models of PD might address various aspects of the disease and its management, that is, the examination of pathogenetic mechanisms not only in the nigrostriatal system (van Camp et al., 2009; Zhang et al., 2017) but also in other brain regions and outside the brain, the investigation of the compensatory mechanisms under dopamine deficiency, the search of biological markers for presymptomatic parkinsonism, and finally the development of preventive therapy (Ugrumov et al., 2011). Early quantitative DTI studies reported decreased FA in the substantia nigra, indicating dopaminergic nigral degeneration in 1-methyl-4-phenyl-1,2,3,6-tetrahydropyridine (MPTP)-treated animals (Boska et al., 2007). Current technical studies investigated the value of DTI markers in the application to different PD models, such as MPTP and 3,4-methylene-dioxy-methamphetamine (MDMA) lesions, respectively, in the non-human primate: their different patterns could be demonstrated since MPTP-induced lesions were associated with MD increases of within the caudate and the anterior cingulate cortex, whereas MDMA-induced lesions were associated with FA increase within the caudate (Météreau et al., 2018). In another technical study, multiparametric MRI including DTI demonstrated the different characteristics of the rotenone and the 6-hydroxydopamine (6-OHDA) model after substantia nigra injection in rats, since the FA value of the substantia nigra was remarkably lower at 6 weeks than at other time points in the rotenone group, while in the 6-OHDA group, the FA value was decreased at 1 week (Liu L. X. et al., 2018). In the characterization of another model called the MitoPark mouse, which is a genetic model of PD with a dopaminergic neuron-specific knock-out inactivating mitochondrial transcription factor A, DTI demonstrated reduced FA in the corpus callosum and the substantia nigra (Cong et al., 2016). Beyond the different models, preclinical parkinsonism has been characterized by DTI in different species. A voxel-based analysis of a 7 T DTI study in marmosets before and after MPTP administration revealed increased diffusivity in the bilateral nigrostriatal pathway, validated by *ex-vivo* microscopic tractographic images, which showed loss of fiber structures in the MPTP-treated brain (Hikishima et al., 2015) and a longitudinal combined morphometric and DTI study in cynomolgus monkeys revealed widespread and dynamic structural changes not only in the nigrostriatal pathway but also in other cortical, subcortical, and cerebellar areas (Jeong et al., 2018). Further DTI studies (within multimodal imaging protocols) demonstrated significantly altered diffusivity parameters (MD, AD, RD) in the nigrostriatal tract (in correlation with MPTP dose), but not in the substantia nigra or striatum, in the macaque nemestrina after application of MPTP (Shimony et al., 2018) and increased FA in the ipsi- and contralateral striatum after 3 weeks and increase of AxD and MD in the ipsilateral striatum in rats with 6-OHDA striatal lesions (Perlbarg et al., 2018). That way, DTI applications to various PD models could contribute to the mapping of the underlying pathophysiology, together with DKI as a non-Gaussian DTI approach, which demonstrated microstructural alterations when applied to transgenic mice overexpressing human wildtype a-synuclein under the murine Thy-1 promoter, that is, increases in the striatum and thalamus after 3 months and in the substantia nigra after 6 months (Khairnar et al., 2017). Beyond mere descriptive assessments of the disease models, DTI was used in multimodal neuroimaging studies as a measure for therapeutic evaluations. Here, in a first step, levodopa-induced dyskinesia in MPTP/MDMA-intoxicated monkeys, as a model of the "classical" treatment complication in humans, were assessed by PET imaging and MRI including DTI, and severity of levodopa-induced dyskinesia was correlated to MD decreases in the ventral striatum but were no more altered after lesion of serotonergic fibers and the second levodopa period, highlighting that DTI is complementary to PET to decipher pathophysiological mechanisms underlying treatment-associated complications (Beaudoin-Gobert et al., 2018). As an example, for the use in therapy monitoring in a prospective case–control animal study in rats with the 6-OHDA model, simple diffusion delivery (direct microinjection of the drug into the brain tissue) of rasagiline was assessed by DTI and T2* mapping (Fang et al., 2018). The authors could show that FA values of the substantia nigra in the simple diffusion delivery treatment group were significantly higher at week 1 and lower at week 6 than that of the PD control group; given that higher T2* parameters at week 6 showed the same pattern, the authors considered the combination to be more reliable than other traditional methods for evaluating the curative effect of PD drugs in animal models. In summary, DTI, as one element of multimodal neuroimaging, has demonstrated a growing importance over the recent years in preclinical PD models for the assessment of disease-related pathophysiology and started to be used as a marker of therapeutic interventions.

DTI Study of Animal Models of Traumatic Brain Injury

In contrast to chronic neurodegenerative conditions, in which axonal and microstructural changes progress over months or years, in traumatic brain injury (TBI), damage to brain architecture takes place in seconds (primary damage). Nevertheless, further progressive alterations unfold over days or weeks (secondary damage). Furthermore, recent evidence shows that traumatic injury to the brain constitutes a powerful trigger of chronic neurodegenerative processes, in particular related to Tau protein (Chen et al., 2018; Stern et al., 2019). Thus, measuring initial and progressive damage to the brain upon TBI is the key to understand how the acute damage cause immediate neurological deficits and at the same time set in motion neurodegenerative cascades. We identified 23 papers exploiting DTI for the study of mouse models of TBI and 42 applying DTI to rat models.

Because of the sensitivity to axonal disruption, DTI has been extensively used to characterize diffuse axonal damage and long-range white matter tract injury in murine models to TBI. Initial evidence (Mac Donald et al., 2007a) showed that in controlled-cortical-injury TBI model, DTI detected alterations in the corpus callosum white matter underlying the trauma site with a stereotyped evolution of DTI signal over time (Mac Donald et al., 2007b). Notably, the alteration in radial anisotropy displayed the largest effect size and were directly correlated with histological measures of axonal damage (Li et al., 2013; Tu et al., 2016; also in rat models). FA maps have demonstrated substantial microstructural abnormalities also in case of experimental blast injury in mouse (Rubovitch et al., 2011; Hutchinson et al., 2018; Venkatasubramanian et al., 2020; Weiss et al., 2020) as well as in rat models (Budde et al., 2013; Begonia et al., 2014; Kamnaksh et al., 2014; Zhuo et al., 2015; Tang et al., 2017; Badea et al., 2018; Missault et al., 2019; Mohamed et al., 2020; San Martín Molina et al., 2020). DTI appeared sensitive enough to detect changes even in mild TBI models (Hylin et al., 2013; Takeuchi et al., 2013; Long et al., 2015; Li et al., 2016; Herrera et al., 2017; Kikinis et al., 2017; Wendel et al., 2018; Hoogenboom et al., 2019) and in distant locations within the brain up to 1 year after injury (Pischiutta et al., 2018). Interestingly, very-high field intensity DTI (14 T) has been successfully applied *ex vivo* for the analysis of closed TBI (CHIMERA model); this approach revealed abnormalities in FA and in AxD with a sensitivity and spatial resolution comparable to immunohistological approaches (Haber et al., 2017). Recently, DKI has been added to the MRI toolset for TBI investigation and has been able to detect changes in injured cortex in a CCI model of brain injury as soon as 5 h (Hansen et al., 2017; Soni et al., 2019). Although the DKI approach is in principle more sensitive to complex microstructural changes occurring upon trauma in mice and rats (Zhuo et al., 2015; Wang et al., 2018; Braeckman et al., 2019; Yu et al., 2019), its role is not established and remains object of investigation.

DTI has also been employed in the detection of axonal injury and microstructural changes following repeated mild TBI (which mimics the occurrence of head traumas in several sports). In this model, reduced values of axial diffusivity and mean diffusivity in the corpus callosum were found at 7 days post injury, in agreement with histological markers; notably, radial diffusivity was already altered in the cortical gray matter at 24 h but returned to baseline at the 7 days evaluation (Bennett et al., 2012). In a similar repeated-hit model, DTI has revealed disruption of axonal integrity in multiple white matter structures, irrespective of microhemorrhage detection (Robinson et al., 2017); substantial white matter damage was detected by DTI, together with histological approaches, in juvenile mice subject to repeated mild TBI (Yu et al., 2017; Lee et al., 2018). Similar alterations have been detected in rat models of repeated TBI (Calabrese et al., 2014; Singh et al., 2016; Wright et al., 2016; Qin et al., 2018; Kao et al., 2019) as well as in juvenile rat (Fidan et al., 2018; Wortman et al., 2018; Wright et al., 2018) or mouse (Rodriguez-Grande et al., 2018; Clément et al., 2020) cohorts subject to TBI. A few studies have applied *ex-vivo* DTI to obtain high-resolution maps of axonal disruption upon TBI, both in mouse (Weiss et al., 2020) and in rat (Donovan et al., 2014; Laitinen et al., 2015) models of brain trauma.

Finally, DTI-MRI has been used as read-out of treatment efficacy in rodents' models of TBI. In particular, DTI has revealed the beneficial effect on white matter integrity of activation of mitochondrial calcium fluxes (Parent et al., 2020), of autophagy modulators (Medina et al., 2017; Yin et al., 2018), estrogens (Kim et al., 2015, 2017), metamphetamine (Ding et al., 2013), erythropoietin (Robinson et al., 2016, 2018), tissue plasminogen activator (in mice; Xia et al., 2018), mGluR5 (in mice; Byrnes et al., 2012), and dietary modulations (Shultz et al., 2015; Schober et al., 2016; Tan et al., 2016). Notably, the detrimental effect of alcohol in TBI was also investigated by DTI (Kong et al., 2013). Taken together, these studies extensively highlight the sensitivity of DTI as readout of acute and subacute axonal damage in rodents TBI models.

Efforts are currently made to bring DTI to non-murine models of TBI. MRI has been successfully employed to study traumatic damage to piglets (sus scrofa domestia) in order to simulate pediatric TBI (Kinder et al., 2019) as well as to explore therapeutic strategies in adult minipigs (Georgoff et al., 2017; Nikolian et al., 2017). Recently, DTI has been implemented in minipigs (Simchick et al., 2019), revealing a remarkable similarity of the pattern of functional and structural connectivity between men and pigs and underscoring the translational value of porcine models. These experiments prove that the use of DTI-based MRI on swine models is possible but a full DTI study has not yet been performed. Initial studies of the application of DTI in non-human primates for the investigation of TBI are ongoing. Seminal work has shown that DTI can provide outcome measures in non-human primates models of traumatic spinal cord injury (Ma et al., 2016) and the remodeling of brain circuits upon hippocampal damage (Meng et al., 2018). Although non-human primate models of TBI has been established (e.g., King et al., 2010), the logistics and the ethics of non-human primates have so far limited the availability for DTI investigations.

Taken together, these findings identify DTI as a key approach to investigate large-scale and microstructural integrity in preclinical models of TBI, with excellent agreement with histological readouts and the advantage of longitudinal, non-invasive assessment.

DTI Integration With High-Resolution Optical Imaging

There is a growing number of large-scale connectomes for preclinical models obtained with DTI *ex vivo* (Nouls et al., 2018; Allan Johnson et al., 2019) and increasingly *in vivo* (Gimenez et al., 2017; Haber et al., 2017; Müller et al., 2019). At the same time, single-neuron resolution connectomes are being obtained for the whole mouse brain (Ho et al., 2014) or for individual structures (e.g., Commisso et al., 2018) using viral tracing tools and optical imaging. Therefore, the integration of these two techniques appears to be the logical next step. This may take place either in the form of technical approaches enabling the co-acquisition of DTI datasets and MRI-compatible viral tracing or in the form of post-acquisition merging of distinct datasets.

In the domain of *post-hoc* coregistration, the availability of the Allen Brain Connectivity atlas (Ho et al., 2014) has spurred early effort to merge or cross-check DTI atlases with connectivity measures obtained from viral tracing experiments. Initial evaluations in this direction have shown an incomplete match between DTI datasets and tracing datasets, in particular in the connectivity of striatum and cerebellum (Chen et al., 2015). In particular, the DTI connectivity map emerged to be more accurate when the anatomical parcellation was less precise, underscoring the different resolution of the DTI vs. optical imaging. Nevertheless, DTI appears to be reliable in the identification of at least 90% of large projection tracts identified by viral tracing; the misidentified tracts appear to be due to erroneous link of two independent fiber tracts by the tracing algorithm in the DTI dataset (Chen et al., 2015). Therefore, it is anticipated that further improvement of the technology, using machine-learning approaches that can use optical counterparts as "gold standard," will result in improvement in tracing, in particular in terms of reduced false positives (Maier-Hein et al., 2017). Of note, the resolution of the DTI-MRI datasets for murine models is progressively increasing, thanks to the adoption of ultra-high-field, *ex-vivo* acquisition (Allan Johnson et al., 2019). On the other hand, the acquisition of whole-brain optical images in cleared specimens (Ueda et al., 2020), which are going to have the same overall format of MRI images in terms of explored volume and reference points (and therefore could be normalized to standardized templates), may be anticipated to make for easier and faster integration with DTI-MRI.

Nevertheless, a large degree of complementarity, rather than integration, remains between DTI imaging and optical, tracer-based approaches. In fact, the major advantage for MRI application remains the acquisition of data *in vivo*, which is largely impossible with optical methods; however, DTI datasets are intrinsically devoid of directionality so that the polarization of the identified tracts cannot be deduced solely from diffusion metrics. To this respect, viral tracing provides a critical information, since viruses can be engineered to have anterograde or retrograde propagation (e.g., Commisso et al., 2018).

Of note, DTI atlases are being refined for non-murine animal models of disease. For porcine models, DTI imaging has been used to provide a whole-brain map of connectivity (Simchick et al., 2019) as well as enhanced tractography (Knösche et al., 2015). Furthermore, DTI connectome initiatives have been performed on marmoset (Callithrix jacchus) models (Okano and Mitra, 2015) and in rhesus models (Feng et al., 2017; Young et al., 2017). The correlative histological studies are quickly advancing, especially in marmoset (Goulas et al., 2019; Liu C. et al., 2020; Majka et al., 2020), but also in larger non-human primates (e.g., Decramer et al., 2018 and by the PRIME-DE initiative—PRIMatE Data Exchange (PRIME-DE) Global Collaboration Workshop Consortium, 2020). Thus, the current challenge is to obtain correlative DTI-histological mapping on large brains; the most severe limitations appear to be imposed by the difficulties in optical imaging of large samples with cellular resolution, although promising steps have been already undertaken such as the optical clearing of large organs (Zhao et al., 2020).

DISCUSSION

MRI in Preclinical Models of Neurodegeneration

Neuroimaging has provided powerful data on the temporal course of neurobiological changes associated with neurodegenerative disorders and is emerging as a powerful biomarker to define target engagement in therapeutic trials in humans (Masdeu, 2017). Animal studies have a crucial role in neuroscience and have substantially contributed to the understanding of neurodegeneration, and the studies previously presented in the various models of different neurodegenerative disease will pave the way for further DTI-based imaging read-outs in animals, including tracking of changes associated with pharmacological manipulation. Although animal studies are not a substitute for studies in real human biology, animal models provide opportunities for experiments that cannot be performed in humans and thus represent a critical platform upon which translational efforts for treating human neurodegenerative diseases are built (Albanese et al., 2018). Since advanced genetic techniques allow the manipulation of the genome and precise control of gene expression in rodents, transgenic models of human neuropathology are becoming increasingly important. Animal models of brain structure and organization at different neurodegenerative disease stages may define possible read-outs for surrogate markers and enhanced drug trials. Longitudinal studies in animals are of special interest since they can be designed across the entire lifespan of the respective animal in contrast to humans where longitudinal studies have to be designed for many years or even decades to capture a sizeable part of the human lifespan (Gorges et al., 2017). DTI-based analysis of the brain can show disease-related alterations of brain areas, which develop over time. MRI has substantially contributed to the understanding of microstructural brain alterations in animal models in the course of neurodegenerative diseases. Taken together, the broad spectrum of experimental manipulations, which can be longitudinally investigated by the non-invasive DTI approach provides a promising tool for cross-species comparative investigations. The integration of DTI in a multiparametric imaging protocol is a promising approach to integrate microstructural characteristics into a context of the structural and functional networks.

DTI in Translational Imaging

DTI is a powerful tool providing important information regarding alterations in brain microstructure. As DTI has enormous translational potential, the remaining task is to design animal studies exhausting this potential by focusing on clinically relevant parameters, developmental time points, and by providing carefully matched controls. To assess the axonal damage and myelin degradation, the statistical analysis of DTI metrics can be performed by unbiased whole-brain-based voxelwise comparison or by hypothesis-guided ROI-based or TOI-based quantification. When these tools are combined with the strengths of animal models, a more complete picture of the neurobiological targets and mechanisms of neurodegeneration can be developed. A methodological example of harmonized translational imaging in man and in mouse is a recent cohort DTI study in a mouse model of the Phelan-McDermid syndrome. Here, white matter damage in *SHANK3* deficiency has been investigated in a back-translational study of human subjects with Phelan-McDermid syndrome and terminal deletions of chromosome 22q13, including *SHANK3* on the one hand and a *SHANK3* mouse model on the other hand: with the identical DTI analysis cascade, human DTI data and murine DTI data were analyzed by unbiased voxelwise WBSS-based comparison and by hypothesis-guided TOI-based analysis, respectively (Jesse et al., 2020).

Traditional DTI analysis is using the single-tensor model. While this model can adequately analyze alterations in the microstructure in certain brain regions, it is hardly useful for the representation of crossing fibers, posing substantial problems with robust tractography. A step away from single-tensor representations are high angular resolution diffusion imaging (HARDI) (Ozarslan and Mareci, 2003; Cercignani et al., 2012), Q-ball imaging (Tuch, 2004), and NODDI (Barritt et al., 2018; Gatto et al., 2018d). These approaches rely on acquiring a comparatively high number of diffusion gradient directions to cover a full orientation distribution function. HARDI has been performed in excised tissue (D'Arceuil and de Crespigny, 2007; D'Arceuil et al., 2007), and there have been first attempts to apply HARDI or Q-ball imaging in the whole rodent brain at 16.4 T (Alomair et al., 2015). There are no theoretical restrictions for the application of HARDI or Q-ball imaging to animal cohort studies; however, there are many practical challenges such as scanning time. However, NODDI has been applied to detect neurite orientation dispersion of mouse brain microstructure (Wang et al., 2019) or alterations in hippocampal microstructure (Colon-Perez et al., 2019) and also to investigate spinal cords at 17.6 T in an ALS mouse model (G93A-SOD1 mice) for the detection of presymptomatic axonal degeneration (Gatto et al., 2018d). Because simple Gaussian diffusion models do not sufficiently describe water diffusion in complex tissues, a novel diffusion MRI acquisition approach can be applied, that is, hybrid diffusion imaging (HYDI). HYDI can be fit into NODDI to extract diffusion metrics that may be more biologically specific and unbiased by crossing fibers (Wu et al., 2008, 2018; Daianu et al., 2015a,b). In AD research, both HYDI and NODDI have been applied to rat models (Daianu et al., 2015a) or mouse models (Colgan et al., 2016). Due to their elaborate character, it is unclear if these techniques will be clinically significant, but there are aspects that might aid in the research of neurodegenerative diseases, for example, in the discrimination of cortical gray matter as diffusion MRI is sensitive to architectonic differences between a large number of different cortical areas (Ganepola et al., 2018).

Novel developments show the applicability of deep learning-based techniques to obtain DTI with only six gradients directions (Li et al., 2020). The method uses deep convolutional neural networks to learn the nonlinear relationship between diffusion weighted images and tensor-derived maps, bypassing the conventional tensor fitting procedure, which is well-known to be highly susceptible to noise in diffusion weighted imaging. This technique has been reported and it will be shown in the future if it will contribute to significantly reduce the recording time. The role of DKI (Marrale et al., 2016) has not been generally established yet, although—due to its improved sensitivity to complex microstructural changes—successful studies in TBI (Hansen et al., 2017; Soni et al., 2019) and early microstructural changes in the ALS brain (Gatto et al., 2018b,c, 2019) have already been performed; thus, DKI might be considered to be one of the promising techniques to be included in the data acquisition protocols of future experiments.

Limitations of DTI

As a macro- or mesoscale imaging technique, DTI has the advantages of 3D and *in-vivo* imaging, including the opportunity of repeated and longitudinal scanning with an arbitrary number of DTI recordings and follow-up scans. The ratio of the microstructural feature size to voxel size is improved in small animal imaging as compared with human or primate imaging; nevertheless, a DTI voxel always contains the averaged information of diffusion covering hundreds of axons as well as the surrounding water molecules. Thus, any DTI metric is a measurement of the physical properties of a volume element without any specific restriction to axonal microstructure. Therefore, DTI metrics determination is only an indirect assessment of fiber density and cell packing, degree of myelination, and individual fiber diameter. Diffusion anisotropy is influenced by axonal integrity or myelin degradation, which are affected by neurodegenerative processes.

There have been many efforts to develop sophisticated techniques to extract relevant information on axonal integrity or myelin degradation to get insights into neurodegenerative processes. This ranges from advanced recording techniques, such as Q-ball, HARDI, or NODDI to extensive postprocessing algorithms, that is, parameterization to one FA value or fiber tracking reconstructions. However, it is an intrinsic property of DTI (which is related to the image recording at a macro- or mesoscale) that any FT technique can only represent the probable fiber bundle course rather than individual axons. As a macro- or mesoscale imaging technique DTI has the advantages of 3D and *in-vivo* imaging, which contains the opportunity of repeated and longitudinal scanning with an arbitrary number of DTI recordings and follow-up scans. The ratio microstructural feature size to voxel size is improved in small animal imaging compared to human or primate imaging; nevertheless, a DTI voxel always contains the averaged information of diffusion covering hundreds of axons as well as the surrounding water molecules. Thus, any DTI metric is a measurement of the physical properties of a volume element without any specific restriction to axonal microstructure. Therefore, DTI metrics determination is only an indirect measurement of density of fibers and cell packing, degree of myelination, and individual fiber diameter. Diffusion anisotropy is influenced by axonal integrity or myelin degradation, which are thought to be mainly affected by neurodegenerative processes.

Future Aspects

A future aspect of microstructure imaging by DTI (including tractography) is the combination of the detected alteration patterns with further MRI-based techniques such as structural imaging and intrinsic functional connectivity imaging, which can be the basis for connectome imaging as a comprehensive map of neural connections of the species nervous system (Rilling and van den Heuvel, 2018). These techniques have successfully been applied to humans and will further strengthen the translational insights into a complex multiparametric comprehensive structural-functional organization of the animal brains. Such MRI studies can then be expanded, for example, by radioligand neuroimaging or advanced optical imaging (see section DTI Integration With High-Resolution Optical Imaging). There is particular interest in performing these advanced neuroimaging analyses at the group level, given that a trend for bottom-up initiatives is emerging within the neuroscientific community, starting with small-scale projects by single groups that expand upon self-organized collaborations of researchers and infrastructures in "meso-scale" collaborations and develop to grand-scale projects (Kassubek, 2017). Joined forces with a focus on the analysis of specific preclinical models for neurodegeneration might be a solution to the existing challenges especially in preclinical imaging by the combination of neuroimaging data: preferably in a prospectively harmonized design than *ex post facto*, DTI might be one promising advanced imaging candidate in that sense in the light of standardized acquisition protocols with relative robustness. In the context of models of neurodegenerative diseases, both the analysis of disease-related brain changes including the correlation with the clinical phenotype and the analysis of white matter plasticity (Sampaio-Baptista and Johansen-Berg, 2017; Sampaio-Baptista et al., 2020) might facilitate the translational approach of these studies to clinical data.

DATA AVAILABILITY STATEMENT

The original contributions presented in the study are included in the article/supplementary material, further inquiries can be directed to the corresponding author.

AUTHOR CONTRIBUTIONS

H-PM and JK drafted the manuscript. FR and VR revised the manuscript for intellectual content. All authors performed literature investigation, agreed to be accountable for the content of the work, and finally approved the manuscript.

FUNDING

FR was supported by the Deutsche Forschungsgemeinschaft (DFG) as member of the SFB1149 Danger Response, disturbance Factors and Regenerative Potential after Acute Trauma and by BMBF (FKZ 01EW1705A) in the context of the ERANET-NEURON initiative.

ACKNOWLEDGMENTS

We would like to thank the Ulm University Center for Translational Imaging MoMAN for its support.

REFERENCES

Aggarwal, M., Mori, S., Shimogori, T., Blackshaw, S., and Zhang, J. (2010). Three-dimensional diffusion tensor microimaging for anatomical characterization of the mouse brain. *Magn. Reson. Med.* 64, 249–261. doi: 10.1002/mrm.22426

Aggarwal, M., Zhang, J., Miller, M. I., Sidman, R. L., and Mori, S. (2009). Magnetic resonance imaging and micro-computed tomography combined atlas of developing and adult mouse brains for stereotaxic surgery. *Neuroscience* 162, 1339–1350. doi: 10.1016/j.neuroscience.2009.05.070

Agosta, F., Weiler, M., and Filippi, M. (2015). Propagation of pathology through brain networks in neurodegenerative diseases: from molecules to clinical phenotypes. *CNS Neurosci Ther.* 21, 754–767. doi: 10.1111/cns.12410

Albanese, S., Greco, A., Auletta, L., and Mancini, M. (2018). Mouse models of neurodegenerative disease: preclinical imaging and neurovascular component. *Brain Imaging Behav.* 12, 1160–1196. doi: 10.1007/s11682-017-9770-3

Alexander, D. C., Pierpaoli, C., Basser, P. J., and Gee, J. C. (2001). Spatial transformations of diffusion tensor magnetic resonance images. *IEEE Trans. Med. Imaging* 20, 1131–1139. doi: 10.1109/42.963816

Allan Johnson, G., Wang, N., Anderson, R. J., Chen, M., Cofer, G. P., Gee, J. C., et al. (2019). Whole mouse brain connectomics. *J. Comp. Neurol.* 527, 2146–2157. doi: 10.1002/cne.24560

Alomair, O. I., Brereton, I. M., Smith, M. T., Galloway, G. J., and Kurniawan, N. D. (2015). *In vivo* high angular resolution diffusion-weighted imaging of mouse brain at 16.4 Tesla. *PLoS ONE* 10:e0130133. doi: 10.1371/journal.pone.0130133

Anckaerts, C., Blockx, I., Summer, P., Michael, J., Hamaide, J., Kreutzer, C., et al. (2019). Early functional connectivity deficits and progressive microstructural alterations in the TgF344-AD rat model of alzheimer's disease: a longitudinal MRI study. *Neurobiol Dis.* 124, 93–107. doi: 10.1016/j.nbd.2018.11.010

Badea, A., Kamnaksh, A., Anderson, R. J., Calabrese, E., Long, J. B., and Agoston, D. V. (2018). Repeated mild blast exposure in young adult rats results in dynamic and persistent microstructural changes in the brain. *Neuroimage Clin.* 18, 60–73. doi: 10.1016/j.nicl.2018.01.007

Badea, A., Wu, W., Shuff, J., Wang, M., Anderson, R., Qi, Y., et al. (2019). Identifying vulnerable brain networks in mouse models of genetic risk factors for late onset alzheimer's disease. *Front. Neuroinform.* 13:72. doi: 10.3389/fninf.2019.00072

Barritt, A. W., Gabel, M. C., Cercignani, M., and Leigh, P. N. (2018). Emerging magnetic resonance imaging techniques and analysis methods in amyotrophic lateral sclerosis. *Front. Neurol.* 9:1065. doi: 10.3389/fneur.2018.01065

Basser, P. J., Mattiello, J., and LeBihan, D. (1994). MR diffusion tensor spectroscopy and imaging. *Biophys J.* 66, 259–267. doi: 10.1016/S0006-3495(94)80775-1

Beaudoin-Gobert, M., Météreau, E., Duperrier, S., Thobois, S., Tremblay, L., and Sgambato, V. (2018). Pathophysiology of levodopa-induced dyskinesia: insights from multimodal imaging and immunohistochemistry in non-human primates. *Neuroimage* 183, 132–141. doi: 10.1016/j.neuroimage.2018.08.016

Begonia, M. T., Prabhu, R., Liao, J., Whittington, W. R., Claude, A., Willeford, B., et al. (2014). Quantitative analysis of brain microstructure following mild blunt and blast trauma. *J. Biomech.* 47, 3704–3711. doi: 10.1016/j.jbiomech.2014.09.026

Bennett, A. J., and Ringach, D. L. (2016). Animal research in neuroscience: a duty to engage. *Neuron* 92, 653–657. doi: 10.1016/j.neuron.2016.10.034

Bennett, R. E., Mac Donald, C. L., and Brody, D. L. (2012). Diffusion tensor imaging detects axonal injury in a mouse model of repetitive closed-skull traumatic brain injury. *Neurosci. Lett.* 513, 160–165. doi: 10.1016/j.neulet.2012.02.024

Bitner, B. R., Perez-Torres, C. J., Hu, L., Inoue, T., and Pautler, R. G. (2012). Improvements in a mouse model of alzheimer's disease through SOD2 overexpression are due to functional and not structural alterations. *Magn. Reson. Insights* 5, 1–6. doi: 10.4137/MRI.S9352

Blamire, A. M. (2018). MR approaches in neurodegenerative disorders. *Prog. Nucl. Magn. Reson. Spectrosc.* 108, 1–16. doi: 10.1016/j.pnmrs.2018.11.001

Boska, M. D., Hasan, K. M., Kibuule, D., Banerjee, R., McIntyre, E., Nelson, J. A., et al. (2007). Quantitative diffusion tensor imaging detects dopaminergic neuronal degeneration in a murine model of Parkinson's disease. *Neurobiol. Dis.* 26, 590–596. doi: 10.1016/j.nbd.2007.02.010

Braak, H., Brettschneider, J., Ludolph, A. C., Lee, V. M., Trojanowski, J. Q., Del Tredici, K., et al. (2013). Amyotrophic lateral sclerosis–a model of corticofugal axonal spread. *Nat. Rev. Neurol.* 9, 708–714. doi: 10.1038/nrneurol.2013.221

Braeckman, K., Descamps, B., Pieters, L., Vral, A., Caeyenberghs, K., and Vanhove, C. (2019). Dynamic changes in hippocampal diffusion and kurtosis metrics following experimental mTBI correlate with glial reactivity. *Neuroimage Clin.* 21:101669. doi: 10.1016/j.nicl.2019.101669

Brandstack, N., Kurki, T., Laalo, J., Kauko, T., and Tenovuo, O. (2016). Reproducibility of tract-based and region-of-interest, DTI analysis of long association tracts. *Clin. Neuroradiol.* 26, 199–208. doi: 10.1007/s00062-014-0349-8

Brennan, F. H., Cowin, G. J., Kurniawan, N. D., and Ruitenberg, M. J. (2013). Longitudinal assessment of white matter pathology in the injured mouse spinal cord through ultra-high field (16.4 T) *in vivo* diffusion tensor imaging. *Neuroimage* 82, 574–585. doi: 10.1016/j.neuroimage.2013.06.019

Brett, M., Johnsrude, I. S., and Owen, A. M. (2002). The problem of functional localization in the human brain. *Nat. Rev. Neurosci.* 3, 243–249. doi: 10.1038/nrn756

Budde, M. D., Shah, A., McCrea, M., Cullinan, W. E., Pintar, F. A., and Stemper, B. D. (2013). Primary blast traumatic brain injury in the rat: relating diffusion tensor imaging and behavior. *Front. Neurol.* 4:154. doi: 10.3389/fneur.2013.00154

Byrnes, K. R., Loane, D. J., Stoica, B. A., Zhang, J., and Faden, A. I. (2012). Delayed mGluR5 activation limits neuroinflammation and neurodegeneration after traumatic brain injury. *J. Neuroinflamm.* 9:43. doi: 10.1186/1742-2094-9-43

Cai, Y., McMurray, M. S., Oguz, I., Yuan, H., Styner, M. A., Lin, W., et al. (2011). Use of high resolution 3D diffusion tensor imaging to study brain white matter development in live neonatal rats, *Front. Psychiatry* 2:54. doi: 10.3389/fpsyt.2011.00054

Calabrese, E., Du, F., Garman, R. H., Johnson, G. A., Riccio, C., Tong, L. C., et al. (2014). Diffusion tensor imaging reveals white matter injury in a rat model of repetitive blast-induced traumatic brain injury, *J. Neurotrauma.* 31, 938–950. doi: 10.1089/neu.2013.3144

Cercignani, M., Embleton, K., Parker, G. J., and Bozzali, M. (2012). Group-averaged anatomical connectivity mapping for improved human white matter pathway visualisation *NMR Biomed.* 25, 1224–1233. doi: 10.1002/nbm.2793

Chen, H., Liu, T., Zhao, Y., Zhang, T., Li, Y., Li, M., et al. (2015). Optimization of large-scale mouse brain connectome via joint evaluation of DTI and neuron tracing data. *Neuroimage.* 115, 202–213. doi: 10.1016/j.neuroimage.2015.04.050

Chen, S. T., Siddarth, P., Merrill, D. A., Martinez, J., Emerson, N. D., Liu, J., et al. (2018). FD DNP-PET tau brain protein binding patterns in military personnel with suspected chronic traumatic encephalopathy. *J. Alzheimers Dis.* 65, 79–88. doi: 10.3233/JAD-171152

Chiò, A., Pagani, M., Agosta, F., Calvo, A., Cistaro, A., and Filippi, M. (2014). Neuroimaging in amyotrophic lateral sclerosis: insights into structural and functional changes. *Lancet Neurol.* 13, 1228–1240. doi: 10.1016/S1474-4422(14)70167-X

Chuang, N., Mori, S., Yamamoto, A., Jiang, H., Ye, X., Xu, X., et al. (2011). An MRI-based atlas and database of the developing mouse brain. *NeuroImage* 54, 80–89. doi: 10.1016/j.neuroimage.2010.07.043

Clément, T., Lee, J. B., Ichkova, A., Rodriguez-Grande, B., Fournier, M. L., Aussudre, J., et al. (2020). Juvenile mild traumatic brain injury elicits distinct spatiotemporal astrocyte responses. *Glia* 68, 528–542. doi: 10.1002/glia.23736

Colgan, N., Siow, B., O'Callaghan, J. M., Harrison, I. F., Wells, J. A., Holmes, H. E., et al. (2016). Application of neurite orientation dispersion and density imaging (NODDI) to a tau pathology model of Alzheimer's disease. *Neuroimage* 125, 739–744. doi: 10.1016/j.neuroimage.2015.10.043

Colon-Perez, L. M., Ibanez, K. R., Suarez, M., Torroella, K., Acuna, K., Ofori, E., et al. (2019). Neurite orientation dispersion and density imaging reveals white matter and hippocampal microstructure changes produced by interleukin-6 in the TgCRND8 mouse model of amyloidosis. *Neuroimage* 202:116138. doi: 10.1016/j.neuroimage.2019.116138

Commisso, B., Ding, L., Varadi, K., Gorges, M., Bayer, D., Boeckers, T. M., et al. (2018). Stage-dependent remodeling of projections to motor cortex in ALS mouse model revealed by a new variant retrograde-AAV9. *Elife* 7:e36892. doi: 10.7554/eLife.36892

Cong, L., Muir, E. R., Chen, C., Qian, Y., Liu, J., Biju, K. C., et al. (2016). Multimodal MRI evaluation of the mitopark mouse model of parkinson's disease. *PLoS ONE* 11:e0151884. doi: 10.1371/journal.pone.0151884

Daianu, M., Jacobs, R. E., Weitz, T. M., Town, T. C., and Thompson, P. M. (2015a). Multi-shell hybrid diffusion imaging (HYDI) at 7 tesla in TgF344-AD transgenic alzheimer rats. *PLoS ONE* 10:e0145205. doi: 10.1371/journal.pone.0145205

Daianu, M., Jahanshad, N., Villalon-Reina, J. E., Prasad, G., Jacobs, R. E., Barnes, S., et al. (2015b). 7T multi-shell hybrid diffusion imaging (HYDI) for mapping brain connectivity in mice. *Proc. SPIE Int. Soc. Opt. Eng.* 9413:941309. doi: 10.1117/12.2081491

D'Arceuil, H., and de Crespigny, A. (2007). The effects of brain tissue decomposition on DTI and tractography. *Neuroimage* 36, 64–68. doi: 10.1016/j.neuroimage.2007.02.039

D'Arceuil, H. E., Westmoreland, S., and de Crespigny, A. J. (2007). An approach to high resolution diffusion tensor imaging in fixed primate brain. *Neuroimage* 35, 553–565. doi: 10.1016/j.neuroimage.2006.12.028

Dawson, T. M., Golde, T. E., and Lagier-Tourenne, C. (2018). Animal models of neurodegenerative diseases. *Nat. Neurosci.* 21, 1370–1379. doi: 10.1038/s41593-018-0236-8

Decramer, T., Swinnen, S., van Loon, J., Janssen, P., and Theys, T. (2018). White matter tract anatomy in the rhesus monkey: a fiber dissection study. *Brain Struct. Funct.* 223, 3681–3688. doi: 10.1007/s00429-018-1718-x

Ding, G. L., Chopp, M., Poulsen, D. J., Li, L., Qu, C., Li, Q., et al. (2013). MRI of neuronal recovery after low-dose methamphetamine treatment of traumatic brain injury in rats. *PLoS ONE* 8:e61241. doi: 10.1371/journal.pone.0061241

Donovan, V., Kim, C., Anugerah, A. K., Coats, J. S., Oyoyo, U., Pardo, A. C., et al. (2014). Repeated mild traumatic brain injury results in long-term white-matter disruption, *J. Cereb. Blood Flow. Metab.* 34, 715–723. doi: 10.1038/jcbfm.2014.6

Duan, F., Zhao, T., He, Y., and Shu, N. (2015). Test-retest reliability of diffusion measures in cerebral white matter: a multiband diffusion MRI study. *J. Magn. Reson. Imaging* 42, 1106–1116. doi: 10.1002/jmri.24859

Duong, T. Q. (2010). Diffusion tensor and perfusion MRI of non-human primates. *Methods.* 50, 125–135. doi: 10.1016/j.ymeth.2009.08.001

Fang, Y., Zheng, T., Liu, L., Gao, D., Shi, Q., Dong, Y., et al. (2018). Role of the combination of FA and T2* parameters as a new diagnostic method in therapeutic evaluation of parkinson's disease. *J. Magn. Reson. Imaging* 48, 84–93. doi: 10.1002/jmri.25900

Feng, L., Jeon, T., Yu, Q., Ouyang, M., Peng, Q., Mishraet, V., et al. (2017). Population-averaged macaque brain atlas with high-resolution *ex vivo* DTI integrated into *in vivo* space. *Brain Struct. Funct.* 222, 4131–4147. doi: 10.1007/s00429-017-1463-6

Fidan, E., Foley, L. M., New, L. A., Alexander, H., Kochanek, P. M., Hitchens, T. K., et al. (2018). Metabolic and structural imaging at 7 tesla after repetitive mild traumatic brain injury in immature rats. *ASN Neuro.* 10:1759091418770543. doi: 10.1177/1759091418770543

Field, A. S., Wu, Y. C., and Alexander, A. L. (2005). Principal diffusion direction in peritumoral fiber tracts: color map patterns and directional statistics. *Ann. N. Y. Acad. Sci.* 1064, 193–201. doi: 10.1196/annals.1340.037

Figini, M., Zucca, I., Aquino, D., Pennacchio, P., Nava, S., Di Marzio, A., et al. (2015). *In vivo* DTI tractography of the rat brain: an atlas of the main tracts in Paxinos space with histological comparison. *Magn. Reson. Imaging* 33, 296–303. doi: 10.1016/j.mri.2014.11.001

Frank, L. R., Jung, Y., Inati, S., Tyszka, J. M., and Wong, E. C. (2010). High efficiency, low distortion 3D diffusion tensor imaging with variable density spiral fast spin echoes (3D DW VDS RARE). *Neuroimage* 49, 1510–1523. doi: 10.1016/j.neuroimage.2009.09.010

Frisoni, G. B., Fox, N. C., Jack, C. R Jr., Scheltens, P., and Thompson, P. M. (2010). The clinical use of structural MRI in alzheimer disease. *Nat. Rev. Neurol.* 6, 67–77. doi: 10.1038/nrneurol.2009.215

Ganepola, T., Nagy, Z., Ghosh, A., Papadopoulo, T., Alexander, D. C., and Sereno, M. I. (2018). Using diffusion MRI to discriminate areas of cortical grey matter. *Neuroimage* 182, 456–468. doi: 10.1016/j.neuroimage.2017.12.046

Garin-Muga, A., and Borro, D. (2014). Review and challenges of brain analysis through DTI measurements. *Stud. Health Technol. Inform.* 207, 27–36. doi: 10.3233/978-1-61499-474-9-27

Gatto, R. G., Amin, M., Finkielsztein, A., Weissmann, C., Barrett, T., Lamoutte, C., et al. (2019). Unveiling early cortical and subcortical neuronal degeneration in ALS mice by ultra-high field diffusion M RI. *Amyotroph. Lateral Scler. Frontotemporal. Degener.* 20, 549–561. doi: 10.1080/21678421.2019.1620285

Gatto, R. G., Amin, M. Y., Deyoung, D., Hey, M., Mareci, T. H., and Magin, R. L. (2018a). Ultra-high field diffusion MRI reveals early axonal pathology in spinal cord of ALS mice. *Transl. Neurodegener.* 7:20. doi: 10.1186/s40035-018-0122-z

Gatto, R. G., Li, W., Gao, J., and Magin, R. L. (2018b). *In vivo* diffusion MRI detects early spinal cord axonal pathology in a mouse model of amyotrophic lateral sclerosis, *NMR Biomed.* 31:e3954. doi: 10.1002/nbm.3954

Gatto, R. G., Li, W., and Magin, R. L. (2018c). Diffusion tensor imaging identifies presymptomatic axonal degeneration in the spinal cord of ALS mice. *Brain Res.* 1679, 45–52. doi: 10.1016/j.brainres.2017.11.017

Gatto, R. G., Mustafi, S. M., Amin, M. Y., Mareci, T. H., Wu, Y. C., and Magin, R. L. (2018d). Neurite orientation dispersion and density imaging can detect presymptomatic axonal degeneration in the spinal cord of ALS mice. *Funct Neurol.* 33, 155–163.

Gatto, R. G., and Weissmann, C. (2019). Diffusion tensor imaging in preclinical and human studies of huntington's disease: what have we learned so far? *Curr. Med. Imaging Rev.* 15, 521–542. doi: 10.2174/1573405614666181115113400

Genovese, C. R., Lazar, N. A., and Nichols, T. (2002). Thresholding of statistical maps in functional neuroimaging using the false discovery rate. *Neuroimage.* 15, 870–878. doi: 10.1006/nimg.2001.1037

Georgoff, P. E., Nikolian, V. C., Halaweish, I., Chtraklin, K., Bruhn, P. J., Eidy, H., et al. (2017). Resuscitation with lyophilized plasma is safe, and improves neurological recovery in a long-term survival model of swine subjected to traumatic brain injury hemorrhagic shock and polytrauma. *J. Neurotrauma* 34, 2167–2175. doi: 10.1089/neu.2016.4859

Gimenez, U., Boulan, B., Mauconduit, F., Taurel, F., Leclercq, M., Denarier, E., et al. (2017). 3D imaging of the brain morphology and connectivity defects in a model of psychiatric disorders MAP6-KO mice. *Sci. Rep.* 7:10308. doi: 10.1038/s41598-017-10544-2

Gorges, M., Roselli, F., Müller, H. P., Ludolph, A. C., Rasche, V., and Kassubek, J. (2017). Functional connectivity mapping in the animal model: principles and applications of resting-state FMRI. *Front. Neurol.* 8:200. doi: 10.3389/fneur.2017.00200

Goulas, A., Majka, P., Rosa, M. G. P., and Hilgetag, C. C. (2019). A blueprint of mammalian cortical connectomes. *PLoS Biol.* 17:e2005346. doi: 10.1371/journal.pbio.2005346

Goveas, J., O'Dwyer, L., Mascalchi, M., Cosottini, M., Diciotti, S., De Santis, S., et al. (2015). Diffusion MRI in neurodegenerative disorders. *Magn. Reson. Imaging* 33, 853–876. doi: 10.1016/j.mri.2015.04.006

Guilfoyle, D. N., Gerum, S., and Hrabe, J. (2011). Murine diffusion imaging using snapshot interleaved EPI acquisition at 7T. *J. Neurosci. Methods* 199, 10–14. doi: 10.1016/j.jneumeth.2011.04.011

Gutman, D. A., Keifer, O. P Jr., Magnuson, M. E., Choi, D. C., Majeed, W., Keilholz, S., et al. (2012). A DTI tractography analysis of infralimbic and prelimbic connectivity in the mouse using high-throughput MRI. *Neuroimage* 63, 800–811. doi: 10.1016/j.neuroimage.2012.07.014

Gyengesi, E., Calabrese, E., Sherrier, M. C., Johnson, G. A., Paxinos, G., Watson, C. (2014). Semi-automated 3D segmentation of major tracts in the rat brain: comparing DTI with standard histological methods. *Brain Struct. Funct.* 219, 539–550. doi: 10.1007/s00429-013-0516-8

Haber, M., Hutchinson, E. B., Sadeghi, N., Cheng, W. H., Namjoshi, D., Cripton, P., et al. (2017). Defining an analytic framework to evaluate quantitative MRI markers of traumatic axonal injury: preliminary results in a mouse closed head injury model. *eNeuro* 4:ENEURO.0164-17.2017. doi: 10.1523/ENEURO.0164-17.2017

Hansen, B., Khan, A. R., Shemesh, N., Lund, T. E., Sangill, R., Eskidsen, S. F., et al. (2017). White matter biomarkers from fast protocols using axially symmetric diffusion kurtosis imaging. *NMR Biomed.* 30:3741. doi: 10.1002/nbm.3741

Hara, Y., Motoi, Y., Hikishima, K., Mizuma, H., Onoe, H., Matsumoto, S. E., et al. (2017). Involvement of the septo-hippocampal cholinergic pathway in association with septal acetylcholinesterase upregulation in a mouse model of tauopathy. *Curr. Alzheimer Res.* 14, 94–103. doi: 10.2174/1567205013666160602235800

Harms, M. P., Kotyk, J. J., and Merchant, K.M. (2006). Evaluation of white matter integrity in *ex vivo* brains of amyloid plaque-bearing APPsw transgenic mice using magnetic resonance diffusion tensor imaging. *Exp. Neurol.* 199, 408–415. doi: 10.1016/j.expneurol.2006.01.002

Harsan, L. A., Paul, D., Schnell, S., Kreher, B. W., Hennig, J., Staiger, J. F., et al. (2010). In vivo diffusion tensor magnetic resonance imaging and fiber tracking of the mouse brain. *NMR Biomed.* 23, 884–896. doi: 10.1002/nbm.1496

Hayashi, T., Shimazawa, M., Watabe, H., Ose, T., Inokuchi, Y., Ito, Y., et al. (2013). Kinetics of neurodegeneration based on a risk-related biomarker in animal model of glaucoma. *Mol. Neurodegener.* 8:4. doi: 10.1186/1750-1326-8-4

Herrera, J. J., Bockhorst, K., Kondraganti, S., Stertz, L., Quevedo, J., and Narayana, P. A. (2017). Acute white matter tract damage after frontal mild traumatic brain injury, *J. Neurotrauma* 34, 291–299. doi: 10.1089/neu.2016.4407

Herrmann, K. H., Schmidt, S., Kretz, A., Haenold, R., Krumbein, I., Metzler, M., et al. (2012). Possibilities and limitations for high resolution small animal MRI on a clinical whole-body 3T scanner. *MAGMA* 25, 233–244. doi: 10.1007/s10334-011-0284-5

Hikishima, K., Ando, K., Yano, R., Kawai, K., Komaki, Y., Inoue, T., et al. (2015). Parkinson disease: Diffusion MR imaging to detect nigrostriatal pathway loss in a marmoset model treated with 1-methyl-4-phenyl-1,2,3,6-tetrahydropyridine. *Radiology* 275, 430–437. doi: 10.1148/radiol.14140601

Ho, Y. M., Au, N. P., Wong, K. L., Chan, C. T., Kwok, W. M., Law, G. L., et al. (2014). A Lysosome-Specific Two-Photon Phosphorescent Binuclear Cyclometalated Platinum(II) probe for *in vivo* imaging of live neurons. *Chem. Commun.* 50, 4161–4163. doi: 10.1039/c3cc48934e

Holmes, H. E., Colgan, N., Ismail, O., Ma, D., Powell, N. M., O'Callaghan, J. M., et al. (2016). Imaging the accumulation and suppression of tau pathology using multiparametric MRI. *Neurobiol. Aging* 39, 184–194. doi: 10.1016/j.neurobiolaging.2015.12.001

Hoogenboom, W. S., Rubin, T. G., Ye, K., Cui, M. H., Branch, K. C., Liu, J., et al. (2019). Diffusion tensor imaging of the evolving response to mild traumatic brain injury in rats *J. Exp. Neurosci.* 13:1179069519858627. doi: 10.1177/1179069519858627

Hutchinson, E. B., Schwerin, S. C., Avram, A. V., Juliano, S. L., and Pierpaoli, C. (2018). Diffusion MRI the detection of alterations following traumatic brain injury. *J. Neurosci. Res.* 96, 612–625. doi: 10.1002/jnr.24065

Hylin, M. J., Orsi, S. A., Zhao, J., Bockhorst, K., Perez, A., Moore, A. N., et al. (2013). Behavioral and histopathological alterations resulting from mild fluid percussion injury. *J. Neurotrauma* 30, 702–715. doi: 10.1089/neu.2012.2630

Irie, R., Kamagata, K., Kerever, A., Ueda, R., Yokosawa, S., Otake, Y., et al. (2018). The relationship between neurite density measured with confocal microscopy in a cleared mouse brain and metrics obtained from diffusion tensor and diffusion kurtosis imaging. *Magn. Reson. Med. Sci.* 17, 138–144. doi: 10.2463/mrms.mp.2017-0031

Jeong, H. S., Lee, S. R., Kim, J. E., Lyoo, I. K., Yoon, S., Namgung, E., et al. (2018). Brain structural changes in cynomolgus monkeys administered with 1-methyl-4-phenyl-1,2,3,6-tetrahydropyridine: A longitudinal voxel-based morphometry and diffusion tensor imaging study. *PLoS One* 13:e0189804. doi: 10.1371/journal.pone.0189804

Jesse, S., Müller, H. P., Schoen, M., Asoglu, H., Bockmann, J., Huppertz, H. J., et al. (2020). Severe white matter damage in SHANK3 deficiency: a human and translational study. *Ann. Clin. Transl. Neurol.* 7, 46–58. doi: 10.1002/acn3.50959

Jiang, Y., and Johnson, G. A. (2009). Microscopic diffusion tensor imaging of the mouse brain. *NeuroImage* 50, 465–471. doi: 10.1016/j.neuroimage.2009.12.057

Jones, D. K. (2004). The effect of gradient sampling schemes on measures derived from diffusion tensor MRI a monte carlo study. *Magn. Reson. Med.* 51, 807–815. doi: 10.1002/mrm.20033

Jucker, M., and Walker, L. C. (2013). Self-propagation of pathogenic protein aggregates in neurodegenerative diseases. *Nature* 501, 45–51. doi: 10.1038/nature12481

Jucker, M., and Walker, L. C. (2018). Propagation and spread of pathogenic protein assemblies in neurodegenerative diseases. *Nat. Neurosci.* 21, 1341–1349. doi: 10.1038/s41593-018-0238-6

Kamnaksh, A., Budde, M. D., Kovesdi, E., Long, J. B., Frank, J. A., and Agoston, D. V. (2014). Diffusion tensor imaging reveals acute subcortical changes after mild blast-induced traumatic brain injury. *Sc.i Rep.* 4:4809. doi: 10.1038/srep04809

Kao, Y. J., Lui, Y. W., Lu, C. F., Chen, H. L., Hsieh, B. Y., and Chen, C. Y. (2019). Behavioral and structural effects of single and repeat closed-head injury. *AJNR Am. J. Neuroradiol.* 40, 601–608. doi: 10.3174/ajnr.A6014

Kassubek, J. (2017). The application of neuroimaging to healthy and diseased brains: present and future. *Front. Neurol.* 8:61. doi: 10.3389/fneur.2017.00061

Kassubek, J., and Müller, H. P. (2016). Computer-based magnetic resonance imaging as a tool in clinical diagnosis in neurodegenerative diseases. *Expert Rev. Neurother.* 16, 295–306. doi: 10.1586/14737175.2016.1146590

Kastyak-Ibrahim, M. Z., Di Curzio, D. L., Buist, R., Herrera, S. L., Albensi, B. C., Del Bigio, M. R., et al. (2013). Neurofibrillary tangles and plaques are not accompanied by white matter pathology in aged triple transgenic-Alzheimer disease mice. *Magn. Reson. Imaging* 31, 1515–1521. doi: 10.1016/j.mri.2013.06.013

Kerbler, G. M., Hamlin, A. S., Pannek, K., Kurniawan, N. D., Keller, M. D., Rose, S. E., et al. (2013). Diffusion-weighted magnetic resonance imaging detection of basal forebrain cholinergic degeneration in a mouse model. *Neuroimage* 66, 133–141. doi: 10.1016/j.neuroimage.2012.10.075

Khairnar, A., Ruda-Kucerova, J., Szabó, N., Drazanova, E., Arab, A., Hutter-Paier, B., et al. (2017). Early and progressive microstructural brain changes in mice overexpressing human α- Synuclein detected by diffusion kurtosis imaging. *Brain Behav. Immun.* 61, 197–208. doi: 10.1016/j.bbi.2016.11.027

Kikinis, Z., Muehlmann, M., Pasternak, O., Peled, S., Kulkarni, P., Ferris, C., et al. (2017). Diffusion imaging of mild traumatic brain injury in the impact accelerated rodent model A pilot study. *Brain Inj.* 31, 1376–1381. doi: 10.1080/02699052.2017.1318450

Kim, H., Cam-Etoz, B., Zhai, G., Hubbard, W. J., Zinn, K. R., and Chaudry, I. H. (2015). Salutary effects of estrogen sulfate for traumatic brain injury. *J. Neurotrauma* 32, 1210–1216. doi: 10.1089/neu.2014.3771

Kim, H., Yu, T., Cam-Etoz, B., van Groen, T., Hubbard, W. J., and Chaudry, I. H. (2017). Treatment of traumatic brain injury with 17α-ethinylestradiol-3-sulfate in a rat model. *J. Neurosurg.* 127, 23–31. doi: 10.3171/2016.7.JNS161263

Kim, J. H., Wu, T. H., Budde, M. D., Lee, J. M., and Song, S. K. (2011). Noninvasive detection of brainstem and spinal cord axonal degeneration in an amyotrophic lateral sclerosis mouse model. *NMR Biomed.* 24, 163–169. doi: 10.1002/nbm.1567

Kinder, H. A., Baker, E. W., Wang, S., Fleischer, C. C., Howerth, E. W., Duberstein, K. J., et al. (2019). Traumatic brain injury results in dynamic brain structure changes leading to acute and chronic motor function deficits in a pediatric piglet model. *J. Neurotrauma* 36, 2930–2942. doi: 10.1089/neu.2018.6303

King, C., Robinson, T., Dixon, C. E., Rao, G. R., Larnard, D., and Nemoto, C. E. (2010). Brain temperature profiles during epidural cooling with the ChillerPad in a monkey model of traumatic brain injury. *J. Neurotrauma* 27, 1895–1903. doi: 10.1089/neu.2009.1178

Knösche, T. R., Anwander, A., Liptrot, M., and Dyrby, T. B. (2015). Validation of tractography: comparison with manganese tracing. *Hum. Brain Mapp.* 36, 4116–4134. doi: 10.1002/hbm.22902

Kong, L., Lian, G., Zheng, W., Liu, H., Zhang, H., and Chen, R. (2013). Effect of alcohol on diffuse axonal injury in rat brainstem: diffusion tensor imaging and aquaporin-4 expression study. *Biomed. Res. Int.* 2013:798261. doi: 10.1155/2013/798261

Kumar, M., Nasrallah, I. M., Kim, S., Ittyerah, R., Pickup, S., Li, J., et al. (2014). High-resolution magnetic resonance microscopy and diffusion tensor imaging to assess brain structural abnormalities in the murine mucopolysaccharidosis VII model. *J. Neuropathol. Exp. Neurol.* 73, 39–49. doi: 10.1097/NEN.0000000000000023

Kunimatsu, A., Aoki, S., Masutani, Y., Abe, O., Hayashi, N., Mori, H., et al. (2004). The optimal trackability threshold of fractional anisotropy for diffusion tensor tractography of the corticospinal tract. *Magn. Reson. Med. Sci.* 3, 11–17. doi: 10.2463/mrms.3.11

Laitinen, T., Sierra, A., Bolkvadze, T., Pitkänen, A., and Gröhn, O. (2015). Diffusion tensor imaging detects chronic microstructural changes in white and gray matter after traumatic brain injury in rat. *Front. Neurosci.* 9:128. doi: 10.3389/fnins.2015.00128

Lee, J. B., Affeldt, B. M., Gamboa, Y., Hamer, M., Dunn, J. F., Pardo, A. C., et al. (2018). Repeated pediatric concussions evoke long-term oligodendrocyte and white matter microstructural dysregulation distant from the injury. *Dev. Neurosci.* 40, 358–375. doi: 10.1159/000494134

Li, H., Liang, Z., Zhang, C., Liu, R., Li, J., Zhang, W., et al. (2020). Deep learning for highly accelerated diffusion tensor imaging. arXiv:2002.01031[eess.IV].

Li, S., Sun, Y., Shan, D., Feng, B., Xing, J., Duan, Y., et al. (2013). Temporal profiles of axonal injury following impact acceleration traumatic brain injury in rats–a comparative study with diffusion tensor imaging and morphological analysis. *Int. J. Legal. Med.* 127, 159–167. doi: 10.1007/s00414-012-0712-8

Li, W., Long, J. A., Watts, L., Shen, Q., Liu, Y., Jang, Z., et al. (2016). Spatiotemporal changes in diffusion, T2 and susceptibility of white matter following mild traumatic brain injury. *NMR Biomed.* 29, 896–903. doi: 10.1002/nbm.3536

Liu, C., Ye, F. Q., Newman, J. D., Szczupak, D., Tian, X., Yen, C. C., et al. (2020). A resource for the detailed 3D mapping of white matter pathways in the marmoset brain. *Nat. Neurosci.* 23, 271–280. doi: 10.1038/s41593-019-0575-0

Liu, C., Ye, F. Q., Yen, C. C., Glen, D., Leopold, D. A., and Silva, A. C. (2018). A digital 3D atlas of the marmoset brain based on multi-modal MRI. *Neuroimage* 169, 106–116. doi: 10.1016/j.neuroimage.2017.12.004

Liu, L., Liu, Y., Li, N., Huang, R., Zheng, X., Huang, L., et al. (2020). Multiple inflammatory profiles of microglia and altered neuroimages in APP/PS1 transgenic AD mice. *Brain Res. Bull.* 156, 86–104. doi: 10.1016/j.brainresbull.2020.01.003

Liu, L. X., Du, D., Wang, Z. Q., Fang, Y., Zheng, T., Dong, Y. C., et al. (2018). Differences in brain pathological changes between rotenone and 6-hydroxydopamine parkinson's disease models. *Neural. Regen. Res.* 13, 1276–1280. doi: 10.4103/1673-5374.235076

Liu, Z., Wang, Y., Gerig, G., Gouttard, S., Tao, R., Fletcher, T., et al. (2010). Quality control of diffusion weighted images. *Proc. SPIE. Int. Soc. Opt. Eng.* 7628:76280J. doi: 10.1117/12.844748

Lodygensky, G. A., West, T., Stump, M., Holtzman, D. M., Inder, T. E., and Neil, J. J. (2010). *In vivo* MRI analysis of an inflammatory injury in the developing brain. *Brain Behav. Immun.* 24, 759–767. doi: 10.1016/j.bbi.2009.11.005

Long, J. A., Watts, L. T., Chemello, J., Huang, S., Shen, Q., and Duong, T. Q. (2015). Multiparametric and longitudinal MRI characterization of mild traumatic brain injury in rats. *J. Neurotrauma* 32, 598–607. doi: 10.1089/neu.2014.3563

Ma, Z., Zhang, Y. P., Liu, W., Yan, G., Li, Y., Shields, L. B. E., et al. (2016). A controlled spinal cord contusion for the rhesus macaque monkey. *Exp. Neurol.* 279, 261–273. doi: 10.1016/j.expneurol.2016.02.008

Mac Donald, C. L., Dikranian, K., Bayly, P., Holtzman, D., and Brody, D. (2007a). Diffusion tensor imaging reliably detects experimental traumatic axonal injury and indicates approximate time of injury. *J. Neurosci.* 27, 11869–11876. doi: 10.1523/JNEUROSCI.3647-07.2007

Mac Donald, C. L., Dikranian, K., Song, S. K., Bayly, P. V., Holtzman, D. M., and Brody, D. L. (2007b). Detection of traumatic axonal injury with diffusion tensor imaging in a mouse model of traumatic brain injury. *Exp. Neurol.* 205, 116–131. doi: 10.1016/j.expneurol.2007.01.035

Maier-Hein, K. H., Neher, P. F., Houde, J. C., Côté, M. A., Garyfallidis, E., Zhong, J., et al. (2017). The challenge of mapping the human connectome based on diffusion tractography. *Nat. Commun.* 8:1349. doi: 10.1038/s41467-017-01285-x

Majka, P., Bai, S., Bakola, S., Bednarek, S., Chan, J. M., Jermakow, N., et al. (2020). Open access resource for cellular-resolution analyses of corticocortical connectivity in the marmoset monkey. *Nat. Commun.* 11:1133. doi: 10.1038/s41467-020-14858-0

Manno, F. A. M., Isla, A. G., Manno, S. H. C., Ahmed, I., Cheng, S. H., Barrios, F. A., et al. (2019). Early stage alterations in white Matter and decreased functional interhemispheric hippocampal connectivity in the 3xTg mouse model of alzheimer's disease. *Front. Aging Neurosci.* 11:39. doi: 10.3389/fnagi.2019.00039

Marcuzzo, S., Bonanno, S., Figini, M., Scotti, A., Zucca, I., Minati, L., et al. (2017). A longitudinal DTI and histological study of the spinal cord reveals early pathological alterations in G93A-SOD1 mouse model of amyotrophic lateral sclerosis. *Exp. Neurol.* 293, 43–52. doi: 10.1016/j.expneurol.2017.03.018

Marrale, M., Collura, G., Brai, M., Toschi, N., Midiri, F., La Tona, G., et al. (2016). Physics techniques and review of neuroradiological applications of diffusion kurtosis imaging (DKI). *Clin. Neuroradiol.* 26, 391–403. doi: 10.1007/s00062-015-0469-9

Masdeu, J. C. (2017). Future directions in imaging neurodegeneration. *Curr. Neurol. Neurosci. Rep.* 17:9. doi: 10.1007/s11910-017-0718-1

Mattiello, J., Basser, P. J., and Lebihan, D. (1994). Analytical expressions for the b matrix in NMR diffusion imaging and spectroscopy. *J. Magn. Reson. A.* 108:131–141.

Mayer, D., Zahr, N. M., Adalsteinsson, E., Rutt, B., Sullivan, E. V., and Pfefferbaum, A. (2007). *In vivo* fiber tracking in the rat brain on a clinical 3T MRI system using a high strength insert gradient coil. *Neuroimage* 35, 1077–1085. doi: 10.1016/j.neuroimage.2007.01.006

Medina, D. L., Settembre, C., and Ballabio, A. (2017). Methods to monitor and manipulate TFEB activity during autophagy. *Methods Enzymol.* 588, 61–78. doi: 10.1016/bs.mie.2016.10.008

Meng, Y., Hu, X., Zhang, X., and Bachevalier, J. (2018). Diffusion tensor imaging reveals microstructural alterations in corpus callosum and associated transcallosal fiber tracts in adult macaques with neonatal hippocampal lesions. *Hippocampus* 28, 838–845. doi: 10.1002/hipo.23006

Météreau, E., Beaudoin-Gobert, M., Duperrier, S., Thobois, S., Tremblay, L., and Sgambato-Faure, V. (2018). Diffusion tensor imaging marks dopaminergic and serotonergic lesions in the Parkinsonian monkey. *Mov. Disord.* 33, 298–309. doi: 10.1002/mds.27201

Missault, S., Anckaerts, C., Blockx, I., Deleye, S., Van Dam, D., Barriche, N., et al. (2019). Neuroimaging of subacute brain inflammation microstructural changes predicts long-term functional outcome after experimental traumatic brain injury. *J. Neurotrauma* 36, 768–788. doi: 10.1089/neu.2018.5704

Mohamed, A. Z., Corrigan, F., Collins-Praino, L. E., Plummer, S. L., Soni, N., and Nasrallah, F. A. (2020). Evaluating spatiotemporal microstructural alterations following diffuse traumatic brain injury. *Neuroimage Clin.* 25:102136. doi: 10.1016/j.nicl.2019.102136

Mori, S., and van Zijl, P. C. M. (2002). Fiber tracking: principles and strategies - a technical review. *NMR Biomed*. 15, 468–480. doi: 10.1002/nbm.781

Müller, H.-P., Kassubek, J., Vernikouskaya, I., Ludolph, A. C., Stiller, D., and Rasche, V. (2013). Diffusion tensor magnetic resonance imaging of the brain in APP transgenic mice: a cohort study. *PLoS ONE* 8:e67630. doi: 10.1371/journal.pone.0067630

Müller, H.-P., Unrath, A., Huppertz, H.-J., Ludolph, A. C., and Kassubek, J. (2012b). Neuroanatomical patterns of cerebral white matter involvement in different motor neuron diseases as studied by diffusion tensor imaging analysis. *Amyotroph. Lateral Scler*. 13, 254–264. doi: 10.3109/17482968.2011.653571

Müller, H.-P., Unrath, A., Sperfeld, A. D., Ludolph, A. C., Riecker, A., and Kassubek, J. (2007). Diffusion tensor imaging and tractwise fractional anisotropy statistics: quantitative analysis in white matter pathology. *Biomed. Eng.* 6:42. doi: 10.1186/1475-925X-6-42

Müller, H.-P., Vernikouskaya, I., Ludolph, A. C., Kassubek, J., and Rasche, V. (2012a). Fast diffusion tensor magnetic resonance imaging of the mouse brain at ultrahigh-field: aiming at cohort studies. *PLoS ONE* 7:e53389. doi: 10.1371/journal.pone.0053389

Müller, H. P., Brenner, D., Roselli, F., Wiesner, D., Abaei, A., and Gorges, M. (2019). Longitudinal diffusion tensor magnetic resonance imaging analysis at the cohort level reveals disturbed cortical and callosal microstructure with spared corticospinal tract in the TDP-43G298S ALS mouse model. *Transl. Neurodegener.* 8:27. doi: 10.1186/s40035-019-0163-y

Müller, H. P., and Kassubek, J. (2018). MRI-Based mapping of cerebral propagation in amyotrophic lateral sclerosis. *Front. Neurosci.* 12:655. doi: 10.3389/fnins.2018.00655

Nair, G., Tanahashi, Y., Low, H. P., Billings-Gagliardi, S., Schwartz, W. J., and Duong, T. Q. (2005). Myelination and long diffusion times alter diffusion-tensor-imaging contrast in myelin-deficient shiverer mice. *Neuroimage*. 28, 165–174. doi: 10.1016/j.neuroimage.2005.05.049

Nikolian, V. C., Georgoff, P. E., Pai, M. P., Dennahy, I. S., Chtraklin, K., Eidy, H., et al. (2017). Valproic acid decreases brain lesion size and improves neurologic recovery in swine subjected to traumatic brain injury, hemorrhagic shock, and polytrauma. *J. Trauma Acute Care Surg*. 83, 1066–1073. doi: 10.1097/TA.0000000000001612

Nishioka, C., Liang, H. F., Barsamian, B., and Sun, S. W. (2019). Amyloid-beta induced retrograde axonal degeneration in a mouse tauopathy model. *Neuroimage* 189, 180–191. doi: 10.1016/j.neuroimage.2019.01.007

Nouls, J. C., Badea, A., Anderson, R. B. J., Cofer, G. P., and Allan Johnson, G. (2018). Diffusion tensor imaging using multiple coils for mouse brain connectomics. *NMR Biomed*. 31:e3921. doi: 10.1002/nbm.3921

Oguz, I., Farzinfar, M., Matsui, J., Budin, F., Liu, Z., Gerig, G., et al. (2014). DTIPrep: quality control of diffusion-weighted images. *Front. Neuroinform.* 8:4. doi: 10.3389/fninf.2014.00004

Oguz, I., McMurray, M. S., Styner, M., and Johns, J. M. (2012). The translational role of diffusion tensor image analysis in animal models of developmental pathologies. *Dev. Neurosci.* 34, 5–19. doi: 10.1159/000336825

Oh, S. W., Harris, J. A., Ng, L., Winslow, B., Cain, N., Mihalas, S., et al. (2014). A mesoscale connectome of the mouse brain. *Nature*. 508, 207–214. doi: 10.1038/nature13186

Okano, H., and Mitra, P. (2015). Brain-mapping projects using the common marmoset. *Neurosci. Res.* 93, 3–7. doi: 10.1016/j.neures.2014.08.014

Ozarslan, E., and Mareci, T. H. (2003). Generalized diffusion tensor imaging and analytical relationships between diffusion tensor imaging and high angular resolution diffusion imaging. *Magn. Reson. Med.* 50, 955–965. doi: 10.1002/mrm.10596

Pajevic, S., and Pierpaoli, C. (1999). Color schemes to represent the orientation of anisotropic tissues from diffusion tensor data: application to white matter fiber tract mapping in the human brain. *Magn. Reson. Med.* 42, 526–540. doi: 10.1002/(SICI)1522-2594(199909)42:3<526::AID-MRM15>3.0.CO;2-J

Palazzi, X., and Bordier, N. (2008). *The Marmoset Brain in Stereotaxic Coordinates.* New York, NY: Springer. doi: 10.1007/978-0-387-78385-7

Panic, N., Leoncini, E., de Belvis, G., Ricciardi, W., and Boccia, S. (2013). Evaluation of the endorsement of the preferred reporting items for systematic reviews and meta-analysis (PRISMA) statement on the quality of published systematic review and meta-analyses. *PLoS ONE* 8:e83138. doi: 10.1371/journal.pone.0083138

Parent, M., Chitturi, J., Santhakumar, V., Hyder, F., Sanganahalli, B. G., and Kannurpatti, S. S. (2020). Kaempferol treatment after traumatic brain injury during early development mitigates brain parenchymal microstructure neural functional connectivity deterioration at adolescence. *J Neurotrauma*. 37:966-974. doi: 10.1089/neu.2019.6486

Paxinos, G., and Franklin, K. B. J. (2007). *The mouse brain in stereotaxic coordinates. 3rd Edn.* New York, NY: Academic press; Elsevier

Paxinos, G., and Watson, C. (2013). *The Rat Brain in Stereotaxic Coordinates. 7th Edn*. New York, NY: Academic Press; Elsevier.

Perlbarg, V., Lambert, J., Butler, B., Felfli, M., Valabrègue, R., Privat, A. L., et al. (2018). Alterations of the nigrostriatal pathway in a 6-OHDA rat model of parkinson's disease evaluated with multimodal MRI. *PLoS ONE* 13:e0202597. doi: 10.1371/journal.pone.0202597

Petrella, L. I., Castelhano, J. M., Ribeiro, M., Sereno, J. V., Gonçalves, S. I., Laço, M. N., et al. (2018). A whole brain longitudinal study in the YAC128 mouse model of Huntington's disease shows distinct trajectories of neurochemical, structural connectivity and volumetric changes. *Hum. Mol. Genet.* 27, 2125–2137. doi: 10.1093/hmg/ddy119

Pierpaoli, C., and Basser, P. J. (1996). Toward a quantitative assessment of diffusion anisotropy. *Magn. Reson. Med.* 36, 893–906. doi: 10.1002/mrm.1910360612

Pischiutta, F., Micotti, E., Hay, J. R., Marongiu, I., Sammali, E., Tolomeo, D., et al. (2018). Single severe traumatic brain injury produces progressive pathology with ongoing contralateral white matter damage one year after injury. *Exp. Neurol.* 300, 167–178. doi: 10.1016/j.expneurol.2017.11.003

Politis, M. (2014). Neuroimaging in parkinson disease: from research setting to clinical practice. *Nat. Rev. Neurol.* 10, 708–722. doi: 10.1038/nrneurol.2014.205

PRIMatE Data Exchange (PRIME-DE) Global Collaboration Workshop and Consortium. (2020). Accelerating the evolution of nonhuman primate neuroimaging. *Neuron* 105, 600–603. doi: 10.1016/j.neuron.2019.12.023

Qin, Y., Li, G. L., Xu, X. H., Sun, Z. Y., Gu, J. W., and Gao, F. B. (2018). Brain structure alterations and cognitive impairment following repetitive mild head impact: an *in vivo* MRI behavioral study in rat. *Behav. Brain. Res.* 340, 41–48. doi: 10.1016/j.bbr.2016.08.008

Qin, Y. Y., Li, M. W., Zhang, S., Zhang, Y., Zhao, L. Y., Lei, H., et al. (2013). *In vivo* quantitative whole-brain diffusion tensor imaging analysis of APP/PS1 transgenic mice using voxel-based and atlas-based methods. *Neuroradiology* 55, 1027–1038. doi: 10.1007/s00234-013-1195-0

Ratering, D., Baltes, C., Nordmeyer-Massner, J., Marek, D., and Rudin, M. (2008). Performance of a 200-MHz cryogenic RF probe designed for MRI and MRS of the murine brain. *Magn. Reson. Med.* 59, 1440–1447. doi: 10.1002/mrm.21629

Rilling, J. K., and van den Heuvel, M. P. (2018). Comparative primate connectomics. *Brain Brain Behav. Evol.* 91, 170–179. doi: 10.1159/000488886

Risser, L., Sadoun, A., Mescam, M., Strelnikov, K., Lebreton, S., Boucher, S., et al. (2019). *In vivo* localization of cortical areas using a 3D computerized atlas of the marmoset brain. *Brain Struct. Funct.* 224, 1957–1969. doi: 10.1007/s00429-019-01869-x

Robinson, S., Berglass, J. B., Denson, J. L., Berkner, J., Anstine, C. V., Winer, J. L., et al. (2017). Microstructural and microglial changes after repetitive mild traumatic brain injury in mice. *J. Neurosci. Res.* 95, 1025–1035. doi: 10.1002/jnr.23848

Robinson, S., Winer, J. L., Berkner, J., Chan, L. A., Denson, J. L., Maxwell, J. R., et al. (2016). Imaging and serum biomarkers reflecting the functional efficacy of extended erythropoietin treatment in rats following infantile traumatic brain injury. *J. Neurosurg. Pediatr.* 17, 739–755. doi: 10.3171/2015.10.PEDS15554

Robinson, S., Winer, J. L., Chan, L. A. S., Oppong, A. Y., Yellowhair, T. R., Maxwell, J. R., et al. (2018). Extended erythropoietin treatment prevents chronic executive functional and microstructural deficits following early severe traumatic brain injury in rats. *Front. Neurol.* 9:451. doi: 10.3389/fneur.2018.00451

Rodriguez-Grande, B., Obenaus, A., Ichkova, A., Aussudre, J., Bessy, T., Barse, E., et al. (2018). Gliovascular changes precede white matter damage and long-term disorders in juvenile mild closed head injury. *Glia*. 66, 1663–1677. doi: 10.1002/glia.23336

Rubovitch, V., Ten-Bosch, M., Zohar, O., Harrison, C. R., Tempel-Brami, C., Stein, E., et al. (2011). A mouse model of blast-induced mild traumatic brain injury. *Exp. Neurol.* 232, 280–289. doi: 10.1016/j.expneurol.2011.09.018

Rumple, A., McMurray, M., Johns, J., Lauder, J., Makam, P., Radcliffe, M., et al. (2013). 3-dimensional diffusion tensor imaging (DTI) atlas of the rat brain. *PLoS ONE* 8:e67334. doi: 10.1371/journal.pone.0067334

Sahara, N., Perez, P. D., Lin, W. L., Dickson, D. W., Ren, Y., Zeng, H., et al. (2014). Age-related decline in white matter integrity in a mouse model of tauopathy: an *in vivo* diffusion tensor magnetic resonance imaging study. *Neurobiol. Aging* 35, 1364–1374. doi: 10.1016/j.neurobiolaging.2013.12.009

Sampaio-Baptista, C., Diosi, K., and Johansen-Berg, H. (2019). Magnetic resonance techniques for imaging white. Matter. *Methods Mol. Biol.* 1936, 397–407. doi: 10.1007/978-1-4939-9072-6_22

Sampaio-Baptista, C., and Johansen-Berg, H. (2017). White matter plasticity in the adult brain. *Neuron* 96, 1239–1251. doi: 10.1016/j.neuron.2017.11.026

Sampaio-Baptista, C., Vallès, A., Khrapitchev, A. A., Akkermans, G., Winkler, A. M., Foxley, S., et al. (2020). White matter structure and myelin-related gene expression alterations with experience in adult rats. *Prog Neurobiol.* 187:101770. doi: 10.1016/j.pneurobio.2020.101770

San Martín Molina, I., Salo, R. A., Abdollahzadeh, A., Tohka, J., Gröhn, O., and Sierra, A. (2020). *In vivo* diffusion tensor imaging in acute and subacute phases of mild traumatic brain injury in rats. *eNeuro* 7:ENEURO.0476-19.2020. doi: 10.1523/ENEURO.0476-19.2020

Schober, M. E., Requena, D. F., Abdullah, O. M., Casper, T. C., Beachy, J., Malleske, D., et al. (2016). Dietary docosahexaenoic acid improves cognitive function tissue sparing magnetic resonance imaging indices of edema and white matter injury in the immature rat after traumatic brain injury. *J. Neurotrauma* 33, 390–402. doi: 10.1089/neu.2015.3945

Shen, Z., Lei, J., Li, X., Wang, Z., Bao, X., and Wang, R. (2018). Multifaceted assessment of the APP/PS1 mouse model for alzheimer's disease: applying MRS DTI. *ASL Brain Res.* 1698, 114–120. doi: 10.1016/j.brainres.2018.08.001

Shepherd, T. M., Ozarslan, E., King, M. A., Mareci, T. H., and Blackband, S. J. (2006). Structural insights from high-resolution diffusion tensor imaging and tractography of the isolated rat hippocampus. *Neuroimage* 32, 1499–1509. doi: 10.1016/j.neuroimage.2006.04.210

Shi, X., Ma, X., Wu, W., Huang, F., Yuan, C., and Guo, H. (2015). Parallel imaging and compressed sensing combined framework for accelerating high-resolution diffusion tensor imaging using inter-image correlation. *Magn. Reson. Med.* 73, 1775–1785. doi: 10.1002/mrm.25290

Shibata, S., Komaki, Y., Seki, F., Inouye, M. O., Nagai, T., and Okano, H. (2015). Connectomics: comprehensive approaches for whole-brain mapping. *Microscopy (Oxf)* 64, 57–67. doi: 10.1093/jmicro/dfu103

Shimony, J. S., Rutlin, J., Karimi, M., Tian, L., Snyder, A. Z., Loftin, S. K., et al. (2018). Validation of diffusion tensor imaging measures of nigrostriatal neurons in macaques. *PLoS ONE* 13:e0202201. doi: 10.1371/journal.pone.0202201

Shu, X., Qin, Y. Y., Zhang, S., Jiang, J. J., Zhang, Y., Zhao, L. Y., et al. (2013). Voxel-based diffusion tensor imaging of an APP/PS1 mouse model of alzheimer's disease. *Mol. Neurobiol.* 48, 78–83. doi: 10.1007/s12035-013-8418-6

Shultz, S. R., Wright, D. K., Zheng, P., Stuchbery, R., Liu, S. J., Sashindranath, M., et al. (2015). Sodium selenate reduces hyperphosphorylated tau and improves outcomes after traumatic brain injury. *Brain* 138, 1297–1313. doi: 10.1093/brain/awv053

Sierra, A., Laitinen, T., Lehtimäki, K., Rieppo, L., Pitkänen, A., and Gröhn, O. (2011). Diffusion tensor MRI with tract-based spatial statistics and histology reveals undiscovered lesioned areas in kainate model of epilepsy in rat. *Brain Struct. Funct.* 216, 123–135. doi: 10.1007/s00429-010-0299-0

Simchick, G., Shen, A., Campbell, B., Park, H. J., West, F. D., and Zhao, Q. (2019). Pig brains have homologous resting-state networks with human brains. *Brain Connect.* 9, 566–579. doi: 10.1089/brain.2019.0673

Singh, K., Trivedi, R., Devi, M. M., Tripathi, R. P., and Khushu, S. (2016). Longitudinal changes in the DTI measures, anti-GFAP expression and levels of serum inflammatory cytokines following mild traumatic brain injury. *Exp. Neurol. 275,* 427–435. doi: 10.1016/j.expneurol.2015.07.016

Sinke, M. R. T., Otte, W. M., Christiaens, D., Schmitt, O., Leemans, A., van der Toorn, A., et al. (2018). Diffusion MRI-based cortical connectome reconstruction: dependency on tractography procedures and neuroanatomical characteristics. *Brain Struct. Funct.* 223, 2269–2285. doi: 10.1007/s00429-018-1628-y

Smith, S. M., Jenkinson, M., Johansen-Berg, H., Rueckert, D., Nichols, T. E., Mackay, C. E., et al. (2006). Tract-based spatial statistics: voxelwise analysis of multi-subject diffusion data. *Neuroimage* 31, 1487–1505. doi: 10.1016/j.neuroimage.2006.02.024

Snow, W. M., Dale, R., O'Brien-Moran, Z., Buist, R., Peirson, D., Martin, M., et al. (2017). *In vivo* Detection of gray matter neuropathology in the 3xTg mouse model of alzheimer's disease with diffusion tensor imaging. *J. Alzheimers Dis.* 58, 841–853. doi: 10.3233/JAD-170136

Song, S. K., Kim, J. H., Lin, S. J., Brendza, R. P., and Holtzman, D. M. (2004). Diffusion tensor imaging detects age-dependent white matter changes in a transgenic mouse model with amyloid deposition. *Neurobiol. Dis.* 15, 640–647. doi: 10.1016/j.nbd.2003.12.003

Song, S. K., Yoshino, J., Le, T. Q., Lin, S.-J., Sun, S.-W., Cross, A. H., et al. (2005). Demyelination increases radial diffusivity in corpus callosum of mouse brain. *Neuroimage* 26, 132–140. doi: 10.1016/j.neuroimage.2005.01.028

Soni, N., Mohamed, A. Z., Kurniawan, N. D., Borges, K., and Nasrallah, F. (2019). Diffusion magnetic resonance imaging unveils the spatiotemporal microstructural gray matter changes following injury in the rodent brain, *J. Neurotrauma* 36, 1306–1317. doi: 10.1089/neu.2018.5972

Stern, R. A., Adler, C. H., Chen, K., Navitsky, M., Luo, J., Dodick, D. W., et al. (2019). Tau positron-emission tomography in former national football league players. *N. Engl. J. Med*. 380, 1716–1725. doi: 10.1056/NEJMoa1900757

Sun, S. W., Liang, H. F., Mei, J., Xu, D., and Shi, W. X. (2014). In vivo diffusion tensor imaging of amyloid-Œ≤-induced white matter damage in mice. *J. Alzheimers Dis*. 38, 93–101. doi: 10.3233/JAD-130236

Sun, S. W., Song, S. K., Harms, M. P., Lin, S. J., Holtzman, D. M., Merchant, K. M., et al. (2005). Detection of age-dependent brain injury in a mouse model of brain amyloidosis associated with Alzheimer's disease using magnetic resonance diffusion tensor imaging. *Exp. Neurol*. 191, 77–85. doi: 10.1016/j.expneurol.2004.09.006

Takeuchi, S., Nawashiro, H., Sato, S., Kawauchi, S., Nagatani, K., Kobayashi, H., et al. (2013). A better mild traumatic brain injury model in the rat. *Acta Neurochir. Suppl*. 118, 99–101. doi: 10.1007/978-3-7091-1434-6_17

Tan, X. L., Wright, D. K., Liu, S., Hovens, C., O'Brien, T. J., and Shultz, S. R. (2016). Sodium selenate, a protein phosphatase 2A activator, mitigates hyperphosphorylated tau and improves repeated mild traumatic brain injury outcomes. *Neuropharmacology* 108, 382–393. doi: 10.1016/j.neuropharm.2016.05.001

Tang, S., Xu, S., Fourney, W. L., Leiste, U. H., Proctor, J. L., Fiskum, G., et al. (2017). Central nervous system changes induced by underbody blast-induced hyperacceleration: an *in vivo* diffusion tensor imaging magnetic resonance spectroscopy study. *J. Neurotrauma*. 34, 1972–1980. doi: 10.1089/neu.2016.4650

Totenhagen, J. W., Lope-Piedrafita, S., Borbon, I. A., Yoshimaru, E. S., Erickson, R. P., and Trouard, T. P. (2012). *In vivo* assessment of neurodegeneration in niemann-pick type C mice by quantitative T2 mapping and diffusion tensor imaging. *J. Magn. Reson. Imaging*. 35, 528–536. doi: 10.1002/jmri.22837

Tu, T. W., Williams, R. A., Lescher, J. D., Jikaria, N., Turtzo, L. C., and Frank, J. A. (2016). Radiological-pathological correlation of diffusion tensor and magnetization transfer imaging in a closed head traumatic brain injury model. *Ann. Neurol*. 79, 907–920. doi: 10.1002/ana.24641

Tuch, D. S. (2004). Q–ball imaging. *Magn. Reson. Med*. 52, 1358–1372. doi: 10.1002/mrm.20279

Ueda, H. R., Ertürk, A., Chung, K., Gradinaru, V., Chédotal, A., Tomancak, P., et al. (2020). Tissue clearing and its applications in neuroscience. *Nat. Rev. Neurosci*. 21, 61–79. doi: 10.1038/s41583-019-0250-1

Ugrumov, M. V., Khaindrava, V. G., Kozina, E. A., Kucheryanu, V. G., Bocharov, E. V., Kryzhanovsky, G. N., et al. (2011). Modeling of presymptomatic and symptomatic stages of parkinsonism in mice. *Neuroscience*. 181, 175–188. doi: 10.1016/j.neuroscience.2011.03.007

Underwood, C. K., Kurniawan, N. D., Butler, T. J., Cowin, G. J., and Wallace, R. H. (2011). Non-invasive diffusion tensor imaging detects white matter degeneration in the spinal cord of a mouse model of amyotrophic lateral sclerosis. *Neuroimage* 55, 455–461. doi: 10.1016/j.neuroimage.2010.12.044

van Camp, N., Blockx, I., Verhoye, M., Casteels, C., Coun, F., Leemans, A., et al. (2009). Diffusion tensor imaging in a rat model of Parkinson's disease after lesioning of the nigrostriatal tract. *NMR Biomed*. 22, 697–706. doi: 10.1002/nbm.1381

Venkatasubramanian, P. N., Pina-Crespo, J. C., Mathews, K., Rigby, P. H., Smith, M., Duckworth, J. L., et al. (2020). Initial biphasic fractional anisotropy response to blast-induced mild traumatic brain injury in a mouse model. *Mil. Med*. 185, 243–247. doi: 10.1093/milmed/usz307

Wang, M. L., Yu, M. M., Yang, D. X., Liu, Y. L., Wei, X. E., and Li, W. B. (2018). Longitudinal microstructural changes in traumatic brain injury in rats: a diffusional kurtosis imaging histology and behavior study. *AJNR Am. J. Neuroradiol*. 39, 1650–1656. doi: 10.3174/ajnr.A5737

Wang, N., Zhang, J., Cofer, G., Qi, Y., Anderson, R. J., White, L. E., et al. (2019). Neurite orientation dispersion and density imaging of mouse brain microstructure. *Brain Struct. Funct*. 224, 1797–1813. doi: 10.1007/s00429-019-01877-x

Weiss, C., Lendacki, F. R., Rigby, P. H., Wyrwicz, A. M., Disterhoft, J. F., and Spiess, J. (2020). Conditioned contextual freezing is a neurobehavioral biomarker of axonal injury indicated by reduced fractional anisotropy in a mouse model of blast-induced mild traumatic brain injury. *Shock* 53, 744–753. doi: 10.1097/SHK.0000000000001424

Wells, J. A., O'Callaghan, J. M., Holmes, H. E., Powell, N. M., Johnson, R. A., Siow, B., et al. (2015). *In vivo* imaging of tau pathology using multi-parametric quantitative MRI. *Neuroimage* 111, 369–378. doi: 10.1016/j.neuroimage.2015.02.023

Wendel, K. M., Lee, J. B., Affeldt, B. M., Hamer, M., Harahap-Carillo, I. S., Pardo, A. C., et al. (2018). Corpus callosum vasculature predicts white matter microstructure abnormalities after pediatric mild traumatic brain injury. *J. Neurotrauma* 36:5670. doi: 10.7591/9781501711046-011

Whittaker, H. T., Zhu, S., Di Curzio, D. L., Buist, R., Li, X. M., Noy, S., et al. (2018). T(1), diffusion tensor, and quantitative magnetization transfer imaging of the hippocampus in an Alzheimer's disease mouse model. *Magn. Reson. Imaging*. 50, 26–37. doi: 10.1016/j.mri.2018.03.010

Wortman, R. C., Meconi, A., Neale, K. J., Brady, R. D., McDonald, S. J., Christie, B. R., et al. (2018). Diffusion MRI abnormalities in adolescent rats given repeated mild traumatic brain injury. *Ann. Clin. Transl. Neurol*. 5, 1588–1598. doi: 10.1002/acn3.667

Wright, D. K., O'Brien, T. J., Mychasiuk, R., and Shultz, S. R. (2018). Telomere length and advanced diffusion MRI as biomarkers for repetitive mild traumatic brain injury in adolescent rats. *Neuroimage Clin*. 18, 315–324. doi: 10.1016/j.nicl.2018.01.033

Wright, D. K., Trezise, J., Kamnaksh, A., Bekdash, R., Johnston, L. A., Ordidge, R., et al. (2016). Behavioral, blood, and magnetic resonance imaging biomarkers of experimental mild traumatic brain injury. *Sci Rep*. 6:28713. doi: 10.1038/srep28713

Wu, D., Xu, J., McMahon, M. T., van Ziojl, P. C. M., Mori, S., Northington, F. J., et al. (2013). In vivo high-resolution diffusion tensor imaging of the mouse brain. *Neuroimage* 83, 18–26. doi: 10.1016/j.neuroimage.2013.06.012

Wu, Y. C., Field, A. S., and Alexander, A. L. (2008). Computation of diffusion function measures in q-space using magnetic resonance hybrid diffusion imaging, *IEEE Trans. Med. Imaging*. 27, 858–865. doi: 10.1109/TMI.2008.922696

Wu, Y. C., Field, A. S., Duncan, I. D., Samsonov, A. A., Kondo, Y., Tudorascu, D., et al. (2011). High b-value and diffusion tensor imaging in a canine model of dysmyelination and brain maturation. *Neuroimage* 58, 829–837. doi: 10.1016/j.neuroimage.2011.06.067

Wu, Y. C., Mustafi, S. M., Harezlak, J., Kodiweera, C., Flashman, L. A., and McAllister, T. W. (2018). Hybrid diffusion imaging in mild traumatic brain injury, *J. Neurotrauma*. 35, 2377–2390. doi: 10.1089/neu.2017.5566

Xia, Y., Pu, H., Leak, R. K., Shi, Y., Mu, H., Hu, X., et al. (2018). Tissue plasminogen activator promotes white matter integrity and functional recovery in a murine model of traumatic brain injury. *Proc. Natl. Acad. Sci. U.S.A*. 115, E9230–E9238. doi: 10.1073/pnas.1810693115

Yin, Y., Li, E., Sun, G., Yan, H. Q., Foley, L. M., Andrejczuk, L. A., et al. (2018). Effects of, DHA on hippocampal autophagy and lysosome function after traumatic brain injury. *Mol. Neurobiol*. 55, 2454–2470. doi: 10.1007/s12035-017-0504-8

Young, J. T., Shi, Y., Niethammer, M., Grauer, M., Coe, C. L., Lubach, G. R., et al. (2017). The UNC-wisconsin rhesus macaque neurodevelopment database: a structural MRI and DTI database of early postnatal development. *Front. Neurosci*. 11:29. doi: 10.3389/fnins.2017.00029

Yu, F., Shukla, D. K., Armstrong, R. C., Marion, C. M., Radomski, K. L., Selwyn, R. G., et al. (2017). Repetitive model of mild traumatic brain injury produces cortical abnormalities detectable by magnetic resonance diffusion imaging histopathology and behavior. *J. Neurotrauma* 34, 1364–1381. doi: 10.1089/neu.2016.4569

Yu, M., Wang, M., Yang, D., Wei, X., and Li, W. (2019). Dynamics of blood brain barrier permeability and tissue microstructure following controlled cortical impact injury in rat: a dynamic contrast-enhanced magnetic resonance imaging and diffusion kurtosis imaging study. *Magn. Reson. Imaging*. 62, 1–9. doi: 10.1016/j.mri.2019.01.017

Zerbi, V., Kleinnijenhuis, M., Fang, X., Jansen, D., Veltien, A., van Asten, J., et al. (2013). Gray and white matter degeneration revealed by diffusion in an alzheimer mouse model. *Neurobiol. Aging*. 34, 1440–1450. doi: 10.1016/j.neurobiolaging.2012.11.017

Zhang, D., Guo, L., Zhu, D., Li, K., Li, L., Chen, H., et al. (2013). Diffusion tensor imaging reveals evolution of primate brain architectures. *Brain Struct. Funct.* 218, 1429–1450. doi: 10.1007/s00429-012-0468-4

Zhang, J., Rs, L. J., Yarowsky, P., Huang, H., van Zijl, P., and Mori, S. (2003). Three dimensional anatomical characterization of the developing mouse brain by diffusion tensor microimaging. *NeuroImage*. 20, 1639–1648. doi: 10.1016/S1053-8119(03)00410-5

Zhang, R. Z., Tao, C. Y., Chen, W., Wang, C. H., Hu, Y., Song, L., et al. (2016). Dynamic Diffusion tensor imaging reveals structural changes in the bilateral pyramidal tracts after brain stem hemorrhage in rats. *Front. Neuroanat.* 10:33. doi: 10.3389/fnana.2016.00033

Zhang, W., Zhang, L., Liu, L., and Wang, X. (2017). Time course study of fractional anisotropy in the substantia nigra of a parkinsonian rat model induced by 6-OHDA. *Behav Brain Res*. 328, 130–137. doi: 10.1016/j.bbr.2017.03.046

Zhang, X., Kirsch, J. E., and Zhong, X. (2016). Artifact correction in diffusion, MRI of non-human primate brains on a clinical 3T scanner. *J. Med. Primatol*. 45, 21–27. doi: 10.1111/jmp.12204

Zhang, X., Tong, F., Li, C. X., Yan, Y., Kempf, D., Nair, G., et al. (2015). Temporal evolution of ischemic lesions in nonhuman primates: a diffusion and perfusion MRI study. *PLoS ONE* 10:e0117290. doi: 10.1371/journal.pone.0117290

Zhao, S., Todorov, M. I., Cai, R., Maskari, R. A., Steinke, H., Kemter, E., et al. (2020). Cellular and molecular probing of intact human organs. *Cell* 180, 796–812.e19. doi: 10.1016/j.cell.2020.01.030

Zhao, X., Hui, E., Chan, K., Cai, K., Guo, H., Lai, P., et al. (2008). Identifying rodent olfactory bulb structures with micro-DTI. *Conf. Proc. IEEE Eng. Med. Biol. Soc.* 2008, 2028–2031. doi: 10.1109/IEMBS.2008.4649589

Zhuo, J., Keledjian, K., Xu, S., Pampori, A., Gerzanich, V., Simard, J. M., et al. (2015). Changes in diffusion kurtosis imaging and magnetic resonance spectroscopy in a direct cranial blast traumatic brain injury (dc-bTBI) model. *PLoS ONE.* 10:e0136151. doi: 10.1371/journal.pone.0136151

Conflict of Interest: The authors declare that the research was conducted in the absence of any commercial or financial relationships that could be construed as a potential conflict of interest.

frontiers
in Neuroscience

ORIGINAL RESEARCH
published: 09 November 2020
doi: 10.3389/fnins.2020.584161

X-ray Phase Contrast Tomography Serves Preclinical Investigation of Neurodegenerative Diseases

Francesca Palermo[1,2†], Nicola Pieroni[1,3†], Laura Maugeri[1], Ginevra Begani Provinciali[1], Alessia Sanna[1], Inna Bukreeva[1], Lorenzo Massimi[1‡], Maura Catalano[1], Margie P. Olbinado[4], Michela Fratini[1], Antonio Uccelli[5,6], Giuseppe Gigli[7], Nicole Kerlero de Rosbo[5§], Claudia Balducci[8§] and Alessia Cedola[1*§]

[1] TomaLab, Institute of Nanotechnology, CNR, Rome, Italy, [2] Dipartimento di Fisica, Università della Calabria, Rende, Italy, [3] Dipartimento di Morfogenesi e Ingegneria Tissutale, Sapienza Università di Roma, Rome, Italy, [4] Swiss Light Source, Paul Scherrer Institut X-ray Tomography Group, Villigen, Switzerland, [5] Department of Neurosciences, Rehabilitation, Ophthalmology and Maternal-Fetal Medicine (DINOGMI), University of Genoa, Genoa, Italy, [6] Ospedale Policlinico San Martino IRCCS, Genoa, Italy, [7] Institute of Nanotechnology, CNR, Università del Salento, Lecce, Italy, [8] Istituto di Ricerche Farmacologiche Mario Negri IRCCS, Milan, Italy

OPEN ACCESS

Edited by:
Yu-Chien Wu,
Indiana University Bloomington,
United States

Reviewed by:
Chengcheng Zhu,
University of Washington,
United States
Sara Garbarino,
University of Genoa, Italy

****Correspondence:***
Alessia Cedola
alessia.cedola@cnr.it

†These authors have contributed equally to this work and share first authorship

‡Present address:
Lorenzo Massimi,
Department of Medical Physics and Biomedical Engineering,
University College London, London,
United Kingdom

§These authors have contributed equally to this work and share last authorship

Specialty section:
This article was submitted to Brain Imaging Methods, a section of the journal Frontiers in Neuroscience

Received: *16 July 2020*
Accepted: *09 October 2020*
Published: *09 November 2020*

Citation:
Palermo F, Pieroni N, Maugeri L, Provinciali GB, Sanna A, Bukreeva I, Massimi L, Catalano M, Olbinado MP, Fratini M, Uccelli A, Gigli G, Kerlero de Rosbo N, Balducci C and Cedola A (2020) X-ray Phase Contrast Tomography Serves Preclinical Investigation of Neurodegenerative Diseases. Front. Neurosci. 14:584161. doi: 10.3389/fnins.2020.584161

We report a qualitative study on central nervous system (CNS) damage that demonstrates the ability of X-ray phase contrast tomography (XPCT) to confirm data obtained with standard 2D methodology and permits the description of additional features that are not detected with 2D or other 3D techniques. In contrast to magnetic resonance or computed tomography, XPCT makes possible the high-resolution 3D imaging of soft tissues classically considered "invisible" to X-rays without the use of additional contrast agents, or without the need for intense processing of the tissue required by 2D techniques. Most importantly for studies of CNS diseases, XPCT enables a concomitant multi-scale 3D biomedical imaging of neuronal and vascular networks ranging from cells through to the CNS as a whole. In the last years, we have used XPCT to investigate neurodegenerative diseases, such as Alzheimer's disease (AD) and multiple sclerosis (MS), to shed light on brain damage and extend the observations obtained with standard techniques. Here, we show the cutting-edge ability of XPCT to highlight in 3D, concomitantly, vascular occlusions and damages, close associations between plaques and damaged vessels, as well as dramatic changes induced at neuropathological level by treatment in AD mice. We corroborate data on the well-known blood-brain barrier dysfunction in the animal model of MS, experimental autoimmune encephalomyelitis, and further show its extent throughout the CNS axis and at the level of the single vessel/capillary.

Keywords: X-ray phase contrast tomography, preclinical disease models, Alzheimer's disease, multiple sclerosis, 3D imaging

INTRODUCTION

Neurodegeneration is a process by which a progressive loss of neuronal structure and function occurs in many central nervous system (CNS) pathologies; it is generally associated with neuroinflammation. Neurodegenerative diseases are presently incurable and current therapies have minimal or no significant effect in reversing the CNS damage.

The research in human neurological diseases has greatly benefited from pre-clinical research in experimental *in vitro* and *in vivo* models. In this context, for example, several of the therapeutic approaches that have led in the past 30 years to an increasing number of drugs for multiple sclerosis (MS), such as glatiramer acetate (Ben-Nun et al., 1996) and natalizumab (Yednock et al., 1992) in particular, have been developed in its murine model, experimental autoimmune encephalomyelitis (EAE) (Constantinescu et al., 2011).

However, new efforts are necessary for the comprehension of disease mechanisms and monitoring of therapeutic approaches. In particular, the research in neurodegenerative diseases requires tools enabling the visualization of disease-relevant networks, such as the vascular and neuronal networks (VN and NN), and of affected cells, as well as the monitoring of treatment efficacy. The techniques currently used to investigate damage in the VN and NN at cellular level suffer from several limitations. In particular, 2D imaging (immuno-histochemistry and electron microscopy) restricts spatial coverage, entails destructive sample preparation, and is only applicable at the *ex vivo* level. Although jumping from 2D to 3D represented an outstanding breakthrough in the general quality of imaging and information obtained, magnetic resonance imaging (MRI), positron emission tomography (PET), and X-ray-computed tomography fail to provide a satisfactory answer to the unmet medico-imaging needs for these diseases. Thus, MRI and PET are limited in terms of spatial resolution, and X-ray computed tomography, whilst providing 3D visualization of X-ray-absorbing tissues, fails in the analysis of soft tissues, such as the CNS.

These severe limitations in 3D imaging can be overcome by the more advanced X-ray phase contrast tomography (XPCT), which provides much higher resolution and contrast at cellular level also in soft tissues. XPCT makes possible the simultaneous multi-scale 3D biomedical imaging of neuronal and vascular networks, ranging from cells through to brain as a whole. XPCT revolutionizes X-ray imaging and removes its main limitation of poor image contrast arising from low attenuation differences. XPCT increases the contrast of all details and enables the detection of features classically considered as "X-ray invisible."

A key ability of XPCT is the possibility to generate a 3D *multiscale* image of the whole brain, which displays information on the NN and VN *simultaneously* (Fratini et al., 2015; Bukreeva et al., 2017; Begani Provinciali et al., 2020). In previous works (Cedola et al., 2017; Massimi et al., 2019, 2020), we exploited this unique feature of XPCT to evaluate morphological alterations in the VN and NN, both in EAE and in the APP/PS1dE9 mouse model of Alzheimer's disease (AD).

In this work, we move forward in these studies toward a deeper understanding of *specific* hot issues in MS and AD. Namely, in EAE, effective 3D imaging has allowed us to confirm disease-related alterations in blood-brain barrier (BBB) permeability, demonstrating its spreading throughout the affected tissue. In the APP/PS1 mouse model, we have investigated the effect of a new therapeutic approach on β–amyloid (Aβ) plaques, the main neuropathological hallmark of AD (Jack et al., 2010).

MATERIALS AND METHODS

Sample Preparation

Experimental autoimmune encephalomyelitis sample: An eight-week-old C57Bl/6J female mouse, weighing 18.5 g, purchased from Harlan Italy, was immunized as described before (Mendel et al., 1995) by subcutaneous injection (200 μl total) at two sites in the flank with an emulsion of 200 μg myelin oligodendrocyte glycoprotein (MOG) peptide 35–55 (Espikem) in incomplete Freund adjuvant (Difco) containing 600 μg Mycobacterium tuberculosis (strain H37Ra; Difco). The mouse was injected (100 μl total) in the tail vein with 400 ng pertussis toxin (Sigma-Aldrich) immediately and 48 h after immunization. The mouse was scored daily for clinical manifestations of EAE on a scale of 0–5 (Mendel et al., 1995), and sacrificed by CO2 inhalation at onset of clinical manifestations (day 11 after immunization), with a clinical score of 3.5. The brain and spinal cord were dissected out, with the spinal cord being divided into 3 parts, cervical (C1–C7), thoracic (T1–T13, and lumbar/sacrococcygeal (L1–S4). The tissues were fixed in 4% paraformaldehyde for 24 h, then stored in 70% ethanol until XPCT.

All animals are housed in pathogen-free conditions and treated according to the Italian and European guidelines (Decreto Legislativo 4 marzo 2014, n. 26, legislative transposition of Directive 2010/63/EU of the European Parliament and of the Council of 22 September 2010 on the protection of animals used for scientific purposes), with food and water *ad libitum*. The research protocol was approved by the Ethical Committee for Animal Experimentation of the University of Genoa (Prot. 319).

AD samples: APPswe/PS1dE9 transgenic male mice [B6C3 – Tg(APPswe, PSEN1dE9)85Dbo/Mmjax mice], which express a chimeric mouse/human amyloid precursor protein (Mo/HuAPP695swe) and a mutant human presenilin 1 (PS1-dE9), were purchased from Jackson Laboratories (United States). They are referred to thereafter as AD mice.

All animals were housed in a SPF facility in groups of 4 in standard mouse cages containing sawdust with food (2018S Envigo diet) and water *ad libitum*, under conventional laboratory conditions (room temperature: 20 ± 2°C; humidity: 60%) and a 12/12 h light/dark cycle. The IRFMN adheres to the principles set out in the following laws, regulation, and policies governing the Care and Use of Laboratory Animals: Italian Governing Law (D.lgs 26/2014; Authorization n. 19/2008-A issued March 6, 2008 by Ministry of Health); Mario Negri Institutional Regulations and Policies providing internal authorization for persons conducting animal experiments (Quality Management System Certificate – UNI EN ISO 9001:2015 – Reg. N° 6121); the NIH Guide for the Care and Use of Laboratory Animals (2011 edition) and EU directives and guidelines (EEC Council Directive 2010/63/UE). The statement of Compliance (Assurance) with the Public Health Service (PHS) Policy on Human Care and Use of Laboratory Animals has been reviewed (9/9/2014; Animal Welfare Assurance #A5023-01). The mice were used for the experiment at 18 months of age. One AD mouse was treated intranasally (25 μl total volume for both nostrils) once weekly for eight consecutive weeks with the concentrated secretome of mesenchymal stem cells (MSC), that is the conditioned supernatant of cultured MSC (MSC-CS), as described previously (Santamaria et al., 2020); the other untreated mouse received concentrated medium intranasally according to the same regimen. Mice were killed under CO_2 inhalation. For micro-XPCT, the brains were removed and post-fixed in 4% paraformaldehyde overnight and subsequently stored in 70% ethanol at 4°C until XPCT. For holo-nano-XPCT and nano-XPCT, the brains were removed and specific regions (frontal cortex, hippocampus) were cut and placed in 0.1 M cacodylate buffer pH 7.2, containing 2.5% glutaraldehyde for 3 h at room temperature. Brain samples were postfixed in osmium tetroxide (1% in 0.1 M cacodylate buffer, pH 7.2; 1 h) and uranyl acetate (1% in water; 1 h). Samples were then dehydrated through a graded ethanol series (70/95/100%), put in propylene oxide, and embedded in resin (Poly-Bed; Polysciences, Inc., Warrington, PA, United States) at 42°C overnight and for 2 days at 60°C. The blocks were kept at 4°C.

Micro-XPCT

The XPCT experiments were performed at the ID17 beamline of the European Synchrotron Radiation Facility (ESRF, Grenoble, France) and at the ANATOMIX beamline of Synchrotron SOLEIL (Paris, France), in free-space propagation mode (Bravin et al., 2012).

Data acquisition at ID17 was performed using monochromatic incident X-ray energy of 35 keV. The sample-detector distance was set at 2.3 m. The detector has an effective pixel size of 3.05 μm. The tomography was produced by means of 2000 projections covering a total angle range of 180°. The acquisition time for each angular position was 300 ms. The total sample volume was acquired in about 15 min. Data pre-processing, phase retrieval, and tomographic reconstruction were performed with SYRMEP Tomo Project software (Brun et al., 2017; Massimi et al., 2018) and optimized scripts.

The experiment at ANATOMIX beamline was carried out with a filtered white beam peaked around 20 keV. The propagation distance was 0.2 m. The effective pixel size was 3.25, resulting from 2× optics coupled with Orca Flash 4.0 camera (sensor type CMOS, sensor array size 2048 × 2048, pixel size 6.5 μm 16-bit nominal dynamic range). The experiment was performed acquiring 4000 projections in 360° scan mode. 360° scan mode or extended field of view (FOV) mode (half-acquisition mode) pertain specifically to the acquisition of sample horizontally larger than the FOV of the camera. In this acquisition mode, the sample is positioned outside the rotation center of the stage so that half of the sample is outside the FOV. We acquired over an angular range of 360°. The projections acquired during the first 180° provide information on the first part of the sample, while the projections acquired from 180 to 360° provide information on the sample region which was initially out of the FOV. Data pre-processing, phase retrieval, and tomographic reconstruction were performed with PyHST software package. The tomography color scale is a gray-shade scale from black to white. Least dense tissues appear black, structures with highest density appear white.

Holographic Nano-XPCT

The holographic (holo-)nano-XPCT experiment was carried out at Nano-Imaging ID16A beamline of the ESRF. A pair of multilayer-coated Kirkpatrick-Baez optics was used to focus the X-rays (∼30 nm) at 17 keV. The sample is put in the divergent beam downstream of the focus to produce magnified phase contrast images. The projection geometry also allows zooming into specific regions of a large sample by combining scans with different magnifications and FOV (Mokso et al., 2007; Bartels et al., 2015). By measuring the Fresnel diffraction patterns at different effective propagation distances, the phase maps of the sample can be retrieved via holographic reconstruction, this so-called phase-retrieval procedure (Cloetens et al., 1999) being implemented using GNU Octave software. Magnified radiographs were recorded onto an X-ray detector using a FReLoN-charged coupled device. For one tomography scan, 1500 projections were acquired with 0.32 s exposure time and 50 nm effective pixel size. Tomography scans at four different foci-to-sample distances were acquired to complete one holotomography scan. The tomographic reconstruction was obtained with ESRF PyHST software package. In this kind of images, the shades of gray are proportional to electron density, with black corresponding to the highest value of the density spectrum, whereas white corresponds to the lowest value, hence to features of lowest density.

Nano-XPCT

The nano-XPCT experiment was performed at TOMCAT beamline of the Swiss Light Source at Paul Scherrer Institut (Villigen, Switzerland). An incident monochromatic x-ray beam with an energy of 17 keV was used. In order to obtain an effective pixel size of 325 nm, a 20× lens was coupled with a pco.edge 5.5 camera (sCMOS-technology, 2560 × 2160 pixels, 6.5 μm pixel size and a 16-bit nominal dynamic range). The experiment was performed in free-space propagation mode, with a single propagation distance of 50 mm. For one tomography scan, 1500 projections were acquired with 0.12 s exposure time. Data reconstruction was obtained with TOMCAT plug-in of ImageJ software. As for micro-XPCT, the gray scale is proportional to the electron density of the tissues.

Image Analysis

We removed the ring artifacts by improved frequency filtering (Massimi et al., 2018). Image analysis was performed using ImageJ software[1]. To enhance the contrast, we used *z*-projection of maximum and minimum intensity. *Z*-Projection consists in projecting an image stack along the axis perpendicular to the image plane (the so-called "*z*" axis). Performing the projection of the maximum (or minimum) intensity creates an output image of which each pixel contains the maximum (or minimum) value over all images in the stack at the particular pixel location. On the one hand, maximum intensity projection (MAX) enlightens high density structures such as neurons and amyloid plaques. On the other hand, minimum intensity projection (MIN) emphasizes low-density details such as the lumen of the vessels.

---

[1] https://imagej.net/Fiji

To simultaneously visualize features with low and high density, images obtained from MAX and MIN were added together.

XPCT provides intrinsic 3D information of the samples measured. Three-dimensional spatial distribution of anatomical structures can be effectively rendered using VG studio Max software. To isolate and enlighten particular structures, image segmentation is required. This procedure groups features with the same density by selecting the corresponding portion of the gray-level-histogram intensity. The segmentation and 3D rendering, performed with VGstudioMax, can be exploited to simultaneously visualize different structures, furthering the study of the interaction among biological networks.

RESULTS

XPCT for Brain Imaging

The ambitious objective to explore the CNS from the whole organ down to the single cell through a detailed 3D imaging, whilst preserving tissue chemistry and structure, can nowadays be achieved through XPCT. Its most compelling achievement is the possibility to investigate the highly complex VN and NN in the context of the tissue as a whole and, therefore, compare physiological vs. pathological states at the level of crucial disease targets.

In order to explore the complexity of the tissue, standard X-ray tomography of the brain requires the application of contrast agents, as shown in **Figure 1A**. As can be seen, the difference in contrast between the cortex and the thalamus is clear, and the corpus callosum and the mammillothalamic tract are well defined. However, despite the use of contrast agent, little information can be extracted on nerve cells in the cortex and on nerve fibers (**Figure 1A**). Contrary to standard X-ray tomography, the contrast in the XPCT images is not proportional to the X-ray attenuation inside the sample but is proportional to the refraction of the X-ray beam crossing the sample. Since in the biomedical samples the refraction effect can be 1000 times higher with respect to the absorption effect, XPCT is a unique technique of tomography to image low-absorbing tissues. **Figure 1B** shows the same anatomic district imaged in **Figure 1A**, using XPCT, but the richness of details in this case is quite impressive with respect to **Figure 1A**. Even though a contrast agent was not used (see below), the vascularization in the cortex clearly appears, and the cells and fibers are imaged with optimal contrast.

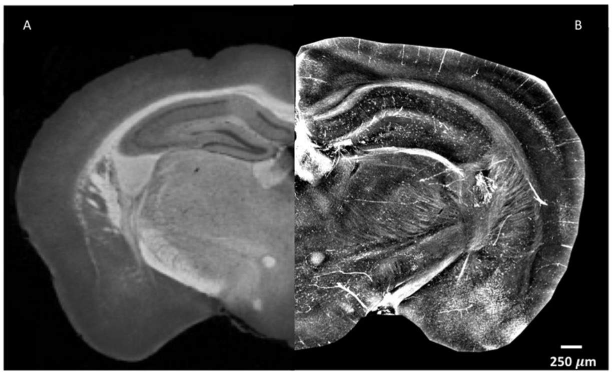

FIGURE 1 | XPCT is a powerful technique that provides high-contrast resolution without requirement for a contrast agent. The image shown puts together parts of naïve mouse brain with the left side assessed by standard X-ray micro-tomography with a mixture of 1% iodine and 90% methanol as contrast agent **(A)** as reported in Zikmund et al. (2018) JINST 13 C02039, while the right side was generated by XPCT **(B)**. Small variations in density appear much more evident in XPCT imaging. Both images were obtained as *z*-projection of maximum intensity over 300 μm.

Figure 2 shows XPCT of a naïve mouse brain region where the VN (**Figures 2A–C**) and NN (**Figures 2D–F**) are virtually extracted independently by an image post-processing, i.e., segmentation process (see section "Materials and Methods"). **Figure 2B** presents a detail of the vascular network, while a zoomed image of the small capillary network obtained through holo-nano-XPCT is shown in **Figure 2C**. In the latter image, holo-nano-XPCT distinguishes two different types of cells: the black-appearing cells at the capillary walls, which are compatible with endothelial cells, and cells surrounding the capillary, which display a white cytoplasm and a dark nucleus. Of note, nano-XPCT and holo-nano-XPCT are presently the unique techniques able to image the 3D capillary network. **Figure 2E** shows the hippocampal NN, while **Figure 2F** displays a magnification of the tissue where a cell with typical pyramidal neuron morphology with dark cytoplasm, and surrounded by round cells, is clearly defined.

EAE

Multiple sclerosis is a neurodegenerative autoimmune disease of the CNS associated with neuroinflammation, demyelination, axonal damage, and neuronal loss. The use of an appropriate animal model, such as EAE induced by MOG peptide, a chronic neurological disease with progressive caudo-rostral paralysis associated with demyelination and axonal loss (Mendel et al., 1995), facilitates the study of the disease mechanisms. In a previous XPCT study (Cedola et al., 2017), we demonstrated the presence of EAE-mediated vascular alterations down to the capillary network, and shed light on how the disease affects the tissues and on how treatment with MSC reverts the damage to some extent.

In these previous studies of murine CNS tissue, we had perfused the mice with saline and heparin to remove the blood, or with MICROFIL®, a compound that fills vessels and enhances the opacity of the microvascular network (Fratini et al., 2015; Bukreeva et al., 2017; Cedola et al., 2017). In the present study, we made the serendipitous discovery that blood itself makes for a better contrast agent, with less manipulations. Indeed, we had planned to use gadolinium as a contrast agent to enhance the visibility of the vessels. We injected gadolinium intravenously, as it is used in human disease, and compared the images of the tissues with those from mice we had injected with PBS. Unexpectedly, we found that the XPCT images of brain samples from mice injected with gadolinium (data not shown) did not show better contrast than those from mice injected with PBS, where the presence of iron in the blood permits the visualization of the vessels. Accordingly, we have subsequently assessed the vascular networks in non-perfused

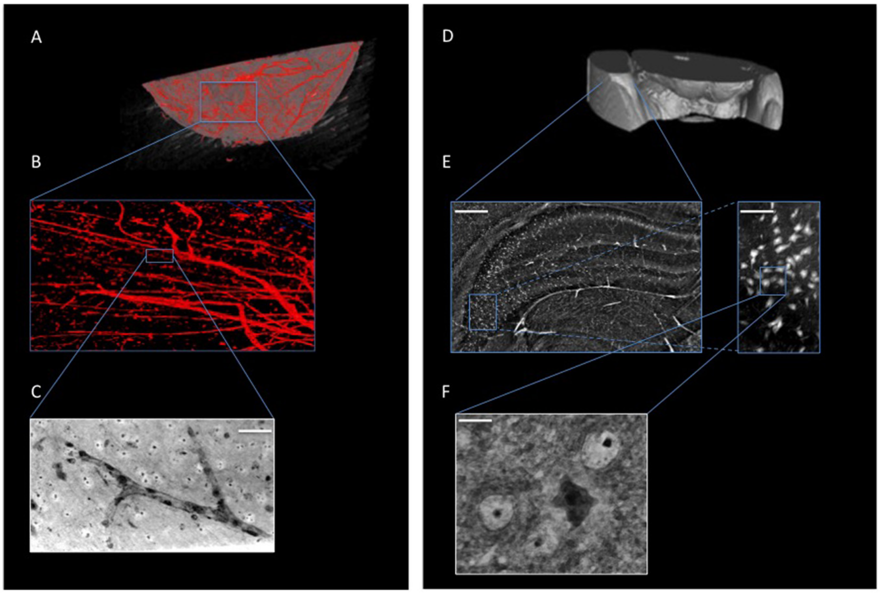

FIGURE 2 | XPCT is a multiscale 3D technique that enables the simultaneous visualization of different anatomical structures within biological tissues without sectioning or staining, and allows the imaging from whole-organ level down to nanometric details. **(A,B)** 3D-rendering of naïve mouse brain vasculature (in red). **(C)** Holo-nano-XPCT image of a single capillary (acquired at ID16, ESRF; scale bar, 50 μm). **(D–F)** XPCT images showing the multiscale approach to analyze the neuronal network down to the single cell; **(E)** Inset of **(D)** showing a micro-XPCT detail of brain in the hippocampal region (scale bar, 250 μm) and a magnification (scale bar, 80 μm) demonstrating the ability of micro-XPCT to go down to cell level; micro-XPCT measures were acquired at ID17, ESRF. **(F)** Holo-nano-XPCT image highlighting the ability of XPCT to distinguish different cell types within the tissue (acquired at ID16, ESRF; scale bar, 10 μm).

mice that had not received contrast agent. More importantly for our study, the presence of iron in the blood also permits the visualization of extravasated material, as a result of BBB dysfunction. In 2D analysis, extravasation from CNS blood vessels, in particular capillaries, is detected most appropriately in mice upon intravenous injection of immunofluorescent material of high molecular weight, such as FITC-labeled dextran 70, prior to sacrifice, and appears in optical fluorescence microscopy as "clouds" of material diffusing in the parenchyma (Ferrara et al., 2016). Similar "clouds" can be seen in the XPCT images of brain and spinal cord from EAE-affected mice (**Figures 3–5**). EAE is an experimental disease where neurological impairment proceeds as a caudo-rostral ascending paralysis that is associated with inflammation and accumulating vasogenic edema, followed by demyelination and axonal damage. A dysfunctional blood-CNS barrier is first observed in the lumbar spinal cord, spreading to the upper spinal cord regions to reach the cerebellum. **Figure 3** shows XPCT images of the lumbar spinal cord of a naïve mouse (**Figures 3A,C**) and of an EAE-affected mouse at the onset of the disease (day 11 after immunization; **Figures 3B,D**). In both sagittal (**Figures 3A,B**) and axial (**Figures 3C,D**) views, 3D analysis with XPCT shows clear alterations in this region. Thus, while we see well-defined vessels arising from the longitudinal spinal artery in the naïve mouse lumbar spinal cord (**Figure 3A**), these appear very fuzzy and surrounded by numerous "clouds" in the lumbar spinal cord of the EAE-affected mouse (**Figure 3B**), reflecting the intense BBB dysfunction at this stage of the disease. The 3D axial view of the lumbar spinal cord of the EAE-affected mouse shows very clearly a large accumulation of cells close to vessels (**Figure 3D**), which would be typical of an EAE lesion with infiltrating inflammatory cells, and is never observed in naïve mouse spinal cord (**Figure 3C**). In **Figure 4**, we see a 3D-rendering of spinal cord volume where localized extravasated material (bright gray) is clearly visible (panel A); in panel B, the 3D-rendering of the lesion in **Figure 4A**, emphasizes the surroundings of the vessel (red) by small cells (white) that differ from morphologically neuron-like cells (purple). Clouds reflecting BBB dysfunction together with accumulation of cells are also observed in the volume from the cervical region of the spinal cord (SC) up to the brain stem (BS), and cerebellum (Cer) of the same EAE-affected mouse, albeit at apparently much reduced frequencies (**Figure 5A**), as would be expected. Details of these three CNS regions are reported in **Figures 5B,C** (Cer), **5D,E** (BS), and **5F,G** (SC). The blue arrows (**Figures 5B,D,F**, and **G**) and circles indicate the areas where an extravasation is evident and appears as a white "cloud" close to an interruption or a thinner tract of the vessel. A clear gathering of small bright spots around the "clouds" (see in particular **Figure 5E**) suggests the presence of inflammatory cells in these areas, that could be compatible with infiltrating inflammatory T cells and macrophages, and/or microgliosis, which have all been extensively described in EAE (Constantinescu et al., 2011).

The scope of the present report was to provide an overview of the unique possibilities of XPCT and of the quality of the 3D images obtained that has allowed us to understand the extent of the BBB dysfunction in EAE. Rather than providing biological statistics, we have therefore presented a qualitative study with one mouse sample per condition. However, the high quality

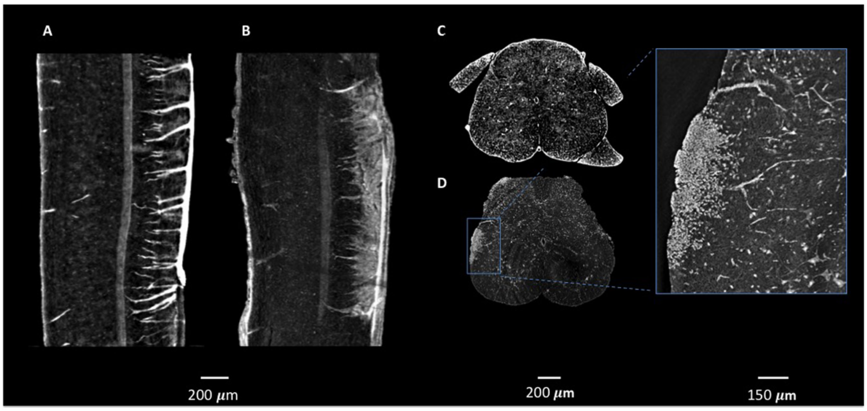

FIGURE 3 | Micro-XPCT imaging of BBB leakage and lesion in lumbar spinal cord of EAE-affected mouse. **(A–D)** XPCT images showing the sagittal **(A,B),** and axial **(C,D)** views of the lumbar spinal cord in a naïve mouse **(A,C),** and an EAE-affected mouse at disease onset **(B,D)**, where vessels appear surrounded by numerous "clouds" of extravasated material **(B)** reflecting the intense BBB dysfunction in the EAE-affected mouse, and the accumulation of cells around the leaky vessels **(D)** is commensurate with the classical EAE lesion. Images were obtained as MAX of volumes acquired at ID17, ESRF **(A–C)** and at ANATOMIX, Soleil **(D)**. (**A–B**: MAX over 50 μm; **C,D**: MAX over 10 μm).

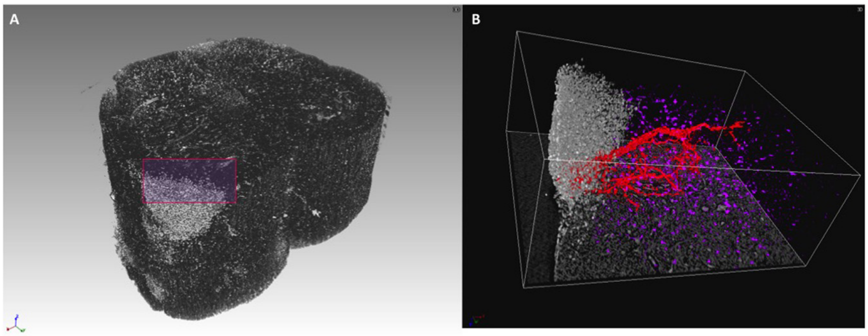

FIGURE 4 | 3D rendering of lumbar spinal cord lesion in EAE-affected mouse. **(A)** 3D rendering of a lumbar spinal cord volume (about 1-mm length) of EAE-affected mouse imaged with micro-XPCT at ANATOMIX, Soleil. **(B)** Detail of a lesion from **(A)** rendered and segmented in 3D. Images were obtained with VGstudioMax.

of our images has enabled us to quantify the number of BBB alterations at different time points throughout the disease, which have indicated an increased trend as function of the disease stage (manuscript in preparation).

Alzheimer's Disease

We have exploited XPCT to study the APP/PS1dE9 mouse model of AD (Balducci and Forloni, 2011), a progressive neurodegenerative disorder associated with aberrant production of Aβ depositing in the brain as extracellular plaques, especially in the cortical and the hippocampal areas (Huang and Mucke, 2012). APP/PS1dE9 mice develop crucial AD signatures including extracellular and intravascular plaque deposition, cognitive impairment, and neuroinflammation. **Figures 6A,B** shows an XPCT image of an APP/PS1dE9 mouse brain section. Here, a large number of plaques appear as small bright spots (highly dense tissue) of a few tens of microns in size in both the cortex and the hippocampus. We used holo-nano-XPCT to achieve single plaque details, such as the presence of neurites – appearing as black dense spots – inside and around the plaque corona (**Figure 6B**). In AD, the deposition of Aβ inside the vessels determines their lumen reduction or even occlusions, as well as wall breakages, culminating in a reduced cerebral blood flow (Klohs, 2019). Holo-nano-XPCT can reveal fine details from a 3D volume (**Figure 7**, left panel) to capillary and cell levels. As can be seen in the inset of **Figure 7** (right panel), holo-nano-XPCT has the ability to reveal the presence of intralumen deposits completely occluding the capillary. In this inset, holo-nano-XPCT also highlights the difference between healthy neurons featured by a dark-appearing dense cytoplasm (yellow arrow) and the degenerated ones with a low-density, white cytoplasm (red arrow) (Kuljis et al., 1997).

Through holo-nano- and nano-XPCT, we could also investigate structural changes in APP/PS1dE9 mouse brain at an advanced stage of the disease, treated either with vehicle or with a conditioned secretome collected from mouse bone marrow MSC. These MSC had been primed with APP/PS1dE9 mouse brain homogenate, in order to mimic a typical AD microenvironment, which licenses the cells to assume a neuroreparative/immunomodulatory phenotype reflected

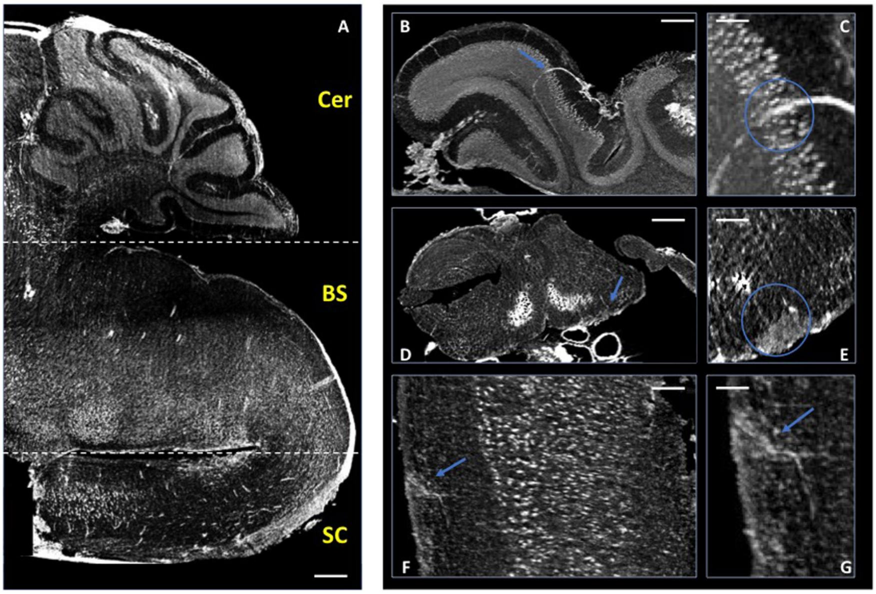

FIGURE 5 | Micro-XPCT imaging of EAE-affected mouse CNS. **(A)** Micro-XPCT image showing a sagittal view of the cerebellum (Cer), brain stem (BS), and cervical section of the spinal cord (SC) of an EAE-affected mouse at disease onset (MAX over 150 μm; scale bar, 300 μm). **(B,C)** Micro-XPCT image of a detail of vessel in the cerebellum is shown in **(B)**, with a zoomed image of the same region shown in **(C)** (MAX over 130 μm; scale bar, 100 and 50 mm, respectively). **(D,E)** Inflammatory lesion with BBB leakage in the brain stem **(D)** zoomed in **(E)** (MAX over 65 μm; scale bar, 350 and 100 μm, respectively), and in the cervical portion of spinal cord **(F)**, zoomed in **(G)** (MAX over 30 μm; scale bar, 90 and 50 μm, respectively). Blue arrows indicate lesions, with blue circles encompassing the vessels and extravasated material. Images were acquired at ANATOMIX, Soleil.

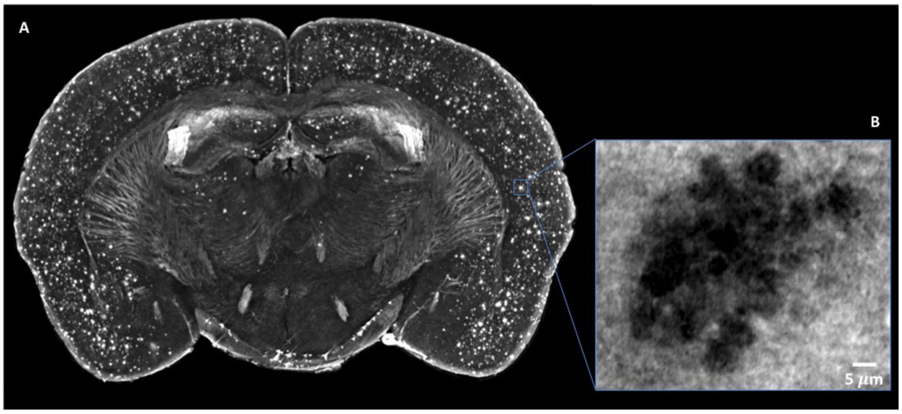

FIGURE 6 | Micro-XPCT reveals the widespread distribution of Aβ plaques in cortex of 22-month-old AD mouse. **(A)** Maximum z-projection (over 100 μm) of micro-XPCT of AD mouse brain clearly shows dramatic presence of Aβ deposits localized all over the cortex. **(B)** shows an holo-nano-XPCT magnification of a Aβ plaque in an AD mouse cortex (the gray levels are inverted in the **(A)** and **(B)**, see the text). Images were acquired at ID16, ESRF.

in their secretome (MSC-CS). In a very recent study, we demonstrated the enormous therapeutic potential of MSC-CS intranasally administered in 22-month-old APP/PS1dE9 mice at a very advanced disease stage. MSC-CS reduced brain amyloidosis, neuroinflammation and hippocampal atrophy, increased neuronal density in both the cortex and the hippocampus, and improved mouse longevity considerably (Santamaria et al., 2020). By applying holo-nano- and nano-XPCT, we could achieve the resolution to visualize plaque and vessel details, which point to a significant effect of the treatment on the microenvironment whereby the treatment is associated with destructured plaques (**Figures 8**, **9** and **Supplementary Movies 1** and **Supplementary Movies 2**). Thus, while in the brain from the vehicle-treated AD mouse we detected highly dense Aβ plaques surrounded by blood vessels almost completely occluded by the presence of Aβ deposits in their lumen (**Figure 10A**), in the AD mouse treated with MSC-CS cleaner vessels could be observed in close proximity to less dense neuritic plaques (**Figure 10B**). This latter vessel condition was highly comparable to what can be observed in the healthy WT mouse (**Figure 10C**).

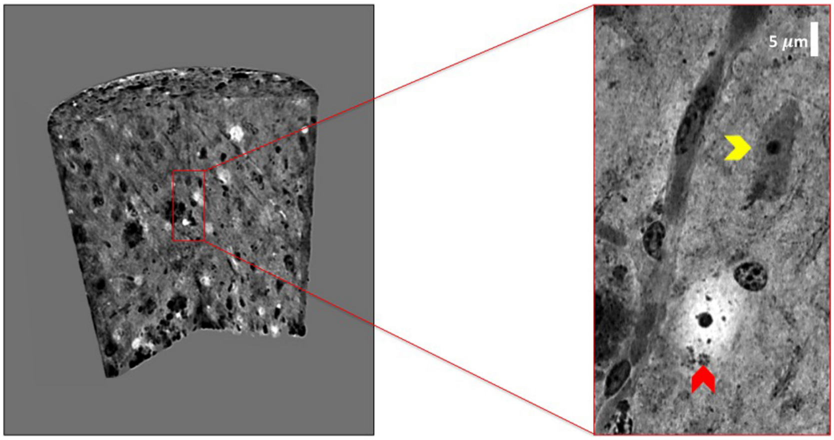

FIGURE 7 | Holo-nano-XPCT enables the visualization of neuropathological findings in AD mouse brain tissue at capillary and cell levels. The volume of AD mouse brain tissue was rendered with 3D Viewer ImageJ plug-in. The inset shows a detail of a capillary revealing the presence of intralumen Aβ deposits. As can be seen in the inset, the high sensitivity of XPCT imaging allows the clear detection of cells with very different cytoplasm density, which might reflect the known presence of degenerated neurons (low cytoplasm density; red arrow), together with seemingly healthy neurons (high cytoplasm density; yellow arrow). Images were acquired at ID16 and ESRF.

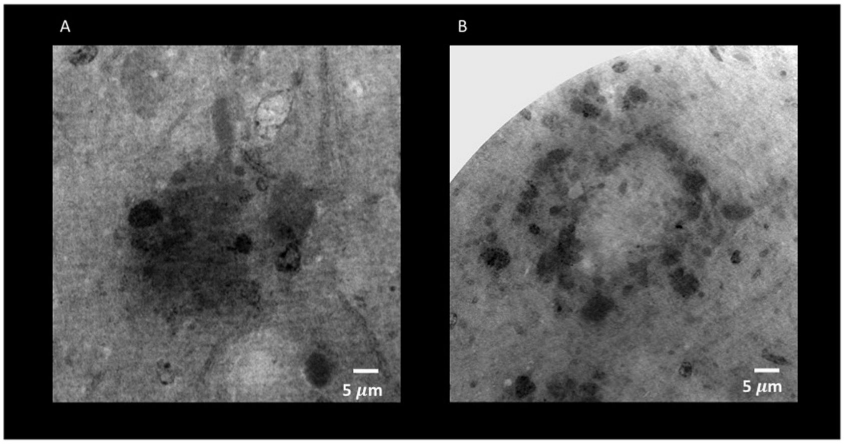

FIGURE 8 | Holo-Nano-XPCT allows the visualization of fine details inside equal-sized areas of AD mouse cortex, revealing destructured plaques in AD mouse treated with MSC-CS. The high resolution of this powerful technique highlights differences in the structure of Aβ plaques in untreated **(A)** and MSC-CS-treated **(B)** mouse cortex. Images were acquired at ID16 and ESRF.

DISCUSSION

To investigate crucial neuropathological signatures and therapeutic efficacy at fine level would require direct imaging of the whole brain in a 3D fashion, allowing for simultaneous analyses of (i) brain alterations in various cell populations (neuronal loss, gliosis, peripheral infiltrates); (ii) structural changes in terms of cell density and organization (brain atrophy); (iii) modifications in vascular networks and integrity (cerebral amyloid angiopathy, BBB modifications). This would be far more informative than the standard histological examination of isolated slices of brain tissue having undergone blood removal, freezing at extremely low temperature, and manipulation with aggressive fixatives and various detergents. Indeed, the conventional indirect immunohistochemical techniques require chemical tissue manipulations to add fluorescence/chromogenic reporters. MRI helps to circumvent these problems, but remains limited by a spatial resolution of a few mm or several tens of microns in preclinical studies. These limitations are overcome by X-ray tomography, which, however, has a poor performance in imaging soft tissues. This is why XPCT, which does not require processing of the tissue and makes possible multi-scale 3D imaging of NN and VN ranging from cells through to brain as a whole, can offer a valuable alternative. XPCT can reach up to a 1000-fold gain in contrast resolution with respect to conventional tomography and is therefore particularly useful for low-absorbing bio-medical samples. In particular, due to its high resolution and large FOV, XPCT is rapidly gaining importance in the investigation of neurodegenerative diseases, such as AD and

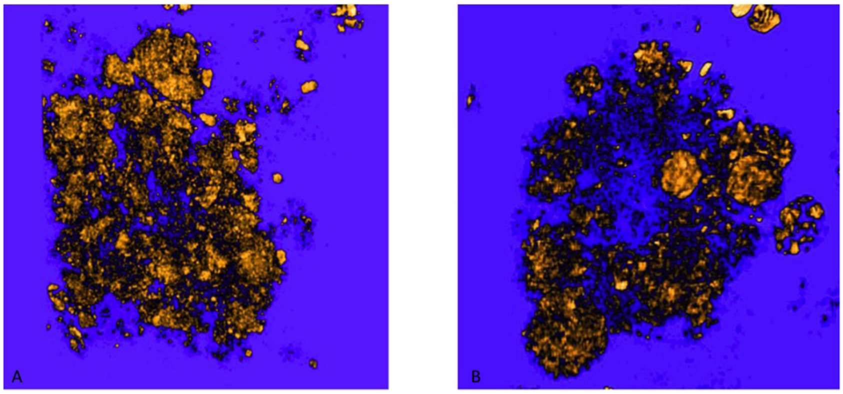

FIGURE 9 | 3D rendering of Aβ plaques in untreated and MSC-CS treated mouse cortex. **(A)** and **(B)** correspond to panels **(A,B)** of **Figure 8**, respectively. Images were obtained with VGstudioMax.

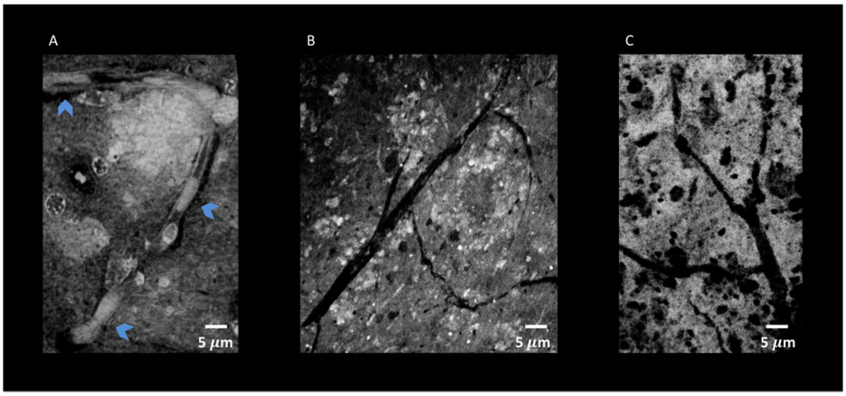

FIGURE 10 | Nano-XPCT and holo-nano-XPCT permit the visual dissection of vessels in MSC-CS-treated and untreated AD mouse cortex. **(A)** Nano-XPCT image showing the almost complete occlusion of vessel lumen by Aβ deposits in vehicle-treated AD mouse brain. The image was acquired at ID16, ESRF. **(B)** Holo-nano-XPCT image showing cleaner vessels in the brain of AD mouse treated with MSC-CS. **(C)** Nano-XPCT image of vessels in a healthy wild-type mouse brain. Images were acquired at TOMCAT and SLS. All the images are the sum of MAX and MIN over 20 μm. Gray levels have been made consistent: white represents highest-density structures, black corresponds to less dense features.

MS. The use of animal models to mimic neurodegenerative disorders allows the investigation of neuropathogenic mechanisms and the monitoring of disease progression and therapeutic efficacy.

To the best of our knowledge, this is the first study that has been able to show the extent of BBB damage in EAE at the level of the single vessel/capillary. BBB dysfunction plays a paramount role in the development of EAE and MS and has been extensively studied. Until MRI and the development of means to apply it in small animals, BBB dysfunction was, and still is, generally studied at 2-dimensional level with biochemical, histological, and immunohistochemical methods (Kassner and Merali, 2015), that have included the assessment of extravasated albumin and/or IgG in CNS through immunoblotting (Kerlero de Rosbo et al., 1985), proteomic analysis (Han et al., 2008; Farias et al., 2012; Rosenling et al., 2012), and Evan's blue or radiological labeling (LeVine, 2016). More recently, other injected tracers have included horseradish peroxidase that can be visualized through immunohistochemistry upon application of its substrate to 2D slices (Muller et al., 2005) and fluorescein isothiocyanate-labeled high molecular weight (70 kDa) dextran visualized by fluorescent microscopy of tissue slices (Ferrara et al., 2016). All these techniques require processing of the tissues to a greater or lesser extent, and do not allow the concomitant assessment of entire VN or NN. Multi-photon and two-photon microscopy is an *in vivo* method of assessing BBB disruption (Abulrob et al., 2008); however, albeit with high spatial and temporal resolution, it only permits the visualization of surface microvasculature because of poor tissue penetration (no more than 1-mm depth) and light scattering; it would therefore be inadequate to assess lesions in EAE in general, in particular perivascular and cortical lesions (Constantinescu et al., 2011). MRI has been used for 3D assessment of BBB dysfunction in EAE (Rausch et al., 2003; Nathoo et al., 2014), which enabled the demonstration of gadolinium-enhanced areas indicative of leakage across the BBB. However, unlike XPCT, the resolution of MRI does not reach the singular vessel or cell levels. Thus, to clearly show cell infiltration and accumulation of cells at BBB damage areas necessitates the adjunct use of 2D histology/immunohistochemistry (Kassner and Merali, 2015) with difficulty in matching the exact co-location of the lesion with both techniques. The injection of iron oxide-based nanoparticles that label macrophages in the CNS (Rausch et al., 2003) has also been used in conjunction with MRI, albeit with caution as such nanoparticles might not be easily distinguished by MRI from iron naturally deposited due to the disease process. In contrast, XPCT is able to visualize the fine location of the BBB leakage, together with its consequences, that is infiltrating and resident cell accumulation, in a single assessment on tissue that has not undergone extensive denaturation or processing. We believe that, as the technique improves, we will be able to track BBB lesions *in vivo* to thereby monitor disease progression and assess the efficacy of therapeutic approaches.

While our studies were the first to apply XPCT to evaluate VN and NN in EAE (Fratini et al., 2015), XPCT was used to assess the AD mouse model, showing the presence of plaques (Astolfo et al., 2016). In the present qualitative study, XPCT enabled us to demonstrate capillary occlusions and damages, close associations between plaques and damaged vessels, as well as dramatic changes induced by MSC-CS treatment in AD mice. Indeed, we could evidence clearing of Aβ deposits inside the vessels, as well as impressive changes in plaque structure and density.

The use of only one animal per group could be taken as a limitation of our study. However, rather than obtaining statistical data for a quantitative study, our aim was to emphasize the innovative aspect of XPCT in detecting pathological differences even at cellular level, in preclinical models of neurodegenerative diseases.

Our results put in evidence the essential use of XPCT as a cutting-edge technique able to provide further depth in the imaging of the damaged brain, without lengthy and/or destructive processing. While the present work does not provide statistically significant biological results, it shows how biological problems should be tackled to confirm and extend the observations obtained with standard techniques.

DATA AVAILABILITY STATEMENT

All datasets presented in this study are included in the article/**Supplementary Material**.

ETHICS STATEMENT

The animal study was reviewed and approved by Ethical Committee for Animal Experimentation of the University of Genoa (Prot. 319) and the Istituto di Ricerche Farmacologiche Mario Negri IRCCS.

AUTHOR CONTRIBUTIONS

AC, CB, and NKdeR conceived and designed the experiments and participated to the discussion of the results and wrote the manuscript. MF, FP, NP, LM, GP, AS, and AC performed the experiments and contributed to the data analysis. IB, AC, MF, FP, NP, LM, GP, AS, IB, and GG have contributed to the discussion of the results and to the final revision of the manuscript. MC performed the data analysis. All the authors contributed to the final writing of the manuscript.

FUNDING

The FISR Project "Tecnopolo di nanotecnologia e fotonica per la medicina di precisione" (funded by MIUR/CNR, CUP B83B17000010001) and the TECNOMED project (funded by Regione Puglia, CUP B84I18000540002). The bilateral project CNR/RFBR (2018–2020) – accordo CNR-RFBR delle Relazioni Internazionali (CUP B86C17000210005).

ACKNOWLEDGMENTS

The authors would like to thank Alberto Bravin for his very active support during the measurements. The authors would like also to thank the staff of ID17 and ID16 at ESRF the staff of ANATOMIX at Soleil and the staff of TOMCAT at SLS for technical assistance during the experiments, and G. Ferrara for induction of EAE in mice.

SUPPLEMENTARY MATERIAL

The Supplementary Material for this article can be found online at: https://www.frontiersin.org/articles/10.3389/fnins.2020.584161/full#supplementary-material

REFERENCES

Abulrob, A., Brunette, E., Slinn, J., Baumann, E., and Stanimirovic, D. (2008). Dynamic analysis of the blood-brain barrier disruption in experimental stroke using time domain in vivo fluorescence imaging. *Mol. Imaging* 7, 248–262.

Astolfo, A., Lathuiliere, A., Laversenne, V., Schneider, B., and Stampanoni, M. (2016). Amyloid-β plaque deposition measured using propagation-based X-ray phase contrast CT imaging. *J. Synchrotron Radiat.* 23, 813–819. doi: 10.1107/s1600577516004045

Balducci, C., and Forloni, G. (2011). APP transgenic mice: their use and limitations. *Neuromolecular Med.* 13, 117–137. doi: 10.1007/s12017-010-8141-7

Bartels, M., Krenkel, M., Cloetens, P., Mobius, W., and Salditt, T. (2015). Myelinated mouse nerves studied by X-ray phase contrast zoom tomography. *J. Struct. Biol.* 192, 561–568. doi: 10.1016/j.jsb.2015.11.001

Begani Provinciali, G., Pieroni, N., Bukreeva, I., Fratini, M., Massimi, L., Maugeri, L., et al. (2020). X-ray phase contrast tomography for the investigation of amyotrophic lateral sclerosis. *J. Synchrotron Radiat.* 27, 1042-1048.

Ben-Nun, A., Mendel, I., Bakimer, R., Fridkis-Hareli, M., Teitelbaum, D., Arnon, R., et al. (1996). The autoimmune reactivity to myelin oligodendrocyte glycoprotein (MOG) in multiple sclerosis is potentially pathogenic: effect of copolymer 1 on MOG-induced disease. *J Neurol* 243(4 Suppl. 1), S14–S22.

Bravin, A., Coan, P., and Suortti, P. (2012). X-ray phase-contrast imaging: from pre-clinical applications towards clinics. *Phys. Med. Biol.* 58:R1.

Brun, F., Massimi, L., Fratini, M., Dreossi, D., Bille, F., Accardo, A., et al. (2017). SYRMEP Tomo Project: a graphical user interface for customizing CT reconstruction workflows. *Adv. Struct. Chem. Imaging* 3:4. doi: 10.1186/s40679-016-0036-8

Bukreeva, I., Campi, G., Fratini, M., Spano, R., Bucci, D., Battaglia, G., et al. (2017). Quantitative 3D investigation of Neuronal network in mouse spinal cord model. *Sci. Rep.* 7:41054. doi: 10.1038/srep41054

Cedola, A., Bravin, A., Bukreeva, I., Fratini, M., Pacureanu, A., Mittone, A., et al. (2017). X-Ray Phase Contrast Tomography Reveals Early Vascular Alterations and Neuronal Loss in a Multiple Sclerosis Model. *Sci. Rep.* 7:5890. doi: 10.1038/s41598-017-06251-7

Cloetens, P., Ludwig, W., Baruchel, J., Van Dyck, D., Van Landuyt, J., Guigay, J., et al. (1999). Holotomography: Quantitative phase tomography with micrometer resolution using hard synchrotron radiation x rays. *Appl. Phys. Lett.* 75, 2912–2914. doi: 10.1063/1.125225

Constantinescu, C. S., Farooqi, N., O'Brien, K., and Gran, B. (2011). Experimental autoimmune encephalomyelitis (EAE) as a model for multiple sclerosis (MS). *Br. J. Pharmacol.* 164, 1079–1106. doi: 10.1111/j.1476-5381.2011.01302.x

Farias, A. S., Martins-de-Souza, D., Guimaraes, L., Pradella, F., Moraes, A. S., Facchini, G., et al. (2012). Proteome analysis of spinal cord during the clinical course of monophasic experimental autoimmune encephalomyelitis. *Proteomics* 12, 2656–2662. doi: 10.1002/pmic.201200044

Ferrara, G., Errede, M., Girolamo, F., Morando, S., Ivaldi, F., Panini, N., et al. (2016). NG2, a common denominator for neuroinflammation, blood–brain barrier alteration, and oligodendrocyte precursor response in EAE, plays a role in dendritic cell activation. *Acta Neuropathol.* 132, 23–42. doi: 10.1007/s00401-016-1563-z

Fratini, M., Bukreeva, I., Campi, G., Brun, F., Tromba, G., Modregger, P., et al. (2015). Simultaneous submicrometric 3D imaging of the micro-vascular network and the neuronal system in a mouse spinal cord. *Sci. Rep.* 5:8514. doi: 10.1038/srep08514

Han, M. H., Hwang, S. I., Roy, D. B., Lundgren, D. H., Price, J. V., Ousman, S. S., et al. (2008). Proteomic analysis of active multiple sclerosis lesions reveals therapeutic targets. *Nature* 451, 1076–1081. doi: 10.1038/nature06559

Huang, Y., and Mucke, L. (2012). Alzheimer mechanisms and therapeutic strategies. *Cell* 148, 1204–1222. doi: 10.1016/j.cell.2012.02.040

Jack, C. R. Jr., Knopman, D. S., Jagust, W. J., Shaw, L. M., Aisen, P. S., Weiner, M. W., et al. (2010). Hypothetical model of dynamic biomarkers of the Alzheimer's pathological cascade. *Lancet Neurol.* 9, 119–128. doi: 10.1016/s1474-4422(09)70299-6

Kassner, A., and Merali, Z. (2015). Assessment of Blood-Brain Barrier Disruption in Stroke. *Stroke* 46, 3310–3315. doi: 10.1161/strokeaha.115.008861

Kerlero de Rosbo, N., Bernard, C., Simmons, R., and Carnegie, P. (1985). Concomitant detection of changes in myelin basic protein and permeability of blood-spinal cord barrier in acute experimental autoimmune encephalomyelitis by electroimmunoblotting. *J. Neuroimmunol.* 9, 349–361. doi: 10.1016/s0165-5728(85)80035-7

Klohs, J. (2019). An integrated view on vascular dysfunction in Alzheimer's disease. *Neurodegener. Dis.* 19, 109–127. doi: 10.1159/000505625

Kuljis, R. O., Xu, Y., Aguila, M. C., and Baltimore, D. (1997). Degeneration of neurons, synapses, and neuropil and glial activation in a murine Atm knockout model of ataxia-telangiectasia. *Proc. Natl. Acad. Sci. U.S.A.* 94, 12688–12693. doi: 10.1073/pnas.94.23.12688

LeVine, S. M. (2016). Albumin and multiple sclerosis. *BMC Neurol.* 16:47. doi: 10.1186/s12883-016-0564-9

Massimi, L., Brun, F., Fratini, M., Bukreeva, I., and Cedola, A. (2018). An improved ring removal procedure for in-line x-ray phase contrast tomography. *Phys. Med. Biol.* 63:045007. doi: 10.1088/1361-6560/aaa706

Massimi, L., Bukreeva, I., Santamaria, G., Fratini, M., Corbelli, A., Brun, F., et al. (2019). Exploring Alzheimer's disease mouse brain through X-ray phase contrast tomography: from the cell to the organ. *NeuroImage* 184, 490–495. doi: 10.1016/j.neuroimage.2018.09.044

Massimi, L., Pieroni, N., Maugeri, L., Fratini, M., Brun, F., Bukreeva, I., et al. (2020). Assessment of plaque morphology in Alzheimer's mouse cerebellum using three-dimensional X-ray phase-based virtual histology. *Sci. Rep.* 10, 1–10.

Mendel, I., Kerlero de Rosbo, N., and Ben-Nun, A. (1995). A myelin oligodendrocyte glycoprotein peptide induces typical chronic experimental autoimmune encephalomyelitis in H-2b mice: fine specificity and T cell receptor V beta expression of encephalitogenic T cells. *Eur. J. Immunol.* 25, 1951–1959. doi: 10.1002/eji.1830250723

Mokso, R., Cloetens, P., Maire, E., Ludwig, W., and Buffière, J.-Y. (2007). Nanoscale zoom tomography with hard x rays using Kirkpatrick-Baez optics. *Appl. Phys. Lett.* 90:144104. doi: 10.1063/1.2719653

Muller, D. M., Pender, M. P., and Greer, J. M. (2005). Blood–brain barrier disruption and lesion localisation in experimental autoimmune encephalomyelitis with predominant cerebellar and brainstem involvement. *J. Neuroimmunol.* 160, 162–169. doi: 10.1016/j.jneuroim.2004.11.011

Nathoo, N., Yong, V. W., and Dunn, J. F. (2014). Understanding disease processes in multiple sclerosis through magnetic resonance imaging studies in animal models. *Neuroimage Clin.* 4, 743–756. doi: 10.1016/j.nicl.2014.04.011

Rausch, M., Hiestand, P., Baumann, D., Cannet, C., and Rudin, M. (2003). MRI-based monitoring of inflammation and tissue damage in acute and chronic relapsing EAE. *Magn. Reson. Med.* 50, 309–314. doi: 10.1002/mrm.10541

Rosenling, T., Stoop, M. P., Attali, A., van Aken, H., Suidgeest, E., Christin, C., et al. (2012). Profiling and identification of cerebrospinal fluid proteins in a rat EAE model of multiple sclerosis. *J. Proteome Res.* 11, 2048–2060. doi: 10.1021/pr201244t

Santamaria, G., Brandi, E., La Vitola, P., Grandi, F., Ferrara, G., Pischiutta, F., et al. (2020). Intranasal delivery of mesenchymal stem cell secretome repairs the brain of Alzheimer's mice. *Cell Death Differ* doi: 10.1038/s41418-020-0592-2 [Epub ahead of print].

Yednock, T. A., Cannon, C., Fritz, L. C., Sanchez-Madrid, F., Steinman, L., and Karin, N. (1992). Prevention of experimental autoimmune encephalomyelitis by antibodies against alpha 4 beta 1 integrin. *Nature* 356, 63–66. doi: 10.1038/356063a0

Zikmund, T., Novotná, M., Kavková, M., Tesařová, M., Kaucká, M., Szarowská, B., et al. (2018). High-contrast differentiation resolution 3D imaging of rodent brain by X-ray computed microtomography. *J. Instrum.* 13:C02039.

Conflict of Interest: The authors declare that the research was conducted in the absence of any commercial or financial relationships that could be construed as a potential conflict of interest.

The reviewer SG declared a shared affiliation with several of the authors, AU and NKdeR, to the handling editor at the time of review.

frontiers in Neuroscience

CORRECTION
published: 17 February 2021
doi: 10.3389/fnins.2021.657368

Corrigendum: X-ray Phase Contrast Tomography Serves Preclinical Investigation of Neurodegenerative Diseases

Francesca Palermo[1,2†], Nicola Pieroni[1,3†], Laura Maugeri[1], Ginevra Begani Provinciali[1], Alessia Sanna[1], Inna Bukreeva[1], Lorenzo Massimi[1‡], Maura Catalano[1], Margie P. Olbinado[4], Michela Fratini[1], Antonio Uccelli[5,6], Giuseppe Gigli[7], Nicole Kerlero de Rosbo[5§], Claudia Balducci[8§] and Alessia Cedola[1*§]

[1] TomaLab, Institute of Nanotechnology, CNR, Rome, Italy, [2] Dipartimento di Fisica, Università della Calabria, Rende, Italy, [3] Dipartimento di Morfogenesi e Ingegneria Tissutale, Sapienza Università di Roma, Rome, Italy, [4] Swiss Light Source, Paul Scherrer Institut X-ray Tomography Group, Villigen, Switzerland, [5] Department of Neurosciences, Rehabilitation, Ophthalmology and Maternal-Fetal Medicine (DINOGMI), University of Genoa, Genoa, Italy, [6] Ospedale Policlinico San Martino IRCCS, Genoa, Italy, [7] Institute of Nanotechnology, CNR, Università del Salento, Lecce, Italy, [8] Istituto di Ricerche Farmacologiche Mario Negri IRCCS, Milan, Italy

Approved by:
Frontiers Editorial Office, Frontiers Media SA, Switzerland

***Correspondence:**
Alessia Cedola
alessia.cedola@cnr.it

† These authors have contributed equally to this work and share first authorship

‡ Present address:
Lorenzo Massimi, Department of Medical Physics and Biomedical Engineering, University College London, London, United Kingdom

§ These authors have contributed equally to this work and share last authorship

Specialty section:
This article was submitted to Brain Imaging Methods, a section of the journal Frontiers in Neuroscience

Received: *22 January 2021*
Accepted: *27 January 2021*
Published: *17 February 2021*

Citation:
Palermo F, Pieroni N, Maugeri L, Provinciali GB, Sanna A, Bukreeva I, Massimi L, Catalano M, Olbinado MP, Fratini M, Uccelli A, Gigli G, Kerlero de Rosbo N, Balducci C and Cedola A (2021) Corrigendum: X-ray Phase Contrast Tomography Serves Preclinical Investigation of Neurodegenerative Diseases. Front. Neurosci. 15:657368. doi: 10.3389/fnins.2021.657368

Keywords: X-ray phase contrast tomography, preclinical disease models, Alzheimer's disease, multiple sclerosis, 3D imaging

A Corrigendum on

X-ray Phase Contrast Tomography Serves Preclinical Investigation of Neurodegenerative Diseases
by Palermo, F., Pieroni, N., Maugeri, L., Provinciali, G. B., Sanna, A., Bukreeva, I., et al. (2020). Front. Neurosci. 14:584161. doi: 10.3389/fnins.2020.584161

In the original article, there were several errors, as detailed below.

Author List, Affiliations, and Author Contributions

Giuseppe Gigli was not included as an author in the published article. The corrected Author Contributions Statement appears below.

Author Contributions

AC, CB, and NKdeR conceived and designed the experiments and participated to the discussion of the results and wrote the manuscript. MF, FP, NP, LM, GP, AS, and AC performed the experiments and contributed to the data analysis. IB, AC, MF, FP, NP, LM, GP, AS, IB, and GG have contributed to the discussion of the results and to the final revision of the manuscript. MC performed the data analysis. All the authors contributed to the final writing of the manuscript.

In the original article, the affiliation for author Giuseppe Gigli was also not included. We have added the affiliation for Giuseppe Gigli as 7 - Institute of Nanotechnology, CNR, Università del Salento, Lecce, Italy.

Additionally, there was an error in the order of the authors in the author list of the original article. Inna Bukreeva should be the sixth author in the list. The original article has now been updated.

Text Corrections

In the original article, there was a mistake in the caption for Figure 1 as published. Figure 1A was adapted from Figure 3F of T. Zikmund et al 2018 JINST 13 C02039, but the reference to the paper was erroneously omitted. The corrected caption appears below.

Figure 1. XPCT is a powerful technique that provides high-contrast resolution without requirement for a contrast agent. The image shown puts together parts of naïve mouse brain with the left side assessed by standard X-ray micro-tomography with a mixture of 1% iodine and 90% methanol as contrast agent (A) as reported in Zikmund et al. (2018) JINST 13 C02039, while the right side was generated by XPCT (B). Small variations in density appear much more evident in XPCT imaging. Both images were obtained as z-projection of maximum intensity over 300 μm.

In addition, the full citation for Zikmund et al. (2018) JINST 13 C02039 will be added to the reference list of the original article.

The authors apologize for these errors and state that they do not change the scientific conclusions of the article in any way. The original article has been updated.

REFERENCES

Zikmund, T., Novotná, M., Kavková, M., Tesařová, M., Kaucká, M., Szarowská, B., et al. (2018). High-contrast differentiation resolution 3D imaging of rodent brain by X-ray computed microtomography. *J. Instrum.* 13:C02039.

frontiers in Neuroscience

ORIGINAL RESEARCH
published: 22 January 2021
doi: 10.3389/fnins.2020.592063

Diffusion Basis Spectrum Imaging Detects Axonal Loss After Transient Dexamethasone Treatment in Optic Neuritis Mice

Tsen-Hsuan Lin[1]*, Jie Zhan[1,7], Chunyu Song[2], Michael Wallendorf[3], Peng Sun[1], Xuan Niu[1], Ruimeng Yang[1,6], Anne H. Cross[4,5] and Sheng-Kwei Song[1,2,5]

[1] Department of Radiology, Washington University School of Medicine, St. Louis, MO, United States, [2] Department of Biomedical Engineering, Washington University in St. Louis, St. Louis, MO, United States, [3] Division of Biostatistics, Washington University School of Medicine, St. Louis, MO, United States, [4] Department of Neurology, Washington University School of Medicine, St. Louis, MO, United States, [5] Hope Center for Neurological Disorders, Washington University School of Medicine, St. Louis, MO, United States, [6] Department of Radiology, Guangzhou First People's Hospital, School of Medicine, South China University of Technology, Guangzhou, China, [7] Department of Radiology, The First Affiliated Hospital, Nanchang University, Jiangxi, China

OPEN ACCESS

Edited by:
*Rodolfo Gabriel Gatto,
University of Illinois at Chicago,
United States*

Reviewed by:
*Noam Shemesh,
Champalimaud Foundation, Portugal
Darius Gerlach,
Helmholtz Association of German
Research Centers (HZ), Germany
Ahmed Toosy,
University College London,
United Kingdom*

***Correspondence:**
*Tsen-Hsuan Lin
tsenhsuanlin@wustl.edu*

Specialty section:
*This article was submitted to
Neurodegeneration,
a section of the journal
Frontiers in Neuroscience*

Received: *06 August 2020*
Accepted: *28 December 2020*
Published: *22 January 2021*

Citation:
*Lin T-H, Zhan J, Song C,
Wallendorf M, Sun P, Niu X, Yang R,
Cross AH and Song S-K (2021)
Diffusion Basis Spectrum Imaging
Detects Axonal Loss After Transient
Dexamethasone Treatment in Optic
Neuritis Mice.
Front. Neurosci. 14:592063.
doi: 10.3389/fnins.2020.592063*

Optic neuritis is a frequent first symptom of multiple sclerosis (MS) for which corticosteroids are a widely employed treatment option. The Optic Neuritis Treatment Trial (ONTT) reported that corticosteroid treatment does not improve long-term visual acuity, although the evolution of underlying pathologies is unclear. In this study, we employed non-invasive diffusion basis spectrum imaging (DBSI)-derived fiber volume to quantify 11% axonal loss 2 months after corticosteroid treatment (vs. baseline) in experimental autoimmune encephalomyelitis mouse optic nerves affected by optic neuritis. Longitudinal DBSI was performed at baseline (before immunization), after a 2-week corticosteroid treatment period, and 1 and 2 months after treatment, followed by histological validation of neuropathology. Pathological metrics employed to assess the optic nerve revealed axonal protection and anti-inflammatory effects of dexamethasone treatment that were transient. Two months after treatment, axonal injury and loss were indistinguishable between PBS- and dexamethasone-treated optic nerves, similar to results of the human ONTT. Our findings in mice further support that corticosteroid treatment alone is not sufficient to prevent eventual axonal loss in ON, and strongly support the potential of DBSI as an *in vivo* imaging outcome measure to assess optic nerve pathology.

Keywords: axonal loss, optic neuritis (ON), multiple sclerosis (MS), diffusion MRI, dexamethasone, anti-inflammation, Diffusion basis spectrum imaging (DBSI)

INTRODUCTION

Multiple sclerosis (MS) is an inflammatory demyelinating disease affecting the central nervous system (CNS), including brain, optic nerves, and spinal cord. Anti-inflammation treatment using corticosteroids is often used to suppress relapses. Corticosteroids are thought to shorten duration of MS relapses but not to alter the long-term outcome. Optic neuritis (ON) occurs frequently, often as the initial episode, in MS (Michalski et al., 1981; Gonzalez-Hernandez et al., 2015). Corticosteroids are widely used to treat ON in MS patients (Beck et al., 1993; Bennett et al., 2015) and are also effective in reducing clinical signs of murine experimental autoimmune encephalomyelitis (EAE) (Dustman and Snyder, 1981), an animal model of MS. Corticosteroids have multiple effects, including anti-inflammatory and immunosuppressive effects, reduction of blood–brain barrier (BBB) permeability and alteration of ion channel activity (Levitan et al., 1991; Boumpas et al., 1993; Wust et al., 2008; Myhr and Mellgren, 2009; Coutinho and Chapman, 2011). The seminal Optic Neuritis Treatment Trial (ONTT) reported no long-term functional benefits from either intravenous or oral corticosteroid treatment of acute ON, but did find expedited recovery of visual function (Valberg et al., 1981; Gal et al., 2015). Known adverse effects of corticosteroids in humans are many, including reduced glucose metabolism, cataract formation, joint injury and loss of bone density. Experimentally, several reports have also shown neuronal cell loss in animal models (Diem et al., 2003; Lieberman et al., 2011; Muller et al., 2014). Hence, we have taken a longitudinal and non-invasive imaging assessment of the evolution of optic nerve pathology in murine ON, culminating in histological assessment, to improve the understanding of the impact of corticosteroid treatment.

Magnetic resonance imaging (MRI) plays a vital role in diagnosing and assessing disease progression in people with MS. For instance, contrast-enhanced lesions and chronic T1-weighted hypointensities reflect inflammation, and axonal loss, respectively, but are at best only semi-quantitative (Ge, 2006; Ceccarelli et al., 2012; Llado et al., 2012). Axonal loss is a critical mechanism of irreversible neurological disability (Kornek et al., 2000; Wujek et al., 2002; Medana and Esiri, 2003). A non-invasive biomarker to quantify the extent of axonal loss and residual axon injury would greatly improve the understanding of evolution of injury and help stratify therapies for individual MS. Magnetization transfer ratio (MTR) and *N*-acetyl aspartate to creatine ratio determined by magnetic resonance spectroscopy (MRS) are usually considered the best imaging biomarkers for myelin and axon integrity, respectively, in people with MS (Davie et al., 1999; Bjartmar et al., 2000; Schmierer et al., 2004). Diffusion-tensor-imaging (DTI)-derived axial diffusivity (AD, also denoted as $\lambda_{\parallel}$) and radial diffusivity (RD, also denoted as $\lambda_{\perp}$) have been used to more specifically assess axonal injury, and demyelination. However, the DTI model is confounded by coexisting pathologies such as inflammation and axon loss on AD and RD (Wang et al., 2011b; Chiang et al., 2014). Therefore, we developed diffusion basis spectrum imaging (DBSI) to analyze diffusion-weighted images obtained with multi-direction and multi-b-value schemes. DBSI more accurately detects and quantifies co-existing white-matter pathologies in EAE-affected mice and people with MS (Wang et al., 2007, 2011a, 2014, 2015; Chiang et al., 2014).

Optic neuritis frequently occurs in murine EAE, as seen in people with MS. In the current study, we performed longitudinal DBSI to assess injury progression in the optic nerves of EAE-affected mice undergoing treatment with a widely used corticosteroid, dexamethasone (Dex) (Wust et al., 2008; Coutinho and Chapman, 2011) followed by post-MRI immunohistochemical validation. The study was set up to reflect a typical scenario for human ON, with treatment of individual mice beginning only after signs of reduced visual acuity (VA) and stopping after 2 weeks.

MATERIALS AND METHODS

All experimental procedures involving animals were approved by Washington University Institutional Animal Care and Use Committee (IACUC) and conformed to the NIH Policy on Responsibility for Care and Use of Animals.

Experimental Autoimmune Encephalomyelitis (EAE) Mouse Model

Fifteen 7-week-old, female C57BL/6 mice were obtained from Jackson Laboratory (Bar Harbor, ME, United States). Before immunization, mice were housed with 12-h dark/light cycle for 2 weeks. EAE was induced by active immunization with 50 μg MOG_{35-55} peptide emulsified (1:1) in incomplete Freund's adjuvant (IFA) and Mycobacterium tuberculosis. Pertussis toxin (300 ng; PTX, List Laboratories, Campbell, CA, United States) was injected intravenously on the day of MOG_{35-55} immunization and 2 days later (Wang et al., 2007).

Visual Acuity (VA)

Mouse VA was assessed using the Virtual Optometry System (OptoMotry, Cerebral Mechanics, Inc., Canada). Briefly, the virtual rotating columns were projected on the LCD monitors with different spatial frequencies in cycles/degree (c/d). The mouse head movement in response to the virtual column rotations was noted. The spatial frequency was starting from 0.1 c/d with step size of 0.05 c/d until the mouse stopped responding. The VA was defined as the highest spatial frequency to which the mouse responded to the virtual rotating columns. Each mouse was confirmed to have normal VA before immunization. After immunization, daily VA was assessed until VA $\leq$ 0.25 c/d, our definition for the onset of ON in MOG_{35-55} EAE mice (Chiang et al., 2014; Lin et al., 2014a,b). The first day of VA $\leq$ 0.25 c/d both Dex- and PBS-treated group was 13.4 ± 3.7 days post immunization. Upon Dex treatment commencement, VA was performed twice a week and 1 day before MRI scans.

Dexamethasone Administration

When VA $\leq$ 0.25 c/d, ON-affected mice underwent daily intraperitoneal injection of Dex (3 mg/kg, Sigma Inc., MO, United States) or PBS for 2 weeks. The first day of VA $\leq$ 0.25 c/d in both Dex and PBS groups was 13.4 ± 3.7 days post immunization. Mice were alternately assigned to receive PBS or Dex until the 9th pair. The last EAE mouse was assigned to PBS group. Daily clinical scores were assessed using a standard 0–5 scoring system (Wang et al., 2014).

Diffusion-Weighted MRI Data Acquisition

Mice were anesthetized for imaging as previously described (Lin et al., 2017). *In vivo* MRI experiments were performed on a

4.7-T Agilent DirectDrive^{TM} small-animal MRI system (Agilent Technologies, Santa Clara, CA, United States) equipped with a Magnex/Agilent HD imaging gradient coil (Magnex/Agilent, Oxford, United Kingdom) capable of pulsed-gradient strengths of up to 58 G/cm and a gradient rise time $\leq$ 295 μs. An actively decoupled 1.7-cm receive coil was placed on the top of the mouse head for MR signal reception. The animal holder assembly, including the receive coil was placed inside an 8-cm actively decoupled volume transmit coil. Diffusion-weighted MRI data were acquired with 25-direction diffusion weighting scheme (Batchelor et al., 2003) using a multi-echo spin-echo diffusion-weighted imaging sequence (Tu et al., 2010). The following parameters were used to acquire diffusion-weighted MRI data: TR = 1.5 s, TE = 35 ms, inter-echo delay = 20.7 ms, FOV = 22.5 × 22.5 mm^2, matrix size = 192 × 192 (zero-filled to 384 × 384), slice thickness = 0.8 mm, 25 different *b*-values (max *b*-value = 2,200 s/mm^2), one b = 0 s/mm^2, Δ = 18 ms, δ = 6 ms, total scan time = 2 h 4 min (Chiang et al., 2014; Lin et al., 2017). The final target image view was perpendicular to optic nerve and obtained as previously described (Spees et al., 2013; Lin et al., 2014b). A train of two echoes was co-added to form the final MR images to increase accumulated signal-to-noise ratio. Diffusion-weighted MRI was performed four times on each mouse: 2 weeks before immunization (baseline), at the end of 2-week treatment (2 weeks after onset of ON), and 1 and 2 months after stopping treatment (chronic, no longer treated) (**Figure 1A**).

Diffusion Basis Spectrum Imaging (DBSI) and Diffusion Tensor Imaging (DTI)

Data was analyzed with DBSI multi-tensor and conventional DTI single-tensor analysis packages developed in-house with MATLAB (Wang et al., 2011a, 2015). The imaging data were modeled according to Eq. 1:

$$S_k = \sum_{i=1}^{N_{Aniso}} f_i e^{-\left|\vec{b_k}\right| \lambda_{\perp i}} e^{-\left|\vec{b_k}\right| (\lambda_{\parallel i} - \lambda_{\perp i}) \cos^2 \psi_{ik}} + \int_a^b f(D)\, e^{-\left|\vec{b_k}\right| D} dD \quad (k = 1,\ 2,\ 3, \ldots,\ 25)\,. \tag{1}$$

The quantities S_k and $\left|\vec{b_k}\right|$ are the signal and *b*-value of the k^{th} diffusion gradient, N_{Aniso} is the number of anisotropic tensors (fiber tracts), Ψ_{ik} is the angle between the k^{th} diffusion gradient and the principal direction of the i^{th} anisotropic tensor, $\lambda_{||i}$ and $\lambda_{\perp i}$ are the AD and RD of the i^{th} anisotropic tensor, f_i is the signal intensity fraction for the i^{th} anisotropic tensor, and a and b are the low and high diffusivity limits for the isotropic diffusion spectrum (reflecting cellularity and edema) $f(D)$. For a coherent fiber bundle like the optic nerve, $N_{Aniso} = 1$. DBSI derived f_i represents the density of axons derived from retinal ganglion cells (fiber fraction) in the image voxel, after resolving intra-voxel pathological and structural complications. Based on prior work, DBSI derived $\lambda_{||}$ and $\lambda_{\perp}$ reflect axon and myelin integrity respectively: $\downarrow \lambda_{||}$ = axonal injury and $\uparrow \lambda_{\perp}$ = demyelination. Our previous experimental findings suggest that the restricted isotropic diffusion fraction reflecting cellularity can be derived by the summation of $f(D)$ at $0 \leq \text{ADC} \leq 0.6\ \mu\text{m}^2$/ms. The summation of the remaining $f(D)$ at $0.6 < \text{ADC} < 3\ \mu\text{m}^2$/ms represents "hindered" isotropic diffusion, which denotes regions of tissue loss, increased inter-axonal space, vasogenic edema and CSF. The summation of $f(D)$ at $\text{ADC} = 3\ \mu\text{m}^2$/ms represents free water.

Regions of interest (ROI) were manually drawn with ImageJ[1] (NIH, United States) at the center of each optic nerve on the diffusion-weighted image (the edge voxel of optic nerve were avoided), which corresponded to the diffusion gradient direction perpendicular to optic nerves, to minimize partial volume effects. ROIs were then transferred to the parametric maps to calculate the mean value for individual DBSI metrics.

ROI for DBSI Fiber Volume

A separate ROI encompassing the whole optic nerve was drawn on cross-sectional images obtained with diffusion weighting gradient direction orthogonal to optic nerve (larger than the ROIs for other DBSI metrics). The ROI included the edge voxel of optic nerve. DBSI-derived fiber volume was calculated from the optic nerve volume (the entire ROI on DWI) multiplied by the corresponding DBSI fiber fraction. The dilution effect of inflammation and surrounding CSF is considered in the fiber volume computation in the manner.

Immunohistochemistry (IHC) of Optic Nerves

Following the final MR examination, mice were perfused with 1% phosphate-buffered saline followed by 4% paraformaldehyde in 1% phosphate-buffered saline. The brain was excised and post-fixed for 24 h before being transferred to 1% phosphate-buffered saline for storage at 4°C. For histological analysis, mouse optic nerves were embedded in 2% agar (Blewitt et al., 1982). The agar block was then embedded in paraffin wax and 5 μm thick transverse slices were sectioned for IHC. Sections were deparaffinized, rehydrated, and then blocked using 1% bovine serum albumin (BSA, Sigma Inc., MO, United States) and 5% normal goat serum solution for 30 min at room temperature to prevent non-specific binding and to increase antibody permeability. Slides were incubated overnight at 4°C with purified anti-neurofilament marker pan axonal cocktail (1:300, SMI-312, BioLegend, United States), or purified anti-neurofilament H (NF-H), phosphorylated antibody (1:300, SMI-31; BioLegend, United States) to stain total axons or only non-injured axons, respectively. Rabbit anti-myelin basic protein (MBP) antibody (1:300, Sigma Inc., MO, United States) was used to stain myelin blobs from breakdown or intact myelin sheaths (Song et al., 2003; Costello et al., 2006b; Urolagin et al., 2012). After rinsing, goat anti-mouse IgG or goat anti-rabbit IgG conjugated Alexa 488 (1:240, Invitrogen, United States) was applied to visualize immunoreactivity of phosphorylated neurofilament and MBP. Finally, slides were covered using Vectashield Mounting Medium with 4′,6-diamidino-2-phenylindole (DAPI, Vector Laboratory,

---

[1] https://imagej.nih.gov/ij/

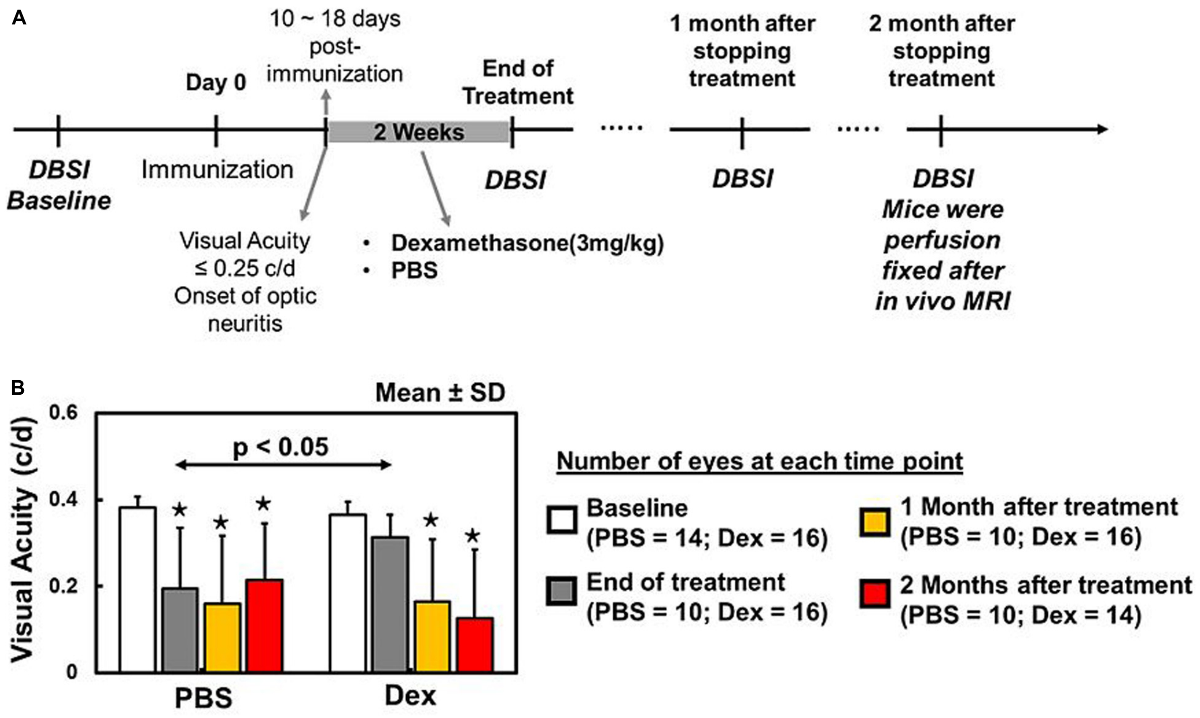

FIGURE 1 | Baseline DBSI prior to active immunization of EAE mice **(A)**. Daily intraperitoneal PBS or dexamethasone injection started at the onset of optic neuritis (i.e., visual acuity (VA) < 0.25 c/d) and continued for 2 weeks. DBSI was performed at the end of the 2-week treatment, with 1- and 2-month follow-ups after the initial scan **(A)**. Dexamethasone-treated eyes exhibited baseline visual acuity (VA) that was significantly higher than PBS-treated eyes during treatment period **(B)**. One and two months after concluding treatment, VA of PBS and dexamethasone groups were significantly lower than their baseline **(B)**. There was no difference between PBS and dexamethasone groups **(B)**. The VA data suggested that dexamethasone treatment could only retain intermittent visual function during treatment period. * indicates $p < 0.05$, comparing to baseline.

Inc., Burlingame, CA, United States) to stain cell nuclei (Costello et al., 2006b; Wang et al., 2007, 2011a). Images were acquired with a Nikon Eclipse 80i fluorescence microscope equipped with 100 × oil objective and a black-and-white CCD camera with MetaMorph software (Universal Imaging Corporation, Sunnyvale, CA, United States) for entire optic nerve with the montage function.

Histological Data Analysis

The whole field of SMI-31, MBP, and DAPI stained images at 100× magnification was captured with the same fluorescence light intensity and exposure time for each image. All captured images were converted to 8-bit gray scale and analyzed using threshold, edge enhancement, analyze particles and gray level watershed segmentation functions in ImageJ (see text footnote 1, NIH, United States). Nucleus counts were performed by signal intensity threshold on DAPI staining (Lin et al., 2014a,b).

Statistical Analysis

Three PBS-treated EAE mice and one Dex-treated EAE mouse died before the end of the 2-week treatment. Two PBS-treated EAE mice died before the MRI scan at 1 month after treatment. At conclusion of the study, five PBS-treated and seven Dex-treated EAE mice had survived through the final DBSI scan (2 months after treatment) and histologic analysis.

For all the boxplots, whiskers extend to the minimum/maximum and the means are marked as diamonds. VA or MRI measurements were taken on each eye at baseline, end of 2-week treatment, and at 1 and 2 months after treatment. Data were analyzed with a mixed random effects repeated measures model with side, time, treatment, and time by treatment interaction as fixed effects. Degrees of freedom were adjusted with Kenward–Rogers method. A first order auto-regressive covariance structure was used to account for repeated measures. Contrasts were estimated for change from baseline. The associations of histology data with DBSI measurements at 2 months after treatment were analyzed by mixed random effects regression with correlation calculated as the mean of Pearson correlations on left and right sides.

RESULTS

Recovery of Visual Function During Dexamethasone Treatment Period

Visual acuity in Dex-treated eyes were comparable to its baseline ($p = 0.1615$, **Figure 1B**) and significantly improved than PBS-treated eyes at the end of 2-week treatment ($p = 0.0242$, **Figure 1B**). One and two months after stopping treatment, both Dex- and PBS-treated eyes were significantly lower than

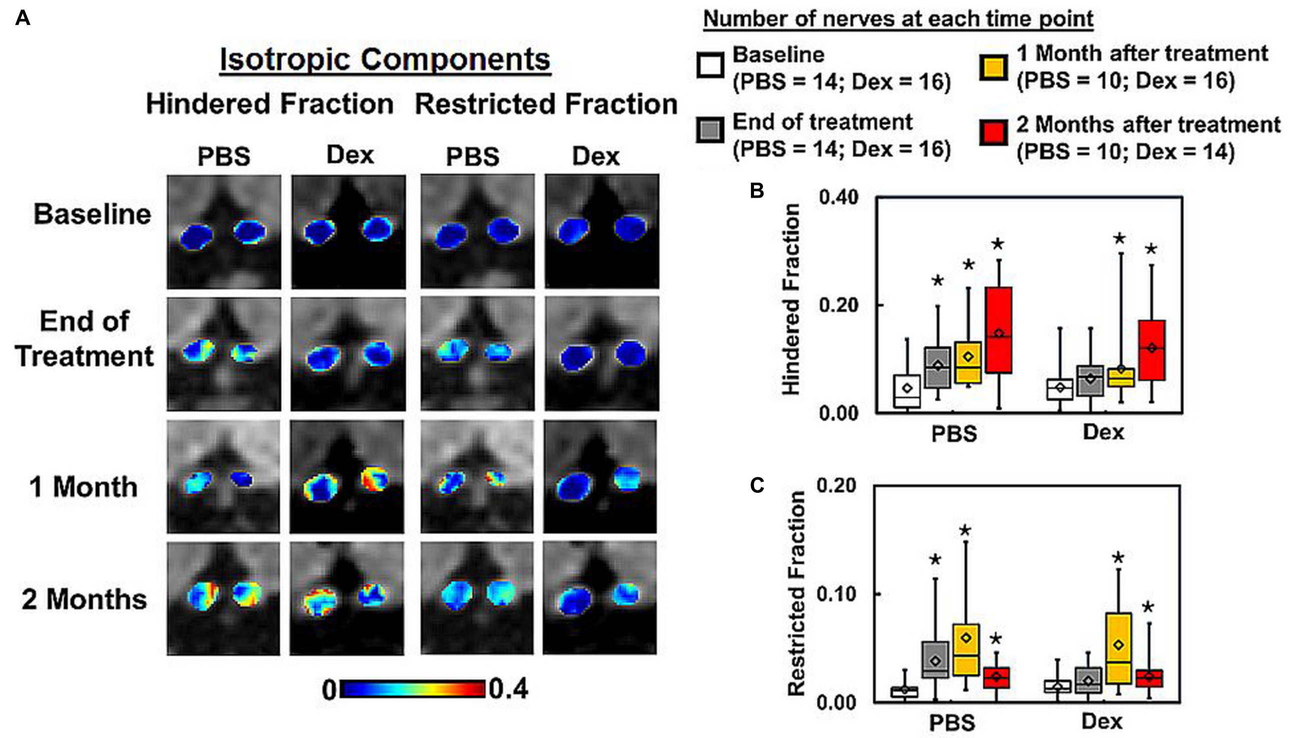

FIGURE 2 | DBSI-derived hindered (putative vasogenic edema marker) and restricted (putative cellularity marker) isotropic diffusion tensor fraction maps **(A)** from the representative PBS- and dexamethasone-treated mice were compared. Dexamethasone suppressed inflammation, i.e., the putative inflammation markers did not differ from baseline values including hindered ($p = 0.51$) and restricted ($p = 0.46$) fractions, at the end of 2-week treatment **(B,C)**. In contrast, hindered ($p < 0.05$) and restricted ($p < 0.05$) fractions significantly increased (reflecting prominent inflammation) at the end of 2-week PBS treatment. At 1 and 2 months after cessation of PBS or dexamethasone treatment, hindered ($p < 0.05$) and restricted ($p < 0.05$) isotropic diffusion fractions increased compared to baseline **(A–C)**. Summary box plots show that these isotropic diffusion metrics were elevated to similar degree in both PBS- and dexamethasone-treated optic nerves at 1 and 2 months **(B,C)**. The latter suggest the ineffectiveness of dexamethasone after cessation of treatment. There was no statistically significant difference between treatment groups at each matched time point. * indicates $p < 0.05$, comparing to baseline.

their baseline ($p < 0.0001$, **Figure 1B**) and no difference between two groups ($p = 0.3992$ and $p = 0.3570$ for 1 and 2 months, respectively).

DBSI: Acute Anti-inflammatory Effects of Dexamethasone

Comparing to the baseline (within each treatment group), significantly increased DBSI hindered (elevated by 90% from baseline, $p = 0.038$, **Figure 2B** and **Table 1**) and restricted isotropic (increased by 285% from baseline, $p = 0.0074$, **Figure 2C** and **Table 1**) diffusion fractions were seen in optic nerves at the end of the 2-week PBS treatment (**Figure 2**). In contrast, moderate but not statistically significantly increased DBSI hindered (28%, $p = 0.52$, **Figure 2B** and **Table 1**) and restricted isotropic (48%, $p = 0.46$, **Figure 2C** and **Table 1**) fractions were seen 2 weeks after the Dex-treatment. The extent of increased hindered isotropic diffusion fraction (putative marker of edema, increased inter-axonal space, or tissue loss) and restricted isotropic diffusion fraction (putative marker of cellularity) was significantly increased at 2 months after Dex- (187%, $p = 0.0002$ and 174%, $p = 0.0071$ from baseline, respectively and **Table 1**) or PBS-treatments (147%, $p = 0.0009$ and 207%, $p = 0.0093$ from baseline, respectively and **Table 1**). With our limited mouse number, none of the DBSI metrics exhibited a statistically significant difference between the two treatment groups at any of the examined time points.

DBSI: Delayed Axon/Myelin Injury With Dexamethasone Administration

At the end of 2-week treatments, DBSI $\lambda_{||}$ (putative marker of axonal injury) of Dex-treated optic nerves was not decreased compared with the baseline value ($p = 0.96$, **Table 1**). DBSI $\lambda_{||}$ of PBS-treated optic nerves moderately decreased by 13% from the baseline value although not reaching statistical significance ($p = 0.11$, **Figure 3B** and **Table 1**). Compared to the baseline, DBSI $\lambda_{\perp}$ (putative marker of myelination) in PBS-treated optic nerves increased by 41% ($p = 0.01$, **Table 1**) while Dex-treated DBSI $\lambda_{\perp}$ increased non-significantly by 16% (**Figure 3C** and **Table 1**). A moderate but not significant DBSI $\lambda_{||}$ decrease was observed in both PBS- and Dex-treated optic nerves at 1 month (decreased by 4% and 2% respectively, **Table 1**) and 2 months (decreased by 8% and 6% respectively, **Table 1**) after treatment (**Figure 3B**). Increased DBSI $\lambda_{\perp}$ was seen at 1 month after PBS treatment (increased by 59% from baseline, $p = 0.006$, **Figure 3C** and **Table 1**) but was not significantly increased in Dex-treated optic nerves (increased by 20% from baseline,

TABLE 1 | Group averaged of DTI or DBSI metrics of EAE mice with PBS ($n = 7$ for baseline and end of treatment, $n = 5$ for 1 and 2 months after treatment) and dexamethasone ($n = 8$ for baseline, end of treatment, and 1 month after treatment, $n = 7$ for 2 months after treatment) treatment.

		Baseline	End treatment	1 month	2 months
DTI ADC (μm^2/ms)	PBS	0.74 ± 0.03	0.74 ± 0.06	0.74 ± 0.06	0.72 ± 0.06
	Dexamethasone	0.73 ± 0.03	0.74 ± 0.07	0.71 ± 0.06	0.73 ± 0.04
DBSI axial diffusivity (μm^2/ms)	PBS	1.88 ± 0.15	*1.76 ± 0.22	*1.80 ± 0.18	*1.73 ± 0.21
	Dexamethasone	1.86 ± 0.11	1.86 ± 0.16	*1.82 ± 0.18	*1.76 ± 0.10
DTI axial diffusivity (μm^2/ms)	PBS	1.72 ± 0.25	*1.49 ± 0.38	*1.52 ± 0.21	*1.50 ± 0.24
	Dexamethasone	1.74 ± 0.12	1.70 ± 0.22	*1.56 ± 0.18	*1.49 ± 0.18
DBSI radial diffusivity (μm^2/ms)	PBS	0.18 ± 0.52	*0.26 ± 0.09	*0.29±0.08	0.23 ± 0.06
	Dexamethasone	0.19 ± 0.05	0.23 ± 0.05	0.23 ± 0.05	*0.26 ± 0.08
DTI radial diffusivity (μm^2/ms)	PBS	0.25 ± 0.16	0.35 ± 0.11	0.35 ± 0.10	0.33 ± 0.06
	Dexamethasone	0.21 ± 0.04	0.26 ± 0.05	0.30 ± 0.07	0.36 ± 0.11
DBSI non-restricted fraction	PBS	0.05 ± 0.04	*0.09 ± 0.05	*0.09 ± 0.05	*0.08 ± 0.12
	Dexamethasone	0.04 ± 0.04	0.05 ± 0.04	*0.08 ± 0.07	*0.12 ± 0.07
DBSI restricted fraction	PBS	0.02 ± 0.01	*0.06 ± 0.05	*0.06 ± 0.05	*0.05 ± 0.05
	Dexamethasone	0.02 ± 0.02	0.03 ± 0.02	*0.05 ± 0.04	*0.06 ± 0.04
DBSI fiber signal fraction	PBS	0.79 ± 0.07	*0.70 ± 0.07	*0.73 ± 0.07	*0.71 ± 0.11
	Dexamethasone	0.79 ± 0.05	0.79 ± 0.04	0.75 ± 0.09	*0.69 ± 0.10
DWI-derived optic nerve volume (mm^3)	PBS	0.09 ± 0.01	0.11 ± 0.02	0.10 ± 0.01	0.09 ± 0.02
	Dexamethasone	0.10 ± 0.01	0.10 ± 0.01	0.10 ± 0.01	0.10 ± 0.03
DBSI-derived fiber volume (mm^3)	PBS	0.073 ± 0.007	0.073 ± 0.012	0.071 ± 0.014	0.065 ± 0.013
	Dexamethasone	0.078 ± 0.006	0.075 ± 0.006	0.077 ± 0.014	*0.070 ± 0.019

**Indicates $p < 0.05$, comparing to baseline.*

$p = 0.15$, **Figure 3C** and **Table 1**). A moderate but not significant DBSI $\lambda_\perp$ increase by 27% from baseline was seen at 2 months after PBS ($p = 0.27$, **Table 1**). In contrast, the Dex-treated group had 35% DBSI $\lambda_\perp$ increase from baseline ($p = 0.02$, **Figure 3C** and **Table 1**). However, DTI $\lambda_{||}$ (**Figures 4A,B** and **Table 1**) and DBSI $\lambda_\perp$ (**Figures 4A,C** and **Table 1**) results were exaggerated and consistent with the change of DBSI hindered (**Figure 2B**) and restricted (**Figure 2C**) fraction, suggesting DTI result might be contaminated inflammatory pathology. In addition, DTI ADC (**Figure 4D** and **Table 1**) could not reflect damage in either PBS- or Dex-treated optic nerves.

Dexamethasone Treatment Failed to Prevent Axonal Loss

Optic nerve DBSI fiber fraction (putative marker of apparent axon density) was decreased in PBS-treated but not Dex-treated mice at the end of the 2-week treatment (decreased from baseline by 12%, $p = 0.0008$ vs. 1%, $p = 0.37$ respectively, **Figures 5A,B** and **Table 1**). Significant optic nerve volume increase was detected in the PBS-treated optic nerves (increased by 13% from baseline, $p = 0.0147$, **Figure 5C** and **Table 1**) at the end of the 2-week treatment. In contrast, there was no detectable change in nerve volume at any measured time point in Dex-treated optic nerves (decreased by 2% from baseline, $p = 0.6232$, **Figure 5C** and **Table 1**) at the end of 2-week treatment. Comparing to Dex-treated group, significant lower fiber signal fraction was observed at the end of 2-week treatment ($p = 0.0381$, **Figure 5B** and **Table 1**). Meanwhile, significant increased nerve volume was detected at the end of 2-week treatment ($p = 0.0012$, **Figure 5C** and **Table 1**). Significantly lower fiber signal fraction was seen in both PBS- and Dex-treated optic nerves at 2 months after treatment (decreased by 10%, $p = 0.0005$ and 13%, $p < 0.0001$ from baseline respectively, **Figure 5B** and **Table 1**). There was no difference of fiber fraction ($p = 0.858$, **Figure 5B** and **Table 1**), nerve volume ($p = 0.7252$, **Figure 5C** and **Table 1**), and DBSI-derived fiber volume ($p = 0.7096$, **Figure 5D** and **Table 1**) between PBS- and Dex-treated groups at 2 months after treatment. These results suggest that Dex treatment offers no long-term benefits related to axon preservation.

Immunohistochemistry (IHC) Staining of Optic Nerve

Comparing IHC of naïve optic nerve (**Figures 6A–D**), IHC of PBS-treated (**Figures 6E–H**) and Dex-treated (**Figures 6I–L**) optic nerves at end of the experiment showed decreased SMI-31 (intact phosphorylated axons) and SMI-312 (intact plus injured axons) staining intensity with irregular distribution of expanded hyper-intense areas due to axonal injury and axonal swelling (white arrows, **Figures 6E,G,I,K**), which were detected by DBSI fiber signal fraction (**Figures 6a,e,i**) and DBSI $\lambda_{||}$ (**Figures 6c,g,k**). Reduced MBP (myelin basic protein) staining intensity and irregular hyper-intense spots (white arrows, **Figures 6F,J**) resulting from demyelination and possible myelin debris was seen in both PBS- and Dex-treated optic nerves, and the results was consistent with DBSI $\lambda_\perp$ (**Figures 6b,f,j**). Increased DAPI counts (number of cell nuclei) was also observed in PBS- and Dex-treated optic nerves (**Figures 6H,L**) and consistent with DBSI restricted fraction (**Figures 6d,h,l**). Decreased SMI-312 staining intensity in PBS- and Dex-treated optic nerves were associated with noticeable axonal loss (**Figures 6E,I**). SMI312 area, MBP fraction, SMI31 counts, and DAPI counts associated with DBSI-derived fiber volume

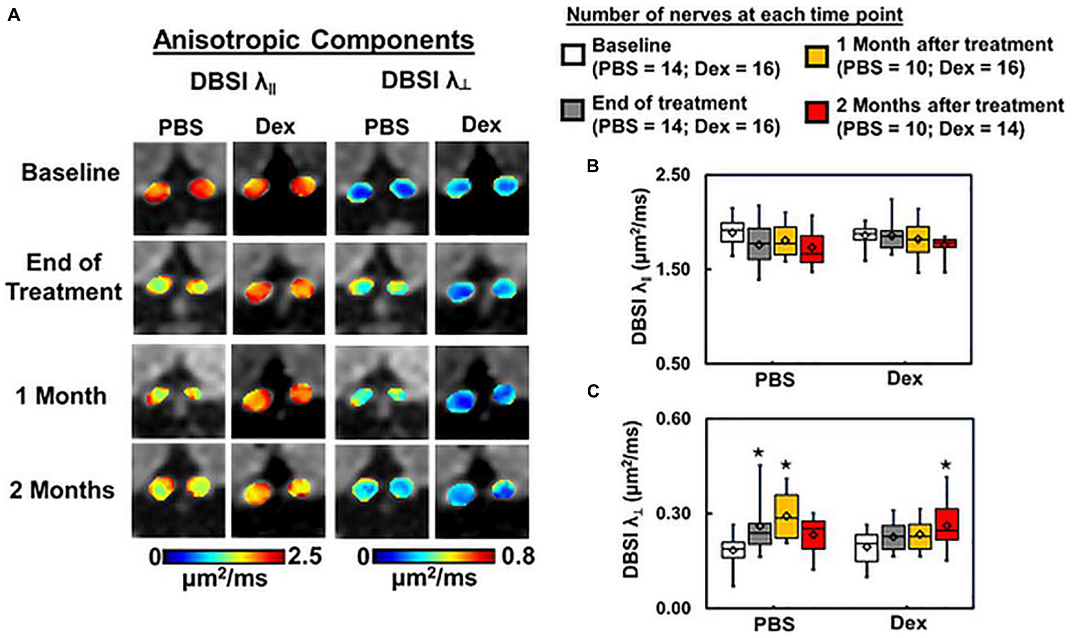

FIGURE 3 | DBSI-derived axial ($\lambda_{\parallel}$) and radial ($\lambda_{\perp}$) diffusivity maps **(A)** from the same two representative mice as in **Figure 2**. Optic nerves from the PBS-treated mouse developed axon and myelin injury as revealed by the decreased $\lambda_{\parallel}$ and increased $\lambda_{\perp}$ **(A)**. In contrast, optic nerves from the dexamethasone treated mouse were minimally affected, as reflected by the near baseline $\lambda_{\parallel}$ and $\lambda_{\perp}$ values at the end of 2-week treatment **(A)**. Box plots of DBSI-derived $\lambda_{\parallel}$ **(B)** and $\lambda_{\perp}$ **(C)** from the two cohorts of mice revealed that at the end of the 2-week treatment period, DBSI-derived $\lambda_{\parallel}$ decreased by 7% ($p = 0.11$) in the PBS cohort, while no change was seen in the Dex-treated cohort. DBSI-derived $\lambda_{\perp}$ increased by 41% ($p < 0.05$) and 16% ($p = 0.24$) in PBS- and Dex-treated EAE mice, respectively, at the end of 2-week treatment. At 1 month after treatment, moderate but not statistically significant DBSI $\lambda_{\parallel}$ decrease was observed in both PBS- and dexamethasone-treated optic nerves comparing to their baseline (decreased by 4% and 2% respectively, **B**). Significantly elevated DBSI $\lambda_{\perp}$ was seen at 1 month after PBS treatment (increased by 59%, $p < 0.05$, **C**) but not statistically significant in dexamethasone-treated optic nerves (increased by 20%, $p = 0.14$, **C**) comparing to their baseline. Two months after treatment, DBSI $\lambda_{\perp}$ increase was apparent at 2 months after ending PBS (increased by 27%, $p = 0.28$, **C**) and dexamethasone treatment (increased by 35%, $p = 0.02$, **C**) from baseline. There was no statistical difference between treatment groups at each single time point. *Indicates $p < 0.05$, comparing to baseline.

(**Figure 7A**, directly correlated), DBSI $\lambda_{\perp}$ (**Figure 7E**, inversely correlated), DBSI $\lambda_{||}$ (**Figure 7I**, directly correlated), DBSI restricted isotropic fraction (**Figure 7M**, inversely correlated), suggesting that DBSI derived pathological metrics revealed the severity of axonal loss, demyelination, axonal injury, and cell infiltration. In this study, the change of DBSI $\lambda_{\perp}$ was also associated with SMI312 area (**Figure 7B**, inversely correlated), SMI31 counts (**Figure 7J**, inversely correlated), and DAPI counts (**Figure 7N**, directly correlated). The change of DBSI-derived fiber volume was associated with SMI31 counts (**Figure 7K**, directly correlated) and DAPI counts (**Figure 7O**, inversely correlated). The change of DBSI $\lambda_{||}$ was associated with MBP (**Figure 7D**, directly correlated). The change of DBSI restricted fraction was associated with SMI31 (**Figure 7L**, inversely correlated). Correlations among IHC and DBSI metrics indicate that optic nerve pathologies were inter-dependent reflecting the inter-dependence among inflammation, demyelination, and axonal injury in optic neuritis of EAE mice. IHC scatter plot distributions overlapped between treatment groups at 2 months, suggesting that the 2-week treatment dexamethasone treatment had little impact on long-term optic nerve pathologies. Overall, the data indicate that *in vivo* findings of DBSI metrics reflected underlying neuropathology.

DISCUSSION

Diffusion basis spectrum imaging has shown success in modeling non-Gaussian diffusion phenomena with multiple Gaussian functions for biological tissues and environment in MS subjects and EAE mice (Wang et al., 2011a, 2015; Chiang et al., 2014; Lin et al., 2017). In this study, we used DBSI to assess the effects of 2-week Dex treatment on optic nerve integrity in murine ON serially over the subsequent 2 months, with immunohistochemistry at the conclusion of study time course to assess optic nerve neuropathology. A two-sample Student's *t*-test of DBSI restricted fraction (putative biomarker for inflammation) was used to estimate the sample size ($n = 7$) needed to achieve the statistical significance. During the experiment, five PBS-treated EAE mice died at various time points leading to the small sample size for this study. Despite the small cohort size, the longitudinal comparison within individual EAE mice demonstrated the difference between PBS- and Dex-treatments. It is much close to clinical need to design the personal treatment strategy, especially for people with MS (Gajofatto and Benedetti, 2015). Our findings were still consistent with the classic human ONTT trial (Gal et al., 2012), finding that a short course of corticosteroids led to improved visual function in the short-term while it

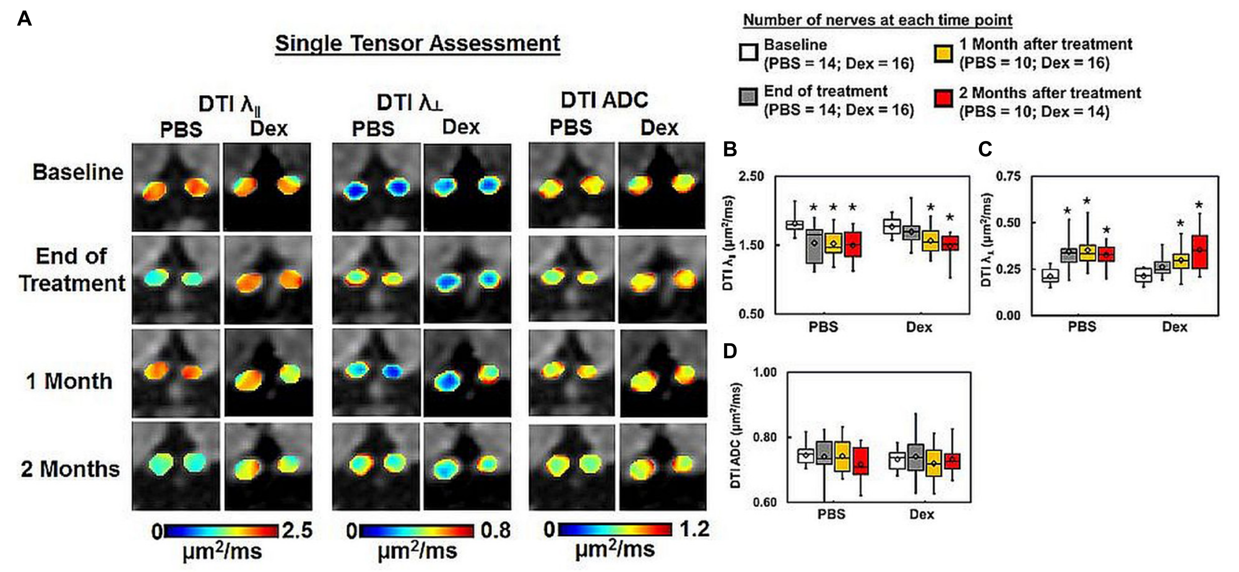

FIGURE 4 | DTI-derived axial ($\lambda_{\parallel}$) and radial ($\lambda_{\perp}$) diffusivity, and ADC maps **(A)** from the same two representative mice as in **Figure 2**. PBS-treated optic nerves showed exaggerated DTI $\lambda_{\parallel}$ decrease **(B)** and DTI $\lambda_{\perp}$ increase **(C)** than DBSI $\lambda_{\parallel}$ (**Figure 3B**) and DBSI $\lambda_{\perp}$ (**Figure 3C**). DTI-derived ADC showed no difference within or between groups **(D)**. * indicates $p < 0.05$, comparing to baseline.

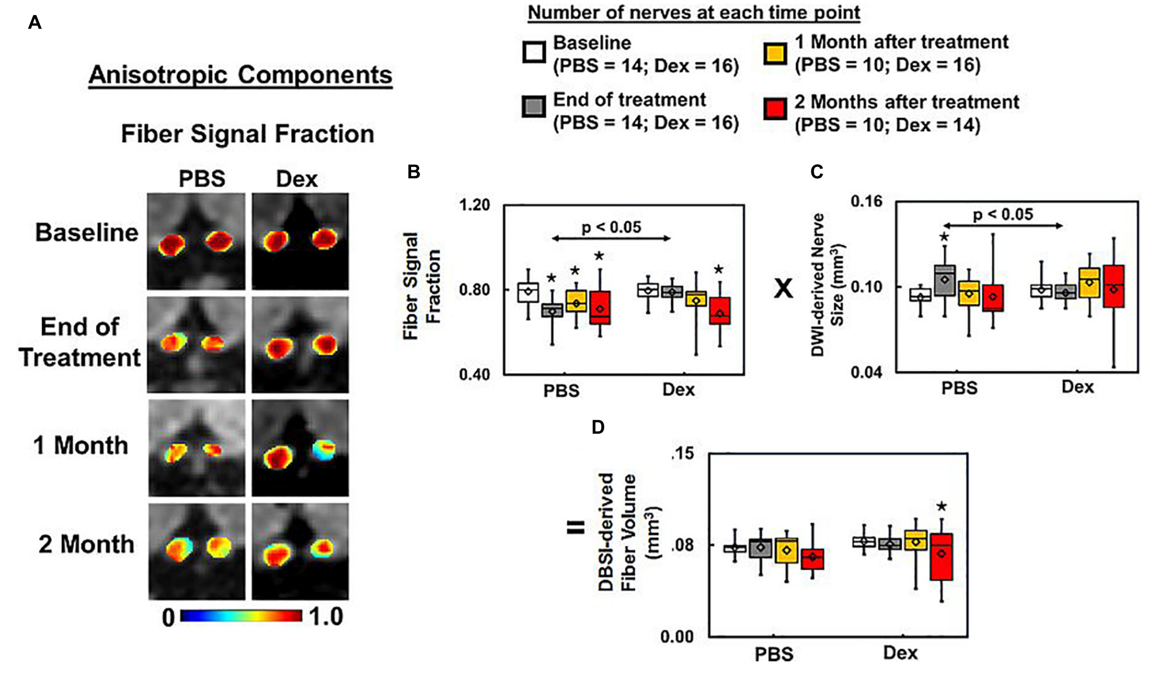

FIGURE 5 | DBSI fiber signal fraction is the portion of the total diffusion signal within an image voxel that is putative biomarker of axonal density **(A)**. Decreased axonal density from baseline was apparent at all time-points ($p < 0.05$) after ON onset in the PBS treated mice, and at 1 and 2 months after Dex ($p < 0.05$) treatment (**A**, same representative mice of **Figures 2**, **3**). Dexamethasone treatment effectively maintained the baseline fiber signal fraction at 2 weeks after treatment, slightly decreased by ∼10% from baseline without reaching statistical significance at 1 and 2 months afterward (**B**, $p = 0.37$). The DBSI "fiber volume" **(D)** was derived as DBSI anisotropic diffusion fiber signal fraction **(B)** multiplied by DWI-derived nerve volume **(C)** to reflect total fiber signal amount without dilution effects from cell inflammation/edema, putatively estimating the extent of axon loss **(D)**. DBSI-derived fiber volume quantifies the severity of axonal loss although not a true volume. At 2 months after treatment, axonal loss was seen in both PBS- and dexamethasone-treated optic nerves, suggesting that dexamethasone was not able to prevent irreversible axonal degeneration. * indicates $p < 0.05$, comparing to baseline.

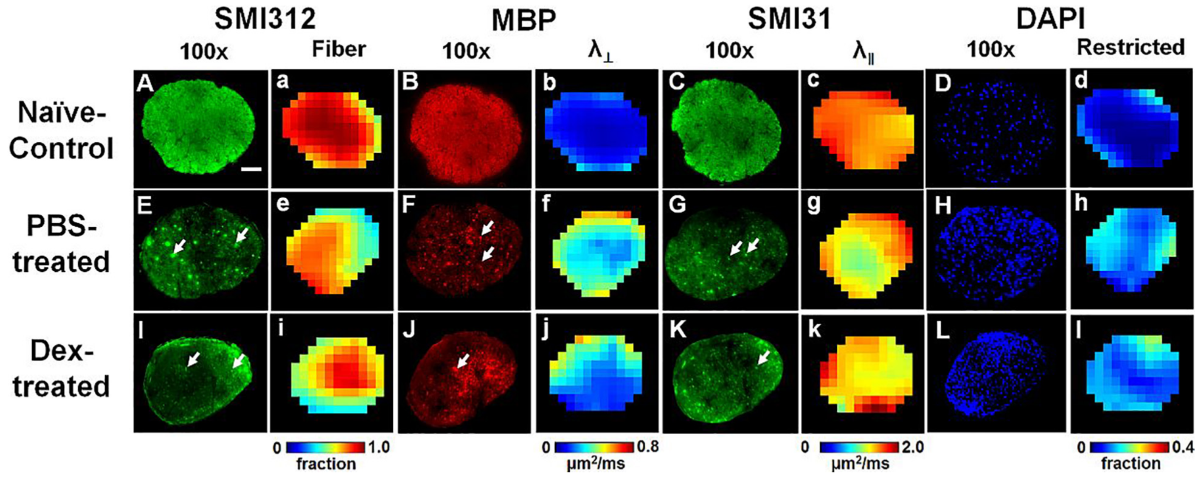

FIGURE 6 | Representative 100× immunohistochemical staining images of total neurofilament (SMI-312, staining both injured and intact axons, **A,E,I**), myelin basic protein (MBP, assessing myelin integrity, **B,F,J**), phosphorylated neurofilament (SMI-31, reflecting intact axons, **C,G,K**), and 4′, 6-dianidino-2-phenylindole (DAPI, detecting nuclei, **D,H,L**) from naïve control (row 1), PBS-treated (row 2), and dexamethasone-treated (row 3) optic nerves at end of DBSI time course (2 months after treatment). The corresponding DBSI fiber signal fraction (the total signal of optic nerve tracts, **a,e,i**), radial diffusivity ($\lambda_{\perp}$, myelin integrity of residual optic nerve tracts, **b,f,j**), axial diffusivity ($\lambda_{\parallel}$, axonal integrity of residual optic nerve tracts, **c,g,k**) and restricted fraction (cellularity, **d,h,l**) metrics demonstrate injury patterns of optic nerve. Results here show different degrees of tissue damage in optic nerves from mice with optic neuritis treated with PBS versus dexamethasone. The results are consistent with *in vivo* DBSI findings that short-term treatment with dexamethasone does not protect optic nerves after the cessation of treatment. Optic nerves developed axonal injury (decreased staining intensity and swollen axons, the white arrows, in SMI-312, MBP and SMI-31 panels), demyelination (decreased staining intensity for MBP), axonal loss (decreased SMI-32 staining intensity and tissue shrinkage), and increased cellularity (increased DAPI staining). White scale bar: 50 μm.

failed to preserve visual function in the long-term (**Figure 1B**). Histologically, similar degrees of optic nerve axonal injury/loss were observed in both PBS- and Dex-treated mice at 2 months after the 2-week treatment. To the best of our knowledge, this is the first study to non-invasively and longitudinally examine the effects of corticosteroids on the evolution of optic nerve pathologies of ON mice.

Corticosteroids suppress inflammation through inhibiting vascular permeability, suppressing leukocyte emigration into sites of inflammation, and reducing production of inflammatory mediators (Perretti and Ahluwalia, 2000; Coutinho and Chapman, 2011). Although corticosteroids are commonly employed to treat acute inflammation, they have known associated adverse effects, some of which are cumulative (Ohno et al., 1987; Buchman, 2001; Myhr and Mellgren, 2009), limiting its long-term use. Our findings were consistent with ONTT conclusion that no long-tern benefits of steroids for VA improvement. We speculate that timing of treatment commencement may play a critical role in treatment efficacy. Thus, with accurate and non-invasive assessment of optic nerve pathologies using DBSI that is capable of detect subclinical pathologies could improve the treatment efficacy by affording an early treatment before clinical manifestations detectable in MS (Noyes and Weinstock-Guttman, 2013; Kavaliunas et al., 2017). In the current study, we started at 0.1–0.3 mg/kg dexamethasone (Donia et al., 2010) that resulted in inconsistent and limited effects on EAE mice. Our final working dose of dexamethasone for treating ON (10 × clinical dose) is comparable to that used in previous reports to treat optic neuritis of MOG$_{35-55}$ EAE mice (Wust et al., 2008; Donia et al., 2010). The anti-inflammation effect of Dex seen in the report was also detected in the present study, manifested as the lower restricted isotropic diffusion fraction than PBS-treated EAE mice by comparing to baseline within group.

Axonal loss is believed to be the primary substrate of irreversible neurological disability in MS (van Waesberghe et al., 1999; Bjartmar et al., 2000; Wujek et al., 2002; Van Asseldonk et al., 2006). Optical coherence tomography (OCT) has been increasingly relied upon as a non-invasive biomarker of axonal loss for people with MS (Costello et al., 2006a; Lagreze et al., 2009; Saidha et al., 2015). DTI-derived fractional anisotropy (FA) has also been implied to reflect axonal injury. However, acute inflammation-associated cell infiltration and vasogenic edema might lead to optic nerve swelling. Both DTI and OCT results might be masked by these inflammations associated changes. Our results indicated that DTI $\lambda_{\parallel}$ and $\lambda_{\perp}$ was affected by the progression of inflammation overestimating axonal pathologies (**Figures 2B,C**). Thus, DTI metrics would fail to accurately reflect axonal injury or demyelination in the presence of axonal loss and/or inflammation. In contrast, DBSI not only detects inflammatory pathologies but also reflects axonal injury and demyelination without confounding effects of inflammation. DBSI-derived fiber volume, i.e., DBSI fiber fraction multiplied by optic nerve volume, quantified axonal loss of the optic nerve and spinal cord in the presence of acute inflammation-associated swelling (Lin et al., 2017, 2019). In the present study, DBSI-derived fiber volume reflected histology-detected axonal loss, and non-invasively reflected the failure of dexamethasone to prevent long-term optic nerve axonal loss in living mice.

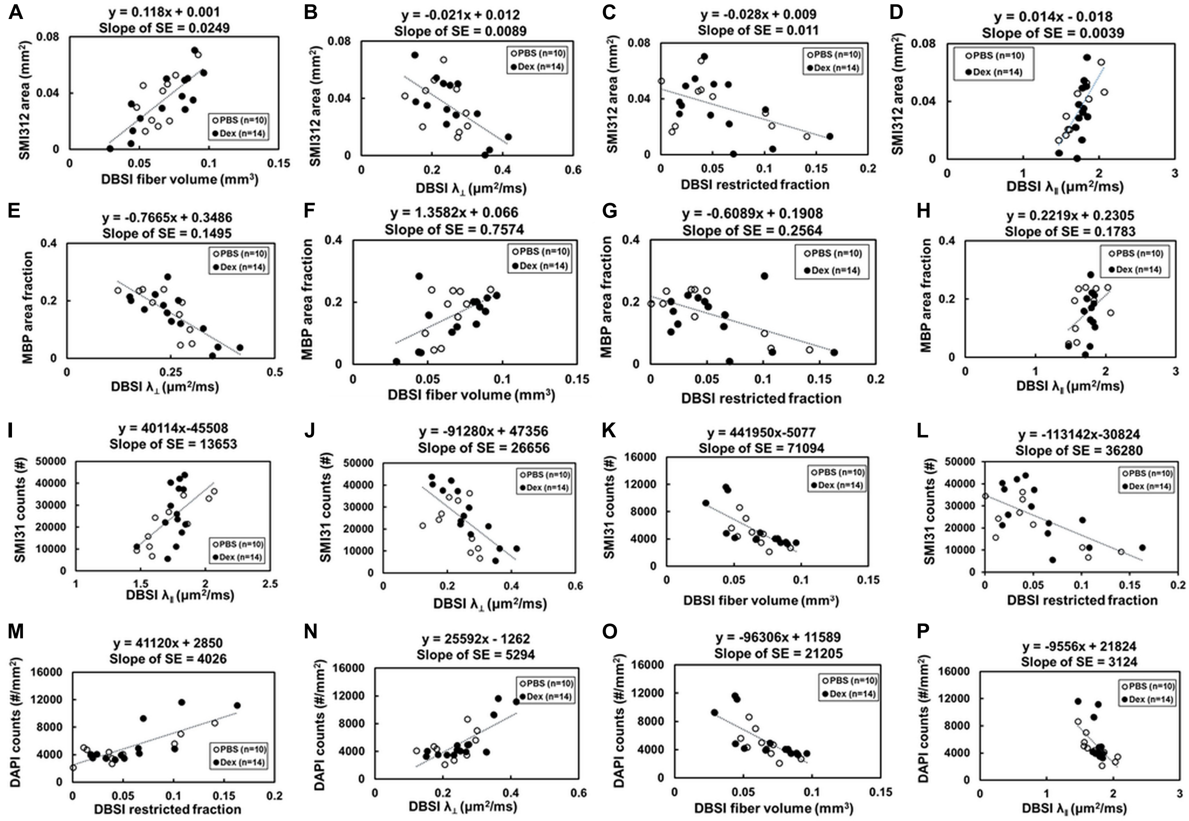

FIGURE 7 | Optic nerve tissues were extracted and prepared for IHC staining after the last imaging time point (2 months post-treatment). The correlations of IHC and DBSI metrics were **(A–P)** were shown. The IHC biomarkers included SMI-312 area (absolute value of positive staining counts, **A–D**), MBP area fraction (the ratio of positive staining counts and total tissue area, **E–H**) and SMI-31 counts **(I–L)**, and DAPI counts **(M–P)** to reflect severity of axonal loss, demyelination, axonal injury, and cellularity, respectively. Total axonal counts as expected directly correlated with DBSI fiber volume **(A)** and DBSI-$\lambda_{||}$ **(D)**, inversely correlated with DBSI-$\lambda_{\perp}$ (direct correlation with myelin integrity) and DBSI restricted diffusion fraction (increased inflammation impact axonal integrity). Similarly, MBP area (myelination integrity) directly corrected with DBSI axonal volume **(F)** and DBSI-$\lambda_{||}$ (**H**, i.e., axonal integrity impacted myelin integrity), and inversely correlated with DBSI-$\lambda_{\perp}$ (**E**, increased myelination integrity) and DBSI-restricted fraction (**G**, increased inflammation also damaged myelin). Intact axonal staining (SMI-31) directly correlated with DBSI-$\lambda_{||}$ **(I)** and axonal volume **(L)**, i.e., DBSI axonal integrity markers, and inversely correlated with DBSI-$\lambda_{\perp}$ (directly correlated with myelin integrity) and DBSI restricted fraction (**L**, inflammation damaged myelin integrity). Cellularity (DAPI staining) directly correlated with DBSI restricted fraction **(M)** and DBSI-$\lambda_{\perp}$ (directly correlated with myelin damage), and inversely correlated with DBSI fiber volume **(O)** and DBSI-$\lambda_{||}$ (i.e., inversely correlated with axonal integrity). Results reflect that axonal pathologies in EAE optic nerves are inter-dependent due to the pathological dependence.

In the current study, SMI312, MBP, SMI31, and DAPI were used to validate the specificity and sensitivity of DBSI-derived fiber volume, DBSI $\lambda_{\perp}$, DBSI $\lambda_{||}$, and DBSI restricted fraction. However, the inter-dependence among IHC biomarkers and DBSI metrics seen in the current study (**Figure 7**) reflects the potential causal relationships among underlying pathologies of optic neuritis in EAE mice. The results imply that DBSI metrics may not uniquely correlated with the target pathologies since one cannot definitively isolated inter-relationship between metrics. This observation is likely to hold true for all MRI derived biomarkers that are derived based on morphological changes without molecular specificity. For complex pathologies in diseases such as multiple sclerosis, it would be difficult to definitively validate any pathological biomarkers since the underlying pathologies are inter-dependent.

Histological validation of *in vivo* MRI findings needs to take into account of the evolution of pathologies of MS/EAE to elucidate the potential inter-correlations among coexisting individual pathological components. For example, if at a lesion or normal appearing white matter site where inflammation induces subsequence axonal injury at the same site or in close vicinity, then inflammation and axonal injury would correlate with each other. Under this scenario, an inflammatory marker could correlate with axonal injury or vice versa. Our previous numerous studies on EAE mice and postmortem MS specimens favorably suggest that DBSI-derived pathological metrics are adequate biomarkers of pathologies of axon, myelin, and inflammation origin. However, due to the unspecific nature of MRI biomarkers of white matter injury it would require researchers to be cautious in applying these markers in complex pathologies present in MS/EAE.

In summary, we employed serial DBSI to assess optic nerve pathology longitudinally in living EAE mice. Optic nerve responses to dexamethasone and PBS treatments, showing short-term but not long-term benefits of corticosteroids, which recapitulated observations from the ONTT in ON patients. Upon comparing *in vivo* DBSI to neuropathology, we demonstrated that DBSI-derived fiber volume can serve as a quantitative biomarker of axonal loss. Measurement of axonal loss is important, as it underpins permanent neurological impairment. The current study provides an important validation of DBSI-derived pathological markers in response to a treatment, and uniquely quantifies axonal loss *in vivo*.

DATA AVAILABILITY STATEMENT

The raw data supporting the conclusions of this article will be made available by the authors, without undue reservation.

ETHICS STATEMENT

The animal study was reviewed and approved by Washington University Institutional Animal Care and Use Committee (IACUC) and conformed to the NIH Policy on Responsibility for Care and Use of Animals.

AUTHOR CONTRIBUTIONS

T-HL, AC, and S-KS contributed to the concept and experimental design. T-HL, PS, and CS contributed to the protocol and code development. T-HL, JZ, CS, MW, XN, RY, and S-KS contributed to the generation, collection, and analysis of data. T-HL, AC, RY, MW, and S-KS contributed to the manuscript drafting. AC and S-KS contributed to the critical review of the manuscript. T-HL, JZ, CS, MW, PS, XN, RY, AC, and S-KS contributed to the manuscript approval. All authors contributed to the article and approved the submitted version.

FUNDING

This study was supported in part by the grants from National Institute of Health R01-NS047592 (S-KS), P01-NS059560 (AC), U01- EY025500 (S-KS), National Multiple Sclerosis Society (NMSS) RG 4549A4/1 (S-KS), RG1701-26617 (S-KS), FG-1507-05315 (T-HL), and Department of Defense Idea Award W81XWH-12-1-0457 (S-KS). The National Natural Science Foundation of China 81971574 (RY), the Guangzhou Science and Technology Project, P.R. China 202002030268 (RY), and Natural Science Foundation of Guangdong Province in China 2018A030313282 (RY). AC was supported in part by the Manny and Rosalyn Rosenthal-Dr. John L. Trotter MS Center Chair in Neuroimmunology of Barnes-Jewish Hospital Foundation.

ACKNOWLEDGMENTS

The authors thank Mr. Bob Mikesell for excellent technical assistance.

REFERENCES

Batchelor, P. G., Atkinson, D., Hill, D. L., Calamante, F., and Connelly, A. (2003). Anisotropic noise propagation in diffusion tensor MRI sampling schemes. *Magn. Reson. Med.* 49, 1143–1151. doi: 10.1002/mrm.10491

Beck, R. W., Cleary, P. A., Trobe, J. D., Kaufman, D. I., Kupersmith, M. J., Paty, D. W., et al. (1993). The effect of corticosteroids for acute optic neuritis on the subsequent development of multiple sclerosis. the optic neuritis study group. *N. Engl. J. Med.* 329, 1764–1769.

Bennett, J. L., Nickerson, M., Costello, F., Sergott, R. C., Calkwood, J. C., Galetta, S. L., et al. (2015). Re-evaluating the treatment of acute optic neuritis. *J. Neurol. Neurosurg. Psychiatry* 86, 799–808.

Bjartmar, C., Kidd, G., Mork, S., Rudick, R., and Trapp, B. D. (2000). Neurological disability correlates with spinal cord axonal loss and reduced N-acetyl aspartate in chronic multiple sclerosis patients. *Ann. Neurol.* 48, 893–901. doi: 10.1002/1531-8249(200012)48:6<893::aid-ana10>3.0.co;2-b

Blewitt, E. S., Pogmore, T., and Talbot, I. C. (1982). Double embedding in agar/paraffin wax as an aid to orientation of mucosal biopsies. *J. Clin. Pathol.* 35:365. doi: 10.1136/jcp.35.3.365-b

Boumpas, D. T., Chrousos, G. P., Wilder, R. L., Cupps, T. R., and Balow, J. E. (1993). Glucocorticoid therapy for immune-mediated diseases: basic and clinical correlates. *Ann. Intern. Med.* 119, 1198–1208. doi: 10.7326/0003-4819-119-12-199312150-00007

Buchman, A. L. (2001). Side effects of corticosteroid therapy. *J. Clin. Gastroenterol.* 33, 289–294. doi: 10.1097/00004836-200110000-00006

Ceccarelli, A., Bakshi, R., and Neema, M. (2012). MRI in multiple sclerosis: a review of the current literature. *Curr. Opin. Neurol.* 25, 402–409. doi: 10.1097/wco.0b013e328354f63f

Chiang, C. W., Wang, Y., Sun, P., Lin, T. H., Trinkaus, K., Cross, A. H., et al. (2014). Quantifying white matter tract diffusion parameters in the presence of increased extra-fiber cellularity and vasogenic edema. *Neuroimage* 101, 310–319. doi: 10.1016/j.neuroimage.2014.06.064

Costello, F., Coupland, S., Hodge, W., Lorello, G. R., Koroluk, J., Pan, Y. I., et al. (2006a). Quantifying axonal loss after optic neuritis with optical coherence tomography. *Ann. Neurol.* 59, 963–969. doi: 10.1002/ana.20851

Costello, F., Coupland, S., Hodge, W., Lorello, G. R., Koroluk, J., Pan, Y. I., et al. (2006b). Quantifying axonal loss after optic neuritis with optical coherence tomography. *Ann. Neurol.* 59, 963–969. doi: 10.1002/ana.20851

Coutinho, A. E., and Chapman, K. E. (2011). The anti-inflammatory and immunosuppressive effects of glucocorticoids, recent developments and mechanistic insights. *Mol. Cell. Endocrinol.* 335, 2–13. doi: 10.1016/j.mce.2010.04.005

Davie, C. A., Silver, N. C., Barker, G. J., Tofts, P. S., Thompson, A. J., Mcdonald, W. I., et al. (1999). Does the extent of axonal loss and demyelination from chronic lesions in multiple sclerosis correlate with the clinical subgroup? *J. Neurol. Neurosurg. Psychiatry* 67, 710–715. doi: 10.1136/jnnp.67.6.710

Diem, R., Hobom, M., Maier, K., Weissert, R., Storch, M. K., Meyer, R., et al. (2003). Methylprednisolone increases neuronal apoptosis during autoimmune CNS inflammation by inhibition of an endogenous neuroprotective pathway. *J. Neurosci.* 23, 6993–7000. doi: 10.1523/jneurosci.23-18-06993.2003

Donia, M., Mangano, K., Quattrocchi, C., Fagone, P., Signorelli, S., Magro, G., et al. (2010). Specific and strain-independent effects of dexamethasone in the prevention and treatment of experimental autoimmune encephalomyelitis in rodents. *Scand. J. Immunol.* 72, 396–407. doi:10.1111/j.1365-3083.2010.02451.x

Dustman, R. E., and Snyder, E. W. (1981). Life-span change in visually evoked potentials at central scalp. *Neurobiol. Aging* 2, 303–308. doi: 10.1016/0197-4580(81)90039-7

Gajofatto, A., and Benedetti, M. D. (2015). Treatment strategies for multiple sclerosis: when to start, when to change, when to stop? *World J. Clin. Cases* 3, 545–555. doi: 10.12998/wjcc.v3.i7.545

Gal, R. L., Vedula, S. S., and Beck, R. (2012). Corticosteroids for treating optic neuritis. *Cochrane Database. Syst. Rev.* 4:CD001430.

Gal, R. L., Vedula, S. S., and Beck, R. (2015). Corticosteroids for treating optic neuritis. *Cochrane Database. Syst. Rev.* 8:CD001430.

Ge, Y. (2006). Multiple sclerosis: the role of MR imaging. *AJNR Am. J. Neuroradiol.* 27, 1165–1176.

Gonzalez-Hernandez, J. A., Pita-Alcorta, C., Wolters, C. H., Padron, A., Finale, A., Galan-Garcia, L., et al. (2015). Specificity and sensitivity of visual evoked potentials in the diagnosis of schizophrenia: rethinking VEPs. *Schizophr. Res.* 166, 231–234. doi: 10.1016/j.schres.2015.05.007

Kavaliunas, A., Manouchehrinia, A., Stawiarz, L., Ramanujam, R., Agholme, J., Hedstrom, A. K., et al. (2017). Importance of early treatment initiation in the clinical course of multiple sclerosis. *Mult. Scler.* 23, 1233–1240. doi: 10.1177/1352458516675039

Kornek, B., Storch, M. K., Weissert, R., Wallstroem, E., Stefferl, A., Olsson, T., et al. (2000). Multiple sclerosis and chronic autoimmune encephalomyelitis: a comparative quantitative study of axonal injury in active, inactive, and remyelinated lesions. *Am. J. Pathol.* 157, 267–276.

Lagreze, W. A., Gaggl, M., Weigel, M., Schulte-Monting, J., Buhler, A., Bach, M., et al. (2009). Retrobulbar optic nerve diameter measured by high-speed magnetic resonance imaging as a biomarker for axonal loss in glaucomatous optic atrophy. *Invest. Ophthalmol. Vis. Sci.* 50, 4223–4228. doi: 10.1167/iovs.08-2683

Levitan, E. S., Hemmick, L. M., Birnberg, N. C., and Kaczmarek, L. K. (1991). Dexamethasone increases potassium channel messenger RNA and activity in clonal pituitary cells. *Mol. Endocrinol.* 5, 1903–1908. doi: 10.1210/mend-5-12-1903

Lieberman, D. M., Jan, T. A., Ahmad, S. O., and Most, S. P. (2011). Effects of corticosteroids on functional recovery and neuron survival after facial nerve injury in mice. *Arch. Facial. Plast. Surg.* 13, 117–124.

Lin, T. H., Chiang, C. W., Perez-Torres, C. J., Sun, P., Wallendorf, M., Schmidt, R. E., et al. (2017). Diffusion MRI quantifies early axonal loss in the presence of nerve swelling. *J. Neuroinflammation* 14:78.

Lin, T. H., Kim, J. H., Perez-Torres, C., Chiang, C. W., Trinkaus, K., Cross, A. H., et al. (2014a). Axonal transport rate decreased at the onset of optic neuritis in EAE mice. *Neuroimage* 100C, 244–253. doi: 10.1016/j.neuroimage.2014.06.009

Lin, T. H., Spees, W. M., Chiang, C. W., Trinkaus, K., Cross, A. H., and Song, S. K. (2014b). Diffusion fMRI detects white-matter dysfunction in mice with acute optic neuritis. *Neurobiol. Dis.* 67, 1–8. doi: 10.1016/j.nbd.2014.02.007

Lin, T. H., Sun, P., Hallman, M., Hwang, F. C., Wallendorf, M., Ray, W. Z., et al. (2019). Noninvasive quantification of axonal loss in the presence of tissue swelling in traumatic spinal cord injury mice. *J. Neurotrauma.* 36, 2308–2315. doi: 10.1089/neu.2018.6016

Llado, X., Oliver, A., Cabezas, M., Freixenet, J., Vilanova, J. C., Quiles, A., et al. (2012). Segmentation of multiple sclerosis lesions in brain MRI: a review of automated approaches. *Inform. Sci.* 186, 164–185. doi: 10.1016/j.ins.2011.10.011

Medana, I. M., and Esiri, M. M. (2003). Axonal damage: a key predictor of outcome in human CNS diseases. *Brain* 126, 515–530. doi: 10.1093/brain/awg061

Michalski, A., Radil, T., and Zernicki, B. (1981). Diminution of cortical visually evoked potentials during the following eye-movement in the cat. *Acta Neurobiol. Exp.* 41, 623–632.

Muller, G. J., Hasseldam, H., Rasmussen, R. S., and Johansen, F. F. (2014). Dexamethasone enhances necrosis-like neuronal death in ischemic rat hippocampus involving mu-calpain activation. *Exp. Neurol.* 261, 711–719. doi: 10.1016/j.expneurol.2014.08.009

Myhr, K. M., and Mellgren, S. I. (2009). Corticosteroids in the treatment of multiple sclerosis. *Acta Neurol. Scand. Suppl.* 189, 73–80. doi: 10.1111/j.1600-0404.2009.01213.x

Noyes, K., and Weinstock-Guttman, B. (2013). Impact of diagnosis and early treatment on the course of multiple sclerosis. *Am. J. Manag. Care* 19, s321–331.

Ohno, R., Hamaguchi, K., Sowa, K., Tanaka, H., and Watanabe, Y. (1987). High-dose intravenous corticosteroids in the treatment of multiple sclerosis. *Jpn. J. Med.* 26, 212–216. doi: 10.2169/internalmedicine1962.26.212

Perretti, M., and Ahluwalia, A. (2000). The microcirculation and inflammation: site of action for glucocorticoids. *Microcirculation* 7, 147–161. doi: 10.1111/j.1549-8719.2000.tb00117.x

Saidha, S., Al-Louzi, O., Ratchford, J. N., Bhargava, P., Oh, J., Newsome, S. D., et al. (2015). Optical coherence tomography reflects brain atrophy in multiple sclerosis: a four-year study. *Ann. Neurol.* 78, 801–813. doi: 10.1002/ana.24487

Schmierer, K., Scaravilli, F., Altmann, D. R., Barker, G. J., and Miller, D. H. (2004). Magnetization transfer ratio and myelin in postmortem multiple sclerosis brain. *Ann. Neurol.* 56, 407–415. doi: 10.1002/ana.20202

Song, S. K., Sun, S. W., Ju, W. K., Lin, S. J., Cross, A. H., and Neufeld, A. H. (2003). Diffusion tensor imaging detects and differentiates axon and myelin degeneration in mouse optic nerve after retinal ischemia. *Neuroimage* 20, 1714–1722. doi: 10.1016/j.neuroimage.2003.07.005

Spees, W. M., Lin, T. H., and Song, S. K. (2013). White-matter diffusion fMRI of mouse optic nerve. *Neuroimage* 65, 209–215. doi: 10.1016/j.neuroimage.2012.10.021

Tu, T. W., Budde, M. D., Quirk, J. D., and Song, K. S. (2010). Using absorption-mode images to improve in vivo DTI quality. *Proc. Intl. Soc. Mag. Reson. Med.* 18:4001.

Urolagin, S. B., Kotrashetti, S. M., Kale, T. P., and Balihallimath, L. J. (2012). Traumatic optic neuropathy after maxillofacial trauma: a review of 8 cases. *J. Oral Maxillofac. Surg.* 70, 1123–1130. doi: 10.1016/j.joms.2011.09.045

Valberg, A., Olsen, B. T., and Marthinsen, S. (1981). Peripheral contrast reversal inhibits visually evoked potentials in the fovea. *Vis. Res.* 21, 947–950. doi: 10.1016/0042-6989(81)90197-8

Van Asseldonk, J. T. H., Van Den Berg, L. H., Kalmijn, S., Van Den Berg-Vos, R. M., Polman, C. H., Wokke, J. H. J., et al. (2006). Axon loss is an important determinant of weakness in multifocal motor neuropathy. *J. Neurol. Neurosurg. Psychiatry* 77, 743–747. doi: 10.1136/jnnp.2005.064816

van Waesberghe, J. H. T. M., Kamphorst, W., De Groot, C. J. A., Van Walderveen, M. A. A., Castelijns, J. A., Ravid, R., et al. (1999). Axonal loss in multiple sclerosis lesions: magnetic resonance imaging insights into substrates of disability. *Ann. Neurol.* 46, 747–754. doi: 10.1002/1531-8249(199911)46:5<747::aid-ana10>3.0.co;2-4

Wang, X., Cusick, M. F., Wang, Y., Sun, P., Libbey, J. E., Trinkaus, K., et al. (2014). Diffusion basis spectrum imaging detects and distinguishes coexisting subclinical inflammation, demyelination and axonal injury in experimental autoimmune encephalomyelitis mice. *NMR Biomed.* 27, 843–852. doi: 10.1002/nbm.3129

Wang, X., Li, X. S., and Wang, W. C. (2007). Transnasal endoscopic optic canal decompression for traumatic optic neuropathy without light reception. *Zhonghua Er Bi Yan Hou Tou Jing Wai Ke Za Zhi* 42, 625–626.

Wang, Y., Sun, P., Wang, Q., Trinkaus, K., Schmidt, R. E., Naismith, R. T., et al. (2015). Differentiation and quantification of inflammation, demyelination and axon injury or loss in multiple sclerosis. *Brain* 138, 1223–1238. doi: 10.1093/brain/awv046

Wang, Y., Wang, Q., Haldar, J. P., Yeh, F. C., Xie, M., Sun, P., et al. (2011a). Quantification of increased cellularity during inflammatory demyelination. *Brain* 134, 3590–3601. doi: 10.1093/brain/awr307

Wang, Y., Wang, Q., Haldar, J. P., Yeh, F. C., Xie, M., Sun, P., et al. (2011b). Quantification of increased cellularity during inflammatory demyelination. *Brain J. Neurol.* 134, 3590–3601. doi: 10.1093/brain/awr307

Wujek, J. R., Bjartmar, C., Richer, E., Ransohoff, R. M., Yu, M., Tuohy, V. K., et al. (2002). Axon loss in the spinal cord determines permanent neurological disability in an animal model of multiple sclerosis. *J. Neuropathol. Exp. Neurol.* 61, 23–32. doi: 10.1093/jnen/61.1.23

Wust, S., Van Den Brandt, J., Tischner, D., Kleiman, A., Tuckermann, J. P., Gold, R., et al. (2008). Peripheral T cells are the therapeutic targets of glucocorticoids in experimental autoimmune encephalomyelitis. *J. Immunol.* 180, 8434–8443. doi: 10.4049/jimmunol.180.12.8434

Conflict of Interest: The authors declare that the research was conducted in the absence of any commercial or financial relationships that could be construed as a potential conflict of interest.

frontiers in Neuroscience

ORIGINAL RESEARCH
published: 24 February 2021
doi: 10.3389/fnins.2021.611451

Diffusion Tensor Imaging Detects Acute Pathology-Specific Changes in the P301L Tauopathy Mouse Model Following Traumatic Brain Injury

Neha Soni, Rodrigo Medeiros, Khawlah Alateeq, Xuan Vinh To and Fatima A. Nasrallah*

Queensland Brain Institute, The University of Queensland, St. Lucia, QLD, Australia

Traumatic brain injury (TBI) has been linked with tauopathy. However, imaging methods that can non-invasively detect tau-protein abnormalities following TBI need further investigation. This study aimed to investigate the potential of diffusion tensor imaging (DTI) to detect tauopathy following TBI in P301L mutant-tau-transgenic-pR5-mice. A total of 24 9-month-old pR5 mice were randomly assigned to sham and TBI groups. Controlled cortical injuries/craniotomies were performed for TBI/sham groups followed by DTI data acquisition on days 1 and 7 post-injury. DTI data were analyzed by using voxelwise analysis and track-based spatial statistics for gray matter and white matter. Further, immunohistochemistry was performed for total-tau and phosphorylated-tau, astrocytes, and microglia. To detect the association of DTI with these pathological markers, a correlation analysis was performed between DTI and histology findings. At day 1 post-TBI, DTI revealed a widespread reduction in fractional anisotropy (FA) and axial diffusivity (AxD) in the TBI group compared to shams. On day 7, further reduction in FA, AxD, and mean diffusivity and increased radial diffusivity were observed. FA was significantly increased in the amygdala and cortex. Correlation results showed that in the ipsilateral hemisphere FA reduction was associated with increased phosphorylated-tau and glial-immunoreactivity, whereas in the contralateral regions, the FA increase was associated with increased immunostaining for astrocytes. This study is the first to exploit DTI to investigate the effect of TBI in tau-transgenic mice. We show that alterations in the DTI signal were associated with glial activity following TBI and would most likely reflect changes that co-occur with/without phosphorylated-tau. In addition, FA may be a promising measure to identify discrete pathological processes such as increased astroglia activation, tau-hyperphosphorylation or both in the brain following TBI.

Keywords: traumatic brain injury, diffusion tensor imaging, transgenic, tau-hyperphosphorylation, astrocytes, microglia, fractional anisotropy, P301L-mutation

Edited by:
Yu-Chien Wu,
Indiana University Bloomington,
United States

Reviewed by:
Ken Sakaie,
Case Western Reserve University,
United States
Alejandra Sierra,
University of Eastern Finland, Finland
Jose Guerrero-Gonzalez,
University of Wisconsin–Madison,
United States

Correspondence:
Fatima A. Nasrallah
f.nasrallah@uq.edu.au

Specialty section:
This article was submitted to
Brain Imaging Methods,
a section of the journal
Frontiers in Neuroscience

Received: *29 September 2020*
Accepted: *25 January 2021*
Published: *24 February 2021*

Citation:
Soni N, Medeiros R, Alateeq K,
To XV and Nasrallah FA (2021)
Diffusion Tensor Imaging Detects
Acute Pathology-Specific Changes
in the P301L Tauopathy Mouse Model
Following Traumatic Brain Injury.
Front. Neurosci. 15:611451.
doi: 10.3389/fnins.2021.611451

INTRODUCTION

Traumatic brain injury (TBI) has recently been deemed a leading risk factor for dementias such as Alzheimer's disease (AD) or chronic traumatic encephalopathy (Fleminger et al., 2003; Hay et al., 2016; Li et al., 2017). People sustaining a TBI are 24% more likely to develop dementia, which increases with the severity and number of injuries (Fann et al., 2018). Distinctive but overlapping features of TBI and AD, apart from the associated cognitive deficits, are the deposition of fragments of the β-amyloid peptide to form plaques, and aggregation of hyperphosphorylated forms of the microtubule-associated protein tau to form intracellular neurofibrillary tangles (NFTs) (Tran et al., 2011a,b; Johnson et al., 2012; Magnoni et al., 2012). Clinicopathological studies show that NFTs are associated with brain function loss and the cognitive deficits reported in TBI and AD with the density of NFTs reflecting the degree of dementia (Yoshiyama et al., 2005; Johnson et al., 2016; Buckley et al., 2017). These findings indicate that tau is a valuable marker for the diagnosis of the long-term sequelae of TBI (Johnson et al., 2012). Immunohistochemical and biochemical methods have remained the gold standards for the detection of tau pathology in clinical, as well as experimental studies. In 5 to 7-month-old mice expressing wild-type human tau, accelerated tau pathology in the hippocampus, progressive astrogliosis, cognitive, and locomotor impairments were identified 6 weeks post-injury (Zhang et al., 2019). In a 3×Tg-AD mouse model overexpressing human tau and β-amyloid, accelerated hyperphosphorylation of tau and tau aggregates were observed 1 week after a single TBI (Tran et al., 2011a). Although both clinical and pre-clinical studies have proposed tau as a potential marker linking TBI to AD, the evidence has been largely based on *post mortem* evaluations and cannot be implemented in clinical settings. Moreover, the structural and pathological features of tauopathy have made its detection challenging even with *ex vivo* tools, hindering a concrete conclusion regarding its role in the link between TBI and AD (Hanger et al., 2009; Castellani and Perry, 2019). Therefore, there is a need to develop some *in vivo* tools to detect tau pathology at the early stages of disease in order to determine its effects during an individual's lifespan.

Diffusion tensor imaging (DTI) is a magnetic resonance imaging (MRI) modality that uses magnetic field gradients to detect diffusivity parameters of water molecules as they undergo diffusion in biological tissues; and these diffusivities may be affected by pathological processes (Beaulieu, 2002; Alexander et al., 2007). Tau protein is soluble and responsible for microtubular stability. In the hyperphosphorylated state, it begins to aggregate in the form of insoluble paired helical filaments, and water mobility on the surface of the tau protein is highly affected in its transition from monomeric to aggregated forms (Fichou et al., 2015). Reduced fractional anisotropy (FA) and increased MD have also been reported in hippocampal regions of early AD patients; however, no studies were performed to understand the pathological underpinnings of these changes (Rose et al., 2008). In the rTg4510 tau transgenic mouse model, a strain with massive tau expression and neurodegeneration, reduced FA and increased radial diffusivity (RD) were noticed in white matter regions with tau aggregates (Sahara et al., 2014; Wells et al., 2015). In the triple transgenic 3×Tg mouse model of AD, decreased FA and axial diffusivity (AxD) were associated with the depositions of both amyloid-β and hyperphosphorylated tau in the hippocampal region (Snow et al., 2017). Although, DTI has been shown to detect hyperphosphorylated tau in AD patients and experimental models, no study is available that has investigated the potential of this method to detect tau abnormalities following severe TBI. Given that TBI involves a complex pathology and survivors can develop tauopathy within a week (Tran et al., 2011a; Rubenstein et al., 2017), it is crucial to understand if and how DTI reflects tau hyperphosphorylation in other confounding pathologies associated with brain injuries at its early stages.

Neuroinflammation is a crucial intrinsic process that has been implicated in the pathological events of tau aggregation and can be robustly induced by TBI (Johnson et al., 2013; Bemiller et al., 2017; Laurent et al., 2018; Pischiutta et al., 2018). Active glial cells (astrocytes and microglia) can increase tau hyperphosphosphorylation, followed by its aggregation (Leyns and Holtzman, 2017; Laurent et al., 2018). DTI has been shown to detect post-TBI neuroinflammation (Budde et al., 2011; Soni et al., 2018), but in AD, neuroinflammation has mostly been investigated using positron emission tomography imaging (Lagarde et al., 2018). Recently, Wang et al. (2015) proposed that DTI can detect inflammation in pre-clinical stages of AD by identifying reduced diffusivity measures (AD, MD, and RD). Thus, the evaluation of DTI to detect tau-induced structural brain abnormality at the early stages of TBI and to differentiate them from neuroinflammation-like pathologies can put more insight into DTI's detection potential in TBI.

This work applies a DTI-histopathological approach to examine the effect of TBI on tau pathology progression in both white and gray matter structures in pR5 mice. pR5 mice overexpress the human tau isoform with a P301L mutation and a well-developed model to study tauopathy (Gotz et al., 2001). Since tauopathy is a key process that is triggered following TBI in the AD brain, confirmed both biochemically and histopathologically, we demonstrate, for the first time, the potential of DTI to map the spatial and temporal profile of the pathological processes following TBI in a tau transgenic mouse model.

MATERIALS AND METHODS

Animals and Study Design

Twenty-four 9-month-old male and female P301L tau transgenic mouse (line pR5) (21–35 g) generated on a C57B1/6 × DBA2F1 background, and backcrossed onto C57B1/6 were used (Gotz et al., 2001). Transgenic mice were randomly allocated into two TBI and two sham groups at two respective time points, i.e., days 1 and 7 post-injury. To ensure the validity and precision of the statistical analysis, we used six mice per group. This study was approved by the Animal Research Ethics Committee of the University of Queensland (Animal Ethics Committee number: QBI/SCMB/036/16/MAIC). All the experiments were performed in accordance with the Australian code of practice for the care and use of animals for scientific purposes.

All animals were housed in the animal facility of the Center for Advanced Imaging, UQ, and acclimatized for a week before commencing surgeries. The TBI groups received a controlled cortical impact (CCI), whereas the sham groups underwent only craniotomy without an impact followed by MRI scan at the respective time points. All animals were immediately perfused after the MRI scans for histological studies. The study design is illustrated in **Figure 1**.

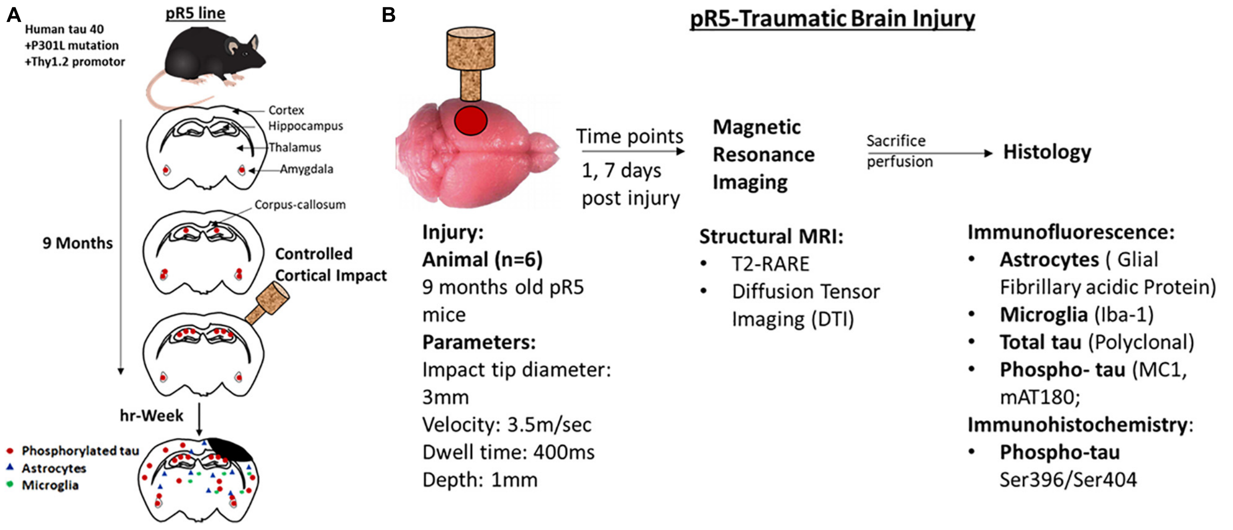

FIGURE 1 | Representation of experimental design and experiments performed at different time points. **(A)** A schematic representation of the pathological progression in pR5 mice before and after injury in 9-month-old mice. **(B)** Experimental design, 9-month-old pr5 mice (n = 6/group) were exposed to controlled cortical impact followed by structural MRI scans at days 1 and 7, followed by histological analysis for astrocytes, microglia, total tau, and phospho-tau.

Controlled Cortical Impact Model of Traumatic Brain Injury

Focal open skull injuries were performed using a CCI injury model following the same protocol described in our previous paper (Soni et al., 2018). Briefly, animals were anesthetized with 1.5–1.8% of isoflurane in a mixture of compressed air and oxygen (1:0.8) and fixed in a stereotactic frame with ear bars and a bite bar. Eye gel was applied to the eyes to avoid dryness. Craniotomy was performed on the left side of the brain, and the bone flap was removed from the craniotomy region with the dura intact. All mice in the TBI groups were exposed to a cortical impact using the CCI device (model-TBI 0310; Precision System and Instrumentation LLC.) with a 3 mm diameter piston tip. The brain was hit with an impact velocity = 3.5 m/s, depth = 1 mm, and dwell time = 400 ms, whereas, in the sham groups, only craniotomy was performed. In all cases, the bone flap was replaced, and the skin was sutured after the procedure in all mice. Animals were removed from the stereotaxic frame and placed on a heating pad for recovery. 0.5 ml of saline was injected subcutaneously in three different regions in all the animals for rehydration. All the mice were active within 5–10 min following injury and were kept in cages with *ad libitum* access to water gel and wet food.

MRI Data Acquisition

All animals were handled for a minimum of 2 weeks prior to the scan. Animals were conditioned to handling for 5–10 min each day for a week before the surgery. On the day of surgery, each mouse was handled for 3–5 min before being placed in the anesthetic chamber, and then they were handled each day until the day of scanning. On the day of the scan, animals were also handled for 3–5 min before the induction of anesthesia to minimize stress. All TBI and sham animals underwent MRI scanning on days 1 and 7. MRI scans were performed on a 9.4T MRI scanner (Bruker BioSpin, Germany) equipped with a cryogenically cooled transmit and receive coil, controlled by a console running Paravision 6.0.1 (Bruker BioSpin, Germany) Deep anesthesia was induced by 3% of isoflurane in a mixture of compressed air/O_2 (0.6/0.4) at 1 l/min, followed by 1.5–2% of isoflurane for maintenance. Deeply anesthetized rodents were then placed on an MRI-compatible cradle (Bruker Biospin) in the head first, supine position, and the head was fixed using ear bars and a bite bar to avoid movement. The respiration rate and rectal temperature were monitored by an MRI-compatible rodent physiological monitoring system (Model 1030, SA Instruments Inc.). Three—dimensional (3D) T2-weighted (T2w) imaging data sets were acquired using a rapid acquisition with relaxation enhancement (RARE) sequence with the following parameters: repetition time (TR) = 7200 ms, echo time (TE) = 39 ms, averages = 4, slice thickness = 0.3 mm, field of view (FoV) = 19.2 × 19.2 × 15.6 mm, and matrix = 192 × 192 × 52 totaling to 11 min 31 s of acquisition time/animal. DTI data were acquired using an axial gradient echo-planar imaging sequence using TR = 10,000 ms, TE = 25 ms, averages = 2, number of slices = 48, slice thickness = 0.3 mm, FoV = 18 × 18 × 15.6 mm, and matrix = 100 × 100 × 48, 2 b0 volumes, 33 non—collinear directions with b—value 750 s/mm^2 with acquisition time of 11 min 40 s of acquisition time/animal. A reverse-phase image was acquired for DTI, which was used in data pre-processing.

MRI Data Analysis

T2-weighted and DTI data sets were analyzed using the FMRIB Software Library version 5.0.9 (FSL)[1]. First, all T2w images were corrected for motion using the MCFLIRT tool (FMRIB's Software Library) (Smith et al., 2004), followed by inhomogeneity

---

[1] https://fsl.fmrib.ox.ac.uk/fsl/fslwiki

correction using the N4BiasFieldCorrection function of the advanced normalization tools (ANTs Version: 2.1.0-gGIT-N). Corrected T2w datasets were then skull-stripped using brain masks created with the 3D Pulsed-Couple Neural Networks tool (Chou et al., 2011) and brain images were extracted. Skull-stripped individual T2w images were affinely registered to the Australian Mouse Brain Mapping Consortium template[2] using FMRIB's FLIRT. The registered images were averaged to create the first iteration of a study-specific template. This first iteration study-specific template was used as reference for non-linear registration of individual images using FMRIB's FNIRT. The non-linearly registered individual images were averaged to generate the final study specific template to which a final round of non-linear registration of individual T2w images was performed.

Firstly, we used the reverse phase encoding volume pair as input for TOPUP (Andersson et al., 2003) to estimate distortion then correct all DWIs, then the MCFLIRT tool (FMRIB's Software Library) (Smith et al., 2004) was used to adjust for eddy current distortion. The DTI data were then corrected for signal inhomogeneity using N4 Field bias correction from ANTS (ANTs Version: 2.1.0-gGIT-N). The FSL-diffusion Toolkit (DTI-FIT) (Behrens et al., 2003) was used for local fitting of the diffusion tensors to generate the maps for the DTI parameters FA, MD, AxD, and RD using *b*-values 0 and 750 s/mm. To register the data to the study specific template, we firstly co-registered the individual's B0 maps to the corresponding T2 images and then apply the warp files from T2-to-study template to register the DTI measures to the same common space of study specific template. All estimated DTI maps were registered to the study-specific T2w template for inter-group voxelwise permutation testing.

To improve the sensitivity, objectivity, and interpretability of the white matter changes, voxel-based analysis style-TBSS (track-based spatial statistics) was performed by using the standard pipeline in FSL, FMRIB (Smith et al., 2006, 2007). In this analysis method, all FA maps in a common study−specific T2w template space were first averaged to create the mean FA template, followed by generation of the mean skeletonized FA maps (representation of fiber tracts). The individual skeletonized mean FA map was further used to generate a distance map. The distance map, together with the FA map thresholded at 0.2 and the anterior commissure as the reference, was used to get a TBSS skeleton for the individual FA maps and subsequently for all other individual metrics (AxD, RD, and MD skeletonized) to show changes in the white matter tracks. The mean FA template was used as an underlay to represent the diffusion changes in the white matter. A demonstration of DTI image registration efficiency and TBSS skeletonization procedure can be found in **Supplementary Figures 1, 2**. Which demonstrated the efficiency of image registration, its short comings with regards to larger white matter tracts while acceptable for large homogenous gray matter structures, and TBSS efficiency and accuracy in improve the matching across subjects and reflect, for example, missing white matter tracts in the lesion area.

For region-of-interest based analyses, we mainly focused on the regions with maximal changes seen on statistical difference maps obtained from the voxel-based analysis. These regions involved the corpus callosum (middle region), ipsilateral (ip) and contralateral (cn) external capsule, and the internal capsule. In the gray matter, the cn-dentate gyrus, CA1 region (the ipsilateral hippocampus was washed away during brain processing for histology), ipsilateral and contralateral amygdala, cortex, and thalamus were explored. Regions-of-interest were drawn manually on the study-specific template using the Australian mouse brain mapping consortium template (Watson et al., 2017) and the Allen adult mouse brain atlas[3] as a reference (Soni et al., 2020). Diffusion and anisotropy values were extracted from the regions-of-interest and correlated with the measures from immunohistochemistry, namely, phosphorylated tau, microglia, and astrocytes.

Histology Preparation and Analysis

Immediately after MRI scans, the mice were deeply anesthetized with isoflurane and perfused transcardially with 11 ml 0.1 M phosphate-buffered saline containing 1% sodium nitrite (PBS, pH 7.4) followed by 11 ml 4% formaldehyde (prepared from paraformaldehyde) dissolved in 0.1 M PBS. Perfusates were delivered using an automated syringe pump [10 ml–14.48 mm diameter BD (New Jersey, United States) syringes were used] programed to deliver perfusates at 90 ml/h. Brains were excised and immersion-fixed in 4% PFA overnight at 4°C and then stored in PBS supplemented with 0.05% sodium azide. Prior to slicing, the brains were cryoprotected with 30% sucrose for 48 h. The frozen brains were sectioned coronally (40 μm thick) using a Leica SM2010R freezing microtome and collected serially in PBS with 0.02% sodium azide and kept at 4°C until used for immunohistology. In accordance with the 3rd edition of the Franklin and Paxinos, 1997 mouse brain atlas, five coronal mouse brain sections were selected (between Bregma −0.5 and −4.5 mm) for each immunohistology staining (Every 25th coronal section of 40 μm thickness). Allen mouse brain atlas (see text footnote 3) was also referred to cross verify regions of interest for clarity.

Immunohistochemistry

For immunohistochemistry, free-floating brain sections were rinsed thrice with tris-buffer saline (TBS, pH 7.5) and then incubated with 30% H_2O_2 in methanol in TBS for 30 min to quench the endogenous peroxidase activity. This was followed by TBS washing and citrate buffer treatment at 95°C for 10 min for antigen retrieval. Sections were then treated in 0.1% Triton X-100 in TBS (TBS-A; pH = 7.5) for 15 min, followed by blocking in 2% bovine serum albumin in TBS and Triton X-100 (TBS-B; pH = 7.5) for 30 min. Brain sections were further incubated with the primary antibody for phosphorylated-tau [rabbit pSer (396 + 404) (Thermo Fisher; 1:1,000)] with 5% normal-horse-serum and kept on the shaker overnight at 4°C. The tissues were washed gently for 15 min the next morning. Prior to the secondary antibody treatment, sections were blocked with 5% normal-horse-serum diluted in TBS-B for 30 min and then incubated with secondary biotinylated horse

---

[2] http://imaging.org.au/AMBMC/Model

[3] https://alleninstitute.org/

anti-rabbit immunoglobulin-G (Vector Laboratories; 1:500) for an hour. After 20 min of blocking with TBS-B, the sections underwent Avidin-Biotin Complex (ABC) reagent treatment (Vector laboratories) for 30 min, followed by 3,3′-Diaminobenzidine (DAB) treatment with hydrogen peroxide at room temperature. The DAB treatment time was strictly controlled to obtain comparable results. The sections were then rinsed with TBS and mounted on superfrost-plus slides. After drying, the slides were cover-slipped with the mounting medium and allowed to dry overnight.

Immunofluorescence

For total tau, immunofluorescence was performed. Except for H_2O_2 and citrate buffer treatment, the initial steps were similar to those used for immunohistochemistry. Brain sections were then incubated with primary antibody (polyclonal rabbit anti-human) (Dako; 1:1,000) for total tau. Goat anti-rabbit 488 (Life Technologies; 1:200) was used as the secondary antibody. The sections were rinsed, mounted, dried, and cover-slipped. Double immunofluorescence was performed for astrocytes and microglia using glial fibrillary acidic protein (GFAP) and ionized calcium-binding adaptor molecule 1 (Iba1) markers, anti-GFAP chicken polyclonal antibody (Abcam; 1:1,000) and anti-Iba1 rabbit monoclonal antibody (Wako; 1:1,000). Goat anti-rabbit 555 (Life Technologies; 1:200) and goat-anti chicken 488 (Life Technologies; 1:200) secondary antibodies were used.

Quantification

Sections were examined for staining under an upright microscope (Axio Imager Green). For the quantification, slides were scanned using a Metafer VSlide scanner (MetaSystems) using a Zeiss Axio Imager Z2. Each section of the slides was then cropped into individual images using the 3D crop tool of the interactive microscopy image analysis software (Imaris; Bitplane). For the histology figures, selected areas of interests were acquired using a spinning-disk confocal system (Marianas; 3i, Inc.) consisting of an Axio Observer Z1 (Carl Zeiss), CSU-W1 spinning-disk head (Yokogawa Corporation), ORCA-Flash4.0 v2 sCMOS camera (Hamamatsu Photonics), using 63× magnification oil immersion objective. Images were acquired as 20 μm Z-stacks with 0.5 μm intervals and the 3D stacks were maximum intensity Z-projected to create a single 2D image for figures.

The percentage area of phosphorylated-tau positive immunoreactivity was calculated as described previously (Bodea et al., 2017). Total five serial sections per animal were used for the histological quantification. Using ImageJ, two sample boxes, one large and one small were created. These two sample boxes were utilized to create multiple ROIs of the same dimensions that were then placed on the respective areas of interest on the slices (corpus callosum, internal capsule, external capsule, cortex, dentate gyrus, CA1, thalamus, and amygdala). Please refer to **Supplementary Figure 3** for the ROI details. These regions were chosen on the basis of voxel-based analysis results of DTI maps. To be consistent, same ROIs were used for all the animals with slight adjustments for the regions if needed. For total-tau, astrocyte and microglia sections were corrected for the background using the rolling ball algorithm, then thresholded using the automated ImageJ threshold (moment), where staining was not visible in the negative control. Cell number and percent area covered by cells were then calculated using the particle analyzer tool. Any region that has multiple boxes, average values were calculated. The graphs are platted statistically while the images shown are the representative images from a random subject of each group. Slight differences in the contrast in the representative images could be during data acquisition from the automatic scanning, however the data acquisition parameters were well optimized and consistent for the data. Visual analysis was performed to check the major deformations, link to the data repository can be provided if needed.

Statistical Analysis

For voxel-based analysis, an unpaired two-sample *t*-test was used to calculate the differences between the TBI and sham animals for the DTI parameters using the FSL—randomize tool with the number of permutations set to exhaustive. The FSL-threshold-free cluster enhancement corrected difference maps, thresholded at p-value ≤ 0.05 results, were reported.

For region-of-interest-based analysis, prior to fitting the statistical models, we examined the normality of the data using the Shapiro–Wilk test. All the data sets were normally distributed, so parametric tests were used for the analysis. One-way ANOVA with *post hoc* analysis using Tukey's multiple comparisons test was used. Data analysis was completed and plotted using GraphPad Prism version 7.04 (GraphPad Software Inc.). The results are presented as mean ± standard error measurement. $^{*}p$-value ≤ 0.05, $^{**}p$-value ≤ 0.001, and $^{***}p$-value ≤ 0.0001 were considered significant.

In order to investigate the possible association between DTI measures, tau pathology, and neuroinflammation, Pearson's multiple correlations were performed. The calculated R^2 or the coefficient of correlation values and corrected p-values are reported in the results. A p-value ≤ 0.05 was considered significant. As we have $n = 6$, it was not enough separate the data and perform correlation within separate groups. Thus, both sham and TBI groups were combined for correlation.

RESULTS

In this study, the effects of TBI on the microstructure of the white and gray matter were examined by determining the associated changes of water diffusion using DTI, with corresponding pathological analyses in the same animals from histological specimens. Here, we report the whole brain voxel-based analysis results. Further, we discuss our immunohistochemistry findings and their correlation with DTI measures (FA, MD, AxD, and RD) in several white matter and gray matter regions selected on the basis of the voxel-based analysis results.

Diffusion Tensor Imaging Reveals Changes in the White Matter of pR5 Mice Following TBI

Figure 2 represents significantly affected white matter regions after TBI as compared sham controls. From the TBSS results

(**Figure 2A**), FA was significantly low in pR5 mice following TBI compared to sham-treated pR5 mice in the white matter regions ipsilateral to the lesion side involving the corpus callosum, external capsule, fimbria, stria terminalis and internal capsule, optic tracks, and external medullary lamina of the thalamus on day 1 post-injury. FA reduction was also seen in the contralateral-external capsule of the pR5 TBI mice. On day 7, in addition to the above-mentioned regions, a significant reduction in FA was observed in the corpus callosum, fimbria, and internal capsule in the TBI mice compared to the sham mice. In the case of diffusivity changes, on day 1 post-injury, a significantly reduced AxD was noted in the ipsilateral and contralateral fimbria and external capsule in the TBI mice as compared to the sham mice, whereas RD and MD were significantly higher. A similar increase in RD and MD was observed in the corpus callosum, ipsilateral internal capsule, and contralateral internal capsule. On day 7 post-injury, a significant AxD reduction was evident in the corpus callosum and the contralateral fimbria, internal capsule, and external capsule regions in the TBI group versus the sham group. Unlike on day 1, RD and MD changes were negligible except in the ipsilateral external capsule, where increased RD and MD changes were noted in the TBI mice. These results indicate that DTI measures were potentially detecting the white matter abnormalities induced by TBI in tau transgenic mice.

DTI Reveals Changes in the Gray Matter in pR5 Mice Following TBI

Diffusion tensor imaging results shown in **Figure 3** reveal significant destruction in the gray matter microstructural regions. In voxel-based analysis findings (**Figure 3A**), on day 1 post-injury, there was a significant reduction in FA in the ipsilateral caudate-putamen and the thalamus in the TBI group as compared to the sham group. On day 7, together with the

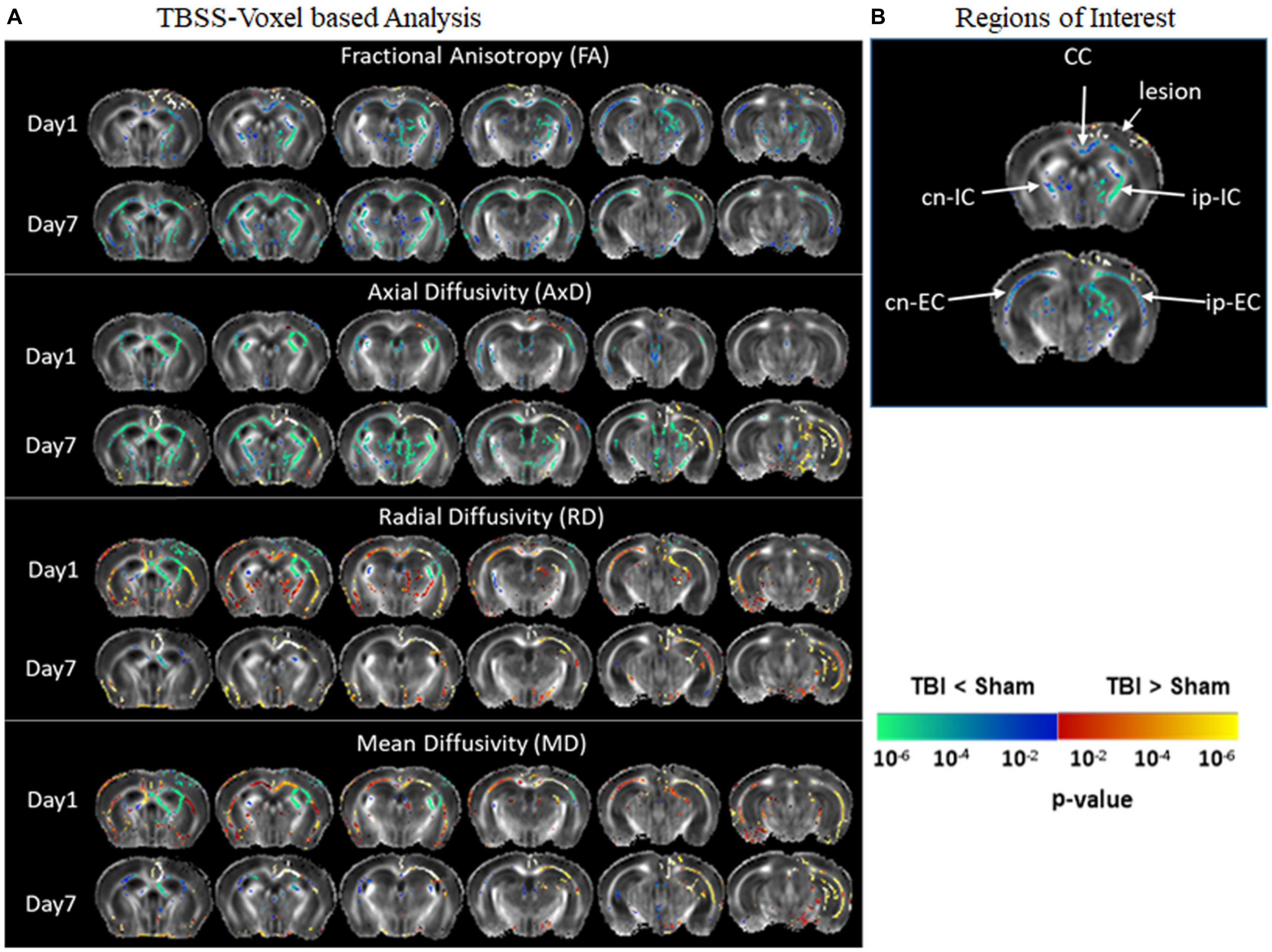

FIGURE 2 | Alterations in DTI measures (FA, AxD, MD, and RD) in white matter representing statistical differences between pR5-sham and pR5-TBI groups over 1 week. **(A)** Tract-based spatial statistical Intergroup difference maps for DTI parameters fractional anisotropy (FA), axial diffusivity (AxD), mean diffusivity (MD), and radial diffusivity (RD) between sham ($n = 6$) and TBI groups ($n = 6$) at different time points overlaid on the FA-template (columns). Yellow–red indicates TBI > sham, and blue–green indicates TBI < sham. The statistical map was thresholded at p-value ≤ 0.05, unpaired two-sample t-test, implemented as permutation tested for the General Linear Model. **(B)** Showing the regions of interest chosen for the correlation analysis involving the corpus callosum, ipsilateral internal capsule, contralateral internal capsule, ipsilateral external capsule, and contralateral external capsule.

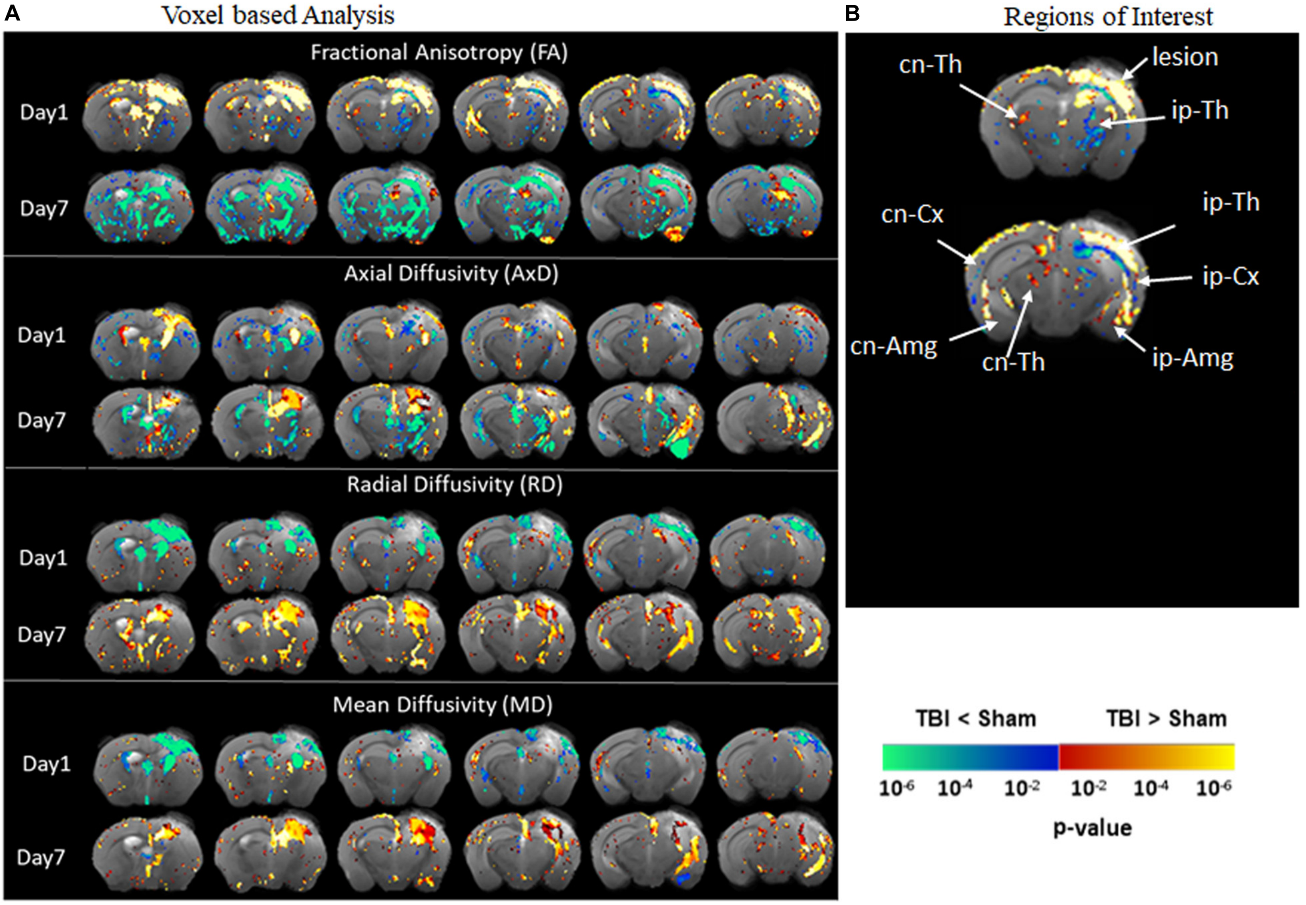

FIGURE 3 | Alterations in DTI measures (FA, AxD, MD, and RD) in gray matter representing statistical differences between pR5-sham and pR5-TBI groups 1 week after TBI. **(A)** Voxel-by-voxel statistical analysis results of DTI parameters fractional anisotropy (FA), axial diffusivity (AxD), mean diffusivity (MD), and radial diffusivity (RD) between sham and TBI groups at different time points overlaid on the FA-template (columns). Yellow–red indicates TBI > sham, and blue–green indicates TBI < sham. The statistical map was thresholded at p-value ≤ 0.05, unpaired two-sample t-test, implemented as permutation tested for the General Linear Model. Fractional anisotropy changes were extremely high after 7 days post-injury in the gray matter. **(B)** Showing the regions of interest chosen in the correlation analysis, involving ipsilateral and contralateral thalamus, amygdala, cortex, and contralateral hippocampal regions. MRI regions of interest are also presented in **Supplementary Figure 3B**.

ipsilateral regions, a significantly reduced FA was apparent in the contralateral regions involving the caudate-putamen, cortex, and hippocampus (CA1 and dentate gyrus). The FA was significantly increased in the piriform amygdala, cortex, and in the deep gray matter in close proximity to the lesion. A significant reduction in AxD in the TBI group versus the sham group was mainly found in the ipsilateral and contralateral cortex, the ipsilateral thalamic area closer to the injury site, and in the caudal hippocampus on day 1 post-injury. On day 7, a widespread reduction in AxD in the TBI group as compared to the sham group was observed in the regions involving the ipsilateral caudate-putamen, thalamus, and amygdala. Unlike on day 1, a significant increase in the AxD was seen in the cortex and caudal hippocampus. The RD and MD were significantly increased in cortical and thalamic areas in the TBI group versus the sham group after day 1 post-injury. On day 7, significant increases in RD and MD were noted only in the cortex of TBI group as compare to sham group. Overall, these results indicate that TBI induced structural abnormalities in tau transgenic mice were significantly altering all DTI measures. Both increased and decreased FA changes were noted in different in gray matter regions.

Increased Tau Phosphorylation Post-injury in pR5 Mice

Immunohistochemistry revealed post-injury increase in tau hyperphosphorylation at the epitope site ser396 + 404 in several white and gray matter regions (**Figures 4A**, **5A**). This increased pathology was potentially reflected by the various DTI measures as shown in our correlation analysis, represented in **Figures 4C**, **5C**.

Statistically (**Figure 4B**), on day 1, a significant increase in the percentage of Ser396 + 404-positive area was observed in the cn-internal capsule in the TBI group (3.638 ± 0.7967; $p = 0.0482$) versus the sham group (0.5933 ± 0.1722). Immunoreactivity for phosphorylated tau was not altered

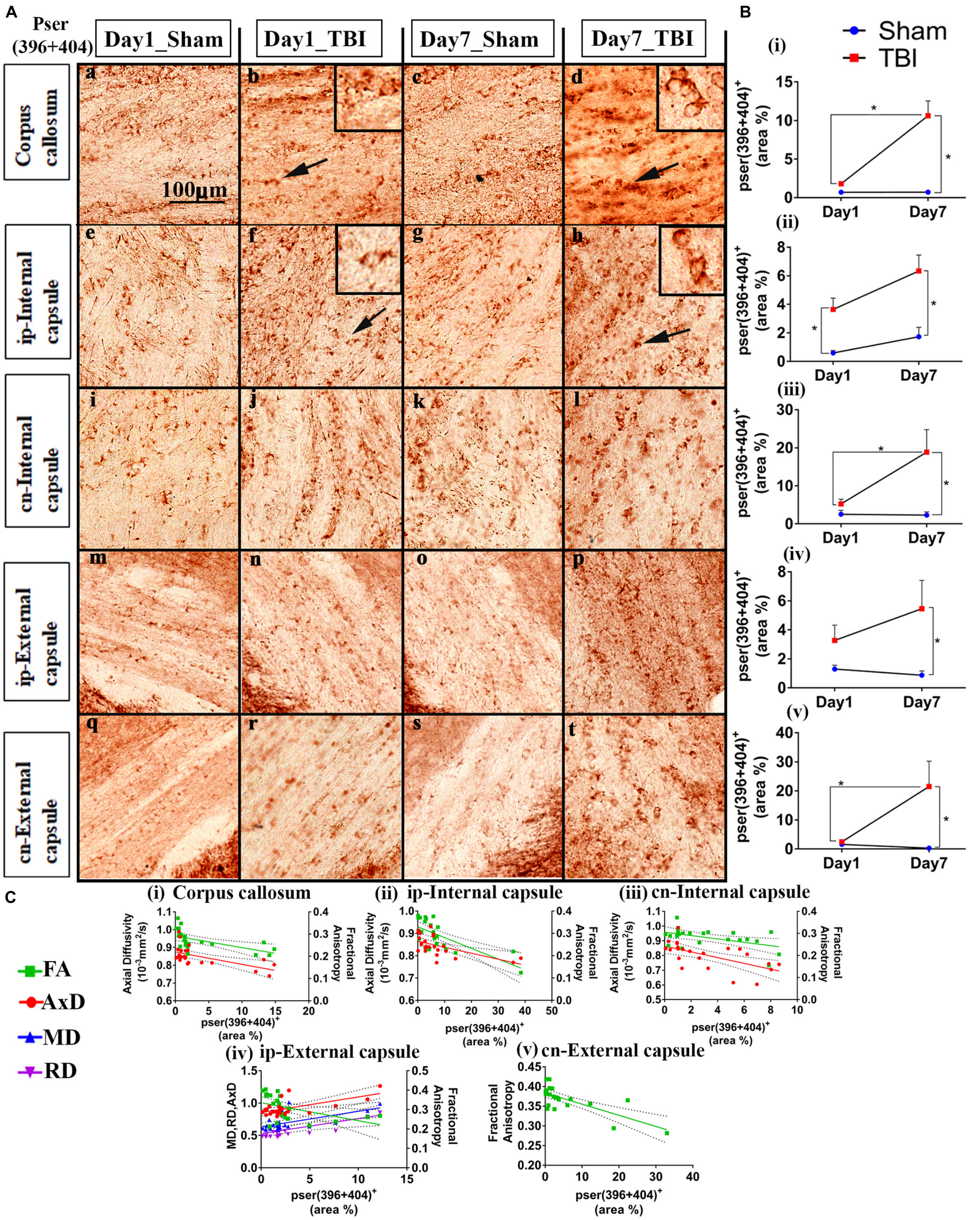

FIGURE 4 | Controlled cortical impact increases phosphorylation in the white matter of injured pR5 mice: **(A)** Phosphorylation at the pSer396 + 404 epitopes of tau was detected in different white matter regions, including the corpus callosum (a–d), ipsilateral internal capsule (e–h), contralateral internal capsule (i–l), ipsilateral external capsule (m–p), and contralateral external capsule (q–t) of pR5 mice post-injury (*n* = 6 pR5 TBI mice and *n* = 6 pR5-sham mice at days 1 and 7). Scale bar: 100 µm. Zoom-in view of phospho-tau positive cells indicated with the black arrows are shown in the square boxes. **(B)** (i–v), Phosphorylation at the pSer396 + 404 epitopes was markedly increased in all the regions (corpus callosum, ipsilateral internal capsule, contralateral internal capsule, ipsilateral external capsule, and contralateral external capsule) on day 7 post-injury in the pR5-TBI group versus the pR5-sham group, whereas no significant differences were observed on day 1 pR5-TBI group versus the pR5-sham group except contralateral internal capsule (iii). One-way ANOVA with Tukey's multiple comparison test, $^*p \leq 0.05$, $^{**}p \leq 0.001$, $^{***}p \leq 0.0001$). **(C)** (i–v), Anisotropy was significantly reduced with hyperphosphorylation in all regions (corpus callosum, ipsilateral internal capsule, contralateral internal capsule, ipsilateral external capsule, and contralateral external capsule). A negative correlation was also found with axial diffusion in corpus callosum, ipsilateral internal capsule, contralateral internal capsule, and contralateral external capsule whereas in ipsilateral external capsule axial diffusivity (AxD) was increased significantly with increased phosphorylation. Radial diffusivity (RD) and mean diffusivity (MD) were also increased markedly with phosphorylation in the ipsilateral external capsule (**C** (iv)) (Pearson multiple correlations *p*-value ≤ 0.05).

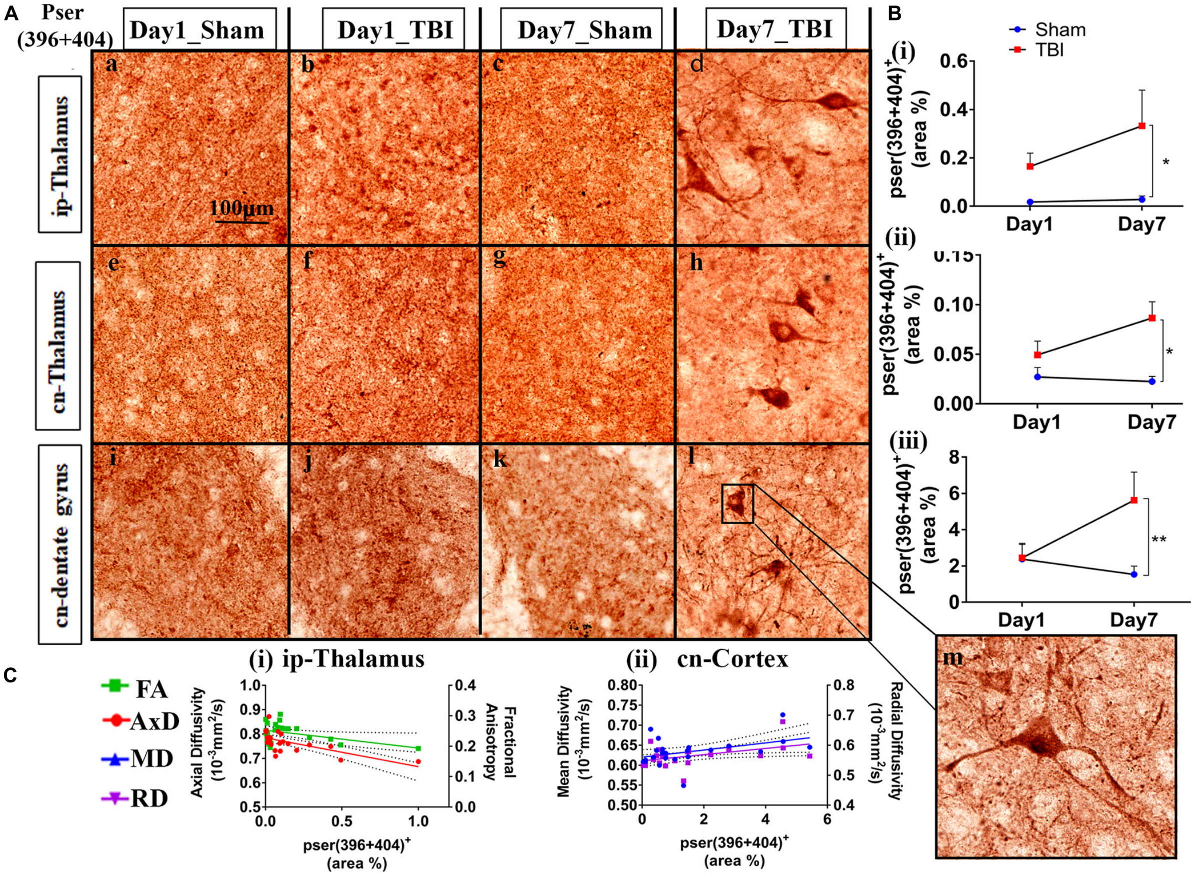

FIGURE 5 | Phosphorylation occurred in additional gray matter regions 1-week post-TBI in injured pR5 mice: **(A)** Phosphorylation at the pSer396 + 404 epitopes of tau was detected in the ipsilateral thalamus (a–d), contralateral thalamus (e–h), and contralateral dentate gyrus (i–l) ($n = 6$ pR5 TBI mice and $n = 6$ pR5-sham mice at days 1 and 7). Scale bar: 100 µm. **(B)** (i–iii), Phosphorylation at the pSer396 + 404 epitopes was evidently increased in the regions on day 7 post-injury in the pR5-TBI group versus the pR5-sham group, whereas no significant differences were observed in the day 1 pR5-TBI group versus the pR5-sham group (one-way ANOVA with Tukey's multiple comparisons test, $^{*}p \leq 0.05$, $^{**}p \leq 0.001$). **(C)** (i–ii), Fractional anisotropy (FA) and axial diffusivity (AxD) were significantly reduced with increased phosphorylation in the ipsilateral thalamus. Although hyperphosphorylation was not significant in the cortex, radial and mean diffusivity was significantly correlating with tau hyperphosphorylation in the cortex (Pearson multiple correlations p-value ≤ 0.05).

in the ip-external capsule (3.271 ± 1.056; $p = 0.6090$), ip-internal capsule (5.254 ± 1.250; $p = 0.9211$), and corpus callosum (1.799 ± 0.0858; $p = 0.8524$) compared to the sham group; ip-external capsule (1.293 ± 0.2726), ip-internal capsule (2.514 ± 1.046), and corpus callosum (0.7057 ± 0.1883). On day 7, immunoreactivity for phosphorylated tau was significantly higher in all selected regions-of-interest in the TBI group [ip-external capsule (5.456 ± 1.951; $p = 0.0426$), ip-internal capsule (18.81 ± 5.868; $p = 0.0057$), cn-internal capsule (6.331 ± 1.119; $p = 0.0020$), and corpus callosum (10.61 ± 1.911; $p = 0.0001$)] as compared to the day 7 sham group [ip-external capsule (0.8712 ± 0.2962), ip-internal capsule (2.299 ± 0.8450), cn-internal capsule (1.733 ± 0.6496), and corpus callosum (0.7123 ± 0.1344)]. In the corpus callosum (10.61 ± 1.911; $p = 0.0001$), ip-internal capsule (18.81 ± 5.868; $p = 0.0257$), and cn-external capsule (21.51 ± 8.695; $p = 0.0439$), immunoreactivity for phosphorylated tau in the day 7 TBI group was even higher than in the day 1 TBI group [corpus callosum (1.799 ± 0.0858), ip-internal capsule (5.254 ± 1.250), and cn-external capsule (2.434 ± 0.4153)]. Notably, immunoreactivity for phosphorylated tau was more abundant in contralateral regions than ipsilateral regions. There was no significant increase in total tau levels (data not shown).

Upon correlation with the DTI measures (**Figure 4C**), a negative correlation was seen between the percentage of ser396 + 404 positive area and FA in the corpus callosum ($R^2 = 0.3330$; $p = 0.0039$), ip-external capsule ($R^2 = 0.2269$; $p = 0.0216$), ip-internal capsule ($R^2 = 0.5076$; $p = 0.0001$), cn-external capsule ($R^2 = 0.5435$; $p = 0.0001$), and cn-internal capsule ($R^2 = 0.2483$; $p = 0.0155$). A negative correlation was also observed with AxD in the corpus callosum ($R^2 = 0.3654$; $p = 0.0022$), ip-internal capsule ($R^2 = 0.3438$; $p = 0.0026$), and cn-internal capsule ($R^2 = 0.3710$; $p = 0.0020$). Interestingly, a positive correlation was noted in the ip-external capsule phosphorylated-tau and diffusivity measures of AxD ($R^2 = 0.3969$; $p = 0.0013$), MD ($R^2 = 0.3509$; $p = 0.0029$), and RD ($R^2 = 0.3004$; $p = 0.0068$). Overall, these results indicate that decreased FA is associated with increased tau pathology.

In the gray matter (**Figure 5B**), no significant changes were observed on day 1 post-TBI. On day 7, a significant increase in the phosphorylated-tau positive area was seen only in the ip-thalamus (0.3324 ± 0.1478; p = 0.0488), cn-thalamus (0.08643 ± 0.01638; p = 0.0062), and cn-dentate gyrus (5.619 ± 1.554; p = 0.0318) in the TBI group versus the day 7 sham group [ip-thalamus (0.01743 ± 0.0055), cn-thalamus (0.02256 ± 0.0052), cn-dentate gyrus (1.533 ± 0.4619)]. In other regions involving the ip-cortex (3.099 ± 1.498; p = 0.4406), cn-cortex (2.353 ± 0.7649; p = 0.3659), cn-amygdala (4.896 ± 2.076; p = 0.5464), and cn-CA1 (18.13 ± 4,775; p = 2.447), a non-significant increase was noted as compared to the respective sham group [ip-cortex (0.6220 ± 0.3059), cn-cortex (0.9850 ± 0.3171), cn-amygdala (1.432 ± 0.6714), and cn-Ca1 (7.971 ± 3.573)]. These findings indicate that cn-dentate gyrus and ip- and cn-thalamus were the two main gray regions that were affected with tau pathology within a week in the pR5 mice after injury.

Similar to the white matter, a negative correlation of phosphorylated-tau area was observed with FA (R^2 = 0.1865; p = 0.0396) and AxD (R^2 = 0.3938; p = 0.0013) but only in the ip-thalamus. In the cn-cortex, a positive correlation was observed with MD (R^2 = 0.1802; p = 0.0435) and RD (R^2 = 0.2020; p = 0.0314) (**Figure 5C**). This suggests that a decrease in FA in the gray matter is associated with increased tau hyperphosphorylation.

Increased GFAP Expression Post-injury in pR5 Mice

Overall, increased GFAP expression was evident one day post-TBI that peaked after 7 days in the TBI groups as compared to the sham group (**Figures 6A**, **7A**). In the case of astrocytes, changes were noted in both the percentage of GFAP-positive cell areas (reported below) and GFAP-positive cell count (outlined in **Supplementary Table 1**). DTI measures-FA, AxD, MD, and RD-showed significant changes with the increased expression of GFAP in several regions of the brain.

In the white matter (**Figure 6B**), on day 1, a significant increase percentage of GFAP-positive cell area was observed in the ip-internal capsule in the TBI group (3.909 ± 0.5325; p = 0.0075) versus the sham group (1.611 ± 0.3459). No significant increase in percentage of GFAP positive cell area was seen in the cn-internal capsule (2.560 ± 0.3460; p = 0.0693), and corpus callosum (2.714 ± 0.3160; p = 0.2327) when compared to the day 1 sham group; cn-internal capsule (1.427 ± 0.1885), corpus callosum (1.640 ± 0.2749). On day 7, percentage of GFAP-positive staining was significantly higher in the TBI groups in all selected white matter regions, including ip-internal capsule (4.679 ± 0.5405, p = 0.0149), corpus callosum (6.165 ± 0.4585; p = 0.0001), ip-external capsule (7.089 ± 1.014, p = 0.0027), and cn-external capsule (7.570 ± 0.4892, p = 0.0003) versus sham regions; ip-internal capsule (2.576 ± 0.2912), corpus callosum (1.893 ± 0.4579), ip-external capsule (3.364 ± 1.156), and cn-external capsule (3.670 ± 0.6898). These findings show that GFAP immunostaining in the white matter increase within a week of injury in the pR5 mice.

In correlating with the DTI measures (**Figure 6C**), a negative correlation was seen between the percentage of GFAP positive cell area and FA in the corpus callosum (R^2 = 0.3989; p = 0.0012), an ip-internal capsule (R^2 = 0.3075; p = 0.0049), and with AxD in the corpus callosum (R^2 = 0.3140; p = 0.0054), ip-internal capsule (R^2 = 0.3920; p = 0.0011), cn-internal capsule (R^2 = 0.4124; p = 0.0010), and cn-external capsule (R^2 = 0.3734; p = 0.0019). A positive correlation was observed with AxD (R^2 = 0.2210; p = 0.0236), MD (R^2 = 0.3083; p = 0.0060), and RD (R^2 = 0.3344; p = 0.0038) in the ip-external capsule. Overall, this indicates that a decrease in anisotropy and an increase in diffusion in the white matter were associated with an increase in astrocytes.

In the gray matter (**Figure 7B**), a significant increase in GFAP expression was seen only in the ip-thalamus (0.9537 ± 0.1991, p = 0.0300) and ip-cortex (0.9743 ± 0.1880, p = 0.0160) on day 1 in the TBI versus the sham group [ip-thalamus (0.2697 ± 0.1126) and ip-cortex (0.4305 ± 0.0474)], with a significant increase in the ip-thalamus (3.486 ± 0.2074, p = 0.0001), ip-cortex (2.867 ± 0.1161, p = 0.0001), cn-cortex (0.8618 ± 0.1270; p = 0.0004), ip-amygdala (3.900 ± 0.0990, p = 0.0001), cn-CA1 (6.119 ± 0.1884, p = 0.0001), and cn-dentate gyrus (5.619 ± 1.554, p = 0.0318) being observed at 7 days post-injury as compared to shams [ip-thalamus (0.2617 ± 0.0755), ip-cortex (0.4200 ± 0.0463), cn-cortex (0.2523 ± 0.0579), ip-amygdala (0.9060 ± 0.1575), cn-CA1 (2.944 ± 0.2041), and cn-dentate gyrus (1.533 ± 0.4619)]. These results suggest that GFAP immunostaining in gray matter was increased within a week in pR5 mice post-injury.

A negative correlation (**Figure 7C**) in the ip-thalamus (R^2 = 0.2048; p = 0.0301) and a positive correlation in the ip-cortex (R^2 = 0.3148; p = 0.0053) and ip-amygdala (R^2 = 0.2759; p = 0.0101) were observed with FA. A negative correlation was also seen with AxD in the ip-thalamus (R^2 = 0.2837; p = 0.0089) and ip-amygdala (R^2 = 0.2682; p = 0.0114). In the ip-amygdala, GFAP expression also negatively correlated with MD (R^2 = 0.2467; p = 0.0159). These findings demonstrate region-dependent increases and decreases in FA in association with an increase in GFAP immunostaining. Together with the phosphorylated-tau results, the increase in FA was associated with increased GFAP immunostaining with no tauopathy, and the FA decrease was associated with increased GFAP immunostaining with tauopathy.

Increased Microglial Cell Number 7 Days Post-injury

Unlike astrocytes, we did not observe any increase in microglial number (Iba1+ cell count) on day 1; however, active microglial cells were seen in the thalamus region (**Figure 8A**). A significant increase in microglial cell number was noted only 7 days after injury in both the white matter (**Figures 9A,B**) corpus callosum (9.796 ± 1.259, p = 0.0001), ip-external capsule (10.88 ± 0.3521, p = 0.0001), ip-internal capsule (60.33 ± 9.124, p = 0.0002), and the gray matter (**Figures 8A,B**) in the TBI group (ip-thalamus (93.83 ± 10.54; p = 0.0001) versus the sham groups–corpus callosum (2.019 ± 0.1608), ip-external capsule (2.042 ± 0.2534), ip-internal capsule (19.42 ± 1.546),

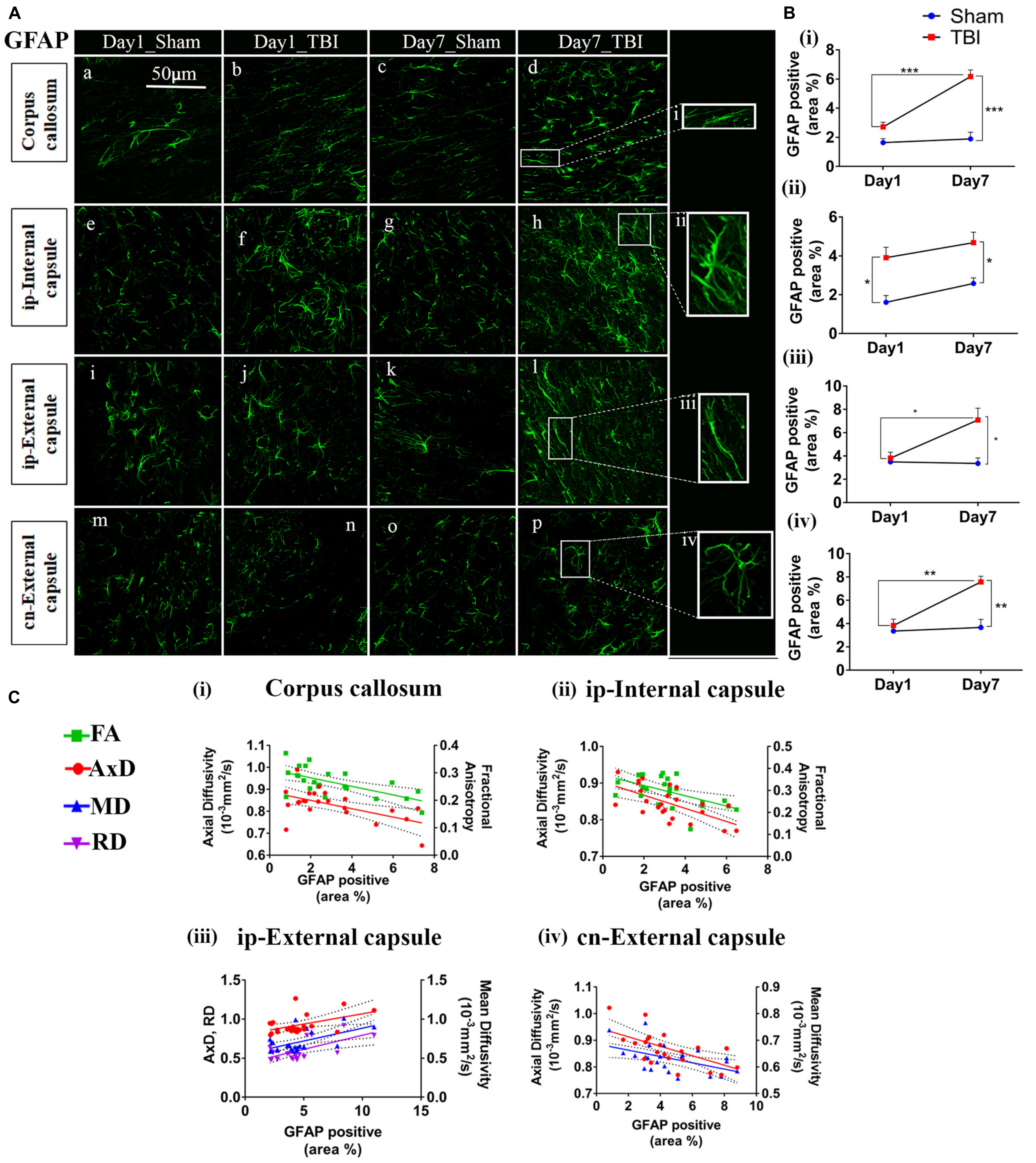

FIGURE 6 | Increased astrogliosis in white matter early after injury in pR5 mice: **(A)** Increase in glial fibrillary acidic protein (GFAP) positive cell area percentage was noticed in white matter regions containing the corpus callosum (a–d), ipsilateral internal capsule (e–h), ipsilateral external capsule (i–l), and contralateral external capsule (m–p) of injured pR5 mice (*n* = 6 pR5 TBI mice and *n* = 6 pR5-sham mice at days 1 and 7). Scale bar: 50 μm. **(B)** (i–iv), GFAP positive cell area was significantly increased in all the regions (corpus callosum, ipsilateral internal capsule, ipsilateral external capsule, and contralateral external capsule) on day 7 post-injury in pR5-TBI group versus the pR5-sham group, whereas no significant differences were observed the day 1 pR5-TBI group versus the pR5 sham group except ipsilateral internal capsule (**B** (iii)) (one-way ANOVA with Tukey's multiple comparison test, $^*p \leq 0.05$, $^{**}p \leq 0.001$, $^{***}p \leq 0.0001$). **(C)** (i–iv), Anisotropy was significantly reduced with gliosis in the corpus callosum and ipsilateral internal capsule. Axial diffusion (AxD) was also measurably reduced in the corpus callosum, ipsilateral internal capsule, and contralateral external capsule whereas in the ipsilateral external capsule, axial diffusivity (AxD) was increased significantly with gliosis. Radial and mean diffusivity were also increased in the ipsilateral external capsule with gliosis, whereas, in the contralateral external capsule, mean diffusivity (MD) was reduced with gliosis (Pearson multiple correlations *p*-value ≤ 0.05).

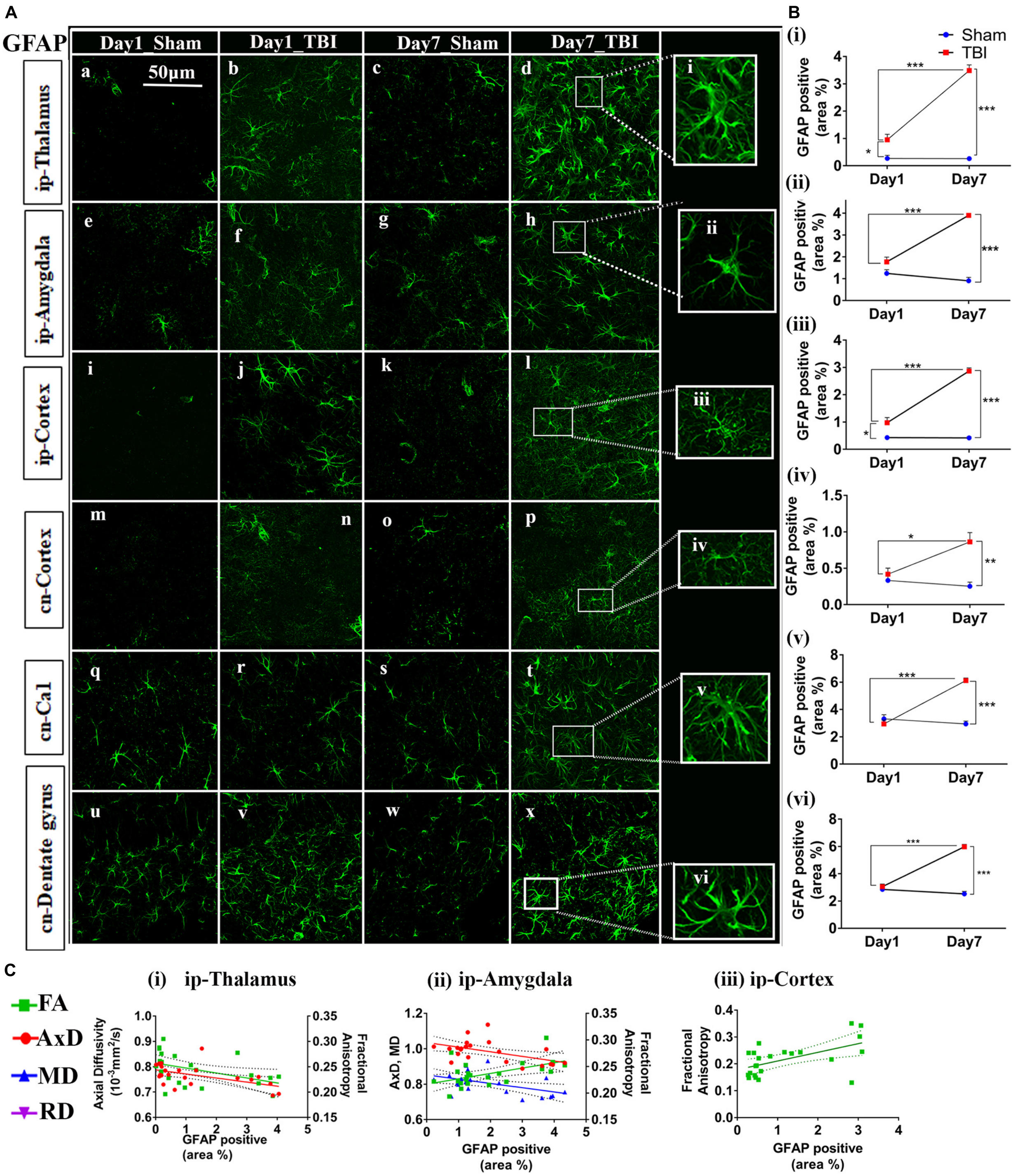

FIGURE 7 | Augmented astrogliosis post-TBI in the gray matter of injured pR5 mice: **(A)** Statistically significant increase in glial fibrillary acidic protein (GFAP)-positive cell area percentage in the gray matter regions, including the ipsilateral thalamus (a–d), ipsilateral amygdala (e–h), ipsilateral cortex (i–k), contralateral cortex (m–p), contralateral CA1 (q–t), and contralateral dentate gyrus (u–x) of pR5 TBI groups versus sham groups ($n = 6$ pR5 TBI mice and $n = 6$ pR5-sham mice at days 1 and 7). Scale bar: 50 μm. Extended views of astrocytes from all regions were shown (i–viii) indicating the differences in the shape of the astrocytes. **(B)** (i–vi), GFAP-positive percentage cell area was significantly higher in the ipsilateral thalamus and ipsilateral cortex on day 1 post-injury in pR5-TBI mice versus the pR5-sham mice control group. On day 7, the percent positive area was evidently increased in ipsilateral thalamus, ipsilateral amygdala, ipsilateral cortex, contralateral cortex, contralateral CA1, and contralateral dentate gyrus (One-way ANOVA with Tukey's multiple comparison test, $^*p \leq 0.05$, $^{**}p \leq 0.001$, $^{***}p \leq 0.0001$). **(C)** (i–iii), Anisotropy was significantly reduced in the ipsilateral thalamus and increased in the ipsilateral amygdala with gliosis. Axial diffusion was also measurably reduced in the ipsilateral thalamus and ipsilateral amygdala. Reduced mean diffusivity was also noted in the ipsilateral amygdala with increased gliosis (Pearson multiple correlations p-value ≤ 0.05).

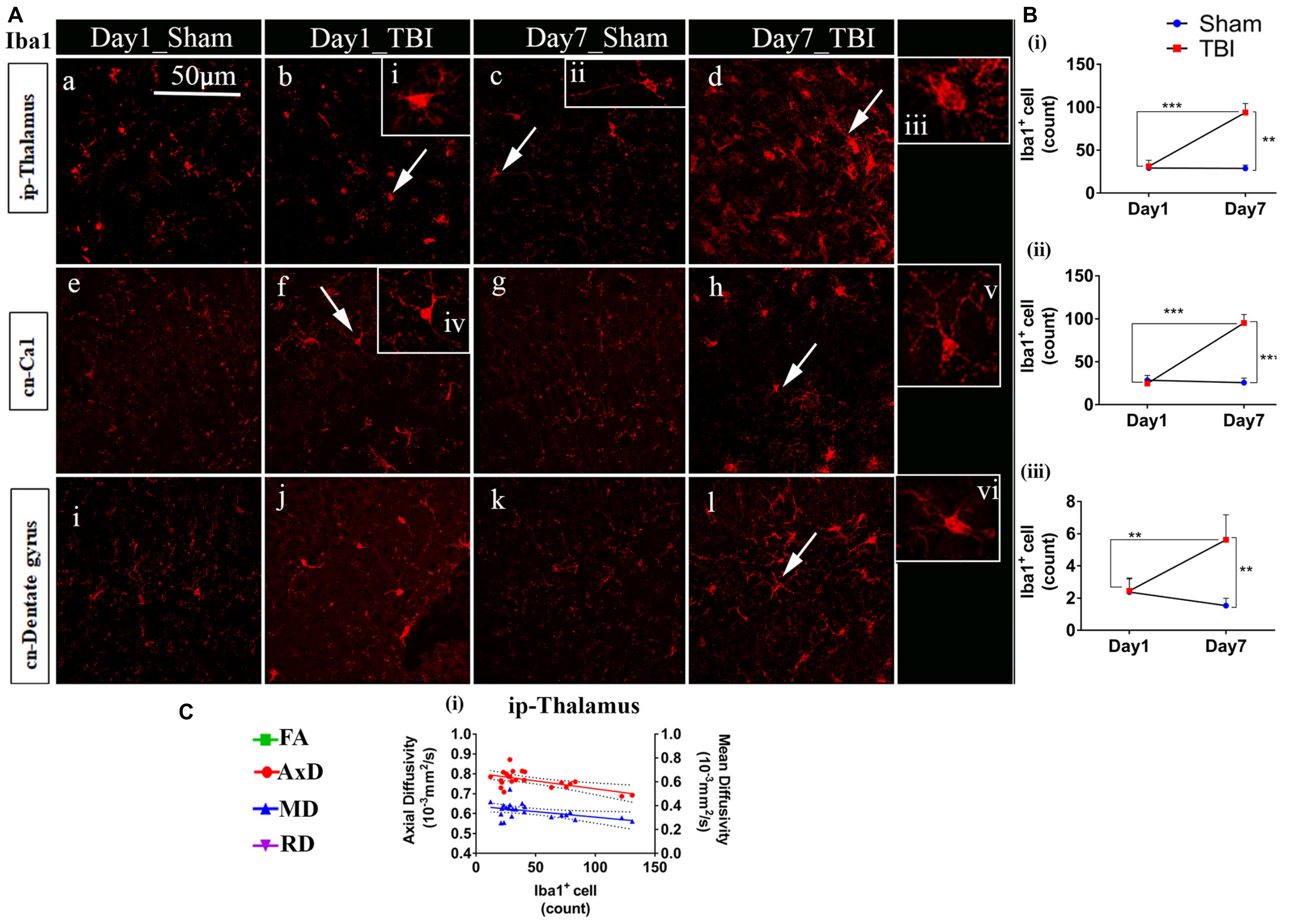

FIGURE 8 | Increased microglia activity in gray matter post-TBI in pR5 mice: **(A)** Iba1+ cell counts were evident in gray matter regions, ipsilateral thalamus (a–d), contralateral CA1 hippocampal region (e–h), and contralateral dentate gyrus (i–l). Extended iba1+ cells (i–vi) demonstrate a difference between active and inactive microglia cells at days 1 and 7 (*n* = 6 pR5 TBI mice and *n* = 6 pR5-sham mice for days 1 and 7). Scale bar: 50 μm. **(B)** (i–iii), A significant increase in microglia count in the ip-thalamus, contralateral CA1, and contralateral dentate gyrus were noticed at day 7 post-injury (One-way ANOVA with Tukey's multiple comparison test, $^*p \leq 0.05$, $^{**}p \leq 0.001$, $^{***}p \leq 0.0001$). **(C)** Significant negative correlations are observed between Iba1+ cell counts and DTI measures fractional anisotropy (FA), and axial diffusivity (AxD) ipsilateral thalamus (**C** (i)) (Pearson multiple correlations *p*-value ≤ 0.05).

and ip-thalamus (28.75 ± 3.857). Notably, in the contralateral regions, a significant increase was observed in the cn-external capsule (7.542 ± 0.9820, $p = 0.0001$), CA1 (95.17 ± 9.862, $p = 0.0001$), and dentate gyrus (73.78 ± 5.007, $p = 0.0003$) at day 7 in the TBI group versus the sham group; cn-external capsule (2.042 ± 0.3501), Ca1 (25.67 ± 5.354), and dentate gyrus (32.39 ± 6.159) regions. These results indicate that microglial activity increases within a week of TBI in pR5 mice.

Although correlated with DTI (**Figures 8C**, **9C**), microglial counts negatively correlated with FA in the ip-external capsule ($R^2 = 0.2010$; $p = 0.0319$), ip-internal capsule ($R^2 = 0.2581$; $p = 0.0113$), and with AxD in the ip-internal capsule ($R^2 = 0.2755$; $p = 0.0085$) and ip-thalamus ($R^2 = 0.3631$; $p = 0.0023$). A positive correlation was observed with AxD ($R^2 = 0.4300$; $p = 0.0007$), MD ($R^2 = 0.6658$; $p = 0.0001$), and RD ($R^2 = 0.7362$; $p = 0.0001$) in ip-external capsule and negative correlation with MD ($R^2 = 0.2143$; $p = 0.0261$) in the ip-thalamus. Together, these findings reveal that the white matter anisotropy was mainly affected by the increase in microglial activity whereas in the gray matter diffusivity was primarily affected.

DISCUSSION

This work revealed evolving and progressive microstructural alterations in tau animals as early as 1 day post-injury that propagated to the contralateral hemisphere within a week, and were associated with TBI-accelerated tauopathy. In the white matter, the reduction in FA and AxD and an increase in MD and RD at day 1 were followed by a decrease in FA, AxD, and MD, and increased RD at seven days post-injury in the TBI-pR5 group compared to shams. In the gray matter, FA was markedly increased in the amygdala and cortex, but remained significantly decreased in the thalamic and hippocampal regions for 1 week as compared to the sham group. The reduced FA was consistently associated with increased expression of

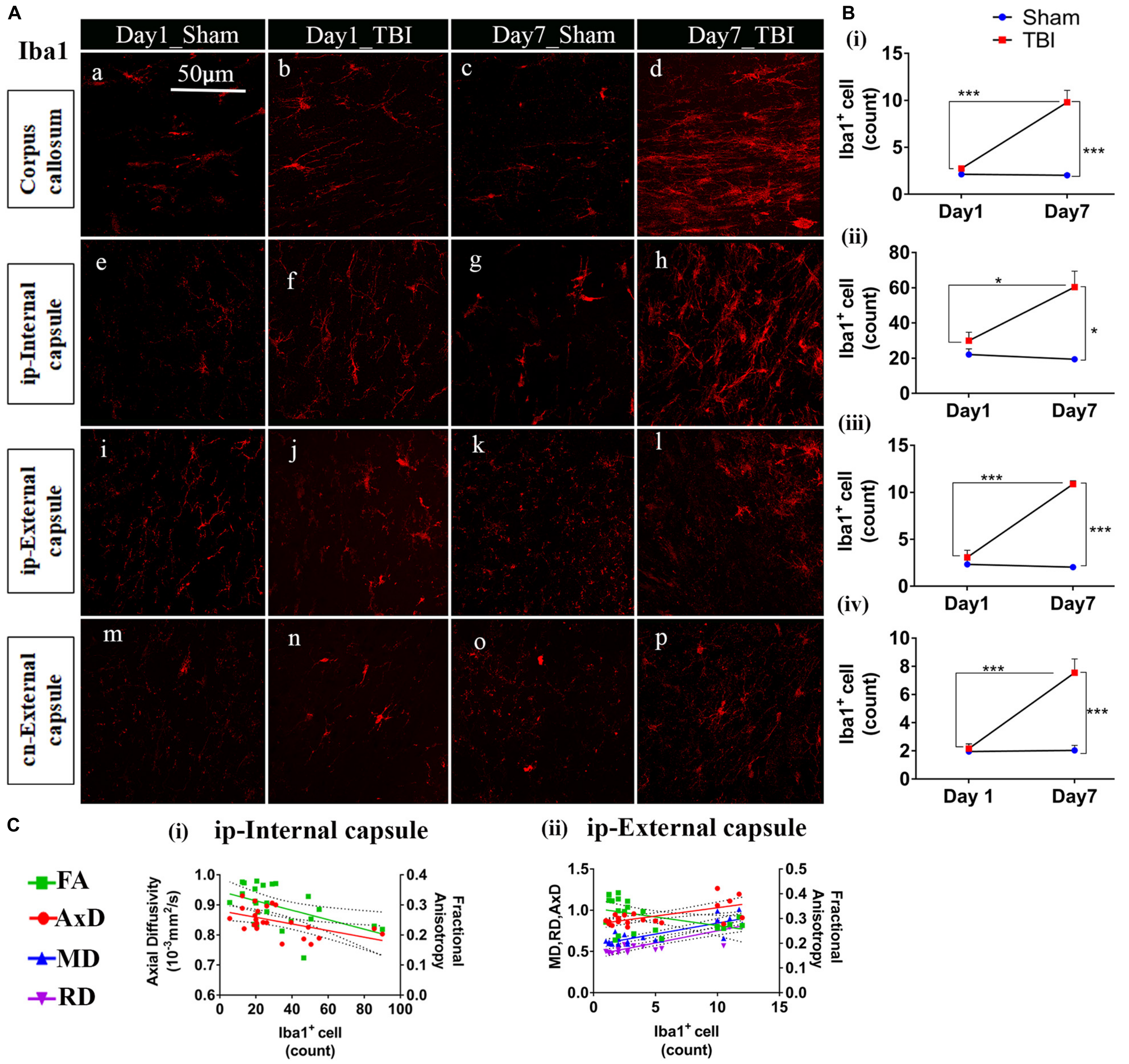

FIGURE 9 | TBI induces microglial increase in the white matter of pR5 mice: **(A)** Increased Iba1+ cell count in white matter regions, including the corpus callosum (a–d), ipsilateral internal capsule (e–h), ipsilateral external capsule (i–l), and contralateral external capsule (m–p), ($n = 6$ pR5 TBI mice and $n = 6$ pR5-sham mice for days 1 and 7-time points). Scale bar: 50 µm. **(B)** (i–iv), Iba1+ cells were significantly higher in day 7 pR5 TBI mice versus sham mice in all four regions (One-way ANOVA with Tukey's multiple comparison test, $^{*}p \leq 0.05$, $^{**}p \leq 0.001$, $^{***}p \leq 0.0001$). **(C)** (i,ii), Fractional anisotropy decreased with increased microglia count in the ipsilateral internal capsule and ipsilateral external capsule. Axial diffusivity was decreased in the ipsilateral internal capsule while increased in the ipsilateral external capsule with an increase in microglia count. Along with this, mean and radial diffusivity were also increased with microglia level in the ipsilateral external capsule (Pearson multiple correlations p-value ≤ 0.05).

phosphorylated tau evident after day 1 in the white matter followed by its propagation to the gray matter within 1 week, in line with neuroinflammation. An increased FA on the other hand, particularly reflected a prominent increase in neuroinflammation without any significant increase in tau phosphorylation. Overall, we observed regional changes in the DTI signal, particularly in FA, that could reflect either increased phosphorylation of tau, neuroinflammation, or both.

Tauopathy has been documented as a possible linking factor between TBI and AD (Johnson et al., 2012). Pathological isoforms of tau have been detected immunohistochemically and biochemically in postmortem TBI brain at various different time points and are shown to affect the behavioral function associated with respective brain areas (Zanier et al., 2018; Zhang et al., 2019). *In vivo* detection of tauopathy at an early stage post-TBI is underexplored. The findings presented here advance our current understanding of TBI-accelerated tauopathy in experimental models by providing information about the early pathological and microstructural changes in a tau transgenic mouse model post single severe injury. This work exploits DTI along with histology to measure widespread pathology in pR5 mice for a period of 1-week post-TBI. This is the first study to apply DTI to investigate the effect of TBI in tau transgenic animals.

In the past few years, tauopathies following TBI have been the hypothesized link with AD (McKee and Daneshvar, 2015). In clinicopathological studies, postmortem TBI brains analyzed at different time points exhibited extensive tau phosphorylation that was associated with cognitive deficits in the patients (Zanier et al., 2018; Zhang et al., 2019). Consistent with previous studies (Acosta et al., 2017; Zhao et al., 2017), we document immunohistologically, a similar increase in tau phosphorylation following TBI. Hyperphosphorylation appeared at day 1 post-injury in the ipsilateral internal capsule then spread to the gray matter regions, specifically to the ipsilateral and contralateral thalamus and the contralateral dentate gyrus after 1 week. Such early changes in tau phosphorylation were consistent with another study that utilized the CCI model in a triple-transgenic mouse (3×Tg-AD), where an increase in phosphorylated-tau expression in the fimbria and the CA1 region of the hippocampus, along with the deposition of amyloid-β plaques within 1 week of the injury were reported (Tran et al., 2011a). Unlike Tran et al., we did not see any increase in total tau levels, which was consistent with the report of Zhang et al. (2019) who reported no changes in total tau levels even 6 weeks after injury. In pR5 mice, NFT formation is initiated at around 6 months in the amygdala and also detectable in the CA1 region at 20 months of age (Deters et al., 2008). In general, the literature supports that aging accelerates the course of AD pathogenesis. Tau hyperphosphorylation was evident in the hippocampus of pR5 mice at 9 months of age post-TBI in our study as compared the typical 20 months of age as reported by previous studies (Gotz et al., 2001; Deters et al., 2008).

The role of neuroinflammation in tau pathogenesis has also been extensively documented (Curran and O'Connor, 2001; Sutinen et al., 2012; Morales et al., 2013; Collins-Praino and Corrigan, 2017; Leyns and Holtzman, 2017; Laurent et al., 2018). In both clinical and experimental models, TBI can augment tau pathology if it coexists with active glial cells (Johnson et al., 2012, 2013; Ojo et al., 2013; Nilson et al., 2017). We noted the presence of reactive astrocytes and activated microglia in regions presenting with increased hyper-phosphorylation, such as the ipsilateral thalamus and contralateral dentate gyrus, corpus callosum, and internal and external capsule. Both microglia and astrocytes have been shown to be promoters for tau hyper-phosphorylation by either increasing the release of pro-inflammatory mediators in their active states that further increases the activity of kinases responsible for tau phosphorylation or by altering other involved pathways (Curran and O'Connor, 2001; Sutinen et al., 2012).

Diffusion tensor imaging is a well-established imaging tool that has been known to detect TBI-induced microstructural abnormalities in the brain (Alexander et al., 2007; Lo et al., 2009; Budde et al., 2011; Soni et al., 2018). Here we have shown, FA and AxD were reduced in the TBI group in the ip-thalamus, corpus callosum, external capsule, and internal capsule compared to the sham transgenic mice with immunohistochemical evidence of increases in tau phosphorylation in these same regions. These findings were consistent with Sahara et al. (2014) where DTI changes in rTg4510 tau transgenic mice were studied with respect to tau pathology, regardless of injury, a similar reduction in FA in the white matter was associated with tau hyper-phosphorylation in rTg4510 mice. In 3×Tg mice, decreased FA was reported primarily in the hippocampal region which was associated with depositions of both Aβ plaques and hyperphosphorylated tau (Snow et al., 2017). Here we noticed tau phosphorylation and reduced FA in the dentate gyrus; however, the correlation was not significant, most likely related to the sensitivity limitations of DTI (Taoka et al., 2009). Another reason could be that the pR5 mouse model used in this study is a tau transgenic mouse with no amyloid pathology; therefore, unlike 3×Tg mice, the changes we noticed were only associated with hyperphosphorylated tau. It should be noted that contradictory to our findings, Wells et al. (2015) reported an opposite trend of FA change in the areas of high tau burden, including the cortex and hippocampus but not in the thalamus where NFT density was significantly low. We also noticed increased FA in a few regions involving the cortical areas close to the injury site–amygdala, ipsilateral epithalamic, and contralateral-ventral thalamic region–but did not find any correlation with phosphorylated-tau increase. It is possible that phosphorylated tau in its aggregated form alters the directionality and diffusion of water in a different manner; however, as we did not look at NFTs, this cannot be confirmed with the current data. Altogether, our results indicate that the post-TBI increase in phosphorylated-tau may induce structural impairments that are measurable with DTI.

The DTI changes observed may be further complicated by the associated neuroinflammatory processes. Astrocytes, that are responsible for upholding homeostasis in the central nervous system (Sofroniew and Vinters, 2010). They are typically been shown to have star like shape and isotropic morphology (Schiweck et al., 2018). However, advanced visualization techniques revealed that shape of astrocytes is complex and keeps changing depending on the region and physiology of the brain (Fernaud-Espinosa et al., 1993). In pathological conditions, such as brain insults, gliomas and neurodegenerative disorders astrocytes appear in different structural forms depending on the severity or stages of the pathological condition (Schiweck et al., 2018). This can either highlight its isotropic behavior or shift it toward anisotropy and can affect directionality of water diffusion. In TBI, some reports have demonstrated isotropic gliosis in gray matter, where astrocytes maintain their distinct shapes but become hypertrophic that may lead to visible decrease in FA (Edlow et al., 2016). Contradictory to these findings, some others have depicted anisomorphic gliosis following injury (Budde et al., 2011; Laitinen et al., 2015; Soni et al., 2018). These studies indicated that astrocytes present in close proximity to injury site have the characteristics to change their shapes by expanding their busy processes toward lesion that lead to anisotropic structure causing increase in FA (Budde et al., 2011; Laitinen et al., 2015; Soni et al., 2018). These astrocytes named as palisading astrocytes are also responsible for the formation of glial scars. In AD, along with morphological variations astrocytes are also demonstrated to have spatial association with the pathological tau which may contribute in disease progression concurrently (Sidoryk-Wegrzynowicz et al., 2017; Kovacs et al., 2018).

In this study, on day 1 post-injury, we observed increase in astrocytes but we did not observe any increase in tau and microglia count. Therefore, slight reduction in FA seen on day 1 can either be because of increased astrocytes, or damage to the fiber bundle attached to the thalamic region or edema. However, as we did not see any significant changes in AxD, RD, and MD thalamic region and also no change in ad was noted in white matter tracks, it is likely indicated toward glial pathology. Generally, microglia activation starts earlier than astrocytes post-TBI but because gliosis had already been reported at 9 months of age in Pr5 animals, it might be possible that TBI induction in these animals resulted in increased astrocyte expression prior to microglial activation seen on days 1 and 7 (Skripuletz et al., 2013; Jha et al., 2019). In our previous TBI study on wild type mouse, we observed an increased FA in the ipsilateral thalamus post 7 days of injury, which was reflecting the anisotropic gliosis (Soni et al., 2018). Whereas in our current study, we observed FA increase only in the cortical area very close to the injury site which can be because of palisading astrocytes and amygdala may reflect neurodegeneration supported by reduction in AD and MD. In thalamus, FA changes were supporting isotropic nature of astrocytes leading to reduction in FA on day 7 post-injury. These differences in FA can be driven by a combined effect of astrocytes, phosphorylated tau and active microglia also seen in the thalamic region on day 7 post-injury. While the association of DTI parameters with neuroinflammatory markers in both gray matter and white matter regions has been extensively studied post-TBI (Budde et al., 2011; Bennett et al., 2012; Soni et al., 2018), the alterations induced by the combined effect of neuroinflammatory markers along with tauopathy has not been explored. In our study, we observed a negative correlation of GFAP expression with FA and AxD change in the areas with phosphorylated-tau increases. This FA reduction with respect to gliosis was opposite to other CCI studies on wild-type rodents, where increased FA was shown to reflect gliosis (Budde et al., 2011; Xu et al., 2011; Soni et al., 2018). This inconsistent pattern could be explained by the additional presence of phosphorylated-tau and microglia in the thalamus of transgenic mice post-injury, that might be absent in those wild-type rodents. Thus, it could be suggested that these changes are either driven by both the astrocytes or phosphorylated tau together or dominated by phosphorylated tau (Sahara et al., 2014; Snow et al., 2017). In contrast to the thalamus, in the ip-amygdala and cortex, we observed a positive correlation between astrocytes and FA, which was consistent with the TBI studies (Budde et al., 2011; Soni et al., 2018). Thus, it justifies that the changes were only driven by astrocytes as the phosphorylated-tau burden in these areas did not differ between sham and TBI groups. The negative correlation of microglia counts with MD and AxD in the thalamus suggested that the increase in the microglial cell density in the thalamic region could restrict water diffusion in the area. However, as TBI initiated multifaceted mechanisms and DTI measures might be affected by a multitude of factors other than phosphorylation and neuroinflammatory processes, investigation of other processes would contribute further to the specificity of these effects. Other pathological mechanisms, such as axonal injury, amyloid deposition (Tran et al., 2011b; Genrikhs et al., 2017), neuronal death (Murakami et al., 1998; Genrikhs et al., 2017), neurogenesis (Tran et al., 2006), and demyelination (Guglielmetti et al., 2016) may also contribute to the changes observed in DTI measures specifically FA (Rola et al., 2006). Axonal injury to the axons may perturb the dissociation of tau protein from the microtubules leading to microtubular destabilization and increased tau protein levels in the brain tissue, cerebrospinal fluid, and serum/plasma (Zemlan et al., 1999; Smith et al., 2003; Johnson et al., 2013). When evaluated in TBI patients and experimental models it has been found that both total tau and phosphorylated tau levels were significantly increased and were affecting memory functions (Zhao et al., 2017; Zanier et al., 2018). These findings suggested that axonal injury is not the only mechanism responsible for TBI associated tauopathy. Axonal damage dissociates tau protein from the microtubule and may provide a surge to other underlying pathological mechanisms that can further accelerate and worsen the tau pathology by initiating tau hyperphosphorylation and oligomer formation. Axonal injury together with inflammation, cell death and myelin damage can affect diffusion differently at one and 7 days after the injury. Therefore, investigating transgenic models, where key processes are more prominent and elevated than others, may be a key approach to highlighting the DTI alterations that may be more reflective of those processes.

Our study has several limitations, which if addressed, could aid in a better understanding of the associated pathological process. This study shows that TBI affects increasing tau pathology in the pR5 mice, it is unable to conclude whether TBI has more of an effect in the presence of tau pathology since no comparison was made in normal mice. Therefore, the inclusion of non-transgenic sham and TBI littermates would have provided a suitable baseline for comparisons. Further, behavioral assessments of cognition were not performed. The lack of cognitive testing in this study means that this study cannot define the functional impact of the DTI and pathological changes that we have detected, and this warrants future study. The investigation at longer follow-up times would provide insight into the trajectory of tau propagation in pR5 mice and allow the development of better diagnosis paradigm. Although DTI changes were observed in the regions with a high burden of phospho-tau, astrocytes and microglia due to its nature of detecting complex pathologies, it cannot be said that the changes observed in DTI measures are specifically due to these pathological events as the direct correlation were not performed. The limitation on direct matching of DTI and histological measurements are inherent to the methods themselves: MRI can image the whole brain while in general, histology can only image a few very thin sections per animal. Even a single MRI slice is approximately 10 times thicker than one histological slice. Nevertheless, the specific correlation of a histopathological process with a specific trend of diffusion imaging metric change is a complicated issue. For example, a specific pathology may result in a predictable biomarker on DTI or NODDI; however, different pathologies may create the same diffusion metric change (Jelescu and Budde, 2017). Furthermore, in complex conditions like concussion or TBI, pathologies generally do not occur alone. Astrogliosis, microgliosis, and axonal injury generally occur together as a consequence of TBI in mice (Namjoshi et al., 2016, 2017; Bashir et al., 2020; To et al., 2020). Thus, we placed greater importance on maintaining consistency within the same modality (MRI or histology) across different subjects rather than across different modalities (MRI and histology) within the same subject. For consistency across all subjects with MRI, the same ROI covering the defined by the AMBMC atlas was used. For histology, we used the same box ROI size for different subjects covering approximately the same area. Greater importance was placed on determining the capability of DTI on detecting the effects of injury by comparing the sham and controls and demonstrating the underlying pathologies underpinning in injured animals. The correlation between DTI and histological measurements were serendipitous in nature. Also, Fourier or structure tensor-based analyses (Budde et al., 2011) can provide anisotropy to directly compare to FA. However, as this was the first MRI study in TBI-tau transgenic mice model, our purpose was to first understand the pathological cascade if there is any pathological change at early stage and how it can affect DTI measures for which it was important to perform staining. As from this study it is now clear the microstructural changes involved in this double model are mainly affecting FA. In our proposed future study, we will be specifically performing a correlation study and will be using Fourier or structure tensor-based analyses. Another major limitation of this study was the lack of evaluation of sex differences which indeed can increase our understating of disease progression and spatiotemporal changes with time (Wright et al., 2017a,b). A comprehensive comparison of disease progression is a critical step which is required to implement the diagnostic and therapeutic tools at a clinical level thus can be suggested to include in the future studies. Further, a sample size of $n = 6$ per group was used for this study. to calculate the sample size of this study we conducted a power analysis based on our previously published work; we obtained a standard deviation obtained in the DTI measures (FA and mean diffusivity) from first study, which was 20% relative to the mean, six mice per surgery group were required to be able to observe a 22% difference with alpha of 0.05 and 80% power. Further, with the standard deviation found in immunohistochemistry in the pilot experiments (which was 25% relative to the mean), we needed six mice per surgery group to be able to observe 27% of differences at the 0.05 significance level and 80% power. However, considering the heterogeneous of the model and pathologies evolved post-injury in CCI, we suggest the use of large data sets for similar future studies.

CONCLUSION

In conclusion, the detection of the cumulative effects of TBI in the AD brain is limited because of the myriad of ongoing processes. We highlight that DTI, and in particular, FA patterns as promising methods to discern tauopathy-related pathology compared to combined tau and neuroinflammatory processes in the brain. These findings are supported by our histological measures of tau, microglia, and astrogliosis. We suggest FA as a potential *in vivo* marker to detect TBI-associated tauopathy and this would be the first study to demonstrate the spatio-temporal profile of DTI microstructural changes following TBI in a transgenic tau model. Our findings advance the current understanding of diagnostic tools for the detection of TBI-accelerated tauopathy in experimental animal models.

DATA AVAILABILITY STATEMENT

The raw data supporting the conclusions of this article will be made available by the authors, without undue reservation.

ETHICS STATEMENT

The animal study was reviewed and approved by Animal Research Ethics Committee of the University of Queensland (Animal Ethics Committee number: QBI/SCMB/036/16/MAIC).

AUTHOR CONTRIBUTIONS

NS and FN have contributed to design of the study and data interpretation. NS contributed to generate the animal model, data acquisition, analysis, drafting the manuscript. RM revised the manuscript for important intellectual content. XVT contributed to manuscript revision during the review process. KA helped in data acquisition. FN provided approval for publication of the content. All authors contributed to the article and approved the submitted version.

FUNDING

The work was supported by the Motor Accident Insurance Commission (MAIC) (Grant: 2014000857), the Queensland Government, Australia, for the research grant to Fatima Nasrallah.

ACKNOWLEDGMENTS

We thank the Australian Government support through NCRIS and the National Imaging Facility (NIF) for the operation of 9.4T MRI at the Center of Advanced Imaging (CAI), UQ. We acknowledge the histology and advanced microscopy facility at the Queensland Brain Institute (QBI), UQ with a special thanks to Arnaud Gaudin and Robert Sullivan for their guidance.

SUPPLEMENTARY MATERIAL

The Supplementary Material for this article can be found online at: https://www.frontiersin.org/articles/10.3389/fnins.2021.611451/full#supplementary-material

Supplementary Figure 1 | Example of distortion-corrected data from a sham subject, demonstrating SNR.

Supplementary Figure 2 | Examples of registered FA maps from sham and CCI animals of days 2 and 7. Each individual's registered FA maps (grayscale background) were shown with the corresponding skeletonized FA maps (rainbow scaled overlays). Generally, thinner white matter tracts (e.g., the external capsule on contralateral side) were well-matched across subjects, evidenced by the thin FA skeleton consistently covering the whole tract. Thicker white matter tracts, i.e., areas with high FA, (e.g., the corpus callosum and internal capsule, indicated on first row with purple arrows) had slight mismatches, in terms of the tract thickness and/or the FA skeleton did not always pass through the same location along the tract. TBSS skeletonizing process improve the spatial matching of these white matter tracts and overall, the skeletonizing process was accurate, i.e., the FA skeleton always fall within larger FA tracts. TBSS also reflected situation where the white matter tract was disrupted in lesion area in the CCI animals, for example the ipsilateral external capsule (indicated by light blue arrows). On the registered FA maps, the external capsule in the lesion area disappeared and the corresponding FA skeleton passing through the area, the FA value was significantly lower to than the contralateral external capsule FA skeletonized FA tract (∼0.1, below the TBSS FA threshold). The white matter tracts were grossly aligned and consequently the more homogenous (in terms of DTI metrics pattern) gray matter area was sufficiently well-matched for voxel-wise spatial statistics. This is relevant since TBSS does not provide results on DTI changes in the gray matter.

Supplementary Figure 3 | Figure representing the sections and regions of interest chosen for region-based quantification: **(A)** Representative images from the developing Allen mouse brain atlas to demonstrate the bregma region (−0.5 to −4.5 mm) used for immunohistochemistry analysis and quantification. **(B)** Images of the MRI slices from the same bregma region were chosen to demonstrate the Regions-of-interest that were drawn manually on the study-specific template using the Australian mouse brain mapping consortium template (Watson et al., 2017) and the Allen adult mouse brain atlas (https://alleninstitute.org/) as a reference. All slices between the bregma regions −0.5 to −4.5 mm were covered in the ROI mask. **(C)** Representative serial coronal sections chosen for immunohistochemistry quantification. Regions of interest were Amygdala, thalamus, hippocampus (CA1 and dentate gyrus), cortex (closer to the amygdala region), corpus callosum, internal and external capsule shown with different colors on the slices. Two sample boxes (one large and one small) were used to create multiple ROIs for all the slices, that were used to quantify pathologies in different areas as shown in different colors in the figure. To be consistent with the size of the ROIs, same set of ROIs for all the five sections were used for all the animals with slight adjustment in the location if needed.

Supplementary Figure 4 | Histology sections of a representative sham mouse stained for p-tau.

REFERENCES

Acosta, S. A., Tajiri, N., Sanberg, P. R., Kaneko, Y., and Borlongan, C. V. (2017). Increased amyloid precursor protein and tau expression manifests as key secondary cell death in chronic traumatic brain injury. *J. Cell. Physiol.* 232, 665–677. doi: 10.1002/jcp.25629

Alexander, A. L., Lee, J. E., Lazar, M., and Field, A. S. (2007). Diffusion tensor imaging of the brain. *Neurotherapeutics* 4, 316–329.

Andersson, J. L., Skare, S., and Ashburner, J. (2003). How to correct susceptibility distortions in spin-echo echo-planar images: application to diffusion tensor imaging. *Neuroimage* 20, 870–888. doi: 10.1016/s1053-8119(03)00336-7

Bashir, A., Abebe, Z. A., McInnes, K. A., Button, E. B., Tatarnikov, I., Cheng, W. H., et al. (2020). Increased severity of the CHIMERA model induces acute vascular injury, sub-acute deficits in memory recall, and chronic white matter gliosis. *Exp. Neurol.* 324:113116. doi: 10.1016/j.expneurol.2019.113116

Beaulieu, C. (2002). The basis of anisotropic water diffusion in the nervous system - a technical review. *NMR Biomed.* 15, 435–455. doi: 10.1002/nbm.782

Behrens, T. E. J., Woolrich, M. W., Jenkinson, M., Johansen-Berg, H., Nunes, R. G., Clare, S., et al. (2003). Characterization and propagation of uncertainty in diffusion-weighted MR imaging. *Magn. Reson. Med.* 50, 1077–1088.

Bemiller, S. M., Mccray, T. J., Allan, K., Formica, S. V., Xu, G. X., Wilson, G., et al. (2017). TREM2 deficiency exacerbates tau pathology through dysregulated kinase signaling in a mouse model of tauopathy. *Mol. Neurodegenerat.* 12:74.

Bennett, R. E., Mac Donald, C. L., and Brody, D. L. (2012). Diffusion tensor imaging detects axonal injury in a mouse model of repetitive closed-skull traumatic brain injury. *Neurosci. Lett.* 513, 160–165. doi: 10.1016/j.neulet.2012.02.024

Bodea, L. G., Evans, H. T., Van Der Jeugd, A., Ittner, L. M., Delerue, F., Kril, J., et al. (2017). Accelerated aging exacerbates a pre-existing pathology in a tau transgenic mouse model. *Aging Cell* 16, 377–386. doi: 10.1111/acel.12565

Buckley, R. F., Hanseeuw, B., Schultz, A. P., Vannini, P., Aghjayan, S. L., Properzi, M. J., et al. (2017). Region-specific association of subjective cognitive decline with tauopathy independent of global beta-amyloid burden. *JAMA Neurol.* 74, 1455–1463. doi: 10.1001/jamaneurol.2017.2216

Budde, M. D., Janes, L., Gold, E., Turtzo, L. C., and Frank, J. A. (2011). The contribution of gliosis to diffusion tensor anisotropy and tractography following traumatic brain injury: validation in the rat using Fourier analysis of stained tissue sections. *Brain* 134, 2248–2260. doi: 10.1093/brain/awr161

Castellani, R. J., and Perry, G. (2019). Tau biology, tauopathy, traumatic brain injury, and diagnostic challenges. *J. Alzheimers Dis. JAD* 67, 447–467. doi: 10.3233/jad-180721

Chou, N., Wu, J., Bai Bingren, J., Qiu, A., and Chuang, K. H. (2011). Robust automatic rodent brain extraction using 3-D pulse-coupled neural networks (PCNN). *IEEE Trans. Image Process* 20, 2554–2564. doi: 10.1109/tip.2011.2126587

Collins-Praino, L. E., and Corrigan, F. (2017). Does neuroinflammation drive the relationship between tau hyperphosphorylation and dementia development following traumatic brain injury? *Brain Behav. Immun.* 60, 369–382. doi: 10.1016/j.bbi.2016.09.027

Curran, B., and O'Connor, J. J. (2001). The pro-inflammatory cytokine interleukin-18 impairs long-term potentiation and NMDA receptor-mediated transmission in the rat hippocampus in vitro. *Neuroscience* 108, 83–90. doi: 10.1016/s0306-4522(01)00405-5

Deters, N., Ittner, L. M., and Gotz, J. (2008). Divergent phosphorylation pattern of tau in P301L tau transgenic mice. *Eur. J. Neurosci.* 28, 137–147. doi: 10.1111/j.1460-9568.2008.06318.x

Edlow, B. L., Copen, W. A., Izzy, S., Bakhadirov, K., Van Der Kouwe, A., Glenn, M. B., et al. (2016). Diffusion tensor imaging in acute-to-subacute traumatic brain injury: a longitudinal analysis. *BMC Neurol.* 16:2. doi: 10.1186/s12883-015-0525-8

Fann, J. R., Ribe, A. R., Pedersen, H. S., Fenger-Gron, M., Christensen, J., Benros, M. E., et al. (2018). Long-term risk of dementia among people with traumatic brain injury in Denmark: a population-based observational cohort study. *Lancet Psychiatry* 5, 424–431. doi: 10.1016/s2215-0366(18)30065-8

Fernaud-Espinosa, I., Nieto-Sampedro, M., and Bovolenta, P. (1993). Differential activation of microglia and astrocytes in aniso- and isomorphic gliotic tissue. *Glia* 8, 277–291. doi: 10.1002/glia.440080408

Fichou, Y., Schiro, G., Gallat, F. X., Laguri, C., Moulin, M., Combete, J., et al. (2015). Hydration water mobility is enhanced around tau amyloid fibers. *Proc. Natl. Acad. Sci. U.S.A.* 112, 6365–6370. doi: 10.1073/pnas.1422824112

Fleminger, S., Oliver, D. L., Lovestone, S., Rabe-Hesketh, S., and Giora, A. (2003). Head injury as a risk factor for Alzheimer's disease: the evidence 10 years on; a partial replication. *J. Neurol. Neurosurg. Psychiatry* 74, 857–862. doi: 10.1136/jnnp.74.7.857

Franklin, K., and Paxinos, G. (1997). *The Mouse Brain in Stereotaxic Coordinates.* San Diego, CA: Academic Press.

Genrikhs, E. E., Voronkov, D. N., Kapkaeva, M. R., Isaev, N. K., and Stelmashook, E. V. (2017). Focal unilateral traumatic brain injury causes delayed neurodegenerative changes in the brain of rats. *Bull. Exp. Biol. Med.* 164, 211–213. doi: 10.1007/s10517-017-3960-2

Gotz, J., Chen, F., Barmettler, R., and Nitsch, R. M. (2001). Tau filament formation in transgenic mice expressing P301L tau. *J. Biol. Chem.* 276, 529–534. doi: 10.1074/jbc.m006531200

Guglielmetti, C., Veraart, J., Roelant, E., Mai, Z., Daans, J., Van Audekerke, J., et al. (2016). Diffusion kurtosis imaging probes cortical alterations and white matter pathology following cuprizone induced demyelination and spontaneous remyelination. *Neuroimage* 125, 363–377. doi: 10.1016/j.neuroimage.2015.10.052

Hanger, D. P., Anderton, B. H., and Noble, W. (2009). Tau phosphorylation: the therapeutic challenge for neurodegenerative disease. *Trends Mol. Med.* 15, 112–119. doi: 10.1016/j.molmed.2009.01.003

Hay, J., Johnson, V. E., Smith, D. H., and Stewart, W. (2016). Chronic traumatic encephalopathy: the neuropathological legacy of traumatic brain injury. *Annu. Rev. Pathol.* 11, 21–45. doi: 10.1146/annurev-pathol-012615-044116

Jelescu, I. O., and Budde, M. D. (2017). Design and validation of diffusion MRI models of white matter. *Front. Phys.* 28:61. doi: 10.3389/fphy.2017.00061

Jha, M. K., Jo, M., Kim, J. H., and Suk, K. (2019). Microglia-astrocyte crosstalk: an intimate molecular conversation. *Neuroscientist* 25, 227–240. doi: 10.1177/1073858418783959

Johnson, K. A., Schultz, A., Betensky, R. A., Becker, J. A., Sepulcre, J., Rentz, D., et al. (2016). Tau positron emission tomographic imaging in aging and early Alzheimer disease. *Ann. Neurol.* 79, 110–119. doi: 10.1002/ana.24546

Johnson, V. E., Stewart, J. E., Begbie, F. D., Trojanowski, J. Q., Smith, D. H., and Stewart, W. (2013). Inflammation and white matter degeneration persist for years after a single traumatic brain injury. *Brain* 136, 28–42. doi: 10.1093/brain/aws322

Johnson, V. E., Stewart, W., and Smith, D. H. (2012). Widespread tau and amyloid-beta pathology many years after a single traumatic brain injury in humans. *Brain Pathol.* 22, 142–149. doi: 10.1111/j.1750-3639.2011.00513.x

Kovacs, G. G., Xie, S. X., Robinson, J. L., Lee, E. B., Smith, D. H., Schuck, T., et al. (2018). Sequential stages and distribution patterns of aging-related tau astrogliopathy (ARTAG) in the human brain. *Acta Neuropathol. Commun.* 6:50.

Lagarde, J., Sarazin, M., and Bottlaender, M. (2018). In vivo PET imaging of neuroinflammation in Alzheimer's disease. *J. Neural Transm.* 125, 847–867. doi: 10.1007/s00702-017-1731-x

Laitinen, T., Sierra, A., Bolkvadze, T., Pitkanen, A., and Grohn, O. (2015). Diffusion tensor imaging detects chronic microstructural changes in white and gray matter after traumatic brain injury in rat. *Front. Neurosci.* 9:128. doi: 10.3389/fnins.2015.00128

Laurent, C., Buee, L., and Blum, D. (2018). Tau and neuroinflammation: what impact for Alzheimer's disease and tauopathies? *Biomed. J.* 41, 21–33. doi: 10.1016/j.bj.2018.01.003

Leyns, C. E. G., and Holtzman, D. M. (2017). Glial contributions to neurodegeneration in tauopathies. *Mol. Neurodegener.* 12:50.

Li, Y. J., Li, Y. M., Li, X. T., Zhang, S., Zhao, J. C., Zhu, X. F., et al. (2017). Head Injury as a Risk Factor for Dementia and Alzheimer's Disease: A Systematic Review and Meta-Analysis of 32 Observational Studies. *PLoS One* 12:e0169650. doi: 10.1371/journal.pone.0169650

Lo, C., Shifteh, K., Gold, T., Bello, J. A., and Lipton, M. L. (2009). Diffusion tensor imaging abnormalities in patients with mild traumatic brain injury and neurocognitive impairment. *J. Comput. Assist. Tomogr.* 33, 293–297. doi: 10.1097/rct.0b013e31817579d1

Magnoni, S., Esparza, T. J., Conte, V., Carbonara, M., Carrabba, G., Holtzman, D. M., et al. (2012). Tau elevations in the brain extracellular space correlate with reduced amyloid-beta levels and predict adverse clinical outcomes after severe traumatic brain injury. *Brain* 135, 1268–1280. doi: 10.1093/brain/awr286

McKee, A. C., and Daneshvar, D. H. (2015). The neuropathology of traumatic brain injury. *Handb. Clin. Neurol.* 127, 45–66. doi: 10.1016/b978-0-444-52892-6.00004-0

Morales, I., Jimenez, J. M., Mancilla, M., and Maccioni, R. B. (2013). Tau oligomers and fibrils induce activation of microglial cells. *J. Alzheimers. Dis.* 37, 849–856. doi: 10.3233/jad-131843

Murakami, N., Yamaki, T., Iwamoto, Y., Sakakibara, T., Kobori, N., Fushiki, S., et al. (1998). Experimental brain injury induces expression of amyloid precursor protein, which may be related to neuronal loss in the hippocampus. *J. Neurotrauma* 15, 993–1003. doi: 10.1089/neu.1998.15.993

Namjoshi, D. R., Cheng, W. H., Bashir, A., Wilkinson, A., Stukas, S., Martens, K. M., et al. (2017). Defining the biomechanical and biological threshold of murine mild traumatic brain injury using CHIMERA (closed head impact model of engineered rotational acceleration). *Exp. Neurol.* 292, 80–91. doi: 10.1016/j.expneurol.2017.03.003

Namjoshi, D. R., Cheng, W. H., Carr, M., Martens, K. M., Zareyan, S., Wilkinson, A., et al. (2016). Chronic exposure to androgenic-anabolic steroids exacerbates axonal injury and microgliosis in the CHIMERA mouse model of repetitive concussion. *PLoS One* 11:e0146540. doi: 10.1371/journal.pone.0146540

Nilson, A. N., English, K. C., Gerson, J. E., Barton Whittle, T., Nicolas Crain, C., Xue, J., et al. (2017). Tau oligomers associate with inflammation in the brain and retina of tauopathy mice and in neurodegenerative diseases. *J. Alzheimers. Dis.* 55, 1083–1099. doi: 10.3233/jad-160912

Ojo, J. O., Mouzon, B., Greenberg, M. B., Bachmeier, C., Mullan, M., and Crawford, F. (2013). Repetitive mild traumatic brain injury augments tau pathology and glial activation in aged hTau mice. *J. Neuropathol. Exp. Neurol.* 72, 137–151. doi: 10.1097/nen.0b013e3182814cdf

Pischiutta, F., Micotti, E., Hay, J. R., Marongiu, I., Sammali, E., Tolomeo, D., et al. (2018). Single severe traumatic brain injury produces progressive pathology with ongoing contralateral white matter damage one year after injury. *Exp. Neurol.* 300, 167–178. doi: 10.1016/j.expneurol.2017.11.003

Rola, R., Mizumatsu, S., Otsuka, S., Morhardt, D. R., Noble-Haeusslein, L. J., Fishman, K., et al. (2006). Alterations in hippocampal neurogenesis following traumatic brain injury in mice. *Exp. Neurol.* 202, 189–199. doi: 10.1016/j.expneurol.2006.05.034

Rose, S. E., Janke, A. L., and Chalk, J. B. (2008). Gray and white matter changes in Alzheimer's disease: a diffusion tensor imaging study. *J. Magn. Reson. Imaging* 27, 20–26. doi: 10.1002/jmri.21231

Rubenstein, R., Chang, B., Yue, J. K., Chiu, A., Winkler, E. A., Puccio, A. M., et al. (2017). Comparing plasma phospho tau, total tau, and phospho tau-total tau ratio as acute and chronic traumatic brain injury biomarkers. *JAMA Neurol.* 74, 1063–1072. doi: 10.1001/jamaneurol.2017.0655

Sahara, N., Perez, P. D., Lin, W. L., Dickson, D. W., Ren, Y., Zeng, H., et al. (2014). Age-related decline in white matter integrity in a mouse model of tauopathy: an in vivo diffusion tensor magnetic resonance imaging study. *Neurobiol. Aging* 35, 1364–1374. doi: 10.1016/j.neurobiolaging.2013.12.009

Schiweck, J., Eickholt, B. J., and Murk, K. (2018). Important shapeshifter: mechanisms allowing astrocytes to respond to the changing nervous system during development, injury and disease. *Front. Cell. Neurosci.* 12:261. doi: 10.3389/fncel.2018.00261

Sidoryk-Wegrzynowicz, M., Gerber, Y. N., Ries, M., Sastre, M., Tolkovsky, A. M., and Spillantini, M. G. (2017). Astrocytes in mouse models of tauopathies acquire early deficits and lose neurosupportive functions. *Acta Neuropathol. Commun.* 5:89.

Skripuletz, T., Hackstette, D., Bauer, K., Gudi, V., Pul, R., Voss, E., et al. (2013). Astrocytes regulate myelin clearance through recruitment of microglia during cuprizone-induced demyelination. *Brain* 136, 147–167. doi: 10.1093/brain/aws262

Smith, C., Graham, D. I., Murray, L. S., and Nicoll, J. A. (2003). Tau immunohistochemistry in acute brain injury. *Neuropathol. Appl. Neurobiol.* 29, 496–502. doi: 10.1046/j.1365-2990.2003.00488.x

Smith, S. M., Jenkinson, M., Johansen-Berg, H., Rueckert, D., Nichols, T. E., Mackay, C. E., et al. (2006). Tract-based spatial statistics: voxelwise analysis of multi-subject diffusion data. *Neuroimage* 31, 1487–1505. doi: 10.1016/j.neuroimage.2006.02.024

Smith, S. M., Jenkinson, M., Woolrich, M. W., Beckmann, C. F., Behrens, T. E., Johansen-Berg, H., et al. (2004). Advances in functional and structural MR image analysis and implementation as FSL. *Neuroimage* 23(Suppl. 1), S208–S219.

Smith, S. M., Johansen-Berg, H., Jenkinson, M., Rueckert, D., Nichols, T. E., Miller, K. L., et al. (2007). Acquisition and voxelwise analysis of multi-subject diffusion data with tract-based spatial statistics. *Nat. Protoc.* 2, 499–503. doi: 10.1038/nprot.2007.45

Snow, W. M., Dale, R., O'brien-Moran, Z., Buist, R., Peirson, D., Martin, M., et al. (2017). In vivo detection of gray matter neuropathology in the 3xTg mouse model of Alzheimer's disease with diffusion tensor imaging. *J. Alzheimers Dis.* 58, 841–853. doi: 10.3233/jad-170136

Sofroniew, M. V., and Vinters, H. V. (2010). Astrocytes: biology and pathology. *Acta Neuropathol.* 119, 7–35. doi: 10.1007/s00401-009-0619-8

Soni, N., Mohamed, A. Z., Kurniawan, N. D., Borges, K., and Nasrallah, F. (2018). Diffusion MRI unveils the spatiotemporal microstructural grey matter changes following injury in the rodent brain. *J. Neurotrauma.* 36, 1306–1317. doi: 10.1089/neu.2018.5972

Soni, N., Vegh, V., To, X. V., Mohamed, A. Z., Borges, K., and Nasrallah, F. A. (2020). Combined diffusion tensor imaging and quantitative susceptibility mapping discern discrete facets of white matter pathology post-injury in the rodent brain. *Front. Neurol.* 11:153. doi: 10.3389/fneur.2020.00153

Sutinen, E. M., Pirttila, T., Anderson, G., Salminen, A., and Ojala, J. O. (2012). Pro-inflammatory interleukin-18 increases Alzheimer's disease-associated amyloid-beta production in human neuron-like cells. *J. Neuroinflammation* 9:199.

Taoka, T., Morikawa, M., Akashi, T., Miyasaka, T., Nakagawa, H., Kiuchi, K., et al. (2009). Fractional anisotropy-threshold dependence in tract-based diffusion tensor analysis: evaluation of the uncinate fasciculus in Alzheimer disease. *Am. J. Neuroradiol.* 30, 1700–1703.

To, X. V., Benetatos, J., Soni, N., Liu, D., Abraha, H. M., Yan, W., et al. (2020). Ultra-high-field diffusion tensor imaging identifies discrete patterns of concussive injury in the rodent brain. *J. Neurotrauma.* [Epub ahead of print].

Tran, H. T., Laferla, F. M., Holtzman, D. M., and Brody, D. L. (2011a). Controlled cortical impact traumatic brain injury in 3xTg-AD mice causes acute intra-axonal amyloid-beta accumulation and independently accelerates the development of tau abnormalities. *J. Neurosci.* 31, 9513–9525. doi: 10.1523/jneurosci.0858-11.2011

Tran, H. T., Sanchez, L., Esparza, T. J., and Brody, D. L. (2011b). Distinct temporal and anatomical distributions of amyloid-beta and tau abnormalities following controlled cortical impact in transgenic mice. *PLoS One* 6:e25475. doi: 10.1371/journal.pone.0025475

Tran, L. D., Lifshitz, J., Witgen, B. M., Schwarzbach, E., Cohen, A. S., and Grady, M. S. (2006). Response of the contralateral hippocampus to lateral fluid percussion brain injury. *J. Neurotrauma* 23, 1330–1342. doi: 10.1089/neu.2006.23.1330

Wang, Q., Wang, Y., Shimony, J. S., Fagan, A. M., Cairns, N. J., Ances, B., et al. (2015). Diffusion tensor imaging detected neurodegeneration in preclinical Alzheimer disease. *Alzheimers Dement. J. Alzheimers Assoc.* 11, 77–78.

Watson, C., Janke, A. L., Hamalainen, C., Bagheri, S. M., Paxinos, G., Reutens, D. C., et al. (2017). An ontologically consistent MRI-based atlas of the mouse diencephalon. *Neuroimage* 157, 275–287. doi: 10.1016/j.neuroimage.2017.05.057

Wells, J. A., O'callaghan, J. M., Holmes, H. E., Powell, N. M., Johnson, R. A., Siow, B., et al. (2015). In vivo imaging of tau pathology using multi-parametric quantitative MRI. *Neuroimage* 111, 369–378. doi: 10.1016/j.neuroimage.2015.02.023

Wright, D. K., Liu, S., Van Der Poel, C., Mcdonald, S. J., Brady, R. D., Taylor, L., et al. (2017a). Traumatic brain injury results in cellular, structural and functional changes resembling motor neuron disease. *Cereb. Cortex* 27, 4503–4515.

Wright, D. K., O'brien, T. J., Shultz, S. R., and Mychasiuk, R. (2017b). Sex matters: repetitive mild traumatic brain injury in adolescent rats. *Ann. Clin. Transl. Neurol.* 4, 640–654. doi: 10.1002/acn3.441

Xu, S., Zhuo, J., Racz, J., Shi, D., Roys, S., Fiskum, G., et al. (2011). Early microstructural and metabolic changes following controlled cortical impact injury in rat: a magnetic resonance imaging and spectroscopy study. *J. Neurotrauma* 28, 2091–2102. doi: 10.1089/neu.2010.1739

Yoshiyama, Y., Uryu, K., Higuchi, M., Longhi, L., Hoover, R., Fujimoto, S., et al. (2005). Enhanced neurofibrillary tangle formation, cerebral atrophy, and cognitive deficits induced by repetitive mild brain injury in a transgenic tauopathy mouse model. *J. Neurotrauma* 22, 1134–1141.

Zanier, E. R., Bertani, I., Sammali, E., Pischiutta, F., Chiaravalloti, M. A., Vegliante, G., et al. (2018). Induction of a transmissible tau pathology by traumatic brain injury. *Brain* 141, 2685–2699.

Zemlan, F. P., Rosenberg, W. S., Luebbe, P. A., Campbell, T. A., Dean, G. E., Weiner, N. E., et al. (1999). Quantification of axonal damage in traumatic brain injury: affinity purification and characterization of cerebrospinal fluid tau proteins. *J. Neurochem.* 72, 741–750. doi: 10.1046/j.1471-4159.1999.0720741.x

Zhang, Y., Wu, F., Iqbal, K., Gong, C. X., Hu, W., and Liu, F. (2019). Subacute to chronic Alzheimer-like alterations after controlled cortical impact in human tau transgenic mice. *Sci. Rep.* 9:3789.

Zhao, Z. A., Ning, Y. L., Li, P., Yang, N., Peng, Y., Xiong, R. P., et al. (2017). Widespread hyperphosphorylated tau in the working memory circuit early after cortical impact injury of brain (Original study). *Behav. Brain Res.* 323, 146–153.

Conflict of Interest: The authors declare that the research was conducted in the absence of any commercial or financial relationships that could be construed as a potential conflict of interest.

frontiers in Neuroscience

ORIGINAL RESEARCH
published: 04 March 2021
doi: 10.3389/fnins.2021.625167

RAFF-4, Magnetization Transfer and Diffusion Tensor MRI of Lysophosphatidylcholine Induced Demyelination and Remyelination in Rats

Klara Holikova[1], Hanne Laakso[2], Raimo Salo[2], Artem Shatillo[3], Antti Nurmi[3], Martin Bares[4,5], Jiri Vanicek[1], Shalom Michaeli[6], Silvia Mangia[6], Alejandra Sierra[2] and Olli Gröhn[2]*

[1] Department of Medical Imaging, St. Anne's University Hospital Brno and Faculty of Medicine, Masaryk University, Brno, Czechia, [2] A.I. Virtanen Institute for Molecular Sciences, University of Eastern Finland, Kuopio, Finland, [3] Charles River Laboratories, Kuopio, Finland, [4] First Department of Neurology, St. Anne's University Hospital Brno and Faculty of Medicine, Masaryk University, Brno, Czechia, [5] Department of Neurology, School of Medicine, University of Minnesota, Minneapolis, MN, Untied States, [6] Center for Magnetic Resonance Research, University of Minnesota, Minneapolis, MN, Untied States

OPEN ACCESS

Edited by:
Yu-Chien Wu,
Indiana University Bloomington,
United States

Reviewed by:
Yunyan Zhang,
University of Calgary, Canada
Maria Concepcion Garcia Otaduy,
University of São Paulo, Brazil

***Correspondence:**
Olli Gröhn
olli.grohn@uef.fi

Specialty section:
This article was submitted to
Brain Imaging Methods,
a section of the journal
Frontiers in Neuroscience

Received: 02 November 2020
Accepted: 01 February 2021
Published: 04 March 2021

Citation:
Holikova K, Laakso H, Salo R,
Shatillo A, Nurmi A, Bares M,
Vanicek J, Michaeli S, Mangia S,
Sierra A and Gröhn O (2021) RAFF-4,
Magnetization Transfer and Diffusion
Tensor MRI
of Lysophosphatidylcholine Induced
Demyelination and Remyelination
in Rats. Front. Neurosci. 15:625167.
doi: 10.3389/fnins.2021.625167

Remyelination is a naturally occurring response to demyelination and has a central role in the pathophysiology of multiple sclerosis and traumatic brain injury. Recently we demonstrated that a novel MRI technique entitled Relaxation Along a Fictitious Field (RAFF) in the rotating frame of rank n (RAFFn) achieved exceptional sensitivity in detecting the demyelination processes induced by lysophosphatidylcholine (LPC) in rat brain. In the present work, our aim was to test whether RAFF4, along with magnetization transfer (MT) and diffusion tensor imaging (DTI), would be capable of detecting the changes in the myelin content and microstructure caused by modifications of myelin sheets around axons or by gliosis during the remyelination phase after LPC-induced demyelination in the corpus callosum of rats. We collected MRI data with RAFF4, MT and DTI at 3 days after injection (demyelination stage) and at 38 days after injection (remyelination stage) of LPC (n = 12) or vehicle (n = 9). Cell density and myelin content were assessed by histology. All MRI metrics detected differences between LPC-injected and control groups of animals in the demyelination stage, on day 3. In the remyelination phase (day 38), RAFF4, MT parameters, fractional anisotropy, and axial diffusivity detected signs of a partial recovery consistent with the remyelination evident in histology. Radial diffusivity had undergone a further increase from day 3 to 38 and mean diffusivity revealed a complete recovery correlating with the histological assessment of cell density attributed to gliosis. The combination of RAFF4, MT and DTI has the potential to differentiate between normal, demyelinated and remyelinated axons and gliosis and thus it may be able to provide a more detailed assessment of white matter pathologies in several neurological diseases.

Keywords: myelin, demyelination, remyelination, MRI, diffusion, rotating frame relaxation

---

Abbreviations: MRI, magnetic resonance imaging; MR, magnetic resonance; DTI, diffusion tensor imaging; MT, magnetization transfer; RAFF, relaxation along a fictitious field; MTR, magnetization transfer ratio; LPC, lysophosphatidylcholine; MD, mean diffusivity; FA, fractional anisotropy; RD, radial diffusivity; AD, axial diffusivity; FSL, FMRIB's Software Library; ROI, region of interest; OD, optical density.

INTRODUCTION

Myelin is essential for the proper functioning of the central nervous system. It not only accelerates the propagation of electrical impulses along myelinated fibers, but it also provides protection and nutrients to neurons (Saab and Nave, 2017). Disturbances in the integrity of myelin can cause a wide variety of motor, sensory and cognitive symptoms, and demyelination, e.g., damage or loss of myelin sheaths has been associated with several diseases including multiple sclerosis (Noseworthy et al., 2000), Alzheimer's disease (Nasrabady et al., 2018), and traumatic brain injury (Armstrong et al., 2016a).

Remyelination is a natural regenerative response to demyelination. Both acquired and genetic demyelinations are followed by remyelination, and this has been found to play an important role especially in multiple sclerosis (Prineas and Connell, 1979; Hirano, 1989) and traumatic brain injury (Armstrong et al., 2016b). Oligodendrocytes create new myelin sheaths that cover the demyelinated axons; however, the newly formed myelin sheaths are typically thinner than the original myelin sheaths and/or may have a different structure and altered conduction properties (Zhao et al., 2005; Franklin and Ffrench-Constant, 2008). Remyelination is a key step in the patient's recovery process, as electrical impulses propagate too slowly along demyelinated axons to allow normal brain function. Non-invasive quantitative imaging of changes in myelin content and microstructure can provide critical information about demyelination and remyelination processes and be useful for monitoring the progression of diseases and responses to treatment.

There are several methods available which can be used for imaging of demyelination, however, MRI is able to map myelin only indirectly (Heath et al., 2018). Direct detection of myelin is difficult as the movement restriction of lipid chains in the myelin bilayer causes a fast relaxation decay of the MR signal, although it may become more feasible by adopting zero echo time imaging approaches (Wilhelm et al., 2012; Seifert et al., 2017). Diffusion MRI, in particular diffusion tensor imaging (DTI), monitors the microscopic motion of water molecules that occur in brain tissues as a part of the diffusion process. As myelin sheaths restrict water diffusion, DTI can detect abnormalities in the structure of white matter, although it is not specific for the myelin compartment as many other cell structures contribute to the restriction of diffusion in tissue. Magnetization transfer (MT) MRI is an indirect method that was proposed many years ago for the detection of demyelination (Wolff and Balaban, 1989). This method utilizes the exchange of magnetization between the hydrogen nuclei of semisolid macromolecules and hydrogen protons in free water; as a consequence, semisolid tissue components such as myelin structures can modulate the MR image contrast. One limitation to the use of MT for monitoring myelin is that other macromolecular tissue components, as well as changes in the water content due to edema, also affect the MT contrast. Multi-exponential T2 can serve as a potential indicator of the myelin content in white matter. However, the relative size of the short-T2 component around 8–50 ms is defined as myelin associated water, and this has often been interpreted as the myelin content (Dula et al., 2010). While the water fraction of myelin has been found to correlate with the myelin content, the exact relationship between the short T2 component and the myelin content is not well understood (Tozer et al., 2005).

A novel rotating frame relaxation method operating in non-adiabatic regime, entitled Relaxation Along a Fictitious Field (RAFF) (Liimatainen et al., 2010, 2011) in the rotating frame of rank n (RAFFn) (Liimatainen et al., 2015), was recently presented and shown to have excellent sensitivity for myelin detection both in normal brain (Hakkarainen et al., 2016) and in demyelinated lesions induced by lysophosphatidylcholine (LPC) injections into the corpus callosum and in the dorsal tegmental tract (Lehto et al., 2017) of the rat brain and in dysmyelination (Satzer et al., 2015) in mouse brain. The correlation of relaxation time constants detected with RAFF4 (TRAFF4) with the myelin content obtained in a previous study (Lehto et al., 2017) was ascribed to the increased sensitivity of RAFFn to slow/ultra-slow motional regimes. These have correlation times of motion in the ms range (Liimatainen et al., 2015; Satzer et al., 2015; Hakkarainen et al., 2016), likely reflecting the exchange of myelin associated water as well as the conformational dynamics of methylene functional groups within myelin. The highest correlation between relaxation time constants and the myelin content was achieved with RAFF4 and RAFF5 techniques as compared to T1, T2 and conventional spin-lock rotating frame relaxation contrasts (Satzer et al., 2015; Hakkarainen et al., 2016) in the rat brain. In addition, RAFFn provides the distinct advantage of resulting in a substantially lower specific absorption rate (SAR) as compared to conventional continuous wave (CW) (Liimatainen et al., 2010, 2015).

While our previous work demonstrated the clear advantages of RAFFn in the detection of demyelination (Lehto et al., 2017), the process of remyelination was not assessed by multimodal MRI. In the present work, we hypothesize that by combining microstructural imaging, DTI, and methods specific to myelin content, RAFFn and/or MT, it is possible to characterize both the myelin content and the integrity of myelin sheaths during remyelination. To test this hypothesis, we used LPC-induced demyelination in the rat corpus callosum, and conducted a longitudinal study using multiparametric MRI data during both the acute demyelination and chronic remyelination phases and compared the results with histological findings.

MATERIALS AND METHODS

Animal Model

A total of 26 adult male Sprague-Dawley rats (Charles River, Germany; 300–350 g) were used in this study. Rats were group housed with a 12 h light/12 h dark cycle and had *ad libitum* access to food and water. All animal procedures were approved by the Animal Ethics Committee of the Provincial Government of Southern Finland and conducted in accordance with the guidelines set by the European Commission Directive 2010/63/EEC.

All surgical procedures were done under inhalation anesthesia using 1.8–2.2% isoflurane in 30%/70% O_2/N_2O. To induce demyelinated lesions, stereotaxic injections of the LPC solution (volume of 1.5 μl; concentration: 10 mg/ml; L-α-lysophosphatidylcholine from egg yolk; L-4129 Sigma-Aldrich, St. Louis, United States) were administered into the corpus callosum of the rat brain with stereotactic coordinates of 0.4 mm caudal from bregma, 1.4 mm left from bregma, and 2.6 mm from the brain surface ($n = 17$). Control animals ($n = 9$) underwent the identical protocol but were injected with 1.5 μl of vehicle solution of 0.1 M sodium phosphate buffer solution instead of LPC.

Pilot Study

A pilot study was first performed to clarify the time course of the demyelination/-remyelination process in the LPC model under our experimental conditions. It has been previously described that demyelination without an inflammatory reaction peaks at day 3 after LPC injection (Waxman et al., 1979; Lehto et al., 2017). However, it was our intention to determine the time course of remyelination. In the pilot experiment, 5 LPC rats were imaged at 7 T MRI (Bruker Pharmascan, Entlingen, Germany) with an actively decoupled quadrature receiver rat head coil and volume transmit coil pair every 2–3 days for 38 days using a high-resolution T2-weighted fast spin-echo (FSE) sequence with the following parameters: TR = 2.6 s, averages = 8, $TE_{eff} = 42.7$ ms, rare factor = 8, FOV = 25.6×25.6 mm^2, matrix size = 256×256, number of slices = 24 and slice thickness = 0.3 mm) with total imaging time of 10 min 55 s. Immediately after the final scanning, the animals were perfused for histology.

MRI Protocol to Study Demyelination and Remyelination

The remaining rats ($n = 21$) were imaged on day 3 after the LPC ($n = 12$) or vehicle ($n = 9$) injection, when there was already a significant demyelination without any inflammatory reaction or any signs of remyelination (Waxman et al., 1979), and again on day 38 after the injection when there should be a marked remyelination according to our pilot study. All MRI procedures were performed with the 7 T MRI system described above. The location of injections was localized using T2-weighted FSE acquisitions. The center of the imaging slice for RAFF4, MT, and DTI (middle slice), on both day 3 and day 38, was positioned to align with the center of the T2-weighted slice next (caudal) to the slice covering the injection site to exclude any mechanical damage induced by the injection.

For the relaxation and MT measurements, a FSE pulse sequence was used as the readout portion of the sequence. The parameters for the readout were TR = 4 s, $TE_{eff} = 8.3$ ms, $n_{echo} = 8$, FOV = 32.0×32.0 mm^2, matrix size = 256×256, number of slices = 1 and slice thickness = 0.5 mm with a total acquisition time of 16 min for one relaxation time constant map.

The RAFFn method has been presented in detail previously (Liimatainen et al., 2015). Here, we used RAFF4; to generate RAFFn contrast, trains of RAFFn pulses assembled in P-packets ($PP^{-1}\ P_{\pi}\ P_{\pi}{}^{-1}$) were used as described before (Liimatainen et al., 2010). The duration of each RAFF4 pulse, defined as $T_p = 4\pi/(\sqrt{2}\omega_1{}^{\max})$, was set to 4.525 ms and the peak RF amplitude was $\gamma B_1 = 324$ Hz. The RAFF4 pulse train durations were 0, 109, 217, 326, and 434 ms. Separate measurements were performed with and without an adiabatic full passage (AFP) inversion pulse (hyperbolic secant (HS1) pulse, $T_p = 8$ ms, $\gamma B_1 = 2{,}500$ Hz) preceding the RAFFn pulse trains (Liimatainen et al., 2010).

RAFF4 was calculated by a non-linear least-squares fitting approach simultaneously on data obtained with initial -z′ and +z′ magnetization orientations (Liimatainen et al., 2010). Equation 1 was used to model the observed exponential decay and the approach to steady state,

$$S_{\pm Z}(t) = S_{0,\pm Z}\, e^{-Rt} - S_{SS}(1 - e^{-Rt}) \tag{1}$$

Here, S_0 is the initial signal intensity (t = 0), R is the relaxation rate constant describing the decay, and S_{SS} is the steady-state intensity at $t \to \infty$.

In acquiring MT metrics, we used the modified inversion MT protocol with two consecutive acquisitions as described previously (Mangia et al., 2011). Separate measurements were performed with the magnetization initially aligned along the $+z$ axis during off-resonance irradiation, or $-z$ axis to allow the signal to recover, i.e., without or with initial global inversion achieved by an adiabatic full passage (AFP) pulse, in analogy to the acquisitions with RAFF4. A square saturation pulse with $\gamma B_1 = 200$ Hz was placed at 8 kHz off-resonance with an incremental duration (0.0, 0.3, 0.6, 0.9, 1.2 s). T_{1sat}, M_{SS} (steady state magnetization) and M_0 (fully relaxed magnetization in the absence of RF), were calculated using pixel-by-pixel analysis, as described by Mangia et al. (2011). MTR was also calculated as $MTR = 1–M_{SS}/M_0$.

For DTI, segmented spin-echo EPI was used with TR = 1 s, TE = 31.8 ms, $n_{shots} = 2$, number of averages = 48, FOV = 21.3×14.4 mm^2, matrix size = 170×115, number of slices = 5, slice thickness = 0.5 mm, b = 2,000 s/mm^2, diffusion directions = 42 leading to a total acquisition time of 1 h 18 min. Mean diffusivity (MD), fractional anisotropy (FA), and radial and axial diffusivity (RD, AD) maps were calculated from DTI data. DTI data were corrected for motion and eddy current-induced image distortions using Explore DTI (Leemans et al., 2009). Relaxation time constants and parametric maps from MT and DTI were reconstructed from signal intensities using pixel-by-pixel fitting in MATLAB (MathWorks, Natick, MA) and FMRIB's Software Library (FSL).

Region-of-Interest (ROI) Analysis

All the images from both time points were co-registered to the RAFF4 images from day 3 using Advanced Normalization Tools (ANTs)[1]. Two ROIs in the corpus callosum, one contralateral and one ipsilateral to the injection site, were manually drawn on T2-weighted images in every animal and transferred to the co-registered stack of parametric maps using the Aedes software package[2] When drawing the ROIs, we chose one slice caudally to the injection site based on the day 3 images and we used the

---

[1] http://stnava.github.io/ANTs/

[2] http://aedes.uef.fi

same location on day 38. Mean values from each ROIs from every map were used in the statistical analysis. In the vehicle injected animals, the ROIs were drawn at the vehicle injection site similarly as conducted for the LPC- injected animals.

Histological Procedures and Analysis

After the last MRI session, all animals were transcranially perfused first with 0.9% NaCl (30 ml/min, 2 min, 4°C) followed by 4% paraformaldehyde solution in 0.1 M phosphate buffer (pH 7.4) (30 ml/min, 25 min, 4°C). After perfusion, the brains were removed from the skull, and post-fixed for 4 h in 4% paraformaldehyde solution. Then, the brains were cryoprotected in 20% glycerol in 0.02 M potassium phosphate-buffered saline (pH 7.4) for 36 h, and frozen in dry ice, and stored at −70°C until sectioning.

The brains were sectioned into five series of 30 μm thick coronal sections using a sliding microtome. The first series was stored in 10% formalin at room temperature, and second to fifth series were stored in a cryoprotectant tissue-collecting solution (30% ethyleneglycol, 25% glycerol in 0.05 M PBS) at −20°C until staining.

Selected sections from the first series of sections were stained with Nissl (thionin) to assess changes in the cytoarchitecture of the corpus callosum. We stained up to 10 sections covering and exceeding the lesioned area as revealed in MRI on day 3. Consecutive sections from the second series were stained with gold chloride to assess the myeloarchitecture of the corpus callosum (Laitinen et al., 2010).

The optical density of Nissl- and myelin-stained sections was quantified in locations corresponding to the ROIs in the MRI analysis. Three consecutive sections were selected based on the MRI images where the ROI was drawn for analysis. The histological sections were selected based on anatomical landmarks, and the ROIs for optical density were drawn in the same anatomical location as in the MRI images in the ipsi- and contralateral corpus callosum. The three consecutive sections represent 450 μm in the rostral-caudal direction, which provides good coverage of the slice thickness of 500 μm in MRI. High-resolution photomicrographs of both Nissl- and myelin-stained sections of the corpus callosum were obtained using a light microscope (Zeiss Axio Imager2, White Plains, NY, United States) equipped with a digital camera (Zeiss Axiocam color 506). The whole corpus callosum area was imaged in each section by using the tile mode with an objective of 20×. Acquisition, alignment and format conversion were performed with Zen software (Blue edition, v2.6, Carl Zeiss Microscopy GmbH, United States).

The optical density (OD) on Nissl- and myelin-stained sections was quantified using ImageJ software (version 1.47, http://rsb.info.nih.gov/ij/, NIH, United States). First, the color photomicrographs were converted into 16-bit gray scale images, and then the gray scale was inverted to facilitate the interpretation of intensity values in the image to the intensities observed in the myelin-stained sections. We obtained the intensity values from each ROI from Nissl and myelin-stained sections. In order to correct for possible staining differences between sections and brains, the intensity values were corrected against the background intensity with no cell/myelin as in the cortical areas. OD was estimated as (I_{ref} − I_{cc})/I_{ref}, and for each ROI, the OD value was the average of the three consecutive sections. The estimation of the area of demyelination was conducted on the myelin-stained sections by selecting the area with a low content of myelin ipsi- and/or contralaterally. This selection was limited to the area of demyelination included in the previously drawn ROI for intensity.

Statistical Analysis

Data were analyzed using GraphPad Prism software (version 5.03 for Windows, La Jolla, CA, United States). Numerical results are represented as mean and standard deviation. Differences between vehicle- and LPC-injected rats were assessed using the two-sample *t*-test, and differences between ipsi- and contralateral corpus callosum within the same brain using the paired *t*-test. The contribution of myelinated axons and cell density to the MRI metrics was assessed using Pearson's linear correlation of the ROI analysis results from MRI and OD of myelin- and Nissl-stained sections. The change of the MRI parameters between days 3 and 38 was assessed using paired-samples *t*-test separately for ipsi- and contralateral ROIs of vehicle- and LPC-injected rats. The Benjamini-Hochberg false discovery rate method was used for multiple comparison corrections, and FDR-threshold $q < 0.05$ was chosen for statistical significance (Benjamini and Hochberg, 1995).

RESULTS

The time course of the relative signal changes in T2-weighted images after LPC injection is shown in **Figure 1**. This pilot experiment showed that a clear lesion could be detected on day 3 in the corpus callosum, followed by a gradual recovery of the T2-weighted signal intensity in the subsequent time points (**Figure 1G**). This is consistent with the demyelination/remyelination process described for the LPC model in white matter (Woodruff and Franklin, 1999). Based on this experiment, we chose day 3 as the time point for demyelination and day 38 for remyelination.

On day 3, all the LPC animals exhibited a lesion in the MRI maps with the lesion mainly in the ipsilateral corpus callosum, but also extending to the contralateral side (**Figure 2**). The group-wise results and comparisons in absolute units are shown in **Figure 3**, while **Table 1** shows relative differences and *q*-values (FDR corrected *p*-values) facilitating a comparison between modalities. The relative differences were calculated as (LPC-Vehicle)/Vehicle)*100%. All MRI metrics revealed the significant and robust effect of demyelination following LPC-injected animals in the ipsilateral site (**Figure 3**). The largest relative differences were detected by RAFF4, FA and AD (48, −50, −54%, respectively), while MTR, T1sat and RD showed more modest (−18, 21, 26%) but still very clear changes between the demyelinated ipsilateral area and a similar area in vehicle treated animals (**Table 1**). The contralateral side also showed statistically significant but smaller changes between LPC and vehicle injected animals. Diffusion parameters, especially AD,

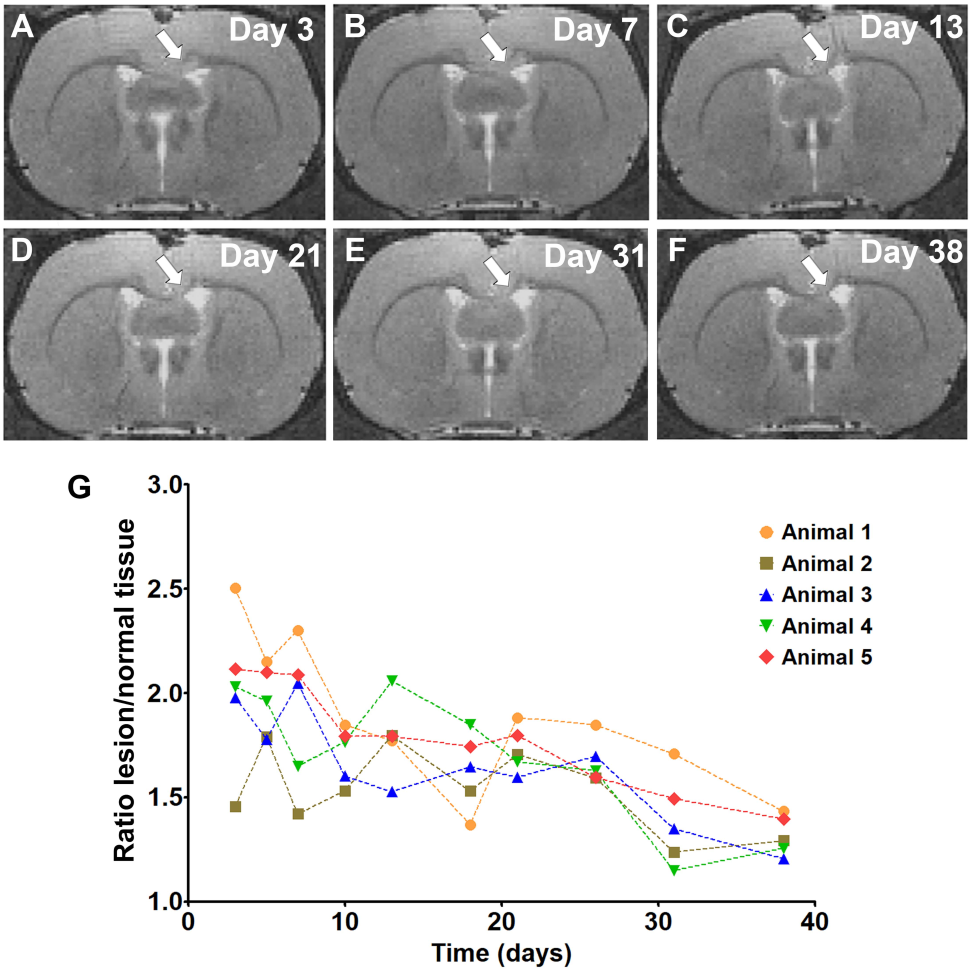

FIGURE 1 | T2 weighted images showing the lesion in the corpus callosum (white arrow) and its development from day 3 to day 38 **(A–F)**. The graph represents the signal intensity ratio between lesioned and normal tissue on individual days **(G)**.

FA and RD (–16, –22, 18%) were most sensitive at detecting the contralateral changes; these were caused most likely by the diffusion of LPC from the ipsilateral side to the contralateral side.

On day 38, all the LPC-injected animals revealed at least a partial recovery of the lesion in the MRI maps (**Figure 4**). Nonetheless, significant differences were still observed on day 38 between LPC and vehicle injected animals in the ipsilateral side in all other MRI metrics except the MD (**Figure 5**). When comparing MRI outcomes on day 3 (demyelination) to day 38 (remyelination), significant differences were detected in all MRI metrics (**Table 1**). In particular, the recovery toward normal values on the ipsilateral side of the LPC injected animals was detected with RAFF4 (from 48 to 17%, difference in ipsilateral side of LPC rats, from day 3 to day 38), MTR (from –18 to –7%), T1sat (from 21 to 10%), MD (from –31 to 1%), FA (from –51 to –22%), AD (from –54 to –16%). Furthermore, RD displayed a further robust increase (from 26 to 45%) from days 3 to 38.

Figure 6 shows the quantitative assessment of the histological results as well as representative examples of myelin- and Nissl-stained sections from vehicle- and LPC-injected animals. On day 38, the optical density (OD) analysis on myelin-stained sections revealed a small but significant decrease in the myelin content when comparing the ipsi- and contralateral ROIs in the corpus callosum in the LPC-injected brains (q = 0.02) (**Figure 6A**). We found a significant increase of the demyelinated area in animals after LPC injection in comparison to vehicle animals, ipsilaterally (q = 0.0085) but not contralaterally (q = 0.11) (**Figure 6B**). The demyelinated area was small as compared to the total area of the ROI analyzed in the OD analysis; these results demonstrate that the remyelination was well advanced but not completed at 38 days after the injection (**Figures 6D–G**). Additionally, we found that myelin alterations were taking place along the corpus callosum structure, which may be an indication of ongoing remyelinating processes (**Figure 6F**).

The analysis on Nissl-stained sections revealed increased cell density, which can be attributed to gliosis. The OD analysis on Nissl-stained sections showed that values in both ipsi- (q = 0.0032) and contralateral (q = 0.0085) ROIs of the corpus callosum significantly increased when comparing vehicle and LPC animals (**Figure 6C**). The increased cell density area overlapped with the demyelinated area (**Figures 6G,K**) and myelin alterations (**Figures 6F,J**) observed in myelin staining. These results demonstrate that the persistent demyelination was accompanied by inflammatory processes which were still ongoing at 38 days after the LPC infection.

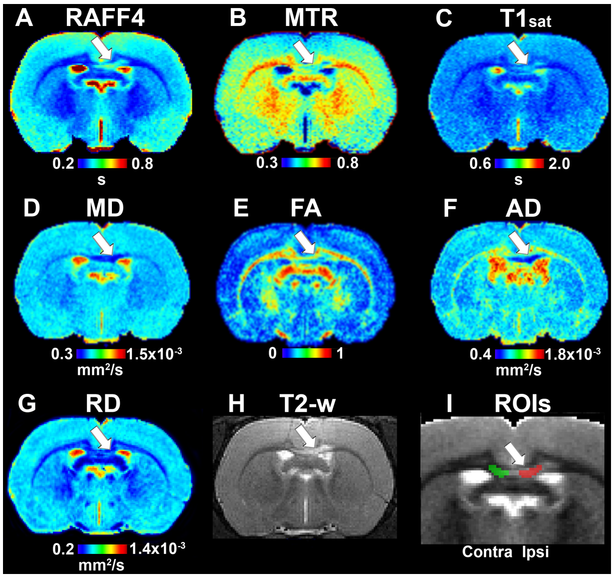

FIGURE 2 | Quantitative MRI maps in the demyelination phase, on day 3: RAFF4 **(A)**, magnetization transfer ratio, MTR **(B)**, T1sat **(C)**, mean diffusivity, MD **(D)**, fractional anisotropy, FA **(E)**, axial diffusivity, AD **(F)**, radial diffusivity, RD **(G)**, T2w image with lesion **(H)** and representative example of ROIs for analyzing the lesion on a grayscale RAFF4 map **(I)**. White arrow points to the lesion in the corpus callosum.

None of the MRI parameters correlated with the OD of myelin staining in the lesion area in the remyelination phase, however, RD, FA and AD correlated with the OD assessed with Nissl staining ($q < 0.05$) (**Table 2**).

DISCUSSION

In the present work, we investigated the capabilities of quantitative RAFF4, MTR, T1sat and DTI metrics to detect LPC-induced demyelination and remyelination in rat brain corpus callosum. We confirmed the previously demonstrated high sensitivity of RAFF4, MTR, and DTI for detecting demyelination (Lehto et al., 2017). This is the first time when RAFF4 was tested for investigating the myelination status during the remyelination phase. Our main finding was that the remyelination phase was associated with a partial recovery of RAFF4, MTR, and T1sat, FA and AD, while RD remained abnormally high and MD showed a complete recovery on day 38 after LPC injection, i.e., a time point when there was histological evidence of marked remyelination and gliosis.

Our results confirmed the sensitivity of RAFF4 and MTR to detect demyelination at 3 days after the LPC injection into the corpus callosum when only mild gliosis was present (Lehto et al., 2017). The demyelination phase was also associated with a distinct pattern in the DTI metric's changes, namely decreases in FA, AD, and MD, and an increase in RD. In our previous study, the LPC induced demyelination in the corpus callosum was characterized by a clearly decreased myelin content as detected by myelin staining. However, in that study we also observed

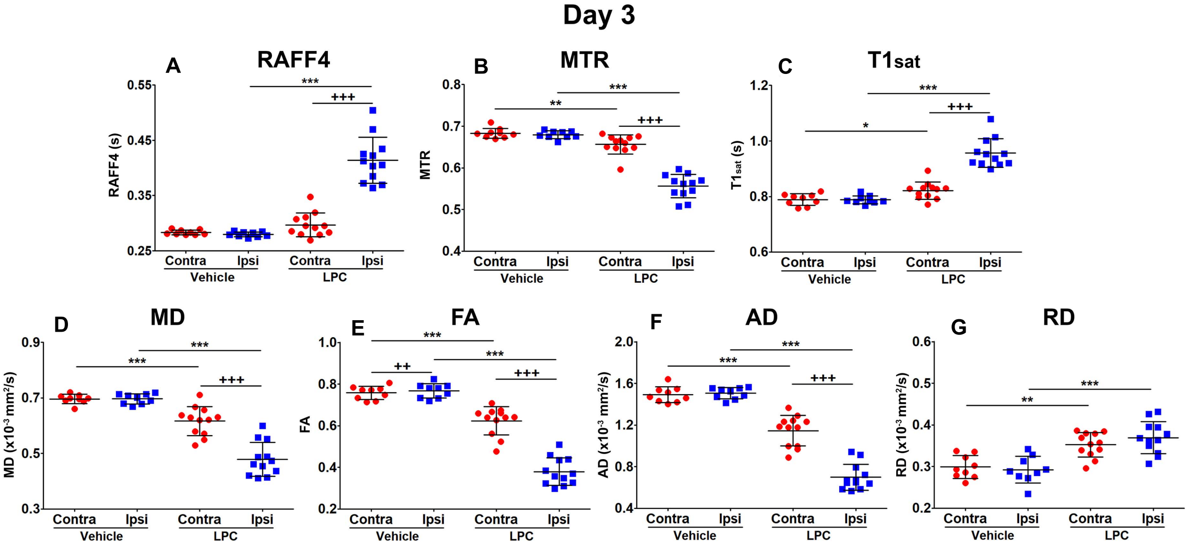

FIGURE 3 | Region of interest analysis of MRI parameters in the demyelination phase, on day 3: RAFF4 **(A)**, magnetization transfer ratio, MTR **(B)**, T1sat **(C)**, mean diffusivity MD **(D)**, fractional anisotropy, FA **(E)** and axial and radial diffusivity, AD **(F),** and RD **(G)**. Values obtained from the ipsilateral and contralateral sides of LPC injected ($n = 12$) rats and from the corresponding ROI in the vehicle injected ($n = 9$) rats. Mean ± SD, paired (+) or unpaired (*) *t*-test, FDR corrected *p*-values: *<0.05, ** or ++<0.01, *** or +++<0.001.

TABLE 1 | Relative differences with statistical significances in the MRI metrics.

			RAFF4	MTR	T1sat	MD	FA	AD	RD
Day 3	Ipsi	%	48.01	–18.16	21.33	–31.18	–50.51	–53.55	26.24
		t	9.53	–12.57	9.44	–10.29	–15.89	–18.11	4.86
		q	6.12e–08	1.10e–09	6.12e–08	2.33e–08	2.77e–11	5.35e–12	0.00017
	Contra	%	4.86	4.13	–3.92	–11.43	–17.80	–23.14	17.84
		t	1.88	–3.21	2.71	–4.41	–5.51	–6.39	4.25
		q	0.088	0.0061	0.018	0.00044	6.86e–05	1.58e–05	0.00061
Day 38	Ipsi	%	17.02	–7.06	9.99	1.27	–22.33	–15.91	44.67
		t	6.03	–4.88	5.49	1.03	–5.39	–5.11	5.81
		q	2.94e–05	0.00017	6.86e–05	0.33	7.89e–05	0.00012	4.23e–05
	Contra	%	0.68	–1.11	2.78	–3.02	–17.54	–16.39	30.48
		t	0.40	–1.282	2.52	–1.85	–5.18	–5.30	4.98
		q	0.70	0.23	0.025	0.089	0.00011	8.71e–05	0.00015
Day 38 - Day 3	LPC Ipsi	%	–22.90	15.81	–12.07	42.14	60.16	75.64	12.02
		t	–7.18	10.22	–7.11	12.33	6.96	12.70	1.85
		q	9.16e–05	5.57e–06	9.16e–05	1.24e–06	9.54e–05	1.24e–06	0.12
	LPC Contra	%	–7.86	5.00	–4.72	6.78	1.33	7.19	7.41
		t	–4.65	4.67	–3.69	2.07	0.077	1.19	2.05
		q	0.0016	0.0016	0.0077	0.095	0.97	0.33	0.095
	Vehicle Ipsi	%	–3.30	1.85	–3.21	–4.53	–0.32	–4.94	–2.31
		t	–6.58	2.81	–5.79	–3.48	–0.23	–2.06	–0.68
		q	0.00060	0.043	0.0013	0.017	0.89	0.10	0.58
	Vehicle Contra	%	–4.27	1.92	–3.58	–3.12	0.13	–2.81	–2.83
		t	–9.84	2.72	–5.63	–2.36	–0.0051	–1.02	–0.74
		q	6.69e–05	0.046	0.0014	0.075	1.00	0.41	0.56

**Percentage on day 3 and day 38: ((LPC-Vehicle)/Vehicle)*100%. q value is the p-value that has been adjusted for the false discovery rate. Percentage on day 38 vs. day 3: ((day 38 - day 3)/day 3)*100 LPC and vehicle ipsi- and contralaterally. q-value on day 38 vs. day 3: (value on day 38-value on day 3) vs. zero.*

some remaining disorganized pockets in the myelin sheaths with myelin debris being evident in electron microscopy (Lehto et al., 2017). In the present experiments, the pattern of changes in DTI metrics in demyelination phase, was mostly consistent with our previous work, however, now we did find increased RD, a parameter which was unchanged in our previous study. The present finding is in agreement with the general view that increased RD is an indication of demyelination (Song et al., 2005). The difference to the previous study may originate from differences in LPC patches leading to more severe demyelination. This is also consistent with the somewhat relatively larger changes in RAFF4 and MTR observed in the present study as compared to those reported by Lehto et al. (2017).

The remyelination phase was characterized by a close-to-normal myelin content as confirmed by OD analysis of myelin-stained histological sections. Unlike on day 3, when only very mild gliosis was present, on day 38 increased cellular density was detected in Nissl staining, likely due to gliosis. As increased cellularity affects relaxation, MT and diffusion, this makes the interpretation of the results more complicated, resembling more realistically the human pathology where myelin damage typically triggers gliosis, and thus these pathological features overlap. At the late time point, we observed a recovery of RAFF4 toward the normal values measured in the healthy tissue, which is consistent with remyelination. It has been shown that RAFF4 is sensitive to the correlation time regime in the ms-range (Satzer et al., 2015; Hakkarainen et al., 2016), which likely corresponds to exchange and dipolar interactions of myelin and water as well as dipolar interaction with methylene groups. Therefore, the high sensitivity of RAFF4 to myelin, also during the remyelination phase, was expected.

MT showed a similar recovery toward baseline as RAFF4. However, the relative difference to controls was smaller than in RAFF4, reflecting its lower sensitivity to myelination changes in the demyelination phase. Previously, RAFF4 had been shown to correlate with myelin density to a greater extent than MT in normal brain (Hakkarainen et al., 2016) and in LPC-induced demyelinated lesions in dorsal tegmental tract (dtg) of the rat brain (Lehto et al., 2017). It should be emphasized, however, that there is a distinct difference between relaxation mechanisms during RAFF4 and MT. RAFF4 is a rotating frame method operating in the rotating frame of rank 4, and thus has contributions from longitudinal, T1r, and transverse, T2r, relaxation pathways (Liimatainen et al., 2015). In addition to anisochronous and isochronous exchange and dipolar interactions contributing to RAFF4, RAFF4 share cross-relaxation pathways with MT (van Zijl et al., 2018). Therefore, these two techniques provide only partially overlapping information when characterizing tissue integrity. This substantial distinction in the relaxation mechanisms contributing to RAFF4 and MT is reflected in the differential sensitivity of RAFF4 and MT to demyelination, dismyelination and remyelination processes in the brain (Satzer et al., 2015). It is also worth noting that RAFFn offers the possibility of achieving the desired fictitious field by making use of a frequency swept pulse which improves the flexibility in handling SAR issues in human applications (Liimatainen et al., 2015).

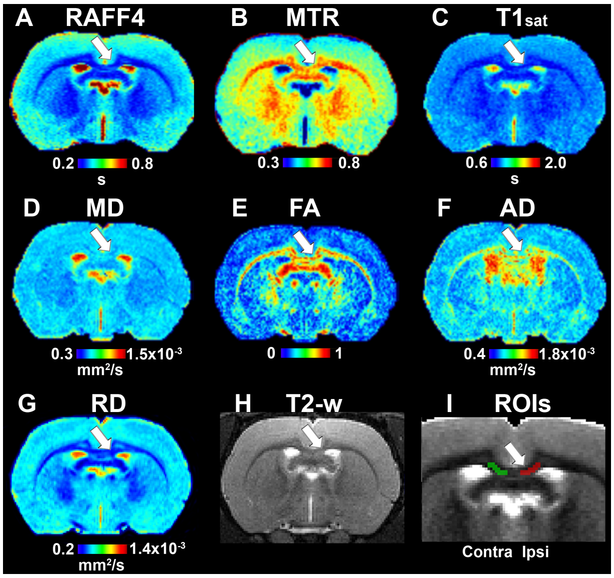

FIGURE 4 | Quantitative MRI maps in the remyelination phase, on day 38. Relaxation time constant map of RAFF4 **(A)**, magnetization transfer ratio, MTR **(B)**, T1sat **(C)**, mean diffusivity, MD **(D)**, fractional anisotropy, FA **(E)**, axial diffusivity, AD **(F)**, radial diffusivity, RD **(G)**, T2w image with the lesion **(H)** and a representative example of ROIs for analyzing lesion on a grayscale RAFF4 map **(I)**. White arrow points to the lesion in the corpus callosum.

The pattern of changes detected in DTI metrics in the remyelination phase was likely conveying information from multiple factors including the thickness and microstructure of the myelin sheaths as well as the cell density. The partial recoveries of FA and AD are similar to those detected with RAFF4 and may reflect the rebuilding of myelin sheaths and the clearance of the myelin debris. The increase in RD is consistent with the fact that the remyelinated sheaths are structurally different from intact myelin sheaths (Raine, 1984; Oluich et al., 2012; Podbielska et al., 2013; Pfeiffer et al., 2019), i.e., they are likely more permeable to water. MD was the only MRI parameter that returned to the normal level on day 38. It is well known from cancer studies that MD inversely correlates with the cellularity of the tissue (Chenevert et al., 2000) and therefore the increased cellularity due to gliosis likely contributes to the pseudo-normalization of MD. The extension to more complex diffusion MRI models has the potential to extract more specific information related to these processes (Luo et al., 2019).

MRI changes were also detected on the contralateral side of the injection between LPC and vehicle injected animals. This is likely attributable to diffusion of LPC along axons in corpus callosum such that LPC reached also the contralateral side. Interestingly, changes in cell density in Nissl, attributed to gliosis, were pronounced on the contralateral side on day 38, probably explaining the higher sensitivity of diffusion

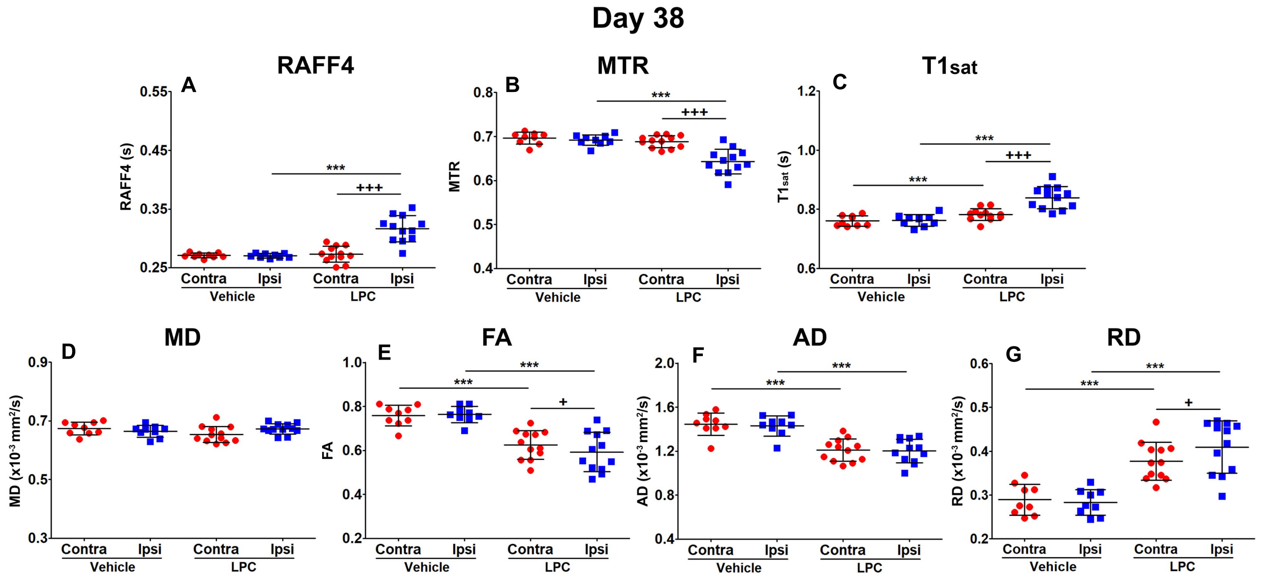

FIGURE 5 | Region of interest analysis of MRI parameters in the remyelinization phase, on day 38: RAFF4 **(A)**, magnetization transfer ratio, MTR **(B)**, T1sat **(C)**, mean diffusivity MD **(D)**, fractional anisotropy, FA **(E)** and axial and radial diffusivity, AD **(F)** and RD **(G)**. Values obtained from the ipsilateral and contralateral side of LPC injected ($n = 12$) rats and from the corresponding ROI in the vehicle injected ($n = 9$) rats. Mean ± *SD*, paired (+) or unpaired (*) *t*-test, FDR corrected *p*-values: + < 0.05, *** or +++<0.001.

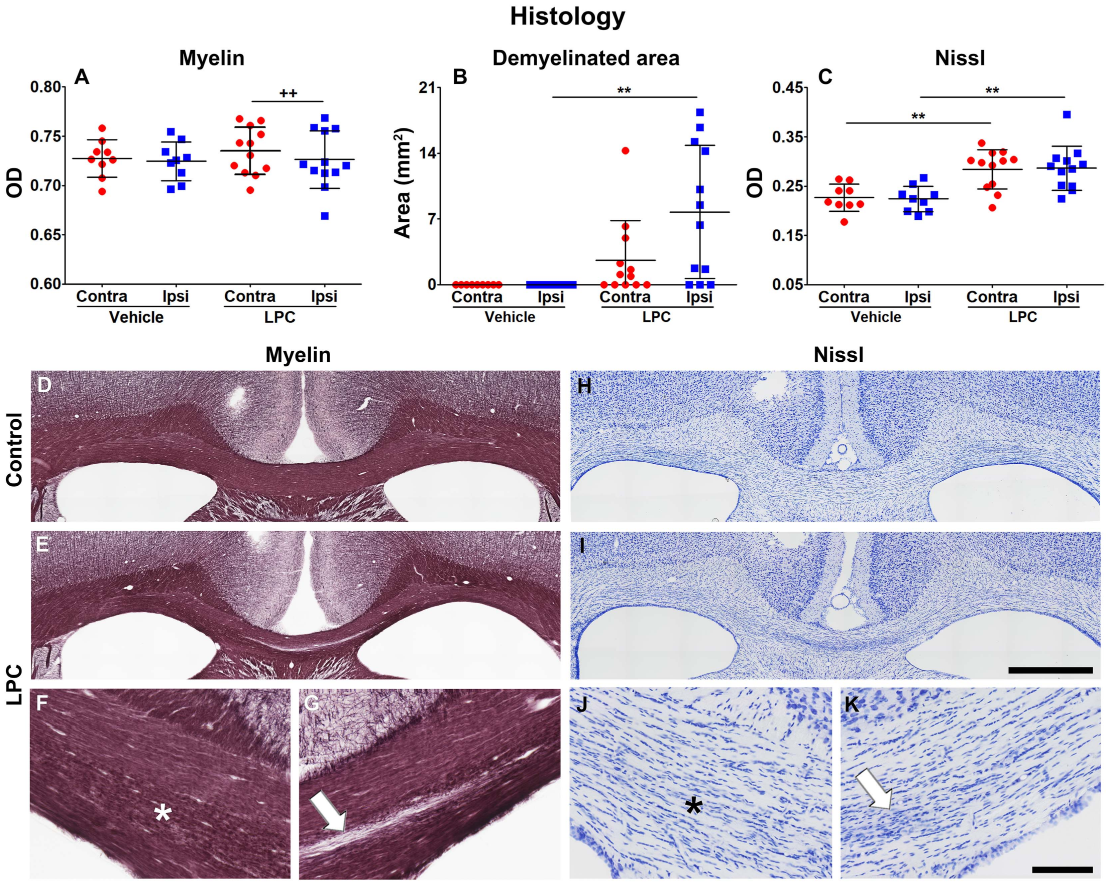

FIGURE 6 | Histologic assessment of the myelin and Nissl stainings at 38 days after vehicle or LPC injection. OD **(A)** and demyelinated area **(B)** analyses of the myelin-stained sections, and OD analysis of the Nissl-stained **(C)** sections. Values were obtained from the ipsi- and contralateral corpus callosum of vehicle- ($n = 9$) and LPC-injected ($n = 12$) rats. Results are shown as mean ± *SD*. The unpaired *t*-test compared the same hemispheres between vehicle- and LPC-injected rats (**$p < 0.01$), and the paired *t*-test ipsi- and contralateral hemispheres within the same animals ($^{++}p < 0.01$). Photomicrographs of vehicle- and LPC-injected animals in myelin **(D–G)** and Nissl **(H–K)** stains of representative rats. The white arrow points to the ongoing demyelinated area and the presence of gliosis, and the asterisk indicates the area with ongoing myelin alterations accompanied by gliosis. Scale bar: 1 mm **(D,E,H,I)** and 200 μm **(F,G,J,K)**.

TABLE 2 | Correlation between MRI metrics and the OD of myelin- and Nissl-stained sections.

	Myelin OD		**Nissl OD**	
	R	***p***	**R**	***p***
AD	−0.18086	0.25171	−0.63062	7.5945e–06
FA	−0.14081	0.37376	−0.67323	1.0335e–06
RD	0.13148	0.40656	0.64884	3.3607e–06
MD	−0.13111	0.40787	−0.071477	0.65284
MTR	0.014335	0.92821	−0.29864	0.054724
RAFF4	0.036727	0.81738	0.2594	0.097141
T1SAT	0.086483	0.58604	0.36175	0.018572

Critical p-value (q < 0.05): 7.5945e–06.

changes than were evident with RAFF4 or MT. None of the MRI parameters correlated significantly with optical density of myelin staining in the remyelination phase. This is likely because the optical densities were close to normal in the lesioned area and therefore there was a narrow range of values both for MRI and optical density. This, together with confounding effect of gliosis on MRI parameters, explains the non-significant correlation values between MRI parameters and myelin density in the remyelination phase, even though there was an evident recovery of MRI parameters, especially RAFF4 and MTR, from demyelination values. The influence of gliosis on diffusion metrics is consistent with the earlier reports of Budde et al. (2011). Consistently, we observed a correlation between cellularity in Nissl staining and diffusion parameters but not with RAFF4 or MT parameters, further emphasizing the different sensitivities of these techniques to detect myelination and cellularity.

One limitation of our study is that in spite of careful manual alignment of histology with MRI by an expert in the field, the partial volume effect and the challenge of selecting the same ROIs in MRI and histology could have influenced our results. In addition, the limited sampling in histology vs. the slice thickness in MRI may have affected our assessments of the correlations.

CONCLUSION

Our data confirms the sensitivity of RAFF4 and MT for detecting the myelin content in demyelinated lesions, but now reveals that remyelination is associated with a recovery of RAFF4 and MT toward normal values. DTI metrics displayed a distinct pattern of changes in the remyelination phase, likely reflecting on-going changes not only in the myelin content but also in the architecture of the myelin sheaths as well as the presence of gliosis. The combination of RAFF4, MT and DTI has the potential to differentiate between normal, demyelinated and remyelinated axonal bundles and gliosis, thus making possible a unique non-invasive characterization of white matter pathologies in several neurological diseases. Further studies will be required to evaluate the sensitivity of multiple MRI modalities to detect remyelination in areas with more isotropic fiber distributions, where RAFF4 has demonstrated its superiority over DTI (Lehto et al., 2017).

DATA AVAILABILITY STATEMENT

The raw data supporting the conclusions of this article will be made available by the authors, without undue reservation.

ETHICS STATEMENT

The animal study was reviewed and approved by the Animal Ethics Committee of the Provincial Government of Southern Finland.

AUTHOR CONTRIBUTIONS

KH, HL, and RS participated in the design of the work, acquisition, analysis, interpretation of data, and preparing the manuscript. AS, AN, MB, and JV participated in the design of the work and preparing the manuscript. ShM and SiM participated in the design of the work, interpretation of the data and preparing the manuscript. AS and OG participated in the design of the work, analysis, interpretation of data and preparing the manuscript. All authors contributed to the article and approved the submitted version.

FUNDING

This project was received funding from the European Union's Horizon 2020 Research and Innovation Programme Under the Marie Skłodowska-Curie Grant Agreement No. 691110 (MICROBRADAM) and Academy of Finland.

ACKNOWLEDGMENTS

We thank Ewen MacDonald Ph.D. for revising the language of the manuscript. The technical assistance with the microinjections, animal handling and histology by Pirjo Hakkarainen and Maarit Pulkkinen is highly appreciated.

REFERENCES

Armstrong, R. C., Mierzwa, A. J., Marion, C. M., and Sullivan, G. M. (2016a). White matter involvement after TBI: clues to axon and myelin repair capacity. *Exp. Neurol.* 275, 328–333. doi: 10.1016/j.expneurol.2015.02.011

Armstrong, R. C., Mierzwa, A. J., Sullivan, G. M., and Sanchez, M. A. (2016b). Myelin and oligodendrocyte lineage cells in white matter pathology and plasticity after traumatic brain injury. *Neuropharmacology* 110, 654–659. doi: 10.1016/j.neuropharm.2015.04.029

Benjamini, Y., and Hochberg, Y. (1995). Controlling the false discovery rate: a practical and powerful approach to multiple testing. *J. R. Stat. Soc. B* 57, 289–300. doi: 10.1111/j.2517-6161.1995.tb02031.x

Budde, M. D., Janes, L., Gold, E., Turtzo, L. C., and Frank, J. A. (2011). The contribution of gliosis to diffusion tensor anisotropy and tractography following traumatic brain injury: validation in the rat using Fourier analysis of stained tissue sections. *Brain* 134:2248. doi: 10.1093/brain/awr161

Chenevert, T., Stegman, L., Taylor, J., Robertson, P., Greenberg, H., and Rehemtulla, A. (2000). Diffusion magnetic resonance imaging: an early surrogate marker of therapeutic efficacy in brain tumors. *ıJ. Natl. Cancer Inst.* 92, 2029–2036. doi: 10.1093/jnci/92.24.2029

Dula, A. N., Gochberg, D. F., Valentine, H. L., Valentine, W. M., and Does, M. D. (2010). Multiexponential T2, magnetization transfer, and quantitative histology in white matter tracts of rat spinal cord. *Magn. Reson. Med.* 63, 902–909. doi: 10.1002/mrm.22267

Franklin, R. J. M., and Ffrench-Constant, C. (2008). Remyelination in the CNS: from biology to therapy. *Nat. Rev. Neurosci.* 9, 839–855. doi: 10.1038/nrn2480

Hakkarainen, H., Sierra, A., Mangia, S., Garwood, M., Michaeli, S., Gröhn, O., et al. (2016). MRI relaxation in the presence of fictitious fields correlates with myelin content in normal rat brain. *Magn. Reson. Med.* 75, 161–168. doi: 10.1002/mrm.25590

Heath, F., Hurley, S. A., Johansen-Berg, H., and Sampaio-Baptista, C. (2018). Advances in noninvasive myelin imaging. *Dev. Neurobiol.* 78, 136–151. doi: 10.1002/dneu.22552

Hirano, A. (1989). Review of the morphological aspects of remyelination. *Dev. Neurosci.* 11, 112–117. doi: 10.1159/000111892

Laitinen, T., Sierra, A., Pitkänen, A., and Gröhn, O. (2010). Diffusion tensor MRI of axonal plasticity in the rat hippocampus. *Neuroimage* 51, 521–530. doi: 10.1016/j.neuroimage.2010.02.077

Leemans, A., Jeurissen, B., Sijbers, J., Jones, D. K. (2009). ExploreDTI: a graphical toolbox for processing, analyzing, and visualizing diffusion MR data. *Proc. Intl. Soc. Mag. Reson. Med.* 17.

Lehto, L. J., Albors, A. A., Sierra, A., Tolppanen, L., Eberly, L. E., Mangia, S., et al. (2017). Lysophosphatidyl choline induced demyelination in rat probed by relaxation along a fictitious field in high rank rotating frame. *Front. Neurosci.* 11:433. doi: 10.3389/fnins.2017.00433

Liimatainen, T., Hakkarainen, H., Mangia, S., Huttunen, J. M. J., Storino, C., Idiyatullin, D., et al. (2015). MRI contrasts in high rank rotating frames. *Magn. Reson. Med.* 73, 254–262. doi: 10.1002/mrm.25129

Liimatainen, T., Mangia, S., Ling, W., Ellermann, J., Sorce, D. J., Garwood, M., et al. (2011). Relaxation dispersion in MRI induced by fictitious magnetic fields. *J. Magn. Reson.* 209, 269–276. doi: 10.1016/j.jmr.2011.01.022

Liimatainen, T., Sorce, D. J., O'Connell, R., Garwood, M., and Michaeli, S. (2010). MRI contrast from relaxation along a fictitious field (RAFF). *Magn. Reson. Med.* 64, 983–994. doi: 10.1002/mrm.22372

Luo, T., Oladosu, O., Rawji, K. S., Zhai, P., Pridham, G., Hossain, S., et al. (2019). Characterizing structural changes with evolving remyelination following experimental demyelination using high angular resolution diffusion MRI and texture analysis. *J. Magn. Reson. Imaging* 49, 1750–1759. doi: 10.1002/jmri.26328

Mangia, S., Federico De, F., Liimatainen, T., Garwood, M., and Michaeli, S. (2011). Magnetization transfer using inversion recovery during off-resonance irradiation. *Magn. Reson. Imaging.* 29, 1346–1350. doi: 10.1016/j.mri.2011.04.002

Nasrabady, S. E., Rizvi, B., Goldman, J. E., and Brickman, A. M. (2018). White matter changes in Alzheimer's disease: a focus on myelin and oligodendrocytes. *Acta Neuropathol. Commun.* 6:22.

Noseworthy, J. H., Lucchinetti, C., Rodriguez, M., and Weinshenker, B. G. (2000). Multiple sclerosis. *N. Engl. J. Med.* 343, 938–952.

Oluich, L.-J., Stratton, J. A. S., Xing, Y. L., Ng, S. W., Cate, H. S., Sah, P., et al. (2012). Targeted ablation of oligodendrocytes induces axonal pathology independent of overt demyelination. *J. Neurosci.* 32:8317. doi: 10.1523/jneurosci.1053-12.2012

Pfeiffer, F., Frommer-Kaestle, G., and Fallier-Becker, P. (2019). Structural adaption of axons during de- and remyelination in the Cuprizone mouse model. *Brain Pathol.* 29, 675–692. doi: 10.1111/bpa.12748

Podbielska, M., Banik, N. L., Kurowska, E., and Hogan, E. L. (2013). Myelin recovery in multiple sclerosis: the challenge of remyelination. *Brain Sci.* 3:1282. doi: 10.3390/brainsci3031282

Prineas, J. W., and Connell, F. (1979). Remyelination in multiple sclerosis. *Ann. Neurol.* 5, 22–31.

Raine, C. (1984). "Morphology of myelin and myelination," in *Myelin*, ed. P. Morell (Boston, MA: Springer), 1–50. doi: 10.1007/978-1-4757-1830-0_1

Saab, A., and Nave, K. (2017). Myelin dynamics: protecting and shaping neuronal functions. *Curr. Opin. Neurobiol.* 47, 104–112. doi: 10.1016/j.conb.2017.09.013

Satzer, D., DiBartolomeo, C., Ritchie, M. M., Storino, C., Liimatainen, T., Hakkarainen, H., et al. (2015). Assessment of dysmyelination with RAFFn MRI: application to murine MPS I. *PLoS One* 10:e0116788. doi: 10.1371/journal.pone.0116788

Seifert, A. C., Li, C., Wilhelm, M. J., Wehrli, S. L., and Wehrli, F. W. (2017). Towards quantification of myelin by solid-state MRI of the lipid matrix protons. *Neuroimage* 163, 358–367. doi: 10.1016/j.neuroimage.2017.09.054

Song, S.-K., Yoshino, J., Le, T., Lin, S.-J., Sun, S.-W., Cross, A., et al. (2005). Demyelination increases radial diffusivity in corpus callosum of mouse brain. *NeuroImage* 26, 132–140. doi: 10.1016/j.neuroimage.2005.01.028

Tozer, D. J., Davies, G. R., Altmann, D. R., Miller, D. H., and Tofts, P. S. (2005). Correlation of apparent myelin measures obtained in multiple sclerosis patients and controls from magnetization transfer and multicompartmental T2 analysis. *Magn. Reson. Med.* 53, 1415–1422. doi: 10.1002/mrm.20479

van Zijl, P., Lam, W. W., Xu, J., Knutsson, L., and Stanisz, G. J. (2018). Magnetization transfer contrast and chemical exchange saturation transfer MRI. Features and analysis of the field-dependent saturation spectrum. *Neuroimage* 168, 222–241. doi: 10.1016/j.neuroimage.2017.04.045

Waxman, S. G., Kocsis, J. D., and Nitta, K. C. (1979). Lysophosphatidyl choline-induced focal demyelination in the rabbit corpus callosum. Light-microscopic observations. *J. Neurol. Sci.* 44, 45–53. doi: 10.1016/0022-510x(79)90221-1

Wilhelm, M. J., Ong, H. H., Wehrli, S. L., Li, C., Tsai, P.-H., Hackney, D. B., et al. (2012). Direct magnetic resonance detection of myelin and prospects for quantitative imaging of myelin density. *Proc. Natl. Acad. Sci. U.S.A.* 109, 9605–9610. doi: 10.1073/pnas.1115107109

Wolff, S. D., and Balaban, R. S. (1989). Magnetization transfer contrast (MTC) and tissue water proton relaxation in vivo. *Magn. Reson. Med.* 10, 135–144. doi: 10.1002/mrm.1910100113

Woodruff, R. H., and Franklin, R. J. M. (1999). Demyelination and remyelination of the caudal cerebellar peduncle of adult rats following stereotaxic injections of lysolecithin, ethidium bromide, and complement/anti-galactocerebroside: a comparative study. *Glia* 25, 216–228. doi: 10.1002/(sici)1098-1136(19990201)25:3<216::aid-glia2>3.0.co;2-l

Zhao, C., Fancy, S. P. J., Kotter, M. R., Li, W.-W., and Franklin, R. J. M. (2005). Mechanisms of CNS Remyelination-the Key to therapeutic advances. *J. Neurol. Sci* 233, 87–91. doi: 10.1016/j.jns.2005.03.008

Conflict of Interest: The authors declare that the research was conducted in the absence of any commercial or financial relationships that could be construed as a potential conflict of interest.

frontiers in Neuroscience

REVIEW
published: 07 April 2021
doi: 10.3389/fnins.2021.583678

Current and Emerging MR Methods and Outcome in Rodent Models of Parkinson's Disease: A Review

Alexandra Petiet[1,2]*

[1] Centre de Neuroimagerie de Recherche, Institut du Cerveau, Paris, France, [2] Inserm U1127, CNRS UMR 7225, Sorbonne Universités, Paris, France

Parkinson's disease (PD) is a major neurodegenerative disease characterized by massive degeneration of the dopaminergic neurons in the substantia nigra pars compacta, α-synuclein-containing Lewy bodies, and neuroinflammation. Magnetic resonance (MR) imaging plays a crucial role in the diagnosis and monitoring of disease progression and treatment. A variety of MR methods are available to characterize neurodegeneration and other disease features such as iron accumulation and metabolic changes in animal models of PD. This review aims at giving an overview of how those physiopathological features of PD have been investigated using various MR methods in rodent models. Toxin-based and genetic-based models of PD are first described. MR methods for neurodegeneration evaluation, iron load, and metabolism alterations are then detailed, and the main findings are provided in those models. Ultimately, future directions are suggested for neuroinflammation and neuromelanin evaluations in new animal models.

Keywords: MRI methods, Parkinson's disease, animal model, diffusion MRI, MR spectroscopy, resting-state functional MRI

Edited by:
Rodolfo Gabriel Gatto,
University of Illinois at Chicago,
United States

Reviewed by:
Sung-Ho Lee,
University of North Carolina at Chapel Hill, United States
Jason Langley,
University of California, Riverside,
United States
Danqing Xiao,
Regis College, United States
Ikuo Tooyama,
Shiga University of Medical Science,
Japan
Puneet Bagga,
St. Jude Children's Research
Hospital, United States

Correspondence:
Alexandra Petiet
alexandra.petiet@icm-institute.org

Specialty section:
This article was submitted to
Brain Imaging Methods,
a section of the journal
Frontiers in Neuroscience

Received: *15 July 2020*
Accepted: *05 March 2021*
Published: *07 April 2021*

Citation:
Petiet A (2021) Current and Emerging MR Methods and Outcome in Rodent Models of Parkinson's Disease: A Review.
Front. Neurosci. 15:583678.
doi: 10.3389/fnins.2021.583678

INTRODUCTION

Parkinson's disease is a major neurodegenerative disease in the elderly affecting 7 to 10 million people worldwide. This disease is characterized by massive degeneration of the dopaminergic (DA) neurons and Lewy body inclusions containing α-synuclein proteins in the subtantia nigra pars compacta (SNc), as well as neuroinflammation. The reduction of DA levels in the striatum (STR) causes the appearance of the clinical symptoms such as akinesia, rigidity, and tremor. The clinical diagnosis can only be done when 50% of those neurons are destroyed (Redgrave et al., 2010). While most forms of PD are sporadic, less than 10% are associated with familial mutations (Dauer and Przedborski, 2003; Thomas and Beal, 2007). Mutations in the *leucin-rich repeat kinase 2* (*LRRK2*) and the α*-synuclein coding* gene (*SNCA*) are responsible for the autosomal-dominant PD, and mutations in the *Parkin* (*PARK2*), the *phosphatase and tensin (Pten)-induced kinase 1* (*PINK1*), and *DJ-1* genes are responsible for the autosomal–recessive PD.

Abbreviations: PD, Parkinson disease; MRI, magnetic resonance imaging; DA, dopamine; LRRK2, leucin-rich repeat kinase 2; SNCA, α-synuclein coding gene; PARK2, Parkin 2; PINK1, phosphatase and tensin (Pten)-induced kinase 1; rs-fMRI, resting-state functional MRI; FC, functional connectivity; R_2^*, transverse relaxation rate ($1/T_2^*$); T_2^*, transverse relaxation time; MRS, magnetic resonance spectroscopy; 6-OHDA, 6-hydroxydopamine; MPTP, 1-methyl-4-phenyl-1,2,3,6-tetrahydropyridine; BBB, blood–brain barrier; fMRI, functional MRI; BOLD, blood oxygenation level-dependent signal; SWI, susceptibility-weighted imaging; QSM, quantitative susceptibility mapping; LPS, lipopolysaccharide; Tg, transgenic; Glu, glutamate; GABA, γ-aminobutyric acid; NAA, *N*-acetyl-aspartate; mIns, myo-inositol; Cre, creatine; Gln, glutamine; Cho, choline; MD, mean diffusivity; FA, fractional anisotropy; AD, axial diffusivity; RD, radial diffusivity; ADC, apparent diffusion coefficient; SNc, substantia nigra pars compacta; STR, striatum; GP, globus pallidus; SNr, substantia nigra pars reticulata; TH, thalamus; STN, subthalamic nucleus; MFB, medial forebrain bundle; M1, primary motor cortex; CC, corpus callosum; SM, sensorimotor cortex; Hc, hippocampus; GPi, globus pallidus interna; GPe, globus pallidus externa; BG, basal ganglia; cp, cerebral peduncle.

Motor dysfunction in PD is classically described by the corticobasal ganglia–thalamocortical motor pathway model and with the direct, indirect, and hyperdirect pathways illustrated in **Figure 1** (Delong, 1990; Honey et al., 2003; Lanciego et al., 2012). The basal ganglia (BG) include the dorsal STR, the globus pallidus (GP) interna and externa, the SNc, the substantia nigra pars reticulata (SNr), the thalamus (TH), and the subthalamic nuclei (STN). The dorsal STR receives excitatory glutamatergic (Glu) inputs from the cortex, while projection neurons from the SN and GP to the TH use inhibitory γ-aminobutyric acid (GABA) neurotransmitters. To close the loop, the motor cortex receives back excitatory Glu projections from the TH. Consequently, inhibition of the TH therefore leads to inhibition of the motor activation. Within the BG, the direct pathway is composed of monosynaptic connections from the dorsal STR to the GP interna, whereas the indirect pathway is composed of polysynaptic connections from the dorsal STR to the GP externa, STN, and to the GP interna. The hyperdirect pathway projects cortical neurons directly to the STN. Coming from the SNc, DA excites or inhibits GABAergic medium spiny neurons via D_1 or D_2 receptors in the STR, respectively. Those structures and neurotransmitters have been the targets for neuroimaging methods developments.

Neuroinflammation also characterizes PD and includes microglial activation, astrocyte proliferation, lymphocyte infiltration, and the presence of proinflammatory cytokines (Glass et al., 2010). Whether inflammation is a cause or consequence of neurodegeneration in PD is still under debate (de Lau and Breteler, 2006; Glass et al., 2010; Tansey and Goldberg, 2010; Cabezudo et al., 2020). Likewise, the protective or deleterious role of inflammation in PD is still unknown (Sofroniew, 2015).

Non-invasive imaging tools have the potential to add critical value for earlier diagnosis and therefore for the development of more efficient treatments against the disease. In this regard, Magnetic Resonance Imaging (MRI) plays a crucial role in the diagnosis and monitoring of disease progression and treatment in both humans and animal models. Neurodegeneration has been evaluated in the SN and nigrostriatal fibers in PD patients using MRI. Changes in diffusion metrics have been reported in the SN of patients [decreased anisotropy and increased mean diffusivity (MD)] and spreading to other gray and white matter regions and tracts, indicating expended loss of microstructural integrity (see review by Weingarten et al., 2015). Likewise, changes in the functional properties of these structures can be detected with resting-state functional MRI (rs-fMRI) (see review by Lehéricy et al., 2012). Reduced functional connectivity (FC) in the SN and in corticostriatal networks was also reported in patients (Helmich et al., 2010; Sharman et al., 2012).

Abnormal iron accumulation in specific brain regions has been observed in several neurodegenerative diseases including PD. Up to 35% increase in the SNc of PD patients has been reported (Dexter et al., 1989; Hirsch et al., 1991). As T_2- and T_2*-weighted imaging are sensitive to the presence of paramagnetic iron, they have been used to evaluate iron deposits in the SN (Lehéricy et al., 2014; see review by Pietracupa et al., 2017). Decreased T_2 values have been measured in the caudate nucleus, putamen, and SN of PD patients (Antonini et al., 1993). Increased nigral transverse relaxation rates R_2^* ($1/T_2^*$) have been reported in PD patients and correlated with disease progression (Ulla et al., 2013; Hopes et al., 2016).

Metabolism alterations in PD patients have been investigated with MR spectroscopy (MRS). While N-acetyl-aspartate (NAA) is a marker of neuronal integrity, myo-inositol (mIns) is a marker of gliosis, and creatine (Cre) is a marker of energy metabolism. Changes in neurotransmitters levels can also inform on the pathological state. For instance, decreased levels of NAA have been reported in the cortex and SN, whereas increased GABA and Glu levels have been found in the pons, putamen, and SN of PD patients (Emir et al., 2012; Levin et al., 2012; Graff-Radford et al., 2014; Gröger et al., 2014).

Animal models have been widely used to improve our understanding of PD features with anatomical, functional, and metabolic MR-based tools. Toxic models based on intracerebral or systemic injections of neurotoxins produce nigrostriatal lesions that replicate many of PD features (see the review by Blandini and Armentero, 2012). The most used models of neurodegeneration are based on injections of the 6-hydroxydopamine (6-OHDA) and the 1-methyl-4-phenyl-1,2,3,6-tetrahydropyridine (MPTP) neurotoxins to produce degeneration of DA neurons in the SN and subsequently of the entire nigrostriatal pathway (Yuan et al., 2005). Although those models are partial models and more acute than the progressive human pathology, they have been extremely useful in mimicking many of PD features accompanied by motor symptoms. Alternatively, genetic-based animal models of PD allow the investigation of the prodromal stage of the disease during the presymptomatic period, as well as the study of specific pathways related to genetic and biochemical alterations (see reviews by Chesselet et al., 2008; Creed and Goldberg, 2018 and by Dawson et al., 2010).

This review aims at giving an overview of how the physiopathological features of PD have been investigated using the most represented MR methods in animal models. It is based on PubMed searches within the last 10 years, and it is limited to rodent models of PD as they have been the most widely used and for their potential in genetic studies. It was elaborated based on a physiopathological perspective to demonstrate how various imaging approaches have been used to investigate PD physiopathology in animals. Rodent models are first described, including toxin-based and genetic-based models. Then structural and functional MR methods are detailed, such as diffusion and rs-fMRI to evaluate neurodegeneration, followed by T_2* and susceptibility imaging to evaluate iron accumulation and MRS to evaluate metabolism changes. Future directions for preclinical MR developments are suggested and include strategies for neuroinflammation and neuromelanin evaluations.

RODENT MODELS

Toxin-Based Models

The 6-OHDA Model

Following the discovery that 6-OHDA could produce selective degeneration of sympathetic adrenergic nerves (Thoenen and Tranzer, 1968), this neurotoxin has been used as a denervation

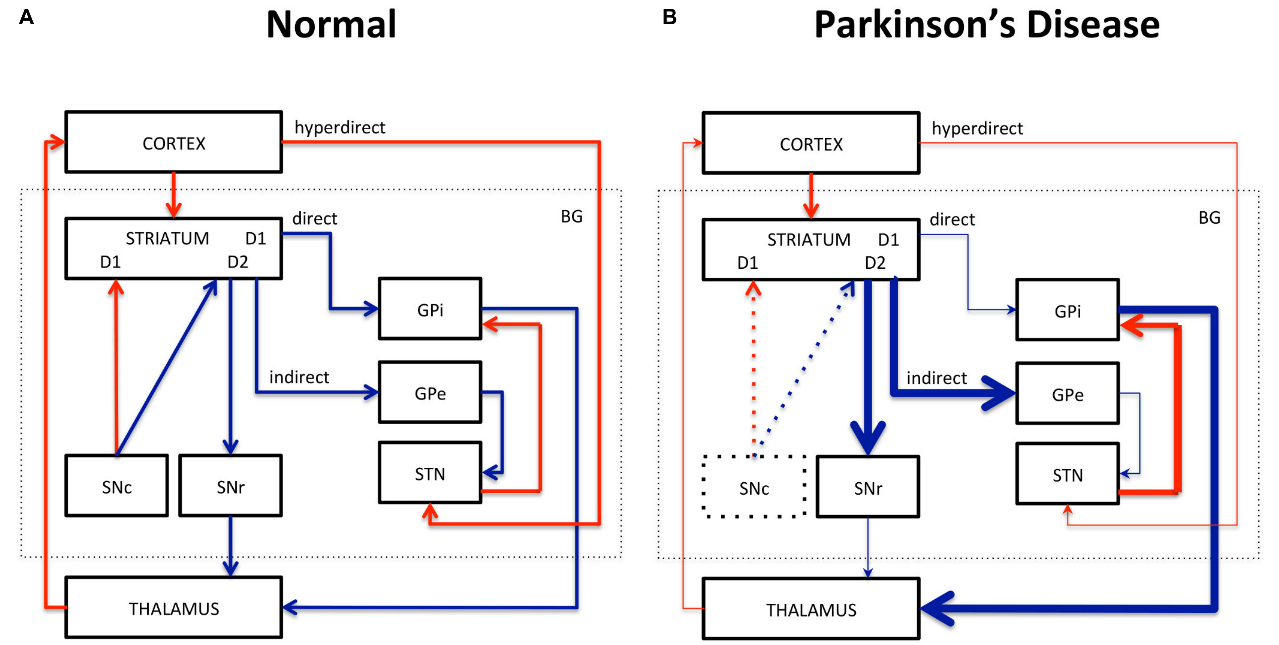

FIGURE 1 | Schematic representation of the corticobasal ganglia–thalamocortical motor pathway model. **(A)** Normal pathway. **(B)** PD pathway. Red arrows correspond to glutamatergic excitatory projection neurons. Blue arrows correspond to GABAergic inhibitory projection neurons. D_1, D_2: striatal receptors. SNc, subtantia nigra pars compacta; SNr, subtantia nigra pars reticulata; STN, subthalamic nucleus; GPi, globus pallidus interna; GPe, globus pallidus externa; BG, basal ganglia. The direct (STR/GPi/TH), indirect (STR/GPe/STN/GPi/TH), and hyperdirect (cortex/STN) pathways are represented. Thick lines represent increased excitation/inhibition. Thin lines represent decreased excitation/inhibition. Dotted lines represent DA neuronal loss in the SNc.

tool in animals (Ungerstedt, 1968; Jonsson, 1980). As a hydroxylated analog of DA, 6-OHDA enters DA neurons through DA transporters. Once in the cytosol, it forms hydrogen peroxide by auto-oxidation reaction. As 6-OHDA does not cross the blood-brain barrier (BBB), it is necessary to administer it directly into the brain with stereotaxic injections. As bilateral injections cause high mortality rates, unilateral injections have been preferred. The mechanism of action varies depending on the injection site along the nigrostriatal pathway. Injections into the SNc or into the medial forebrain bundle (MFB) produce massive and rapid anterograde degeneration of the nigral DA neurons, up to 90%–100% of SN and striatal neurons, and subsequently of the entire nigrostriatal pathway within days. Alternatively, injections into the dorsal STR induce partial lesions of the nigral DA neurons, up to 50%–70% loss within 4 to 6 weeks, which leads to progressive retrograde degeneration of the nigrostriatal pathway more closely mimicking human pathology and allowing longitudinal evaluations (Berger et al., 1991; Przedborski et al., 1995; Shimohama et al., 2003). In the STR, greater than 90% loss of DA can be reached after intrastriatal infusion of 6-OHDA in mice (Xiao et al., 2011).

The MPTP Model

The selective toxicity of MPTP for the nigrostriatal tract was first described by Langston et al. (1983). MPTP is converted to 1-methyl-4-phenylpyridinium ion (MPP^+) and accumulates in the SNc neurons via DA transporters. As MPTP can cross the BBB, it can be injected via the peripheral system. However, systemic MPTP administration fails in rats as the conversion from MPTP to MPP^+ occurs at the BBB preventing influx into the brain (Giovanni et al., 1994; Pienaar et al., 2010; Jagmag et al., 2016; Konnova and Swanberg, 2018); it is therefore alternatively used in mice (Mori et al., 1988). Repeated intraperitoneal injections in mice cause rapid and massive DA neuron loss, which leads to similar symptoms as those found in patients such as akinesia, rigidity, and episodes of tremor (Jackson-Lewis et al., 1995; Tatton and Kish, 1997).

Genetic-Based Models

Autosomal-Dominant Models

The most common mutations in autosomal-dominant PD are the *LRRK2* mutations (Zimprich et al., 2004). This kinase enzyme is normally present in membranes and plays a role in mitochondria, autophagy, and endocytosis (Winklhofer and Haass, 2010; Berwick et al., 2019). Transgenic mice present little to no DA neurodegeneration; however, most of them have abnormalities in the nigrostriatal system, α-synuclein aggregation, or impaired DA release (Li et al., 2009; Jagmag et al., 2016). Likewise, *LRRK2* mutated rats do not show any DA neurodegeneration in the SN but rather behavioral alterations (Daher et al., 2014; Walker et al., 2014; Lee et al., 2015; Shaikh et al., 2015; Sloan et al., 2016).

The *SNCA* gene codes for the presynaptic α-synuclein protein, which is abundantly found in the brain (Maroteaux et al., 1988). Its function is not fully understood; however, it is believed to play a role in synaptic vesicle function, hence of neurotransmitter release (Kahle et al., 2002). Overexpression of α-synuclein produces heterogeneous phenotypes in mice, depending on the promoters used for transgene expression.

Although they lack DA degeneration, some of them present nigrostriatal dysfunctions (Abeliovich et al., 2000; Fleming et al., 2005; Chesselet et al., 2008).

Autosomal–Recessive Models

The *Parkin* (*PARK2*) gene is involved in the ubiquitin proteasome system as an E3 ubiquitin ligase, and mutations of this gene cause loss of function in patients. *Parkin* knockout does not seem to induce nigrostriatal or DA lesions in mice (Perez and Palmiter, 2005). However, overexpression of a mutated form of this gene leads to nigral DA cell depletion, striatal synaptic loss, and decreased striatal DA levels in mice (Lu et al., 2009). Likewise, overexpression of *Parkin* induces mild neurodegeneration in rats (Van Rompuy et al., 2014).

PINK1 is a mitochondrial protein kinase that protects neurons from mitochondrial dysfunction stress. The *PINK1* mutation leads to loss of function mainly affecting the kinase domain in patients (Klein and Westenberger, 2012). *PINK1* knockout does not produce any DA neuronal depletion in mice, but it alters DA neurotransmission and mitochondrial function (Kitada et al., 2007; Gautier et al., 2008; Gispert et al., 2009). In contrast, *PINK1* knockout rats have SN DA neuronal loss, α-synuclein accumulation, mitochondrial defects, and motor dysfunction (Dave et al., 2014; Villeneuve et al., 2016).

DJ-1 is a ThiJ/Pgpl molecular chaperone encoded by the *PARK7* gene and widely expressed in the body. *DJ-1* knockout mice do not exhibit any DA depletion but show some nigrostriatal and mitochondrial abnormalities (Goldberg et al., 2005; Kim et al., 2005; Andres-Mateos et al., 2007).

Other Models

A conditional knockout mouse model with respiratory chain-deficient DA neurons was created in 2007 and named MitoPark mice (Ekstrand et al., 2007). This model is based on the inactivation of the mitochondrial transcription factor A (*Tfam*) gene in DA neurons. Among the different genetic models, those mice present the most PD-like phenotypes including DA cell death, intraneuronal inclusions, and progressive motor dysfunction.

MR METHODS FOR NEURODEGENERATION EVALUATION

Diffusion Imaging

In an unrestricted medium, water molecules undergo random Brownian motion and diffuse freely. Its motion can be hindered by membranes, extracellular hindrance, or tissue heterogeneity. Diffusion-weighted imaging is sensitive to water diffusion through the application of diffusion gradients (Le Bihan, 2003). In the white matter, where fiber bundles constitute physical constraints, water molecules diffuse along a preferred direction along the fibers, which is referred to as anisotropy. The diffusion tensor model, a model of the displacement of water molecules, can provide indices such as the MD, characterizing the overall displacement of water molecules; the fractional anisotropy (FA), characterizing the orientation of diffusion; and the eigenvalues, characterizing the main directions of diffusivities, also derived as axial and radial diffusivities (AD, RD). Although the cellular origin of anisotropy is multifactorial and remains unclear (Chabert and Scifo, 2007), it has been shown that AD changes can be used as an index of axonal damage, whereas RD can be used as an index of myelin damage (Song et al., 2005). In highly oriented fiber bundles, FA is high (close to 1), whereas in regions of crossing fibers, it is low (close to 0).

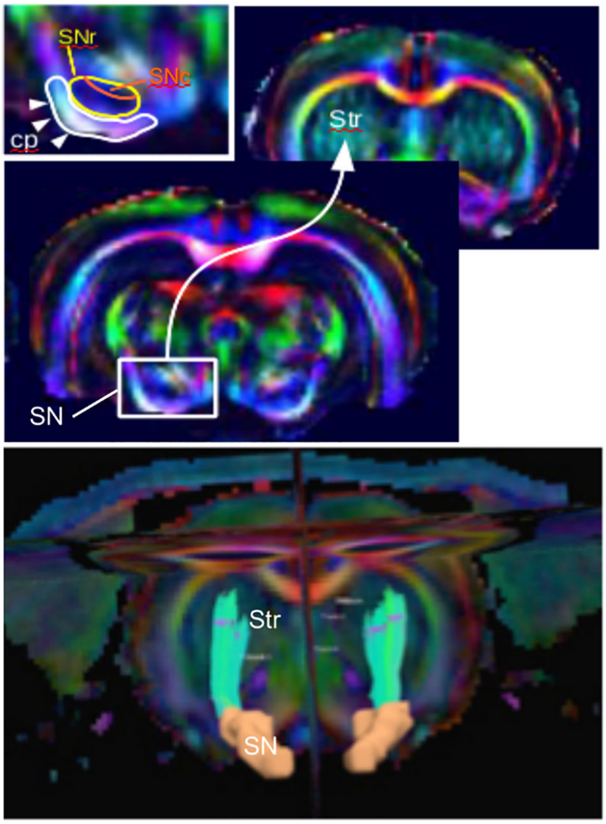

FIGURE 2 | The nigrostriatal pathway illustrated with color-coded diffusion tensor images of a rat brain (coronal views). **(Top)** Zoom into the subtantia nigra (SN) projection to the striatum (Str) and inlet showing the detailed structure with the cerebral peduncle (cp), the SN reticulata (SNr), and the SN compacta (SNc). **(Bottom)** Three-dimensional reconstructed nigrostriatal tract (green) from the SN (orange) to the dorsal Str using diffusion-based tractography.

Diffusion imaging has been used to evaluate microstructural changes in rodents. The SN can be sufficiently resolved from those images, and the nigrostriatal tract can clearly be identified and reconstructed (**Figure 2**). Following MFB injections of 6-OHDA in rats, Monnot et al. (2017) reported decreased FA and increased RD in the ipsilateral SNc and SNr. Those results were supported by a previous study by Soria et al. (2011), which showed bilateral changes in the SN in the same model targeting the MFB. They showed that FA was decreased in the ipsilateral SNr, AD was bilaterally decreased in the SNr, and RD was bilaterally increased in the cortex (Soria et al., 2011). Furthermore, those results were consistent with neurodegeneration and with human findings (Vaillancourt et al., 2009; Rolheiser et al., 2011;

Skorpil et al., 2012; Cochrane and Ebmeier, 2013; Schwarz et al., 2013). In contrast, they were in disagreement with a previous study by Van Camp et al. (2009), which found increased FA in the ipsilateral SN of 6-OHDA rats injected in the STR. This FA increase was attributed to neuroinflammation, but the discrepancy with the other studies might also be due to differences in the injection site (MFB vs. STR). A more recent study by Perlbarg et al. (2018) demonstrated increased FA in the ipsilateral and contralateral STR of 6-OHDA rats who received intrastriatal injections (Perlbarg et al., 2018). This result was consistent with neurodegeneration in a crossing-fiber structure. Indeed, regions of crossing fibers such as the STR have lower FA than regions of linearly oriented fibers such as corpus callosum (CC). Therefore, the selective degeneration of a group of fibers crossing other populations of fibers leads to increase of FA (Winston, 2012). Additionally, they found increased MD in the ipsilateral STR indicating loss of microstructural integrity and in line with human findings. However, in this study, no changes in the SN could be detected presumably because of a lack of sensitivity.

In genetic-based models, neuroimaging studies showed decreased MD, AD, and RD in regions of known α-synuclein accumulation such as the SN, STR, sensorimotor cortex (SM), and TH in α-synuclein transgenic mice (Supplementary data, Khairnar et al., 2015). Those results could be explained by the presumable decrease of free water diffusion caused by the protein aggregation. In a presymptomatic *PINK1* knockout rat model, altered diffusion metrics [reduced anisotropy and apparent diffusion coefficient (ADC)] were observed in the BG and other regions (e.g., hippocampus, brainstem, and cerebellum) (Cai et al., 2019). Those widespread changes throughout the brain have also been described in PD patients (Braak et al., 2004). In the MitoPark mouse model, decreased FA has been measured in the SN and CC, indicating neuronal and fiber degeneration (Cong et al., 2016).

Functional Imaging

Functional connectivity or "synchrony" between and within brain regions refers to temporal correlations between spatially remote neurophysiological events, as measured by fMRI blood oxygenation level-dependent (BOLD) signal (Friston et al., 1993). Using fMRI, low-frequency, spontaneous, and, in some cases, coherent signal fluctuations may be detected in the resting brain (Biswal et al., 1995). Rs-fMRI studies have thus revealed co-activation in distributed networks of cortical and subcortical regions that characterize functional brain networks. Such connectivity may or may not also involve a structural connection (Honey et al., 2009). Most of PD imaging in patients and in animal models has been conducted in the resting state.

Functional connectivity changes have been explored in the nigrostriatal pathway in animal models. Decreased FC was found in the interhemispheric STR and in the ipsilateral cortices of 6-OHDA rats (Monnot et al., 2017; Westphal et al., 2017). Those animals were injected in the MFB and anesthetized with either a mixture of isoflurane and medetomidine (former study) or with medetomidine alone (latter study) during imaging. Likewise, decreased FC between the ipsilateral primary motor cortex (M1) and contralateral TH was reported in the intrastriatal 6-OHDA model using isoflurane alone (Perlbarg et al., 2018). Zhurakovskaya et al. (2019) also reported decreased FC in corticocortical and striatocortical connections of 6-OHDA-injected rats under urethane anesthesia (Zhurakovskaya et al., 2019). Decreased FC is commonly interpreted as direct lesioning effects.

Increased FC was found between the STR and the SM and in the TH of both hemispheres in 6-OHDA rats injected in the MFB (Monnot et al., 2017; Westphal et al., 2017). Similarly, increased FC was found between the ipsilateral STR and the GP, the contralateral M1 and the GP, and the interhemispheric STR and the GP of 6-OHDA rats injected in the STR (Perlbarg et al., 2018). **Figure 3** illustrates the FC maps from the lesioned STR to the rest of the brain in this study and highlights the (non-significant) increased FC between the ipsilateral and contralateral STR in the 6-OHDA group compared to the sham-operated group 3 weeks after lesioning. Increased FC is generally attributed to compensatory effects and reorganization, like it has been observed in PD patients (Helmich et al., 2010; Sharman et al., 2012).

In a presymptomatic *PINK1* knockout rat model, Cai et al. (2019) observed changes in rs-fMRI connectivity in the BG and other regions such as the amygdala, cortex, septum, and pons. They measured decreased connectivity between the TH and STR, whereas the cerebellar nuclei showed increased connectivity within the cerebellum and hippocampus in *PINK1* rats under isoflurane anesthesia. Based on their findings, they suggested a reorganization of connectivity pathways in PINK1 mice, in which the STR to TH connection would be rerouted from the STR to the hippocampus also showing increased connectivity from the cerebellum. They argued on the role of the cerebellum in PD pathology similar to the cerebellar hyperconnectivity found in PD patients (Cerasa et al., 2016; Tuovinen et al., 2018).

MR METHODS FOR IRON ACCUMULATION EVALUATION

T_2* Imaging

It has been shown that iron accumulates in the SN of MPTP and 6-OHDA-lesioned animals (Wang et al., 2004; Hare et al., 2009; Jiang et al., 2010; Lv et al., 2011). Iron deposits can be detected with conventional T_2* imaging. For example, Olmedo et al. (2017) quantified hyposignal levels in the SN of 6-OHDA rats 1 and 4 weeks postinjection in the MFB. They reported significantly increased hypointense pixels (i.e., decreased T_2* signal) in 6-OHDA rats compared to sham rats, which correlated to iron staining with Prussian blue at 4 weeks. Furthermore, Virel et al. (2014) evidenced iron accumulation in the STR of 6-OHDA rats following intrastriatal injections. In this study, they measured increased T_2* hypointensities (i.e., decreased T_2* signal) in the ipsilateral STR as early as 1 week postlesioning and persisting up to 4 weeks. They also showed correlations of those hypointensities with edematous hyperintensities and with iron accumulation revealed with Prussian blue staining at 4 weeks only. In contrast, the SN remained intact, presumably due to milder and delayed depletion in this structure at this later timepoint.

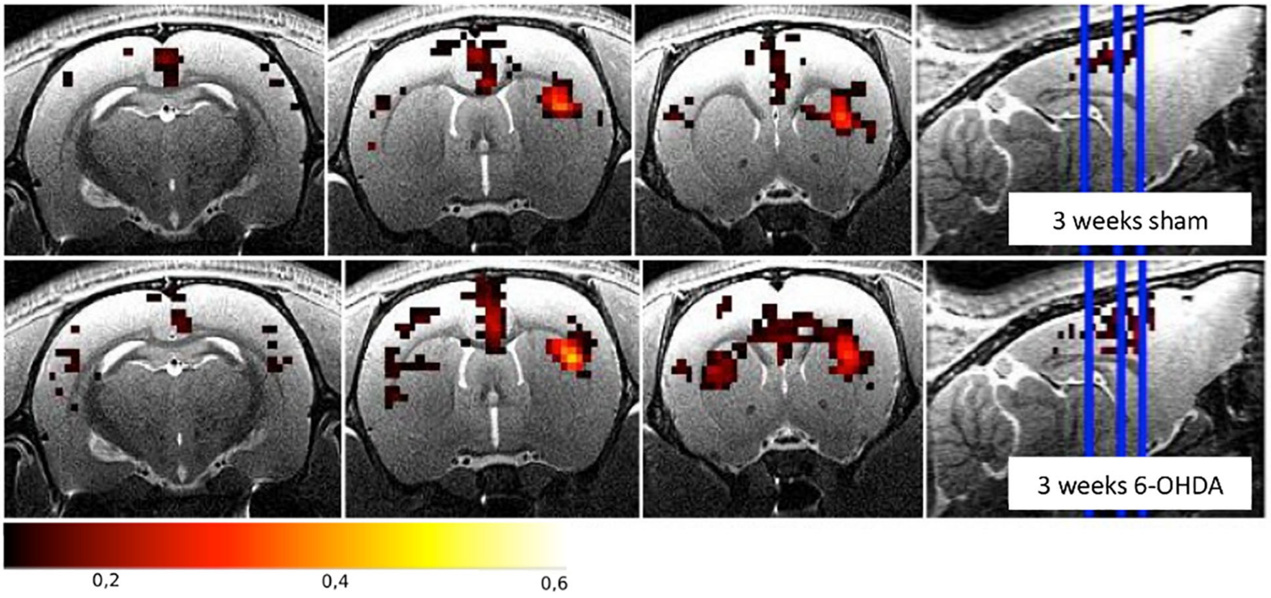

FIGURE 3 | Functional connectivity maps from the right striatum for the sham-operated and the 6-OHDA groups at 3 weeks postinjection in the right hemisphere (i.e., on the right side of the brain on the images). The 6-OHDA group shows a non-significant increase of FC between the left and right striatum. Maps are expressed as correlation coefficient *R*. See Perlbarg et al. (2018) for the full study description.

Decreased T_2* in the SN and STR has also been found in the MitoPark mouse model and was presumably attributed to iron accumulation in the SN as it is a shared feature with PD patients.

Susceptibility Imaging

Other iron-sensitive MRI methods include susceptibility-weighted imaging (SWI) and quantitative susceptibility mapping (QSM), both of which have been used to improve imaging of the SN nigrosomes, STN, and GP interna (Lotfipour et al., 2012; Liu et al., 2013; Schwarz et al., 2014). In SWI methods, the phase data are used to detect susceptibility differences between tissues and are combined to the magnitude data to improve image contrast (Haacke et al., 2004). Increased iron accumulation in PD patients has been measured in deep gray nuclei using SWI (Zhang et al., 2009, 2010; Jin et al., 2011; Wu et al., 2014; Guan et al., 2016; Hopes et al., 2016). QSM is a more recent technique that converts the phase shifts to localize magnetic susceptibility (Haacke et al., 2015). Very little literature is available in PD rodent models applications; nevertheless, increased QSM has been reported in the SN of an MPTP mouse model (Guan and Feng, 2018). This study also evidenced that QSM was a more accurate method than R_2* to detect iron-related changes in the SN, which was supported by a study including PD patients (Hopes et al., 2016). Further improvements of QSM methods have been developed for imaging the mouse brain microstructure at a very high resolution, such that striatal tracts can be reconstructed at 20-μm resolution based on QSM images from postmortem brains (Wei et al., 2016). It has therefore the potential to be used in PD models applications.

MR SPECTROSCOPY FOR METABOLISM EVALUATION

Magnetic resonance spectroscopy is based on the chemical shift and the spin–spin coupling effects. Different nuclei possess different resonant frequencies depending on their chemical environment and local magnetic fields. Their chemical shift is expressed in parts per million (ppm) relative to the standard reference compound tetramethylsilane (Barker et al., 2010).

Magnetic resonance spectroscopy has been used to assess brain metabolic changes in PD models. For example, increased GABA levels have been measured in the STR of MPTP mice and of 6-OHDA rats injected in the MFB (Chassain et al., 2010; Coune et al., 2013). Those results were consistent with human data in which increased GABA levels were found in the pons, putamen, and in the SN of patients (Emir et al., 2012; Gröger et al., 2014). Those findings could be explained by the following mechanism: the STR receives DA projections from the SNc, and knowing that DA inhibits GABAergic spiny neurons via D_2 receptors in the STR, DA denervation should lead to hyperactivation of those neurons (Gerfen, 1992).

Likewise, Glu and glutamine (Gln) levels were found to increase in the STR of MPTP mice (Chassain et al., 2010), consistent with increased Glu in the SN of PD patients (Gröger et al., 2014). In their article, Chassain et al. (2010) explain that this Glu increase inducing changes in the corticostriatal activity is "related to an increased synthesis and release of Glu in the synaptic terminal of the STR." In contrast, decreased Glu levels were measured in the STR of 6-OHDA rats injected in the MFB (Coune et al., 2013).

Decreased NAA levels were found in the ipsilateral STR and in the cortex of 6-OHDA rats injected in the MFB and SN, respectively (Hou et al., 2010; Coune et al., 2013), consistent with neuronal loss also reported in PD patients (Levin et al., 2012; Graff-Radford et al., 2014). However, no changes in NAA levels were found in an MPTP mouse model (Chassain et al., 2010).

Viral vector-based α-synuclein rodent models can be used as an alternative to transgenic models to produce α-synuclein accumulation and subsequent DA cell loss. Intranigral injections of an adeno-associated viral vector coding for human α-synuclein resulted in increased GABA levels in the STR as measured by MRS in rats (Coune et al., 2013). This finding was also reported in a 6-OHDA rat model by the same group and was consistent with MRS data in patients (Emir et al., 2012; Gröger et al., 2014). Furthermore, decreased NAA levels were measured in the SN of rats following intranigral injections. This finding was consistent with nigral cell loss induced in the model and with NAA decrease also found in patients (Clarke and Lowry, 2001; Öz et al., 2006).

Metabolic changes have also been observed in *PINK1* knockout rats using MRS. Villeneuve et al. (2016) found decreased taurine and Cre in the STR of *PINK1* rats. Similarly, decreased taurine and increased Gln were reported in the STR in the same model by Ren et al. (2019). Decreased taurine has been found in patients (Engelborghs et al., 2003) and is associated with mitochondrial function (Hansen et al., 2010). Increased Gln could be attributed to Glu dysregulation as found in the STR of patients (Gardoni and Bellone, 2015).

SUGGESTED FUTURE DIRECTIONS

Evaluation of Neuroinflammation

Inflammation is common to many brain diseases as it has been shown to contribute to neurodegeneration (Ransohoff, 2016). To improve our understanding of the role of inflammation in the etiology of PD, lipopolysaccharide (LPS) animal models have been developed.

LPS Animal Model

The endotoxin LPS is a large molecule found in the outer membrane of Gram-negative bacteria. It binds the CD14/TLR4/MD2 (cluster of differentiation 14/Toll-like receptor 4/myeloid differentiation factor 2) receptor complex, which triggers the activation of proinflammatory pathways and ultimately the activation of microglia (Park and Lee, 2013).

Lipopolysaccharide can be injected in the central or peripheral nervous system to generate various inflammatory responses associated with neurodegeneration (see review by Batista et al., 2019). To induce Parkinson-like features, LPS is injected in the SN or STR, leading to DA degeneration and motor dysfunction in rats (Castano et al., 1998), as well as to macrophage and microglia reactions (Herrera et al., 2000; Gao et al., 2002). Likewise, systemic LPS injections in mice cause microglial activation, progressive loss of nigral DA neurons, and locomotor deficits (Qin et al., 2007).

Lipopolysaccharide models can also be used to assess mitochondrial dysfunction and their contribution to PD pathophysiology. For example, intrastriatal injections of LPS lead to energy dysfunction and neuronal loss in the STR (Hunter et al., 2017). Furthermore, LPS injections can change iron and ferritin levels in nigral glial cells of rats associated with decreased tyrosine hydroxylase staining in the GP and STR (Zhang et al., 2005; Hunter et al., 2008). Interestingly, transgenic mice overexpressing α-synuclein and injected with LPS show increased protein aggregation, chronic nigral DA neuronal loss, and nigral inflammation compared to wild-type mice, suggesting a potentiation role of inflammation on α-synuclein dysfunction (Gao et al., 2011).

In their review, Belloli et al. (2020) give an overview of neuroinflammation imaging markers in PD. Based on the work by Ostrerova-Golts et al. (2000), which provides further data that support the role of toxic iron in α-synuclein aggregation (Ostrerova-Golts et al., 2000), the authors suggest a link between iron concentration and neuroinflammation (Belloli et al., 2020). As SWI can measure iron accumulation, it can therefore be used to assess iron-driven neuroinflammation.

Overall, the use of animal models with LPS-induced inflammation can help our understanding of the neuroinflammatory component of PD. To date, no MRI studies have been conducted on LPS rodent models of PD, which opens new paths to the field. Combined MR methods have the potential to investigate both inflammation and neurodegeneration and to help better define the role of inflammation in the pathophysiology of PD.

Diffusion MR Spectroscopy of Metabolites

Among other complex mechanisms, inflammation involves glial cells activation, and it participates both to the clearance of damaged tissue and to tissue repair. Whether astrocytes play a protective role against inflammation or triggers it is still unknown and constitutes the topic of much ongoing research (Sofroniew, 2015). As brain metabolites are present in specific cell types, they can provide cell-specific markers. For instance, increased levels of choline (Cho) and mIns have been attributed to inflammation and gliosis, respectively (Öz et al., 2014). However, while metabolite concentration changes derived from conventional MRS cannot be attributed to specific pathological mechanisms, diffusion-weighted MRS can probe microstructural changes, such as glial cell swelling upon activation (Palombo et al., 2018). This emerging technique is based on the diffusion properties of metabolites within the intracellular space. For instance, metabolites in hypertrophic cells have more space to diffuse, which should increase their ADC—derived from multiple diffusion spectroscopy experiments.

The diffusivities of Cho and mIns have been proposed as specific markers of cellular hypertrophy triggered during glial activation (Ercan et al., 2016; Ligneul et al., 2019). Ligneul et al. (2019) used a cytokine ciliary neurotrophic factor-induced mouse model in which only hypertrophic reactive astrocytes were detected, whereas neuronal death and microglia were absent. They evidenced that the diffusivity of mIns was the most sensitive and specific marker of astrocytes morphological modulations in those mice.

Evaluation of Neuromelanin

Neuromelanin is the intracellular pigmentation present in nigral DA neurons. While its accumulation in the SN during aging is normal, it is known that its deposition beyond a certain threshold and its specific degeneration can be a marker of the disease (Vila, 2019; Vila et al., 2019). Imaging methods sensitive to neuromelanin have been developed in humans including first spin echo T_1-weighted MRI (Sasaki et al., 2006), and then magnetization transfer MRI after the magnetization transfer effect was found to be responsible for the neuromelanin contrast (Ogisu et al., 2013; Langley et al., 2015). The combination of multicontrast MRI such as SWI and magnetization transfer for iron (found in large amounts in the SNr) and neuromelanin

TABLE 1 | Summary of the MRI/MRS measure changes with the corresponding rodent models.

	Method	Measure	Alterations	Model
Neurodegeneration	Diffusion	FA	Decreased in ipsilateral SN[1]	6-OHDA in MFB
			Decreased in bilateral SN[2]	6-OHDA in MFB
			Decreased in basal ganglia and all regions[3]	Tg PINK1
			Decreased in SN and CC[4]	Tg MitoPark
			Increased in ipsilateral SN[5]	6-OHDA in STR
			Increased in bilateral STR[6]	6-OHDA in STR
		MD	Increased in ipsilateral SN[1]	6-OHDA in MFB
			Increased in bilateral SN[2]	6-OHDA in MFB
			Increased in ipsilateral STR[6]	6-OHDA in STR
			Decreased in SN, STR, SM, TH[7]	Tg α-synuclein
		AD	Decreased in bilateral SN[2]	6-OHDA in MFB
			Decreased in basal ganglia and more regions[3]	Tg PINK1
			Decreased in SN, STR, SmCx, TH[7]	Tg α-synuclein
		RD	Increased in bilateral cortex[2]	6-OHDA in MFB
			Decreased in basal ganglia and more regions[3]	Tg PINK1
			Decreased in STR, Hc, TH[7]	Tg α-synuclein
	rs-fMRI	FC	Decreased in interhemispheric STR[1]	6-OHDA in MFB
			Decreased in ipsilateral cortices[8]	6-OHDA in MFB
			Decreased between ipsilateral M1/contralateral TH[6]	6-OHDA in STR
			Decreased between TH and STR[3]	Tg PINK1
			Decreased corticocortical and striatocortical connections[9]	6-OHDA in STR
			Increased between ipsilateral STR/bilateral SM[1]	6-OHDA in MFB
			Increased in bilateral TH[8]	6-OHDA in MFB
			Increased between ipsilateral STR/GP, contralateral M1/GP, interhemispheric STR/GP[6]	6-OHDA in STR
			Increased between cerebellar nuclei[3]	Tg PINK1
Iron	T_2*	Signal intensity T_2*	Decreased in ipsilateral SN[10]	6-OHDA in MFB
			Decreased in ipsilateral STR[11]	6-OHDA in STR
			Decreased in SN, STR[4]	Tg MitoPark
	QSM	QSM	Increased QSM in SN[12]	MPTP
Metabolism	MRS	GABA	Increased in ipsilateral STR[13]	MPTP
			Increased in ipsilateral STR[14]	6-OHDA in MFB
			Increased in ipsilateral STR[15]	AAV α-synuclein
		Glu	Increased in ipsilateral STR[13]	MPTP
			Decreased in ipsilateral STR[13]	6-OHDA in MFB
		Gln	Increased in STR[13]	MPTP
			Increased in STR[16]	Tg PINK1
		NAA	Decreased in ipsilateral STR[14]	6-OHDA in MFB
			Decreased in cortex[15]	6-OHDA in SN
			No change[13]	MPTP

Rs-fMRI, resting-state functional MRI; MRS, magnetic resonance spectroscopy; FA, fractional anisotropy; MD, mean diffusivity; AD, axial diffusivity; RD, radial diffusivity; FC, functional connectivity; GABA, γ-aminobutyric acid; Glu, glutamate; Gln, glutamine; SN, substantia nigra; STR, striatum; M1, primary motor cortex; TH, thalamus; GP, globus pallidus; MFB, medial forebrain bundle; SM, sensorimotor cortex; Hc, hippocampus; CC, corpus callosum; Tg, transgenic; AAV, adenoviral vector. [1]Monnot et al., 2017; [2]Soria et al., 2011; [3]Cai et al., 2019; [4]Cong et al., 2016; [5]Van Camp et al., 2009; [6]Perlbarg et al., 2018; [7]Khairnar et al., 2015; [8]Westphal et al., 2017; [9]Zhurakovskaya et al., 2019; [10]Olmedo et al., 2017; [11]Virel et al., 2014; [12]Guan and Feng, 2018; [13]Chassain et al., 2010; [14]Coune et al., 2013; [15]Hou et al., 2010; [16]Ren et al., 2019.

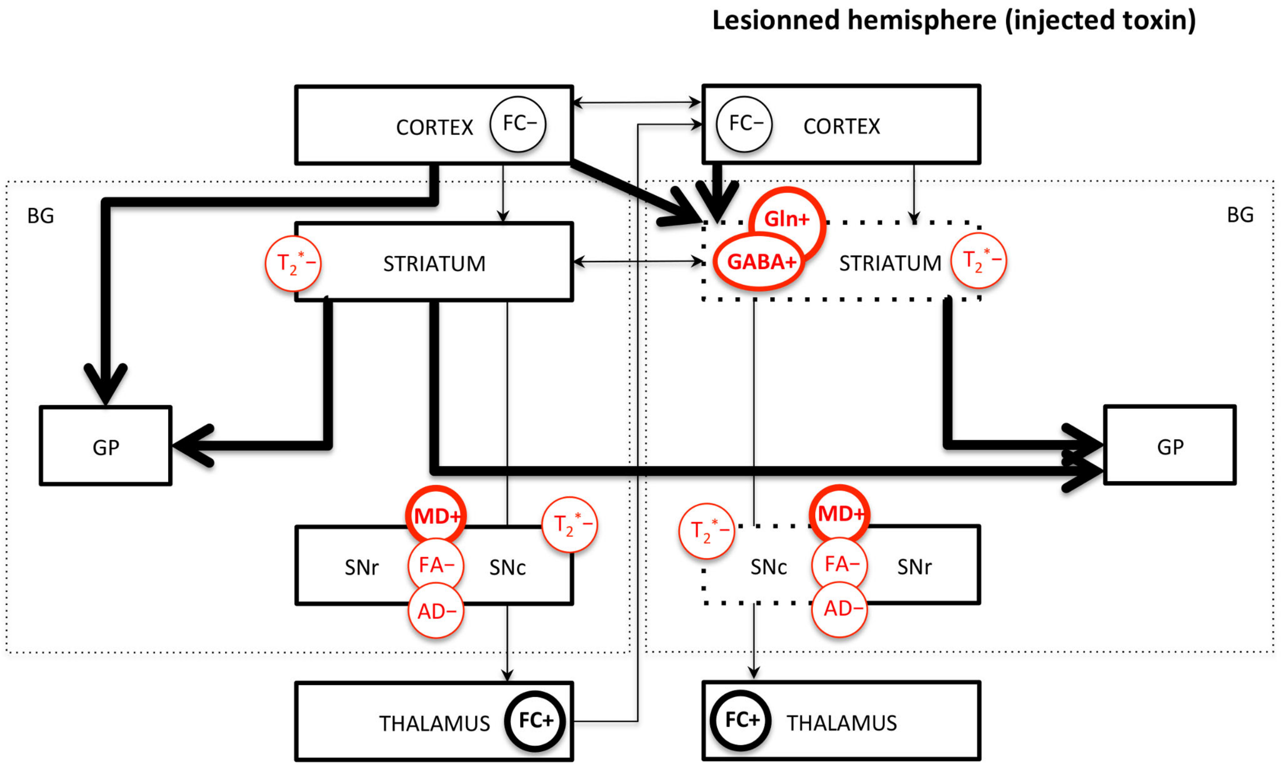

FIGURE 4 | Main MRI/MRS findings in PD rodents affecting the basal ganglia pathways. FC, functional connectivity; MD, mean diffusivity; FA, fractional anisotropy; AD, axial diffusivity; GABA, γ-aminobutyric acid; Gln, glutamine; T_2^*, effective transverse relaxation time. "+" means increase and "-" means decrease of the MR measure. Measures indicated in red are commonly found across studies. Thick/thin lines represent increased/decreased measure. Arrows represent FC changes between structures. For toxic models, the dotted lines represent the lesioned structures; the left/right side of the figure represents the intact/lesioned hemispheres.

(found in the SNc) detection, respectively, has been used to improve the delineation of the SN structures (Langley et al., 2015). Furthermore, diffusion-based tractography can add critical information on structural connections within the BG to better segregate the SNr from the SNc (Menke et al., 2010).

Multicontrast imaging can more easily be performed in anesthetized animals than in humans as scan time is less limited. In addition, the use of ultrahigh magnetic fields can drastically improve the visualization of the SN through increased signal-to-noise ratio (therefore resolution) and increased contrast, as reviewed in Lehéricy et al. (2014). It is therefore expected that the use of 11.7 T and 17 T scanners in rodents should be highly beneficial for better visualizing the details of the SN anatomy.

While neuromelanin is present in the human SNc, its absence in rodents (Marsden, 1961; Barden and Levine, 1983) prevents any investigation in those models. The group of M. Vila recently developed a rat model in which an adeno-associated viral vector expressing human tyrosinase is stereotaxically injected in the SNc region of their brains. Subsequently, those rats overexpressing human tyrosinase produce neuromelanin in the nigral DA neurons (Carballo-Carbajal et al., 2019). This model opens tremendous opportunities for the development of preclinical neuromelanin imaging strategies.

CONCLUSION AND DISCUSSION

The changes in the MRI and MRS measures in the different rodent models presented are summarized in **Table 1**. The discrepancies found in the studies can be explained by several factors: the choice of a genetic or toxic model. Genetic models give insights into widespread cerebral alterations, but they lack the neurodegeneration component for most of them, limiting symptomatic evaluations. In toxic models, the injection site can produce different types of degeneration—massive or partial, rapid or progressive—and can have contrasting effects on the MR measures. The anesthesia protocols, isoflurane or medetomidine alone or a combination of both, which have different modes of action, can impact the rs-fMRI output measures (Williams et al., 2010; Schroeter et al., 2014). The detection sensitivity can also be modulated by different magnetic field strengths (from 7 to 11.7 T) and varying spatial resolutions used in those studies. The effect of iron on water diffusivity can also bias the measurements. Indeed, the presence of iron in the brain causes local magnetic field disturbances, which can lead to reduced water diffusivity if measured by imaging sequences sensitive to those local magnetic changes. In addition, it has been shown that the level of signal-to-noise ratio has an impact on anisotropy measurements, leading to overestimated high eigenvalues and underestimated low eigenvalues

(Pierpaoli and Basser, 1996; Anderson, 2001). Therefore, one could expect to find higher FA in low-signal and iron-rich structures such as the SN. For example, Xu et al. (2015) showed that iron accumulation correlated with decreased MD and increased FA in the putamen of healthy adults. All of those considerations highlight the fact that the interpretation of diffusivity measures is complex and influenced by various mechanisms, such as iron accumulation in the SN and other regions involved in PD, which further contributes to the discrepancies found in the literature. Multimodal imaging combining susceptibility and diffusion sequences may help disentangle the relationship between iron and water diffusivity and could add valuable insights into human and rodent investigations. For instance, Du et al. (2011) demonstrated improved sensitivity and specificity of combined R_2^* and FA measures over the use of single measures to differentiate PD patients from healthy controls.

The limited number of MRI studies in genetic models makes the comparison with toxic models difficult. However, it can be highlighted that decreased FA and AD in the SN and increased GABA and Gln in the STR seem to be the most robust measures across toxic and genetic models. Increased MD seems to be measured only in 6-OHDA models, not in genetic models; however, more studies are needed to confirm this trend. Interestingly, decreased FC and increased FC in various brain regions, as well as interhemispheric changes, are common findings in both toxic and genetic models and suggest overall functional reorganizations. Decreased T_2^* signal or value in the SN and STR is also common across studies. Those major findings are illustrated in **Figure 4**.

All of those imaging measures provide insight into the physiopathology of PD; however, the animal models used do not replicate the entire complexity of the disease. The results should therefore be interpreted with this knowledge. Toxin-based models have been the most widely used in rodents, especially the 6-OHDA rat model; however, genetic-based models are being increasingly used in neuroimaging studies, especially the α-synuclein mouse and the *PINK1* rat models. Gathering more MRI data in various genetic models will help improve our understanding of the role of pathogenic genes in PD. The ideal model should be progressive and age-dependent and include DA depletion together with motor dysfunction as the ones observed in PD patients, as well as inflammation, which is not the case in most models so far. As a consequence, improving animal models is sought after by different groups for either genetic-based rat models (Creed and Goldberg, 2018) or humanized rat models expressing neuromelanin (Carballo-Carbajal et al., 2019).

Ongoing work from various groups aims at improving the specificity of MR-based methods (Petiet et al., 2019). As described above, the diffusivity of mIns as a specific marker of astrogliosis triggers increasing interest for diffusion-weighted MRS developments. Furthermore, this technique has the potential to quantitatively evaluate cell sizes, fiber lengths, and diameters (of either neuronal or glial cells). Indeed, the use of different diffusion time scales allows the quantification of the different parameters governing molecular displacement. Measuring the ADC in the limit of ultrashort diffusion times (<1 ms) allows probing short-range restrictions and cytosol viscosity (Marchadour et al., 2012), whereas measuring ADC in the limit of long diffusion times allows probing long-range restrictions such as cell walls, such that cell geometry and size can be inferred (Najac et al., 2014; Valette et al., 2018). Those technical developments open new fields of investigations in MR-based methods, and they should help better understand the underlying mechanisms.

AUTHOR CONTRIBUTIONS

AP solely contributed to this review, performed bibliographic searches, elaborated the figures and table and wrote the manuscript.

FUNDING

The author thanks the "Institut des Neurosciences Translationnelles" ANR-10-IAIHU-06 and "Infrastructure d'Avenir en Biologie Santé" ANR-11-INBS-0006 for their financial support.

ACKNOWLEDGMENTS

The author thanks the Paris Brain Institute "Movement, Investigation and Therapeutics" team for their fruitful discussions on the topic. The author is also grateful to Vincent Perlbarg and Justine Lambert (from the Institut du Cerveau) for their help in the elaboration of **Figure 3**.

REFERENCES

Abeliovich, A., Schmitz, Y., Farinas, I., Choi-Lundberg, D., Ho, W. H., Castillo, P. E., et al. (2000). Mice lacking α-synuclein display functional deficits in the nigrostriatal dopamine system. *Neuron* 25, 239–252. doi: 10.1016/S0896-6273(00)80886-7

Anderson, A. W. (2001). Theoretical analysis of the effects of noise on diffusion tensor imaging. *Magn. Reson. Med.* 46, 1174–1188. doi: 10.1002/mrm.1315

Andres-Mateos, E., Perier, C., Zhang, L., Blanchard-Fillion, B., Greco, T. M., Thomas, B., et al. (2007). DJ-1 gene deletion reveals that DJ-1 is an atypical peroxiredoxin-like peroxidase. *Proc. Natl. Acad. Sci. U.S.A.* 104, 14807–14812. doi: 10.1073/pnas.0703219104

Antonini, A., Leenders, K. L., Meier, D., Oertel, W. H., Boesiger, P., and Anliker, M. (1993). T2 relaxation time in patients with Parkinson's disease. *Neurology* 43, 697–700. doi: 10.1212/wnl.43.4.697

Barden, H., and Levine, S. (1983). Histochemical observations on rodent brain melanin. *Brain Res. Bull.* 10, 847–851. doi: 10.1016/0361-9230(83)90218-6

Barker, P. B., Bizzi, A., De Stefano, N., Gullapalli, R., and Lin, D. D. M. (2010). *Clinical MR Spectroscopy: Techniques and Applications*. Cambridge: Cambridge University Press.

Batista, C. R. A., Gomes, G. F., Candelario-Jalil, E., Fiebich, B. L., and de Oliveira, A. C. P. (2019). Lipopolysaccharide-induced neuroinflammation as a bridge to understand neurodegeneration. *Int. J. Mol. Sci.* 20:2293. doi: 10.3390/ijms20092293

Belloli, S., Morari, M., Murtaj, V., Valtorta, S., Moresco, R. M., and Gilardi, M. C. (2020). Tranlation imaging in Parkinson's disease: focus on neuroinflammation. *Front. Aging Neurosci.* 12:152. doi: 10.3389/fnagi.2020.00152

Berger, K., Przedborski, S., and Cadet, J. L. (1991). Retrograde degeneration of nigrostriatal neurons induced by intrastriatal 6-hydroxydopamine injection in rats. *Brain Res. Bull.* 26, 301–307. doi: 10.1016/0361-9230(91)90242-c

Berwick, D. C., Heaton, G. R., Azeggagh, S., and Harvey, K. (2019). LRRK2 Biology from structure to dysfunction: research progresses, but the themes remain the same. *Mol. Neurodegener.* 14:49.

Biswal, B., Yetkin, F. Z., Haughton, V. M., and Hyde, J. S. (1995). Functional connectivity in the motor cortex of resting human brain using echo-planar MRI. *Magn. Reson. Med.* 34, 537–541. doi: 10.1002/mrm.1910340409

Blandini, F., and Armentero, M.-T. (2012). Animal models of Parkinson's disease. *FEBS J.* 279, 1156–1166. doi: 10.1111/j.1742-4658.2012.08491.x

Braak, H., Ghebremedhin, E., Rub, U., Bratzke, H., and Del Tredici, K. (2004). Stages in the development of Parkinson's disease-related pathology. *Cell Tissue Res.* 318, 121–134. doi: 10.1007/s00441-004-0956-9

Cabezudo, D., Baekelandt, V., and Lobbestael, E. (2020). Multiple-hit hypothesis in Parkinson's disease: LRRK2 and inflammation. *Front. Neurosci.* 14:376. doi: 10.3389/fnins.2020.00376

Cai, X., Qiao, J., Knox, T., Iriah, S., Kulkarni, P., Madularu, D., et al. (2019). In search of early neuroradiological biomarkers for Parkinson's disease: alterations in resting state functional connectivity and gray matter microarchitecture in PINK1 -/- rats. *Brain Res.* 1706, 58–67. doi: 10.1016/j.brainres.2018.10.033

Carballo-Carbajal, I., Laguna, A., Romero-Gimenez, J., Cuadros, T., Bové, J., Martinez-Vicente, M., et al. (2019). Brain tyrosinase overexpression implicates age-dependent neuromelanin production in Parkinson's disease pathogenesis. *Nat. Commun.* 10:973. doi: 10.1038/s41467-019-08858-y

Castano, A., Herrera, A. J., Cano, J., and Machado, A. (1998). Lipopolysaccharide intranigral injection induces inflammatory reaction and damage in nigrostriatal dopaminergic system. *J. Neurochem.* 70, 1584–1592. doi: 10.1046/j.1471-4159.1998.70041584.x

Cerasa, A., Novellino, F., and Quattrone, A. (2016). Connectivity changes in Parkinson's disease. *Curr. Neurol. Neurosci. Rep.* 16:91. doi: 10.1007/s11910-016-0687-9

Chabert, S., and Scifo, P. (2007). Diffusion signal in magnetic resonance imaging: origin and interpretation in neurosciences. *Biol. Res.* 40, 385–400. doi: 10.4067/S0716-97602007000500003

Chassain, C., Bielicki, G., Keller, C., Renou, J. P., and Durif, F. (2010). Metabolic changes detected in vivo by ^{1}H MRS in the MPTP-intoxicated mouse. *NMR Biomed.* 23, 547–553. doi: 10.1002/nbm.1504

Chesselet, M. F., Fleming, S., Mortazavi, F., and Meurers, B. (2008). Strengths and limitations of genetic mouse models of Parkinson's disease. *Parkinsonism Relat. Disord.* 14, S84–S87. doi: 10.1016/j.parkreldis.2008.04.004

Clarke, C., and Lowry, M. (2001). Systematic review of proton magnetic resonance spectroscopy of the striatum in parkinsonian syndromes. *Eur. J. Neurol.* 8, 573–577. doi: 10.1046/j.1468-1331.2001.00308.x

Cochrane, C. J., and Ebmeier, K. P. (2013). Diffusion tensor imaging in parkinsonian syndromes: a systematic review and meta-analysis. *Neurology* 80, 857–864. doi: 10.1212/WNL.0b013e318284070c

Cong, L., Muir, E. R., Chen, C., Qian, Y., Liu, J., and Biju, K. C. (2016). Multimodal MRI evaluation of the MitoPark mouse model of Parkinson's disease. *PLoS One* 11:e0151884. doi: 10.1371/journal.pone.0151884

Coune, P. G., Craveiro, M., Gaugler, M. N., Mlynarik, V., Schneider, B. L., Aebischer, P., et al. (2013). An in vivo ultrahigh field 14.1T ^{1}H-MRS study on 6-OHDA and α-synuclein-based rat models of Parkinson's disease: GABA as an early disease marker. *NMR Biomed.* 26, 43–50. doi: 10.1002/nbm.2817

Creed, R. B., and Goldberg, M. S. (2018). New developments in genetic rat models of Parkinson's disease. *Mov. Dis.* 33, 717–729. doi: 10.1002/MDS.27296

Daher, J. P. L., Volpicelli-Daley, L. A., Blackburn, J. P., Moehle, M. S., and West, A. B. (2014). Abrogation of–synuclein-mediated dopaminergic neurodegeneration in LRRK2-deficient rats. *Proc. Natl. Acad. Sci. U.S.A.* 111, 9289–9294. doi: 10.1073/pnas.1403215111

Dauer, W., and Przedborski, S. (2003). Parkinson's disease: mechanisms and models. *Neuron* 39, 889–909. doi: 10.1016/s0896-6273(03)00568-3

Dave, K. D., De Silva, S., Sheth, N. P., Ramboz, S., Beck, M. J., Quang, C., et al. (2014). Phenotypic characterization of recessive gene knockout rat models of Parkinson's disease. *Neurobiol. Dis.* 70, 190–203. doi: 10.1016/j.nbd.2014.06.009

Dawson, T. M., Ko, H. S., and Dawson, V. L. (2010). Genetic animal models of Parkinson's disease. *Neuron* 66, 646–661. doi: 10.1016/j.neuron.2010.04.034

de Lau, L. M. L., and Breteler, M. M. B. (2006). Epidemiology of Parkinson's disease. *Lancet Neurol.* 5, 525–535. doi: 10.1016/S1474-4422(06)70471-9

Delong, M. R. (1990). Primate models of movement disorders of basal ganglia origin. *Trends Neurosci.* 13, 281–285. doi: 10.1016/0166-2236(90)90110-v

Dexter, D. T., Wells, F. R., Lees, A. J., Agid, F., Agid, Y., Jenner, P., et al. (1989). Increased nigral iron content and alterations in other metal ions occurring in brain in Parkinson's disease. *J. Neurochem.* 52, 1830–1836. doi: 10.1111/j.1471-4159.1989.tb07264.x

Du, G., Lewis, M. M., Styner, M., Shaffer, M. L., Sen, S., Yang, Q. X., et al. (2011). Combined R2* and diffusion tenser imaging changes in the substantia nigra in Parkinson disease. *Mov. Disord.* 26, 1627–1632. doi: 10.1002/mds.23643

Ekstrand, M. I., Terzioglu, M., Galter, D., Zhu, S., Hofstetter, C., Lindqvist, E., et al. (2007). Progressive parkinsonism in mice with respiratory-chain-deficient dopamine neurons. *Proc. Natl. Acad. Sci. U.S.A.* 104, 1325–1330. doi: 10.1073/pnas.0605208103

Emir, U. E., Tuite, P. J., and Öz, G. (2012). Elevated pontine and putamenal GABA levels in mid-moderate Parkinson disease detected by 7 Tesla proton MRS. *PLoS One* 7:e30918. doi: 10.1371/journal.pone.0030918

Engelborghs, S., Marescau, B., and De Deyn, P. P. (2003). Amino acids and biogenic amines in cere–brospinal fluid of patients with Parkinson's disease. *Neurochem. Res.* 28, 1145–1150. doi: 10.1023/a:1024255208563

Ercan, E., Magro-Checa, C., Valabregue, R., Branzoli, F., Wood, E. T., Steup-Beekman, G. M., et al. (2016). Glial and axonal changes in systemic lupus erythematosus measured with diffusion of intracellular metabolites. *Brain* 139, 1447–1457. doi: 10.1093/brain/aww031

Fleming, S. M., Fernagut, P. O., and Chesselet, M. F. (2005). Genetic mouse models of Parkinsonism: strengths and limitations. *NeuroRx* 2, 495–503. doi: 10.1602/neurorx.2.3.495

Friston, K. J., Frith, C. D., Liddle, P. F., and Frackowiak, R. S. (1993). Functional connectivity: the principal-component analysis of large (PET) data sets. *J. Cereb. Blood Flow Metab.* 13, 5–14. doi: 10.1038/jcbfm.1993.4

Gao, H. M., Jiang, J., Wilson, B., Zhang, W., Hong, J. S., and Liu, B. (2002). Microglial activation-mediated delayed and progressive degeneration of rat nigral dopaminergic neurons: relevance to Parkinson's disease. *J. Neurochem.* 81, 1285–1297. doi: 10.1046/j.1471-4159.2002.00928.x

Gao, H. M., Zhang, F., Zhou, H., Kam, W., Wilson, B., and Hong, J. S. (2011). Neuroinflammation and alpha-synuclein dysfunction potentiate each other, driving chronic progression of neurodegeneration in a mouse model of Parkinson's disease. *Environ. Health Perspect.* 119, 807–814. doi: 10.1289/ehp.1003013

Gardoni, F., and Bellone, C. (2015). Modulation of the glutamatergic transmission by dopamine: a focus on Parkinson, huntington and addiction diseases. *Front. Cell. Neurosci.* 9:25. doi: 10.3389/fncel.2015.00025

Gautier, C. A., Kitada, T., and Shen, J. (2008). Loss of PINK1 causes mitochondrial functional defects and increased sensitivity to oxidative stress. *Proc. Natl. Acad. Sci. U.S.A.* 105, 11364–11369. doi: 10.1073/pnas.0802076105

Gerfen, C. R. (1992). The neostriatal mosaic: multiple levels of compartmental organization. *Trends Neurosci.* 15, 133–139. doi: 10.1016/0166-2236(92)90355-c

Giovanni, A., Sieber, B. A., Heikkila, R. E., and Sonsalla, P. K. (1994). Studies on species sensitivity to the dopaminergic neurotoxin 1-methyl-4- phenyl-1,2,3,6-tetrahydropyridine. part 1: systemic administration. *J. Pharmacol. Exp. Therap.* 270, 1000–1007.

Gispert, S., Ricciardi, F., Kurz, A., Azizov, M., Hoepken, H. H., Becker, D., et al. (2009). Parkinson phenotype in aged PINK1-deficient mice is accompanied by progressive mitochondrial dysfunction in absence of neurodegeneration. *PLoS One* 4:e5777. doi: 10.1371/journal.pone.0005777

Glass, C. K., Saijo, K., Winner, B., Marchetto, M. C., and Gage, F. H. (2010). Mechanisms underlying inflammation in neurodegeneration. *Cell* 140, 918–934. doi: 10.1016/j.cell.2010.02.016

Goldberg, M. S., Pisani, A., Haburcak, M., Vortherms, T. A., Kitada, T., Costa, C., et al. (2005). Nigrostriatal dopaminergic deficits and hypokinesia caused by inactivation of the familial Parkinsonism-linked gene DJ-1. *Neuron* 45, 489–496. doi: 10.1016/j.neuron.2005.01.041

Graff-Radford, J., Boeve, B. F., Murray, M., Ferman, T. J., Tosakulwong, N., Lesnick, T. G., et al. (2014). Regional proton magnetic resonance spectroscopy patterns in dementia with Lewy bodies. *Neurobiol. Aging* 35, 1483–1490. doi: 10.1016/j.neurobiolaging.2014.01.001

Gröger, A., Kolb, R. K., Schäfer, R., and Klose, U. (2014). Dopamine reduction in the substantia nigra of Parkinson's disease patients confirmed by in vivo magnetic resonance spectroscopic imaging. *PLoS One* 9:e84081. doi: 10.1371/journal.pone.0084081

Guan, J.-J., and Feng, Y.-Q. (2018). Quantitative magnetic resonance imaging of brain iron deposition: comparison between quantitative susceptibility mapping and transverse relaxation rate (R2*) mapping. *Nan Fang Yi Ke Da Xue Xue Bao* 38, 305–311. doi: 10.3969/j.issn.1673-4254.2018.03.10

Guan, X., Xuan, M., Gu, Q., Huang, P., Liu, C., Wang, N., et al. (2016). Regionally progressive accumulation of iron in Parkinson's disease as measured by quantitative susceptibility map- ping. *NMR Biomed.* 30:e3489. doi: 10.1002/nbm.3489

Haacke, E. M., Liu, S., Buch, S., Zheng, W., Wu, D., and Ye, Y. (2015). Quantitative susceptibility mapping: current status and future directions. *Magn. Res. Im.* 33, 1–25. doi: 10.1016/j.mri.2014.09.004

Haacke, E. M., Xu, Y., Cheng, Y. C., and Reichenbach, J. R. (2004). Susceptibility weighted imaging (SWI). *Magn. Reson. Med.* 52, 612–618. doi: 10.1002/mrm.20198

Hansen, S. H., Andersen, M. L., Cornett, C., Gradinaru, R., and Grunnet, N. (2010). A role for taurine in mitochondrial function. *J. Biomed. Sci.* 17(Suppl 1):S23.

Hare, D., Reedy, B., Grimm, R., Wilkins, S., Volitakis, I., George, J. L., et al. (2009). Quantitative elemental bio-imaging of Mn, Fe, Cu and Zn in 6-hydroxydopamine induced Parkinsonism mouse models. *Metallomics* 1, 53–58. doi: 10.1039/B816188G

Helmich, R. C., Derikx, L. C., Bakker, M., Scheeringa, R., Bloem, B. R., and Toni, I. (2010). Spatial remapping of cortico- striatal connectivity in Parkinson's disease. *Cereb. Cortex* 20, 1175–1186. doi: 10.1093/cercor/bhp178

Herrera, A. J., Castano, A., Venero, J. L., Cano, J., and Machado, A. (2000). The single intranigral injection of LPS as a new model for studying the selective effects of inflammatory reactions on dopaminergic system. *Neurobiol. Dis.* 7, 429–447. doi: 10.1006/nbdi.2000.0289

Hirsch, E. C., Brandel, J. P., Galle, P., Javoy-Agid, F., and Agid, Y. (1991). Iron and aluminum increase in the substantia nigra of patients with Parkinson's disease: an X-ray microanalysis. *J. Neurochem.* 56, 446–451. doi: 10.1111/j.1471-4159.1991.tb08170.x

Honey, C. J., Sporns, O., Cammoun, L., Gigandet, X., Thiran, J. P., Meuli, R., et al. (2009). Predicting human resting-state functional connectivity from structural connectivity. *Proc. Natl. Acad. Sci. U.S.A.* 106, 2035–2040. doi: 10.1073/pnas.0811168106

Honey, G. D., Suckling, J., Zelaya, F., Long, C., Routledge, C., Jackson, S., et al. (2003). Dopaminergic drug effects on physiological connectivity in a human corticostriato-thalamic system. *Brain* 126, 1767–1781. doi: 10.1093/brain/awg184

Hopes, L., Grolez, G., Moreau, C., Lopes, R., Ryckewaert, G., Carrière, N., et al. (2016). Magnetic resonance imaging features of the nigrostriatal system: biomarker of Parkinson's disease stages? *PLoS One* 11:e0147947. doi: 10.1371/journal.pone.0147947

Hou, Z., Lei, H., Hong, S., Sun, B., Fang, K., Lin, X., et al. (2010). Functional changes in the frontal cortex in Parkinson's disease using a rat model. *J. Clin. Neurosci.* 17, 628–633. doi: 10.1016/j.jocn.2009.07.101

Hunter, R., Ojha, U., Bhurtel, S., Bing, G., and Choi, D. Y. (2017). Lipopolysaccharide-induced functional and structural injury of the mitochondria in the nigrostriatal pathway. *Neurosci. Res.* 114, 62–69. doi: 10.1016/j.neures.2016.09.007

Hunter, R. L., Choi, D. Y., Ross, S. A., and Bing, G. (2008). Protective properties afforded by pioglitazone against intrastriatal LPS in Sprague-Dawley rats. *Neurosci. Lett.* 432, 198–201. doi: 10.1016/j.neulet.2007.12.019

Jackson-Lewis, V., Jakowec, M., Burke, R. E., and Przedborski, S. (1995). Time course and morphology of dopaminergic neuronal death caused by the neurotoxin 1-methyl-4-phenyl-1,2,3,6- tetrahydropyridine. *Neurodegeneration* 4, 257–269. doi: 10.1016/1055-8330(95)90015-2

Jagmag, S. A., Tripathi, N., Shukla, S. D., Maiti, S., and Khurana, S. (2016). evaluation of models of Parkinson's disease. *Front. Neurosci.* 9:503. doi: 10.3389/fnins.2015.00503

Jiang, H., Song, N., Xu, H., Zhang, S., Wang, J., and Xie, J. (2010). Up-regulation of divalent metal transporter 1 in 6-hydroxydopamine intoxication is IRE/IRP dependent. *Cell Res.* 20, 345–356. doi: 10.1038/cr.2010.20

Jin, L., Wang, J., Zhao, L., Jin, H., Fei, G., Zhang, Y., et al. (2011). Decreased serum ceruloplasmin levels characteristically ag- gravate nigral iron deposition in Parkinson's disease. *Brain* 134, 50–58. doi: 10.1093/brain/awq319

Jonsson, G. (1980). Chemical neurotoxins as denervation tools in neuro- biology. *Annu. Rev. Neurosci.* 3, 169–187. doi: 10.1146/annurev.ne.03.030180.001125

Kahle, P. J., Haass, C., Kretzschmar, H. A., and Neumann, M. (2002). Structure/function of alpha-synuclein in health and disease: rational development of animal models for Parkinson's and related diseases. *J. Neurochem.* 82, 449–457. doi: 10.1046/j.1471-4159.2002.01020.x

Khairnar, A., Latta, P., Drazanova, E., Ruda-Kucerova, J., Szabo, N., Arab, A., et al. (2015). Diffusion kurtosis imaging detects microstructural alterations in brain of α-synuclein overexpressing transgenic mouse model of Parkinson's disease: a pilot study. *Neurotox. Res.* 28, 281–289. doi: 10.1007/s12640-015-9537-9

Kim, R. H., Smith, P. D., Aleyasin, H., Hayley, S., Mount, M. P., Pownall, S., et al. (2005). Hypersensitivity of DJ-1-deficient mice to 1-methyl-4-phenyl-1,2,3,6-tetrahydropyrindine (MPTP) and oxidative stress. *Proc. Natl. Acad. Sci. U.S.A.* 102, 5215–5220. doi: 10.1073/pnas.0501282102

Kitada, T., Pisani, A., Porter, D. R., Yamaguchi, H., Tscherter, A., Martella, G., et al. (2007). Impaired dopamine release and synaptic plasticity in the striatum of PINK1-deficient mice. *Proc. Natl. Acad. Sci. U.S.A.* 104, 11441–11446. doi: 10.1073/pnas.0702717104

Klein, C., and Westenberger, A. (2012). Genetics of Parkinson's disease. *Cold Spring Harb. Perspect. Med.* 2:a008888. doi: 10.1101/cshperspect.a008888

Konnova, E. A., and Swanberg, M. (2018). "Animal models of Parkinson's disease," in *Parkinson's Disease: Pathogenesis and Clinical Aspects*, (Brisbane: Codon Publications), doi: 10.15586/codonpublications.parkinsonsdisease.2018.ch5

Lanciego, J. L., Luquin, N., and Obeso, J. A. (2012). Functional neuroanatomy of the basal ganglia. *Cold Spring Harb. Perspect. Med.* 2:a009621. doi: 10.1101/cshperspect.a009621

Langley, J., Huddleston, D. E., Chen, X., Sedlacik, J., Zachariah, N., and Hu, X. (2015). A multicontrast approach for comprehensive imaging of substantia nigra. *Neuroimage* 15, 7–13. doi: 10.1016/j.neuroimage.2015.02.045

Langston, J. W., Ballard, P., Tetrud, J. W., and Irwin, I. (1983). Chronic Parkinsonism in humans due to a product of meperidine-analog synthesis. *Science* 219, 979–980. doi: 10.1126/science.6823561

Le Bihan, D. (2003). Looking into the functional architecture of the brain with diffusion MRI. *Nat. Rev.* 4, 469–480. doi: 10.1038/nrn1119

Lee, J. W., Tapias, V., Di Maio, R., Greenamyre, J. T., and Cannon, J. R. (2015). Behavioral, neurochemical, and pathologic alterations in bacterial artificial chromosome transgenic G2019S leucine-rich repeated kinase 2 rats. *Neurobiol. Aging* 36, 505–518. doi: 10.1016/j.neurobiolaging.2014.07.011

Lehéricy, S., Bardinet, E., Poupon, C., Vidailhet, M., and François, C. (2014). 7 Tesla magnetic resonance imaging: a closer look at substantia nigra anatomy in Parkinson's disease. *Mov. Disord.* 29, 1574–1581. doi: 10.1002/mds.26043

Lehéricy, S., Sharman, M. A., Longo Dos Santos, C., Paquin, R., and Galléa, C. (2012). Magnetic resonance imaging of the substantia nigra in Parkinson's disease. *Mov Disord.* 27, 822–830. doi: 10.1002/mds.25015

Levin, B. E., Katzen, H. L., Maudsley, A., Post, J., Myerson, C., Govind, V., et al. (2012). Whole-brain proton MR spectroscopic imaging in Parkinson's disease. *J. Neuroimaging* 24, 39–44. doi: 10.1111/j.1552-6569.2012.00733.x

Li, Y., Liu, W., Oo, T. F., Wang, L., Tang, Y., Jackson-Lewis, V., et al. (2009). Mutant LRRK2(R1441G) BAC transgenic mice recapitulate cardinal features of Parkinson's disease. *Nat. Neurosci.* 12, 826–828. doi: 10.1038/nn.2349

Ligneul, C., Palombo, M., Hernandez-Garzon, E., Carrillo-de-Sauvage, M. A., Flament, J., Hantraye, P., et al. (2019). Diffusion-weighted magnetic resonance spectroscopy enables cell-specific monitoring of astrocyte reactivity in vivo. *Neuroimage* 191, 457–469. doi: 10.1016/j.neuroimage.2019.02.046

Liu, T., Eskreis-Winkler, S., Schweitzer, A. D., Chen, W., Kaplitt, M. G., Tsiouris, A. J., et al. (2013). Improved subthalamic nucleus depiction with quantitative susceptibility mapping. *Radiology* 269, 216–223. doi: 10.1148/radiol.13121991

Lotfipour, A. K., Wharton, S., Schwarz, S. T., Gontu, V., Schäfer, A., Peters, A. M., et al. (2012). High resolution magnetic susceptibility mapping of the substantia nigra in Parkinson's disease. *J. Magn. Reson. Imaging* 35, 48–55. doi: 10.1002/jmri.22752

Lu, X.-H., Fleming, S. M., Meurers, B., Ackerson, L. C., Mortazavi, F., Lo, V., et al. (2009). Bacterial artificial chromosome transgenic mice expressing a truncated mutant parkin exhibit age-dependent hypokinetic motor deficits, dopaminergic neuron degeneration, and accumulation of proteinase K-Resistant – Synuclein. *J. Neurosci.* 29, 1962–1976. doi: 10.1523/jneurosci.5351-08.2009

Lv, Z., Jiang, H., Xu, H., Song, N., and Xie, J. (2011). Increased iron levels correlate with the selective nigral dopaminergic neuron degeneration in Parkinson's disease. *J. Neural Transm.* 118, 361–369. doi: 10.1007/s00702-010-0434-3

Marchadour, C., Brouillet, E., Hantraye, P., Lebon, V., and Valette, J. (2012). Anomalous diffusion of brain metabolites evidenced by diffusion-weighted magnetic resonance spectroscopy in vivo. *J. Cereb. Blood Flow Metab.* 32:2160. doi: 10.1038/jcbfm.2012.119

Maroteaux, L., Campanelli, J., and Scheller, R. (1988). Synuclein: a neuron-specific protein localized to the nucleus and presynaptic nerve terminal. *J. Neurosci.* 8, 2804–2815. doi: 10.1523/jneurosci.08-08-02804.1988

Marsden, C. D. (1961). Pigmentation in the nucleus substantiae nigrae of mammals. *J. Anat.* 95, 256–261.

Menke, R. A., Jbabdi, S., Miller, K. L., Matthews, P. M., and Zarei, M. (2010). Connectivity-based segmentation of the substantia nigra in human and its implications in Parkinson's disease. *NeuroImage* 52, 1175–1180. doi: 10.1016/j.neuroimage.2010.05.086

Monnot, C., Zhang, X., Nikkhou-Aski, S., Damberg, P., and Svenningsson, P. (2017). Asymmetric dopaminergic degeneration and levodopa alter functional corticostriatal connectivity bilaterally in experimantal parkinsonism. *Exp. Neurol.* 292, 11–20. doi: 10.1016/j.expneurol.2017.02.014

Mori, S., Fujitake, J., Kuno, S., and Sano, Y. (1988). Immunohistochemical evaluation of the neurotoxic effect of 1-methyl-4-phenyl-1,2,3,6-tetrahydropyridine (MPTP) on dopaminergic nigrostriatal neurons of young adult mice using dopamine and tyrosine hydroxylase antibodies. *Neurosci. Lett.* 90, 57–62. doi: 10.1016/0304-3940(88)90786-0

Najac, C., Marchadour, C., Guillermier, M., Houitte, D., Slavov, V., Brouillet, E., et al. (2014). Intracellular metabolites in the primate brain are primarily localized in long fibers rather than in cell bodies, as shown by diffusion-weighted magnetic resonance spectroscopy. *Neuroimage* 90, 374–380. doi: 10.1016/j.neuroimage.2013.12.045

Ogisu, K., Kudo, K., Sasaki, M., Sakushima, K., Yabe, I., Sasaki, H., et al. (2013). 3D neuromelanin-sensitive magnetic resonance imaging with semi-automated volume measurement of the substantia nigra pars compacta for diagnosis of Parkinson's disease. *Neuroradiology* 55, 719–724. doi: 10.1007/s00234-013-1171-8

Olmedo, A., Estevez-Silva, H., Orädd, G., Bjerken, S., Marcellino, D., and Virel, A. (2017). An altered blood-brain barrier contributes to brain iron accumulation and neuroinflammation in the 6-OHDA rat model of Parkinson's disease. *Neuroscience* 362, 141–151. doi: 10.1016/j.neuroscience.2017.08.023

Ostrerova-Golts, N., Petrucelli, L., Hardy, J., Lee, J. M., Farer, M., and Wolozin, B. (2000). The A53T α-synuclein mutation increases iron-dependent aggregation and toxicity. *J. Neurosci.* 20, 6048–6054. doi: 10.1523/jneurosci.20-16-06048.2000

Öz, G., Alger, J. R., Barker, P. B., Bartha, R., Bizzi, A., Boesh, C., et al. (2014). Clinical proton MR spectroscopy in central nervous system disorders. *Radiology* 270, 658–679. doi: 10.1148/radiol.13130531

Öz, G., Terpstra, M., Tkac, I., Aia, P., Lowary, J., Tuite, P., et al. (2006). Proton MRS of the unilateral substantia nigra in the human brain at 4 tesla: detection of high GABA concentrations. *Magn. Reson. Med.* 55, 296–301. doi: 10.1002/mrm.20761

Palombo, M., Shemesh, N., Ronen, I., and Valette, J. (2018). Insights into brain microstructure from in vivo DW-MRS. *Neuroimage* 182, 97–116. doi: 10.1016/j.neuroimage.2017.11.028

Park, B. S., and Lee, J. O. (2013). Recognition of lipopolysaccharide pattern by TLR4 complexes. *Exp. Mol. Med.* 45:e66. doi: 10.1038/emm.2013.97

Perez, F. A., and Palmiter, R. D. (2005). Parkin-deficient mice are not a robust model of parkinsonism. *Proc. Nat. Acad. Sci. U.S A.* 102, 2174–2179. doi: 10.1073/pnas.0409598102

Perlbarg, V., Lambert, J., Butler, B., Felfli, M., Valabrègue, R., Privat, A.-L., et al. (2018). Alterations of the nigrostriatal pathway in a 6-OHDA rat model of Parkinson's disease evaluated with multimodal MRI. *PlosOne* 13:e0202597. doi: 10.1371/journal.pone.0202597

Petiet, A., Adanyeguh, I., Aigrot, M.-S., Poirion, E., Nait-Oumesmar, B., Santin, M., et al. (2019). Ultrahigh field imaging of myelin disease models: toward specific markers of myelin integrity? *J. Comp. Neurol.* 527, 2179–2189. doi: 10.1002/cne.24598

Pienaar, I. S., Götz, J., and Feany, M. B. (2010). Parkinson's disease: insights from non-traditional model organisms. *Prog. Neurobiol.* 92, 558–571. doi: 10.1016/j.pneurobio.2010.09.001

Pierpaoli, C., and Basser, P. J. (1996). Toward a quantitative assessment of diffusion anisotropy. *Magn. Reson. Med.* 36, 893–906. doi: 10.1002/mrm.1910360612

Pietracupa, S., Martin-Bastida, A., and Piccini, P. (2017). Iron metabolism and its detection through MRI in parkinsonian disorders: a systemic review. *Neurol. Sci.* 38, 2095–2101. doi: 10.1007/s10072-017-3099-y

Przedborski, S., Levivier, M., Jiang, H., Ferreira, M., Jackson-Lewis, V., Donaldson, D., et al. (1995). Dose-dependent lesions of the dopaminergic nigrostriatal pathway induced by intrastriatal injection of 6-hydroxydopamine. *Neuroscience* 67, 631–647. doi: 10.1016/0306-4522(95)00066-r

Qin, L., Wu, X., Block, M. L., Liu, Y., Breese, G. R., Hong, J. S., et al. (2007). Systemic LPS causes chronic neuroinflammation and progressive neurodegeneration. *Glia* 55, 453–462. doi: 10.1002/glia.20467

Ransohoff, R. M. (2016). How neuroinflammation contributes to neurodegeneration. *Science* 353, 777–783. doi: 10.1126/science.aag2590

Redgrave, P., Rodriguez, M., Smith, Y., Rodriguez-Oroz, M. C., Lehéricy, S., Bergman, H., et al. (2010). Goal-directed and habitual control in the basal ganglia: implications for parkinson's disease. *Nat. Rev. Neurosci.* 11, 760–772. doi: 10.1038/nrn2915

Ren, X., Hinchie, A., Swomley, A., Powell, D. K., and Butterfield, D. A. (2019). Profiles of brain oxidative damage, ventricular alterations, and neurochemical metabolites in the striatum of PINK1 knockout rats as functions of age and gender: relevance to Parkinson disease. *Free Radic. Biol. Med.* 143, 146–152. doi: 10.1016/j.freeradbiomed.2019.08.008

Rolheiser, T. M., Fulton, H. G., Good, K. P., Fisk, J. D., McKelvey, J. R., Scherfler, C., et al. (2011). Diffusion tensor imaging and olfactory identification testing in early-stage Parkinson's disease. *J. Neurol.* 258, 1254–1260. doi: 10.1007/s00415-011-5915-2

Sasaki, M., Shibata, E., Tohyama, K., Junko, T., Otsuka, K., Tsuchiya, K., et al. (2006). Neuromelanin magnetic resonance imaging of locus ceruleus and substantia nigra in Parkinson's disease. *Neuroreport* 17, 1215–1218. doi: 10.1097/01.wnr.0000227984.84927.a7

Schroeter, A., Schlegel, F., Seuwen, A., Grandjean, J., and Rudin, M. (2014). Specificity of stimulus-evoked fMRI responses in the mouse: the influence of systemic physiological changes associated with innocuous stimulation under four different anesthetics. *Neuroimage* 94, 372–384. doi: 10.1016/j.neuroimage.2014.01.046

Schwarz, S. T., Abaei, M., Gontu, V., Morgan, P. S., Bajaj, N., and Auer, D. P. (2013). Diffusion tensor imaging of nigral degeneration in Parkinson's disease: a region-of-interest and voxel- based study at 3 T and systematic review with meta-analysis. *Neuroimage Clin.* 3, 481–488. doi: 10.1016/j.nicl.2013.10.006

Schwarz, S. T., Afzal, M., Morgan, P. S., Bajaj, N., Gowland, P. A., and Auer, D. P. (2014). The 'swallow tail' appearance of the healthy nigrosome–a new accurate test of Parkinson's disease: a case control and retrospective cross-sectional MRI study at 3T. *PLoS One* 9:e93814. doi: 10.1371/journal.pone.0093814

Shaikh, K. T., Yang, A., Youshin, E., and Schmid, S. (2015). Transgenic LRRK2R1441G rats-a model for Parkinson disease? *PeerJ* 3:e945. doi: 10.7717/peerj.945

Sharman, M., Valabregue, R., Perlbarg, V., Vidailhet, M., Benali, H., Brice, A., et al. (2012). Parkinson's disease patients show reduced cortical-subcortical sensorimotor connectivity. *Mov. Disord.* 28, 447–454. doi: 10.1002/mds.25255

Shimohama, S., Sawada, H., Kitamura, Y., and Taniguchi, T. (2003). Disease model: Parkinson's disease. *Trends Mol. Med.* 9, 360–365. doi: 10.1016/s1471-4914(03)00117-5

Skorpil, M., Söderlund, V., Sundin, A., and Svenningsson, P. (2012). MRI diffusion in Parkinson's disease: using the technique's inherent directional information to study the olfactory bulb and substantia nigra. *J. Parkinsons. Dis.* 2, 171–180. doi: 10.3233/JPD-2012-12091

Sloan, M., Alegre-Abarrategui, J., Potgieter, D., Kaufmann, A. K., Exley, R., Deltheil, T., et al. (2016). LRRK2 BAC transgenic rats develop progressive, L-DOPA-responsive motor impairment, and deficits in dopamine circuit function. *Hum. Mol. Genet.* 25, 951–963. doi: 10.1093/hmg/ddv628

Sofroniew, M. V. (2015). Astrocyte barriers to neurotoxic inflammation. *Nat. Rev. Neurosci.* 16, 249–263. doi: 10.1038/nrn3898

Song, S. K., Yoshino, J., Le, T. Q., Lin, S. J., Sun, S. W., Cross, A. H., et al. (2005). Demyelination increases radial diffusivity in corpus callosum of mouse brain. *Neuroimage* 26, 132–140. doi: 10.1016/j.neuroimage.2005.01.028

Soria, G., Aguilar, E., Tudela, R., Mullol, J., Planas, A. M., and Marin, C. (2011). In vivo magnetic resonance imaging characterization of bilateral structural changes in experimental Parkinson's disease: a T2 relaxometry study combined with longitudinal diffusion tensor imaging and manganese-enhanced magnetic resonance imaging in the 6-hydroxydopamine rat model. *Eur. J. Neurosci.* 33, 1551–1560. doi: 10.1111/j.1460-9568.2011.07639.x

Tansey, M. G., and Goldberg, M. S. (2010). Neuroinflammation in Parkinson's disease: its role in neuronal death and implications for therapeutic intervention. *Neurobiol. Dis.* 37, 510–518. doi: 10.1016/j.nbd.2009.11.004

Tatton, N. A., and Kish, S. J. (1997). *In situ* detection of apoptotic nuclei in the substantia nigra compacta of 1-methyl-4-phenyl- 1,2,3,6-tetrahydropyridine-treated mice using terminal deoxynucleotidyl transferase labelling and acridine orange staining. *Neuroscience* 77, 1037–1048. doi: 10.1016/s0306-4522(96)00545-3

Thoenen, H., and Tranzer, J. P. (1968). Chemical sympathectomy by selective destruction of adrenergic nerve endings with 6- hydroxydopamine. *Naunyn Shmiedebergs Arch. Exp. Pathol. Pharmakol.* 26, 271–288. doi: 10.1007/BF00536990

Thomas, B., and Beal, M. F. (2007). Parkinson's disease. *Hum. Mol. Genet.* 16, R183–R194. doi: 10.1093/hmg/ddm159

Tuovinen, N., Seppi, K., de Pasquale, F., Muller, C., Nocker, M., Schocke, M., et al. (2018). The reorganization of functional architecture in the early-stages of Parkinson's disease. *Parkinsonism Relat. Disord.* 50, 61–68. doi: 10.1016/j.parkreldis.2018.02.013

Ulla, M., Bonny, J. M., Ouchchane, L., Rieu, I., Claise, B., and Durif, F. (2013). Is R2* a new MRI biomarker for the progression of Parkinson's disease? A longitudinal follow-up. *PLoS One* 8:e57904. doi: 10.1371/journal.pone.0057904

Ungerstedt, U. (1968). 6-Hydroxy-dopamine induced degeneration of central monoamine neurons. *Eur. J. Pharmacol.* 5, 107–110. doi: 10.1016/0014-2999(68)90164-7

Vaillancourt, D. E., Spraker, M. B., Prodoehl, J., Abraham, I., Corcos, D. M., Zhou, X. J., et al. (2009). High-resolution diffusion tensor imaging in the substantia nigra of de novo Parkinson disease. *Neurology* 72, 1378–1384. doi: 10.1212/01.wnl.0000340982.01727.6e

Valette, J., Ligneul, C., Marchadour, C., Najac, C., and Palombo, M. (2018). Brain metabolite diffusion from ultra-short to ultra-long time scales: what do we learn, where should we go? *Front. Neurosci.* 12:2. doi: 10.3389/fnins.2018.00002

Van Camp, N., Blockx, I., Verhoye, M., Casteels, C., Coun, F., Leemans, A., et al. (2009). Diffusion tensor imaging in a rat model of Parkinson's disease after lesioning of the nigrostriatal tract. *NMR Biomed.* 22, 697–706. doi: 10.1002/nbm.1381

Van Rompuy, A.-S., Lobbestael, E., Van der Perren, A., Van den Haute, C., and Baekelandt, V. (2014). Long-term overexpression of human wild-type and T240R mutant Parkin in rat substantia nigra induces progressive dopaminergic neurodegeneration. *J. Neuropathol. Exp. Neurol.* 73, 159–174. doi: 10.1097/nen.0000000000000039

Vila, M. (2019). Neuromelanin, aging, and neuronal vulnerability in Parkinson's disease. *Mov. Dis.* 34, 1440–1451. doi: 10.1002/mds.27776

Vila, M., Laguna, A., and Carballo-Carbajal, I. (2019). Intracellular crowding by age-dependent neuromelanin accumulation disrupts neuronal proteostasis and triggers Parkinson disease pathology. *Autophagy* 15, 2028–2030. doi: 10.1080/15548627.2019.1659621

Villeneuve, L. M., Purnell, P. R., Boska, M. D., and Fox, H. S. (2016). Early expression of parkinson's disease-related mitochondrial abnormalities in PINK1 knockout rats. *Mol. Neurobiol.* 53, 171–186. doi: 10.1007/s12035-014-8927-y

Virel, A., Faergemann, E., Orädd, G., and Strömberg, I. (2014). Magnetic resonance imaging (MRI) to study striatal iron accumulation in a rat model of Parkinson's disease. *Plos One* 9:e112941. doi: 10.1371/journal.pone.0112941

Walker, M. D., Volta, M., Cataldi, S., Dinelle, K., Beccano-Kelly, D., Munsie, L., et al. (2014). Behavioral deficits and striatal DA signaling in LRRK2 p.G2019S transgenic rats: a multimodal investigation including PET neuroimaging. *J. Parkinsons Dis.* 4, 483–498. doi: 10.3233/JPD-140344

Wang, J., Jiang, H., and Xie, J. X. (2004). Time dependent effects of 6-OHDA lesions on iron level and neuronal loss in rat nigrostriatal system. *Neurochem. Res.* 29, 2239–2243. doi: 10.1007/s11064-004-7031-5

Wei, H., Xie, L., Dibb, R., Li, W., Decker, K., Zhang, Y., et al. (2016). Imaging whole-brain cytoarchitecture of mouse with MRI-based quantitative susceptibility mapping. *Neuroimage* 15, 107–115. doi: 10.1016/j.neuroimage.2016.05.033

Weingarten, C., Sundman, M. H., Hickey, P., and Chen, N. (2015). Neuroimaging of Parkinson's disease: expanding views. *Neurosci. Biobehav. Rev.* 59, 16–52. doi: 10.1016/j.neubiorev.2015.09.007

Westphal, R., Simmons, C., Mesquita, M. B., Wood, T. C., Williams, S. C. R., Vernon, A. C., et al. (2017). Characterization of the resting-state brain network topology in the 6-hydroxydopamine rat model of Parkinson's disease. *PLoS One* 12:e0172394. doi: 10.1371/journal.pone.0172394

Williams, K. A., Magnuson, M., Majeed, W., LaConte, S. M., Peltier, S. J., Hu, X., et al. (2010). Comparison of alpha-chloralose, medetomidine and isoflurane anesthesia for functional connectivity mapping in the rat. *Magn. Reson. Imaging* 28, 995–1003. doi: 10.1016/j.mri.2010.03.007

Winklhofer, K. F., and Haass, C. (2010). Mitochondrial dysfunction in Parkinson's disease. *Biochim. Biophys. Acta* 1802, 29–44. doi: 10.1016/j.bbadis.2009.08.013

Winston, G. P. (2012). The physical and biological basis of quantitative parameters derived from diffusion MRI. *Quant. Imaging Med. Surg.* 2:25465. doi: 10.3978/j.issn.2223-4292.2012.12.05

Wu, S. F., Zhu, Z. F., Kong, Y., Zhang, H. P., Zhou, G. Q., Jiang, Q. T., et al. (2014). Assessment of cerebral iron content in patients with Parkinson's disease by the susceptibility-weighted MRI. *Eur. Rev. Med. Pharmacol. Sci.* 18, 2605–2608.

Xiao, D., Cassin, J. J., Healy, B., Burdett, T. C., Chen, J.-F., Fredholm, B. B., et al. (2011). Deletion of adenosine A1 or A(2A) receptors reduces L-3,4-dihydroxyphenylalanine-induced dyskinesia in a model of Parkinson's disease. *Brain Res.* 7, 310–318. doi: 10.1016/j.brainres.2010.08.099

Xu, X., Wang, Q., Zhong, J., and Zhang, M. (2015). Iron deposition influences the measurement of water diffusion tensor in the human brain: a combined analysis of diffusion and iron-induced phase changes. *Neuroradiology* 57, 1169–1178. doi: 10.1007/s00234-015-1579-4

Yuan, H., Sarre, S., Ebinger, G., and Michotte, Y. (2005). Histological, behavioral and neurochemical evaluation of medial forebrain bundle and striatal 6-OHDA lesions as rat models of Parkinson's disease. *J. Neurosci. Meth.* 144, 35–45. doi: 10.1016/j.jneumeth.2004.10.004

Zhang, J., Stanton, D. M., Nguyen, X. V., Liu, M., Zhang, Z., Gash, D., et al. (2005). Intrapallidal lipopolysaccharide injection increases iron and ferritin levels in glia of the rat substantia nigra and induces locomotor deficits. *Neuroscience* 135, 829–838. doi: 10.1016/j.neuroscience.2005.06.049

Zhang, J., Zhang, Y., Wang, J., Cai, P., Luo, C., Qian, Z., et al. (2010). Characterizing iron deposition in Parkinson's disease using susceptibility-weighted imaging: an in vivo MR study. *Brain Res.* 1330, 124–130. doi: 10.1016/j.brainres.2010.03.036

Zhang, W., Sun, S. G., Jiang, Y. H., Qiao, X., Sun, X., and Wu, Y. (2009). Determination of brain iron content in patients with Parkinson's disease using magnetic susceptibility imaging. *Neurosci. Bull.* 25, 353–360. doi: 10.1007/s12264-009-0225-8

Zhurakovskaya, E., Leikas, J., Pirttimäki, T., Mon, F. C., Gynther, M., Aliev, R., et al. (2019). Sleep-state dependent alterations in brain functional connectivity under urethane anesthesia in a rat model of early-stage Parkinson's disease. *eNeuro* 6, 1–12. doi: 10.1523/ENEURO.0456-18.2019

Zimprich, A., Biskup, S., Leitner, P., Lichtner, P., Farrer, M., Lincoln, S., et al. (2004). Mutations in LRRK2 cause autosomal-dominant parkinsonism with pleomorphic pathology. *Neuron* 44, 601–607. doi: 10.1016/j.neuron.2004.11.005

Conflict of Interest: The author declares that the research was conducted in the absence of any commercial or financial relationships that could be construed as a potential conflict of interest.